Organic Semiconductor Design, Synthesis and Testing for Solar Energy Applications



Benjamin Willner

Balliol College

University of Oxford

Supervised by Professor Iain McCulloch

Submitted January 2024

This thesis is submitted to the Department of Organic Chemistry, University of Oxford, in partial fulfilment of the requirements for the degree of Doctor of Philosophy

Declaration

I declare that this thesis is my own work and describes my own research unless otherwise stated.

Benjamin Willner 2024

Contents

Page 5 **Chapter 1.** Introduction

Page 75 **Chapter 2.** Development and Investigation of Hydrophilic Processible Polymers of Intrinsic Microporosity for Photocatalytic Hydrogen Production

Page 137 **Chapter 3**. Further Exploration of Intrinsically Microporous Conjugated Polymer Chemistry

Page 179 **Chapter 4.** Small Molecule Electron Transport Materials for Perovskite Solar Cells

Page 210 **Chapter 5.** Thesis Conclusions

Page 213 **Chapter 6.** References

Page 222 **Chapter 7.** Supplementary Information

Abstract

Renewable electricity generation, and particularly renewable H_2 generation is essential to reach net-zero CO_2 global emissions. This thesis explores the use of organic semiconductors to achieve these ends. Direct photocatalytic utilisation of sunlight to produce H_2 from water is thought to be capable of providing the cheapest pathway to renewable H_2 generation in the long term. Heterogeneous catalysis is generally enhanced by large surface areas, however thus far, introduction of porosity in organic semiconductors for photocatalytic H_2 production has not reflected this. To better understand the influence of porosity and hydrophilicity, a family of conjugated intrinsically microporous polymers of varying porosities and hydrophilicities was synthesised. In Chapter 2, the variables of porosity and hydrophilicity were isolated by controlling the molecular design of the polymers. It was found that changing porosity and hydrophilicity independently when other factors are controlled leads to increases in activity. However, it is the *combination of both* properties that sees a synergistic benefit. It was shown through transient absorption spectroscopy (TAS), that two of the pure porous conjugated polymers are capable of almost instantaneous polaron generation in the absence of ascorbic acid, Pt, and less than 1 ppm residual Pd. Through investigating the wetting properties of the porous materials, this was attributed to differences in the accessibility of electrolyte to the porous structures. In Chapter 3, it was shown that by balancing bulky orthogonal tert-butyl spirofluorene flanking groups, it was possible to make solution processable porous conjugated polymers. Finally in Chapter 3, the excellent tunability of organic semiconductors was applied to the design and synthesis of electron transport layers (ETLs) for perovskite solar cells. Six small molecules with frontier molecular orbitals (FMOs) in an energy cascade were synthesised. From these, the ETLs with the deepest LUMOs gave the best performances in solar cells.

Acknowledgements

I would firstly like to thank Professor Iain McCulloch for his support and supervision he has provided me over the course of my MSci and DPhil in his group, and for the time I've spent in his research group. I would also like to thank Dr Catherine Aitchison for the amazing guidance she has given me during her time in the lab. Further to this, I would like to thank all of the excellent researchers I have had the privilege to work with and learn from, in particular fellow DPhil students Junfu, Flo, Sophie, Adam, Helen, Petruta, Matt, Max, Maryam, Luvian, Ellen, Guanru and Yu. I am also immensely grateful to the postdocs in the group who I have learnt so much from and were always willing to offer support. In particular Mark, James, Andy, Christina, Fabien, Wanpeng, Zeinab, Jin, Yunseul and Yuanbao, Weimin and Huchen. I am also grateful to my amazing friends I've made in Balliol and Oxford who have made my time here so much fun, as well as all my friends form Manchester and Imperial College. Lastly, I would like to thank my Mum, Dad, Eileen, Alice and Lottie for never getting me to stop asking 'why?'.

Contributions

- Energy dispersive X-ray Spectroscopy (EDX) measurements were undertaken by **Dr Catherine Aitchison**.
- Water sorption isotherms were measured by **Dr Wanpeng Lu.**
- Transient absorption spectroscopy (TAS) was performed by **Dr Filip Podjaski.**
- Contact angle measurements were conducted by **Dr Robert Jacobs.**
- Density functional theory (DFT) calculations were conducted with the assistance of **Junfu Tian**
- Characterisation of material performance in perovskite solar cells was conducted by **Saqlain Chowdry**

Chapter 1: Introduction

1.1 Context and Motivation

1.1.1. Fossil Fuels

It could be argued that economic value has its origin in the application of work, which requires a source of energy. Since the Agricultural Revolution, the wealth of civilisations was predominantly determined by their agricultural productivity: how readily the land could convert solar energy into a form accessible to its inhabitants. The primary source of labour was domesticated animal or human toil, powered by contemporary solar energy in the form of food crops. This changed in northwest Europe in the mid 18th century at the dawn of the Industrial Revolution, where the true potential of fossil fuels was first realised. Coal enabled the production of iron on a large scale using blast furnaces, and steam engines allowed coal's chemical energy to be converted into concentrated mechanical power, facilitating industrial processes on an unprecedented scale.[1] In 1949 M. K. Hubbert of Shell Oil Company referred to the discovery of vast coal deposits in the British Isles as an "emancipation from this dependence upon contemporary solar energy".[2] This dense ancient solar energy stored in fossil fuels allowed economic output to be largely decoupled from contemporary solar energy. With the utilisation of coal in the 19th century and later oil and natural gas in the 20th century, fossil fuels became integral to transportation, manufacturing, electricity generation and agriculture, and continue to be well into the 21st century.[1]

However, unlocking the energy stored in fossil fuels by combustion emits CO_2 and other deleterious side products. Since the start of the Industrial Revolution, global annual CO_2 emissions have grown year on year, reaching an all-time high of 36.8 Gigatons for 2022, which is likely to be surpassed in 2023.[3] It is now well understood that atmospheric CO_2 concentration has a strong effect on the global climate due to the greenhouse effect, and the continued combustion of fossil fuels to unlock their stored energy is causing catastrophic consequences for the environment and those who inhabit it.[4]

1.1.2. Renewable H_2 to Help Decarbonise the Global Economy

In order to mitigate the worst effects of climate change, there is consensus among governments around the world that the continued combustion of fossil fuels must be curbed. This sentiment was manifested in the 2015 Paris Agreement: a legally binding treaty where representatives of 196 nations agreed to the goal of "holding the increase in the global average temperature to well below 2.0 °C above pre-industrial levels and pursuing efforts to limit the temperature increase to 1.5 °C." [5] In line with this, the United Kingdom government has pledged to achieve net-zero CO_2 emissions by 2050.[6] Though worryingly in 2022 estimates put the current level of average warming at 1.2 °C, highlighting the urgency of the situation.[7]

Fossil fuels have provided around 80% of global energy supply for decades, but it appears the tide is turning, and this figure is expected to reduce this decade. Global investments in renewable energy surpassed fossil fuels for the first time in 2016.[8] Nonetheless, the prospect of net-zero is still distant. In order to achieve it, three broad measures must be taken. Firstly, the global electricity supply must be fully decarbonised by use of renewable energy and nuclear power. Secondly, all emissive activities which can be powered by renewable electricity must be. For example, this means using renewable electricity to heat buildings, and power transport through increased use of electric vehicles. Thirdly, sectors of the economy which cannot be powered by renewable electricity must find alternative non-emissive power sources or use carbon capture as a last resort. The use of H_2 will play a key role in realising these measures.[9,10]

Transition to intermittent renewable electricity sources in the form of solar photovoltaics and wind turbines requires some form of energy storage to regulate mismatches between supply and demand across different timescales. Medium term energy storage is currently overwhelmingly fulfilled by pumped hydro energy storage, where water is pumped uphill to refill reservoirs at times of excess electrical supply, enabling excess electricity to be stored at around 70-80% efficiency.[11,12] Underground compressed air energy storage is another reasonably efficient form of

energy storage. However, both of these technologies require suitable geographic sites which limits their spread.[12] Li-ion batteries also provide a means of storing excess electricity on a short term basis at efficiencies of up to 90%. However, its scalability is limited owing to the inflexible nature of the supply chains for the metals involved, and it is not suitable for long-term yearly energy storage.[9] On the other hand, renewable H_2 as a chemical store of energy can be stored in salt caverns almost indefinitely. When connected to fuel cells, stored H_2 can be converted to electricity at efficiencies of around 55%, or transported via pipelines in a similar manner to natural gas to be used for heating applications.[9] The Dutch government aims to complete a national H_2 transmission network by 2026, connecting major population centres to salt mine H_2 storage facilities, with 85 % of the pipelines using repurposed existing natural gas infrastructure.[13] Meanwhile, while more expensive to liquify and transport compared to natural gas, in 2022 Kawasaki Heavy Industries launched the world's first liquified H_2 tanker, opening up the potential of H_2 as an energy carrier to link areas of surplus energy supply to demand in the global market.[14] This *transportable* nature of chemical fuels is a key advantage over other methods of energy storage.

Renewable H_2 can also play a role in decarbonising sectors of the economy which cannot be electrified. This includes use of fuel cells in heavy vehicles, shipping and steel production, where it can be used as a heat source and reducing agent instead of coke coal which produces CO_2 as a side product.[13,15]

Finally, H_2 is also a crucial component in its own right as an input for the chemical industry, above all in the production of NH_3.[16] NH_3 is produced through the Haber-Bosch process (equation below), which alone accounts for 1.0 % of global energy consumption and 1.4% of CO_2 emissions.[17] Decarbonisation of this process is impossible without renewable H_2. NH_3 is crucial not just in the chemical industry, but also for the production of nitrogen-based fertilisers which consume 70% of global NH_3, and are estimated to sustain about half of global food production.[18]

$$3H_2 + N_2 \leftrightharpoons 2NH_3$$

In summary, while aspirations towards the H_2 economy where H_2 can directly replace the role fossil fuels play in the global economy may be overstated, renewable H_2 is an important tool in the arsenal of measures governments around the world must deploy in order to reach net-zero. Furthermore, H_2 is a vital input to many industrial processes, chiefly nitrogen-based fertiliser production, without which human life on Earth cannot be sustained at current levels. Therefore, renewable H_2 generation is one of the most important challenges faced by humanity this century.

1.2. H_2 Production Methods

1.2.1. Fossil Fuel Derived H_2 Production

Almost all current global H_2 production originates from fossil fuels.[13] In 2021 natural gas was the source of 61 % of H_2 production via steam CH_4 reformation coupled to the water gas shift reaction (equations below), 18 % came from crude oil reformation where heavy hydrocarbons are converted into shorter branched ones by partial dehydrogenation, and 19 % came from coal. Such processes come with heavy CO_2 emissions. [13]

$$\mathrm{CH_4 + H_2O \leftrightharpoons CO + 3H_2}$$

$$\mathrm{CO + H_2O \leftrightharpoons CO_2 + H_2}$$

In an effort to source H_2 from fossil fuels while mitigating emissions, these processes have been coupled to carbon capture and storage. Surprisingly when coupled to steam methane reformation, almost complete CO_2 capture can be achieved at only slight cost increase due to synergistic energy recovery from the reformation process. Another method of low-carbon H_2 production from fossil fuels is pyrolysis, where hydrocarbons are heated in the absence of O_2, producing only H_2 and C which can be easily stored.[13]

It could be argued that fossil fuel derived H_2 coupled to carbon capture and storage could act as a stopgap, fulfilling H_2 supply while nascent H_2 utilisation technologies are developed, and renewable technologies for H_2 production mature. However, it is also argued that is a diversion, allowing multinational companies to continue to profit from fossil fuel extraction.

An alternative renewable source of H_2 is from biomass. This entails growing high energy density crops such as sugarcane and extracting the H_2 therein through pyrolysis or gasification. While these processes emit CO_2, they are considered carbon neutral due to the initial photosynthetic intake of CO_2 in growing the biofuels. Biofuel gasification is expected to soon meet steam methane reformation in price.[19,20] Nonetheless, while biomass can play a role, it competes with valuable arable land for food production, and intensive monoculture agriculture is not without environmental impact, meaning it is less attractive as a H_2 source at large scale.[10]

1.2.2. Water Derived H_2 Production Using Heat

A practically limitless source of H_2 on Earth is water. However due to its stability, water requires a significant amount of energy to split into constituent O_2 and H_2, with a free energy change of +237 kJ mol^{-1} for the reaction (shown below), notwithstanding the overpotentials required.[21]

$$2H_2O \rightarrow 2H_2 + O_2$$

This energy can be supplied thermally in the thermolysis of water, which requires temperatures of 2500 °C. Since reaching temperatures this high generally requires a combustible fuel (defeating the point), thermochemical cycles have been used, employing homogeneous catalysts to enable thermal water splitting at temperatures as low as 550 °C.[22] Using mirror arrays to concentrate solar energy as a heat source would enable this method to produce renewable H_2.[23] However the high temperatures required puts a strain on the longevity of reactors and catalysts, as well as high

installation costs limiting the spread of this technology, through it continues to increase in efficiency and decrease in cost.[24,25]

1.2.3 Water Derived H_2 Production Using Solar Energy

Solar energy is by far the most abundant global energy resource, with 1.2 $x10^{17}$ J s^{-1} supplied to the Earth's surface.[26] In a year, this is greater than all the proven global reserves of fossil fuel energy combined, and dwarfs the energy extraction potential of other sources of renewable energy as shown in Figure 1. [27]

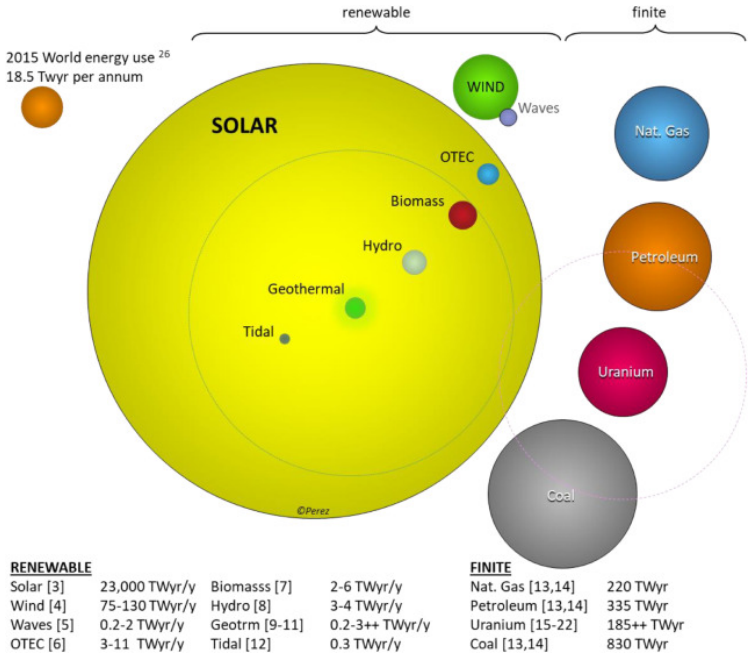

Figure 1. Relative annual energy potential for renewables and total recoverable reserves for non-renewables, represented by area. OTEC is ocean thermal energy conversion. Reproduced from reference under creative commons attribution 4.0 license.[27]

Exploitation of Earth's vast solar energy resources is therefore the most promising resource with which to drive renewable H_2 production. The methods of achieving this are classified as follows:

- *Indirect:* electricity generation by photovoltaics is coupled to water electrolysis.
- *Semi-direct:* photoelectrochemical sunlight assisted electrolysis.
- *Direct:* solar photocatalytic water splitting.

1.2.4. Indirect Solar Water Splitting: Photovoltaics Plus Electrolysis

Using the existing technologies of solar photovoltaic electricity production coupled to electrolysers, it is possible to renewably electrochemically split water and produce H_2 by applying a potential difference between two electrodes causing water oxidation at the anode and reduction at the cathode. In 2021 electrolysis accounted for a negligible 0.1% of global H_2 production. This low contribution is due to its significantly higher cost compared to hydrocarbon reformation, owing to high electricity and installation costs.[13]

Using a high performance triple junction solar cell coupled to polymer electrolyte membrane electrolysers in an integrated system, under laboratory conditions a solar to H_2 conversion efficiency of 30% was reported.[28] However in general, scale up from the cm^2 scale in laboratories to the m^2 scale in commercial industrial settings decreases efficiency considerably.[29] Most installed large-scale electrolyser capacity, and predicted future installations until 2030 are alkaline electrolysers,[13] whose efficiencies are at are up to 60%.[30] Meanwhile the best commercial silicon solar cells are around 20% efficient.[31]

While significant progress has been made in recent decades increasing the efficiency and decreasing the price of these separate processes, the level of additional capital cost to achieve further efficiencies may be considerable. For example, for photovoltaics, the Shockley-Queisser limit sets a theoretical ceiling to single bandgap photovoltaic solar conversion efficiency below 35 %, with existing single junction solar cells getting fairly close to this.[32] Further efficiency improvements require use of tandem solar cells with multiple bandgaps which increases device complexity, likely resulting in a large increase in cost for diminishing efficiency returns.

Owing to the separated nature of electricity generation and electrolysis, the concept of ‘power to gas’ has been proposed. This makes use of the variable cost of electricity, utilising excess renewable electricity at times of oversupply and using this cheap electricity to power electrolysis.[33] However the slow start-up times of current alkaline

electrolysers could be prohibitive for this purpose. Quicker start-up times are provided by polymer electrolyte electrolysers, though capital costs are significantly higher for this less mature electrolyser technology, and lifetimes are lower.[30] Also repeated start-ups and shut-downs of electrolysers can significantly accelerate permanent degradation, reducing electrolyser lifetimes.[30]

There are also inherent inefficiencies with coupled photovoltaics and electrolysis. This could originate in current and voltage mismatches between the generated photovoltaic electricity and the optimal current and voltage conditions for optimal electrolytic efficiency. Accommodating this mismatch requires additional circuit complexity.[28] Furthermore, there are losses incurred from electricity transition from resistance losses,[34] which would be expected to be more acute if the photovoltaic electricity is generated at a significant distance from the electrolysers.

Because of these efficiency limits on indirect solar H_2 production, there has been significant interest in simplifying the process by using solar power to *directly* split water, which is the focus of this thesis.

1.2.5. Semi-Direct Solar Water Splitting: Photoelectrocatalysis

By replacing the cathode or anode of an electrochemical system with a light harvesting semiconductor, it is possible to utilise solar energy to enable photo-assisted electrolysis. This was first reported in 1972 in the famous work by Fujishima and Honda,[35] which is considered to mark the beginning of light driven water splitting research.[36] Here a TiO_2 anode was connected to a Pt cathode in an electrochemical circuit. Irradiation of the TiO_2 anode at wavelengths shorter than 415 nm caused water oxidation on TiO_2 while Pt acted as the cathode to produce H_2, assisted by an electrical bias and a pH gradient.[35]

The overall driving force for water splitting is the combined photovoltage and applied voltage. If the photovoltage exceeds the thermodynamic potential plus overpotential needed to split water (around a minimum of 1.6 V), then this system can run without

any applied potential. In order to generate additional photovoltage, both anode and cathode can be replaced by light absorbing semiconductors, ideally of complimentary absorptions to maximise solar light harvesting.[37]

An advantage of a biased photoelectrochemical system, is that light absorbing semiconductors with unsuitable band potentials to drive water splitting in isolation (such as Fe_2O_3 and $BiVO_4$), can be 'kicked over the line' with the added applied potential. This also enhances favourable band bending and charge separation processes in the semiconductors.[38,39]

Another advantage of a photoelectrochemical system is the separation of H_2 and O_2 evolution sites, so long as protons can be transported between them. This produces pure H_2 without the need for gas separation. This is a particular safety advantage, given coproduction of H_2 and O_2 poses an explosion risk, with the lower explosion limit at 4.0 vol% H_2 in O_2, or 4.9 vol% O_2 in H_2.[40]

By integrating state of the art multiple junction solar cells into photoelectrochemical systems, solar to H_2 conversion efficiencies of 20.8 % have been reported, as depicted in Figure 2. This utilises the excellent light harvesting properties of perovskite and silicon solar cells in tandem, allowing a large enough potential difference to be generated to drive water splitting at the anode and cathode. In such a strategy it is imperative to protect the active layers from degradation caused by electrolyte and was achieved by a conductive barrier between the cell and O_2 evolution catalyst. However its performance did decrease over time, due to photovoltaic and catalyst degradation.[41]

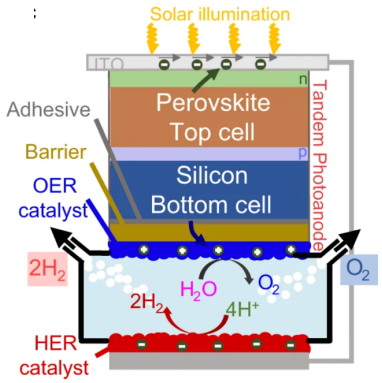

Figure 2. Scheme of high efficiency photoelectrochemical setup. OER is oxygen evolution reaction, HER is hydrogen evolution reaction. Reproduced from reference under creative commons attribution 4.0 license [41]

While able to achieve high solar to H_2 conversion efficiencies on a laboratory scale, photoelectrochemical multicomponent 'wired' systems involve significant reactor design complexity, involving costly materials and fabrication processes. This translates to high capital costs for installation and significant efficiency losses during scale up.[37,42]

1.2.6. Direct Water Splitting: Photocatalysis

The simplest solar water splitting system uses particulate photocatalysts where light absorption and catalysis take place on the same particle. This 'wireless' approach removes the need for long-distance charge transfer between light harvesting and reactive sites, significantly reducing reactor complexity. In fact, some proposed reactor designs are essentially poly(ethene) bags filled with aqueous suspensions of photocatalyst, christened 'baggies' in an influential report by the United States Department of Energy,[43] depicted below in Figure 3.

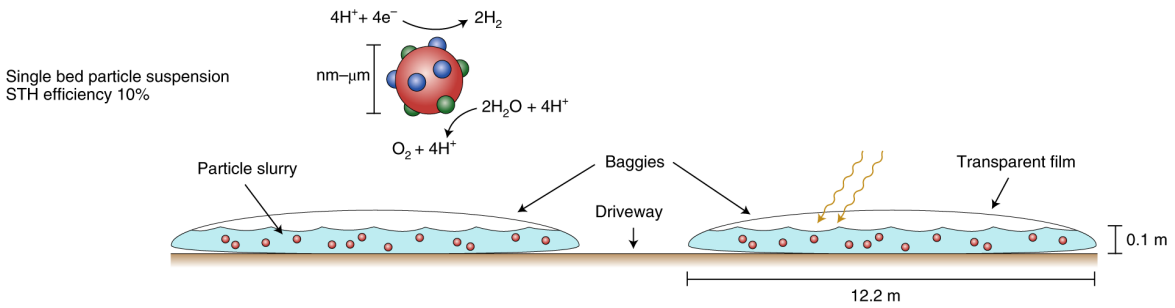

Figure 3. *Direct particulate photocatalysis 'baggies'. STH is solar to hydrogen conversion. Reproduced from reference under creative commons attribution 4.0 license.[44]*

Other reactor designs involve photocatalytic particles suspended in tilted transparent polymer panels,[45–48] which are further immobilised on removable plates[46–48] or membranes[49] to avoid particle sedimentation, removing the need for agitation or stirring to keep the particles suspended. By use of hydrophilic coatings photocatalytic particles were able to be kept wet, while allowing efficient transport of O_2 and H_2 bubbles upwards due to their buoyancy.[45] In the largest scale example of this system to date a 100 m^2 scale array of panels has been constructed in Japan, shown in Figure 4.

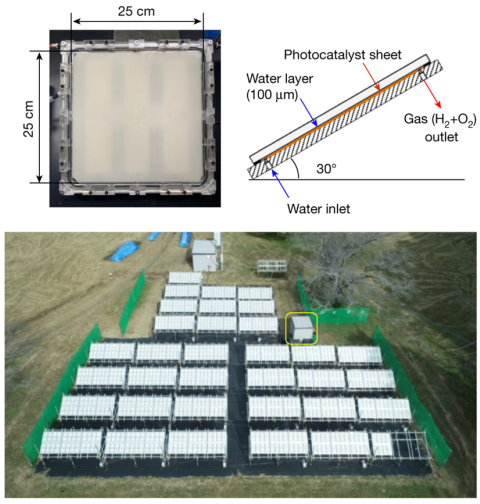

Figure 4. Large scale particulate photocatalysis panels. Reproduced with permission.[50]

Such systems involving coproduction of H_2 and O_2 avoid explosion risk by keeping O_2 and H_2 concentration below 4.0 vol % in the reactor.[51] This can be achieved by removal of the H_2 and O_2 immediately after generation, whereupon separation of the wet mixture can take place using pressure swing adsorption systems.[43] It is estimated that the energetic cost for gas separation is around 1.1 % the free energy of water splitting,[45] though it is also estimated that photocatalytic systems requiring gas separation must produce 11 % more H_2 than those which don't, due to H_2 losses involved in the separation process.[43] In the above example, gas separation was achieved by pumping the wet H_2 and O_2 mixture through membrane separators, utilising hollow polyimide fibres with a higher permittivity of H_2 with respect to O_2. While an important step in demonstrating the large scale feasibility and safety of photocatalytic H_2 production, the use of inorganic UV-active wide bandgap

semiconductor photocatalyst limited the overall solar to H_2 conversion efficiency of the system to 0.76 %.[50]

Nonetheless, the key advantage of such a system is its extremely scalable nature without significant loss in efficiency upon scale up.[45] This is because the components required for photocatalysis are self-contained on particles, and scaling up simply involves adding more particles. So long as they receive enough light, their efficiency is largely independent of scale. The approach of conducting the photocatalytic process on individual discrete particles, rather than large complicated systems can also increase the resilience of the system, as damage to one part of the photoreactor will not harm any circuitry, and have limited effect on the rest of the system.[45]

When installation cost, lifetime, gas handling and separation, and other associated costs were considered, the levelized cost of H_2 production for particulate direct photocatalytic systems was estimated to be \$1.60 kg^{-1}, assuming a solar to H_2 conversion efficiency of 10 %. This is in contrast to a fixed panel photoelectrochemical system costing \$10.40 kg^{-1} at the same efficiency. The cost for 15 % efficient tandem photoelectrochemical systems using tracking mirror concentrator arrays was put at \$4.10 kg^{-1}.[42,44] Nonetheless, the ability of particulate photocatalytic systems to outperform other solar H_2 production methods relies on meeting ambitious solar to H_2 efficiencies, in order to achieve the United States Department of Energy's target of \$2.00 to \$4.00 kg^{-1}.[42,44] This has led many to take 5 % to 10 % solar to H_2 efficiency as the benchmark at which particulate photocatalysis will begin to be economically competitive with current fossil fuel derived H_2 production methods.[44] Though it could be argued that the true social and environmental cost of fossil fuel H_2 production is not factored into its market price, and introduction of a carbon tax on fossil fuel production, or economic subsidies for renewable generation could dramatically change this economic assessment.

1.3. Solar Energy Conversion Requires Semiconductors

1.3.1. What is a Semiconductor?

In solids the electronic orbitals of adjacent atoms overlap. The linear combination of these atomic orbitals gives an equal number of stabilised (bonding) and destabilised (antibonding) molecular orbitals. As more atomic orbitals are combined in such a way, the spacing between energy levels decreases. For large systems, this creates a distribution of molecular orbitals whose difference in energy is so small that the electronic energy levels can be considered as a 'band', where the energy difference between electronic levels is much smaller than the thermally available energy, k_BT.[52–54]

Theoretically, for such a material at 0 K, the highest populated energy state (given each state can accommodate two spin paired electrons owing to the Pauli exclusion principle) is defined as the Fermi energy. However, at normal temperatures, electrons near the Fermi energy have sufficient thermal energy to migrate to higher energy levels. This gives a temperature dependent probability distribution $f(E)$ of the probability of a state with energy E being occupied. This probability is 'smeared' across an energy range of the order k_BT, going from a probability of 1 at lower energies, through a probability of half at the Fermi level, down to a probability of 0 on the other side. At ambient temperatures, it is more useful to consider the Fermi level as the energy at which $f(E) = 0.5$.[52–54]

This Fermi-Dirac distribution gives the probability of finding an electron as a function of energy, however it does not follow that there actually exists an electronic state at such an energy level. Depending on the structure and composition of a material, it will have a different density of available states which electrons may populate. Regions with a nonzero density of states are called bands and the conductivity of solids (whether they be metallic, semiconducting or insulating) is intrinsically tied to their 'band structure', as illustrated in Figure 5.

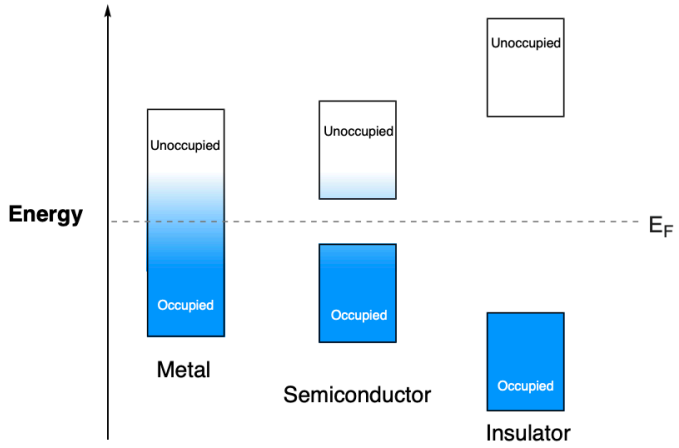

Figure 5. Band representation of metals, semiconductors and insulators

Metals are substances whose Fermi level exists within a partially filled band or where bands overlap. This makes net electron movement under an electric field easy, because there are partially filled electronic states accessible for valence electrons to move around in. Insulators on the other hand have their Fermi level lie between a filled valence band and an empty conduction band.[52–54] The energy gap between the highest energy electronic state in the valence band and the lowest energy electronic state in the conduction band is the bandgap, which for insulators is large (usually considered greater than 3 or 4 eV). Insulators cannot conduct electricity because there are no vacant sites in the electronic energy levels to allow movement of electrons.[54,55] Semiconductors also have their Fermi level within the bandgap, between valence and conduction bands, but crucially this bandgap is narrower than insulators, being generally smaller than 3 or 4 eV.[54,55] At 0 K all semiconductors are electronically insulating, however owing to the smaller bandgaps, at ambient temperatures it is possible for a very small population of electrons from the occupied valence band to become sufficiently thermally excited to transition to the valence band. This leaves behind vacancies in the valence band called holes. Because the excited electron and hole can move through their respective bands, it endows semiconductors with a degree of electrical conductivity. This conductivity increases with temperature as the number of electrons promoted to the valence band increases, increasing the population of charge carriers in both bands. [53,54]

The ability for semiconductors to allow electronic transitions from filled valence bands to empty conduction bands is the origin of their light harvesting properties. Interaction with light can promote an electron from the valence band to the conduction band. The photophysics of this process will be discussed in section 1.4.

1.3.2. Organic Semiconductors

Organic semiconductors can be described in a similar way. They can be understood by considering the series ethene, butadiene and poly(ethyne)shown in Figure 6. Such systems of contiguous π-bonds are said to be conjugated.

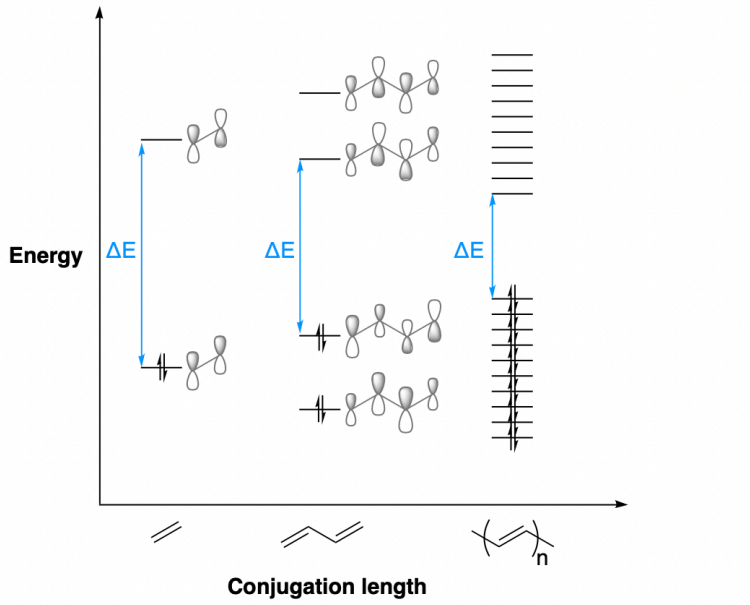

Figure 6. Molecular orbitals formed from p-orbital conjugation for ethene, butadiene and poly(ethyne), with their ground-state electron configurations and band gap ΔE shown.

Conjugated molecules contain adjacent p_z orbitals containing a single electron. Linear combination of these atomic orbitals leads to formation of an equal number of bonding and antibonding molecular orbitals (Figure 6). Bonding interactions are from where the orbitals are aligned in phase, and antibonding when they are out of phase. For ethene there are two possible ways of combining the adjacent p_z orbitals, for butadiene there are four, and for hexatriene there are six. The lowest energy combination of p_z orbitals is where all the orbitals are in phase. As more out of phase orbitals are combined,

creating more nodes, the molecular orbital becomes more antibonding in character and higher in energy.[56,57]

As the number of overlapping atomic orbitals increases, the energy gap between the molecular orbitals decreases, and the energy gap between the highest occupied molecular orbital (HOMO) and the lowest unoccupied molecular orbital (LUMO) also decreases. The HOMO and LUMO can be considered in an analogous way to the valence band maximum and the conduction band minimum.[58] The HOMO-LUMO energy gap is referred to as the bandgap of the organic semiconductor. This narrowing of the bandgap with the number of overlapping p_z orbitals does not continue indefinitely however, which would result in the polymer becoming a conductor. This is due to Peierls distortion, which has its origins in the atomic positions oscillating relative to each other, leaving some atoms further from their neighbour and others compressed together at any one time. This symmetry breaking stabilises the lattice, but simultaneously stops the band gap from closing as conjugation length increases.[58,59]

1.3.3. Organic Semiconductor Terminology

When discussing organic semiconductors, energies are considered relative to a 'local vacuum energy', defined as the electron at rest just outside the solid.[60,61] There are several useful energy parameters for discussing their properties. These include HOMO, LUMO, ionisation potential (E_{IP}), electron affinity (E_{EA}), Fermi level (E_F), fundamental bandgap (E_{fund}), and optical bandgap (E_{opt}). These terms with their definitions are displayed on Figure 7.

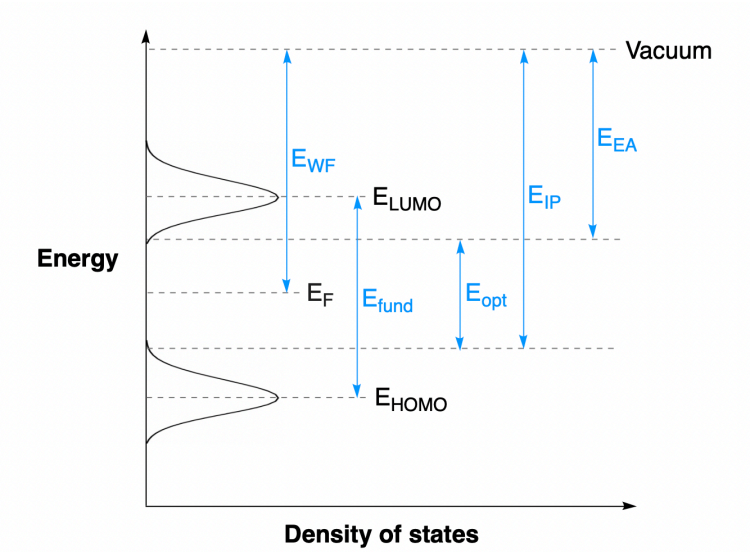

Figure 7. Schematic depiction of organic semiconductor terminology, considering an undoped semiconductor with LUMO and HOMO bands centred at E_{LUMO} and E_{HOMO}, respectively. The ionisation potential E_{IP} is the minimum energy required to remove an electron from the semiconductor to the vacuum level; the electron affinity E_{EA} is the gap between the LUMO and vacuum; The work function E_{WF} corresponds to the energy required to remove an electron from the Fermi level to vacuum. The Fermi level falls halfway between the HOMO and LUMO for undoped semiconductors in their ground state.[60] The gap between HOMO and LUMO is defined as the fundamental band gap (or transport gap). The optical bandgap corresponds to the smallest energy needed for a photoexcitation to take place, usually denoting transition from an S_0 to S_1 electronic state. The optical bandgap is smaller than the fundamental bandgap, with the difference being the binding energy between photoexcited electron in the LUMO and the hole left in the HOMO.[62] Adapted from references[61,63].

When discussing an isolated conjugated molecule, the HOMO and LUMO are easily understood as the frontier molecular orbital energies for that specific molecule. However, when dealing with a bulk organic semiconducting material involving an ensemble of conjugated polymer chains or small molecules, there exists a distribution of HOMO and LUMO energies present in the material, with intermolecular electronic coupling between them. Differences in orientation modify the local energies of their HOMO and LUMO, giving rise to a distribution of energetic states. Therefore, this distribution of HOMO and LUMO energies is treated equivalently to a density of states, as shown in Figure 7.[60,63]

Converting electrochemical potential to absolute energy relative to vacuum is usually taken as 0 V (SHE) = -4.44 eV, bearing in mind the added confusion that the signs of electrochemical potential and absolute energy run in opposite directions.[64] Though others have put this at -4.5 eV,[65] the former value will be used going forwards.

1.3.4. Energy Level Tuning in Organic Semiconductors

Trans-poly(ethyne) is the simplest conjugated polymer. However, its atoms can be substituted with a diverse range of conjugated units. This allows for a high degree of control over the HOMO and LUMO energies. The bandgap can be narrowed by increasing level of conjugation. This can be done by extending conjugation over more atoms, though this can only narrow the bandgap so far owing to the aforementioned reasons. Imposing planarising interactions on the polymer backbone to improve the overlap between adjacent p_z orbitals is another way to improve the conjugation, since deviations from planarity will impair orbital overlap and conjugation. The energies of the HOMO and LUMO energies can further be modified by inductive and resonance effects by the incorporation of electron withdrawing and donating heteroatoms to stabilise or destabilise the energy level in question. In addition, copolymerisation of electron rich and electron deficient monomers can bring about 'push-pull hybridisation', as depicted in Figure 8. This is where there is molecular orbital hybridisation between the two comonomers and the HOMO is predominately located on the electron rich unit, with the LUMO on the electron deficient one. This has the effect of narrowing the bandgap, allowing for excellent light harvesting in the visible region for organic semiconductors, as depicted in Figure 8.[63,66,67]

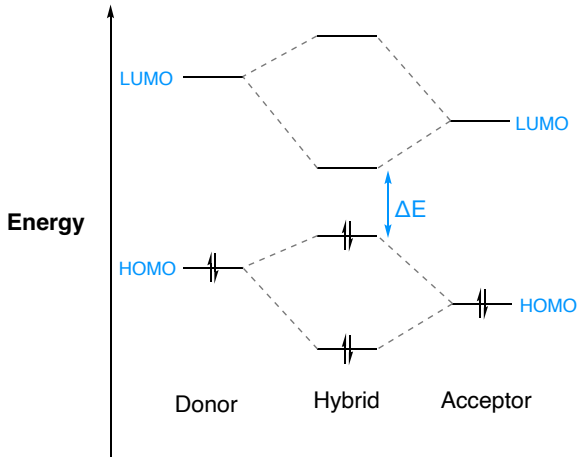

Figure 8. Push-pull or donor-acceptor hybridisation. Adapted from reference[66]

1.4. Principles of Photocatalysis

The scientific method is taught in terms of changing one variable at a time and measuring the effect, enabling the understanding of cause and effect. Science is difficult, and the study of photocatalysis in particular because this approach is rarely possible. The relationship of material properties to their photocatalytic activity depends on many variables which are interrelated; altering one variable changes another simultaneously making structure property elucidations difficult.[68]

1.4.1. Thermodynamics of Water Splitting

Nonetheless, it is clear that some parameters are important in determining photocatalytic activity, chief among them being the HOMO and LUMO energies. In photocatalysis, excited electrons can be considered as reducing agents, and holes can be considered oxidising agents. The reducing and oxidising electrochemical potentials of these species is related to the LUMO and HOMO energies in which they sit. Water splitting involves two coupled half-reactions: water oxidation and proton reduction. Their electrochemical potentials are given under standard conditions below, (these are pH dependent).[69]

$$2H^+ + 2e^- \rightleftharpoons H_2 \qquad E^{\ominus} = 0.00\ V$$

$$2H_2O + 4e^- + 4H^+ \rightleftharpoons O_2 \qquad E^{\ominus} = 1.23\ V$$

For electrolytic water splitting, the electrochemical potential for the cathode and anode must be more negative and more positive than the redox potentials for the reduction and oxidation reactions respectively.[65] For photocatalysis, this is analogous, whereby the energies of the excited electron in the HOMO and the hole in the LUMO must encompass the electrochemical potentials of the two half-reactions, with some extra driving force to provide sufficient overpotential to meet the activation energy for the processes.

The subsequent sections will describe the mechanisms of photocatalysis, assuming the semiconductor possesses suitable HOMO and LUMO energies.

1.4.2. Step 1: Light Absorption and Exciton Creation

Electrons inside molecular orbitals typically resonate at frequencies between 10^{15} and 10^{16} Hz as standing waves. Light can be thought of as orthogonal electric and magnetic waves propagating in step through space. When an electromagnetic wave form passes into the vicinity of a chromophore, its oscillating electrons are subjected to an oscillating electric field which exerts a force on the electrons (the magnetic field is negligible). When the frequency of the electric field matches that of electronic oscillations, it can excite an electron into a higher frequency oscillation, promoting it into an excited state. The wavelength equivalent of the frequencies needed to resonate with electrons in organic molecules are typically in the ultra-violet and visible range, 200-700 nm.[70]

Due to the requirement to conserve energy, the difference in energy between the two electronic states must equal the energy of the absorbed photon: $E_{ground} - E_{excited} = h\nu$. Transitions are generally between the (spin paired) singlet ground state S_0 to singlet excited states S_n, due to the necessity to conserve spin. Although, spin-orbit coupling due to the presence of heavy atoms can provide a mechanism for electrons to flip their spin and access triplet states: $S_0 \rightarrow T_n$.[70,71]

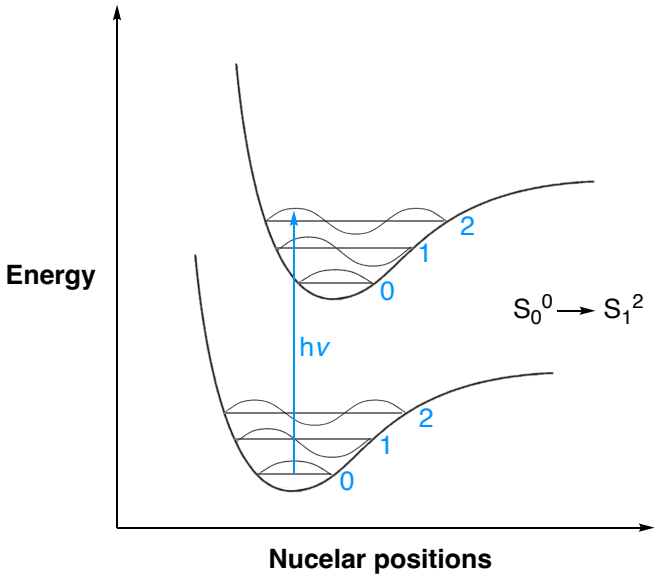

Figure 9. Potential energy surfaces with an electronic transition. Adapted from reference[71]

To understand what determines the probability of light absorption given it has an appropriate frequency, two principles must be applied. The Born-Oppenheimer approximation allows the molecular wavefunction to be separated into electronic and nuclear components, owing to the vastly more massive nature of the nuclei, which allows separate treatment of electrons and nuclei. The Franck-Condon principle takes this further to state that electronic transitions can be considered as instantaneous compared to nuclear motion. That is to say, the timescales of electronic transitions are so fast relative to nuclear vibrations, that on the timescale of photoexcitation, the nuclei don't have time to readjust their relative positions to accommodate the change in electronic distribution. This means nuclear positions are fixed during photoexcitation, allowing electronic transitions to be drawn as vertical arrows between potential energy surfaces, as shown in Figure 9. The probability of a transition depends on the overlap of the nuclear wavefunctions corresponding to vibrational energy levels on the ground and excited electronic states. This is the Franck-Condon factor. When transition from a ground state to an excited state, the rate of transition will depend on how much the excited state nuclear wavefunction looks like the ground one. This can mean an electron transitions from the ground potential energy surface to an excited one in a 'hot' vibrational state which subsequently relaxes to its equilibrium nuclear positions.[70,71] The probability of photon absorption also depends on how easily the electron can couple with the electric field coming from the light. Its change in

distribution caused by the oscillating electric field changes the distribution of charges in the chromophore, creating a transition dipole moment during the electronic transition. The larger the transition dipole moment, the greater the probability of absorption of the photon and electronic excitation.[70,71] This means if the transient dipole is spread over a greater distance, absorption can be stronger. Transition from the HOMO to the LUMO is the lowest energy transition, which is usually S_0 to S_1.[72,73] These frontier molecular orbitals (FMOs) are distributed across several atoms in organic semiconductors. A high degree of spatial overlap between HOMO and LUMO, will favour a high extinction coefficient due to these reasons, in addition to greater degrees of conjugation with long highly planar backbones and the presence of polarisable heteroatoms which are correlated to strong absorption. [70,74–76]

Photoexcitation populates the LUMO with an excited electron, leaving behind a concomitant hole in the HOMO. These oppositely charged species are considered as a Coulombically bound pair called an exciton, where their binding energy E_B is given below depending on electronic charge e, the permittivity of free space ε_0, the dielectric response of the medium ε_r, and the distance between the electron and hole r.[77]

$$E_B = \frac{e^2}{4\pi\varepsilon_0\varepsilon_r r}$$

The exciton binding energy is the energy required to separate the electron and hole. When the exciton binding energy is considerable, the energies of the electron and hole sit within the fundamental bandgap (the difference between HOMO and LUMO).The difference between the optical bandgap and the fundamental bandgap is equal to the exciton binding energy.[78–80]

The Achilles' heel of organic semiconductors could be considered to be their low dielectric response, typically $\varepsilon_r \approx 3$, compared to TiO_2 where $\varepsilon_r \approx 80$.[77] The exciton binding energy is inversely proportional to the dielectric response of the medium, as can be seen in the equation above. This means the excitons produced in organic semiconductors are tightly bound and termed Frenkel excitons, localised across a

small area of the lattice and requiring an energetic driving force to separate.[77,81–83] For organic semiconductors, typical exciton binding energies are 300 to 500 meV.[84] This is in contrast to inorganic semiconductors, whose higher dielectric responses more effectively shield electrons and holes, generating more loosely bound Wannier-Mott excitons spread across a larger area of lattice whose binding energies are generally less than 10 meV.[85] Given the thermal energy available at room temperature k_BT is about 28 meV, the exciton binding energy is thermally surmountable here, generating free polarons in inorganic semiconductors following photoexcitation, where the optical bandgap is much closer to the fundamental bandgap.[83]

1.4.3. Step 2: Exciton Transport to Dissociate (Energy Transfer)

This tightly bound nature of Frenkel excitons in organic semiconductors has serious implications for the photocatalytic process. Excited state lifetimes are typically much shorter than 1 ns, after which time the exciton decays either radiatively by emitting a photon or non-radiatively which converts the excitation energy to heat in a process termed internal conversion.[77] Given exciton dissociation requires an energetic driving force, it follows that the exciton must be able to access this driving force before it decays in order to be productive. This takes the form of an interface with something capable of accepting the electron, leaving the hole behind or vice versa.

Because there is no external electric field applied in organic semiconductor particulate photocatalysts and excitons are charge neutral, diffusion is the only mechanism available to get the exciton to an interface. Exciton diffusion length L_D is guided by a random walk and is defined as the root mean squared displacement of the exciton during its lifetime. It depends on the excited state lifetime of the exciton τ, its diffusion coefficient D in the medium, and the dimensional degrees of freedom available Z.[75,77,86]

$$\mathrm{L_D} = (2\mathrm{ZD}\tau)^{\frac{1}{2}}$$

Exciton diffusion lengths are typically around 10 nm in organic semiconductors.[77,87,88] The mechanism by which exciton diffusion takes place is a series of rapid energy transfer steps as well as slower thermally activated hopping. Here the excitation energy is transferred from donor to acceptor sites in the organic semiconductor. This can take place via Förster resonant energy transfer, which is a through-space interaction involving dipole-dipole interactions between the donor excited state and the acceptor state, enabling the excitation to be transferred from donor to acceptor. This can be intramolecular or intermolecular. More practically, its efficiency can be approximated by the spectral overlap of the donor emission and the acceptor absorption and has a distance dependence of $1/r^6$ between donor and acceptor sites. This makes it more suitable for relatively longer-range energy transfer, from 1 to 5 nm. Dexter energy transfer is another mechanism by which excitons can be transferred, whereby the excited electron in the donor LUMO transfers to the acceptor LUMO, at the same time as an electron from the acceptor HOMO transfers to the donor HOMO. The net effect is transfer of the excited state from donor to acceptor. However Dexter energy transfer requires distances of around 1 nm, so is a much shorter range energy transfer mechanism and is less significant than Förster resonant energy transfer for exciton diffusion.[86] The sequence of energy transfer 'hopping' steps results in a reduction in exciton energy. Organic semiconductors are generally disordered, with a distribution of HOMO-LUMO gaps, so absorption takes place across a wide energy range of states, but this downhill hopping means the excitons end up trapped in a reduced number of lower energy states.[75,77,86]

A greater degree of crystallinity is often beneficial for exciton transport, as it correlates with greater packing density and a narrower density of states.[89] This reduces the likelihood of excitons getting stuck in deep traps which cannot be escaped by thermally activated hopping. Otherwise incorporation of stiff planarised polymer backbones can also help achieve low energetic disorder and promote intramolecular transport along polymer backbones.[90,91]

1.4.4. Step 3: Exciton Dissociation

When an exciton diffuses through the semiconductor to the interface with electrolyte, it is possible for it to come into contact with redox species in solution which may reduce it, filling its vacant HOMO thus liberating the excited electron in the LUMO as an electron polaron.[92,93] A polaron is defined as a radical ion in conjunction with the molecular distortion accommodating its charge. Because of the changes in molecular configuration to accommodate the charge, the polaron sits within the HOMO-LUMO gap.[94] This reductive exciton quenching mechanism will be further discussed in the oxidation half-reaction section (1.5.2.).

Another method of exciton separation is through oxidative quenching, whereby the excited electron can be transferred to a metal cocatalyst on the surface of the semiconductor in electrolyte, liberating a hole polaron.[95] This mechanism of charge separation will be further discussed in the cocatalyst section (1.4.6.).

The third main method to separate excitons is interfacing the semiconductor with another semiconductor of offset energy levels shown in Figure 10. Such an interface between two semiconductors is called a type-II heterojunction, where the higher energy semiconductor is termed the donor and the lower energy the acceptor.

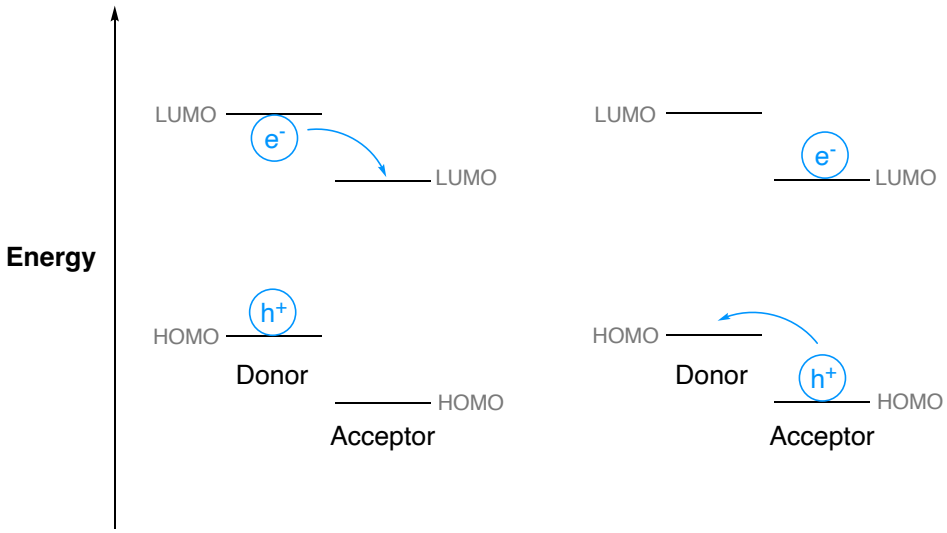

Figure 10. Type-II energetic offset between two semiconductors to promote charge separation

This interface drives exciton separation because transfer of the electron from the donor LUMO to acceptor LUMO lowers the chemical potential of the excited electron

in the exciton. Similarly, holes from excitons generated in the acceptor lowers their chemical potential by transferring to the donor. This happens via formation of a charge transfer exciton created immediately after the electron transfers across the interface into the acceptor. Here the excited electron and hole are still Coulombically bound but located on different semiconductors. Provided it does not recombine, it is then possible for the electron and hole to escape each other's attraction and form polarons in the respective acceptor and donor semiconductors. Charge transfer excitons are able to do this because they are formed in a vibrationally hot state owing to the lower energy of the donor. Subsequent relaxation spatially separates the species, attenuating their binding energy.[77]

The magnitude of energetic offset needed for effective exciton separation is generally taken to be around 0.3 eV or larger, which makes sense as this is of similar magnitude to the exciton binding energy.[78,96] Contrary to this, there have been several reports of high performing organic solar cells where exciton separation is achieved with much smaller energetic offsets.[97–99] However rigorous analysis of the energy levels of the donors and acceptors in question using different techniques has shown these materials to possess larger energetic offsets more in line with exciton binding energy,[100] though this remains an active area of debate in the field.

1.4.5. Step 4: Polaron Transport to Active Sites (Charge Transfer)

Once unbound polarons are generated in the semiconductor, they must be transferred to their catalytic sites to react. Again, there is no electric bias so diffusion is the only real form of transport, though polarons are longer lived than excitons, so their diffusion doesn't have a such a severe lifetime constraint.[101] Polaron diffusion involves a sequence of electron transfer steps as described by Marcus theory.[102,103]

In general, the structural features previously described for effective exciton transport are also applicable to polaron transport, such as coplanar conjugated units with low dihedral angles, where overlap of p_z orbitals is maximised enabling efficient movement of polarons along the π-conjugated region. This encompasses intramolecular polaron

transport and is facilitated by good conjugation along polymer backbones, which reduces the energetic disorder, decreasing the probability of charge carriers getting stuck in deep trap states.[63,104] This can be achieved by covalent bringing units to tie together conjugated units, favourable non-covalent interactions along the backbones, or increasing the rigidity of the bonds by enhancing their quinoidal character.[104–107] It should also be noted that regions of intermolecular π–π interaction are required to allow hopping between conjugated units and enable longer range transport.[57,107]

1.4.6. Step 5: Catalysis

Photophysics is fast and electrocatalysis is relatively slow, given excited state lifetimes are ps to μs, while catalytic processes take place on μs to ms timescales.[70,83,92] Coupling photophysics to electrocatalysis and accommodating their mismatched timescales is essential in understanding photocatalysis.[83] Cocatalysts can play a role in facilitating this.

The final step of photocatalysis is the participation of excitons or polarons in redox reactions with water. Given that these reactive species possess sufficient electrochemical potentials to react, it is imperative they can also surmount the reactions' kinetic barriers. This requires the presence of surface sites able to accumulate charges for the multielectron reactions, as well as lowering the relevant activation energies.[95,108] To this end, use of transition metal cocatalysts is ubiquitous.

In the context of proton reduction, this is mostly performed by Pt nanoparticles intentionally loaded on to the surface of the semiconductor.[109] Pt possesses a deep Fermi energy of 5.6 eV,[110] which is lower in energy than that of typical semiconductors used for photocatalysis. Photogenerated electron polarons can minimise their chemical potential by migration from the semiconductor LUMO to the Pt cocatalyst, which acts as an electron sink accumulating charges. Electron accumulation makes the electrochemical potential of the Pt clusters more negative.[85] Once this is sufficiently negative relative to the electrochemical potential for proton reduction and the overpotential is satisfied, the electrons in the metal can successfully reduce

protons to produce H_2.[85,111] To achieve a steady state of photocatalysis, the potential of the cocatalyst has to be maintained by a constant flow of electrons being fed into it to counteract those leaving it, and continually hold the cocatalyst at a sufficient potential to drive the reduction reaction.[108]

In some systems it is also possible for transition metal clusters to play a role in oxidative exciton quenching by accepting electrons.[95] However the metal nanoclusters can also act as recombination centres where both electron and hole can be accepted and recombine.[112,113] This is particularly the case for single component semiconductor systems when the distribution of metal is fairly uniform. However, an advantage of type-II heterojunction systems is that the photodeposition of Pt can take place preferentially on the reductive sites on the acceptor semiconductor. This limits the ability of photodeposited Pt to act as a recombination centre when it is selectively placed on domains where the concentration of holes is far lower.[114]

In addition to its ability to accumulate charges, Pt is also one of the best known electrocatalysts, expressed in terms of its intrinsic ability to evolve the most H_2 per second with a minimum overpotential.[115] The explanation for this can be understood through a 'volcano curve' (Figure 11), which shows the exchange current density for different metals as a function of their metal-hydrogen (M-H) bond strengths. In acidic conditions, the mechanism for H_2 evolution involves two main steps: adsorption and reduction of protons, followed by their desorption as H_2 molecules as shown in the equations below.[116] When the M-H bond strength is too high on the right slope of the volcano, desorption is disfavoured; when it is too low on the left slope of the volcano, adsorption is disfavoured. It so happens that Pt's bond strength achieves an almost optimal balance of the two.[117,118]

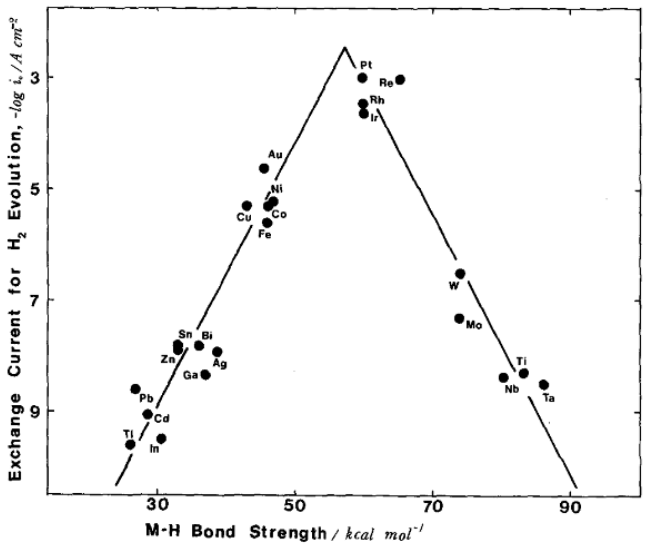

$$H^+ + e^- \rightarrow H_{ad}$$

$$2H_{ad} \rightarrow H_2$$

$$H^+ + H_{ad} + e^- \rightarrow H_2$$

Figure 11. :Left: Volcano plot of rate of H_2 evolution reaction as a function of M-H bond strength. Reproduced with permission.[117]Right: mechanism for proton reduction catalysis.

Organic semiconductors have been reported to be photocatalytically active in the absence of added Pt,[119–122] with computational modelling used to support this. [122–124] However, it has since been highlighted that their transition metal catalysed synthesis leaves behind significant levels of residual metal.[120,121,125] Although it has been reported that the activity does not correlate to amount of residual metal,[120,121] it was found that very low levels (less than 40 ppm) are needed to effectively catalyse H_2 evolution for conjugated polymers, and beyond a given point additional metal does not further increase activity.[126] While it could be possible that organic photocatalysts can function without cocatalysts, as is the case for carbon nitrides (albeit at low levels),[127] it is clear that in general, naked organic semiconductors are very poor photocatalysts without additional cocatalysts.[123]

This presents a challenge for scalability and cost, given that the best organic semiconductors generally require precious metals for their synthesis and function. There has been significant effort to develop molecular catalysts from earth abundant elements to solve this problem, taking inspiration from biological enzymes such has hydrogenase.[128] Among the most active of these under aqueous conditions are nickel du Bois type catalysts, which feature phosphonic acid groups on their outer sphere to make them water soluble.[129] In conjunction with photosensitisers, such molecular

catalysts exhibit relatively high turnover frequencies, However they are quite unstable, degrading in a matter of hours.[129–131] Therefore, despite recent progress, significant stability improvements are required for molecular catalysts to act as a viable alternative to transition metal nanoclusters.

1.5. The Challenge of Water Oxidation and the Use of Sacrificial Reagents

1.5.1 Water Oxidation

Water oxidation is a sluggish 4 proton coupled electron transfer process and is usually the rate-limiting step for water splitting photocatalysis.[132–134] It is unfortunate that the valuable H_2 component of water is produced through a relatively kinetically unchallenging reduction half-reaction, but renewable H_2 production from water is necessarily coupled to an extremely challenging oxidation half-reaction which hampers the whole process, while producing O_2 which is of negligible commercial value.[135] Indeed, the presence of O_2 can be detrimental to proton reduction catalysts,[135] and also enables the competitive reverse water splitting reaction to take place, as well as O_2 reduction to $O_2^{\bullet-}$ and H_2O_2 formation reactions to occur, which all can compete with H_2 evolution.[92,136]

Because of these challenges, if overall water splitting were attempted for every new photocatalyst developed, every measurement would probably yield no H_2 due to the challenging nature of attempting both half-reactions simultaneously. This would make structure property relationships difficult to elucidate. To enable photocatalytic processes to be studied and new photocatalytic systems be developed, sacrificial electron or hole donors are frequently employed which allow each half-reaction to be decoupled in order to gain mechanistic insight.[92,108] For the study of H_2 evolution photocatalysts, sacrificial electron donors are used for this purpose: chiefly triethylamine or ascorbic acid (also called hole scavengers). They are said to be

sacrificial because they are high value starting materials which are easily oxidised in stochiometric quantities to form lower value oxidation products.[137]

Water splitting has a free energy change of +237 kJ mol^{-1}.[21] When the oxidation of water is substituted for oxidation of triethylamine or ascorbic acid oxidation, the overall enthalpy change is significantly less energetical demanding, owing to the less positive electrochemical potentials needed to oxidise them.[134,137]

1.5.2 Ascorbic Acid Oxidation

Ascorbic acid (vitamin C) is known as an antioxidant because of its ability to readily donate electrons (and be preferentially oxidised).[138] As shown in Figure 12, when in aqueous solution, ascorbic acid with a first *pKa* of 4.0 to 4.20[138–141] deprotonates to form its conjugate ascorbate anionic base. After this, there are several possible oxidation pathways proposed in literature, but it is generally supposed that the ascorbate anion species loses an electron and deprotonates to form an ascorbate radical anion. This is then is able to lose a second electron and form dehydroascorbic acid.[137,138,141]

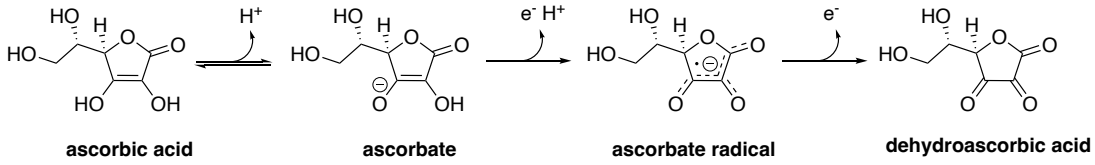

Figure 12. Ascorbic acid oxidation. Adapted from references[137,138,141]

For the purpose of ascorbic acid's use as a sacrificial electron donor to react with semiconductor bound holes, the electrochemical potential for the two electron oxidation has been calculated to be 0.25 V (SHE) at pH 2.60, which is the pH of a 0.1 M solution of ascorbic acid.[142] When converted to an absolute energy scale where 0 V (SHE) = – 4.44 eV (vs vacuum),[64,143] this puts sacrificial electron donation at about -4.69 eV for ascorbic acid, meaning semiconductors whose HOMOs are deeper than this would be expected to be able to undergo sacrificial electron donation from ascorbic acid. By contrast, using 1.23 V (SHE) as the electrochemical potential for

water oxidation and adjusting to pH 2.60 gives a potential of 1.07 V, which after converting relative to vacuum gives -5.51 eV for water oxidation. Clearly ascorbic acid is both thermodynamically and kinetically better able to act as reducing agent compared to water.

In an effort to circumvent the problems associated with water oxidation and take a step away from sacrificial reagents, some researchers have instead targeted different oxidation half-reactions with which to couple water reduction, such as cellulose degradation[144] or various oxidation reactions where the product is of greater commercial value than the starting material.[135,145,146] While the H_2 production rates are predictably far lower than those achieved using sacrificial reagents, this strategy provides a realistic renewable alternative to water splitting for some processes. However, it should be noted there is probably no value-added oxidation candidate for chemical valorisation which can match the scale of demand for H_2, leaving water as the only real candidate for a truly scalable H_2 source.

1.6. Z-Schemes: Managing Absorption and Driving Force

Although the potential difference required to theoretically split water is 1.23 V, due to the overpotentials required and charge separation losses, the potential required is generally greater than 2 V.[51,147,148] Consequently, photocatalyst design faces two opposing constraints: semiconductors require wide band gaps to possess band positions with sufficient overpotential to drive both reduction oxidation half-reactions, but at the same time they must tune their bandgaps to maximise their solar light absorption, which favours narrower bandgaps.

Z-schemes are a way of accommodating these opposing factors. They combine an O_2 evolution photocatalyst (OEP) and a H_2 evolution photocatalyst (HEP) shown in Figure 13. The HEP has a narrow enough bandgap to harvest a large amount of solar light with a LUMO high energy enough to reduce protons, but its HOMO is not deep enough

to provide sufficient driving force to drive water oxidation. This HEP would work with a sacrificial electron donor which is easier to oxidise than water, but instead Z-schemes employ the excited electron on the LUMO of an OEP to reduce the hole on the HEP. This leaves the hole on the HOMO of the OEP deep enough in energy to enable water oxidation. Such a system uses two photoexcitations in two separate semiconductors per excited electron, owing to intentional recombination in the middle. Ideally the bandgaps of the OEP and HEP should be different, allowing complementary solar light absorption.[149]

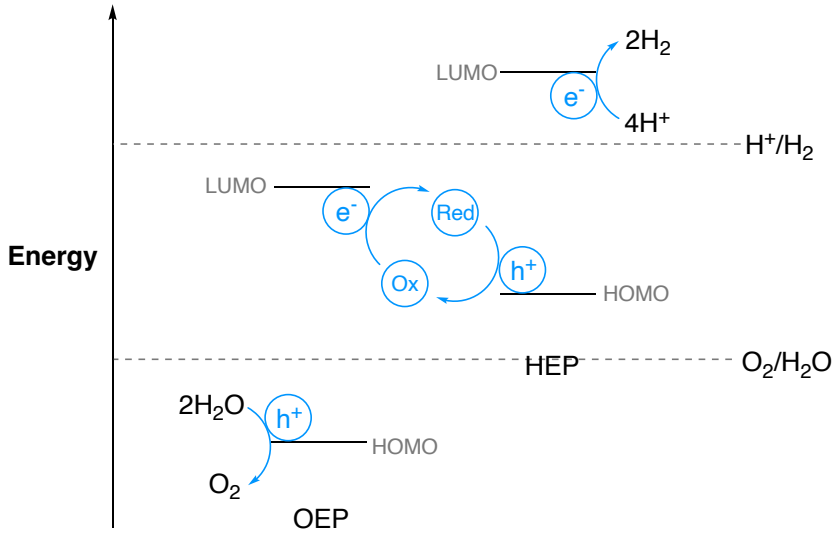

Figure 13. Z-scheme with O_2 evolution photocatalyst (OEP) linked to a H_2 evolution photocatalyst (HEP) via a redox mediator

Biological systems have successfully made use of Z-schemes since the evolution of oxygenic photosynthesis in plants about 2.4 billion years ago.[150] Biological photosynthesis in chlorophyll uses a Z-scheme to drive water oxidation in the first light harvester, photosystem II, while reducing nicotinamide adenine dinucleotide phosphate to store energy for the organism in the second light harvester, photosystem I.[149] Biological Z-schemes enable remarkable quantum efficiencies of above 95%.[151] They do this by a rapid primary electron transfer step from an excited state in photosystem II, which subsequently follows a cascade of short-distance secondary electron transfer steps to bring it in the vicinity of the hole on photosystem I and reduce it, enabling the excited electron in photosystem I to partake in reductive half-reactions.

However, this impressive quantum efficiency comes at the cost of energy efficiency. In order to generate prolonged separated charges to drive the redox processes, many energetically downhill electron transfer steps are incorporated. This comes at an energetic cost, spending about half of the excitation energy to do so.[77,83]

Artificial Z-schemes are challenging to build because they require selective electronic interactions between the two semiconductors. Due to their increased complexity in comparison to single semiconductor photocatalysts, additional backward reaction pathways must be hindered. For example the excited electrons on the HEP must reduce protons, and not holes on the OEP which would cause a short-circuit.[69] Electron transfer between the semiconductors is most commonly achieved by a redox mediator in solution, which can be reversibly reduced by the OEP, enabling it to reduce holes on the HEP and repeat the cycle. Examples include I^-/I_3,[152] IO_3^-/I^- [153–155] and complexes of $Fe^{3+/}Fe^{+2}$,[156] $Mn^{3+/}Mn^{2+}$ [157] and $Co^{3+/}Co^{2+}$,[158] owing to their ability to shuttle between oxidation states. Nonetheless, the intense colours of many of these redox shuttles can cause undesirable competitive light absorption.[149]

There are some redox mediators which can enable selective electron transfer. For example, using the IO_3^-/I^- redox couple in conjunction with WO_3 as an OEP, it has been shown that IO_3^- adsorption is favoured over I^-, which enables selective reduction of IO_3^- by WO_3 excited electrons.[155] A similar selective ability for Fe^{3+} over Fe^{2+} to adsorb on rutile TiO_2 has also been reported.[159,160] Other ways to incorporate selectivity to the redox processes are by selectively depositing gold nanoparticles onto $BiVO_4$ as an OEP, which acts to favour $[Fe(CN)_6]^{3-}$ reduction by the $BiVO_4$.[156]

Z-schemes have also been constructed without the use of redox mediators in solution, such as by fused contact between the semiconductors. Some approaches have connected the OPE and HEP via sheets of conductive carbon,[161] reduced graphene oxide[162] or gold (Figure 14).[163] In these cases, their success seems to rely on the relatively small contact area of the conductive sheet with the semiconductor particles, while they are surrounded by water and decorated with cocatalysts to more rapidly drive water oxidation or proton reduction. For example, the proton reduction reaction

on the HEP must be quicker than the electron flow into the conductive sheet, leading to the reduction of holes on the OEP. Because the particles are surrounded by water and covered in cocatalyst, the rate of the redox half-reactions is quicker than undesired recombination.[162]

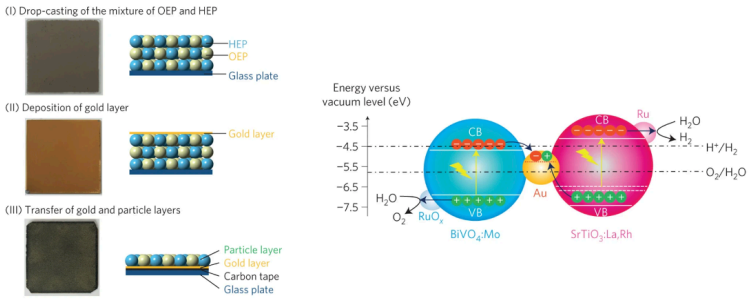

Figure 14. Fused contact Z-scheme using a Au sheet. Reproduced with permission[163]

1.7. The Chemistry of Photocatalysts

1.7.1 Inorganic Photocatalysts

Inorganic semiconductors have some distinct advantages over their organic counterparts. Firstly, due to their high dielectric responses, photoexcitation leads to loosely bound Wannier-Mott type excitons which readily dissociate at room temperature, enabling effective charge separation.[83,101] Secondly, transport of the separated electron and hole charge carriers is generally better than with organics, owing to their band-like charge transport properties and Coulombic shielding offered by their high dielectric responses hindering recombination.[101] Thirdly, inorganic semiconductors more readily undergo band bending, owing to their higher concentration of charge carriers and higher dielectric responses.[101] This is a process whereby a semiconductor is interfaced against another material or electrolyte of a dissimilar Fermi level, and the two Fermi levels equilibrate. This is achieved by net flow of electrons from the higher energy Fermi level material to the lower, creating a depletion layer where the conduction and valence band energies bend in response to the electric field generated by the net movement of charge.[164,165] Depending on the

direction of band bending, the electric field causes selective transport of electrons or holes, and can be beneficial when brought about by the interface with cocatalysts, or in systems where oxidation and reduction surface reactions happen on different semiconductors.[101,166] By contrast, organic semiconductors are considered to have largely 'flat bands'.[101]

These features were elegantly exploited for an $SrTiO_3$:Al photocatalyst shown in Figure 15. It was synthesised into crystals whose dimensions were in the hundreds of nm. It was irradiated in the presence of $RhCl_3$, followed by addition of K_2CrO_4 then $Co(NO_3)_2$. The purpose of this sequential photodeposition process was to selectively coat the {100} crystal facets with a Rh core surrounded by hydrated Cr_2O_3 shell cocatalyst. Given that the Rh cocatalyst catalyses both proton reduction and the reverse O_2 reduction reaction, the role of the hydrated Cr_2O_3 protective shell was to block access of O_2 but allow H_2 to escape, halting the competitive reverse reaction. The water oxidation Co cocatalyst was selectively deposited on the {110} facet. This selective photodeposition onto separate facets was enabled by the small difference in work functions between the different crystal facets. This caused anisotropic electron flow. Through careful elimination of recombination pathways, this photocatalysts achieved a remarkable external quantum efficiency of above 95% at 350 nm.

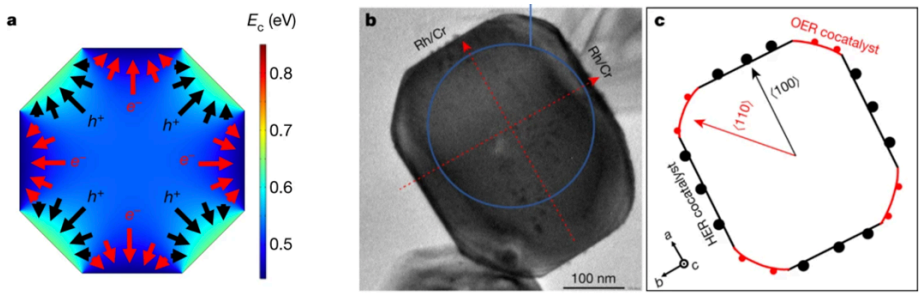

Figure 15. *$SrTiO_3$:Al photocatalyst with over 95% external quantum yield. Reproduced with permission.*[167]

Nonetheless, this impressive efficiency dropped off significantly under visible light, highlighting the key weakness of inorganic semiconductor photocatalysts: in general they harvest lower energy solar photons poorly. About 5% of solar radiation is UV light,

in the range 286-380 nm, while visible light encompasses 45% between 380-780 nm.[168] This means that the wider the bandgap of a photocatalysts, the more efficient it has to be to produce the same amount of H_2 as a photocatalyst with a narrower bandgap, owing to the distribution of solar light.[169] Inorganic semiconductors often have very wide bandgaps, or have indirect bandgaps such as in the case for silicon, which gives it a low extinction coefficient in the visible region.[136,170]

Some narrower bandgap semiconductors such as CdS have been employed as photocatalysts in order to increase solar light harvesting. However its toxicity and photocorrosion, where the S^{2-} anions are oxidised by photogenerated holes has proved an obstacle.[171,172] Other more stable inorganic semiconductors have very deep bands, which enable water oxidation but preclude proton reduction, for example WO_3 or $BiVO_4$ and Fe_2O_3. These have instead found use as components in Z-schemes.[173]

One method to push absorption into the visible range is by elemental substitution. Metal oxides are generally stable but possess very deep conduction bands, producing wide band gaps unable to absorb visible photons.[69] Given the major contribution to their valence bands are O *2p* orbitals, partial substitution of O with N to produce oxynitrides which has a higher energy *2p* orbital has been shown to raise the valence band, enabling visible light driven overall water splitting. Due to the differing oxidation state of N, its substitution must be balanced by introduction of a compensating cation. For example when used to dope ZnO, it was introduced GaN in to produce GaN:ZnO. While allowing for absorption up to 500 nm, it also increased the defect density leading to a low external quantum efficiency of 0.14% at 490 nm.[174] Similarly, introduction of transition metal dopants introduces energetic states from their d-orbitals at positions within the bandgap enabling visible light absorption. However this often comes at the expense of creating recombination centres.[69]

One of the most successful inorganic systems developed utilises Mg doped $In_xGa_{1-x}N$ in a ‘nanowire’ morphology grown off silicon substrates.[175,176] When the ratio of In is varied down the length of the nanowire in the axial direction, it produces different

regions with varying band gaps, enabling absorption up to 600 nm. Meanwhile it was doped by Mg in a gradient laterally, with two sides of the nano wire with differing amount of Mg. This doping gradient causes a built-in electric field, enabling anisotropic charge transport, where electrons migrate to the Mg deficient side, and holes to the Mg rich side. After selectively photodepositing the previously described Rh/ hydrated Cr_2O_3 core shell proton reduction and Co water oxidation cocatalysts cocatalyst owing to the directional charge transport, a solar to H_2 conversion efficiency of 5.2 % was reported, shown in Figure 16.[177]

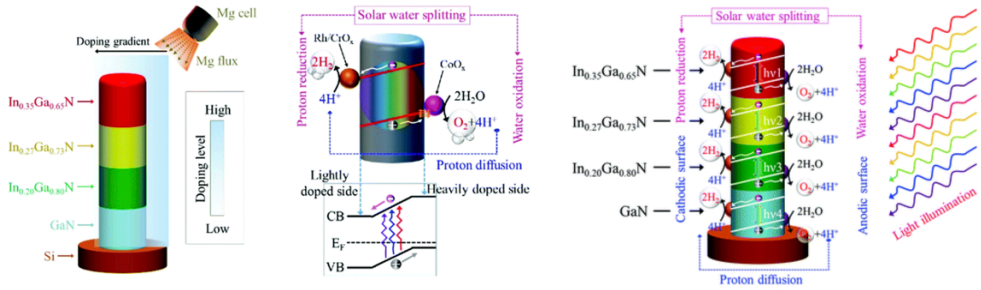

Figure 16. Mg doped $In_xGa_{1-x}N$ nanowires. Reproduced with permission.[177]

In a follow up study, it was found that by utilising the infra-red component of sunlight to heat the photoreactor cell up to an optimal temperature of 70 °C could boost the efficiency to 9.2 %, owing to the beneficial effects of elevated temperature on mass transport and favouring the kinetics of H_2 and O_2 evolution over their reverse reaction on the Rh cocatalyst.[178] The morphology of these finely constructed and precisely doped nanowires requires the use of molecular beam epitaxial growth, which is expensive to operate and scale up.[179] Nonetheless, this state of the art example of record H_2 production from water using sunlight highlights the potential of photocatalysis when the each of the productive steps of the process are maximised, while working to hinder steps which retard the process such as charge carrier recombination and reverse water splitting reactions.

1.7.2. Carbon Nitride Photocatalysts

Carbon nitrides are a nitrogen-rich organic material comprised of sp^2 hybridised C and N atoms in an approximately 3:4 ratio, often with a significant amount of H. It exists in various allotropes, generally arranged in 1,3,5-triazine or heptazine units linked together by imide bridges (Figure 17). The degree of polycondensation and crystallinity varies significantly depending on the starting materials and synthesis conditions.[101,180,181]

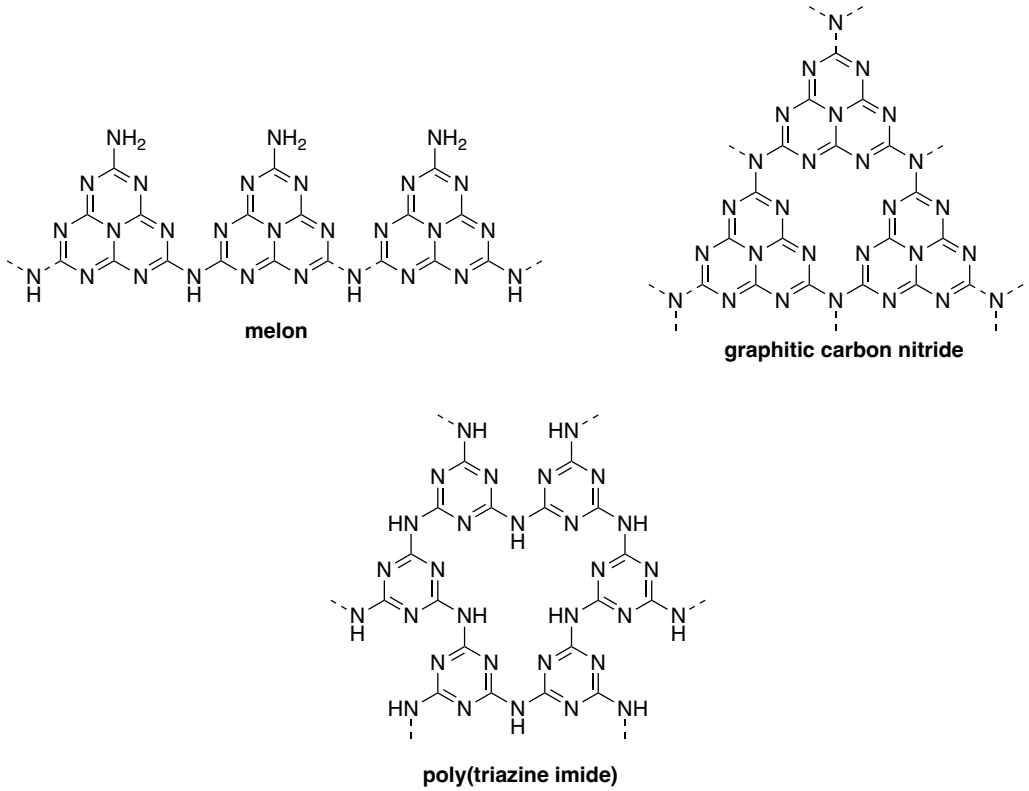

Figure 17. Carbon nitride structures. Adapted from reference.[181]

When synthesised using high temperature solid state synthesis conditions (with no solvent), the lower degree of condensation material melon is predominantly formed (Figure 17 top left).[101] This is a linear polymer of heptazine with pendant amines forming hydrogen-bonds with adjacent polymers to generate a two-dimensional carbon nitride.[182] Such melon type carbon nitride synthesised via the condensation of cyanamide were first reported to be able to act as a photocatalyst for separate H_2 and O_2 evolution from water in the presence of suitable sacrificial electron donors and cocatalysts in 2009.[127] This example of inexpensive non-metal earth abundant

elements simply heated to produce working photocatalysts provoked a great amount of interest in non-metal semiconductors as photocatalyst for H_2 production.[183]

Use of ionothermal (molten salt) solvent synthetic conditions have since been able to achieve greater degrees of polycondensation and crystallinity, enabling formation of graphitic carbon nitride, composed of sheets of heptazine or triazine units stacked via π-π and van der Waals interactions in a three-dimensional structure.[184,185] Their enhanced crystallinity and shorter stacking distances are favourable for polaron transport, based on hopping between the π-π stacked units.[101,186,187]

While synthesis of carbon nitrides is simple, it often leads to ill-defined defect rich structures.[188] This can create a high density of deep trap states (energetic states within the bandgap). Photogenerated electrons can fall into deep trap states, rendering a significant population of electrons unreactive for proton reduction due to the loss of driving force.[189,190] However the nature of the defects is crucial in helping or hindering performance.[101] For example, the inhomogeneous nature of the carbon nitrides has been claimed to be potentially beneficial for charge separation in some cases, through the presence of 'homojunctions', where crystalline and amorphous regions of carbon nitride have a slight type-II energetic offset, facilitating exciton dissociation.[191,192] It seems the presence of some structural inhomogeneity is beneficial for charge separation, but when this leads to the presence of deep traps it can also be detrimental.

A limitation of carbon nitrides is their relatively wide bandgap, absorbing wavelengths generally below 460 nm.[193] Increasing the extent of polycondensation to increase conjugation by reaction at higher temperatures has been shown to push the absorption more into the visible range, enhancing solar light harvesting capabilities and also reducing defects.[189,194,195] However, greater degrees of polycondensation can come at the expense of reducing surface area, as the gaps in the structure get progressively filled in, preventing ingress of electrolyte[196] Extending absorption to longer wavelengths has also been achieved by elemental substitution of atoms in the carbon nitride structure (often referred to as doping).[197–199] However this creation of

electronic states to narrow the bandgap can have the penalty of creating recombination sites.[200]

Despite these limitations, through optimisation of the molten salt composition, a carbon nitride triazine-heptazine copolymer has been reported to achieve an impressive apparent quantum yield of 60 % at 420 nm, using 3 wt % photodeposited Pt and sacrificial electron donor.[201] In addition carbon nitrides have been shown to achieve overall water splitting using Pt and other metal oxide cocatalysts,[192,202,203] as well as when integrated into Z-schemes.[204–208]

Carbon nitrides are a promising material owing to their inexpensive synthesis, chemical stability, and potential for functional group modifications on the sheet edges. However at present the mechanisms by which synthetic precursors and conditions impact the photocatalytic activity of the product is poorly understood, and the issues outlined above concerning the limited chemical versatility (being composed of just alternating C and N atoms), low surface area, as well as processability must be better understood and overcome.[188]

1.7.3. Organic Semiconductor Photocatalysts

Carbon nitride, due to its carbon-based nature, could be classified as an organic semiconductor. However, in its synthesis and behaviour it is more inorganic in character, and its harsh synthetic conditions limit its structural versatility.

By contrast, organic semiconductors synthesised by lower temperature transition metal cross coupling or condensation reactions can tolerate a wider range of functional groups, permitting almost limitless structural diversity.[181] As materials they are characterised by their high extinction coefficients,[72] meaning the thickness required to almost completely absorb incident sunlight is typically around 100 nm.[209,210] This is in contrast to several μm required for silicon due to its indirect bandgap, or up to 1000 nm for typical direct bandgap inorganic semiconductors.[85] Indeed, many organic semiconductors adopt motifs from dye chemistry, capitalising on the materials'

excellent light harvesting capabilities.[211] This allows organic semiconductors to excel at the first step of photocatalysis: absorption of photons to generate a high population of excited states. In addition to this they also have the advantage over their inorganic counterparts of being made of earth-abundant non-toxic elements,[188] while their potential for solution processability makes them amenable to low cost solution processing.[212,213]

Nonetheless, as organic materials with inherently low dielectric responses, photoexcitation leads to the formation of tightly bound Frenkel excitons. [77,81–83] Their major limitation is the charge separation step of photocatalysis. To overcome this, particular emphasis must be paid to interfaces to enable charge separation, either with electrolyte, another semiconductor or cocatalyst. In addition, due to generally worse charge transport properties in comparison to inorganics, attention must also be paid to the distances involved between exciton generation and the interfaces required for charge separation.

1.7.4. Covalent Triazine Frameworks (CTFs): Nitrogen-Rich Open Framework Structures

With the limitations of carbon nitrides in mind, covalent triazine frameworks (CTFs) keep the 1,3,5-triazine motif as a three-branched unit to enable the construction of frameworks, but utilise linker units to connect the triazines, shown in Figure 18.[214] The linker groups offer greater energy level tunability compared to carbon nitrides,[215] as well as acting as ‘struts’ to create an open framework structure. Because the framework is composed of rigid π-conjugated units with low conformational flexibility, the voids created between the struts is locked in, precluding packing and creating permanent porosity.[183,216] This can permit high surface areas, so long as the frameworks do not stack out of line, blocking the pores. In general, porosity can be favourable for photocatalysis when it increases the interfacial area between semiconductor and electrolyte. [121,217–220] The implications of photocatalyst porosity will be further discussed in Chapter 2.

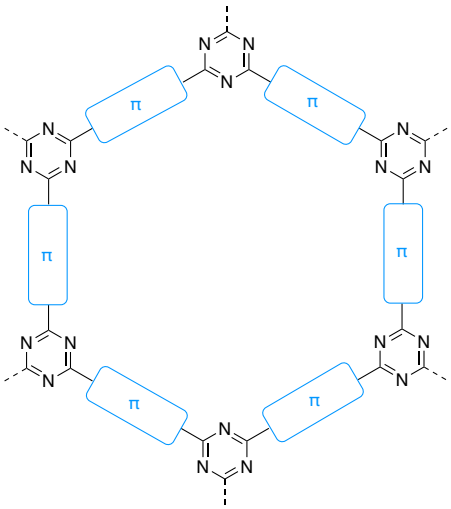

Figure 18. Covalent triazine networks, where triazine units are linked in three directions by π-conjugated linkers

Crystallinity is the degree to which a material possesses periodicity on the atomic scale.[221] Atomic crystallinity in covalently bonded structures requires bond formation under thermodynamic control. This means that under synthetic conditions there is sufficient activation energy to surmount the transition state between reactant and product from either side, enabling bond formation under reversible conditions. The distribution of products is dictated by their relative stabilities, so that the most stable structures form as it reaches equilibrium under the reaction conditions, enabling 'error-correction'. Amorphous covalent structures on the other hand form under kinetic irreversible bond forming conditions.[222,223]

CTFs are commonly synthesised via trimerization of dicyanoarenes, where the nitrile groups coalesce to form the triazines. However, owing to the stability of the aromatic triazine unit, this trimerization typically has poor reversibility rendering the resultant structures amorphous.[224] This can be ameliorated through using more forcing conditions, such as molten zinc chloride as a catalytic solvent to increase crystallinity.[225–227] The ability to allow reversible formation of the triazine unit to promote crystallinity and greater degrees of polymerisation has been shown to lead to more photocatalytically active materials,[228,229] due to improved exciton and polaron transport.[101]

However, harsh, high temperature synthetic conditions needed to ensure the reversibility of the bond forming reactions can simultaneously lead to partial carbonisation side reactions. This is a problem because the black 'soot' like particles compete with light absorption by the semiconductor. [228,230,231] Much of covalent triazine network research has focussed on achieving reversable bond forming reactions to permit crystallinity to emerge while minimising deleterious side reactions.[232,233] In doing so, crystalline CTFs have been reported to photocatalysis overall water splitting with the help of appropriate cocatalysts.[234]

1.7.5. Conjugated Microporous Polymers (CMPs): Porous and Amorphous

CTFs have also been synthesised by pre-forming the tricky triazine unit in monomers, then polymerising them with various appropriately functionalised linkers to form network polymers.[214] While this expands the chemical versatility (away from aromatic nitriles) and avoids unwanted side reactions, it also means the resulting polymers are amorphous, owing to the kinetically controlled irreversible transition metal catalysed coupling bond forming reactions employed.[183] Such materials are classed as conjugated microporous polymers (CMPs). This is general class of network polymer formed through copolymerisation involving branched monomers (with more than two reactive positions). This is capable of producing disordered three-dimensional π-conjugated nets,[235,236] where varying strut length has been shown to offer some control over the pore diameter.[237] It has also been demonstrated that by varying the ratio of monomers of different geometries, it is possible to tune optical bandgap in a continuous fashion.[120]

CMPs have much greater versatility than carbon nitrides due to the diversity of monomers which can be incorporated, but although variation of linker size and composition can impart some control on porosity, pore control is far lower than for ordered crystalline frameworks, where uniform pore size can be predicted from the shape of the framework.[183] Their amorphous nature also makes characterisation challenging, due to their unsuitability for crystallographic techniques and their total

insolubility which further limits their characterisation.[183] This makes structure property relationship elucidation more challenging.

1.7.6. Covalent Organic Frameworks (COFs): Porous and Crystalline

To produce crystalline and porous photocatalysts, reversible bond formation during synthesis is required,[222] while under photocatalytic conditions these bonds should be robust enough to avoid degradation. Covalent organic frameworks (COFs) are such materials, synthesised under reversible thermodynamically controlled conditions. Typically, this involves crosslinking monomers with three or four reactive positions copolymerised with difunctionalised linkers. Crucially the bond forming reactions are reversible, often employing condensation chemistry.[223]

As previously discussed, covalent triazine frameworks may adopt crystalline structures provided the reaction conditions enable reversible bond forming, however in general the forcing conditions required to do this for highly stable triazines can cause partial degradation to other parts of the structures, limiting tolerance to more diverse functional groups.[181] A compromise requires the resultant framework to be not so stable that overly forcing conditions are required to enable its reversible formation, but the bonds holding the framework together must not be so weak that they degrade under photocatalytic application. This has been achieved by the use of azine[238,239] and hydrazone linkages,[240] as well as a modified imine linkage, utilising a two-step reversible imine formation followed by an irreversible enol to keto tautomerism to ‘lock in’ the structure and lend stability to the crystalline imine linked framework due to the presence of a intramolecular hydrogen-bonds.[142,241,242] This linkage is shown below in Figure 19.

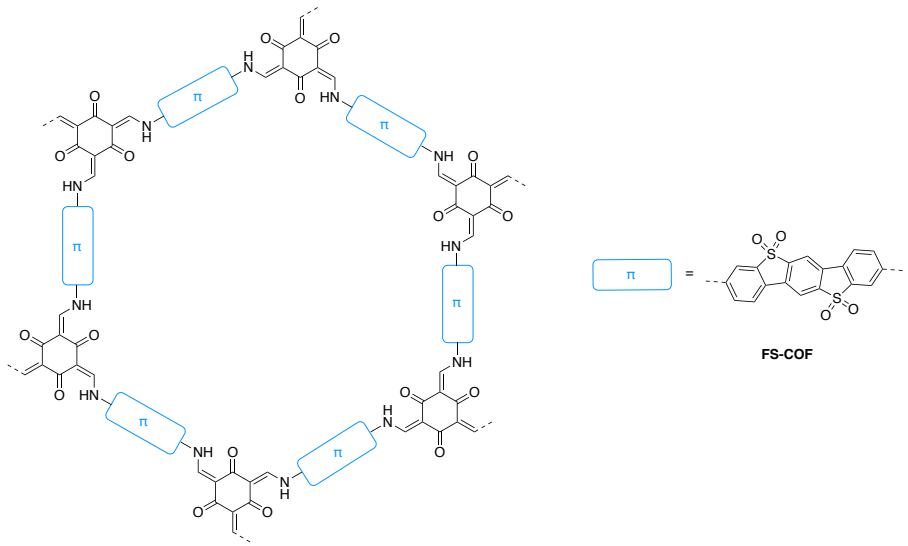

Figure 19. FS-COF from reference[142]

Utilising the stability of this linkage, a study varying the linker composition produced a covalent organic framework **FS-COF** (Figure 19) which gave apparent quantum yields of 3.2% and 1.3% at 420 and 600 nm respectively under sacrificial conditions.[142] When this crystalline covalent organic framework was synthesised by an alternative method to produce an analogous amorphous material, its performance decreased significantly. This is in line with other covalent organic framework studies, reporting higher activities for more crystalline materials with optimised stacking, often achieved by using more planar linkers with reduced biaryl twisting.[142,239,243] This is because highly ordered crystalline π-π stacked structures enable effective exciton and polaron transport, by facilitating axial electronic interaction via π-π interactions and avoiding the presence of defects and charge trapping sites.[244–246] This better enables photogenerated charges to reach their reactive sites which is particularly important if the cocatalyst is not photodeposited inside the pores. Although, consideration of the distribution of cocatalyst is difficult to determine and is often neglected in literature.

Another reason for the high activity of this **FS-COF** is the ability of the highly polar sulfone group to provide wettability. This enabled it to adsorb a large amount of water in its water sorption isotherm compared to similar porous structures without these polar groups.[142]

1.7.7. The Special Properties of Dibenzo[b,d]thiophene Sulfone

Sulfone units have also been incorporated into the backbone of amorphous conjugated microporous polymers. Here **S-SMP3** showed greater water uptake compared to its non-polar analogue **P35**, and its less porous polar analogue **F-SMP3**, shown by their water sorption isotherms shown in Figure 20.[217] It is thought that when pores are hydrophobic, electrolyte entry is restricted.[247,248] This nullifies the benefits of increased surface area when it does not lead to an enlargement of the semiconductor-electrolyte interface. However, in this study the differences in backbone make direct conclusions about hydrophilicity and porosity difficult, owing to the different modes of charge generation between sulfone and non-sulfone containing polymers.[92]

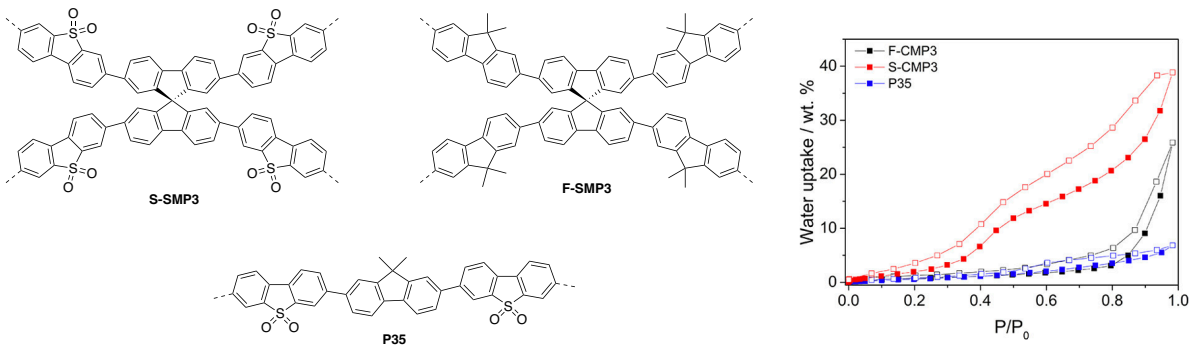

Figure 20. Polymers with their water sorption isotherms from reference. Reproduced from reference under creative commons attribution 4.0 license [217]

Another reason for the high activity of the sulfone unit is its highly polar nature, which enables excellent dispersibility in the aqueous reaction medium.[92,142] Dispersibility is a crucial design parameter for particulate photocatalysts, as poorly dispersed photocatalysts can flocculate or aggregate leading to poor cross-sectional coverage of the irradiated area, enabling much light to be transmitted through the reacting vessel and not be absorbed.[147] Indeed a high-throughput photocatalyst screening study found that dispersibility was a parameter which best correlated with high activity, along with energy level positions.[249]

Dibenzo[b,d]thiophene sulfone units have received much attention due to its high activity, being first employed in linear conjugated polymers.[92,125,250,251] The unit is frequently tested using water, methanol and triethylamine sacrificial electron donor in equal volume,[250–252] with the homopolymer **P10** achieving an apparent quantum yield of 11.6% at 420 nm under such conditions.[92] From transient absorption spectroscopy (TAS) photophysical studies it was found that the presence of the sulfone units correlates to highly efficient generation of extremely long-lived electron polarons. This is due to enhanced water localisation around the backbone owing to its polarity, enabling rapid reductive quenching of excitons by triethylamine scavenger on the ps timescale.[92] These long lived electron polarons localised on the sulfone units then transfer on the μs timescale to close-by residual Pd clusters to reduce protons.[92,93,95]

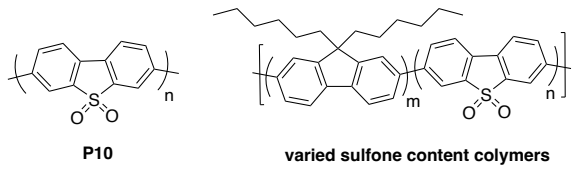

Figure 21. Sulfone containing linear polymers from references.[92,93,95]

P10 has subsequently been shown to be capable of water oxidation in the presence of Co cocatalyst and silver nitrate sacrificial electron acceptor.[253] It was found that the addition of $AgNO_3$ changed the UV-vis spectrum, indicating a pre-association of Ag to the polymer, and the presence of $AgNO_3$ prevented the observation of exciton formation at short timescales, indicating very efficient oxidative exciton quenching by the sacrificial electron acceptor.[253] The same polymer has also been reported to achieve overall water splitting through screening different water oxidation cocatalysts, finding thermally deposited Co which oxidises to CoO enabled rapid reductive exciton quenching to successfully enable overall water splitting to be photocatalysed on single particle systems, albeit at a solar to H_2 conversion efficiency of 0.0047 %.[254] While this is a promising first example of overall water splitting by a linear conjugated polymer photocatalyst, it is clear from spectroscopic investigation that charge separation sulfone containing polymers is largely driven by favourable reductive quenching by sacrificial electron donor, or far less favourable exciton quenching by metallic cocatalysts.

1.7.8. Limitations of Network Polymers

A method of intrinsic charge separation in a material, without relying on sacrificial reagents or cocatalysts, is through the use of type-II heterojunctions as employed in organic photovoltaics.[77,84] The problem is that porous network polymers are insoluble making these difficult to form. Nonetheless, construction of heterostructures in covalent organic frameworks has been achieved by an electron deficient covalent organic framework stacked on top of an electron rich one, enabled by their similar shapes using orthogonal bond forming chemistry, shown in Figure 22. This created a type-II energetic offset, enabling significantly higher photocatalytic activity compared to the two frameworks physically mixed. Transient absorption spectroscopy revealed the intrinsic formation of charge separated states in the material in the ms timescale in the absence of sacrificial electron donor or cocatalyst, showing intrinsic charge generation of the material due to the heterojunction interface. These charges were able to be extracted by photodeposited Pt and ascorbic acid, as well as a redox shuttle, opening up the possibility of use in Z-schemes.[255]

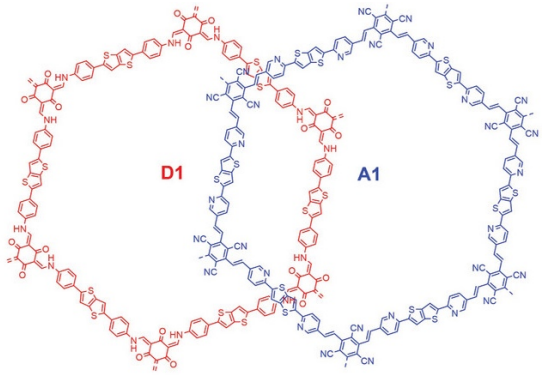

Figure 22. Templated covalent organic framework type-II heterojunction. Reproduced from reference under creative commons attribution 4.0 license.[255]

Nonetheless, formation of such heterojunctions in network polymers is difficult and highly sensitive to finding well matched structural motifs.[255] Covalent organic frameworks in general are highly sensitive to reaction conditions which are difficult to predict, combined with difficulty in scaling up typically lengthy and low yielding reactions.[256] Furthermore, the formation of network polymers requires the incorporation of branched monomers.[257,258] These branching monomers frequently

involve meta linkages[217,259,260] which are cross conjugated.[252,261,262] this diminishes the ability of excitons and polarons to move laterally through the cross conjugated units.[104,236,258] It has been shown that in carbon nitrides, the axial conductivity between sheets is significantly greater than lateral conductivity along sheets,[263] and the lack of lateral conjugation in melon confines excitons to heptazine units.[101] It could be expected that conjugated microporous polymers and covalent organic frameworks would also exhibit such anisotropic charge transport properties when conjugation along the framework is blocked.

Network polymers are also insoluble, which makes morphological modification after polymer synthesis extremely challenging, as their microstructure is mostly fixed following synthesis.[68] Although efforts have been made to exfoliate carbon nitrides and network polymers to increase their surface areas,[264–266] solution processability offers the possibility of far greater morphological control and also means semiconductors of differing energetics can be interfaced against each other to form type-II heterojunctions by simple mixing in solution.

1.7.9. Soluble Linear Conjugated Polymers

The addition of sp^3 hybridised sidechains to conjugated polymers imparts solubility.[67,212] Compounds dissolve when the free energy change associated with dissolution is negative, which depends on the enthalpic and entropic changes during the dissolution process.[267]

Conjugated polymers possess rigid backbones with a low degree of conformational freedom.[212] There exist π-π, van der Waals and dipolar interactions favouring aggregation of organic semiconductors in the solid state.[212] In order to allow these backbones to disaggregate and dissolve, it follows that the cohesive interactions of the polymers must be made less favourable than interaction with solvent. Modification of polymers by attaching long flexible side chains with a high degree of conformational freedom could be expected to modify the cohesive parameters of the polymer.[67,268] The attachment of flexible side chains can also sterically inhibit π-π stacking between

backbones, especially when the side chains are out of plane with the backbone and branched. This could be expected to attenuate the strong cohesive interactions between the polymer backbones.[269] Another factor is the entropic contribution of the flexible side chains during dissolution. It could be expected that their presence would bring about a larger increase in entropy, making dissolution a more energetically favourable process.

Linear conjugated polymers with such solubilising side chains have been extensively studied in other fields of organic electronics such as light emitting diodes,[270] organic transistors[271] and organic photovoltaics.[77] Using similar materials to those employed in organic photovoltaics, it is possible to dissolve conjugated polymers in solvent and spin coat onto glass substrates to form thin film photocatalysts.[272,273] This has the advantage of controlling the semiconductor-electrolyte interface area, circumventing problems associated with particle aggregation or poor dispersibility. However considering exciton diffusion length is generally about ten times smaller than the optical depth of organic semiconductor needed to fully absorb incident sunlight,[77,87,88,95,274] a strategy of coating glass fibres in solution processable conjugated polymer has been demonstrated, which allows incident sunlight to pass through multiple cross-sections of polymer on its way through the reaction vessel.[251]

1.7.10. Nanoparticle Fabrication to Increase External Surface Area

Solution processing also allows the external surface area of particulate photocatalysts to be increased by decreasing particle size. This improves their activity because excitons generally diffuse between 5 to 15 nm before decay.[77,87,88,274] If excitons are photogenerated in the bulk of semiconductor at distances greater than the exciton diffusion length from an interface, they are counterproductive as they absorb photons, but cannot undergo charge separation so waste the excitation energy.[68]

This simplest method of achieving this is nanoprecipitation, which is possible for organic semiconductors which are soluble in a water miscible solvent, typically THF. It works by addition of the THF polymer solution to water under sonication whereupon

the polymer precipitates into nano sized particles (often called Pdots), and the THF is removed.[275–277] Size can be tuned by varying its concentration in the water miscible organic solvent.[278] In some cases stable nanoparticles are able to form without additional amphiphilic compounds.[275,278] It has been proposed that stabilisation can arise from charge accumulation on the surface,[279] however the stabilisation mechanism for such polymer nanoparticles is poorly understood. Nonetheless in many cases polymers irreversibly aggregate following nanoprecipitation owing to the tendency of very small hydrophobic particles to minimise unfavourable interactions with electrolyte through aggregation to maximise more favourable polymer-polymer interfaces.[280] To combat this, it is common for the conjugated polymers to be co-dissolved with amphiphilic molecules or polymers to reduce the surface tension.[276]

By adopting this surfactant stabilised nanoprecipitation approach, conjugated polymer nanoparticles were first shown to be highly photocatalytically active compared to the powder forms of the same polymer.[122,281,282] However morphological stability for these systems was a major problem, with irreversible aggregation under photocatalytic conditions making their activity collapse in a matter of hours.[122,281,283] By replacement of hydrophobic alkyl side chains with more hydrophilic oligo(ethyelene glycol) alternatives, it was shown that more stable nanoparticles could be fabricated without use of surfactant, owing to the reduced unfavorability of the polymer-electrolyte interface.[282,284]

Another method of fabricating organic semiconductor nanoparticles is by mini-emulsion: using a water-immiscible solvent to dissolve the semiconductor such as chloroform and subjecting to high shear force via sonication in the presence of a surfactant to create nano-micelles of semiconductor dissolved in chloroform. After sonication the chloroform is evaporated leaving stable aqueous dispersions of polymer nanoparticles.[285–287]

1.7.11. Hybrid Nanoparticles to Enhance Charge Generation

When two organic semiconductors with offset energy levels are co-dissolved and fabricated into nanoparticles using these aforementioned methods, type-II heterojunctions can be created. This essentially forms nanoparticle bulk heterojunction organic photovoltaic cells decorated with Pt. Using such an approach, miniemulsion nanoparticles containing blended high performance photovoltaic polymer donor and small molecule acceptors **PTB7-Th** and **EH-IDTBR** have been fabricated, depicted in Figure 23. After photodeposition of Pt, the 50-80 nm diameter nanoparticles achieved an AQY of 6.2 % at 700 nm in the presence of ascorbic acid, owing to the strong visible light absorption of the **EH-IDTBR** acceptor, and efficient charge separation at the heterojunction interface.[143] It follows that both donor and acceptor domains must be exposed to the electrolyte interface for high activity. For acceptor domains, this is so electron polarons can reach photodeposited Pt clusters on the surface and catalyse proton reduction. The donor domains must also have access to the electrolyte interface so that holes can be successfully reduced by sacrificial reagent. Morphological control of the donor and acceptor semiconductors' mixing is therefore extremely important. It was found the surfactant has an influence on this, with 2-(3-thienyl)ethyloxybutylsulfonate sodium (TEBS) promoting an intermixed morphology rather than core-shell, enabling more efficient charge separation and dissipation.[143]

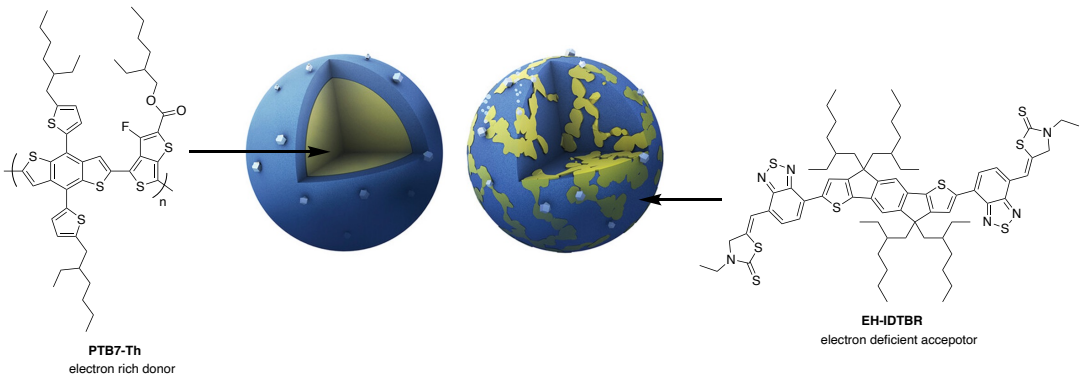

Figure 23. Core shell (left) and intermixed (right) heterojunction nanoparticles with photodeposited Pt: electron rich donor (blue) and electron deficient acceptor (yellow). Reproduced from reference under creative commons attribution 4.0 license.[84]

The excellent ability of such heterojunction nanoparticle systems to intrinsically generate long lived charges was later demonstrated with similar donor acceptor nanoparticle system. This showed remarkably long-lived charge separated electron on the second timescale, in the absence of any Pt or sacrificial electron donor. This was owing to extremely efficient electron transfer from donor to acceptor, and highlights the potential of such a system to efficiently separate excitons in the absence of sacrificial electron donrors.[114]

1.7.12. The Problem with Surfactants

By dissolving many different donor and acceptor organic photovoltaic semiconductors in THF followed by nanoprecipitation, fabrication of donor-acceptor particles made via nanoprecipitation were similarly found to lead to highly active photocatalysts. These blended particles outperformed the physical mixtures of the same ratio of donor and acceptor, to rule out complementary light absorption as causing the improved performance of the blends. Though notably here stability was poor for these surfactant free particles, which flocculated during testing leading to a drop off in H_2 production, as shown in Figure 24. Interestingly, various surfactants were subsequently added during nanoprecipitation to improve stability, however this was accompanied by a drastic decrease in activity compared to the surfactant free particles, opening up questions around the use of surfactants.[288]

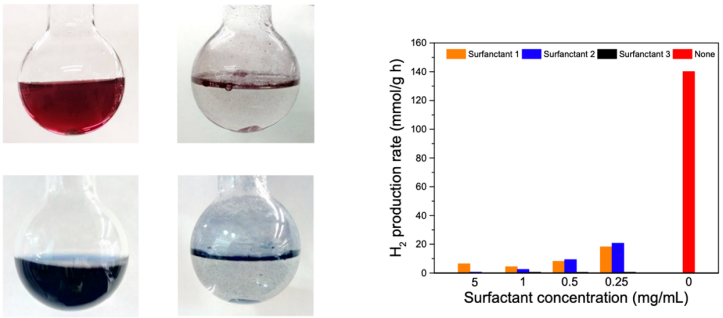

Figure 24. Left: image of nanoparticles before and after testing showing flocculation. Right: graph showing the suppression of H_2 evolution with added surfactant. Reproduced from reference under creative commons attribution 4.0 license[288]

It is striking that for the **PTB7-Th:EH-IDTBR** system (Figure 23), the higher activity of TEBS over sodium dodecyl sulfate (SDS) was attributed to the promotion of an intermixed morphology by TEBS. However single component nanoparticles (pure **PTB7-Th** or pure **EH-IDTBR**) prepared with TEBS were also more active than their SDS analogues, despite similar particle sizes.[143] This suggests that the surfactant must be have additional effects on beyond controlling heterojunction morphology, as there is no heterojunction for single semiconductor nanoparticles. A study reported attributed activity of the SDS nanoparticles compared to TEBS due to SDS forming a denser insulating layer around the nanoparticles which inhibited electron transfer from the semiconductor to photodeposited Pt, and also reduced the amount of Pt that could be successfully photodeposited in the first palce.[289]

There seems to be a compromise between stability and activity, whereby surfactants stabilise nanoparticles but on the other hand surfactants are electronic insulators, which could be expected to inhibit electronic contact between the semiconductor and electrolyte given that they're likely embedded into the surface of the nanoparticles.

Surfactants have been employed to enable processing of conjugated polymers for transistors and photovoltaics in green solvents rather than toxic chlorinated ones. However residual surfactant in the active layers has been shown to be detrimental to long-distance charge transport properties, due to the dense packing of the insulating aliphatic surfactant chains around the semiconductor nanoparticles, worsening interparticle charge transport.[290–292] Taken together, it appears surfactants can do more harm than good, though understanding their role in the photocatalytic process requires more investigation.

1.7.13. The Effect of Dielectric Environment on Photocatalysis

As a discipline, organic photocatalysis has borrowed significant insight from organic photovoltaics, often directly taking high performing photovoltaic materials and putting them into particles with Pt cocatalyst.[114,143,288,289] However, it is important to be mindful of the differences between photovoltaics and photocatalysis: chiefly that water

splitting requires water, meaning semiconductors must be immersed in electrolyte whereas photovoltaics are extremely dry. While this can be a problem for some materials with limited aqueous stability,[293] for other materials this could pose a distinct advantage.

When there are two oppositely charged particles (such as an electron and hole) of magnitude +q and -q at distance r, a dipole moment exists between them, μ. The polarisation of a material is the sum of all the dipole moment vectors per unit volume. The dielectric response, ε_r of a material is a measure of how well a material can screen such polarisation. That is to say, when a dielectric material is placed in an electric field, it is able to reorganise such that it sets up an opposing electric field of its own, counteracting the applied electric field and screening the charges on either side from one another.[294,295]

However, the ability of the material to reorganise and set up an opposing electric field is not instantaneous. This fact imposes a dependence of dielectric charge screening on the frequency of the electric field the material is under. Calling ε_r 'dielectric constant' is misleading because it varies as a function of frequency. There are three main mechanisms whereby dielectrics can reorganise to polarise and set up opposing electric fields. The fastest is electronic polarisation where the electron clouds in the constituent molecules move their average positions relative to the nuclei, creating dipoles and a net polarisation to counteract the applied polarisation. Another mechanism is for ionic materials, where the ions can shift their relative positions in the lattice to generate dipoles and a net polarisation. The slowest mechanism is orientational polarisation, which is where molecules such as water with permanent dipoles can rotate and orientate themselves to oppose applied electric fields. As the frequency of the applied electric field is increased, the three main mechanisms of dielectric polarisation drop off from slowest to fastest, as they're unable to act in time to oppose the applied field. After around 10^{15} Hz none of the mechanisms are able to keep up, and the dielectric response converges to that of vacuum.[294,295]

This is pertinent to photocatalysis because it explains why inorganic semiconductors have higher dielectric responses given the ionic screening mechanism available to them. This is not possible for organic semiconductors which are non-ionic and largely non-polar, so they have limited ability to reorganise in response to an electric field. The frequency dependence of the dielectric response is also important because it follows that the photophysical timescales involved in photocatalysis dictate the dielectric polarisation mechanisms available to the semiconductor to shield the photogenerated electron and hole.

It was predicted that increasing the dielectric response of organic semiconductors could reduce exciton binding energy and decrease geminate and non-geminate recombination in solar cells.[296] This has been put into practice by side chain modification with polar groups, which in cases where charge transport or morphology were not adversely affected, resulted in improved performance in solar cells.[82,297,298] Once separated electron and hole polarons are coulombically attracted to another, it was found that the non-geminate recombination between these species decreased with increasing dielectric response.[82,297]

For increasing the dielectric response to have an effect on exciton separation and geminate recombination as well as non-geminate recombination, it follows that it must also provide dielectric screening at a competitive frequency to the timescales of exciton generation and lifetime. It was reported that this is not the case for conjugated polymers bearing glycol chains inside dry organic photovoltaics, given the chains have a reorientation frequency in the 10^9 Hz (GHz) timescale,[299–301] (though it can reduce polaron recombination, given they are longer lived).[82,297]

However, in a study where glycol sidechains were substituted onto conjugated polymers and fabricated into miniemulsion nanoparticles of consistent size, it was found that the nanoparticles made using glycolated polymers were more active. The difference being that these particles were tested for photocatalysis in aqueous environment, rather than dry solar cells. Investigation of **g-IDTBT** (Figure 25) revealed spontaneous polaron separation in pure water, without Pt or hole scavenger. This

remarkable spontaneous charge generation is extremely uncommon for pure organic semiconductors owing to their high exciton binding energies. This effect of glycol sidechains on charge generation and decreasing recombination was not observed in the anhydrous materials, given glycolation was found to increase water uptake and swelling.[302] This led to the conclusion that the charge generation was due to greater interactions with water for glycolated polymers. Given that water has a higher dielectric response compared to glycol chains, up to the 10^{12} Hz timescale which is competitive with the timescales of exciton lifetimes, the enhanced charge generation was attributed to its dielectric influence.[302,303] Other studies also showed improvements in activity following glycol sidechain substitution,[304,305] however it is likely that the increased performance in these cases was also due to better dispersibility and reduced particle size.

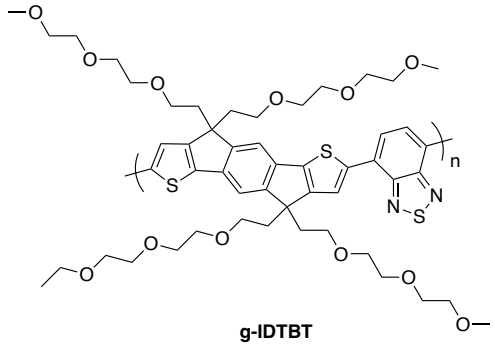

Figure 25. g-IDTBT adapted from reference[302]

1.8. Measuring and Reporting Photocatalytic H_2 Production

In their simplest sense, photocatalytic activity measurements irradiate the photocatalyst and measure how much H_2 is produced. However, when comparing measurements across different laboratories and setups, this can be unreliable due to several factors. Chiefly these are the spectrum and intensity of the light source, the photocatalyst sample preparation and concentration, and the dimensions and composition of the photoreaction cell.

Given that the goal of renewable photocatalytic water splitting is to utilise sunlight to produce H_2, lamps whose spectral output approximates standardised sunlight must be used. For solar energy applications this is conventionally irradiation of 1 Sun using air mass 1.5 (AM 1.5 G), 100 mW cm^{-2}. Use of calibrated photodiodes to calibrate the irradiation intensity is an effective method of ensuring the total photon flux is of a standardised energy, however the wavelength distribution of this energy is variable. Xe lamps are most commonly used in conjunction with mirror modules and cut-off filters to home in on the visible region. In order to ensure reproducibility and transparency in reported activity, it is important to always give the illumination conditions with a measurement.[306]

There is persistent use in the field of mass normalised H_2 production rates, where the activity of a photocatalyst is reported as H_2 produced per mg of photocatalyst per hour. This is misleading because photocatalyst activity is not proportional to its concentration past a given concentration;[147,306,307] testing photocatalysts at very low concentrations will give higher mass normalised rates, illustrated in Figure 26.[147,306] In addition, differences in the dimensions of the reaction chamber also affects the photocatalytic rate.[308] With this in mind, it has been proposed that a more reliable method of ascertaining photocatalytic performance is the area normalised H_2 production rate. This way photocatalysts are measured at concentrations past their activity plateau, and the differences in reactor dimensions are accounted for.[147,258]

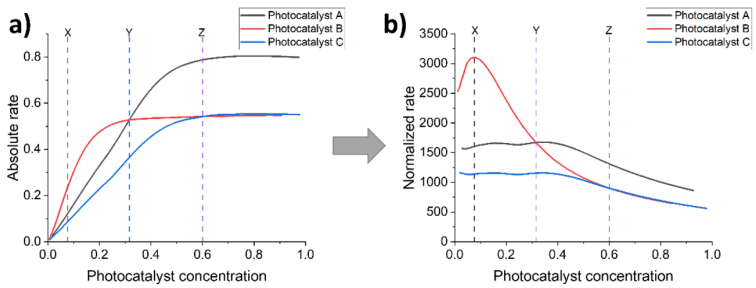

Figure 26. Illustration of the misleading effects of mass normalised activities. Reproduced from reference under creative commons attribution 4.0 license[147]

1.9. Characterising Organic Semiconductors

This section will give an overview of the non-standard techniques employed in this thesis to characterise organic semiconductors.

1.9.1. Photoelectron Spectroscopy in Air (PESA) for HOMO Estimation

Photoelectron spectroscopy is a useful application of the photoelectric effect. Here a sample is irradiated by monochromatic UV light. If its photons exceed the work function, HOMO electrons are emitted from the sample. The photoemitted electrons ionise O_2 in the air, and the O_2^- is detected by the open counter after acceleration by high voltage. The operation in air makes PESA a particularly convenient technique, and its high sensitivity enables very weak UV light intensities to be utilised. [309–311]

For organic semiconductors, the cube route of the photoemission yield with as a function of incident photon energy shows a linear relationship. When tangents are drawn between this and the baseline, the intercept is an estimate of the semiconductor's ionisation energy.[311] An illustrative example is shown in figure 27.

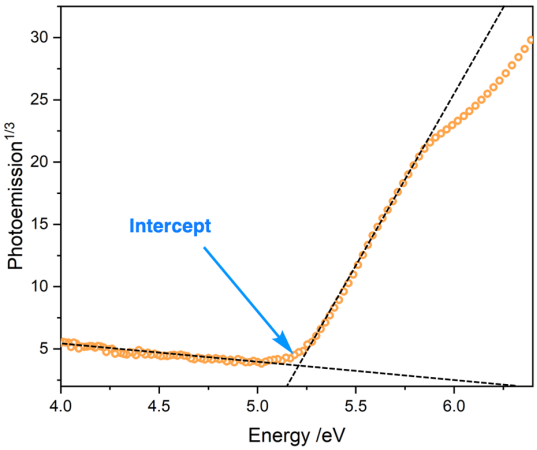

Figure 27. Example photoemission onset determination in PESA

1.9.2. UV-vis Absorption Intercept for Optical Bandgap

The solid-state optical bandgap is commonly measured by conducting UV-vis spectroscopy on a spin coated film of organic semiconductor. By drawing tangents of

the baseline and the absorption (Figure 28), the wavelength of the intercept is converted to a photon energy to obtain this value.[312,313] Adding the optical bandgap to the HOMO energy estimate can give an estimate of the LUMO. Due to the optical bandgap being smaller than the fundamental bandgap, this will be a conservative estimate for the depth of the LUMO, with it likely being higher lying. Therefore, the measurements by which the HOMO and LUMOs were calculated must always be clearly stated, and comparisons of materials should only be made when using the same energy level characterisation methods.

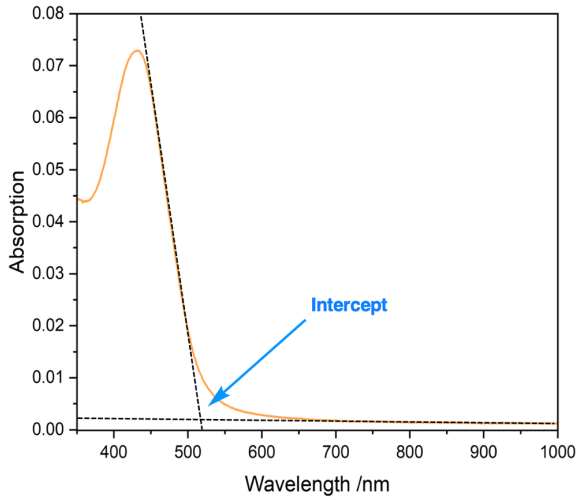

Figure 28. Example optical bandgap determination from absorption onset in UV-vis spectroscopy

1.9.3. Cyclic Voltammetry (CV) for HOMO and LUMO Determination

Cyclic voltammetry is used in organic semiconductor characterisation to measure the potential at which electrons are transferred to and from the material. This gives insight into the ionisation potential and electron affinity of the material, which is a proxy for HOMO and LUMO energy. When put into a three electrode potentiostat setup, where the material is connected to the working electrode, the current flow is measured as a function of applied potential. Positive or negative potential is applied, increasing at a constant rate until a given point, then climbing back down in the other direction. Conventionally, a positive current flow represents an oxidation event (anodic peak) and a negative current flow represents a reduction event (cathodic peak). For

electrochemical measurements, it is important to use an electrolyte which allows current to pass between the electrodes. However, the solvent in which it sits must itself not be reduced or oxidised in the potential range which is to be scanned. This is referred to as a redox window. For this purpose, acetonitrile is common as a solvent in conjunction with an organic solvent soluble electrolyte, owing to its wide redox stability window.[314]

Figure **29** below shows a representative cyclic voltammogram for a reduction event. Tangents of the baseline and the slope of the cathodic peak are used to calculate the reduction onset potential. From this the reduction onset is derived. It is important that in the backwards sweep, when the applied potential is taken back to zero, that the current flow is reversed, for the electron transfer process to be considered reversible.[314]

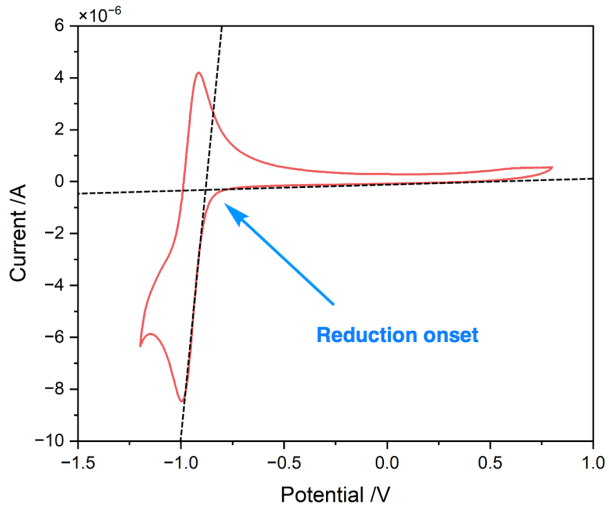

Figure 29. Example reduction potential onset determination in CV

For all electrochemical measurements, the potential must be specified with respect to the reference electrode: Ag/Ag^+ is common for acetonitrile-based measurements for organic semiconductors. However, the equilibrium potential for this the redox processes in reference electrodes depends on the concentration of the ions inside. Variations in concentration can cause reference electrode potentials to deviate. To

counter this ferrocene is used for calibration.[314] Ferrocene gives a clear and reproducible reversible oxidation peaks. The peak maxima are taken for the oxidation and compensating reduction peaks on the reverse sweep, and half-way between these is defined as the half-wave potential, E_{Fc}. Using this value, the ionisation potential and electron affinities, and thereby the HOMO and LUMO estimates can be calculated on an absolute energy scale relative to vacuum. However there are a range of values used to conduct this conversion.[315] The value of 4.8 is commonly used in literature to convert ferrocene's redox half-potential to an absolute energy relative to vacuum.[316–319] This gives the following conversion equation.

$$E_{eV} = 4.8 - \left(E_{Fc}\right) + E_{onset}$$

1.9.4 Calculation of Surface Area by Adsorption Isotherms

The surface area of porous materials can be measured by their gas adsorption properties. N_2 is often used for this purpose due to its inert nature and availability at high purity.[320] First the clean solid adsorbent material under investigation is heated and put under high vacuum to remove any pre-adsorbed species which could influence subsequent adsorption. Next the sample is cooled to using an external liquid N_2 bath around the sample holder, and N_2 molecules are supplied to the sample in a stepwise manner whereupon they encounter the surface of the material. They experience short range electrostatic repulsion owing to clashing electron clouds which is inversely proportional to r^6, and longer-range van der Waals attractions which is inversely proportional to r^{12}, where r is the distance of the adsorbing molecule from the surface. The molecules find a balance between repulsive and attractive forces as a function of distance from the surface, where their energy is minimised and are said to be physiosorbed.[321]

Because physisorption is weak, the energy released during the process is small, as is energy required to desorb. This makes adsorption a reversible process, and the equilibrium amount of adsorbed N_2 depends on the pressure and temperature. The measurement is conducted at a constant temperature giving the measurement its

name of an isotherm, and this chosen temperature is typically very low in order to maximise the amount of gas which can be absorbed.[320] By subjecting a sample at constant temperature to varying pressures of the adsorbing gas using highly accurate pressure transducers, adsorption isotherms can be measured, and the amount of adsorbed gas plotted against relative pressure is measured.[321]

This profile of the adsorption isotherms recorded gives enormous insight into the microstructure of the material. This is because for porous materials, the surface is not a simple plane, but a multifaceted landscape. Here the adsorbate molecules can be surrounded by the surface on more than one side, giving a more favourable adsorption potential energy minimum (the depth of the potential energy well is deeper). This has the effect of increasing the adsorption energy released and lowering the relative pressure at which adsorption can occur. For microporous materials with very small pores (less than 2 nm) which approach the dimensions of the adsorbate gas, this effect gives rise to a distinctive steep concave gradient as the partial pressure increases from the origin, whereas surfaces lacking micropores show a straight line. In general, the larger the pores the grater the relative pressure required to fill them.[321]

Adsorption isotherms are classified into six characteristic types shown in Figure 30 and the first three types are qualitatively described below. Isotherms are plotted as the amount of adsorbate molecules adsorbed against the relative pressure P/P_0, where P is the applied pressure of adsorbate gas and P_0 is the saturation pressure of the gas (when it starts to condense).

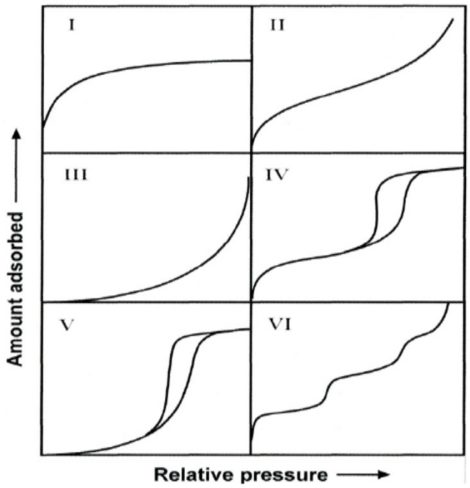

Figure 30. Classification of isotherms. Reproduced from reference under creative commons attribution 4.0 license I[322]

- Isotherm I is often described as a Langmuir isotherm because it shows monolayer adsorption and can be described by the Langmuir equation. This is seen in microporous solids with low external surface area, where very small pores are initially filled causing a rapid spike in adsorbed gas. However, because the pores are so small, they don't allow multilayer absorption, so as the relative pressure is further increased, no more adsorption is possible so it plateaus.[320,321]
- Type II isotherms occur for non-porous or macropore containing porous materials where there is enough space to achieve multilayer adsorption. The inflection point indicates the partial pressure at which monolayer coverage is complete and multilayer coverage begins. At higher relative pressures as it approaches saturation, multilayer adsorption on the surface of non-porous samples, or macropore filling takes place. The adsorbed volume will be higher for the latter than the former.[320,321]
- Type III also depicts multilayer adsorption, but where there is weak physisorption of N_2 onto the surface relative to the strength of gas molecules with each other; condensation is competitive with adsorption and so very high pressures are needed to achieve significant adsorption.[320,321]

After measurement of a material's adsorption isotherm, it is then possible to apply a suitable model and fit the data to estimate the surface area. This most commonly used

for porous compounds displaying type II or IV isotherms is the Brunauer–Emmett–Teller model (BET), which expanded on the Langmuir adsorption model by accounting for multi-layer adsorption.[323] After recording an isotherm graph of volume of gas adsorbed V against relative pressure, P/P_0, the data is put into BET equation shown below: [320,321]

$$\frac{\frac{P}{P_0}}{V\left(1-\frac{P}{P_0}\right)} = \frac{1}{V_m C} + \frac{C-1}{V_m C}\left(\frac{P}{P_0}\right)$$

V_m is the monolayer volume and C is the BET constant which relates to the strength of interaction between the adsorbate molecules and the surface.[320] This equation is plotted with the left hand side of the equation on the y-axis and P/P_0 on the x-axis. Using the values of the intercept and gradient from the plot and using a suitable linear range of P/P_0, it is possible to obtain the monolayer volume, V_m. Using the volume occupied by each adsorbed molecule v, it is then possible to calculate the number of moles of adsorbed gas. Multiplication by Avogadro's number, N_A and the cross-sectional area each molecule occupies, a, gives the surface area, which is then divided by the mass of the porous material whose surface area is being measured, m_s to give the mass normalised BET surface area shown in the equation below: [320,321]

$$A_{BET} = \frac{V_m N_A a}{v m_s}$$

1.9.5. Particle Size Determination

Determination of particle size by laser diffraction (also called static light scattering) has a dynamic range of hundreds of nm up to a few mm, making it ideal to characterise the size of organic semiconductor particle dispersions which are too large to be measured by dynamic light scattering.[324–326]

When light hits a particle, it can be reflected, refracted, absorbed or re-radiated; together these processes are called scattering. The wavelength of light relative to the size of the particle determines how the light is scattered, which for visible light involving particles within the dynamic range, can best be described by Mie theory. Laser diffraction can be used to estimate the sizes of particles in suspension by irradiating the homogenised sample with a laser of visible light, and an array of detectors pick up the scattered light intensity as a function of scattering angle. Given the laser wavelength and the refractive index of the medium, the scattering pattern of particles of different sizes can be predicted. For spherical samples, as a simplification larger angle scattering takes place for smaller particles. Each detector in the array picks up light for a range of angles. After averaging over a range of measurements, a histogram is produced showing the percent of the volume of sample as a function of each detector angle range which represents a size band. This enables the particle size distribution responsible for the scattering to be calculated.[324–326]

However, this distribution is of limited use for comparing different samples. In order to distil the distribution into a single meaningful particle size metric, an average must be taken. For particulate photocatalysts, it is their interface with electrolyte which is the parameter of interest with respect to their photocatalytic activity. Particle size is an important variable because it determines the external surface area to volume ratio, meaning smaller particles give greater surface area. Therefore the surface weighted mean particle diameter is the most relevant, also called the Sauter mean diameter, D[3,2]. For a collection of differently sized particles, D[3,2] gives the diameter of a particle which if there were as many of it to give the same total volume, would give the same total surface area. In other words, it takes a polydisperse group of particles, and gives the diameter of each particle in a monodisperse sample which would have the same total surface area. It can be calculated using the equation below, where n is the number of particles with diameter d.[327]

$$D[3,2] = \frac{\sum_{i=1}^{n} n_i d_i^3}{\sum_{i=1}^{n} n_i d_i^2}$$

1.9.6. Transient Absorption Spectroscopy (TAS)

Transient absorption spectroscopy works by recording the difference in a material's optical absorption between its ground and excited states. Photoexcitation causes a redistribution in a material's electronic structure which provokes readjustment of its equilibrium nuclear positions. This is also the case as excited states form polarons, as the nuclear positions readjust to accommodate the charge. This has the effect of changing the absorption properties of the excited material. By irradiation of the sample with an excitation 'pump' laser excitation, a portion of the molecules in the sample absorb the light and are promoted to an excited state. This is followed by a 'probe' laser pulse of the same wavelength with a delay period, which is controlled by use of a delay stage. By using this technique at a range of wavelengths, the change in absorption between the pump and probe laser pulses, ΔA is measured as a function of wavelength and delay time.[328]

Changes in absorption are generally attributed to the following mechanisms:

- Ground state bleach. This is due to the pump pulse having already excited electrons from the ground to excited state (typically S_0 to S_1), which depletes the population of electrons in ground state, meaning there is a smaller population able to undergo a ground to excited state transition. This gives rise to a negative ΔA.[328]
- Stimulated emission: This is where perturbation by the probe pulse triggers fluorescence (or phosphorescence) of the excited molecules. Because the probe pulse is not absorbed and there is an added photoemission from the sample, it causes a negative ΔA, though due to Stokes' shift the stimulated emission is shifted in wavelength compared to the probe wavelength.[328]
- Excited state absorption: This is absorption of excited state molecules enabling an excited state transition to an even more excited state (such as $S_1 \rightarrow S_n$) and shows a positive ΔA. The probe pulse is kept weak enough that this transition does not deplete the population of excited state molecules significantly due to excited state absorption.[328]

After measuring the ΔA signal as a function of wavelength at different delay periods between pulse and probe, it can be deconvoluted to identify the species responsible for the signals and their respective lifetimes.

Further tools can be used in TAS to elucidate the signal. For example, through use of electron donating or accepting species in solution it is possible to reductively or oxidatively quench excitons and identify the remaining electron or hole polarons respectively.[95]

Chapter 2. Development and Investigation of Hydrophilic Processible Polymers of Intrinsic Microporosity for Photocatalytic H_2 Production

2.1. Introduction: Current Understanding and Questions to Address

In the previous chapter the topic of external surface area for particulate photocatalysts was addressed. In summary, increasing external surface area by solution processing into nanoparticles is an effective strategy to enhance activity[114,143,281–283,288,329] by reducing the average distance between exciton photogeneration and the interface with electrolyte.[68] Though it should be highlighted that the surfactants required to produce stable nanoparticles in this way can be detrimental to photocatalytic activity. This is likely because surfactants impose an insulating barrier between semiconductor, cocatalyst and electrolyte hindering electron transport out of the particle.[283,288,289]

Meanwhile, methods to increase internal surface areas through the introduction of porosity has often failed to increase activity, calling into question its merit as a design principle.[120,183,252,259,260,330] However the failure of this strategy is complicated by a number of factors. Firstly, the methods used to impart porosity, such as incorporation of branched monomers to form porous network polymers, frequently involve meta linkages[217,259,260] which cause cross conjugation[252,261,262], or sterically demanding ortho linkages[259] which induce dihedral twisting[261] and limit the extent of polymerisation.[217,331] This can reduce conjugation lengths, hindering exciton and polaron transport.[104,236,258] Secondly, it has been highlighted that it is predominantly hydrophobic polymers which seem to show the introduction of porosity failing to lead to an increase in activity.[147] This is because the most common method of measuring porosity is by applying BET surface area calculations to nitrogen adsorption isotherms.[332] Photocatalysis takes place in an aqueous environment and just because N_2 can access pores, it does not follow that electrolyte can. By contrast, for hydrophilic structures which achieve porosity without incorporation of unfavourable linkages, porosity has been shown to be conducive to increased activity.[121,217–220] Nonetheless, analysis of the question of how porosity and hydrophilicity interact in the context of photocatalytic H_2 evolution, where these variables can be controlled without significantly disrupting other factors is lacking, and will be addressed in this chapter.

Another feature this chapter and the following will address is the goal of porosity in conjunction with solution processability, insofar as it can be utilised to form type-II heterojunctions. In the previous chapter, the difficulties associated with forming type-II heterojunctions from insoluble porous network polymers, and the relative ease of forming them from solution non-porous processable polymers were discussed. The materials outlined will endeavour to do both: they will target both solution processability and porosity. The class of material capable of this are polymers of intrinsic microporosity.

2.1.1. Intrinsic Microporosity

Polymer chains generally pack in the solid state to maximise favourable intermolecular interactions and minimise unfavourable voids. Most polymers possess enough conformational flexibility to allow their structures to rearrange in such a way to fill these voids.[333] To prevent this, it is possible to 'lock in' excess free volume in polymers during synthesis through crosslinking where after solvent removal, given the crosslinking is rigid and dense enough, pore collapse is prevented.[334] However the introduction of such crosslinking produces insoluble network polymers.[335]

Another design to inhibit polymer packing is the adoption of intrinsic microporosity. This concept applied to polymers was first developed in the 1990s by Budd and McKeown,[335] and was defined as "a continuous network of interconnected intermolecular voids, which forms as a direct consequence of the shape and rigidity of the component macromolecules".[334] Micropores are defined as smaller than 2 nm in width, with macropores above 50 nm and mesopores are anything in between.[323] The porosity is said to be *intrinsic* rather than *extrinsic* because it doesn't rely on the use of templating effects, rapid cooling or solvent removal.[336] The design of such materials depends on the rigid backbones of their constituent polymers which lack rotational freedom, possessing 'awkward' geometries which cannot pack efficiently.[333] Crucially, it was found that intrinsic microporosity can exist alongside solubility.[337,338] Indeed solubility is likely assisted by the inhibited packing which

obstructs close intermolecular cohesive interactions.[335,339,340] An early example **PIM-1** is depicted in Figure 31, featuring its spirocyclic orthogonal group which precludes close packing.[341] Alongside is a two-dimensional diagram of porosity in crystalline (a and b) and amorphous (c and d) materials, where c uses crosslinking and d doesn't, being a representation of an intrinsically microporous polymer. [341]

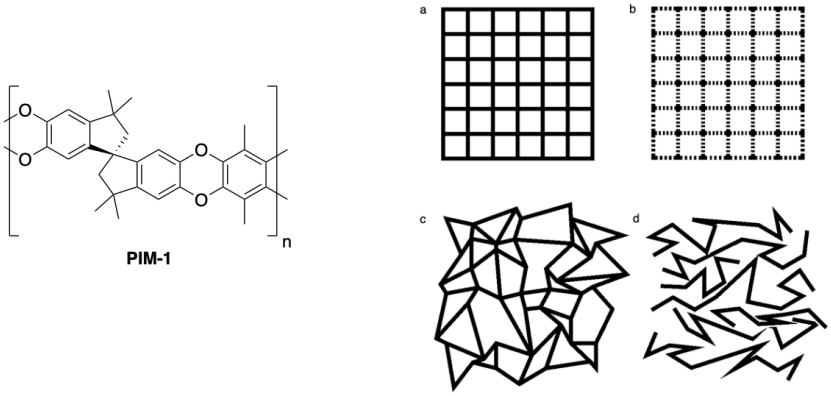

Figure 31. Left: PIM-1. Right: two dimensional representations of porous structures. a. crystalline covalent framework structure (such as a covalent organic frameworks), b. crystalline non-covalent framework structure (such as metal organic frameworks), c. amorphous crosslinked network covalent structure (such as conjugated microporous polymers), d. amorphous non-network non-crosslinked depiction of polymers of intrinsic microporosity, showing porosity without networks. Reproduced from reference under creative commons attribution 4.0 license.[341]

While many examples of intrinsically microporous polymers are non-conjugated, the application of intrinsic microporosity to conjugated polymers is a natural fit, owing to their innately rigid sp^2 hybridised units. Notwithstanding an ambiguous example of a conjugated microporous polymer of intrinsic microporosity,[342] the first well defined series was reported in 2014.[343] This study included two polymer series where the molecular weight of the same repeat unit was varied. Intriguingly it showed surface area to increase with molecular weight, as well as the inclusion of tert-butyl promoting high surface areas.[343] The use of tert-butyl groups has been shown to inhibit π-π interactions between neighbouring molecules and improve stability,[342,344–346] explaining its porosity promoting effect in the series. Another notable feature was the dependence of the porosity on method of precipitation. When dissolved in a 'good' solvent and added to antisolvent, the rapidly precipitated polymer exhibited high nitrogen sorption BET surface areas. However when drop cast or allowed to dry slowly from solution, the surface area can be significantly reduced.[343,347,348] However, none

of these materials were tested for photocatalysis, with reports of solution processable porous polymers for H_2 evolution photocatalysis being relatively few, the most common application for these polymers being membrane separation and gas storage.[333] Novel, polymers for this purpose will be developed in this and the subsequent chapter.

2.1.2. Spirofluorene Motif

Monomers based on the spirofluorene motif were identified as a promising target from which to develop conjugated polymers of intrinsic microporosity. Spiro groups involve two ring systems linked orthogonally by a shared sp^3-hybridised carbon atom.[349]

Such a spiro group between conjugated systems was first reported in 1930 with **spiro-bifluorene** (Figure 32), the simplest example of an sp^3 carbon being bonded on all four sites to aromatic units,[349] and has since been widely studied owing to its intriguing properties. Due to its sterically demanding nature, π-π stacking is hindered for aromatic spiro systems, reducing self-quenching in the solid state leading to enhanced electroluminescence quantum yields, and mean these materials find extensive application in organic light emitting diodes.[350–355] When employed in charge transport materials,[356,357] it was found that linking two aromatic systems via a spiro linkage could raise the glass transition temperature of small molecules by hindering cohesive intermolecular interactions;[350] this endowed greater morphological stability and improved charge transport by keeping the material uniformly amorphous, preventing grain boundaries from forming between crystalline domains.[340] In addition, small molecules involving spiro linkages exhibit enhanced solubility,[340] which has been utilised in organic photovoltaics.[358,359]

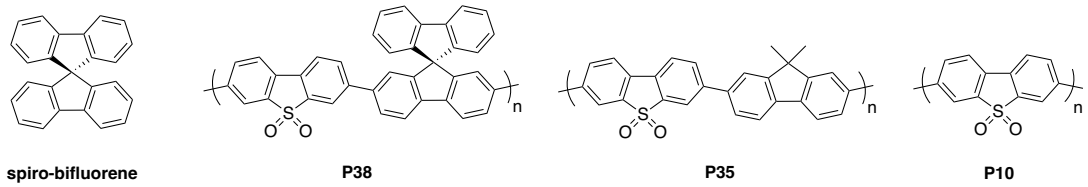

Figure 32. Spiro-bifluorene (left) [349] and insoluble intrinsically microporous polymers, adapted from references [218]

More pertinently for this work, the incorporation of this rigid and sterically demanding motif into conjugated polymers has the ability to impart intrinsic microporosity, while also allowing conjugation along the fluorene units of the polymer backbone.[218] It has previously been employed as a copolymer with dibenzo[b,d]thiophene sulfone **P38**, (Figure 32), to form an intrinsically microporous polymer, with surface area of 352 g m^{-2}. This displayed a higher photocatalytic activity than the non-porous analogue made with dimethyl fluorene **P35** and even outperforming the highly active non-porous **P10**.[218] Nonetheless, none of these polymers were soluble, so in-depth characterisation of their properties was not possible and their potential incorporation into heterojunctions was limited.

2.2. Microporosity Inducing Monomer Design

The spirofluorene motif was taken as a starting point for monomer design owing to its ability to impart intrinsic microporosity while maintaining conjugation along the backbone. It was modified by addition of tert-butyl groups on the fluorene units to add steric bulk promoting porosity and to increase solubility. The fused ring system was also extended to form spirofluorene flanked indacenodithiophene (**Sp-IDT**) and indenofluorene (**Sp-IF**) as target monomers, shown in figure 33. **Sp-IF** extends the planar fused ring character of fluorene (F), and possesses orthogonal tert-butyl substituted spirofluorene arms on either side, which was expected to further enhance the intrinsic microporosity over a single spirofluorene unit.

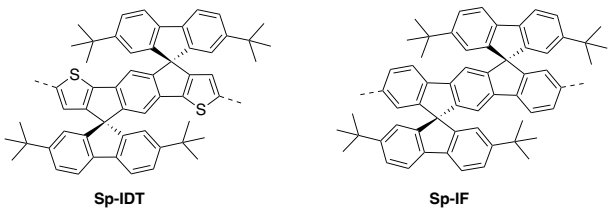

Figure 33. Target monomers for soluble polymers of intrinsic microporosity

With **Sp-IDT** this is also the case, while the flanking thiophene units served several functions. Thiophene is more electron rich than benzene because it has 6 π-electrons shared over 5 atoms, as opposed to 6 atoms. When paired with suitable electron deficient comonomers, this can enable narrowing of the optical bandgap due to push-pull molecular orbital hybridisation.[67] The narrowing of the bandgap is further assisted by thiophene's smaller biaryl twisting angle compared to benzene, whereby it adopts a more planar backbone with improved conjugation.[107] This is due to a reduced steric clash of its ortho-hydrogen in comparison to benzene, as well as its lower aromaticity, The latter factor increases the contribution of the quinoidal resonance form involving more double bond character at the biaryl linkage to the structure.[360]

2.3. Photoreactor and Measurement Conditions

To measure the amount of H_2 evolved by photocatalysts during photocatalytic testing, a bespoke setup was built. Unless stated otherwise, the testing conditions throughout this thesis were conducted as described in this section.

For photocatalysis measurements, typically 5 mg of organic semiconductor was sonicated using a probe sonicator at 200 W in 10 mL NMP for 2 minutes to either disperse or dissolve the semiconductor. This was subsequently added via pipette into an aqueous solution of ascorbic acid and H_2PtCl_6 in a sonicator bath (shown in Figure 34), to give 3 wt % Pt loading assuming quantitate yield. This procedure resembles nanoprecipitation whereby material is dissolved in water miscible solvent then precipitated into water to produce nanoparticles.[281–283,288] However, here the NMP was left in the mixture given its low volatility. Control reactions using NMP without semiconductor showed no H_2 production, indicating that NMP decomposition under light was not a source of H_2, as has also been reported.[264] Instead, the presence of polar organic solvent allows the polymer particles to be dispersed under high powered sonication. Cosolvent in the aqueous mixture also hinders the polymer particles' subsequent aggregation,[264,361,362] enabling them to absorb incident light more effectively. The use of such cosolvents is common in photocatalytic material

testing,[92,250,255,363] and the use of NMP in particular was chosen due to its reported high performance as a cosolvent for insoluble conjugated polymers.[255,264,364]

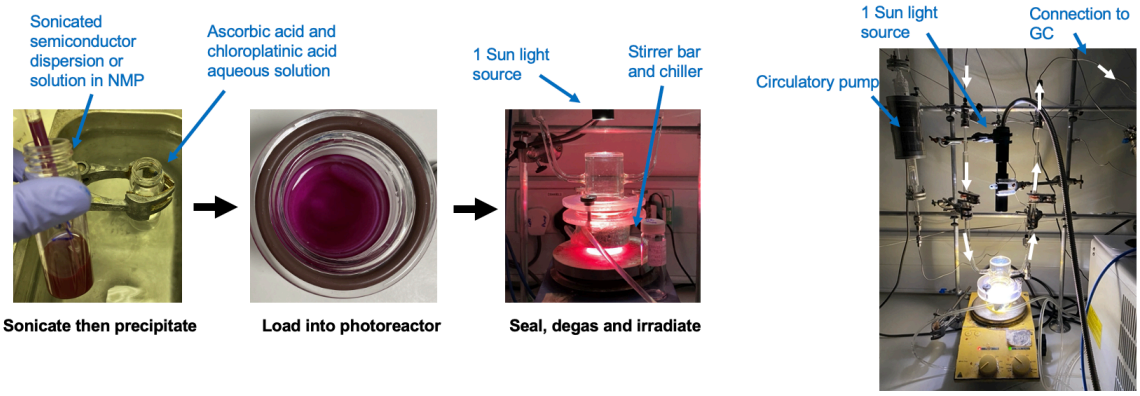

Figure 34. Sample preparation and testing setup for photocatalysis

Once prepared, this photocatalysis mixture was added into a glass cylindrical reactor cell and clamped to create an airtight seal. The arms on either side of the reactor cell were connected to a circulatory pump in a closed loop with a gas chromatograph (GC). The purpose of the circulatory pump was to gently circulate the gas through the tubing to ensure even distribution throughout the headspace, given diffusion was inadequate. A Xe lamp solar simulator fitted with a visible light 390-740 mirror module and an AM 1.5 filter calibrated to 1 Sun using a reference cell was then directed onto the photoreactor cell. The purpose of this was to provide a known and consistent light source which could mimic the solar spectrum. Its spectral output is shown below in Figure 35.

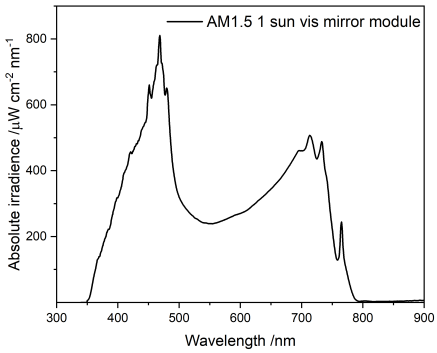

Figure 35. Spectral output in absolute irradiance for Xe light source for photocatalysis experiments

Once in place, the sample was put under vacuum and purged with argon twice, then left at 450-550 mbar argon atmosphere. Ar was chosen to remove O_2 from the system which could cause competing reactions. The measurement was begun once the light is switched on, and the GC was programmed to inject a sample of headspace gas every hour, over the course of 10 hours. During the first stage of illumination, in situ photodeposition takes place. This is a process whereby Pt^{4+} ions from the H_2PtCl_6 are reduced in situ by photogenerated electrons from the semiconductor, causing them to precipitate as Pt metal nanoclusters on the semiconductor. The concomitant holes are quenched by sacrificial electron donor ascorbic acid,[109] as shown by the simplified diagram in figure 36.

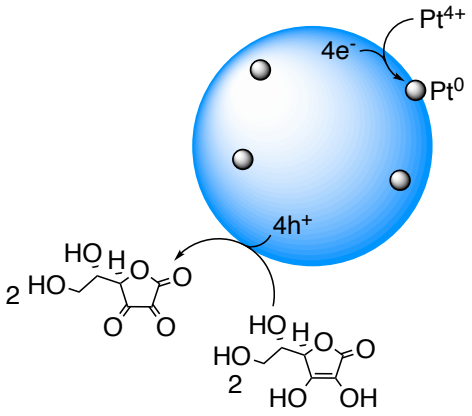

Figure 36. Scheme of photodeposition from H_2PtCl_6 in presence of light and ascorbic acid on organic semiconductor

Following photodeposition, the cumulative moles of H_2 produced are measured.

2.4. Synthesis of Spirofluorene Monomers

2.4.1. Sp-IDT Monomer Synthesis

Indacenodithiophene (IDT) is a common unit in organic electronics.[107] **Sp-IDT** was synthesised by following an adapted literature procedure for IDT (Figure 37), until intermediate **4**.[365]

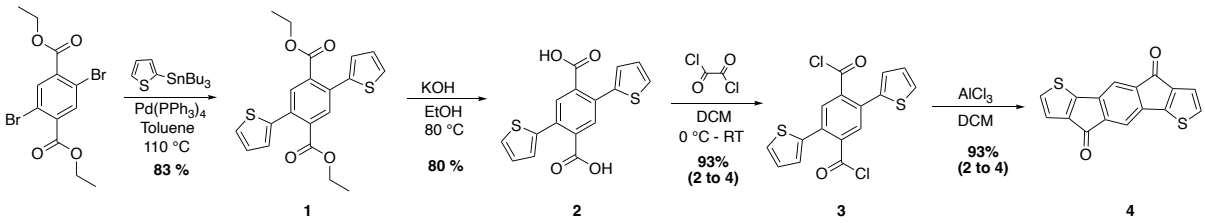

*Figure 37. Scheme showing synthesis of **4***

The first step was Stille coupling to install flanking thiophene units to commercially available 1,4-diethyl-2,5-dibromo-1,4-benzenedicarboxylate. Stille coupling is a powerful transition metal cross coupling reaction, enabling the formation of sp^2 hybridised C-C bonds, with its mechanism shown in Figure 38 below.[366–369]

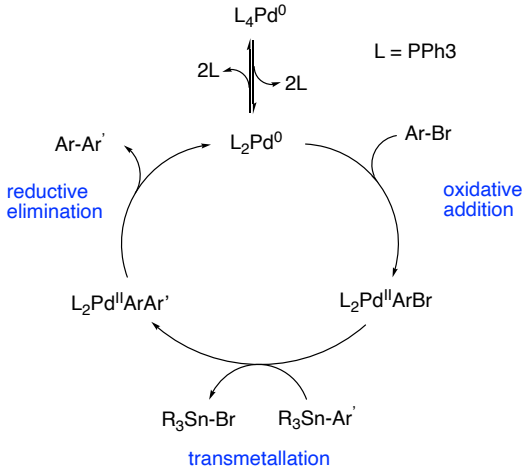

Figure 38. Stille coupling catalytic cycle[366–369]

The analogous Suzuki coupling alternative reaction using thiophene-2-boronic acid was also attempted due to its significantly lower toxicity. This was successful but achieved a much lower yield of 43% compared to 83 % for the Stille coupling. The reason for the lower yield of the Suzuki coupling is likely because of the electron rich character of thiophene promoting protodeboronation. This is where under acidic or basic conditions the borate C-B bond cleaves, substituting the boronic acid or ester with a proton from the solvent.[370] The use of boronic acid pinacol esters over acids can ameliorate this problem,[371] nonetheless protodeboronation is typically faster on electron rich aryl halides.[372]

The next step in the scheme shown in Figure 37 was basic ester hydrolysis of **1** to generate **2**. After this, oxalyl chloride and catalytic DMF were used to transform the carboxylic acid functional groups on **2** to acyl chlorides, driven by release of gaseous side products to give acyl chloride intermediate **3** which was used directly in the next step. The mechanism proceeds via a Vilsmeier-Haack type salt which is attacked by the carboxylic acid to give an acid chloride as shown in Figure 39.[373,374] Finally an intramolecular Friedel-Crafts ring closure was triggered by addition of fresh anhydrous solvent and aluminium trichloride to give the intensely dark-blue insoluble powder **4**.

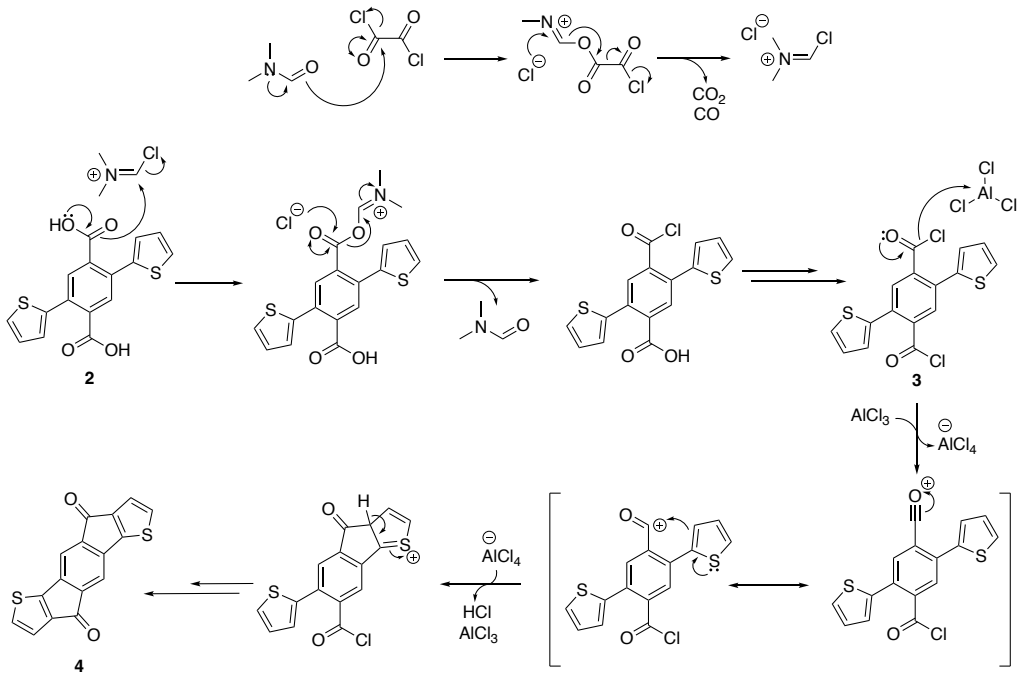

Figure 39. Mechanism for formation of 4

To enable attachment of the tert-butyl substituted spirofluorene units to this IDT core, 4,4′-bis(1,1-dimethylethyl)-1,1′-biphenyl was brominated at the 2-position to produce **5**, following a literature procedure, shown in Figure 40.[375] This directed its subsequent lithiation, after which it was quenched with the dicarbonyl **4** to form an alcohol intermediate which was not purified. With the help of a Lewis acid catalyst, this subsequently underwent ring closure to produce **Sp-IDT**, in a similar fashion to another spirofluorene small molecules from literature.[376]

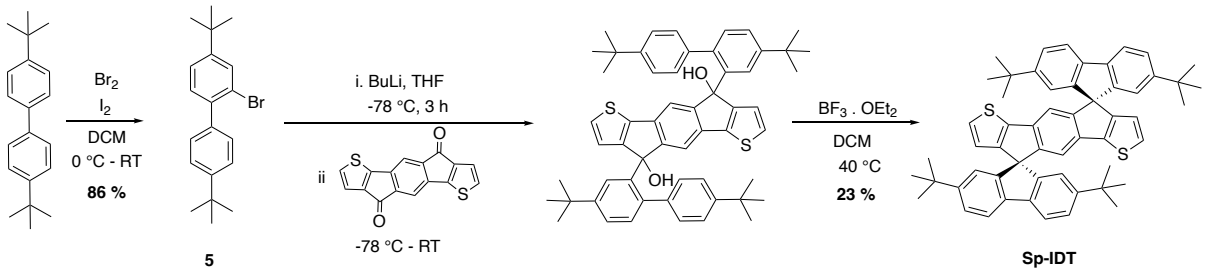

*Figure 40. Scheme for the synthesis of **Sp-IDT** before bromination or stannylation*

Finally, to give **Sp-IDT** reactive handles for polymerisation, it was distannylated via lithiation, followed by a trimethyltin chloride quench. In addition, it was also dibrominated using N-bromo succinimide. This gave more flexibility in terms of potential comonomer partners. These monomers are shown in Figure 41.

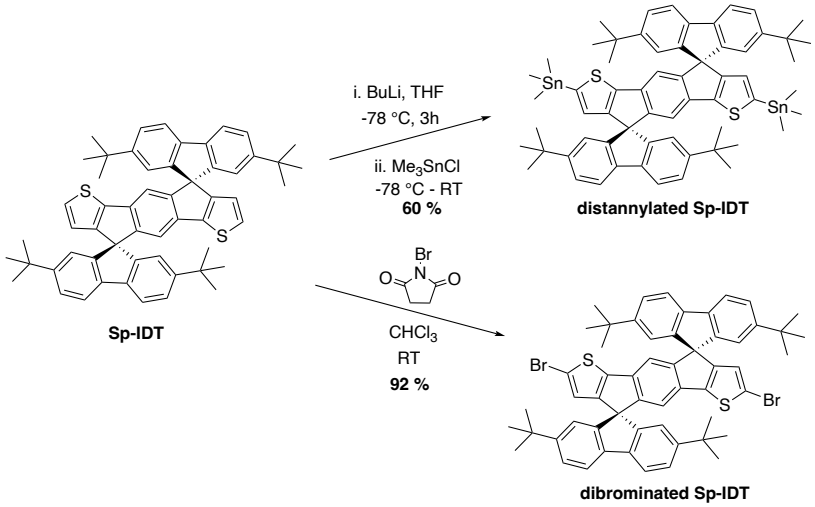

*Figure 41. **Sp-IDT** distannylation and dibromination*

2.4.2. Sp-IF Monomer Synthesis

A similar strategy was adopted for the synthesis of **Sp-IF,** which employed Suzuki coupling to build and elongated aromatic core in **6**. This underwent intramolecular ring closing acylation using concentrated sulfuric acid as solvent and catalyst in a procedure adapted from literature to give the bright pink insoluble powder **7**, shown in figure 42.[377]

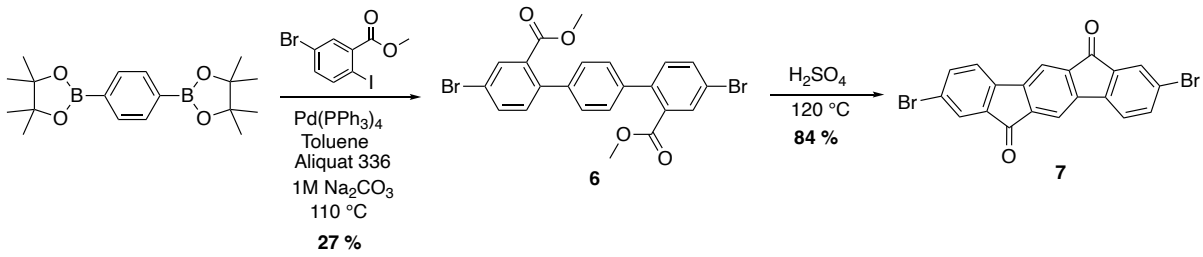

Figure 42. Scheme for the synthesis of 7

This diketone **7** was then used to quench lithiated **5**, followed by acid catalysed ring closure, following a literature procedure,[378] to give dibrominated **Sp-IF** shown in figure 43.

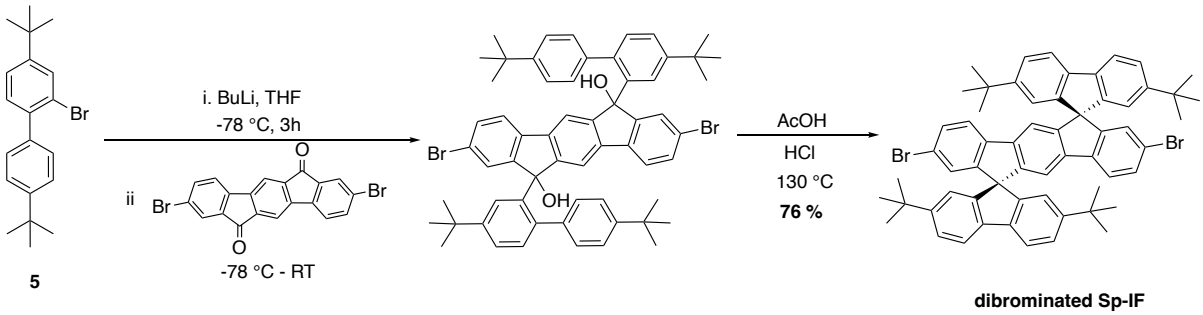

Figure 43. Scheme for the synthesis of dibrominated **Sp-IF**

Distannylation of **Sp-IF** was attempted numerous times. It was unsuccessful by lithiation in THF owing to the insolubility of the starting material. In an attempt to help solubilise it, the starting material was dissolved in a small amount of anhydrous hot toluene, before addition of THF, cooling and addition of ^{n}BuLi. However, this still recovered brominated starting material, indicating a failed lithiation. Miyaura borylation was also unsuccessful in producing a pure borylated monomer. Finally, a Pd catalysed stannylation using bis trimethyltin was attempted. After several doses of catalyst over 3 days this eventually showed product in the NMR. However, its purification proved challenging owing to decomposition, failing to lead to a monomer pure enough for polymerisation.

2.5. First Polymer Attempt: Sp-IDT-BT

The first comonomer unit with which to react the spiro monomers was 2,1,3-benzothiadiazole (**BT**), which was commercially available in both dibrominated and boronic acid pinnacol ester forms. The sp^3 bridges between aromatic units in IDT enforce planarity through covalent bonds, while in IDT-BT, non-covalent interactions between the S of IDT and the protruding H of the BT unit further favour planarity. This results in an extremely small dihedral angle between the aromatic units and a low degree of energetic disorder, resulting in excellent intramolecular charge transport properties.[106,107,379] Given that exciton and polaron transport via intermolecular hopping would be expected to be somewhat impaired for conjugated intrinsically microporous polymers with restricted π-π interactions, using backbones with favourable intramolecular exciton and polaron transport properties was desirable. In addition, BT has an internal dipole which facilitate stronger interactions with water.[380]

The first polymerisation was conducted by reacting dibrominated **Sp-IDT** with commercially available bis-boronic acid pinacol ester of **BT** under Suzuki polymerisation conditions (Figure 44). However, this failed to produce a polymer, given GPC indicated oligomeric molecular weight of 3 repeat units. Changing to homogeneous reaction conditions using DMF as solvent with $Pd(PPh_3)_4$ as catalyst offered no improvement. In general, for copolymerisations it is favourable to make the aryl halide monomer the more electron deficient of the monomer pair, and the aryl boronic ester more electron rich. This is because oxidative addition is faster for electron deficient aryl halides and transmetallation is faster for electron rich aryl boronic esters.[381] The reason for the disappointing polymerisations of the attempted species could therefore be due to the failure to adhere to this principle. Suzuki polymerisations demand a balance between reactivity and stability: the aryl boronic ester should be electron rich enough to be reactive for transmetallation, but not so electron rich that protodeboronation becomes a problem.

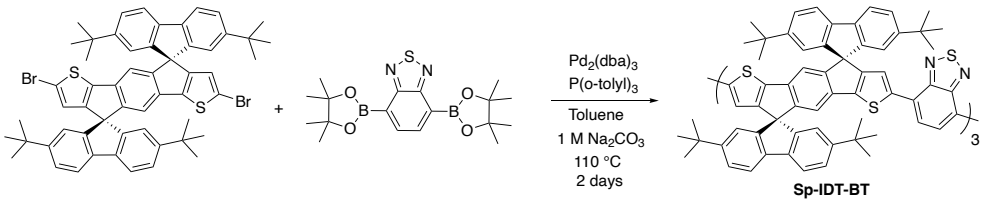

*Figure 44. Low molecular weight oligomer of **Sp-IDT-BT** synthesised by Suzuki polymerisation*

Instead, the distannylated Sp-IDT was copolymerised with dibrominated BT as shown in Figure 45, producing an insoluble blue powder. During Soxhlet purification it couldn't be dissolved in boiling chloroform or chlorobenzene. It is likely that under these conditions, the polymerisation was successful, however at molecular weights typical of polymers rather than oligomers, it is insoluble.

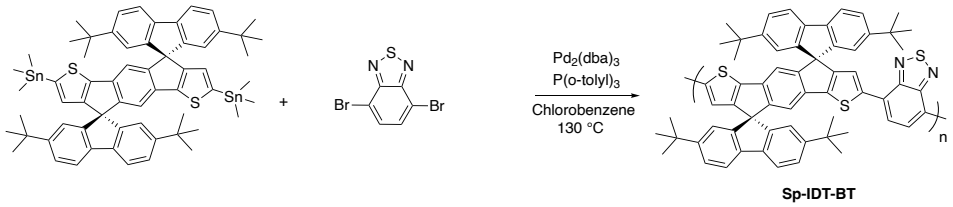

*Figure 45. Synthesis of **Sp-IDT-BT** by Stille polymerisation*

Nonetheless the surface area of this insoluble polymer was characterised by measurement of a N_2 adsorption isotherm, shown in figure 46.

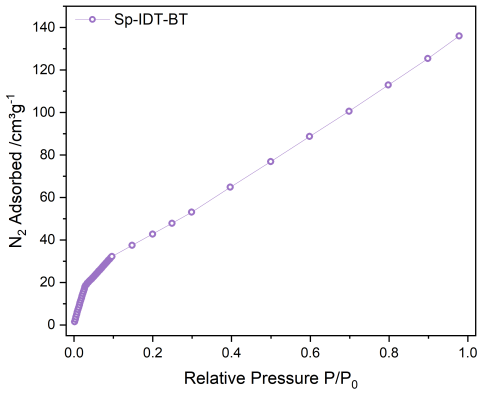

*Figure 46. N_2 adsorption isotherm of **Sp-IDT-BT***

The isotherm showed reasonable porous character, giving a BET surface area estimate of 385 m^2 g^{-1}. This gave confidence in the use of this spiro monomer to

produce porous polymers. However, the assumption that the tert-butyl groups could endow sufficient solubility to counteract the rigid elongated aromatic structure was clearly too optimistic.

The photocatalytic performance of **Sp-IDT-BT** was measured using 3 wt % Pt loading conditions with 0.2 M ascorbic acid and NMP to help it disperse. However, it showed negligible H_2 production, of just over 1 μmol in 10 h. This is not entirely surprising given that literature shows IDT-BT bearing linear alkyl side chains to give very low photocatalytic activity inside miniemulsion nanoparticles, when tested as a single component. Though its performance improved considerably when solution processed into donor acceptor bulk type-II heterojunction nanoparticles.[302] Nonetheless, owing to the insolubility of **Sp-IDT-BT**, a means of blending it with another semiconductor with offset energy levels was precluded, so further work was not pursued using **BT** monomers.

2.6 Comonomer Design: Silyl Ether Protection Strategy

Following this first polymer attempt, it was clear greater consideration of the comonomer design was required. It was concluded some solubilising groups would be needed on the comonomer to make solution processible polymers. However, this raised the problem that adding long flexible side chains to increase the solubility would also be expected to decrease the porosity in a 'pore blocking' effect that has been reported in other porous materials.[382,383] In addition, it was desirable to have hydrophilic groups on the copolymer for the reasons discussed in the previous chapter, such as alcohols or amines to facilitate 'pore wetting'.

With these considerations in mind, a strategy was devised to design comonomers bearing hydrophilic groups, and protecting groups could be attached to temporarily aid solubility during polymerisation and processing. After polymerisation, the protecting groups would be removed to reveal more hydrophilic polymers free of long side chains which would enable porosity.

Protecting groups are powerful tools in organic synthesis. For molecules with many different functional groups present it can become difficult to find reaction conditions which selectively transform the desired functional group while leaving the others intact. Protecting groups temporarily ‘cover up’ functional groups that the chemist does not want to react, and subsequently ‘uncover’ them after the transformation of the target functional group is complete. They are selected to be unreactive during the reaction conditions, but their removal should be possible under specific orthogonal conditions.[56] While protecting groups are most commonly used to solve this chemoselectivity problem, their installation can also have the effect of solubilising the protected molecule. It is possible to modify the protecting group to further enhance this effect, such as adding longer alkyl groups so long as it doesn’t excessively hinder its ability to be deprotected.

To this end, silyl ethers were selected as alcohol protecting groups on the target comonomer. When using protecting groups for small molecule chemistry, it is not of acute importance if the protection and deprotection steps are not totally quantitative, as unreacted material can be removed during purification. However, when conducting post-polymerisation reactions, quantitate reactions are essential as unreacted repeat units on the polymer cannot be removed. Silyl ether protecting groups are attractive because they are stable under basic conditions,[384] permitting stannylation using organolithium during monomer synthesis. They can also be easily and fully deprotected in the presence of fluoride ions in a quantitate manner shown in Figure 47. Fluoride is commonly supplied in the form of tetrabutyl ammonium fluoride (TBAF), whose counterion enables solubility in organic solvents.

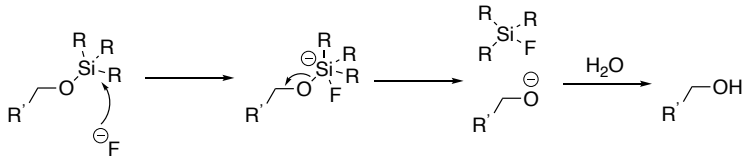

Figure 47. Deprotection of sily ethers using F⁻

The susceptibility of silyl ethers to deprotection is related to the steric bulk of their alkyl groups. Tert-butyl dimethyl silyl was chosen as a target due to its intermediate stability:

enabling survival in the synthetic pathways and purification techniques required to synthesise the monomer and polymers, while being labile enough to be removed from the polymer at the end.[385]

2.7. Alkoxy Benzodithiophene (BDT) Polymer

2.7.1. BDT-Si Monomer Synthesis

The first silyl ether protected target monomer was distannylated tert-butyl dimethyl ether benzodithiophene (**BDT-Si**), shown in Figure 48. This was attractive owing to the phenolic alcohols attached to its core, meaning it could be protected with tert-butyl dimethyl silyl groups to assist solubility, then be deprotected after polymerisation to leave alcohol groups, facilitating close proximity of water to the backbone.

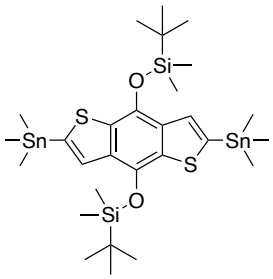

Figure 48. BDT-Si target monomer

This monomer was synthesised by reduction of commercially available benzo[1,2-b:4,5-b′]dithiophene-4,8-dione to give **8** using an adapted literature procedure,[386] which was subsequently protected using tert-butyldimethylsilyl chloride to produce **9**.

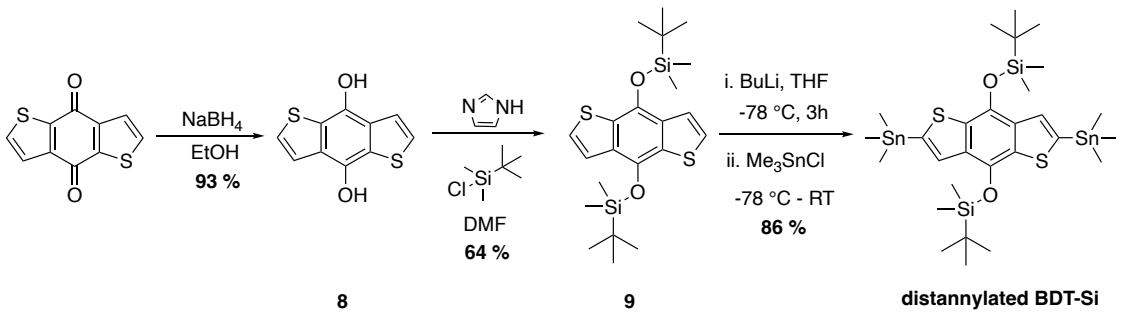

Figure 49. Synthesis of distannylated BDT-Si

A proposed mechanism for the reduction of benzo[1,2-b:4,5-b′]dithiophene-4,8-dione and installation of the tert-butyldimethylsilyl ether protecting group is shown in Figure 50. Here imidazole is thought to act as a catalyst and base to remove the excess protons,[384] though it has also been claimed the solvent DMF can play a catalytic role.[387]

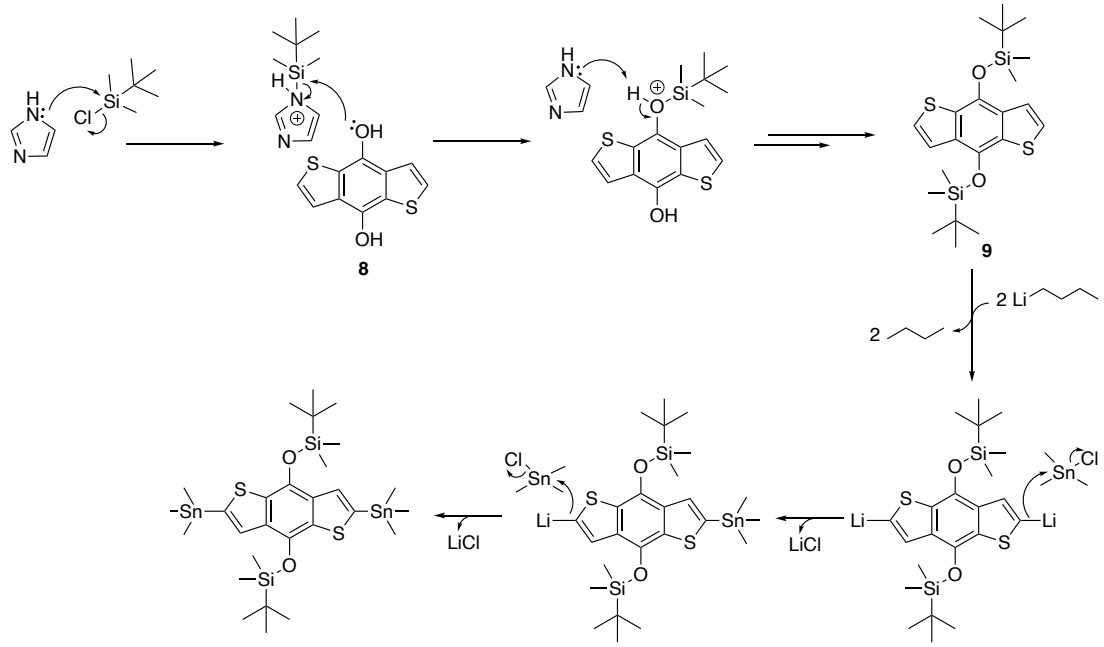

*Figure 50. Mechanism for the synthesis of distannylated **BDT-Si***

2.7.1. Sp-IF-BDT-Si Synthesis and Optoelectronic Properties

The **BDT-Si** monomer was polymerised under Stille conditions with the **Sp-IF** to produce a yellow polymer. GPC estimated average molecular weight as 5 repeat units.

During Soxhlet purification, it was found that chlorobenzene gave the best solubility and was able to recover the most amount of soluble material at the end.

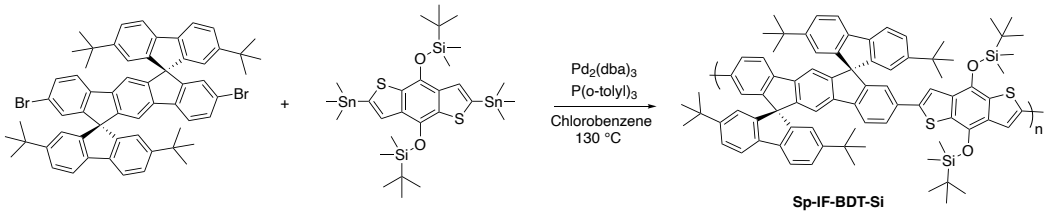

*Figure 51. Polymerisation of **Sp-IF** and **BDT-Si** to form **Sp-IF-BDT-Si***

Its synthesis was subsequently repeated to attempt to achieve a higher molecular weight, however the yield was low because a lot of insoluble material remained in the Soxhlet thimble. This indicated that the 5 repeat units achieved by the first attempt reached the maximum polymer length that is soluble in common organic solvents. Therefore, it was not polymerisation conditions limiting molecular weight but solubility, owing to the insufficiently solubilising tert-butyldimethyl silyl ether side protecting groups.

Nonetheless it was soluble enough in chlorobenzene to spin coat films, and its optoelectronic properties were characterised by UV-vis spectroscopy and PESA (Figure 52). By adding the optical bandgap from UV-vis to the HOMO estimate from PESA, the LUMO energy was estimated. It should be noted that this this LUMO value is an underestimate of LUMO depth (as explained in the previous chapter). Nonetheless, so long as the energy levels for semiconductors in a series are measured using the same method, comparison is reasonable.

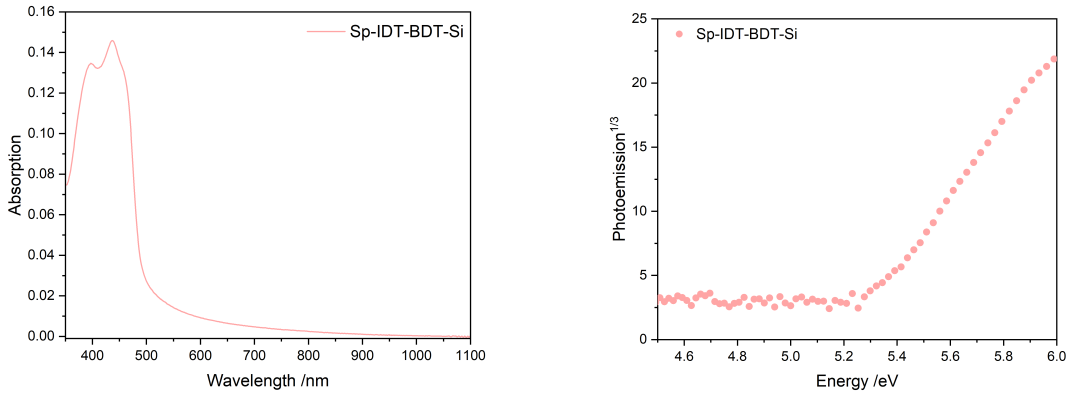

Figure 52. Sp-IF-BDT-Si thin film UV-vis spectrum (left) and PESA (right)

The properties of Sp-IF-BDT-Si are summarised in the table below.

Absorption Onset / nm	Absorption Peak(s) /nm	Optical Bandgap /eV	HOMO (PESA) /eV	LUMO (PESA+ E_g) /eV	M_N /gmol^{-1}	M_W /g mol^{-1}	Poly-dispersity
494	398, 437	2.5	-5.3	-2.8	5894	6920	1.18

2.7.1. Porosity of Sp-IF-BDT-Si

The N_2 sorption isotherm was measured (Figure 53), and BET analysis calcualted a surface area of 417 $m^2\ g^{-1}$. This significant microporous character, even while the silyl groups were attached, was likely due to the rigid and inflexible nature of the tert-butyl dimethyl silyl groups.

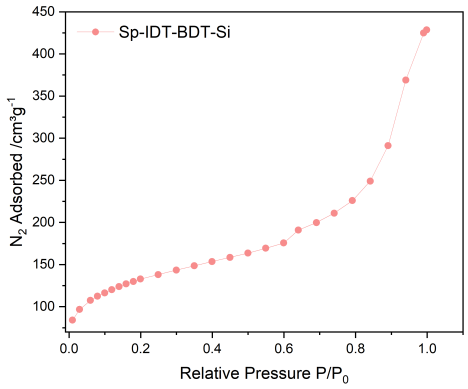

*Figure 53. Left: N_2 adsorption isotherm for **Sp-IF-BDT-Si***

2.7.2. Photocatalytic Activity of Sp-IF-BDT-Si

Sp-IF-BDT-Si was then tested for photocatalysis in a similar manner to **Sp-IDT-BT** using NMP as a dispersant. It showed fairly low H_2 production of 2.09 μmol h^{-1}, however it was thought that owing to the electron rich nature of the polymer, there may have been insufficient driving force for the ascorbic acid oxidation half-reaction.

If ascorbic acid oxidaiton is taken as a two electron proton coupled reaction as has been done elsewhere in literature,[114,142,143] and depicted in Figure 54, increasing pH should make the redox potential for asocrbic acid oxidation more negative (and the absolute energy more positive). Therefore increasing pH this should make asocrbic acid oxidation 'easier', assuming the HOMO and LUMO of the polymer stay the same. This relationship is supported by a computationally modelled Pourbaix diagram for ascorbic acid oxidaiton.[388]

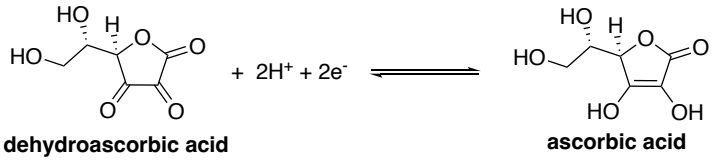

Figure 54. Ascorbic acid redox equation

As explained in the previous chapter, by taking the redox potential for ascorbic acid oxidation at pH 2.6 to be +0.25 V (SHE),[142] this equates to -4.69 eV. Application of the Nernst equation puts the redox potential for proton reduction at pH 2.6 to be -0.15 V (SHE), which equates to -4.29 eV.

As can be seen from the band positions in Figure 55 (left), there is a much larger driving force for the proton reduction half-reaction compared to ascorbic acid oxidation. In photocatalysis, the rates of reduction and oxidation must be matched, and increasing the rate of the limiting half-reaction would be expected to increase the overall rate. In order to investigate the effect of pH on the rate of photocatalysis, the testing solution was neutralised using sodium hydroxide solution. A pH meter was later used to accurately determine the pH of the ascorbic acid sodium hydroxide solution in

the absence of polymer, showing it to be 2.79 without the sodium hydroxide, and 6.43 with the sodium hydroxide present (these conditions will be referred to as 'acidic' or 'neutral'). Both acid and neutral solutions are 0.2 M with respect to ascorbic acid, though with 29 vol % NMP present in both. Aqueous 0.2 M solution of ascorbic acid has been reported to be pH 2.[302] the discrepancy can be explained by the slightly basic nature of NMP, with its slight pH raising effect having been previously reported.[255] In order to see how pH affects the redox potentials for both half-reactions, the Nernst equation was applied to a pH of 6.43, giving a proton reduction protential of -0.38 V (SHE), equating to -4.06 eV. If the same Pourbaix gradient is assumed for the ascorbic acid reaction, this increase in pH would be expected to shift the energy for ascorbic acid oxidation to -4.46 eV. These effects are plotted in Figure 55 (left), illustrating the expected increased driving force for oxidation and decreased driving force for reduction as pH is increased.

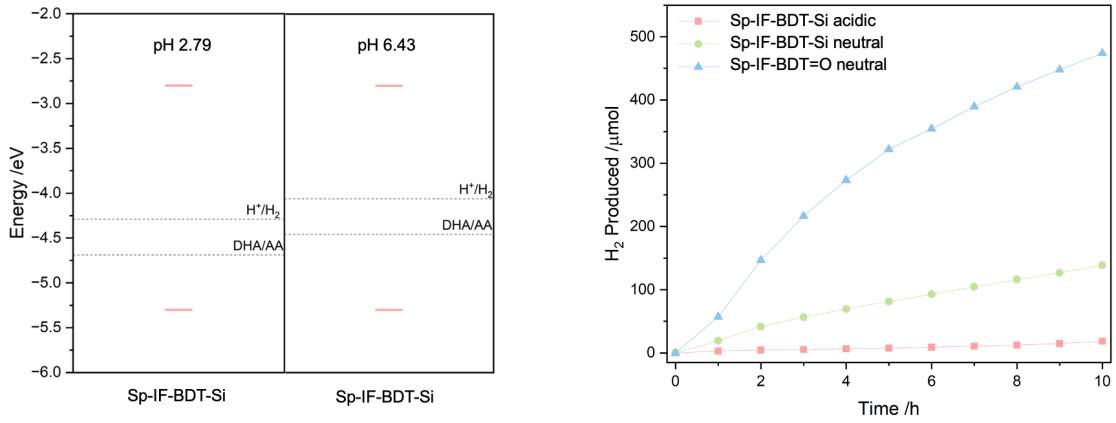

*Figure 55. Left: FMOs of **Sp-IF-BDT-Si** against the expected redox potentials for proton reduction and ascorbic acid oxidation. Right: Photocatalytic activity of **Sp-IF-BDT-Si** under acidic and neutral conditions, as well as its activity after TBAF treatment under neutral conditions*

When the pH was increased as described, **Sp-IF-BDT-Si** showed an increase in average H_2 production rate from 2.09 to 11.40 μmol h^{-1} (Figure 55 right). This is consistent with the idea that the oxidation half-reaction is the rate limiting step.

To deprotect **Sp-IF-BDT-Si**, a portion was next treated with TBAF by addition to a 0.2 M TBAF solution in THF, sonicating and stirring overnight. The suspension was then

poured into methanol, filtered, and washed to remove excess TBAF and silyl fluoride side product. The TBAF treated polymer was no longer soluble in any solvent, and it was also observed to change from yellow to slightly red in colour. It was tested for photocatalytic activity under the same conditions as the neutralised **Sp-IF-BDT-Si** test, and showed a signigicantly higher rate of photocatalysis of 30.58 μmol h^{-1} when tested at neutral pH as shown in Figure 55 (right). **Sp-IF-BDT-Si** shows a tripling in rate after treatment with TBAF.

It was expected that the deprotected polymer contained phenolic alcohols, whose increased hydrophilicity could be accounting for the greater activity. However, the polymers before and after deprotection were too insoluble to adequately tell by NMR. In lieu of this, intermediate **9** (containing the same tert-butyl dimethyl silyl unit) was subjected to the same deprotection conditions as the polymer. It immediately turned bright green then yellow-brown and precipitated. However, d-DMSO NMR of this washed deprotected monomer failed to show the expected alcohol **8**. Instead, its NMR spectrum corresponded to the quinoidal ketone precursor benzo[1,2-b:4,5-b′]dithiophene-4,8-dione, as shown in Figure 56 (left).

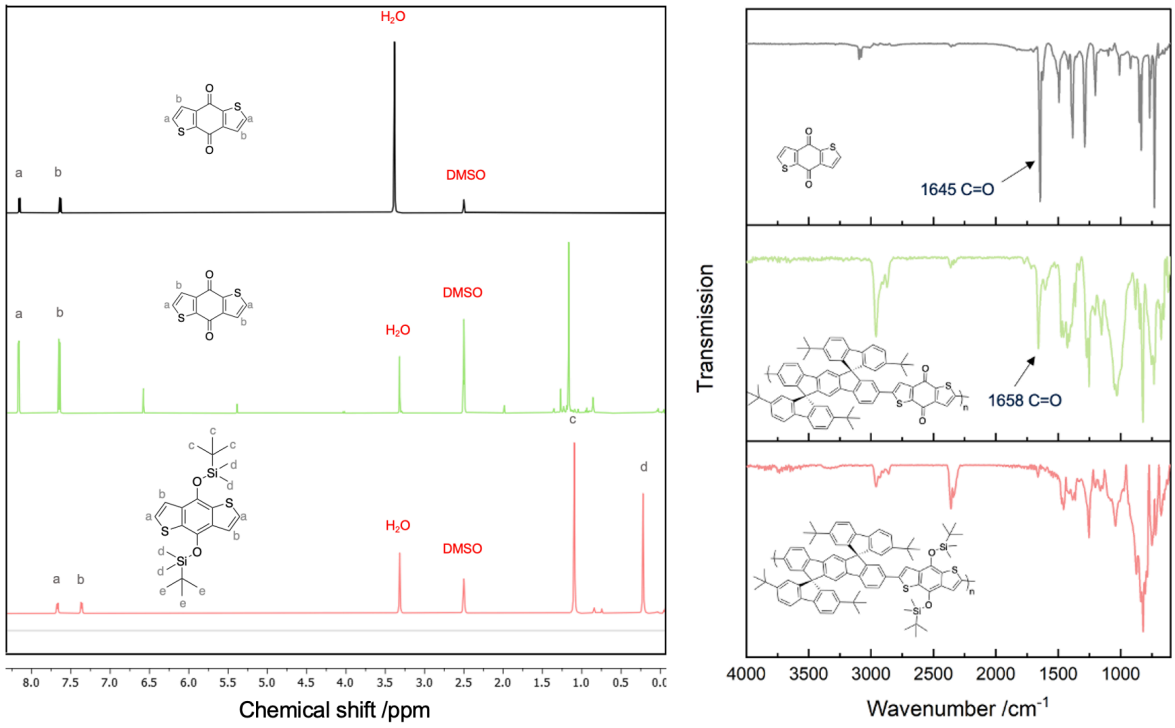

*Figure 56. Left: NMR spectra of benzo[1,2-b:4,5-b′]dithiophene-4,8-dione (top), product of TBAF treatment of **9** (middle) and **9** (bottom). Right: IR spectra of benzo[1,2-b:4,5-b′]dithiophene-4,8-dione (top), TBAF treated **Sp-IF-BDT-Si** (middle) and **Sp-IF-BDT-Si** (bottom)*

To further investigate, IR spectroscopy was conducted on **Sp-IF-BDT-Si** before and after TBAF treatment (Figure 56 right). Rather than showing an expected O-H stretch indicative of an alcohol, it showed the appearance of a new peak at 1658 cm^{-1}. There have been reports of instability of alkoxy benzodithiophene polymers when subjected to electrochemical oxidation before.[389] This happens when a positive potential is applied to the polymer, injecting hole polarons which are stabilised on the benzodithiophene units. It was shown that this injection of holes can trigger a irreversible degradation to form the quinoidal ketone product, resulting in an IR stretch at around 1654 cm^{-1}. This closely matched the new IR peak observed in the TBAF treated **Sp-IF-BDT-Si** at 1658 cm^{-1}. Comparison to the benzo[1,2-b:4,5-b′]dithiophene-4,8-dione precursor also showed a large signal in this region, further supporting the identity of the TBAF treated **Sp-IF-BDT-Si** as the quinoidal ketone polymer **Sp-IF-BDT=O**.

It was unclear mechanistically how the **Sp-IF-BDT-Si** formed the quinoidal ketone in the absence of any electrochemical oxidation. It was however observed that the unprotected hydroxyl benzodithiopehene intermediate **8** reverted back to its quinoidal ketone precursor over time, going from deep green to yellow. This was seen by comparing the NMR of the freshly synthesised **8** from immediately after purification, to having sat in a vial for several weeks. This shows that the hydroxy benzodithiophene is inherently unstable at ambient conditions, making it likely that the tert-butyl dimethyl silyl ether was deprotected on the polymer forming the alcohol, and was subsequently oxidised in the presence of water or O_2.

It was desired to investigate the effects of porosity and hydrophilicity for conjugated polymers, however the transformation of the backbone following deprotection significantly complicated this. Due to the insolubility of Sp-IF-BDT=O, its properties could not be thoroughly investigated. Nonetheless, it clearly changed colour from yellow to red after TBAF treatment. The nature of the conjugated backbone plays a critical role in its light harvesting and electronic behaviour, making forming conclusions about the effect of hydrophilicity on Sp-IF-BDT-Si and Sp-IF-BDT=O invalid. Consequently, this monomer was not investigated further.

2.8 Benzotriazole (BTz) Polymers

2.8.1. Monomer Design Requirements

Moving forward, the solubilising ability of the silyl ether protecting group needed to be increased to enable higher molecular weight and processable polymer to be recovered. Secondly, the deprotection should aim to cause minimal change to the polymer backbone, so as to enable investigation of the effects of hydrophilicity without changing the optoelectronic properties. To achieve this, the alcohol groups on the comonomer would be electronically insulated from the conjugated backbone by an ethylene aliphatic spacer.

2.8.2. Benzotriazole (BTz) Monomer

In the selection of a suitable conjugated platform to attach an ethyl silyl ether, benzotriazole (BTz) was identified. **BTz** is a weaker acceptor compared to BT,[66] and has an alkylation position capable of harbouring a silyl ether. Based on the poor solubility of tert-butyl dimethyl silyl in the previous polymer, and the fact that benzotriazole only has one alkylation position, the larger trihexyl silyl group was selected to offer a greater chance of solubility while still possessing sufficient stability.

The target molecule was identified as trihexyl silyl protected benzotriazole ethyl alcohol (**BTz-Si**) shown in figure 57.

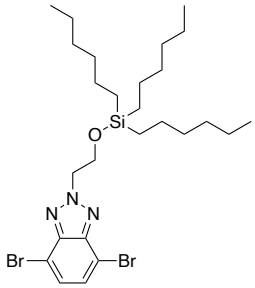

Figure 57. BTz-Si target monomer

2.8.3. BTz-Si Monomer Synthesis

To reach dibromonated BTz, the direct bromination of commercially available benzotriazole was attempted using bromine and HBr (Figure 58) However, this was unsuccessful, probably due to the aqueous conditions using 48 wt% HBr not dissolving the starting material leading to a slow and ineffective heterogenous reaction. Instead, another approach of reducing commercially available dibrominated benzothiadiazole to cleave the heterocyclic ring to give **10**, then forming the triazole ring using $NaNO_3$ giving **11**.[390]

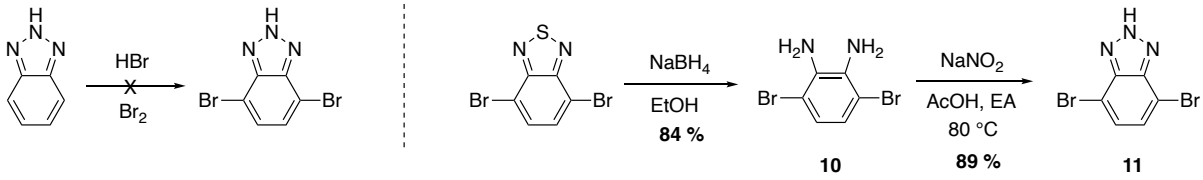

Figure 58. Left: failed bromination of benzotriazole. Right: successful cleavage and closure of dibrominated BT to synthesis 11

A mechanism is suggested in Figure 59 below.

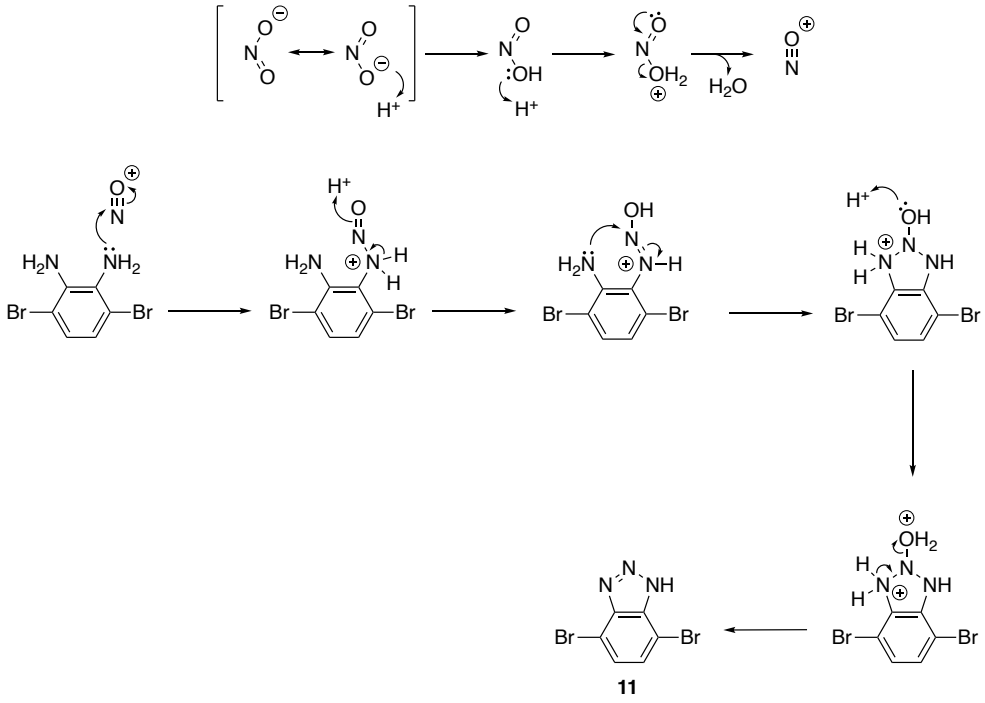

Figure 59. Mechanism for the synthesis of 11

To alkylate **11**, two synthetic pathways were adopted. The first pathway was to deprotonate **11** in the presence of base, enabling nucleophilic attack of commercially available 2-bromoethyl acetate, shown in Figure 60.

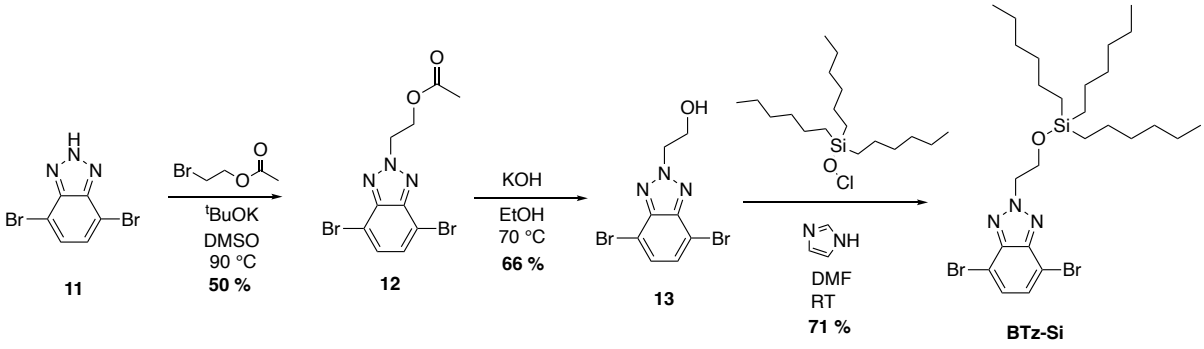

Figure 60. Synthesis of BTz-Si by pathway 1.

This reaction produced a mixture of regioisomers, with a yield of the desired 2-alkyl benzotriazole **12,** of 50 %. This is because BTz exists as tautomers in solution with the H atom hopping across the three N positions. Deprotonation leads to a resonance form where the negative charge is delocalised, with a slightly greater charge density on the N atoms at the N-1 and N-2 positions closest to the fused benzene ring.[391] Consequently nucleophilic attack of the alkyl halide by the delocalised negative charge leads to a mixture of regioisomers, as depicted in Figure 61.

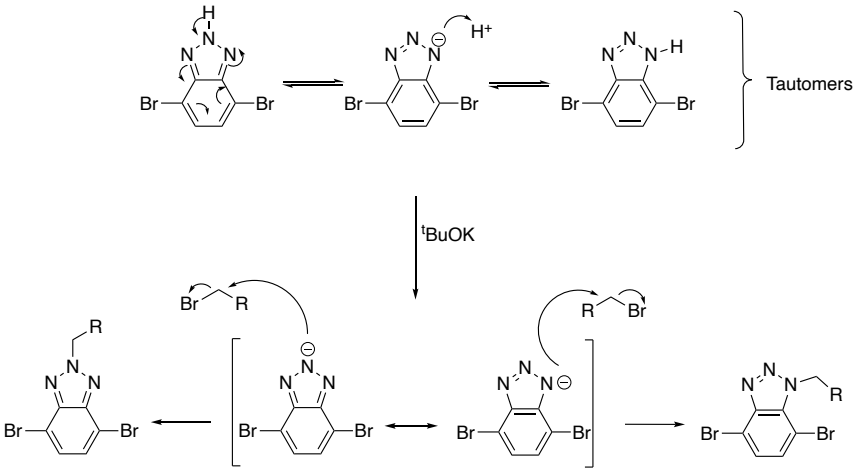

Figure 61. Mechanism of N-1/N-3 side-product formation.

Despite more electron density residing on the N-1/N-3 positions,[391] the N-1/N-3 substituted undesired isomer is fortunately the minor product. This is likely due to the attack from the anionic N-1/N-3 positions facing more steric hinderance and a higher activation energy compared to attack from the N-2 position. The symmetrical N-2 substituted regioisomer is preferred as a monomer over the less symmetric N-1/N-3 substituted one because polymerisation of the latter would lead to regioregularity complications in the resultant polymers. In addition, its position closer to the aryl-bromide could inhibit effective polymerisation on one side of the monomer.

Next, the terminal acetate was hydrolysed under basic conditions to recover the alcohol **13**, which was then protected with trihexylsilyl chloride to form the silyl ether target monomer **BTz-Si** (Figure 60). The strategy is advantageous with respect to minimising the use of costly trihexylsilyl chloride, given the low yield of the benzotriazole alkylation step.

Another pathway requiring fewer steps was to protect the alcohol on the side chain first, and then alkylate dibrominated benzotriazole with this, as shown in Figure 62. This was done by reacting 2-bromoethanol with trihexyl silyl chloride to produce **14**. Using excess 2-bromoethanol in this reaction ensures complete consumption of trihexylsilyl chloride (compared to normal alcohol protection conditions where excess trialkylsilyl chloride is used) and owing to the solubility of 2-bromoethanol in water, aqueous workup yields **14** in high yield and purity. This is subsequently reacted with **11** to give the target monomer **BTz-Si**.

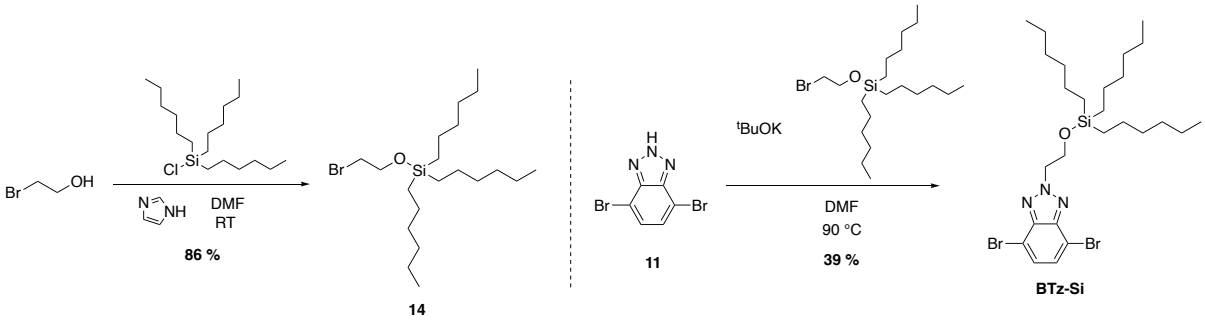

*Figure 62. Synthesis of **BTz-Si** by pathway 2.*

On balance the second pathway was identified as superior, with an overall yield of 34% compared to 23 % for the first. Although the first pathway is more conservative with respect to costly trihexylsilyl chloride and benefitted from a much easier chromatographic separation, with a larger R_f difference between the regioisomers.

2.8.4. Sp-IDT-BTz-Si Synthesis and Optoelectronic Properties

This **BTz-Si** monomer was reacted with distanylated **Sp-IDT** by Stille polymerisation to give the deep purple-pink soluble polymer **Sp-IDT-BTz-Si**, shown in Figure 63.

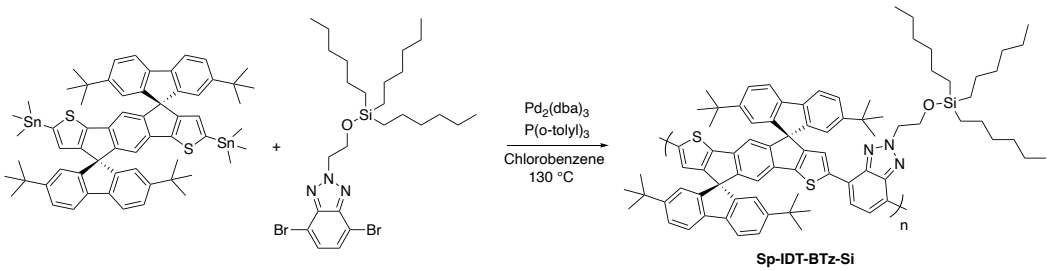

*Figure 63. Polymerisation of **Sp-IDT** and **BTz-Si** to form **Sp-IDT-BTz-Si***

Its optoelectronic properties were characterised by UV-vis spectroscopy and PESA (Figure 64) to obtain an optical bandgap and HOMO energy estimate, using both to obtain a LUMO energy estimate.

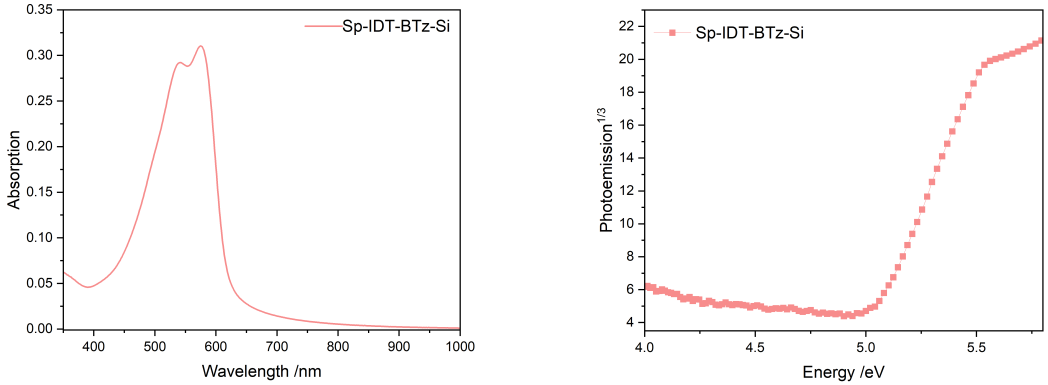

*Figure 64. **Sp-IDT-BTz-Si** thin film UV-vis spectrum (left) and PESA (right)*

The properties of **Sp-IDT-BTz-Si** are summarised in the table below.

Absorption Onset / nm	Absorption Peak(s) /nm	Optical Bandgap /eV	HOMO (PESA) /eV	LUMO (PESA+ E_g) /eV	M_N /gmol^{-1}	M_W /g mol^{-1}	Poly-dispersity
621	542, 575	2.0	-5.1	-3.1	24107	61073	2.53

Its FMO energies with respect to ascorbic acid oxidation and proton reduction are shown in Figure 65, with the half-reaction potentials at pH 6.43, showing it has suitable FMO energies to drive both half-reactions.

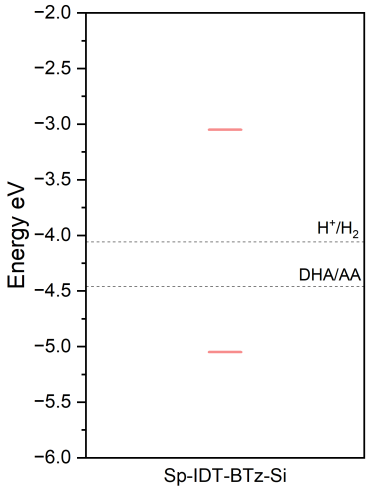

Figure 65. FMOs of Sp-IDT-BTz-Si against the expected redox potentials for proton reduction and ascorbic acid oxidation under neutral conditions.

2.8.4. Sp-IDT-BTz-Si Deprotection

Next, a portion of this **Sp-IDT-BTz-Si** was subjected to deprotection conditions, in the hope of forming its deprotected alcohol analogue **Sp-IDT-BTz-OH** (Figure 66). Due to the basic nature of hydrous TBAF, and out of caution not to damage to the polymer during deprotection, acetic acid was added to neutralise the TBAF deprotection solution. The recovered and washed TBAF treated polymer was now extremely insoluble. While indicative of successful cleavage, its insolubility also made characterisation of the TBAF treated polymer challenging.

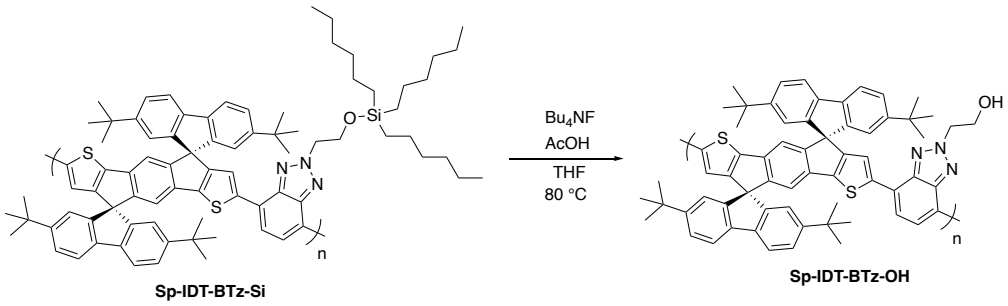

*Figure 66. Deprotection of **Sp-IDT-BTz-Si** to form **Sp-IDT-BTz-OH***

An advantage of using silyl ethers as a protecting group was the ability to use Si as an atomic label, given **Sp-IDT-BTz-Si** only contains Si atoms in the part of the polymer which is removed. Its disappearance could therefore be taken as evidence of successful deprotection. Energy dispersive X-ray Spectroscopy (EDX) measurements were undertaken of **Sp-IDT-BTz-Si** before and after treatment with TBAF for a range of areas on the polymer shown in Figure 67.

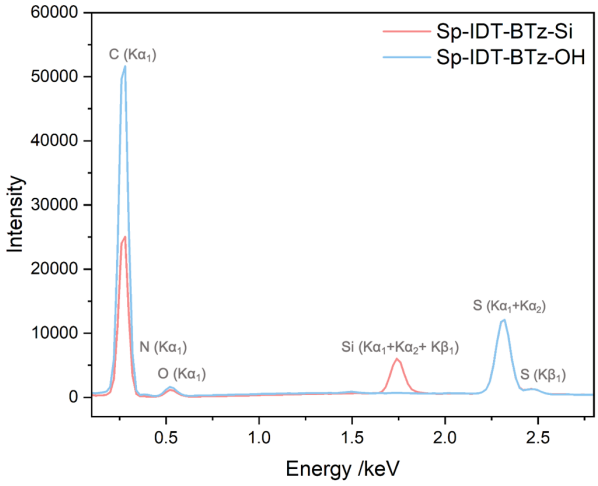

Figure 67. EDX spectra for Sp-IDT-BTz-Si and Sp-IDT-BTz-OH.

The EDX spectra between the areas were averaged and then normalised with respect to the S peak, since **Sp-IDT-BTz-Si** and **Sp-IDT-BTz-OH** have the same number of S atoms per repeat unit (from IDT). The spectra in Figure 67 show the disappearance of the Si peak in the TBAF treated polymer as well as a diminution in the C peak. This indicates successful removal of the silyl ether side chains to below detectable levels.

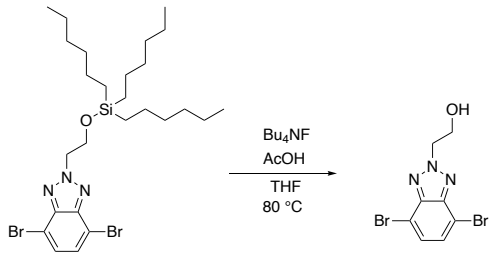

As further evidence for deprotection, a portion of **BTz-Si** monomer was subjected to the same TBAF deprotection conditions as **Sp-IDT-BTz-Si**, enabling its product to be characterised by NMR following an aqueous workup to remove excess TBAF:

extracting with ethyl acetate, and washing with water. The results of the NMR analysis are shown in Figure 68.

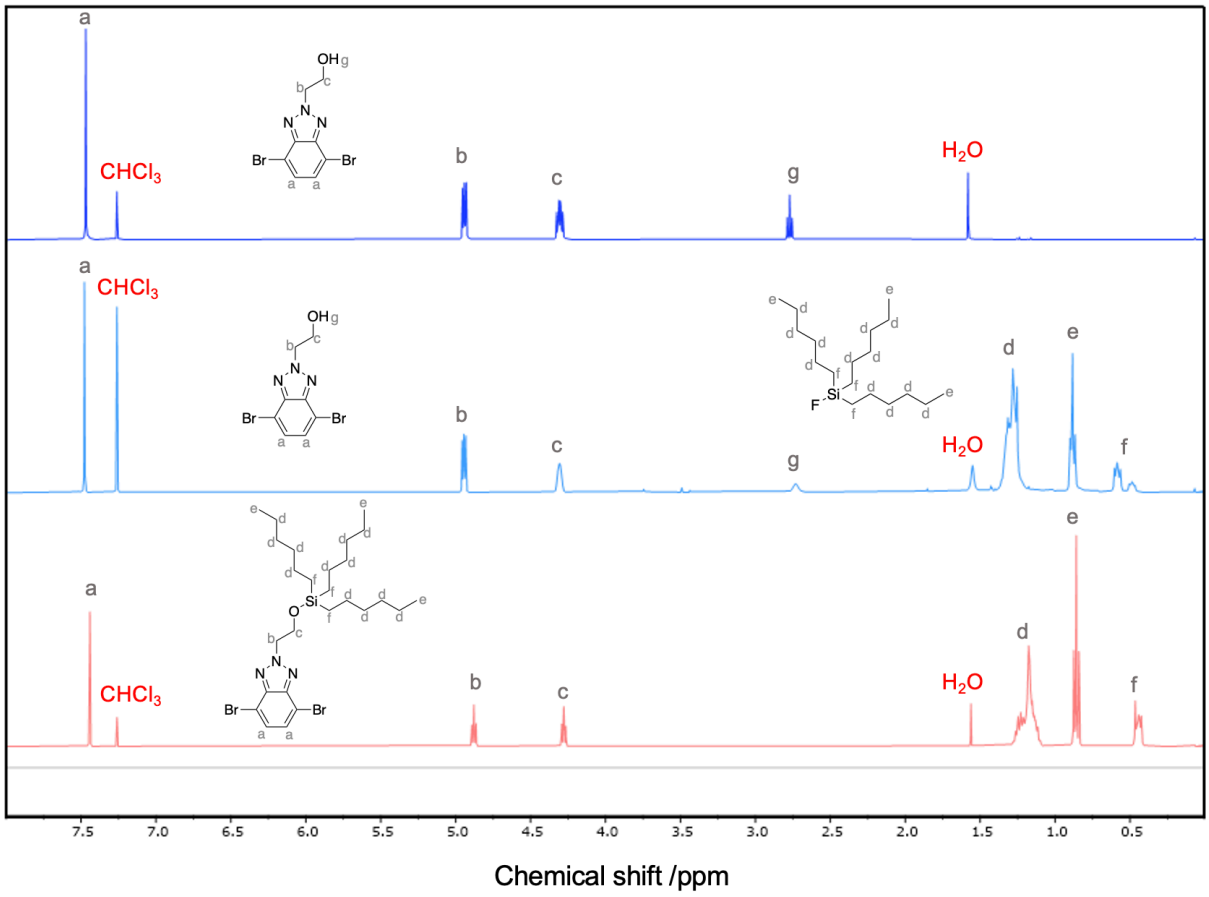

*Figure 68. NMR spectra of **Sp-IDT-BTz-Si** (bottom), TBAF treated **Sp-IDT-BTz-Si** (middle) and intermediate **13** (top)*

It showed complete deprotection of the silyl ether monomer **BTz-Si** to its alcohol analogue **BTz-OH**. The resultant NMR spectrum corresponded to the NMR spectrum of the previously synthesised alcohol intermediate **13** (Figure 68 top). TBAF treatment of **BTz-Si** caused a slight downfield chemical shift for the methylene protons b and c, as well as a new peak g corresponding to a new alcohol proton, given the peaks b:c:g integrated in a 2:2:1 ratio. The TBAF treated product of **BTz-Si** also showed a downfield shift in the peaks for the silyl ether, which were assigned to the cleaved group F-Si(Hex)$_3$ being unremoved by aqueous workup, as this is soluble in ethyl acetate.

Taken together, the NMR spectrum of the TBAF treated monomer with the EDX spectra of **Sp-IDT-BTz-Si** before and after TBAF treatment provide strong evidence for the identity of **Sp-IDT-BTz-Si** after TBAF treatment to its alcohol analogue **Sp-IDT-BTz-OH.**

An advantage of this deprotection technique is that it allows two polymers with differing side chain chemistry to be compared with exactly the same number of repeat units, eliminating variations in polymer chain length as a variable. The porosity and photocatalytic behaviour of **Sp-IDT-BTz-Si** and **Sp-IDT-BTz-OH** were subsequently investigated.

2.8.5. Effect of Deprotection on Porosity of Sp-IDT-BTz-Si

To measure the change in porosity after deprotection, the N_2 adsorption isotherms were measured and BET surface areas calculated for both polymers (Figure 69 left). The silyl protected polymer **Sp-IDT-BTz-Si** was found to be non-porous with a BET surface area of 60 $m^2\ g^{-1}$. By contrast after deprotection, **Sp-IDT-BTz-OH** showed a type I isotherm indicative of a largely microporous structure, with a BET surface area of 528 $m^2\ g^{-1}$. The isotherm software also produced a calculated pore size distribution profile for **Sp-IDT-BTz-OH**, showing a high proportion of under 1 nm pores, with some larger pores above 1 nm (Figure 69 right).

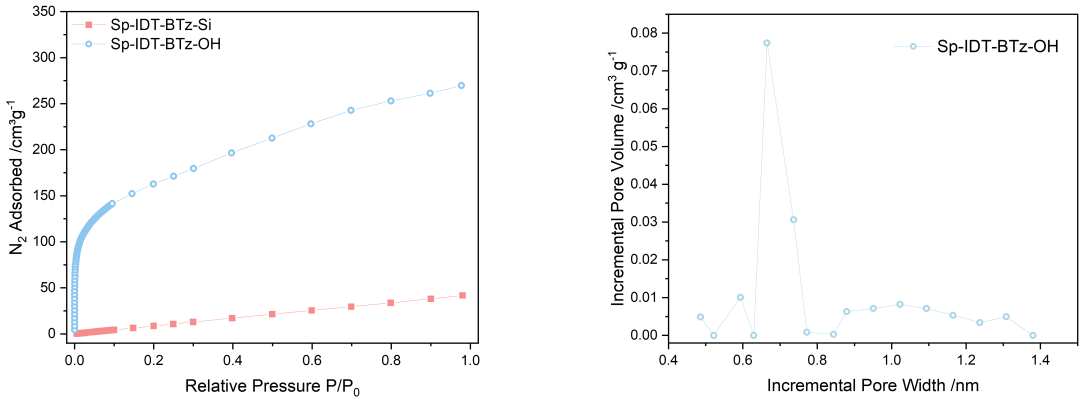

*Figure 69. Left: N_2 adsorption isotherms for **Sp-IDT-BTz-Si** and **Sp-IDT-BTz-OH**. Right: calculated pore size distributions for **Sp-IDT-BTz-OH***

2.8.6. Effect of Deprotection on Photocatalytic Activity of Sp-IDT-BTz-Si

The photocatalytic behaviour of the **Sp-IDT-BTz-Si** and **Sp-IDT-BTz-OH** were investigated next, to see what effect the removal of the protecting group had on its photocatalytic performance. The H_2 production profiles are shown in Figure 70 (left). TBAF treatment caused a significant increase in activity, increasing the rate from 0.56 to 9.40 μmol h^{-1} under neutral conditions.

It was expected that removing the large non-polar trihexyl sily ether groups would improve the dispersibility of the polymer causing an increase in particulate external surface area. To account for differences in external surface area due to differences in particle size, laser diffraction measurements were undertaken on fresh samples of the polymers prepared in the same manner to the photocatalytic tests. The particle size distributions are shown in Figure 70 (right). This analysis showed that the particle size indeed decreased after deprotection, with the D[3,2] surface weighted mean particle diameter decreasing from 7.0 to 4.8 μm.

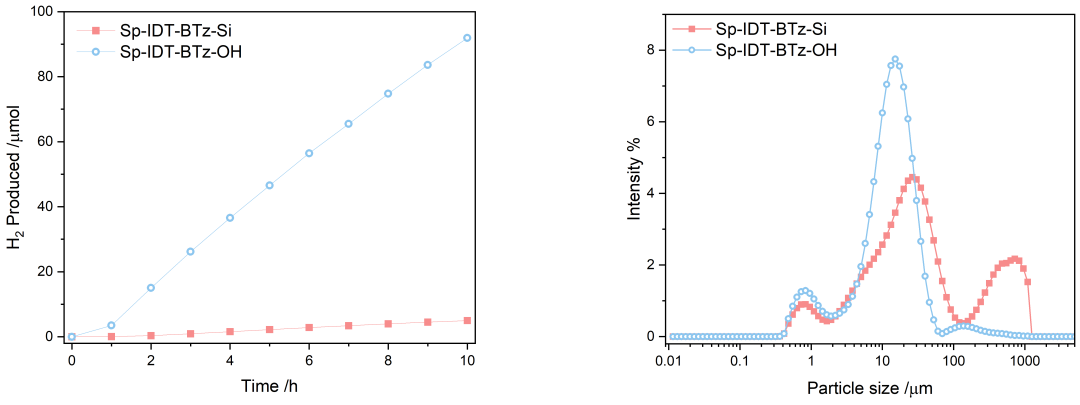

*Figure 70. For **Sp-IDT-BTz-Si** and **Sp-IDT-BTz-OH**. Left: photocatalytic activity under neutral conditions. Right: laser diffraction particle size profile.*

This data for **Sp-IDT-BTz-Si and Sp-IDT-BTz-OH** is shown in the table below.

Polymer	D[3,2] Particle Size / μm	N_2 BET Surface Area / $m^2\ g^{-1}$	Average H_2 Produced Neutral / μmol h^{-1}	Average H_2 Produced Acidic / μmol h^{-1}
Sp-IDT-BTz-Si	7.0	60	0.58	-
Sp-IDT-BTz-OH	4.8	528	9.40	0.96

While the decrease in particle size and concomitant increase in external surface area can partially explain the increase in activity after deprotection, the 16-fold increase was so large, that other factors were likely also making a significant contribution. It was clear from these results that deprotection of the **Sp-IDT-BTz-Si** caused a significant increase in activity. However, the problem was that several important variables were being changed at once: hydrophilicity, porosity, and particle size. In an attempt to tease apart these variables, the next step was to synthesise a porous polymer with the same backbone, but lacking the alcohol moiety, meaning the variable of hydrophilicity could be more closely isolated.

2.9 Hydrophobic Porous Polymers

To investigate the effect of 'turning off' hydrophilicity for porous systems on the photocatalytic activity, an analogue of **Sp-IDT-BTz-OH** was synthesised with an ethyl sidechain, rather than ethyl alcohol, to give **Sp-IDT-BTz-Et**.

This could also shed light on the mechanism by which porosity came about. **Sp-IDT-BTz-Si** was only partially soluble in THF during deprotection. It was unclear whether some of the porosity was originating from the cleavage of bulky silyl ether leaving behind cavities when conducted in the solid state, or whether the bulky spirofluorene repeat units do in fact inhibit packing but the resulting pores were merely 'clogged' with silyl ether, which could be 'unclogged' by cleaving them off using TBAF. The former could be described as extrinsic microporosity, built by removing the silyl template, rather than intrinsic microporosity due to the inherent inability of the polymer to pack in the solid state. If it were the case that the porosity was totally extrinsic due to the removal of the silyl group, then **Sp-IDT-BTz-Et** would be expected to have

significantly lower porosity than **Sp-IDT-BTz-OH**, given that no silyl ethers are there to be removed.

To also investigate the effect of the sidechain length on porosity, the series was expanded by making two additional similar polymers with varying length of side chain, **Sp-IDT-BTz-Hex** and **Sp-IDT-BTz-Dec**. It was expected that as the sidechain length increased, the pores would get 'filled' to a greater degree with the long flexible side chains. The monomers needed to make **Sp-IDT-BTz-Et**, **Sp-IDT-BTz-Hex** and **Sp-IDT-BTz-Dec** were synthesised using the same method as **BTz-Si**, but using ethyl bromide, hexyl bromide and decyl bromide respectively, as shown in Figure 71.

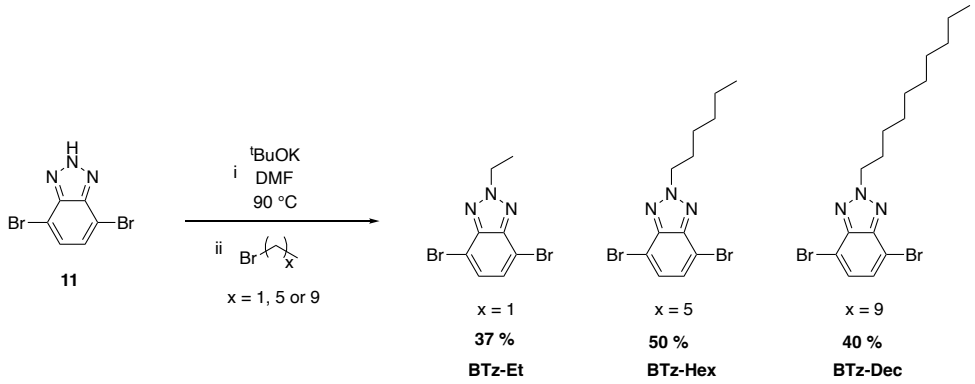

Figure 71. Synthesis of monomers BTz-Et, BTz-Hex and BTz-Dec

These monomers underwent Stille polymerisation in the same manner as **Sp-IDT-BTz-Si** to produce the polymer series, shown below:

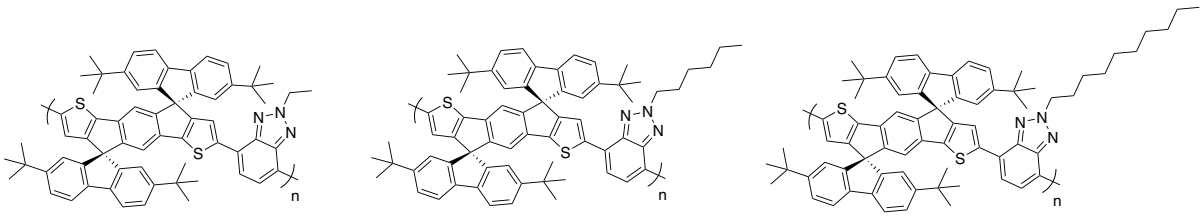

Owing to the insolubility or very low solubility, molecular weight and optoelectronic characterisation could not be performed. However, it was expected that the optoelectronic properties are very similar due to their identical conjugated backbones, though molecular weight was undoubtably a variable that could not be easily controlled

or quantified. Nonetheless, their photocatalytic activities, particle size distributions and N_2 sorption isotherms were characterised, and shown in Figure 72.

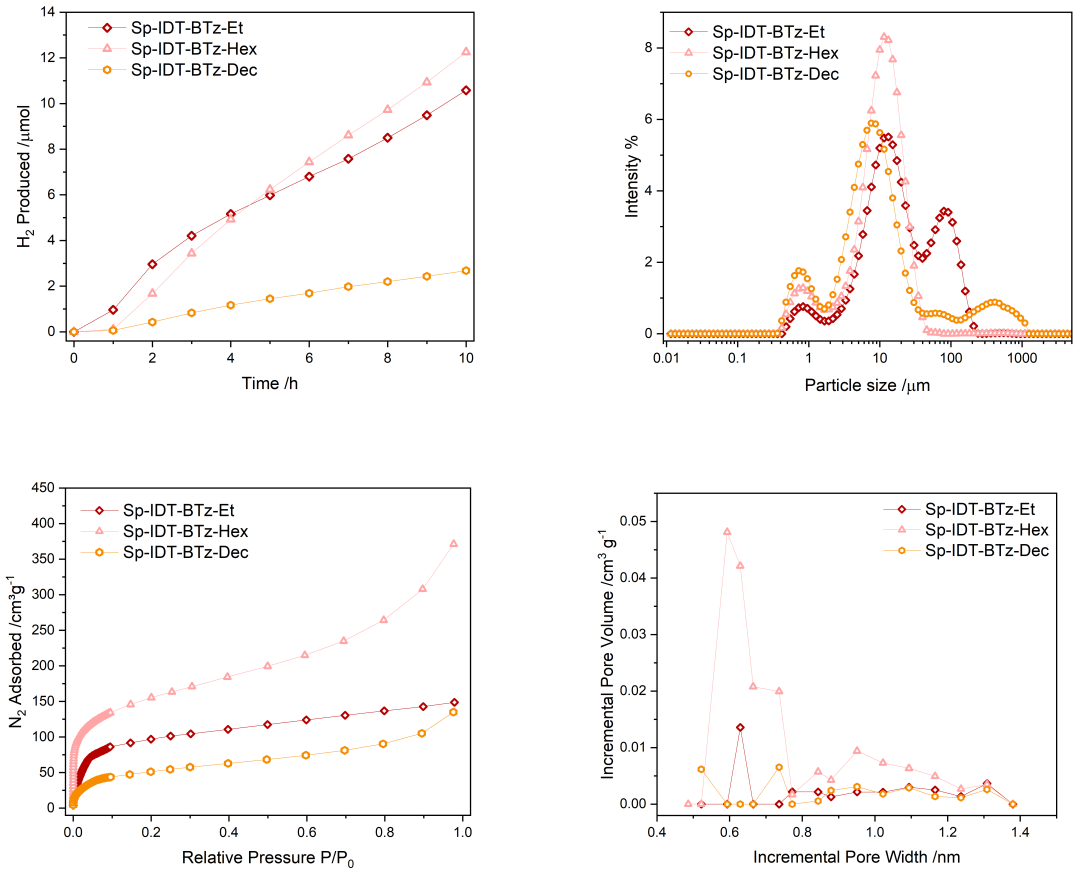

*Figure 72. For **Sp-IDT-BTz-Et**, **Sp-IDT-BTz-Hex** and **Sp-IDT-BTz-Dec**. Top left: photocatalytic activity under neutral conditions. Top right: laser diffraction particle size profiles. Bottom left: N_2 adsorption isotherms. Bottom right: calculated pore size distributions.*

The data for **Sp-IDT-BTz-Et**, **Sp-IDT-BTz-Hex** and **Sp-IDT-BTz-Dec** are summarised in the table below.

Polymer	N_2 BET Surface Area / $m^2\ g^{-1}$	D[3,2] Particle Size / μm	Average H_2 Produced Neutral / $\mu mol\ h^{-1}$
Sp-IDT-BTz-Et	418	7.0	0.89
Sp-IDT-BTz-Hex	503	4.2	1.29
Sp-IDT-BTz-Dec	165	3.4	0.28

Surprisingly, the data shows **Sp-IDT-BTz-Hex** to have the highest BET surface area and photocatalytic activity, though it is close to **Sp-IDT-BTz-Et**, while longest sidechain polymer **Sp-IDT-BTz-Dec** clearly has the lowest porosity and photocatalytic activity as expected. To account for the greater porosity of **Sp-IDT-BTz-Hex** over **Sp-IDT-BTz-Et**, it is possible that the greater solubility of the longer side chains enabled higher molecular weights to be achieved during polymerisation. This has been reported to promote greater porosity in intrinsically microporous polymers.[343] However, this effect could be expected to be counteracted as the side chains get too long, as the **Sp-IDT-BTz-Dec** showed a marked reduction in porosity, likely due to increase filling of void space caused by the longer sidechain.

This series shows a general trend towards greater porosity promoting higher photocatalytic activity. This is despite average particle size decreasing as the alkyl chain gets longer. It is thought that the particle size trend could be because during photocatalytic sample preparation, the polymer is dispersed in NMP under high power sonication where it heats up. The longer side chain polymers dissolve to a greater extent in this. When subsequently pipetted into sonicating water in a nanoprecipitation type procedure, the better dissolution in the NMP for longer side chain polymers produced smaller polymer particles. Looking at the relative intensity of sub μm particles, there is a trend where this increases with sidechain length.

The fact that both **Sp-IDT-BTz-Et** and **Sp-IDT-BTz-Hex** (having no protecting groups removed) display comparable BET surface areas to **Sp-IDT-BTz-OH** gives credence to the idea that the porosity of **Sp-IDT-BTz-OH** originates in the intrinsic inability to pack owing to the spirofluorene group, and not because of an extrinsic templating effect caused by the removal of the silyl group in the solid state.

2.10. Investigating the Effects of Hydrophilicity for Porous Polymers

2.10.1. Sp-IDT-BT-OH and Sp-IDT-BTz-Hex Isolate Hydrophilicity

Given their very similar N_2 adsorption BET surface areas of and 528 and 503 $m^2\ g^{-1}$, **Sp-IDT-BTz-OH** and **Sp-IDT-BTz-Hex** were selected for comparison of the effect of the presence of alcohol functional groups when porosity is constant. Their structures are also shown alongside in Figure 73 for comparison.

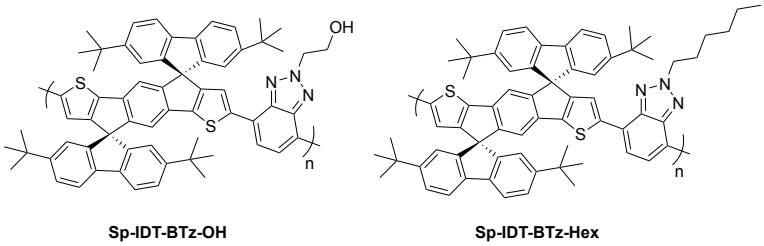

*Figure 73. Structures of **Sp-IDT-BTz-OH** and **Sp-IDT-BTz-Hex**.*

Comparison of these polymers would enable investigation of the effect of the presence of alcohol groups on porous polymers. As can be seen from their comparison in Figure 74 (right), the particle size distributions were also very similar, further isolating the variable of hydrophilicity.

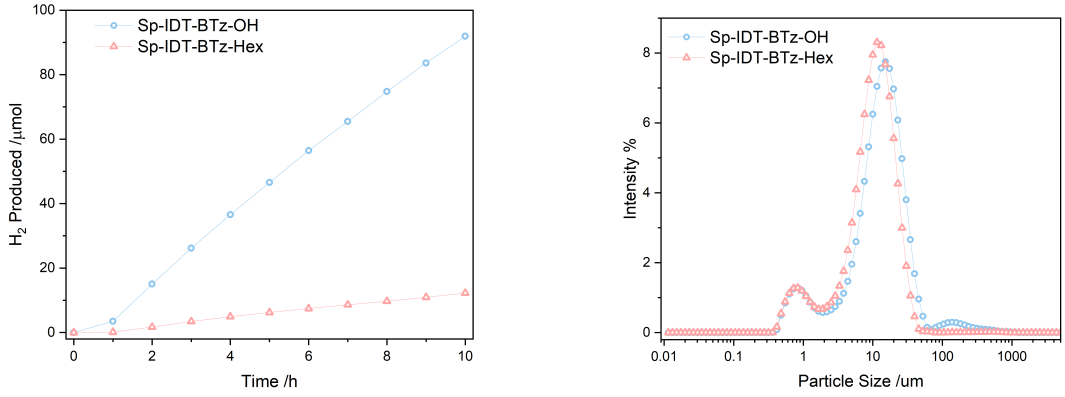

***Figure 74**. For **Sp-IDT-BTz-OH** and **Sp-IDT-BTz-Hex**. Left: photocatalytic activity under neutral conditions. Right: Laser diffraction particle size distributions.*

In order to measure how accessible porosity was to water, water adsorption isotherms for **Sp-IDT-BTz-OH** and **Sp-IDT-BTz-Hex** were measured (Figure 75 right). Given these polymers display very similar N_2 adsorption BET surface areas, differences in water sorption can be indicative of the ability of water to penetrate the internal volume under equilibrium conditions. The N_2 adsorption isotherm is shown alongside for comparison (Figure 75 left).

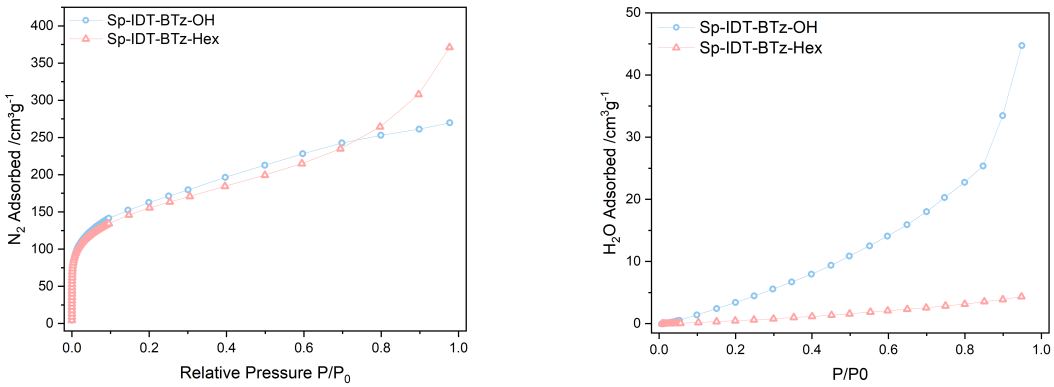

*Figure 75. For **Sp-IDT-BTz-OH** and **Sp-IDT-BTz-Hex**. Left: N_2 adsorption isotherms. Right: H_2O sorption isotherms.*

Parameters for the two polymers are also shown in the table below for comparison.

Polymer	N_2 BET Surface Area / $m^2\ g^{-1}$	D[3,2] Particle Size / μm	Average H_2 Produced Neutral / $\mu mol\ h^{-1}$
Sp-IDT-BTz-OH	528	4.8	9.40
Sp-IDT-BTz-Hex	503	4.2	2.50

Figure 75 shows a large difference in the two water adsorption isotherms, with **Sp-IDT-BTz-OH** being capable of adsorbing significantly more water than **Sp-IDT-BTz-Hex**. **Sp-IDT-BTz-OH** is also nearly four times more photocatalytically active than **Sp-IDT-BTz-Hex**. It was concluded that the presence of alcohol functional groups must be partially responsible for this difference.

2.10.2. fs-TAS to Investigate the Photophysics of Sp-IDT-BTz-OH and Sp-IDT-BTz-Hex

To gain greater mechanistic understanding into the photocatalytic process for these polymers, fs timescale transient absorption spectroscopy (TAS) was conducted. The TAS data shows the change in absorbance ΔA between excited and ground state, plotted as a function of wavelength, from a very short delay between pump and probe of about 0.3 ps, to longer delays up to 5352 ps. This allows the change in absorbance between polymer ground and excited states to be observed as a function of time (see Chapter 1).

The TAS spectra for **Sp-IDT-BTz-OH** and **Sp-IDT-BTz-Hex** were measured 'neat', where the polymers was dispersed in only water and NMP in the same ratio as they were measured for photocatalytic experiments. Then to investigate the behaviour of the polymers after Pt photodeposition, **Sp-IDT-BTz-OH** and **Sp-IDT-BTz-Hex** were also separately dispersed and underwent Pt photodeposition in the presence of ascorbic acid, filtered and washed to remove the ascorbic acid, then redispersed in water and NMP to replicate the photocatalysis dispersion conditions. This allowed TAS spectra for both polymers to be measured with and without photodeposited Pt to investigate its effect. These samples (with and without photodeposited Pt) were also tested in the presence and absence of ascorbic acid to better understand their behaviour.

2.10.3. fs-TAS for Sp-IDT-BTz-OH

The TAS spectrum for the neat deprotected porous polymer **Sp-IDT-BTz-OH,** without Pt or ascorbic acid is shown in Figure 76 (left). The broad, long-wavelngth signal at around 1300 nm, at 0.3 ps after photoexcitation (purple line on Figure 76 left) shows a positive ΔA between excited and ground states. This is assigned to absorbance form excitons. As the delay between pump and probe increases and the change in absorbance from the time of photoexcitation increases, this signal reduces. This

indicates decay of the exciton, with its absorbance completely disappearing by 48 ps. Interestingly, exciton decay in neat **Sp-IDT-BTz-OH** is acompanied by a concomitatnt growth in a positive ΔA at around 960 nm. This was assigned to absorbance of the polymer due to charged states. This demonstrates spontaneous charge generation on the neat polymer, in the absence of ascorbic acid and Pt. By tracking the intensities for the exciton and charge assigned ΔA signals, and mathematically deconvoluting their signals due to their slight overlap, their intensities as a function of time were plotted in Figure 76 (right). This shows rapid charge generation in the neat polymer.

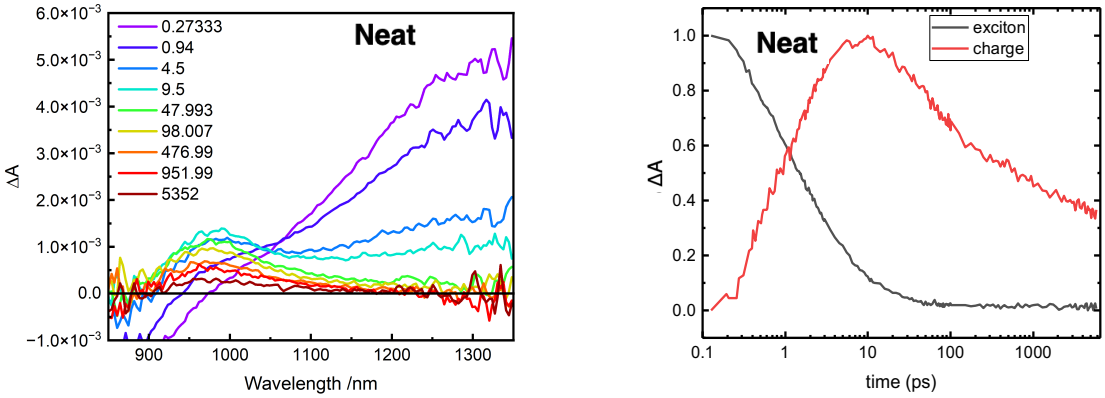

Figure 76. For neat Sp-IDT-BTz-OH. Left: TAS spectra for different pump-probe delay times in ps. Right: mathematically deconvoluted signals for exciton (black) and charge (red) signals.

Figure 76 (right) shows a population of excitons on neat **Sp-IDT-BTz-OH** 0.1 ps after photoexcitation (red line). Its signal appears to decay at the same time as a signal assigned to charged states on the polymer increases in magnitude, peaking around 10 ps, whereupon the charge signal then decays, though persisting into the ns timescale. The charge signal is partially obscured by a negative ΔA signal at short wavelengths on sub 4.5 ps timescales. This is not at the wavelength expected for the ground state photobleach but is instead thought to be an experimental artefact attributed to scattering from the sample. Nonetheless, the relatively long lifetime of the charge signal is very clear, and passes the 6 ns measurement treshold of the fs-TAS experiment, indicating its potential use for photocatalytic reactions.

To better understand the nature of the charge signal, TAS was measured in the presence of ascorbic acid (Figre 77 right). In addition to a degree of rapid reductive quencing of excitons (indicated by the decrease in the magnitude of the exciton signal), the charge signal is almost fully supressed. This strongly suggests that the charge signal is caused by hole polarons on the polymer, since electron polarons would not be expected to be quenched by an electron donor. The fact that no charge signal is present at even the 5-10 ps range suggests that the holes are very rapidly quenched by ascorbic acid. This is consistent with the porous nature of this material, where water and ascorbic acid are likely well permeated throughout the material.

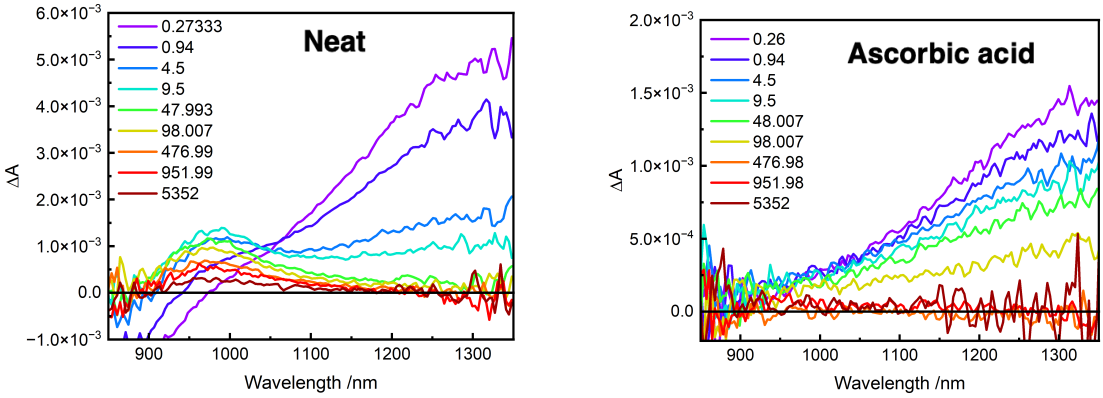

Figure 77. Left: TAS spectra for different pump-probe delay times in ps for Sp-IDT-BTz-OH neat. Right: TAS spectra for different pump-probe delay times in ps for Sp-IDT-BTz-OH in the presence of ascorbic acid.

Owing to the poor dispersion of these polymers (causing scattering by the large particles), the TAS spectra of the bare **Sp-IDT-BTz-OH** (with and without added ascorbic acid) were not conducted at equivalent optical densities to that of the photodeposited Pt **Sp-IDT-BTz-OH** samples. It is therefore not possible to compare the neat and Pt deposited polymers in terms of signal amplitude.

Nontheless examining TAS spectra for the Pt deposited **Sp-IDT-BTz-OH** (Figure 78 left), shows the retaining of the hole polaron signal, inicating Pt is not acting as a significant polaron recombination centre. Whilst the negative ΔA low wavelength artefact of the neat material makes the timescale of charge generation somewhat unclear, it does appear that the Pt deposited sample shows faster growth of the

polaron absorption, with clear signal even at 0.9 ps. This is perhaps due to Pt acting as an 'electron sink' i.e. oxidatively quenching excitons to leave hole polarons on the polymer.[95]

The fs-TAS spactra for the Pt depsoited sample in the presence of ascorbic acid (Figure 78 right), shows the presence of the ascorbic acid leading to almost complete quenching of the 960 nm signal, consitent with efficient quenching of hole polarons by the electron donor.

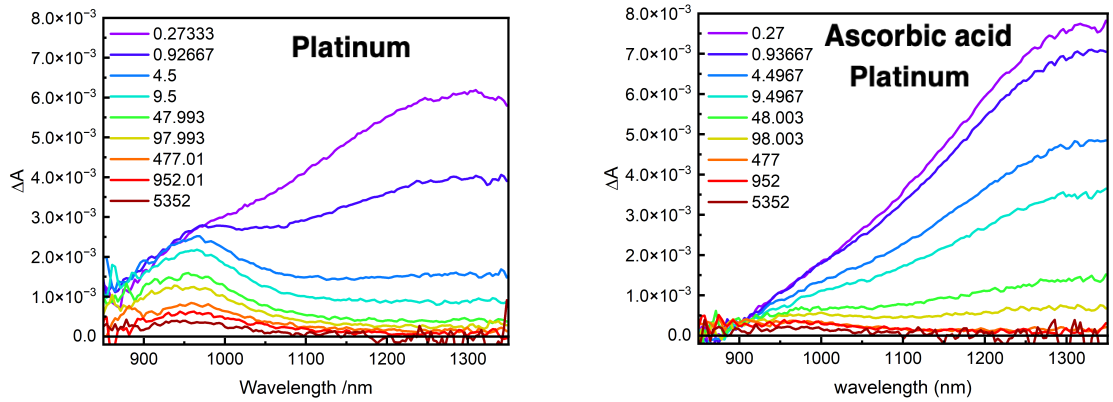

Figure 78. Left: TAS spectra for different pump-probe delay times in ps for photodeposited Pt Sp-IDT-BTz-OH. Right: TAS spectra for different pump-probe delay times in ps for photodeposited Pt Sp-IDT-BTz-OH in the presence of ascorbic acid

2.10.4. Ascorbic Acid Concentration Dependence for Sp-IDT-BTz-OH

In order to better understand role of ascorbic acid in **Sp-IDT-BTz-OH**, the effect of the concentration of ascorbic acid on the rate of photocatalysis (in the presence of Pt) was investigated. This was done by controlling the amount of ascorbic acid that was added to the testing mixture, while adjusting amount of NaOH added to neutralise it and remove pH change as a variable. The H_2 production profile is shown in Figure 79.

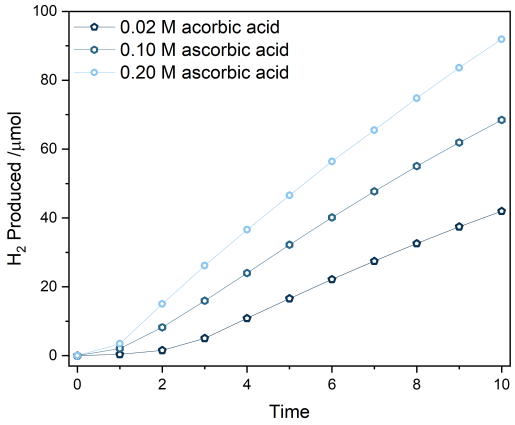

Figure 79. H_2 production profiles for Sp-IDT-BTz-OH with photodeposited Pt under neutral conditions, varying ascorbic acid concentration.

For the 0.2 M ascorbic acid test (which is the normal testing concentration), about 1.3 % of the ascorbic acid was calculated to have been consumed in the 10 h test. This shows that at high concentrations, ascorbic acid concentration still has a large influence on the rate, suggesting hole extraction is a rate limiting process. It is likely that excitons are able to be separated effectively, and the electron polarons efficiently consumed for proton reduction leaving hole polarons left behind, which must be removed to avoid unfavourable charge accumulation. Whilst fs-TAS indicates highly efficient hole extraction, this is on a fully equilibrated sample over a very short time scale. It is possible that diffusion of ascorbic acid throughout the porous structure is a limiting factor across the longer timescales of photocatalysis. Photoinduced absorption spectroscopy (PIAS) measurements under constant illumination (ms-s) timescale are ongoing and should give more of an indication into the materials kinetics under quasi steady-state conditions.

To rule out any effects of residual Pd in the polymer. ICP-MS measurements were conducted, and showed the residual Pd was all less than 3 ppm for **Sp-IDT-BTz-OH** and **Sp-IDT-BTz-Hex**.

2.10.5. fs-TAS for Sp-IDT-BTz-Hex

The TAS spectra for **Sp-IDT-BTz-Hex** were subsequently measured in the same way shown below in Figure 80. On this polymer too, a sustained charge signal is also observed, which is rapidly quenched in the presence of ascorbic acid, suggesting similar photophysics is taking place. At 48 ps on neat **Sp-IDT-BTz-Hex** it can clearly be seen the hole polaron signal remains after the exciton has decayed.

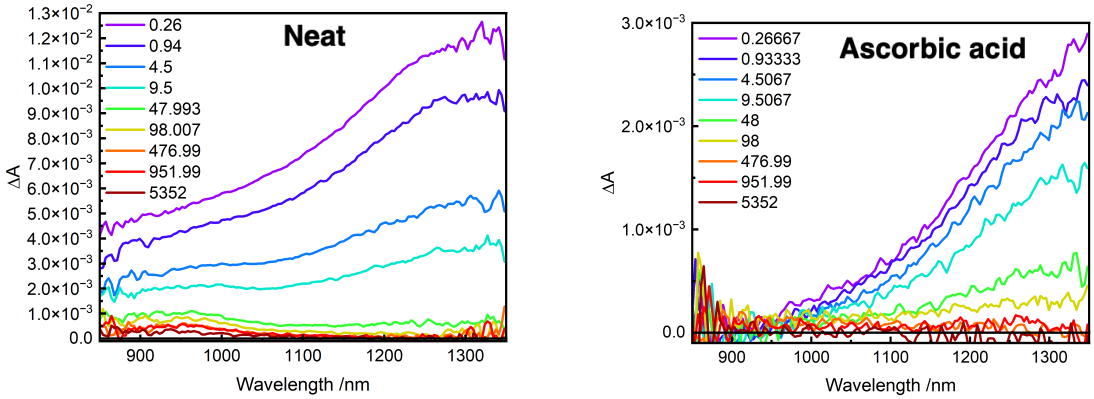

Figure 80. Left: TAS spectra for different pump-probe delay times in ps for Sp-IDT-BTz-Hex. Right: TAS spectra for different pump-probe delay times in ps for Sp-IDT-BTz-Hex in the presence of ascorbic acid

Analysis of the TAS spectra for Pt photodeposited **Sp-IDT-BTz-Hex** shows a similar situation (Figure 81), where the presence of ascorbic acid strongly supresses the hole polaron signal.

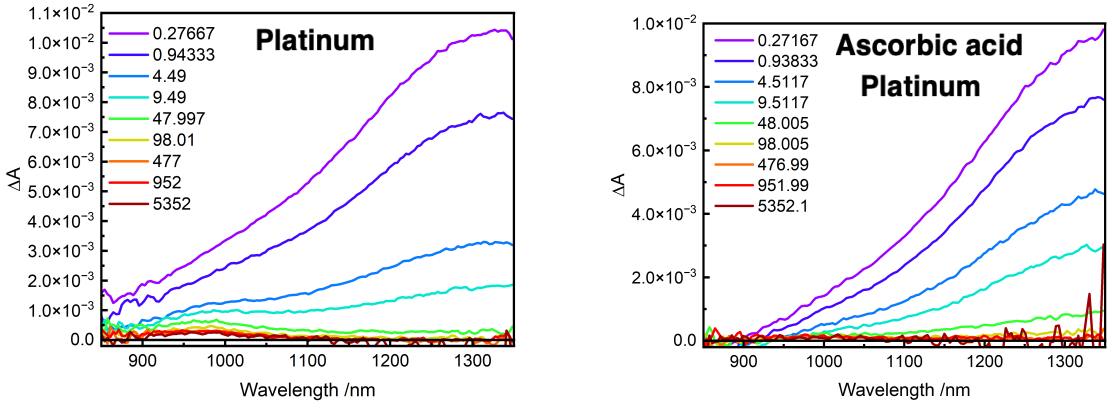

Figure 81. Left: TAS spectra for different pump-probe delay times in ps for photodeposited Pt Sp-IDT-BTz-Hex. Right: TAS spectra for different pump-probe delay times in ps for photodeposited Pt Sp-IDT-BTz-Hex in the presence of ascorbic acid

2.10.6. Relating Photophysics to Photocatalysis

In order to relate these fs-TAS spectra for **Sp-IDT-BTz-OH** and **Sp-IDT-BTz-Hex** to their photocatalytic activities, it is imperative to know the relative amplitudes of the exciton and polaron signals. Qualitatively it appears that the charge signal on the hydrophobic **Sp-IDT-BTz-Hex** is weaker than on **Sp-IDT-BTz-OH.** This would be consistent with its lower activity. Further TAS studies to produce data of sufficient quality for absorption normalisation and comparison, as well as PIAS experiments to get a sense of the relative yields of exciton separation into charges. PIAS measurements are particularly useful for investigating this question as samples are irradiated continuously to allow a build-up of charge.[114] Charge signal decay after illumination stops is characterised by the ΔA between excited and ground states. From the magnitude of the signals as charge is built up, their relative maxima and decay can be compared.

It is highly interesting that **Sp-IDT-BTz-OH** and **Sp-IDT-BTz-Hex** both show exciton separation to generate charge *in the absence* of sacrificial electron donor, heterojunction or cocatalysts. This is rare for single component organic semiconductors which typically lack a thermodynamic driving force to overcome their exciton binding energies. This effect has however been observed in organic semiconductors bearing hydrophilic oligoethylene glycol side chains (as discussed in Chapter 1). This was thought to happen due to swelling and ingress in water caused by the presence of the hydrophilic glycol sidechains, which raised the effective dielectric response in GHz frequency range (on ps timescales). This increased dielectric response in the ps timescale is expected to reduce exciton binding energy, and account for the ability for glycolated polymers to generate charges.[302] Therefore the porosity of **Sp-IDT-BTz-OH** and **Sp-IDT-BTz-Hex** could be having a similar effect here, perhaps due to the presence of water in the free volume.

Nonetheless, until the relative amplitudes of charge generation after normalising for exciton concentration under prolonged illumination conditions (via PIAS) are elucidated, relating the differences in water adsorption for these porous structures to

their TAS behaviour can only be speculative. It could be that the charge signal in **Sp-IDT-Hex** originates from a smaller fraction of **Sp-IDT-BTz-Hex** (compared to **Sp-IDT-BTz-OH**), where water is more accessible such as macropores close to the surface. This would be consistent with the fact that the hole polarons in both polymers are extremely rapidly and efficiently quenched by ascorbic acid, indicating the hole polarons must be accessible to electrolyte (containing the ascorbic acid) on the ps timescale. Were the charges generated in regions inaccessible to ascorbic acid, then it would follow that they would take longer to be quenched, and the polaron signal should persist for longer timescales in the presence of ascorbic acid.

Furthermore, fs-TAS gathers information about the photocatalyst at ps timescales following of photoexcitation from a brief low-energy excitation pulse and doesn't give much information about how the system behaves under greater illumination intensity at steady state conditions (i.e. during photocatalysis), where mass transport becomes relevant. It could be that the greater photocatalytic activity of **Sp-IDT-BTz-OH** originates from better mass transport of ascorbic acid to access its active surface, which cannot be seen in fs-TAS as it does not probe long enough timescales for mass transport effects to impact hole extraction.

2.11. Investigating Hydrophilicity for Non-Porous Polymers

2.11.1. Bu-IDT Monomer Synthesis

As a final additional control, the effects of hydrophilicity for non-porous polymers was investigated by substituting the orthogonal spirofluorene groups with flexible n-butyl side chains. Given their lack of rigidity and steric bulk, it was expected that this substitution would generate non-porous structures of similar optoelectronic properties for comparison. These could then be treated in the same manner with TBAF to trigger deprotection and reveal alcohol groups to enhance the hydrophilicity. The syntheses of this **Bu-IDT** monomer is shown in Figure 82, adapted literature procedure.[365]

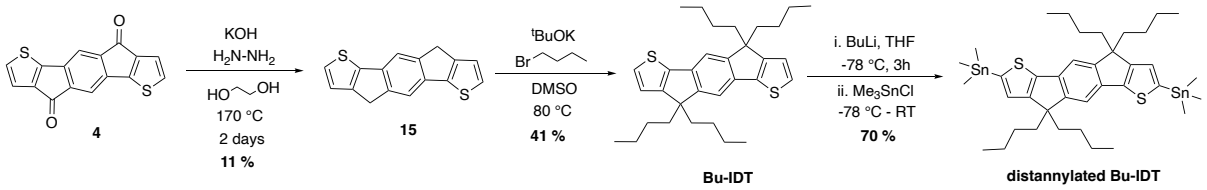

Figure 82. Distannylated Bu-IDT synthesis

Its synthesis involved Wolff-Kishner reduction of **4** to obtain **15**. Its acidic bridging methylene protons were sequentially deprotonated, enabling nucleophilic attack of 1-bromobutane to butylate these positions. Lithiation of **Bu-IDT** followed by quenching with trimethyltin chloride produced the distannylated monomer. A mechanism for the reduction and alkylation is shown below in Figure 83.

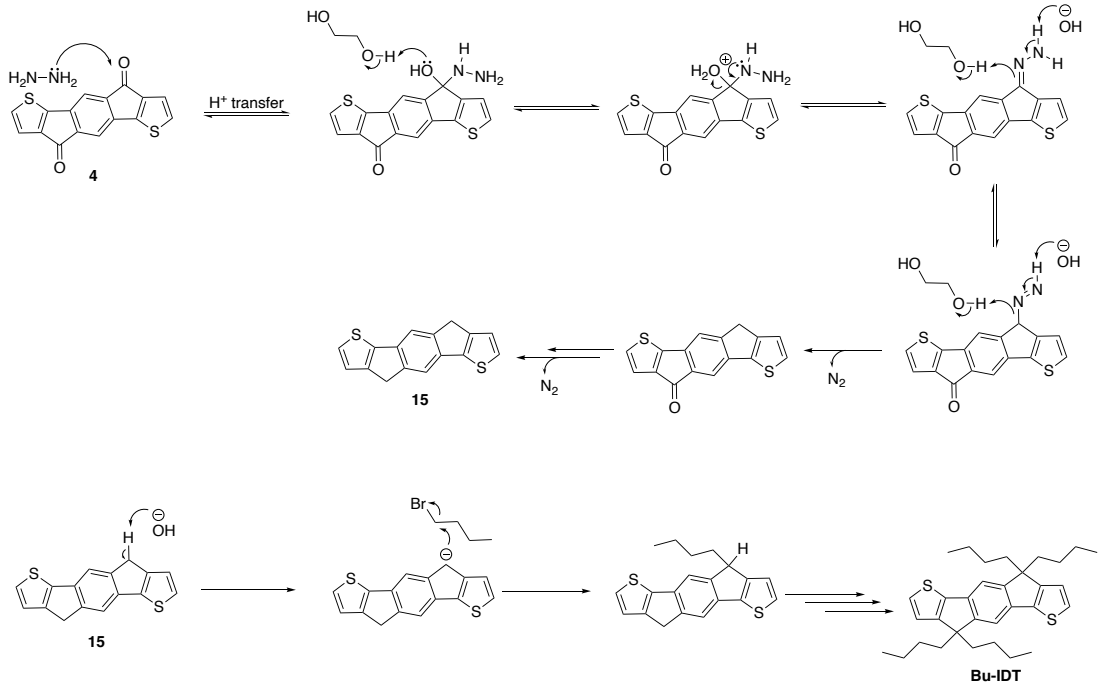

*Figure 83. Mechanism for synthesis of **Bu-IDT***

2.11.2. Bu-IDT-BTz-Si Synthesis and Optoelectronic Properties

The distannlyated **Bu-IDT** monomer then underwent Stille polymerisation with the **BTz-Si** monomer to produce **Bu-IDT-BTz-Si**.

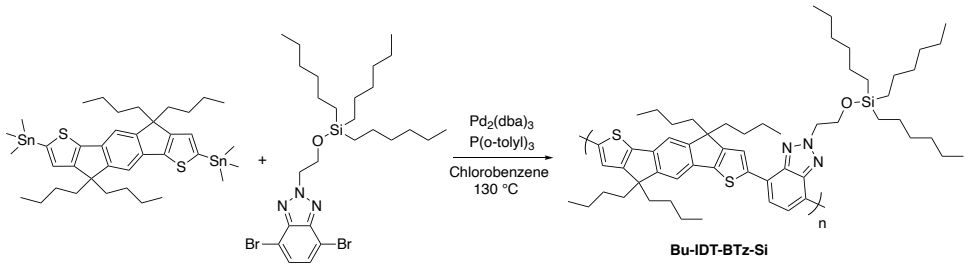

*Figure 84. Synthesis of **Bu-IDT-BTz-Si***

This polymer was designed as a deliberately non-porous analogue of **Bu-IDT-BTz-OH** after deprotection, which still contained an alcohol to keep hydrophilicity similar to enable porosity to be varied. To verify that **Bu-IDT-BTz-Si** was optoelectronically comparable to **Sp-IDT-BTz-Si**, UV-vis spectroscopy was conducted on spin coated films of **Bu-IDT-BTz-Si** compared to **Sp-IDT-BTz-Si**, shown in Figure 85 (left)

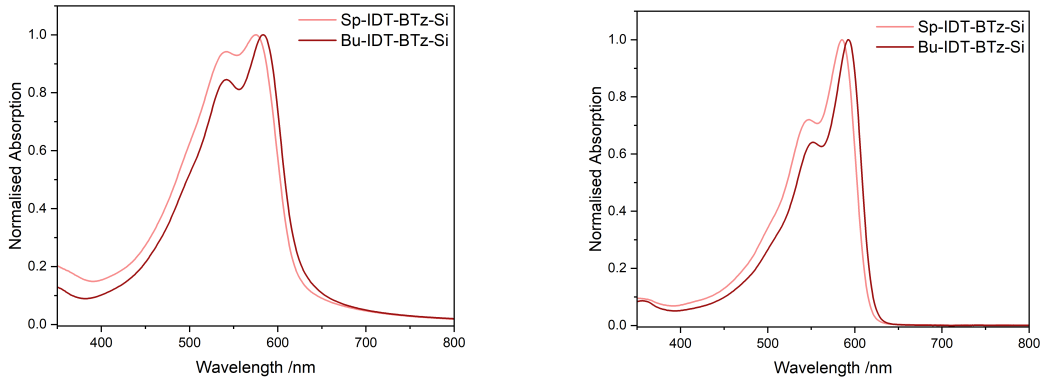

*Figure 85. Left: thin film UV-vis spectra of of **Bu-IDT-BTz-Si** and **Sp-IDT-BTz-Si**. Right: chloroform solution UV-vis spectra of **Bu-IDT-BTz-Si** and **Sp-IDT-BTz-Si***

The properties of **Bu-IDT-BTz-Si** and **Sp-IDT-BTz-Si** are shown in the table below.

Polymer	Absorption Onset / nm	Absorption Peak(s) /nm	Optical Bandgap /eV	HOMO estimate (PESA) /eV	LUMO estimate /eV	M_N /g mol^{-1}	M_W /g mol^{-1}	Poly-dispersity
Sp-IDT-BTz-Si	619	542, 575	2.0	-5.1	-3.1	24107	61073	2.53
Bu-IDT-BTz-Si	625	542, 583	2.0	-5.1	-3.1	27027	45072	1.67

While very similar, it can be seen that **Bu-IDT-BTz-Si** is slightly red shifted with respect to **Sp-IDT-BTz-Si**, with a slight red shift in absorption onset of 6 nm between the spiro and butyl polymers. The slight red shift of **Bu-IDT-BTz-Si** likely originate in differences in solid state packing, whereby enhanced π-π interactions give rise to greater electronic delocalisation in **Bu-IDT-BTz-Si**, given it does not possess bulky spirofluorene groups which are designed to impair stacking in the solid state. The fact that the shift still persists in solution UV-vis (Figure 85 right) is presumably due to aggregation in solution, which is common for conjugated polymers.[89] The shorter wavelength shoulder to the left of the λ_{max} peak on the spectrum is indicative of a 0-1 vibrational transition, where the λ_{max} peak is 0-0. It would be expected that these peaks would be altered upon heating as the chains disaggregate.[392,393]

Nonetheless, the difference in optical bandgap as estimated by UV-vis absorption onset equates to 0.019 eV. Given the magnitude in the differences in photocatalytic activity which will subsequently be discussed, this slight difference in optical bandgap for the two polymers can be considered to be negligible, allowing meaningful comparison between **Bu-IDT-BTz-Si** and **Sp-IDT-BTz-Si**.

2.11.3. Bu-IDT-BTz-Si Deprotection

A portion of **Bu-IDT-BTz-Si** was subjected to treatment with TBAF in the same manner as the other polymers, giving the deprotected polymer, **Bu-IDT-BTz-OH**.

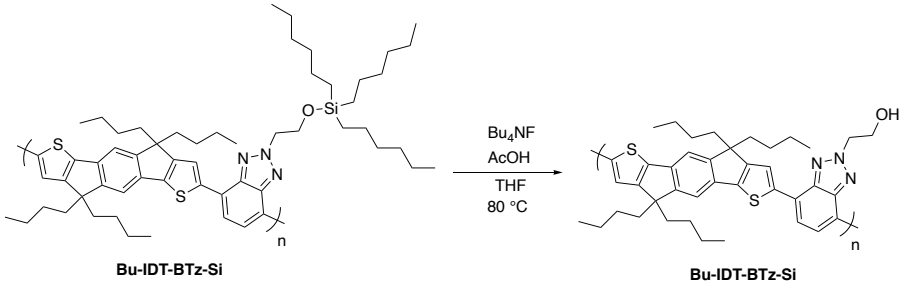

*Figure 86. Deprotection of **Bu-IDT-BTz-Si** to form **Bu-IDT-BTz-OH***

It was found that the cleaved polymer in this case was soluble in THF, owing to the presence of the tetrabutyl side chains on IDT which left it still somewhat soluble after

silyl ether cleavage. Happily, this allowed for NMR analysis of the deprotected polymer using deuterated chlorobenzene, shown in Figure 87.

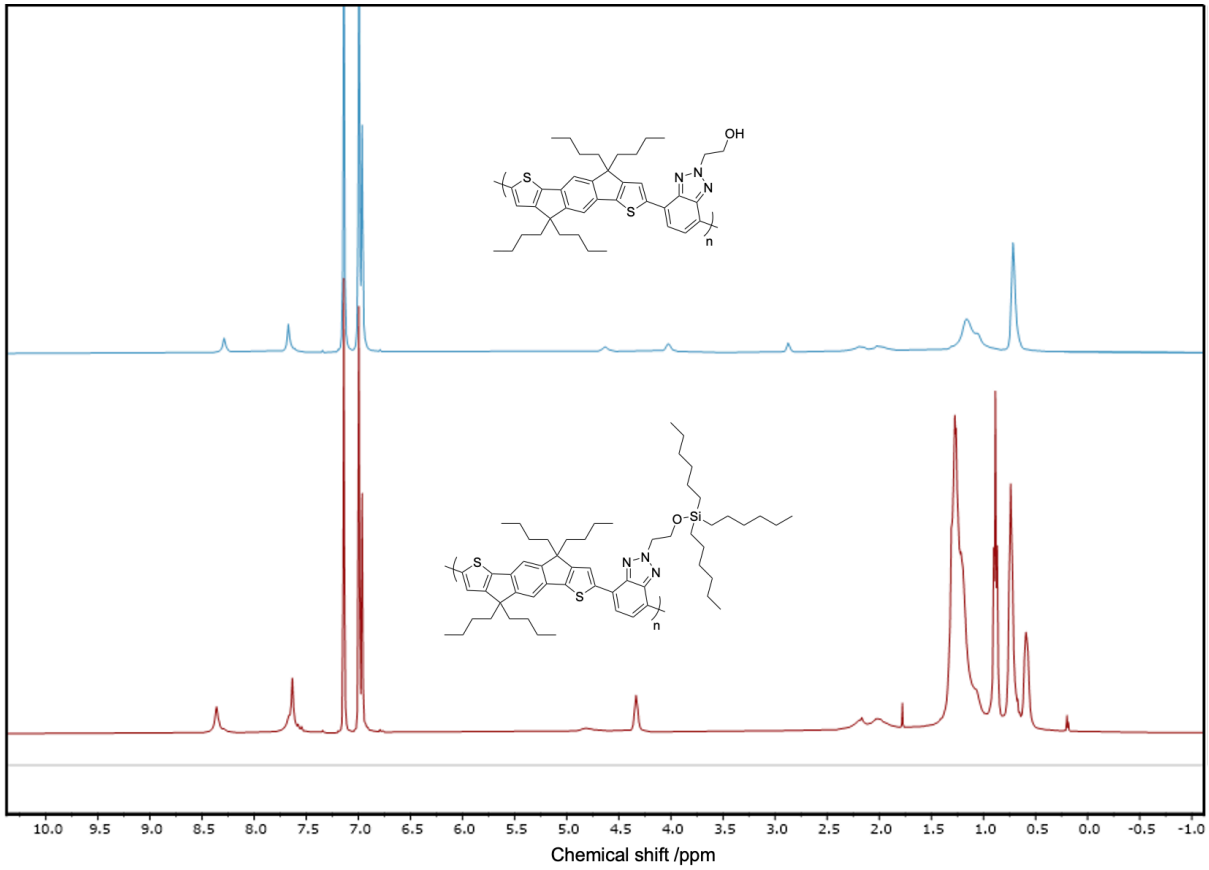

*Figure 87. 400 MHz ^{1}H NMR d-chlorobenzene spectrum for **Bu-IDT-BTz-Si** (bottom) and after deprotection to form **Bu-IDT-BTz-OH** (top)*

Figure 87 shows the disappearance of the silyl protons following TBAF treatment, while the aromatic protons remain the same, indicating the successful deprotection and generation of **Bu-IDT-BTz-OH**. Furthermore, the peaks at 4.63, 4.02 and a new peak at 2.87 ppm integrate in a 2:2:1 ratio, consistent with the presence of an alcohol.

The solution processability of the **Bu-IDT-BTz-OH** was further exploited to conduct thin film and solution UV-vis after deprotection, shown in Figure 88 for thin film (left) and solution (right). This was not possible for **Sp-IDT-BTz-OH** due to its insolubility.

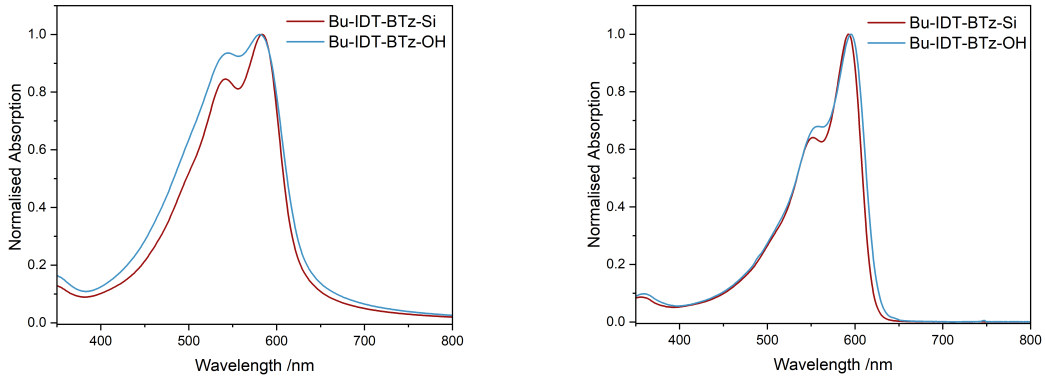

*Figure 88. Left: thin film UV-vis spectra of of **Bu-IDT-BTz-Si** and **Bu-IDT-BTz-OH**. Right: chloroform solution UV-vis spectra of **Bu-IDT-BTz-Si** and **Bu-IDT-BTz-OH**.*

Figure 88 shows minimal change in its UV-vis spectrum change after deprotection. The same films then underwent PESA measurement shown below in Figure 89. This shows no noticeable change in onset, indicating the same HOMO energy for **Sp-IDT-BTz-Si, Bu-IDT-BTz-Si** and **Bu-IDT-BTz-OH**.

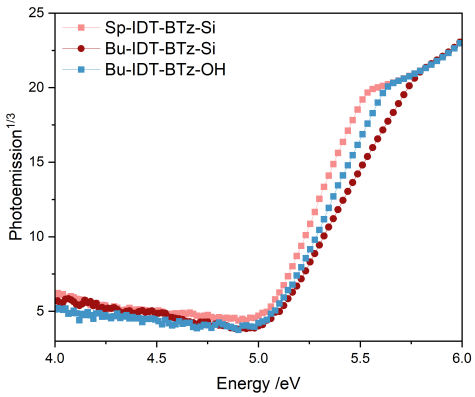

*Figure 89.PESA measurements for **Sp-IDT-BTz-Si**, **Bu-IDT-BTz-Si** and **Bu-IDT-BTz-OH***

Given the very small difference in UV-vis spectra, using **Bu-IDT-BTz-Si** as an optoelectronically similar comparison to **Sp-IDT-BTz-Si** was taken as valid.

Further exploiting the spin coated films of **Bu-IDT-BTz-OH,** contact angle measurements with water droplets were measured, and shown below.

Polymer film	Contact Angle / °	Standard deviation / °
Bu-IDT-BTz-Si	100.9	1.2
Bu-IDT-BTz-OH	87.3	1.1

This shows a reduction in contact angle of 14° after silyl cleavage. However, the reduction in contact angle is modest, with absolute value indicates that **Bu-IDT-BTz-OH** is only barely hydrophilic. This is not that surprising, given each repeat unit has only one alcohol unit, and the **Bu-IDT** comonomer is largely non-polar. Nonetheless it could be that intermediate hydrophilicity is sufficient to promote sufficient pore wetting owing to hydrogen-bonding interactions in the case of **Sp-IDT-BTz-OH**. For this polymer due to its insoluble nature, it was not possible to measure a contact angle, but its water sorption isotherm is good indication of its relative hydrophilicity.

2.11.4. Effect of Deprotection on Porosity of Bu-IDT-BTz-Si

The purpose of **Bu-IDT-BTz-OH** was to provide a non-porous analogue of similar hydrophilicity to **Sp-IDT-BTz-OH**. To verify it was actually non-porous, N_2 adsorption isotherms of **Bu-IDT-BTz-Si** and **Bu-IDT-BTz-OH** were measured and used to calculate the BET surface area. The isotherms are shown in Figure 90, with **Sp-IDT-BTz-Si** and **Sp-IDT-BTz-OH** included for comparison.

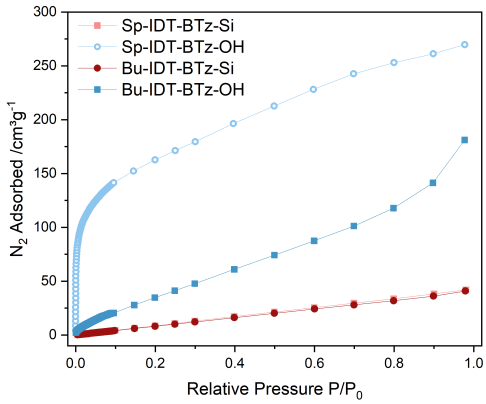

*Figure 90. N_2 adsorption isotherms for **Sp-IDT-BTz-Si**, **Sp-IDT-BTz-OH**, **Bu-IDT-BTz-Si** and **Bu-IDT-BTz-OH***

Bu-IDT-BTz-Si gave a BET surface area of 60 m^2 g^{-1}, while **Bu-IDT-BTz-OH** was calculated to be 69 m^2 g^{-1}, showing both to be non-porous. From the isotherm, it can be seen that **Bu-IDT-BTz-OH** shows a slightly greater surface adsorption compared to **Bu-IDT-BTz-Si**. This increased adsorption is likely due to differences in external surface area of the polymer powder: the sample of **Bu-IDT-BTz-Si** was a shiny polymer film, while **Bu-IDT-BTz-OH** was a fine powder. Nonetheless, BET analysis using the relative pressure range of 0.01 to 0.03 showed **Bu-IDT-BTz-OH** to have a similar surface area to **Bu-IDT-BTz-Si**.

2.11.5. Effect of Deprotection on Photocatalytic Activity of Bu-IDT-BTz-Si

Finally, the photocatalytic activity of **Bu-IDT-BTz-Si** and **Bu-IDT-BTz-OH** were measured. Data for **Sp-IDT-BTz-Si** and **Sp-IDT-BTz-OH** is also shown alongside in Figure 91 for comparison.

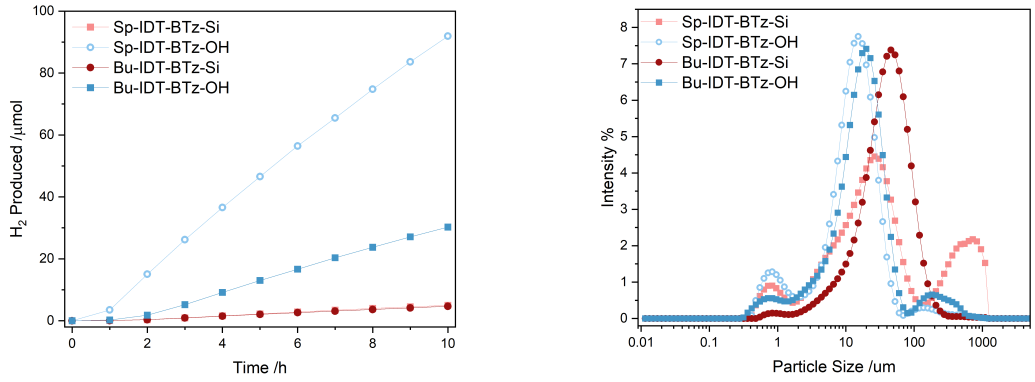

*Figure 91. For **Sp-IDT-BTz-Si**, **Sp-IDT-BTz-OH**, **Bu-IDT-BTz-Si** and **Bu-IDT-BTz-OH**. Left: photocatalytic activity under neutral conditions. Right: Laser diffraction particle size distributions.*

The data for these four polymers is summarised in the table below for comparison.

Polymer	N_2 BET Surface Area / $m^2\ g^{-1}$	D[3,2] Particle Size / μm	Average H_2 Produced Neutral / μmol h^{-1}
Sp-IDT-BTz-Si	60	7.0	0.58
Sp-IDT-BTz-OH	528	4.8	9.40
Bu-IDT-BTz-Si	60	18.5	0.54
Bu-IDT-BTz-OH	69	6.3	3.58

The comparison between non-porous **Bu-IDT-BTz-OH** and porous **Sp-IDT-BTz-OH** is insightful, as they have relatively similar D[3,2] particle sizes and therefore external surface area, yet the porous polymer has triple the H_2 production rate. This provides evidence for the beneficial effect of porosity on photocatalytic activity for polymers with hydrophilic functional groups.

This data shows a marked increase in photocatalytic activity for the non-porous **Bu-IDT-BTz-Si** after conversion to the still non-porous **Bu-IDT-BTz-OH**. Nonetheless there is an almost halving of D[3,2] particle size for Bu-IDT-BTz-OH compared to its protected parent polymer Bu-IDT-BTz-Si, making direct comparison of the effect of hydrophilicity on these non-porous polymer less clear.

2.12. Conclusions and Future Work

In this chapter, novel tert-butyl spirofluorene substituted monomers **Sp-IDT** and **Sp-IF** were synthesised and polymerised to form microporous polymers. Use of **BDT-Si** comonomer units led to irreversible structural changes taking place on constituent polymers under deprotection conditions. IR and NMR investigation, supported by literature led to the conclusion that this was quinoidal ketones. A new comonomer, **BTz-Si** with electronically insulating ethylene groups to decouple the effects of deprotection from the optoelectronic properties of the polymer was designed and synthesised. Deprotection to produce alcohol bearing polymers **Sp-IDT-BTz-OH** and **Bu-IDT-BTz-OH** was demonstrated by XPS and NMR investigation. This provided a platform to conduct an in-depth investigation of the effects of porosity and relative

hydrophilicity on conjugated polymer photocatalysts. The properties of the IDT-BTz polymer series are summarised below.

Polymer	N_2 BET Surface Area / $m^2\ g^{-1}$	D[3,2] Particle Size / μm	Average H_2 Produced Neutral / μmol h^{-1}
Sp-IDT-BTz-Si	60	7.0	0.58
Sp-IDT-BTz-OH	528	4.8	9.40
Sp-IDT-BTz-Et	418	7.0	0.89
Sp-IDT-BTz-Hex	503	4.2	1.29
Sp-IDT-BTz-Dec	165	3.4	0.28
Bu-IDT-BTz-Si	60	18.5	0.54
Bu-IDT-BTz-OH	69	6.3	3.58

It was demonstrated that that microporosity in conjugated polymers is beneficial for photocatalysis, though for polymers lacking hydrophilic moieties this effect is small. This was illustrated by the series **Sp-IDT-BTz-Et**, **Sp-IDT-BTz-Hex** and **Sp-IDT-BTz-Dec**, where lower surface area was correlated with reduced photocatalytic activity, despite smaller average particle sizes. Furthermore, for the hydrophobic polymers, porous **Sp-IDT-BTz-Hex** outperforms non-porous **Sp-IDT-BTz-Si** and **Bu-IDT-BTz-Si**, though differences in particle size differences are also likely contributing to this.

Deprotection to convert silyl ether groups to alcohols, and increase the relative hydrophilicity is shown to be favourable for photocatalytic activity in all cases. This is shown by comparing the non-porous hydrophobic **Bu-IDT-BTz-Si** with its also non-porous more hydrophilic analogue **Bu-IDT-BTz-OH**, though here too particle size was also presumed to be playing a role. For microporous polymers however, this data shows that microporosity *in combination* with hydrophilic moieties is most effective at increasing photocatalytic rate, as shown by the relative activity of the porous and hydrophilic **Sp-IDT-BTz-OH**. Water sorption isotherm measurements of this polymer in comparison to its porous analogue **Sp-IDT-BTz-Hex** which lacked hydrophilic residues revealed a much greater ability of the porous polymer to adsorb water.

To investigate the photophysics taking place in **Sp-IDT-BTz-OH** and **Sp-IDT-BTz-Hex**, fs-TAS experiments revealed that almost instantaneous polaron generation was taking place on both polymers in the absence of ascorbic acid, Pt, and less than 1 ppm residual Pd. Although for now, the relative magnitudes of these charges cannot be quantified in order to link this to photocatalytic activity, it seems likely that charge generation is aided by the polymers' highly porous structure, and in particular the ingress of water therein. This is supported by the extremely rapid quenching of the hole polaron signals by aqueous ascorbic acid, which effectively supresses the signal on low ps timescales. In order to better understand the effects of hydrophilicity in conjugation with porosity, PIAS measurements are underway to probe the photophysics on longer timescales, and to see how this relates to the large difference in water adsorption behaviour between both porous polymers.

Further work on these materials could examine the distribution of photodeposited Pt with respect to the surface of the pores, as well as the effects of mass transport of reagents in the pores, which has been shown elsewhere to be important for photocatalytic activity.[218,394,395]

2.13. Methods

Synthesis procedures can be found in 9. Supplementary Information

2.13.1. TBAF Deprotection

In a large microwave vial, 1.26 g TBAF trihydrate was dissolved in 20 mL THF and 1 mL acetic acid was added to neutralise the basicity of the TBAF. The sample of polymer was added to this, sonicated for 30 minutes and stirred at 80 °C overnight. This was then poured into methanol and filtered, washing with more methanol and acetone to remove any residual TBAF or silyl groups.

2.13.2 Photocatalysis Measurements

Photocatalysis measurements were conducted by adding the aqueous photocatalytic testing medium to a glass quartz cell chilled to 15 °C with tubing around it, under 450-550 mbar argon pressure connected in a closed loop with an 8890 Agilent GC system with a solenoid pump to circulate the headspace. This was irradiated by an Asahi Max 303 330 W xenon lamp fitted with a vis (390-740) mirror module, and AM 1.5 G filter and a collimator (1.0x) lens to direct the light onto the class reactor cell. This intensity of the light on the sample was calibrated to 1 Sun using a Newport calibrated reference cell. Under photocatalytic testing, the reactor headspace was injected into the gas chromatography system every hour for gas detection.

The GC was calibrated using a reference gas and calculating the volume of the reactor headspace using a temporarily attached chamber of known volume. Using the peak area for a known concertation of H_2 and the calculated photoreactor volume, it was possible to then estimate the moles of H_2 produced from the area of the GC peak. This was plotted as a function of time in order to monitor the H_2 production rate and assess the photocatalytic activity of different photocatalytic systems.

For **Sp-IDT-BTz-OH**, the light intensity was measured below the cell when it was empty, containing no sample. It showed an absolute irradiance of 30.3 mW at 575 nm, which is the λ_{max} of the polymer. It was measured again after adding the sample and showed 9.4 mW. These measurements were conducted to tell if the photocatalyst absorbance was saturated.

2.13.3 Laser Diffraction Measurements

The sample preparation was identical to that of photocatalytic testing, except for omitting the addition of H_2PtCl_6. Rather than adding to the photoreactor, these were added to a Mastersizer 2000, diluting up to 800 mL with deionised water. The particle size distributions were measured 10 times, with sonication between measurements. The data for the 10 measurements is then averaged.

2.13.4. Sample Preparation for Transient Absorption Spectroscopy

For the Pt deposited samples, 3.5 mg polymer was dispersed in 2 mL NMP sonicated and pipetted into 5.0 mL water with 27 uL H_2PtCl_6 and 0.25 g ascorbic acid. This was irradiated at 1 Sun under stirring in a 35 ml vial with a small stirrer bar for 5 h. It was poured through a cellulose filter and washed with water several times, making sure to not let the polymer dry out. After washing the polymer was transferred to a vial, and a mixture of 1 mL NMP and 2.5 mL water was added to each, then sonicated at 200 W for 1 minute. Further dilutions for TAS measurements using the same ratio of NMP and water.

2.13.5. Contact Angle Measurements

Contact angles were measured by Dr Robert Jacobs. The polymers were spin coated from concentrations of 5 mg mL^{-1} in chloroform onto glass slides. The contact angles were measured with water droplets on the surface and averaging across two samples of each polymer with three repeats.

Chapter 3: Further Exploration of Intrinsically Microporous Conjugated Polymer Chemistry

3.1. Introduction

Building on the understanding of the effects of porosity and hydrophilicity from the previous chapter, this tert-butyl spirofluorene family of polymers was further explored by incorporating more diverse comonomers.

It was also desirable to generate pairs of porous polymers that have type-II energetic offsets so that porous heterojunction photocatalysts can be fabricated. It was shown in the previous chapter that intrinsic exciton separation is possible in **Sp-IDT-BTz-OH** which is attributed to its hydrophilic porosity. However, even in such cases the presence of a type-II heterojunction is expected to be beneficial, owing to its ability to spatially separate polarons. This is expected to further facilitate exciton separation and hinder polaron recombination. Indeed, it was shown that the glycolated polymer **g-IDTBT** was able to intrinsically generate charges owing to its hydrophilic glycol side chains. However, in this system geminate and non-geminate recombination was still significant, and incorporation of an acceptor to form a type-II heterojunction reduced both of these unfavourable processes.[302]

This chapter will discuss the synthesis, properties, and photocatalytic activity of each of the novel polymers individually in Sections 3.2 and 3.3, then their properties will be compared in more detail in Section 3.4 where the trends will be discussed. Finally in Section 3.5. blends of the polymers will be discussed.

3.2. Investigating the Effect of Spirofluorene Density on Porosity

3.2.1. Maximising Porosity with All tert-Butyl Spirofluorene Polymer

Sp-IDT and **Sp-IF** monomers (synthesised in Chapter 2) were combined, to construct an 'all-spiro' polymer, i.e. incorporating tert-butyl spirofluorene groups on both comonomers. These monomers underwent Stille polymerisation to produce a yellow insoluble polymer **Sp-IDT-IF-Sp**.

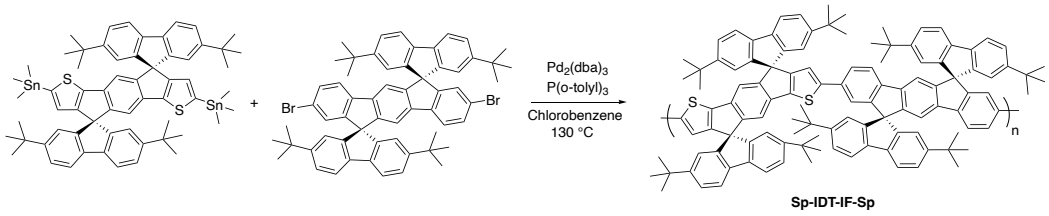

Figure 92. Polymerisation of Sp-IDT and Sp-IF to form Sp-IDT-IF-Sp.

Its insolubility highlighted the importance of the silyl ether comonomer groups for solubility, to counteract the rigidity of the tert-butyl spirofluorene units. Its N_2 sorption isotherm was measured, shown in Figure 93. It displays a high degree of porosity, with a BET surface area of 623 $m^2\ g^{-1}$. Relative to other reported intrinsically microporous polymers in literature, such as **SMP-3** with a BET surface area of 431 $m^2\ g^{-1}$ (discussed in Chapter 2), the porosity of **Sp-IDT-IF-Sp** is relatively high.

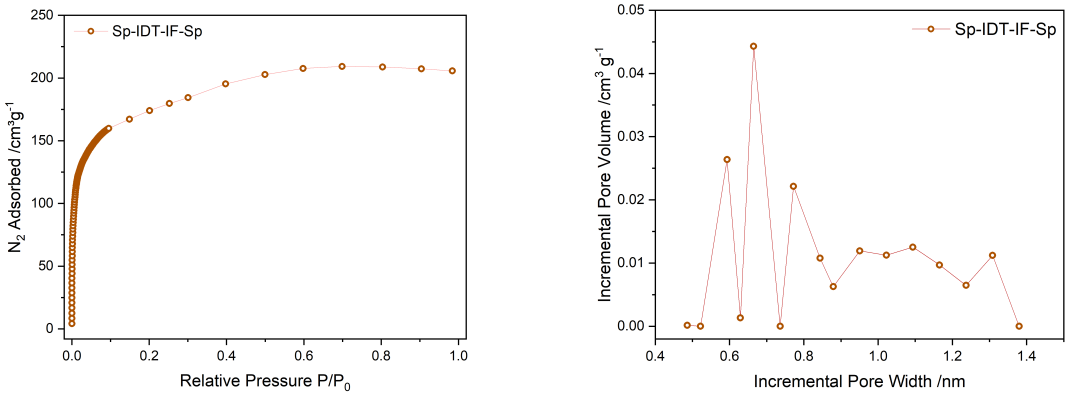

*Figure 93. For **Sp-IDT-IF-Sp**. Left: N_2 adsorption isotherm. Right: calculated pore size distributions*

Its photocatalytic activity and particle size distribution is shown in Figure 94, showing a very low activity of 0.13 μmol h^{-1}. While optoelectronic properties could not be determined due to its insolubility, its poor performance is consistent with the findings of the previous chapter: that high porosity in the absence of hydrophilic moieties does not translate into highly active photocatalysts. This is despite its relatively low average particle size of 7.6 μm, as measured by laser diffraction.

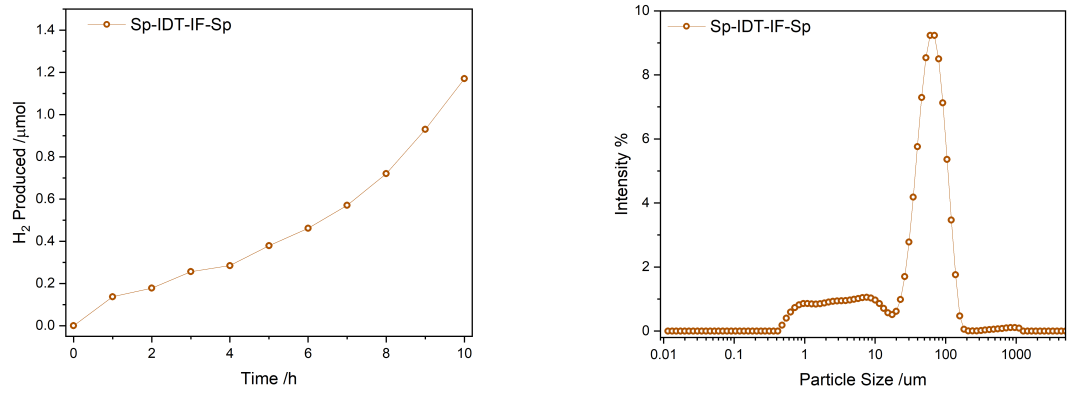

*Figure 94. For **Sp-IDT-IF-Sp**. Left: photocatalytic activity under neutral conditions. Right: laser diffraction particle size profile.*

This data for **Sp-IDT-IF-Sp** is summarised in the table below.

N_2 BET Surface Area / m^2 g^{-1}	D[3,2] Particle Size / μm	Average H_2 Produced Neutral / μmol h^{-1}
623	7.6	0.13

3.2.2 Using a Mono tert-Butyl Spirofluroene Monomer

Next, the opposite effect, reducing the number of tert-butyl spirofluorene units was investigated. A spirofluorene monomer, **Sp-F** was synthesised, which attached tert-butyl spirofluorene to fluorene via the single methylene bridge, producing an analogue of **Sp-IF** with a shorter aromatic core and only one tert-butyl spirofluorene unit. The dibrominated version was formed under similar conditions to **Sp-IF,** which subsequently underwent Miyaura borylation, to produce diborylated **Sp-F** monomer with its synthesis shown below in Figure 95.

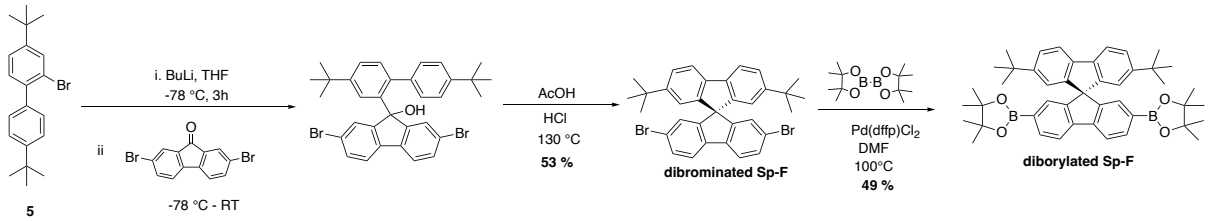

*Figure 95. Synthesis of **Sp-F** monomer*

It was thought that this monomer, owing to its shorter rigid fused ring backbone may enable a higher degree of solubility after side chain cleavage (of the comonomer). This would better enable formation of porous heterojunctions by solution processing of the deprotected polymer, in comparison to **Sp-IDT-BTz-OH** which was insoluble in its deprotected form.

3.2.3. Sp-F-BTz-Si Synthesis and Optoelectronic Properties

To this end, **Sp-F** was copolymerised with **BTz-Si** via Suzuki polymerisation to produce the yellow soluble polymer **Sp-F-BTz-Si**.

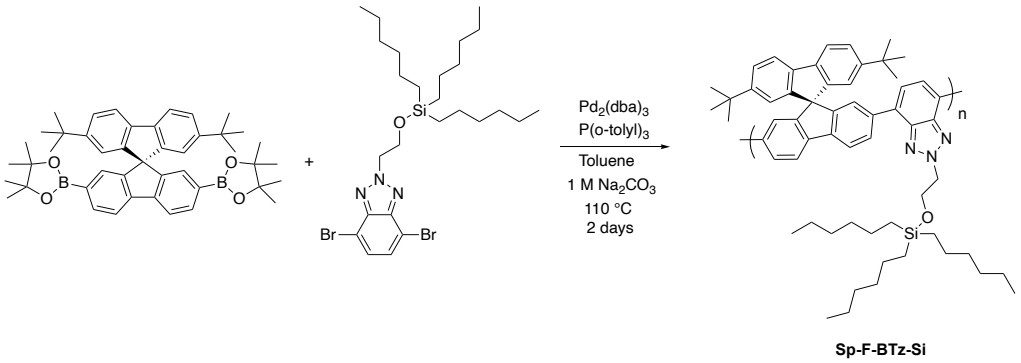

*Figure 96. Polymerisation of **Sp-F** and **BTz-Si** to form **Sp-F-BTz-Si**.*

Its optical bandgap and HOMO were estimated by thin film UV-vis spectroscopy and PESA, shown in Figure 97 and the table below. Compared to **Sp-IDT-BTz-Si** (from Chapter 1) with HOMO and LUMO estimates of -5.1 and -3.1 eV, swapping the IDT unit with F produces HOMO and LUMO estimates of -5.6 and -3.0 eV for **Sp-F-BTz-Si**. This shows that the monomer substitution widens the bandgap significantly. This is likely due to the reduction in conjugation length due to the shorter fused aromatic ring of the F unit, reduced planarity, as well substitution of electron rich IDT for less electron rich F, which dampens push-pull molecular orbital hybridisation.

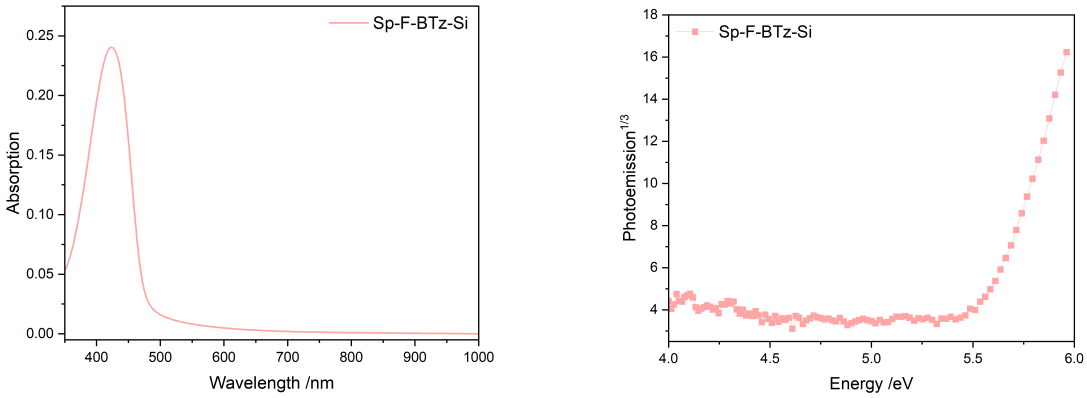

*Figure 97. **Sp-F-BTz-Si** thin film UV-vis spectrum (left) and PESA (right)*

The properties of **Sp-F-BTz-Si** are summarised in the table below.

Absorption Onset / nm	Absorption Peak(s) /nm	Optical Bandgap /eV	HOMO (PESA) /eV	LUMO (PESA+ E_g) /eV	M_N /gmol^{-1}	M_W /g mol^{-1}	Poly-dispersity
475	421	2.6	-5.6	-3.0	22460	30383	1.35

3.2.4. Deprotection of Sp-F-BTz-Si

A portion of **Sp-F-BTz-Si** was deprotected with acetic acid neutralised TBAF in THF to produce **Sp-IDT-F-OH**.

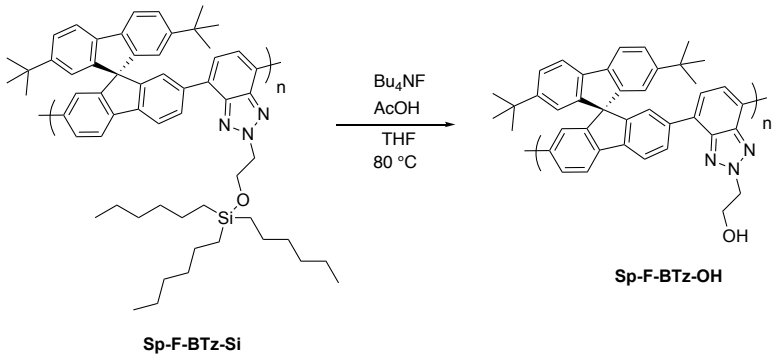

*Figure 98. Deprotection of **Sp-F-BTz-Si** to form **Sp-F-BTz-OH***

Happily, it was still moderately soluble in chloroform after deprotection, enabling NMR characterisation to assess the deprotection. This is shown in Figure 99, indicating the successful removal of silyl groups owing to the disappearance of the silyl ether proton peaks at 1.15, 0.80 and 0.45 ppm. It also showed no change to the aromatic protons, consistent with no degradation of the polymer backbone during deprotection.

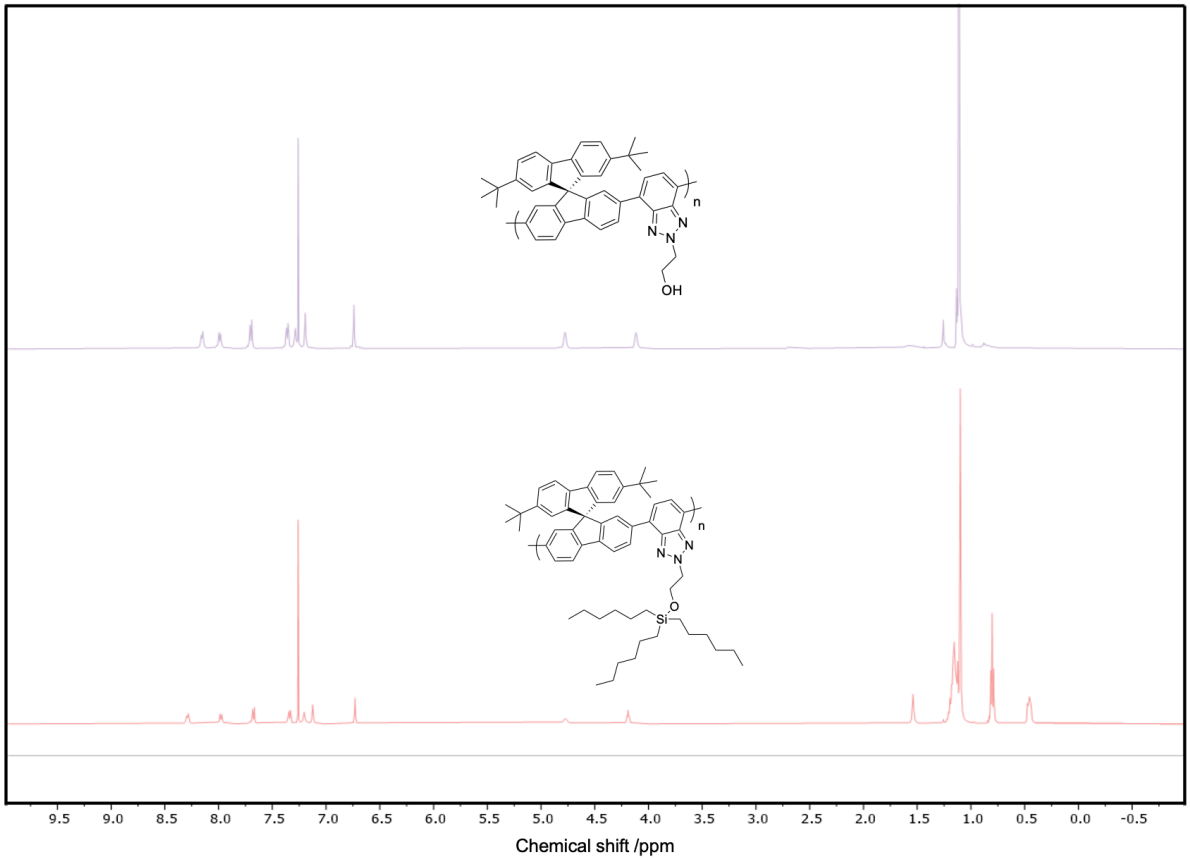

*Figure 99. 500 MHz ^{1}H NMR $CDCl_3$ spectrum for **Sp-F-BTz-Si** (bottom) and after deprotection to form **Sp-F-BTz-OH** (top)*

The relatively good solubility of **Sp-F-BTz-OH** allowed spin coating onto glass slides, enabling UV-vis spectroscopy, PESA and contact angle measurements to be conducted before and after deprotection. These are shown in Figure 100.

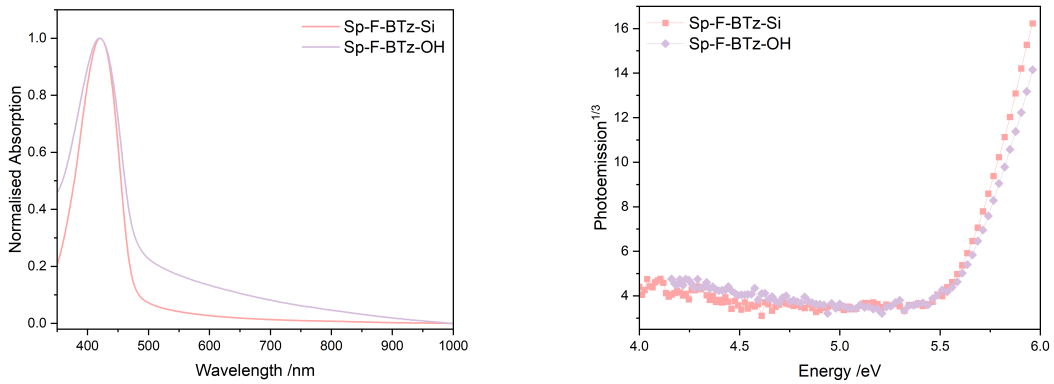

***Figure 100**. For **Sp-F-BTz-Si** and **Sp-F-BTz-OH** spin coated films. Left: UV-vis spectra. Right: PESA measurements*

Contact angle measurements for spin coated films of **Sp-F-BTz-Si** and **Sp-F-BTz-OH** are shown in the table below.

Polymer Film	Contact Angle / °	Standard Deviation / °
Sp-F-BTz-Si	97.3	0.43
Sp-F-BTz-OH	83.9	2.05

It can be seen that deprotection causes no change to the optical bandgap or HOMO, while bringing about a small decrease in contact angle of 13.4 °, indicative of a slight increase in hydrophilicity.

3.2.5. Effect of Deprotection on Porosity of Sp-F-BTz-Si

N_2 sorption isotherms were measured for **Sp-F-BTz-Si** and **Sp-F-BTz-OH**, shown in Figure 101. Unfortunately, it showed neither of the polymers to possess porous character, with BET surface areas below 100 $m^2\ g^{-1}$, even after deprotection. This result will be further discussed in Section 3.4. in comparison with the other polymers.

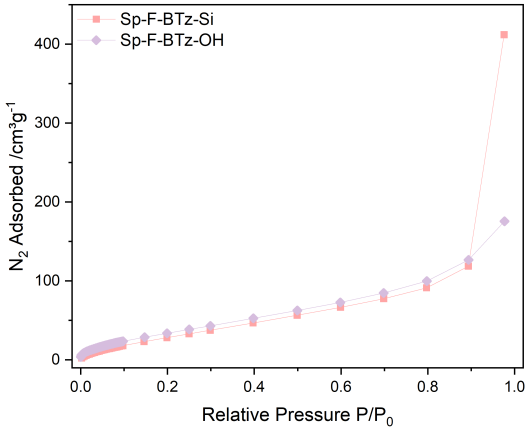

*Figure 101. N_2 adsorption isotherms for **Sp-F-BTz-Si** and **Sp-F-BTz-OH**.*

3.2.6. Effect of Deprotection on Photocatalytic Activity of Sp-F-BTz-Si

The photocatalytic activity and particle size distributions of **Sp-F-BTz-Si** and **Sp-F-BTz-OH** were measured and are displayed in Figure 102. **Sp-F-BTz-OH** shows an increase in activity compared to the protected version, as would be expected based off the behaviour of the non-porous polymers **Bu-IDT-BTz-Si** and **Bu-IDT-Si** in the previous chapter. While greater dispersibility often accounts for the better performance of non-porous hydrophilic polymers due to improved dispersibility, in this case **Sp-F-BTz-Si** and **Sp-F-BTz-OH** have similar average particle sizes. This implies there must be other factors at play explaining the improved performance of the deprotected polymers, as will be further discussed.

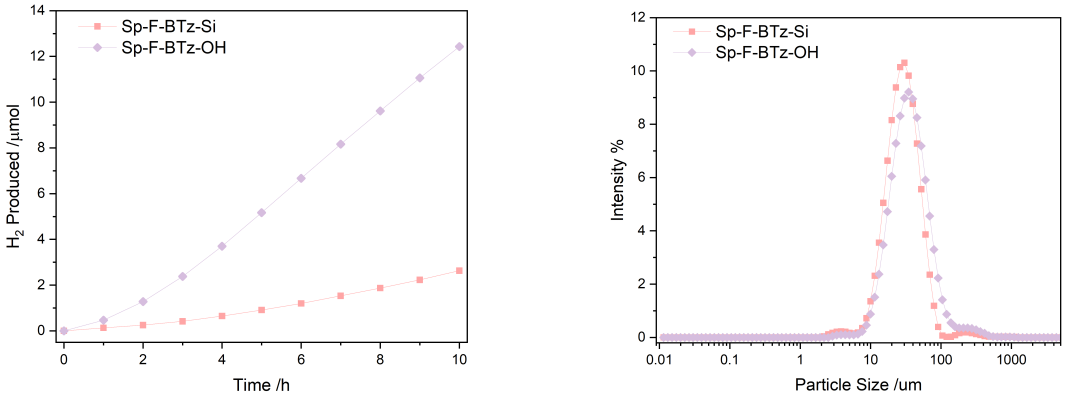

*Figure 102. For **Sp-F-BTz-Si** and **Sp-F-BTz-OH**. Left: photocatalytic activity under neutral conditions. Right: laser diffraction particle size profile*

The photocatalysis and particle size data for **Sp-F-BTz-Si** and **Sp-F-BTz-OH** is shown below.

Polymer	D[3,2] Particle Size / μm	Average H_2 Produced Neutral / μmol h^{-1}
Sp-F-BTz-Si	21.8	0.31
Sp-F-BTz-OH	27.2	1.45

3.3. Varying Sp-IDT Comonomer

3.3.1. F-Si Monomer Synthesis

Fluorene is neither electron rich nor electron deficient, so it would be expected to give a polymer with fairly high energy FMOs and could serve as a potential donor polymer in a heterojunction system. Fluorene is also attractive as a comonomer because it can be doubly alkylated on its bridging sp^3 methylene unit. This is advantageous because it means each repeat unit can bare two silyl protected alcohols compared to one in **Sp-IDT-BTz-Si**, enhancing the potential hydrophilicity of the deprotected polymer and also meaning such large silyl groups as trihexylsily need not be installed to ensure sufficient solubility. For this reason, tert-butyl dimethyl silyl ether protecting groups were used.

The monomer was synthesised by first protecting the alcohol of 2-bromoethanol using tert-butyl dimethyl silyl chloride. Next fluorene was deprotonated enabling nucleophilic attack of the silyl ether bromide twice to give the final monomer, shown in Figure 103.

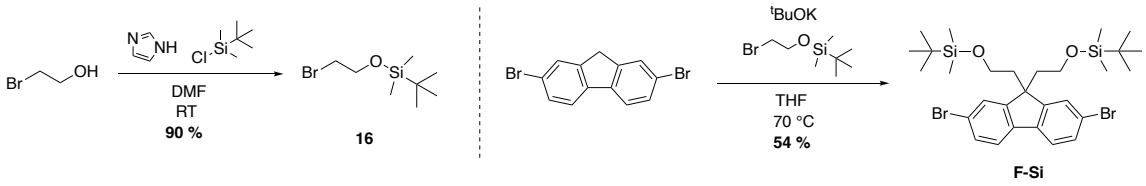

*Figure 103. Synthesis of **F-Si** monomer*

3.3.2. Sp-IDT-F-Si Synthesis and Optoelectronic Properties

The **F-Si** monomer was reacted with distanylated **Sp-IDT** by Stille polymerisation to produce an orange-yellow soluble polymer **Sp-IDT-F-Si**.

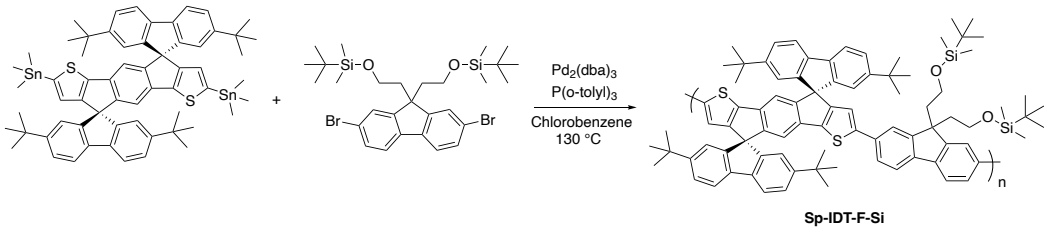

*Figure 104. Polymerisation of **Sp-IDT** and **F-Si** to form **Sp-IDT-F-Si**.*

Its optical bandgap and HOMO were estimated by thin film UV-vis spectroscopy and PESA measurement, shown in Figure 105.

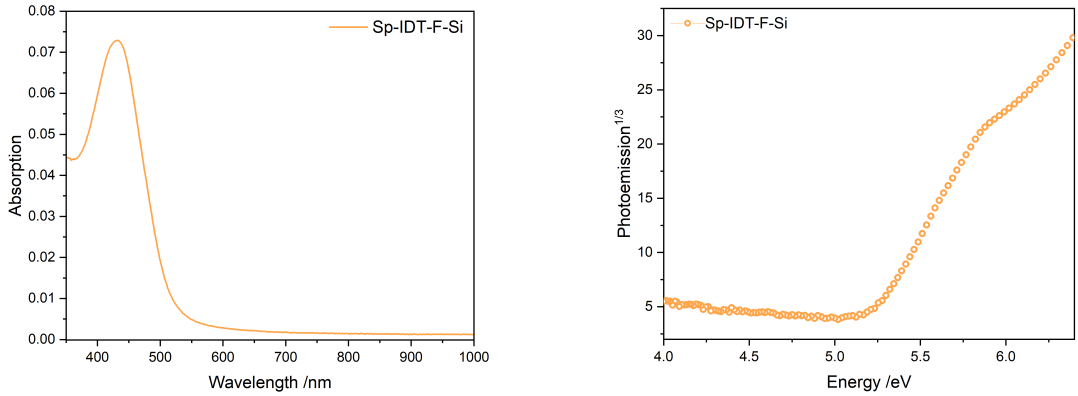

*Figure 105. **Sp-IDT-F-Si** thin film UV-vis spectrum (left) and PESA (right)*

The properties of **Sp-IDT-F-Si** are summarised in the table below.

Absorption Onset / nm	Absorption Peak(s) /nm	Optical Bandgap /eV	HOMO (PESA) /eV	LUMO (PESA+ E_g) /eV	M_N /g mol^{-1}	M_W /g mol^{-1}	Poly-dispersity
510	431	2.4	-5.2	-2.8	12593	23139	1.84

3.3.3. Sp-IDT-F-Si Deprotection

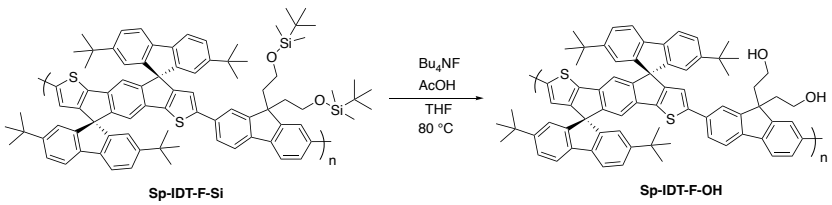

*Figure 106. Deprotection of **Sp-IDT-F-Si** to form **Sp-IDT-F-OH***

A portion of **Sp-IDT-F-Si** was deprotected with acetic acid neutralised TBAF in THF to produce **Sp-IDT-F-OH**. It was sparingly soluble in chloroform after deprotection, enabling NMR characterisation to assess the deprotection (Figure 107)

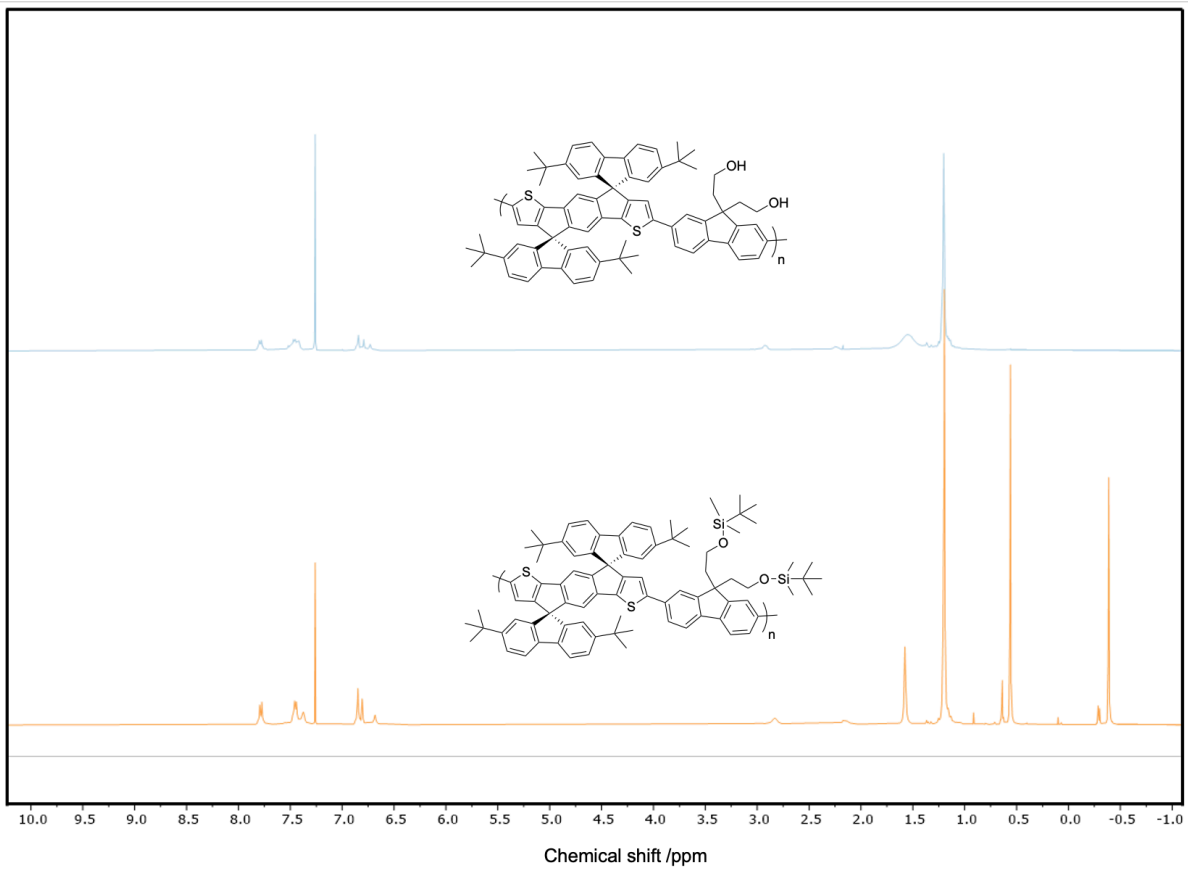

*Figure 107. 500 MHz ^{1}H NMR $CDCl_3$ spectrum for **Sp-IDT-F-Si** (bottom) and after deprotection to form **Sp-IDT-F-OH** (top).*

NMR showed disappearance of the silyl peaks at 0.56 and -0.39 ppm, indicative of successful deprotection. **Sp-IDT-F-OH** was nonetheless much less soluble than **Sp-IDT-F-Si,** so it was not possible to dissolve at high enough concentration to spin coat onto glass slides to measure PESA and UV-vis. It is assumed that this does not vary significantly though, give the NMR shows no change in the aromatic region.

3.3.4 Effect of Deprotection on Porosity of Sp-IDT-F-Si

N_2 isotherms of **Sp-IDT-F-Si** and **Sp-IDT-F-OH** were measured in order to calculate their BET surface areas, shown in Figure 108.

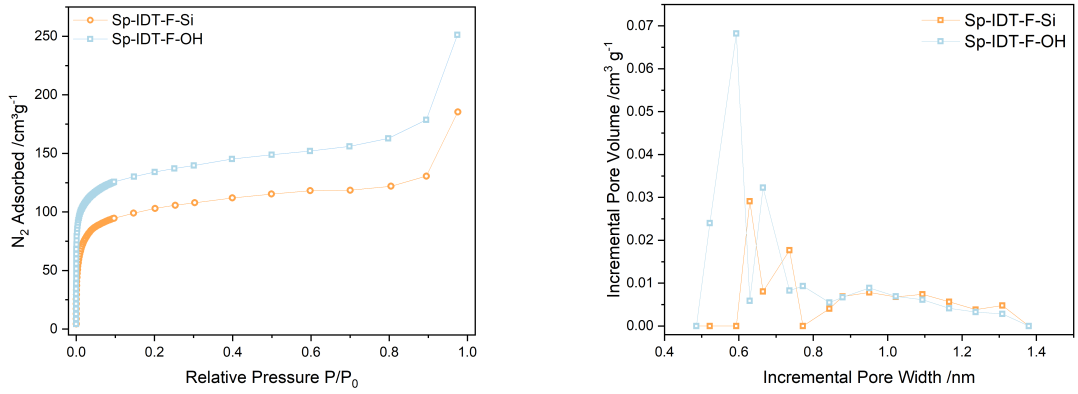

*Figure 108. Left: N_2 adsorption isotherms for **Sp-IDT-F-Si** and **Sp-IDT-F-OH**. Right: calculated pore size distributions for **Sp-IDT-F-OH**.*

Owing to the short and inflexible tert-butyl dimethyl silyl protecting group, **Sp-IDT-F-Si** has relatively high porosity of 376 m^2 g^{-1}. It is likely that its ability to 'clog' the pores is limited, exhibiting similar behaviour to **Sp-IF-BDT-Si** in the previous chapter which was porous while the tert-butyl dimethyl silyl protecting groups were still attached. Deprotection of **Sp-IDT-F-Si** form **Sp-IDT-F-OH** caused a modest increase in porosity, increasing it from 376 to 482 m^2 g^{-1}. Though this is still lower than Sp-IDT-BTz-OH from Chapter 2, with a BET surface area of 528 m^2 g^{-1}.

The water sorption for **Sp-IDT-F-Si** before and after deprotection is shown in Figure 109 (left). This is also compared to the water sorption for the porous hydrophilic polymer Sp-IDT-BTz-OH from the previous chapter in Figure 109 (right) Their structures are shown below for comparison (Figure110).

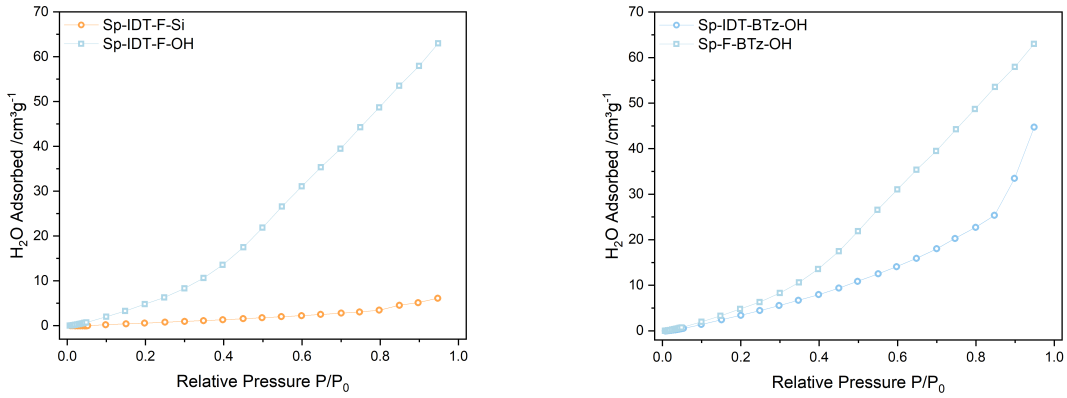

*Figure 109. Left: H_2O adsorption isotherms for **Sp-IDT-F-Si** and **Sp-IDT-F-OH**. Right: H_2O adsorption isotherms for **Sp-IDT-F-OH** and **Sp-IDT-BTz-OH***

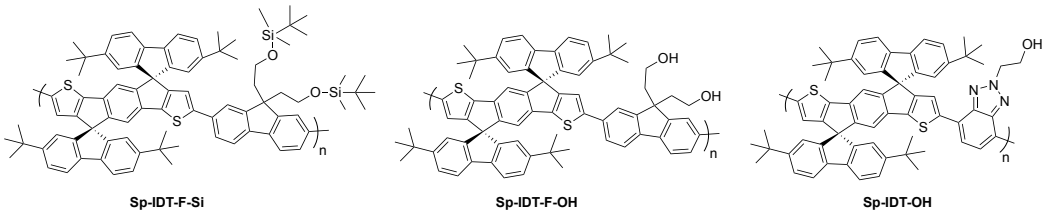

*Figure 110. Structures of **Sp-IDT-F-Si**, **Sp-IDT-F-OH** and **IDT-BTz-OH***

This shows that the silyl ether protecting groups disable water sorption. Given **Sp-IDT-F-Si** and **Sp-IDT-F-OH** have similar N_2 sorption BET surface areas of 376 and 482 $m^2 g^{-1}$ respectively, the lack of water sorption in **Sp-IDT-F-Si** is consistent with hydrophobicity rendering the pores less accessible for water vapour in isotherm measurements.

In addition, **Sp-IDT-F-OH** has a lower BET surface area of 482 g mol^{-1}, in comparison to 528 g mol^{-1} in **Sp-IDT-BTz-OH**. Despite this slightly lower porosity, it shows greater water sorption than **Sp-IDT-F-OH** (Figure 109 right). The reason for this is presumably due to **Sp-IDT-F-OH** possessing twice the number of alcohol functional groups per repeat unit compared to **Sp-IDT-BTz-OH**, facilitating more favourable interactions with water inside the structure. This is consistent with the idea that the presence of alcohols in these polymers facilitates interactions with water.

3.3.5. Effect of Deprotection on Photocatalytic Activity of Sp-IDT-F-Si

When tested for photocatalysis, **Sp-IDT-F-OH** proved to be significantly more active than **Sp-IDT-F-Si**. When the testing solution was neutralised, both **Sp-IDT-F-OH** and **Sp-IDT-F-Si** increased in activity, which is consistent with the high energy FMOs rendering the ascorbic acid oxidation half-reaction rate limiting, as was discussed in section 2.7.2. Laser diffraction measurements were also conducted in order to measure particle size, showing similar particle sizes, with **Sp-IDT-F-OH** being slightly larger than **Sp-IDT-F-Si** (Figure111).

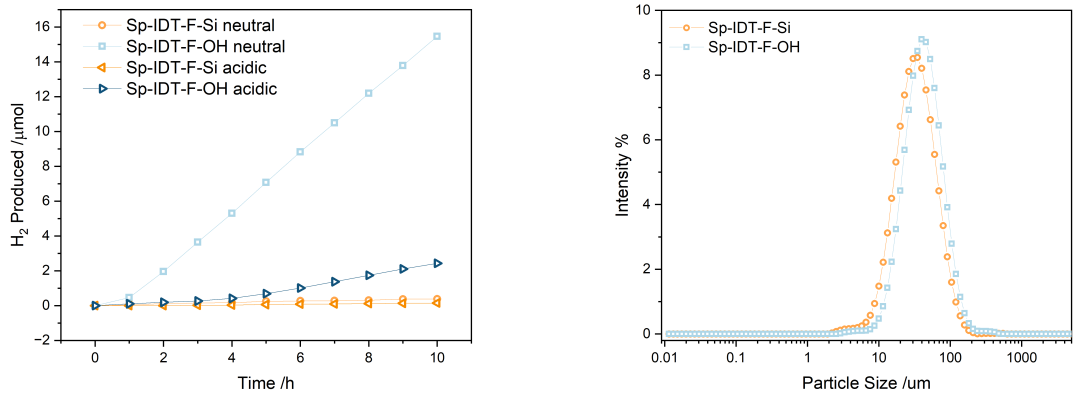

*Figure 111. For **Sp-IDT-F-Si** and **Sp-IDT-F-OH**. Left: photocatalytic activity under neutral and acidic conditions. Right: laser diffraction particle size profile*

The data for **Sp-IDT-F-Si** and **Sp-IDT-F-Si** is summarised in the table below.

Polymer	D[3,2] Particle Size / μm	N_2 BET Surface Area / $m^2\ g^{-1}$	Average H_2 Produced Neutral / μmol h^{-1}	Average H_2 Produced Acidic / μmol h^{-1}
Sp-IDT-F-Si	23.8	376	0.03	0.02
Sp-IDT-F-OH	31.6	482	1.69	0.32

In summary, protected **Sp-IDT-F-Si** and deprotected **Sp-IDT-F-OH** have similar BET surface areas (only increasing modestly after deprotection), and have similar average

particle sizes, however protected **Sp-IDT-F-Si** displays negligible water sorption in comparison to deprotected **Sp-IDT-F-OH**, and extremely low photocatalytic activity. This is attributed to deprotected **Sp-IDT-F-OH** possessing alcohol functional groups, enabling more favourable interactions with water inside the pores. These features reinforce the conclusions from the previous chapter, that porosity without hydrophilic groups to allow ingress of water to the pores is not a successful design strategy for photocatalysis.

3.3.6. NDI-Si Monomer Synthesis

In an effort to make a polymer with more electron deficient character to function as an acceptor in a heterojunction, naphthalene diimide (NDI) was selected as a comonomer. This also featured two alkylation positions, so the intermediate length silyl ether was chosen as a protecting group for pendant alcohols.

NDI-Si monomer synthesis is shown in Figure 112, using a similar strategy to before. First the alcohol of ethanolamine was protected using tributyl silyl chloride to produce **16**, utilising the water-soluble nature of the starting material for easy purification. Next, 2,6-dibromonaphthalene-1,4,5,8-tetracarboxylic dianhydride was heated in the presence of zinc acetate (as a gentle basic catalyst), and **16** to convert the anhydride to a diimide **NDI-Si** monomer, in an adapted literature procedure for NDI alkylation.[396]

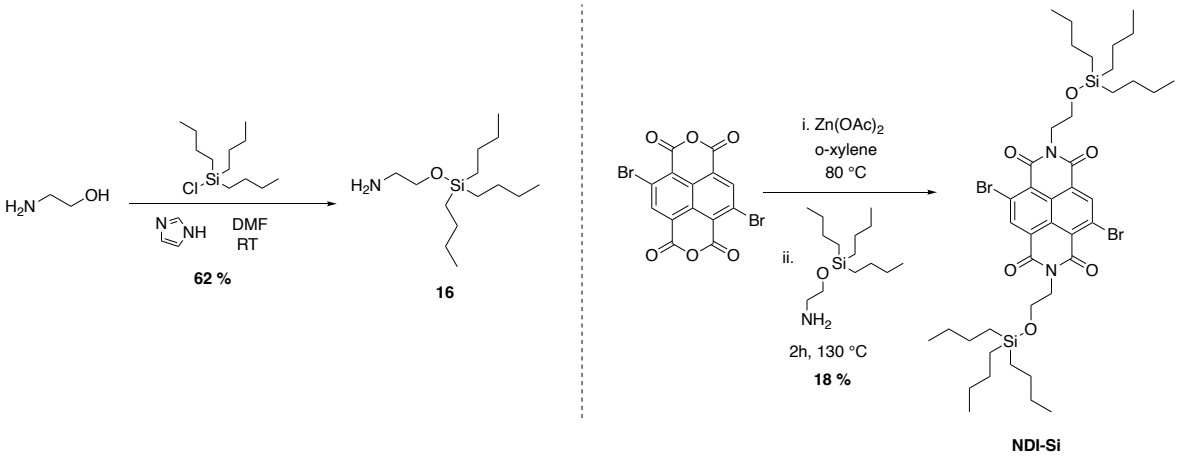

Figure 112. Synthesis of NDI-Si monomer

A proposed mechanism is given in Figure 113. Careful control of reaction time, in step ii, is imperative owing to the highly electron deficient character of the aryl bromide. This is because a nucleophilic aromatic substitution side reaction of the aromatic bromide by the amine is likely to happen. This is hindered by limiting the excess of amine and reaction time.

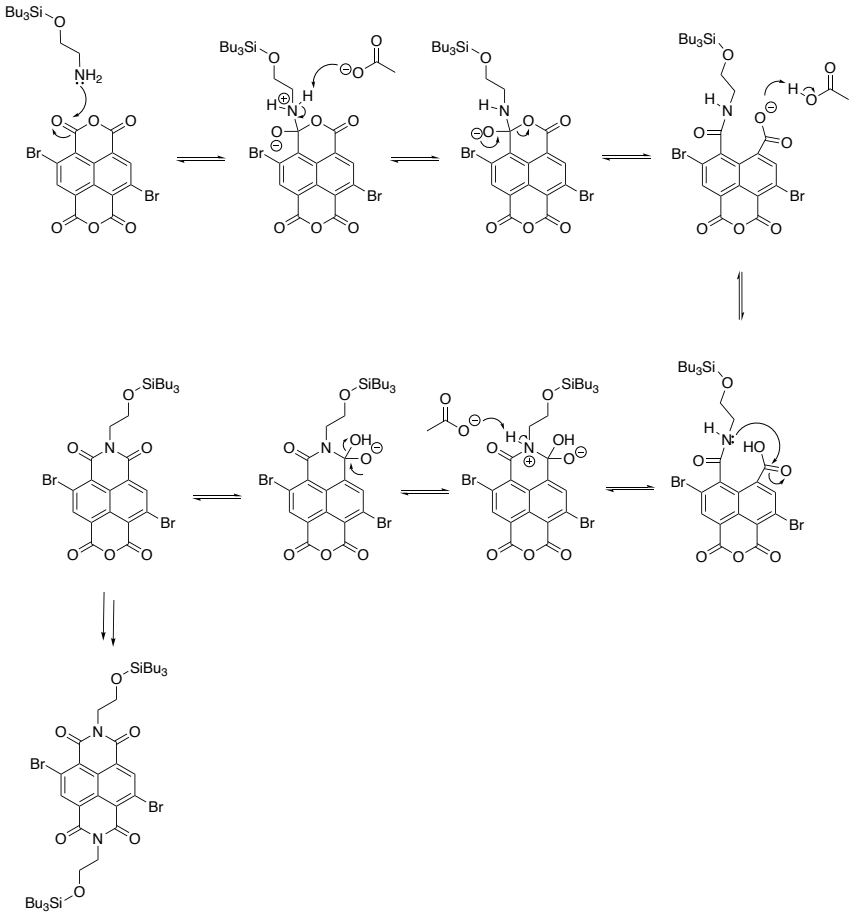

Figure 113. Mechanism for the synthesis of NDI-Si monomer

3.3.7. Sp-IDT-NDI-Si Synthesis and Optoelectronic Properties

The **NDI-Si** monomer was reacted with distanylated **Sp-IDT** by Stille polymerisation to produce a blue soluble polymer **Sp-IDT-NDI-Si**.

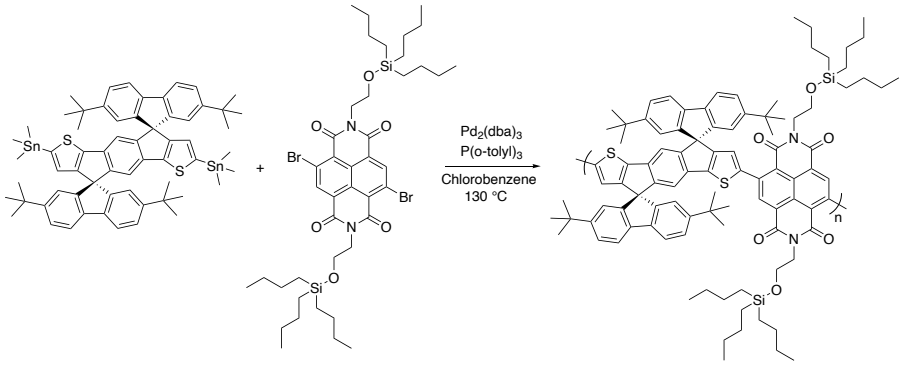

*Figure 114. Polymerisation of **Sp-IDT** and **NDI-Si** to form **Sp-IDT-NDI-Si**.*

UV-vis spectroscopy and PESA measurements were conducted to measure the HOMO and optical bandgap, shown in Figure 115. It shows the strongly electron withdrawing NDI unit causes significant narrowing of the optical bandgap due to push-pull hybridisation, which is beneficial in terms of solar light harvesting.

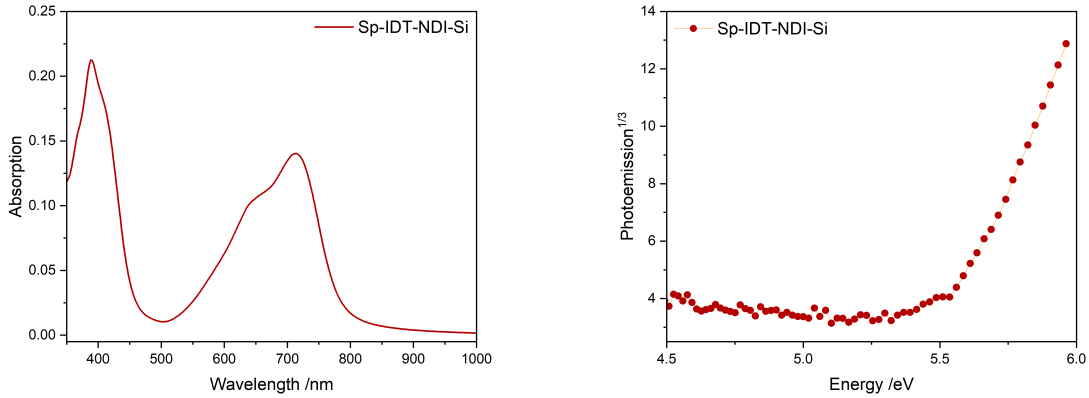

*Figure 115. **Sp-IDT-NDI-Si** thin film UV-vis spectrum (left) and PESA (right)*

The properties of Sp-IDT-NDI-Si are shown in the table below.

Absorption Onset / nm	Absorption Peak(s) /nm	Optical Bandgap /eV	HOMO (PESA) /eV	LUMO (PESA+ E_g) /eV	M_N /g mol^{-1}	M_W /g mol^{-1}	Poly-dispersity
797	340, 714	1.6	-5.5	-3.8	27864	41290	1.48

3.3.8. Sp-IDT-NDI-Si Deprotection

A portion of **Sp-IDT-NDI-Si** was deprotected with acetic acid neutralised TBAF in THF to produce **Sp-IDT-NDI-OH**. Similarly to **Sp-F-BTz-OH**, it was soluble in chloroform after deprotection. This demonstrates that it is possible to achieve solution processability while using the double tert-butyl spirofluorene functionalised monomer **Sp-IDT**.

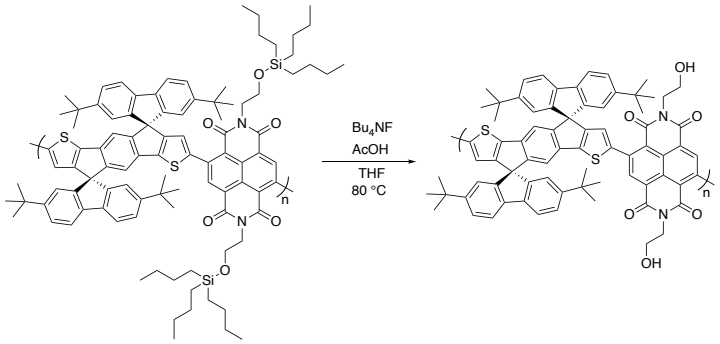

*Figure 116. Deprotection of **Sp-IDT-NDI-Si** to form **Sp-IDT-NDI-OH***

NMR showed successful deprotection by the disappearance of silyl protons at 1.08, 0.64 and 0.39 ppm, with no change to the aromatic peaks, indicating the deprotection conditions did not damage the conjugated backbone, shown in Figure 117.

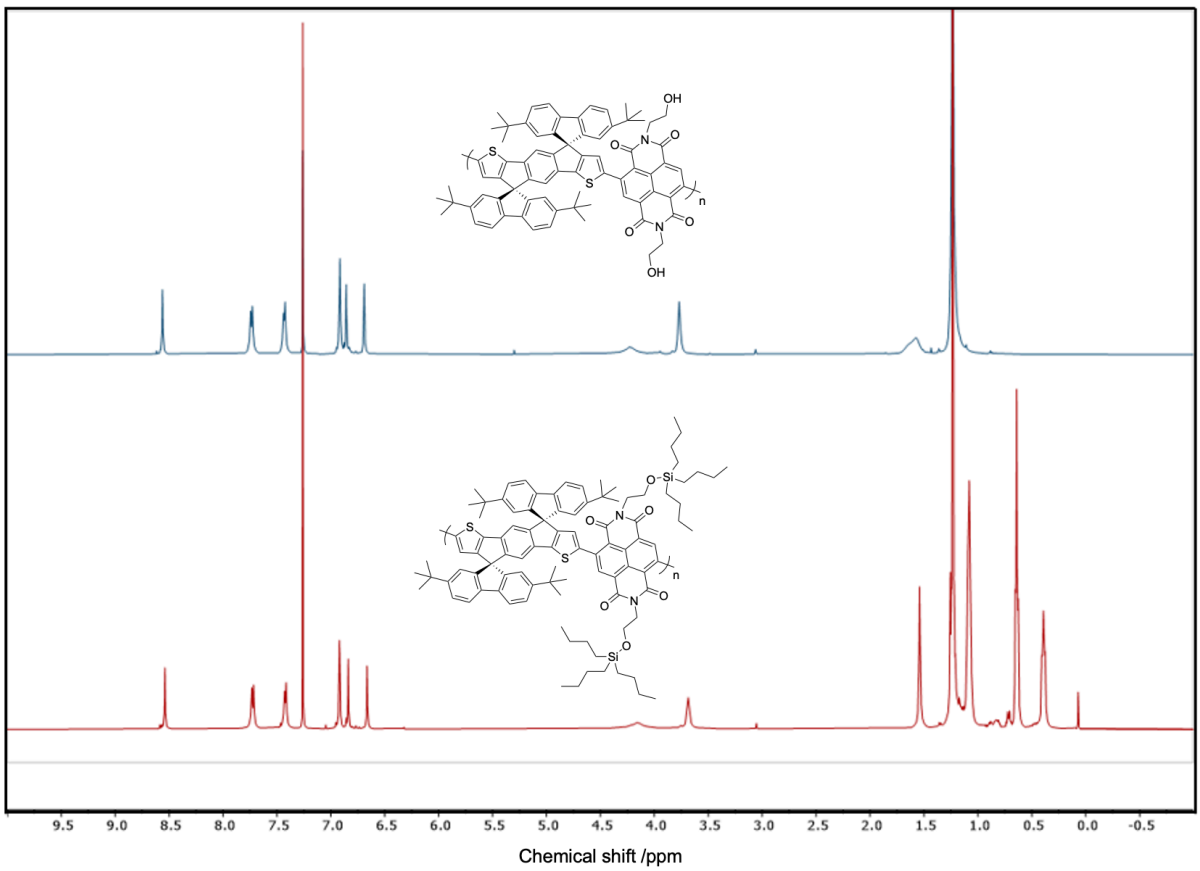

*Figure 117. 500 MHz ^{1}H NMR $CDCl_3$ spectrum for **Sp-IDT-NDI-Si** (bottom) and after deprotection to form **Sp-IDT-NDI-OH** (top).*

The solubility of **Sp-IDT-NDI-OH** permitted spin coating onto glass slides. This allowed UV-vis spectroscopy, PESA and contact angle measurements to be conducted before and after deprotection. These are shown in Figure 118.

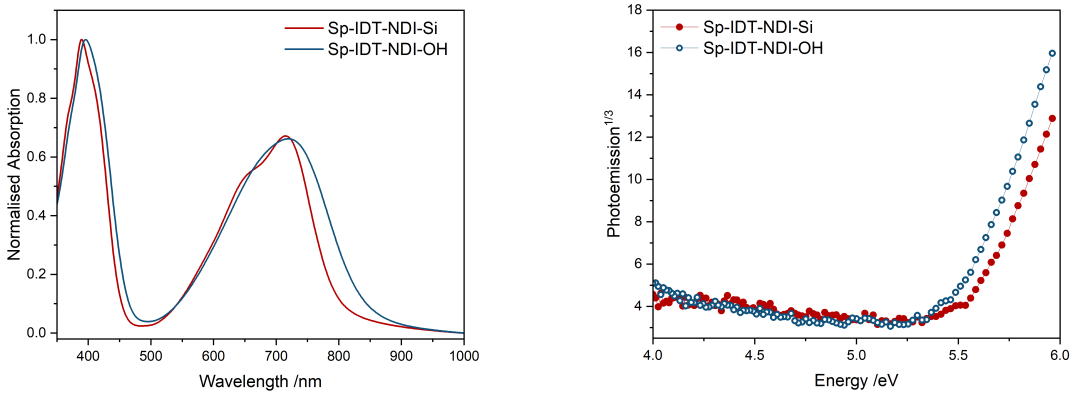

*Figure 118. For **Sp-F-NDI-Si** and **Sp-F-NDI-OH** spin coated films. Left: UV-vis spectra. Right: PESA measurements*

The contact angles for **Sp-NDI-Si** and **Sp-IDT-NDI-OH** are shown in the table below.

Polymer Film	Contact Angle / °	Standard Deviation / °
Sp-IDT-NDI-Si	102.1	1.4
Sp-IDT-NDI-OH	78.0	0.7

After deprotection, the optoelectronic properties were subtly altered. Estimates of the HOMO energy from the PESA photoemission onset show a shift of 0.1 eV, from -5.5 eV in **Sp-IDT-NDI-Si** to -5.4 eV in **Sp-IDT-NDI-OH**. The absorption onset from the UV-vis specrta became slightly broader in **Sp-IDT-NDI-OH**, giving a red shift in absorption onset of 41 nm relative to **Sp-IDT-NDI-Si**. This put the optical bandgap estimate for **Sp-IDT-NDI-OH** to be 1.5 eV, in comparison to 1.6 in **Sp-IDT-NDI-Si**. Although drawing tangents on UV-vis and PESA spectra is limited in accuracy, there does appear to be a noticeable raising in HOMO energy of about 0.1 eV, which is reflected in a slight narrowing of optical bandgap. Given that the NMR shows no change to the aromatic region, this must be an aggregation effect, due to morphological changes after silyl ether deprotection.

Deprotection of **Sp-IDT-NDI-Si** also caused a 24° decrease in contact angle from 102 °to 78 ° with water. This is consistent with increased hydrophilicity owing to the presence of the alcohol, though it is also the smallest contact angle measured for all of the polymers. This is likely caused by the presence of two alcohol functional groups per repeat unit, and the polar nature of the diimide groups.

3.3.9. Effect of Deprotection on Porosity of Sp-IDT-NDI-Si

N_2 adsorption isotherms of **Sp-IDT-NDI-Si** and **Sp-IDT-NDI-OH** were measured in order to calculate their BET surface areas, shown in Figure 119.

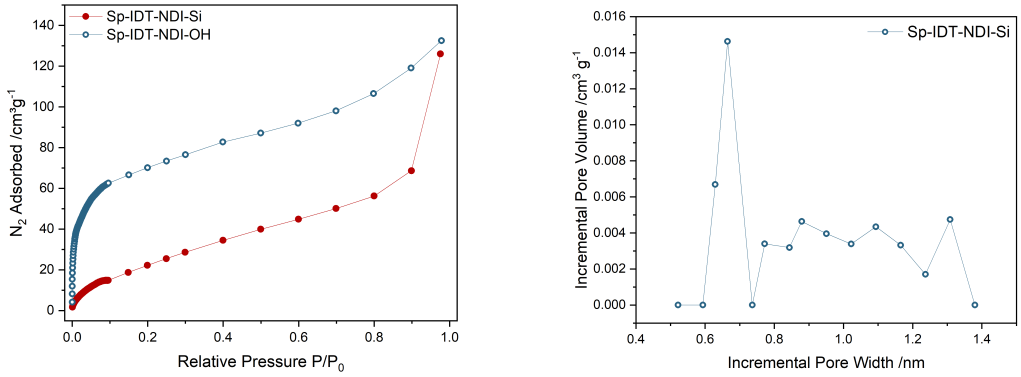

*Figure 119. Left: N_2 adsorption isotherms for **Sp-IDT-NDI-Si** and **Sp-IDT-NDI-OH**. Right: calculated pore size distributions for **Sp-IDT-NDI-OH**.*

This showed that protected **Sp-IDT-NDI-Si** was non-porous and became porous after deprotection to form **Sp-IDT-NDI-OH**, giving a BET surface area of 241 m^2 g^{-1}, in a similar manner to **Sp-IDT-BTz-OH**.

3.3.10. Effect of Deprotection on Photocatalytic Activity of Sp-IDT-NDI-Si

The photocatalytic activity of **Sp-IDT-NDI-Si** was tested under neutralised conditions, showing this polymer to be completely inactive, shown in Figure 120.

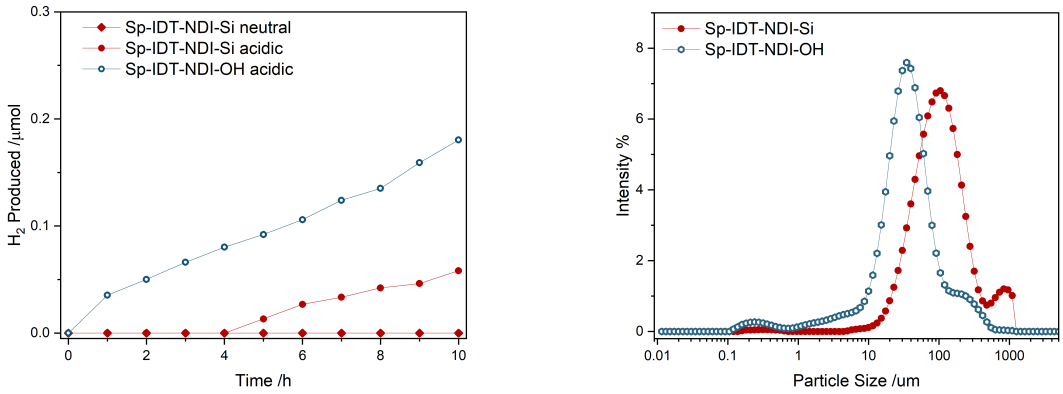

*Figure 120. For **Sp-IDT-NDI-Si** and **Sp-IDT-NDI-OH**. Left: photocatalytic activity under neutral conditions. Right: laser diffraction particle size profiles.*

The testing data for **Sp-IDT-NDI-Si** and **Sp-IDT-NDI-OH** are shown in the table below.

Polymer	D[3,2] Particle Size / μm	N_2 BET Surface Area / $m^2\ g^{-1}$	Average H_2 Produced Neutral / μmol h^{-1}	Average H_2 Produced Acidic / μmol h^{-1}
Sp-IDT-NDI-Si	32.1	58	0.00	0.01
Sp-IDT-NDI-OH	6.3	241	-	0.02

It was thought that in this case, there was insufficient driving force for the reduction half-reaction due to the relatively deep LUMO energy of -3.8 eV. Under neutral conditions, it would be expected that the driving force for proton reduction is decreased, and that testing under acidic conditions (where the ascorbic acid is not neutralised by sodium hydroxide) would increase the rate. This pH effect is expressed in Figure 121 below. It can be seen that the photocatalytic activity of **Sp-IDT-NDI-Si** increased when tested at lower pH, and it increased further after deprotection to form **Sp-IDT-NDI-OH**. This behaviour, where organic semiconductors with deep LUMO energies 'switch off' for photocatalysis as pH is raised, is partially reflected in the higher performance of IDTBR based systems in acidic ascorbic acid, in comparison to basic triethylamine or triethanolamine sacrificial electron donors.[114]

Nonetheless it should be highlighted that the activity of 0.02 μmol h^{-1} is still extremely low, despite this polymer's hydrophilicity. This illustrates the principle, that excessive narrowing of the optical bandgap to maximise solar light harvesting plays a risky game, whereby there is very low driving force for both oxidation and reduction half-reactions. This feature of electron deficient materials with low LUMO energies 'turning off' as pH is raised was also observed during testing of non-fullerene acceptors such as **IDTBR** and **Y6**, though is yet unpublished.

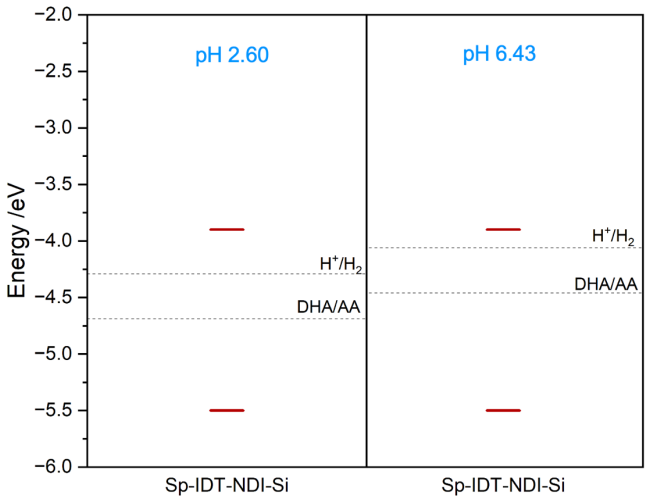

*Figure 121. Predicted redox potentials at pH 2.60 and pH 6.43 and FMOs for **Sp-IDT-NDI-Si.***

3.3.11. DPP-Si Monomer Synthesis

The last monomer to be synthesised was phenyl flanked diketopyrrolopyrrole (DPP). This was attractive due to the presence of two alkylation positions, enabling attachment of silyl ether protected ethyl alcohols. Furthermore, it has previously been reported that phenyl flanked DPP bearing diethylene glycol side chains and copolymerised with benzene, was more photocatalytically active than its alkylated analogues, owing to better dispersibility in water and triethanolamine.[304]

DPP-Si was synthesised following an adapted literature procedure, show in Figure 122.[397] It involved a Finkelstein reaction to convert the previously synthesised **14** to the alkyl halide **17**. **18** then was synthesised and alkylated using **17**.

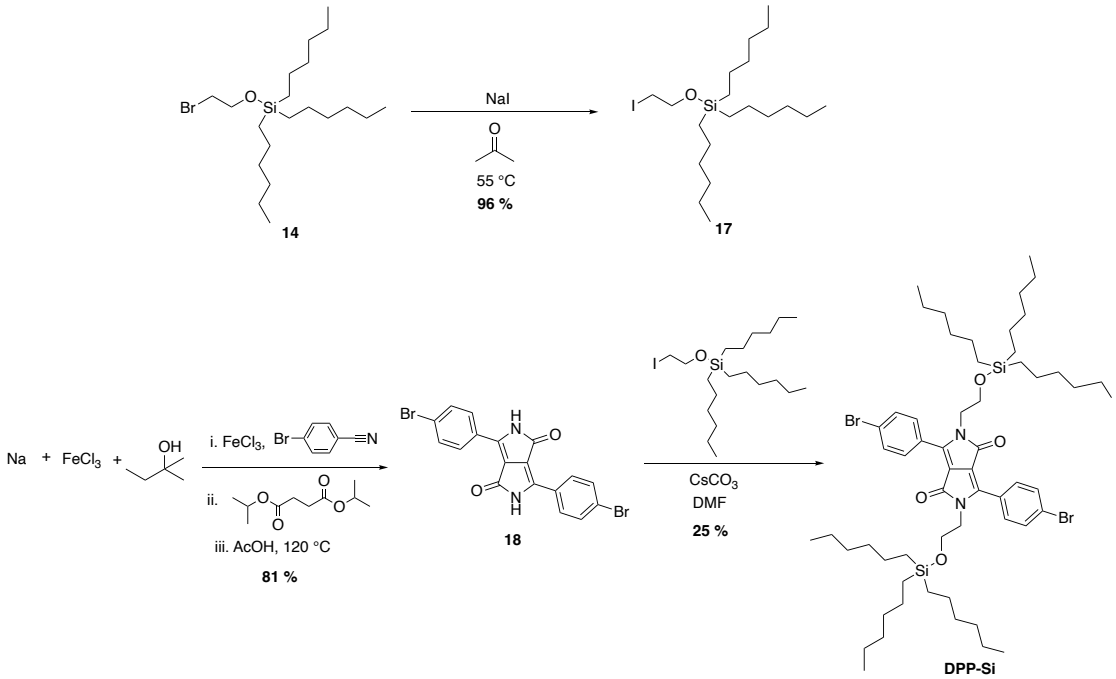

*Figure 122. Synthesis of **DPP-Si** monomer*

A proposed mechanism for the DPP formation reaction is shown in Figure 123. Here 2-methyl-2-butanol acts as solvent and as source of tertiary alkoxide after deprotonation with sodium metal. Tertiary alkoxides are not strong enough to react with benzonitrile, but strong enough to form the enolate of diisopropylsuccinimate, which goes on to attack benzonitrile,[398] activated by the $FeCl_3$. Next the imine tautomerises, followed by a 5-exo-trig ring closure. The cyclic methylene is then able to form an enolate and attack another benzonitrile and repeat the ring closure in a similar manner to form the red insoluble product **18**.

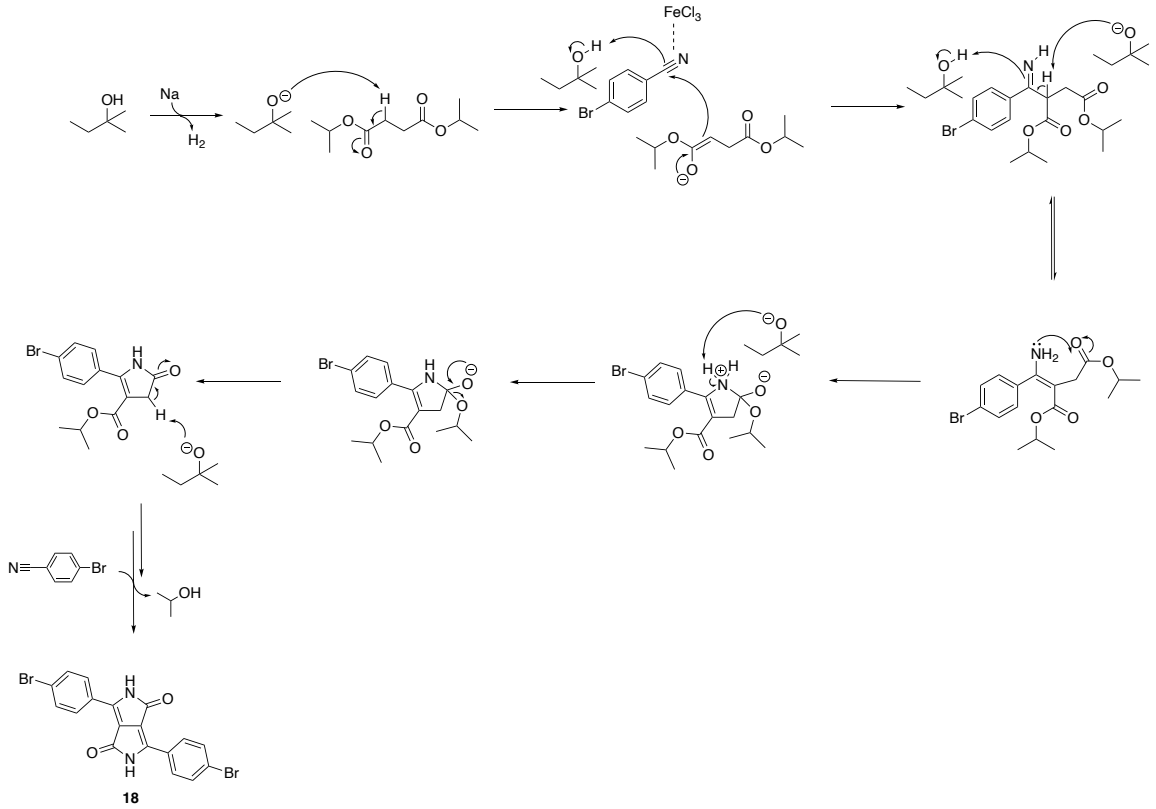

*Figure 123. Mechanism for synthesis of **18***

The next step was to alkylate the **18** using the alkyl iodide **17**. DPP alkylation using alkyl bromides can leave a significant amount of insoluble red powder at the end of the reaction indicative of unreacted **18**, so improving the electrophilicity of the alkyl halide was undertaken by the conversion of **14** to **17**. Next the acidic lactam proton of **18** was deprotonated generating a resonance stabilised anion, which is able to attack the **17** Due to the resonance form involving the O atoms as shown in Figure 124, it is also possible for side products to form during DPP alkylation, including the O,O-alkylated and N,O-alkylated products.[398] These side reactions lower the yield, and must be removed by silica column chromatography.

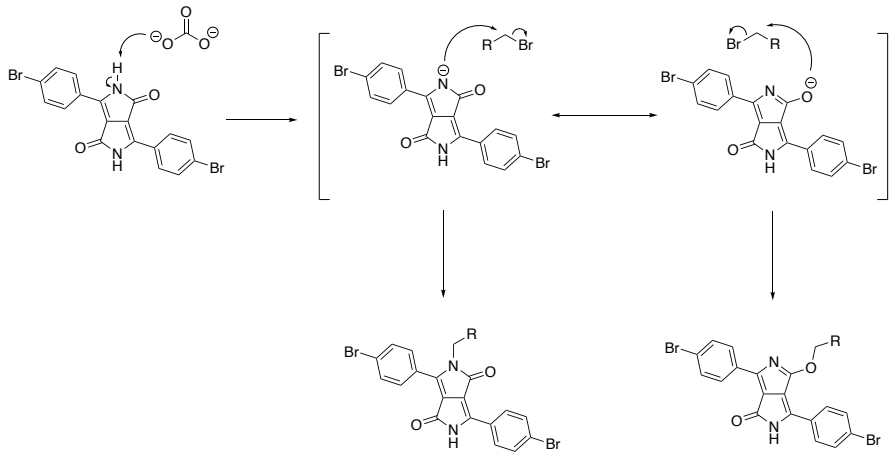

Figure 124. DPP alkylation side-product formation

3.3.12. Sp-IDT-DPP-Si Synthesis and Optoelectronic Properties

The **DPP-Sp** monomer underwent a Stille polymerisation with distannylated **Sp-IDT**, to produce the purple soluble polymer **Sp-IDT-DPP-Si**.

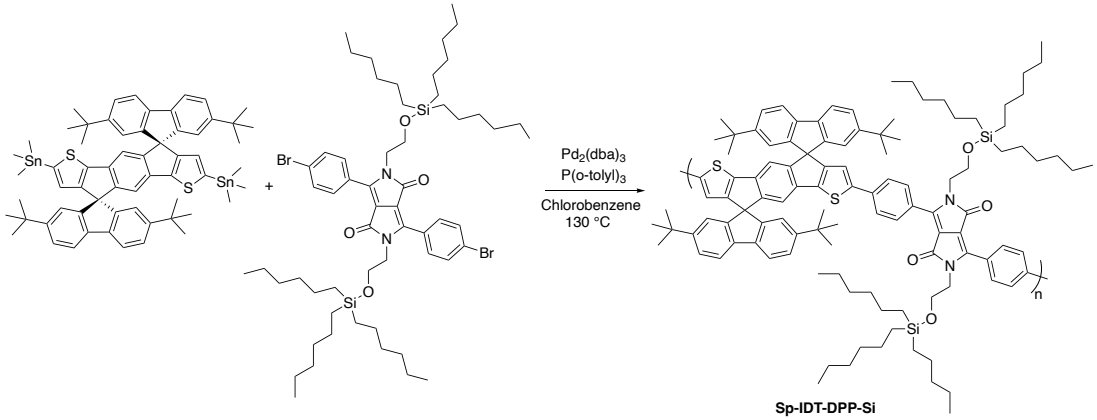

*Figure 125. Polymerisation of **Sp-IDT** and **DPP-Si** to form **Sp-IDT-DPP-Si**.*

PESA and UV-vis spectroscopy were used to estimate its HOMO and optical bandgap, shown in Figure 126.

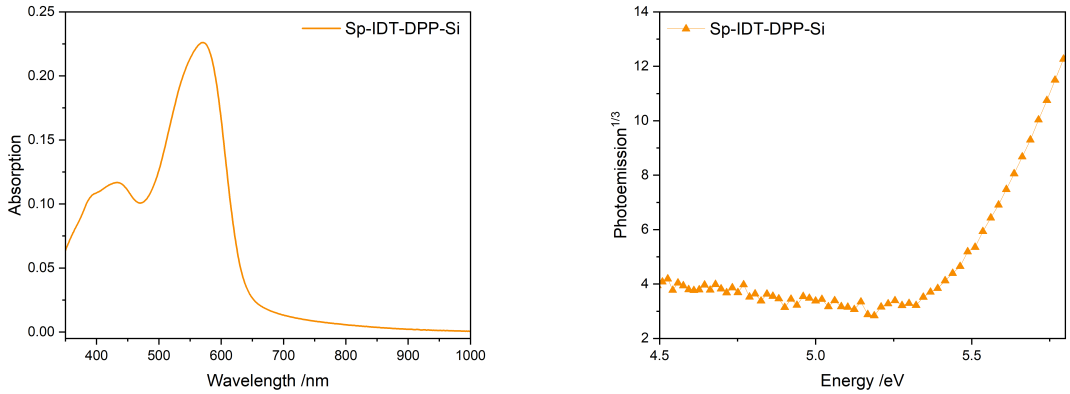

*Figure 126. **Sp-IDT-DPP-Si** thin film UV-vis spectrum (left) and PESA (right)*

The properties of Sp-IDT-DPP-Si are shown in the table below.

Absorption Onset / nm	Absorption Peak(s) /nm	Optical Bandgap /eV	HOMO (PESA) /eV	LUMO (PESA+ E_g) /eV	M_N /g mol^{-1}	M_W /g mol^{-1}	Poly-dispersity
637	432, 570	1.9	-5.4	-3.5	45168	91113	2.02

3.3.13. Sp-IDT-DPP-Si Deprotection

Sp-IDT-NDI-Si was cleaved in the same manner as the preceding polymers. This too produced a reasonably soluble polymer. Successful deprotection was verified by NMR shown in Figure 128.

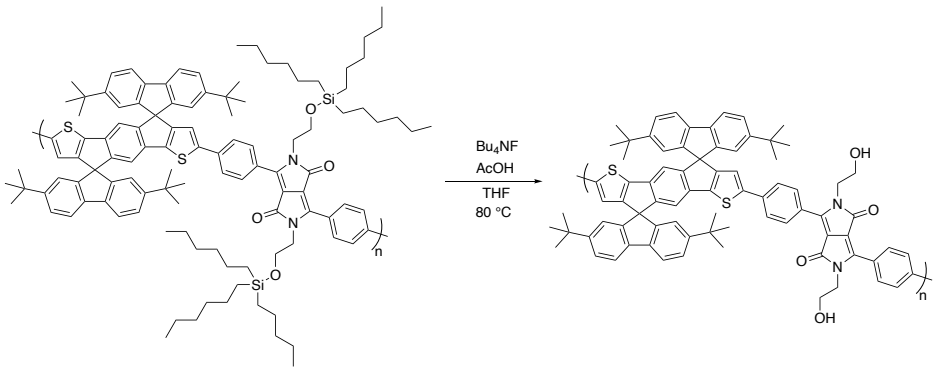

*Figure 127. Deprotection of **Sp-IDT-DPP-Si** to form **Sp-IDT-DPP-OH***

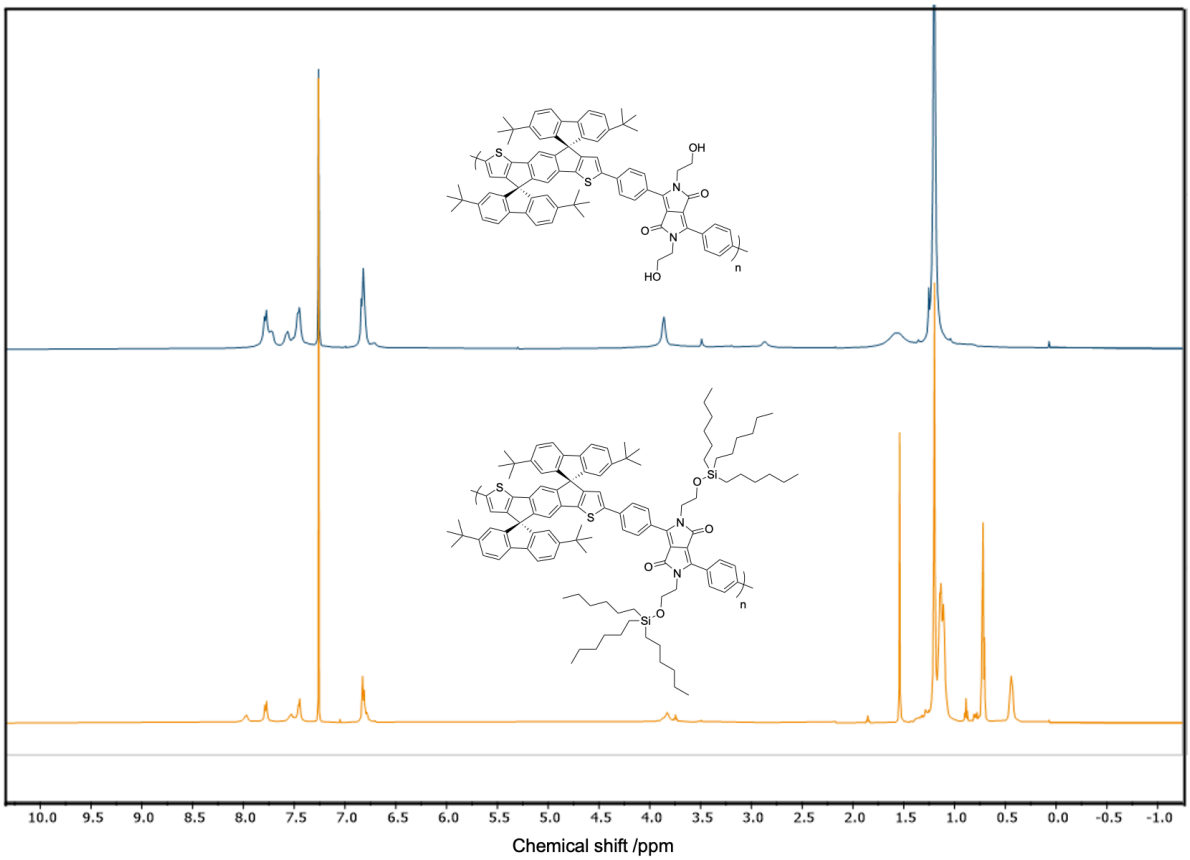

*Figure 128. 500 MHz ^{1}H NMR $CDCl_3$ spectrum for **Sp-IDT-DPP-Si** (bottom) and after deprotection to form **Sp-IDT-DPP-OH** (top).*

UV-vis and PESA showed the deprotection had no effect on the optoelectronic properties of thin films, as shown in Figure 129.

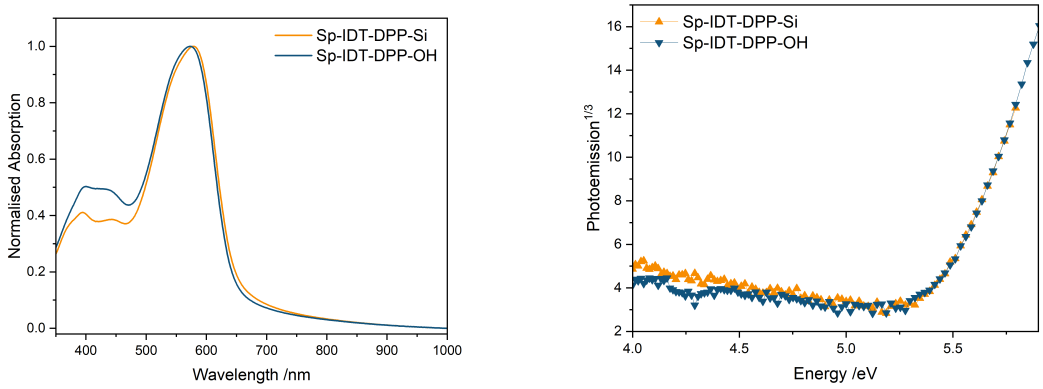

*Figure 129. For **Sp-F-DPP-Si** and **Sp-F-DPP-OH** spin coated films. Left: UV-vis spectra. Right: PESA measurements*

Contact angles with water were also measured on the films, showing a modest reduction in contact angle after deprotection.

Polymer Film	Contact Angle / °	Standard Deviation / °
Sp-IDT-DPP-Si	99.5	0.4
Sp-IDT-DPP-OH	92.8	2.1

3.3.14. Effect of Deprotection on Porosity of Sp-IDT-DPP-Si

Interestingly, the N_2 sorption isotherms (Figure130) showed no porosity after deprotection, while both **Sp-IDT-DPP-Si** and **Sp-IDT-DPP-OH** appeared to be non-porous from their low BET surface areas of 47 and 44 $m^2\ g^{-1}$ respectively.

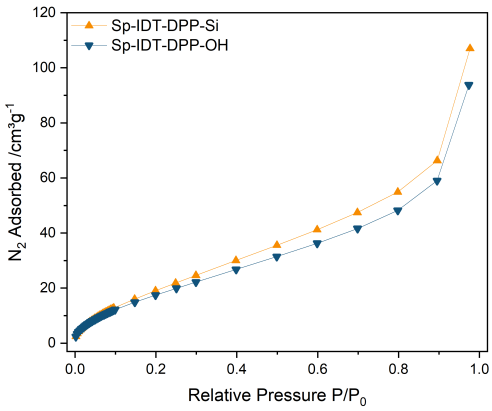

*Figure 130. N_2 adsorption isotherms for **Sp-IDT-DPP-Si** and **Sp-IDT-DPP-OH***

3.3.15. Effect of Deprotection on Photocatalytic Activity of Sp-IDT-DPP-Si

The photocatalytic activity and particle size distributions for **Sp-IDT-DPP-Si** and **Sp-IDT-DPP-OH** are shown in Figure 131. It can be seen that there is an increase in activity when testing **Sp-IDT-DPP-Si** under neutralised conditions, and a significant increase in activity when testing **IDT-DPP-OH** under neutral conditions. This pH effect is similar to what was seen in almost every other polymer tested except **Sp-IDT-NDI-**

OH. This is explained owing to balancing the driving forces for the reduction and oxidation half-reactions, as explained previously. The fact that **Sp-IDT-DPP-OH** and **Sp-IDT-NDI-OH** have similar HOMO energies of -5.4 eV and -5.5 eV respectively, while **Sp-IDT-DPP-OH** has a higher energy LUMO energy of -3.5 eV compared to -3.8 eV in **Sp-IDT-NDI-OH**, gives additional support to the idea that the very low activity of **IDT-NDI-OH** under neutral conditions is due to its LUMO being too low energy.

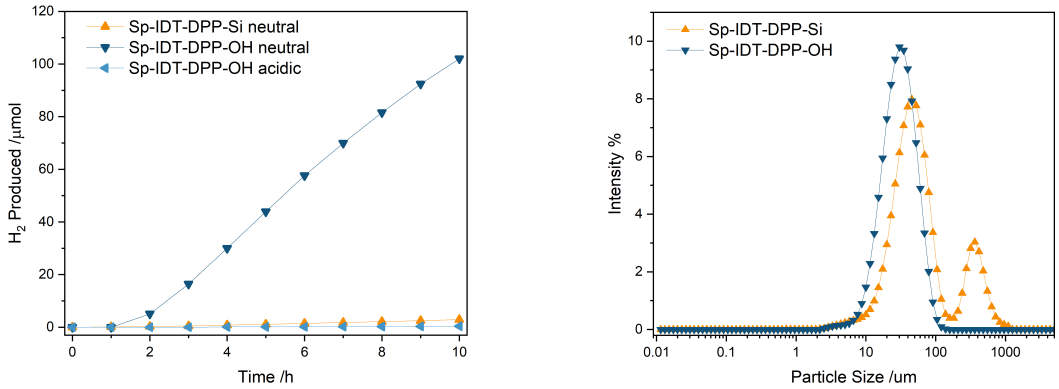

*Figure 131. For **Sp-IDT-NDI-Si** and **Sp-IDT-NDI-OH**. Left: photocatalytic activity. Right: laser diffraction particle size profiles.*

The data for **Sp-IDT-DPP-Si and Sp-IDT-DPP-OH** is shown in the table below.

Polymer	D[3,2] Particle Size / μm	N_2 BET Surface Area / $m^2\ g^{-1}$	Average H_2 Produced Neutral / μmol h^{-1}	Average H_2 Produced Acidic / μmol h^{-1}
Sp-IDT-DPP-Si	34.7	47	0.34	-
Sp-IDT-DPP-OH	22.9	44	12.3	0.05

3.4. Isolated Polymers Summary and Comparison

The photocatalytic parameters of all the soluble polymers and their deprotected counterparts, including **Sp-IDT-BTz-Si** from the previous chapter are summarised in a table below for comparison. A HOMO and LUMO energy diagram for the polymers are also shown below in Figure 132.

Polymer	Optical Bandgap /eV	HOMO (PESA) /eV	LUMO (PESA+ E_g) /eV	N_2 BET Surface Area / m^2 g^{-1}	D[3,2] Particle Size / μm	Average H_2 Produced Neutral / μmol h^{-1}	Average H_2 Produced Acidic / μmol h^{-1}
Sp-IDT-IF-Sp	-	-	-	623	7.6	0.13	-
Sp-IDT-BTz-Si	2.0	-5.1	-3.1	60	7.0	0.58	-
Sp-IDT-BTz-OH	2.0*	-5.1*	-3.1*	528	4.8	9.40	0.96
Sp-F-BTz-Si	2.6	-5.6	-3.0	62	21.8	0.31	-
Sp-F-BTz-OH	2.6	-5.6	-3.0	85	27.2	1.45	-
Sp-IDT-F-Si	2.4	-5.2	-2.8	376	23.8	0.03	0.02
Sp-IDT-F-OH	2.4*	-5.2*	-2.8*	482	31.6	1.69	0.32
Sp-IDT-NDI-Si	1.6	-5.5	-3.8	58	32.1	0.00	0.01
Sp-IDT-NDI-OH	1.5	-5.4	-3.8	241	6.3	-	0.02
Sp-IDT-DPP-Si	1.9	-5.4	-3.5	47	34.7	0.34	-
Sp-IDT-DPP-OH	1.9	-5.4	-3.5	44	22.9	12.3	0.05

*Unable to measure due to insufficient solubility, but assumed to be very similar to the protected polymer

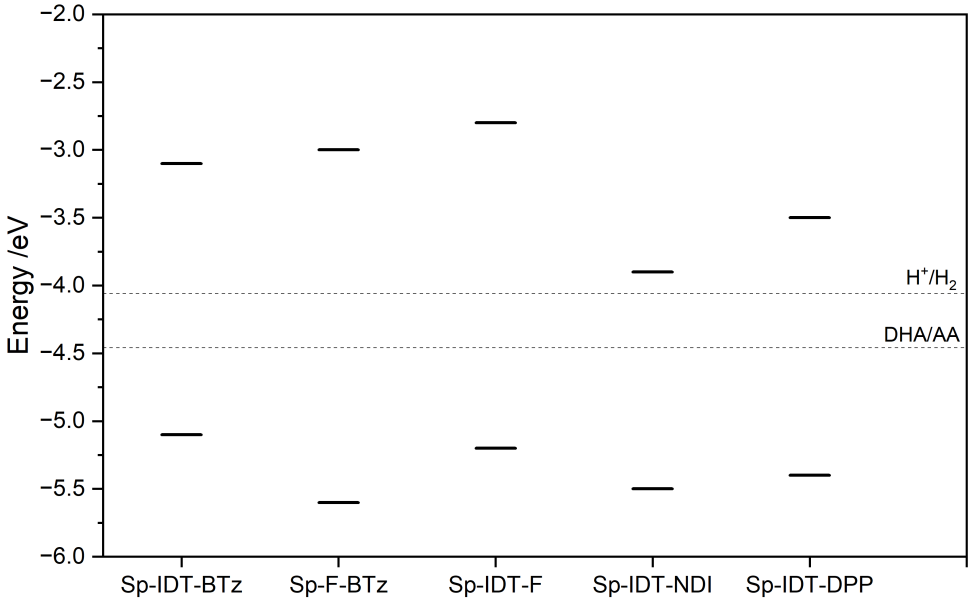

Figure 132. Estimated HOMO and LUMO energies for spin coated films of protected polymers, against predicted redox potentials for half-reactions at pH 6.43 (the pH of the neutralised testing conditions).

3.4.1. Changing Hydrophilicity for Non-Porous Polymers Increases Activity

The activity increases from 0.34 μmol h^{-1} in **Sp-IDT-DPP-Si** to 12.3 μmol h^{-1} in **Sp-IDT-DPP-OH** following deprotection. The reduction in particle size from 34.7 to 22.9 μm is likely a large contributory factor to this significant increase in rate in this case.

However, the rate increases less strongly for the deprotection of **Sp-F-BTz-Si** to form **Sp-F-BTz-OH**. It increases from 0.31 μmol h^{-1} to 1.45 μmol h^{-1} following deprotection. In this case, deprotection of **Sp-F-BTz-Si** to form **Sp-F-BTz-OH** is not accompanied by a simultaneous reduction in particle size, explaining the smaller increase in activity after deprotection in comparison to **Sp-IDT-DPP-Si** and **Sp-IDT-DPP-OH**. Particle size determines the external surface area and given that these polymers were measured to be non-porous, their performance would be expected to be particularly sensitive to

this parameter, given it determines the average distance excitons must travel to dissociate. The fact that non-porous polymers with similar particle sizes also improve in activity after deprotection suggests that additional factors must be at play. This could be due to differences in interactions with ascorbic acid, or interactions with Pt cocatalyst, due to differences in the deposition process between polymer with and without alcohol groups. Quantification of the amount of photodeposited Pt after testing and scanning electron microscopy (SEM) measurements could shed light on this feature in future.

3.4.2 Porosity and Solubility Trends for Deprotected Polymers

Deprotected polymers **Sp-F-BTz-OH** and **Sp-IDT-DPP-OH** are soluble but also non-porous, while **Sp-IDT-BTz-OH** is insoluble and porous, while **Sp-IDT-NDI-OH** is both soluble and porous. It is not immediately obvious from their structures why this should be the case. To better understand these properties, Figure 133 shows the polymers ranked in order of their BET surface areas. The average number of repeat units is indicated, which was calculated from the protected version of the polymers given they share the same backbone. This is because molecular weight has an influence on solubility and also porosity,[343] as was discussed in section 2.1.1.

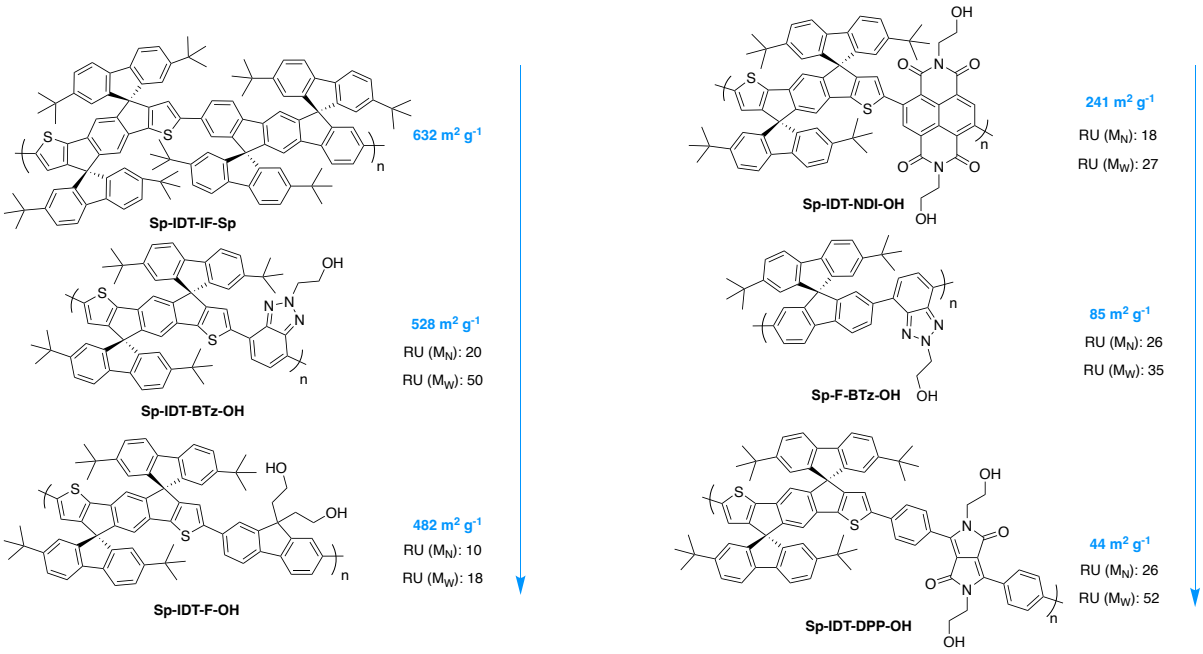

Figure 133. Polymers ranked in order of descending BET surface areas, with the number of repeat units (RU) indicated based on their protected parent molecules' number and weight average molecular weights from GPC

From analysis of these structures in Figure 133, it appears that in general having a greater density of tert-butyl spirofluorene orthogonal flanking groups is consistent with higher porosity, as could be expected. **Sp-IDT-DPP-OH** is non-porous, potentially because the flanking benzene rings either side of DPP are diluting the density of tert-butyl spirofluorene orthogonal flanking groups along the backbone and cause a greater proportion of biaryl bonds per repeat unit which have greater flexibility than the fused aromatic rings in IDT.

There also seems a general trend that porosity and solubility are counteracting. **Sp-IDT-NDI** seems to balance both properties to achieve a reasonable porosity while maintaining solubility. Though it is unfortunate that its other properties such as LUMO being too deep in energy are not conducive to high photocatalytic activity. Trends in performance will be summarised in the conclusions in section 4.6.

3.5. Polymer Blends

3.5.1. Sp-IDT-F : Sp-IDT-NDI Hybrid

The combination of **Sp-IDT-F** donor and **Sp-IDT-NDI** acceptor were selected as heterojunction targets owing to their large HOMO and LUMO offsets and that they displayed porosity after deprotection.

A 1:1 mixture of **Sp-IDT-F-Si** donor and **Sp-IDT-NDI-Si** acceptor was dissolved in chlorobenzene then precipitated into methanol and filtered. This mixture of the silyl ether protected polymers was tested for photocatalysis in the same manner as the other single component polymers: taking 5 mg (in this case this is made up of 2.5 mg of donor and acceptor), sonicated in NMP and then pipetted into the aqueous ascorbic acid and Pt precursor salt testing solution under sonication. This was also tested alongside 2.5 mL of **Sp-IDT-F-Si** donor and **Sp-IDT-NDI-Si** acceptor separately sonicated in NMP and sequentially pipetted into the aqueous testing medium. Both were tested without neutralising the ascorbic acid, owing to the inactivity of **Sp-IDT-NDI-Si** at neutral pH. This is shown in Figure 134. Here it can be seen that the blend of **Sp-IDT-F-Si** : **Sp-IDT-NDI-Si** has much greater activity compared to its constituent polymers tested in isolation under acidic conditions. Furthermore, the physical mixture control test, made from sequentially adding the separately dispersed polymers showed similarly low performance. This is consistent with the blending of the silyl ether protected donor and acceptor increasing activity, potentially through improved charge generation due to electron transfer from donor to acceptor. This high activity is particularly noteworthy given the **Sp-IDT-F-Si** and **Sp-IDT-NDI-Si** have no hydrophilic groups and **Sp-IDT-NDI-Si** is non-porous.

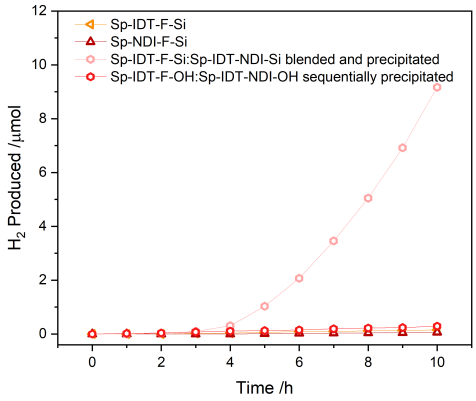

Figure 134. Photocatalytic activity under acidic conditions of Sp-IDT-F-Si and Sp-IDT-NDI-Si in isolation, compared to a 1:1 blend of Sp-IDT-F-Si : Sp-IDT-NDI-Si and a physical mixture of Sp-IDT-F-Si and Sp-IDT-NDI-Si

Next, the blend of **Sp-IDT-F-Si** : **Sp-IDT-NDI-Si** was subjected to deprotection conditions, by adding it to acetic acid neutralised TBAF in THF. After pouring this into methanol, washing and drying, its N_2 sorption isotherm was measured, shown in figure 135 (left). It shows that the material was indeed porous, with a BET surface area of 347 m^2 g.

This was then tested for photocatalysis in the same way, as well as an unblended physical mixture of **Sp-IDT-F-OH** and **Sp-IDT-NDI-OH** added sequentially to the aqueous testing mixture from separately sonicated NMP (Figure 135 right). This however shows that the physical mixture and blend have similar activities, while both are slightly more active than **Sp-IDT-F-OH** in isolation. This implies that the slight improved performance is due to the lack of spectral overlap between **Sp-IDT-F-OH** (which is yellow) and **Sp-IDT-NDI-OH** (which is blue), enabling greater light harvesting. The reason for the failure of the blended then deprotected polymer to outperform its physical mixture is likely due to the deprotection disrupting the blend morphology. **Sp-IDT-NDI-OH** is soluble in THF while **Sp-IDT-F-OH** is only slightly soluble. It could be that after deprotection when it was poured into methanol and filtered, the morphology was significantly disrupted by the deprotection conditions. This explains why its activity resembled that of the physical mixture.

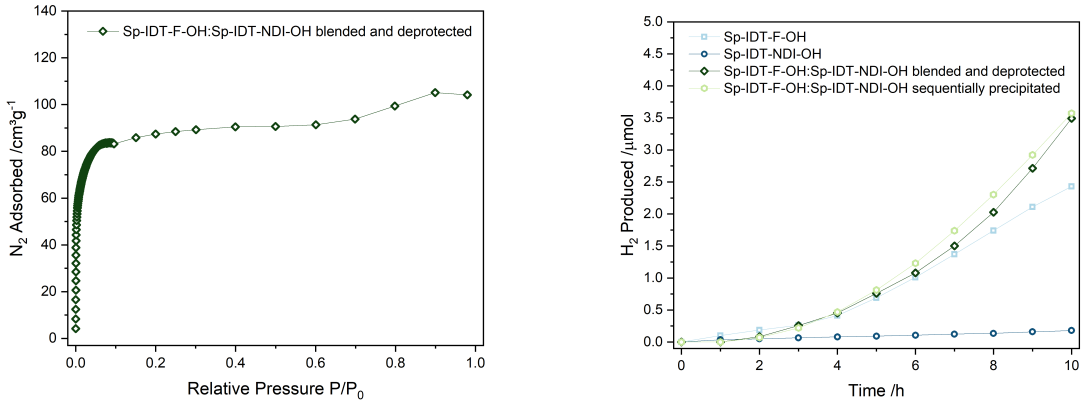

*Figure 135. Left: N_2 adsorption isotherm of 1:1 blend of **Sp-IDT-F-Si : Sp-IDT-NDI-Si** with neutralised TBAF in THF, poured into MeOH, filtered and washed. Right: Photocatalytic activity under acidic conditions of **Sp-IDT-F-OH** and **Sp-IDT-NDI-OH** in isolation, compared to a 1:1 blend of **Sp-IDT-F-Si : Sp-IDT-NDI-Si** treated with TBAF, and a physical mixture of **Sp-IDT-F-OH and Sp-IDT-NDI-OH***

The photocatalysis data for these blends is summarised in the table below.

Polymer	Average H_2 Produced Acidic / μmol h^{-1}
Sp-IDT-F-Si	0.02
Sp-IDT-NDI-Si	0.01
Sp-IDT-F-Si: Sp-IDT-NDI-Si Blended	1.31
Sp-IDT-F-Si: Sp-IDT-NDI-Si Physical mixture	0.03
Sp-IDT-F-OH	0.32
Sp-IDT-NDI-OH	0.02
Sp-IDT-F-OH: Sp-IDT-NDI-OH Blended and Deprotected	0.45
Sp-IDT-F-OH: Sp-IDT-NDI-OH Physical Mixture	0.48

3.5.2. Heterojunction Problems and Potential Solutions

In order to produce a well-functioning heterojunction, it is important not only to select donor and acceptors with a type-II offset and complementary absorption, but also suitable side chains to optimise donor and acceptor miscibility, as well as the ratio of donor and acceptor. This is in order to create domain sizes on the order of exciton diffusion lengths, and charge percolation pathways enabling its extraction to reactive sites.[84]

Further work is required to find conditions which allow good blending of the protected polymers, while employing deprotection conditions which do not disrupt this heterojunction morphology. This means forming heterojunction blends for silyl ether protected polymers, followed by heterogeneous deprotection on them in the solid state.

Another approach could be to utilise polymers in their deprotected form to form blends. This would be possible using **Sp-IDT-NDI-OH** which was soluble in THF, enabling nanoprecipitation, however its photocatalytic activity in isolation was very low. **Sp-IDT-DPP-OH** was also soluble in THF but was non-porous. Furthermore, potential donor polymers such as **Sp-IDT-BTz-OH** and **Sp-IDT-F** were porous but weren't soluble in THF. Therefore, adopting this post-deprotection blending strategy would require deprotected polymers with suitable solubility and mutual miscibility. The mutual miscibilities of silyl ether protected polymers would be expected to be different to the deprotected polymers with alcohol groups, so pursuing either strategy would require optimisation.

3.6. Conclusions and Future Work

It has been found that porosity arises in the deprotected polymers by balancing the density of tert-butyl spirofluorene units along the backbone, where a high density generates higher porosity, but at the expense of solubility. Silyl ether protection of the alcohol groups in these polymers solubilises them, but 'clogs' the porosity as was shown in Chapter 2. The deprotected polymer series also demonstrates that as expected, a greater density of alcohol functional groups on the polymer is more conducive to hydrophilicity, as shown by the greater water sorption of **Sp-IDT-F-OH** compared to **Sp-IDT-BTz-OH**, and the smaller contact angles with water of all of the polymers after deprotection to reveal alcohols.

All of the polymers show increases in performance after deprotection. This is attributed to the transformation of non-polar silyl ether groups to hydrogen-bonding alcohols which increases their hydrophilicity. This is demonstrated by decreases in contact

angles for processable polymers, as well as increases in water sorption. This in general causes decreases in particle sizes which can also contribute to the increase in activity. However, when particle size doesn't vary significantly, deprotection still causes an increase in activity. This could be due to difference in interactions with Pt cocatalyst and ascorbic acid due to the different surface chemistries, a factor which was no investigated here. Further work to quantify the yields of Pt photodeposition on the protected and deprotected polymers will be insightful here.

In this series, the highest performing polymer was actually **Sp-IDT-DPP-OH** with an activity of 12.3 μmol h^{-1}, despite being non-porous (but still with alcohol groups). This shows that although porosity and hydrophilicity are conducive to higher photocatalytic activity, other factors can be more significant, such as HOMO and LUMO positions; **Sp-IDT-DPP-OH** has a slightly narrower bandgap than **Sp-IDT-BTz-OH** but its FMOs are slightly deeper in energy, perhaps providing a better balance between half-reactions. Furthermore, other features relating to exciton and polaron transport in these materials, and the distribution of Pt cocatalyst which were not investigated here will also be expected to play a significant important role when comparing between conjugated backbones.

Sp-IDT-NDI-OH was both porous and hydrophilic (giving the lowest contact angle measured). However, it was nonetheless a very poor photocatalyst. This demonstrates that porosity and hydrophilicity are not always decisive when other factors such as FMO energies do not procure sufficient driving force for the half-reactions.

Nonetheless, the finding in the previous chapter: that porosity is only effective in combination with hydrophilicity, are reinforced in this chapter. This is shown by the deprotection of the already porous **Sp-IDT-F-Si** to form **Sp-IDT-F-OH** which increases the BET surface area from 376 to 482 m^2 g^{-1}, which increases the activity from a barely active 0.03 to 1.70 μmol h^{-1}. Given porosity doesn't change a large amount, the 'switching on' of water sorption shown by the water isotherm measurement is considered responsible for the photocatalytic activity also 'switching on'.

Finally, preliminary measurements of photocatalytic activities for the blend of **Sp-IDT-F-Si** and **Sp-IDT-NDI-Si** appeared to show a significant enhancement upon blending, indicating enhanced exciton separation owing to heterojunction formation. Nonetheless, attempting to deprotect the already blended polymers appears to have destroyed the favourable blend morphology due to the greater solubility of **Sp-IDT-NDI-Si** in THF during deprotection. Further work is required to enable blending protected polymers followed by heterogeneous deprotection without disrupting the blend morphology, or else blending of soluble deprotected polymers.

Chapter 4: Small Molecule Electron Transport Materials for Perovskite Solar Cells

4.1. Introduction

4.1.1. Perovskite Solar Cells

While the previous two chapters have focussed on the use of organic semiconductors for solar H_2 production, this chapter will investigate their application in solar electricity production, in the context of perovskite photovoltaic cells. Photovoltaics operate on similar principles to photocatalysis: semiconducting materials harvest solar energy to generate excited states which must be separated into charge carriers, but instead of using these charge carriers to drive redox reactions, they are instead extracted by electrodes to generate a potential difference in a circuit.

Perovskite refers to a crystal structure with ABX_3 composition. The species which has received the most attention for solar energy application is methyl ammonium lead iodide, $CH_3NH_3PbI_3$. This has a band gap of approximately 1.6 eV which can be increased by halide substitution, being 2.3 eV for Br 3.1 eV for Cl analogues for polycrystalline films.[399]

Perovskite solar cells have shown the steepest increase in efficiency of any photovoltaic material in recent years,[400] with single junction perovskites reporting over 26 % power conversion efficiencies under laboratory conditions.[401] This is explained in part, by their direct bandgaps enabling high extinction coefficients, meaning thinner layers can be used to fully harvest incident sunlight compared to silicon solar cells.[29,32] Additionally, due to high dielectric responses, perovskites produce photogenerated charges much more easily than organics.[402] Also, as a consequence of the relatively thin active layers, the distances these charges need to travel through the material before collection are smaller, keeping charge recombination low.[32] This is further assisted by a relatively high level of defect tolerance, lacking prevalent deep trap states despite their low temperature solution-processing.[29,399,402] This ability to dissolve inexpensive perovskite precursors in polar solvents and cast films to generate active layers in solar cells is a key advantage it shares with soluble organic

semiconductors in the production of low cost photovoltaics, avoiding the use of energy intensive fabrication methods.[29]

Nonetheless, perovskite solar cells also come with serious drawbacks. The active layer is water soluble, so any damage to the casing could result in danger from highly toxic Pb ions.[399] Furthermore, perovskite solar cells are notoriously unstable and temperamental: their constituent ions can move under electric fields making device characterisation challenging, and their performance is highly sensitive to moisture and thermal stress, which can dissolve the perovskite structure, or cause delamination of device layers.[399,403,404]

4.1.2. Charge Transport Layers

Key to the function of high performance perovskites in solar cells is their 'sandwich' arrangement between charge-selective contacts.[399,400] These are interfaces on either side of the perovskite layer which selectively transport excited electrons to the cathodic contact for electron transport layers (ETL), and selectively transport holes to the anodic contact for hole transport layers (HTL). They also have a role in preventing direct contact between the perovskite and electrodes, which can undergo degradation due to diffusion of I^-. ETLs facilitate selective transport of electrons by possessing a LUMO energy level which is aligned to the conduction band minimum (CBM) of the perovskite, while possessing a deep HOMO energy which makes accepting a hole energetically unfavourable, and vice versa with HTLs, depicted in Figure 136. Charge transport layers should also have wide bandgaps so they do not parasitically absorb light at the expense of the perovskite.[405] The development of novel ETL materials will be the focus of this chapter.

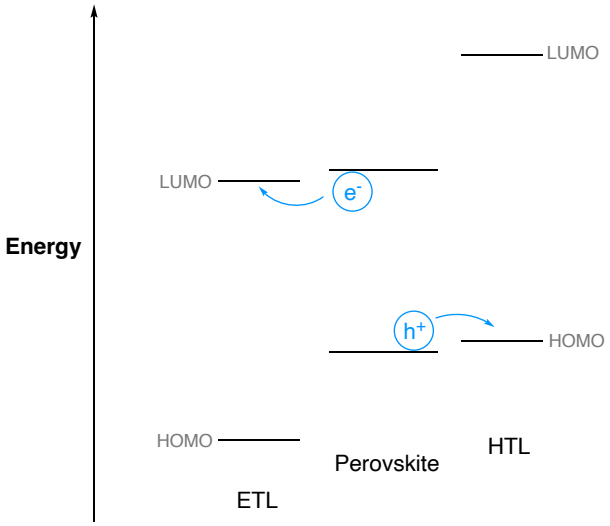

Figure 136. FMOs of Charge Transport Layers in Perovskite Solar Cell

In perovskite solar cells, energetic loss at the charge-selective contacts has been identified as the most significant loss pathway.[400] This can be due to imperfect charge selectivity causing recombination, or inappropriate energetic offsets between the charge transport layers.[399] For ETLs, when the LUMO is higher in energy than the perovskite conduction band minimum, it creates an energetic barrier to electron injection causing charge accumulation at the interface and lowering photocurrent.[399,406] When it is too low it can cause unnecessary energetic losses, decreasing the photovoltage. Therefore, the LUMO of the ETL should be between that of the perovskite conduction band minimum and the cathode to ensure smooth and selective electron transport down a slight energy cascade, meanwhile its HOMO should be as deep as possible to create a wide band gap and avoid parasitic light absorption.[406]

Early perovskite solar cells utilised metal oxides such as TiO_2. However through their absorption of UV light, degradation pathways due to the presence of O defects have been shown.[407,408] In addition, inorganic semiconductors generally form poorer electrical contact compared to their organic analogues.[402]

C_{60} and its derivatives, particularly **PCBM** (Figure 137) have since been very commonly employed as ETL layers or interlayers for perovskite solar cells.[409]

Fullerene has been shown to more effectively quench perovskite photoluminescence compared to TiO_2, indicating greater charge transfer efficiency.[410] In addition, fullerenes are capable of efficient isotropic charge transport, while they also have low extinction coefficients, with poor light absorption in the visible region, minimising parasitic absorption.[411]

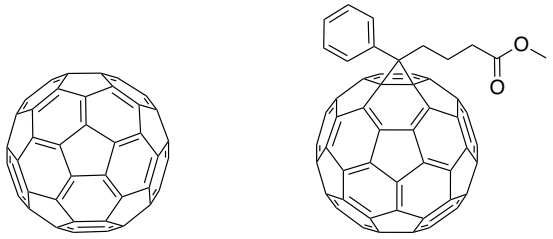

Fullerene C_{60} **Phenyl-C_{61}-butyric acid methyl ester PCBM**

Figure 137. Structures of C_{60} and PCBM

Despite these advantages, fullerenes still cause large voltage losses in perovskite solar cells through imperfect LUMO energy alignment with wide bandgap perovskites,[409] while its LUMO energy is also difficult to tune through chemical modification.[411] Furthermore, fullerenes tend to aggregate, reflected in poor morphological stability in organic solar cells,[411] and are also associated with a high degree of energetic disorder which causes voltage losses when used in perovskite solar cells.[409]

4.2. Design Requirements

In collaboration with the Snaith Group at the University of Oxford (whose focus is on perovskite solar cells), it was desired to design, synthesise and characterise a family of novel ETL materials to replace fullerenes.

Perovskite materials were reported for solar cell application relatively recently in 2009, as photosensitisers in TiO_2 dye sensitised solar cells.[412] Given that perovskites have only just begun to be a focus for research for optoelectronic applications, many of their properties are still poorly understood, including their electronic structure.[413] The band

positions of perovskites change with their composition and morphology which is highly dependent on fabrication method which alters their surface chemistry.[409] How these properties behave in a device can be different to their behaviour in isolation.[413]

The band positions of the collaborator perovskites were already optimised for high efficiency, meaning for the scope of this project, its band positions were considered fixed. Consequently, it was desired to rather tune the LUMO energies of new ETLs to better fit the perovskite, exploiting the superb energetic tunability of organic semiconductors. It was known the conduction band minimum of the perovskite in question was in the region of -4.0 eV. However, due to the aforementioned difficulty in accurately determining this in a device,[409,413] it was desired to produce a range of ETL materials with a range of close LUMO energies in this region to provide the best chance of good alignment. Furthermore, these materials should have wide bandgaps to minimise parasitic absorption.

A final design requirement was for the ETL material to be sublimation processable. Sublimation has many advantages over solution-processing or other deposition techniques in a large-scale context. Firstly, it avoids any complications arising from building layered devices, where the solvent from deposition of the top layer dissolves the layer underneath, which requires solvent orthogonality to avoid.[84] Secondly, use of solvents in general is environmentally harmful, particularly toxic chlorinated solvents which are ubiquitous for organic semiconductor processing.[411] Sublimation avoids solvent use entirely. Furthermore, in an industrial context, sublimation under a vacuum can offer greater control over film thickness and offers an attractive pathway towards commercialisation.[414]

4.3. Molecular Design

4.3.1. Density Functional Theory (DFT) Modelling

The most important property in the ETL molecular design was the LUMO alignment with the perovskite. Because synthesis is time consuming and costly, there was a limit

on how many molecules it was feasible to synthesise in order to test this. In order to open up more 'chemical space' for exploration, density functional theory (DFT) was employed to estimate the LUMO energies of a large range of molecules. This way, the suitability of different molecular designs could be rapidly evaluated, and a wider range of molecules considered.

However, DFT is generally inaccurate at predicting absolute HOMO and LUMO energies, rather, its utility as a tool in molecular design is in comparing relative differences. Therefore, in the calculations, the FMOs for **C_{60}** was also calculated using the same method as a reference, given this already has reasonable alignment in the region of the perovskite CBM. The goal was to design a range of materials with LUMO energies spread across the region of **C60**'s LUMO, as a starting point for energetic tuning. To this end, DFT calculations were performed using Gaussian 09,[415] employing B3LYP functional, and 6-31G (d,p) basis set, using 'empiricaldispersion=gd3' modifier to better simulate the molecules in the solid state.

4.3.2. Isoindigo Motif

Isoindigo was selected as a motif to use as a starting point for FMO energy tuning. Its structure (with position labels for reference) is shown below in Figure 138. Isoindigo is a common building block in organic electronics, owing to its electron deficient character, high planarity, N sites for side chain attachment and scalable synthesis from generally inexpensive reagents.[416,417] Moreover, its more famous isomer, indigo (commonly used to dye blue jeans) is well known for its sublimation properties.[418] Given their similarity, it was assumed that isoindigo would also be capable of sublimation, fulfilling this design requirment.

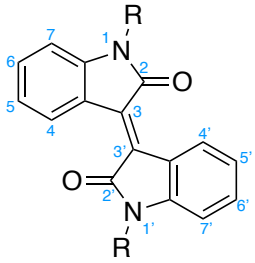

Isoindigo

Figure 138. Isoindigo structure

In deciding the identity of the R groups on Figure 138, it was decided to methylate the N atoms, rather than leaving them protonated. This was to suppress hydrogen-bonding interactions which could be expected to decrease their solubility, making purification more challenging. It was also expected to reduce the intermolecular forces between the molecules to assist sublimation. To tune isoindigo to produce a series of molecules with a spectrum of energies, several organic electronic molecular design techniques were applied.

To raise the FMO energies, giving shallower HOMO and LUMOs, the benzene units in isoindigo were substituted for more electron rich thiophene units to make thienoisoindigo.[419] Another method was substitution of H for a methoxy group at a variety of positions on the benzene rings. O atoms connected to π-systems have a strong electron donating resonance effect due to their lone pairs' electron donation into the π-system, which destabilises the FMOs (despite the electron withdrawing inductive effect of the O atoms).[63]

On the other hand, to lower the FMO energies, substitution of H with F atoms was applied. This stabilises the aromatic system owing to the inductive effect of the electronegative F atom.[56] A similar effect was also achieved by C-H substitution for N (effectively replacing benzene with pyridine) to produce azaisoindigo, to utilise the greater electronegativity of N to stabilise the FMO energies.[420] The final technique to lower the FMOs was substitution of the N atoms of isoindigo to more electronegative O atoms to generate isoxindigo, a motif employed in the dye industry.[421,422]

4.3.3. DFT Calculation FMO Estimates

These modifications are summarised in Figure 139, where their application to the isoindigo motif produced 20 variations. These theoretical structures are numbered **DFT1** to **DFT20**.

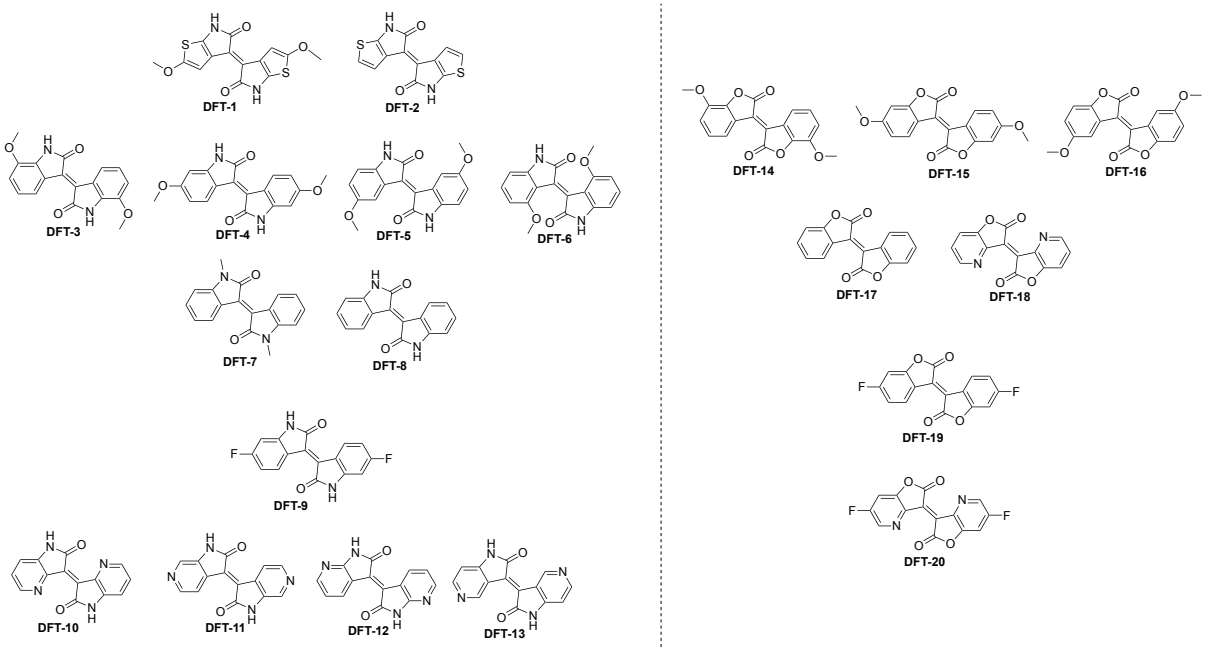

Figure 139. Atomic modifications applied to isoindigo motif to generate a variation in LUMO energies.

After identifying these 20 energetically varied structures, they underwent DFT optimisation and the FMO energies were calculated, with the results summarised in Figure 140, showing good agreement with intuitive predictions.

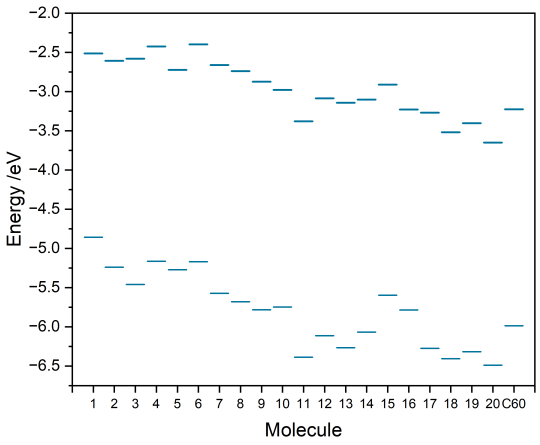

Figure 140. Energy levels of DFT series.

The placement of **C_{60}** on the series (Figure 140 far right) immediately indicated that all the thienoisoindigos and isoindigos with electron donating substituents made the LUMOs far too high. This ruled out molecules **DFT-1** to **DFT-6** as the least promising targets. Furthermore **DFT-18** to **DFT-20** were ruled out as giving too deep LUMOs. Following this, three synthetic targets were narrowed down and identified as giving a reasonable approximation of the FMO energies of C_{60}, while giving energetic 'wiggle room' on either side. Their structures and FMO energies are shown in more detail below in Figure 141, with their FMO energy estimations and shown in the table below.

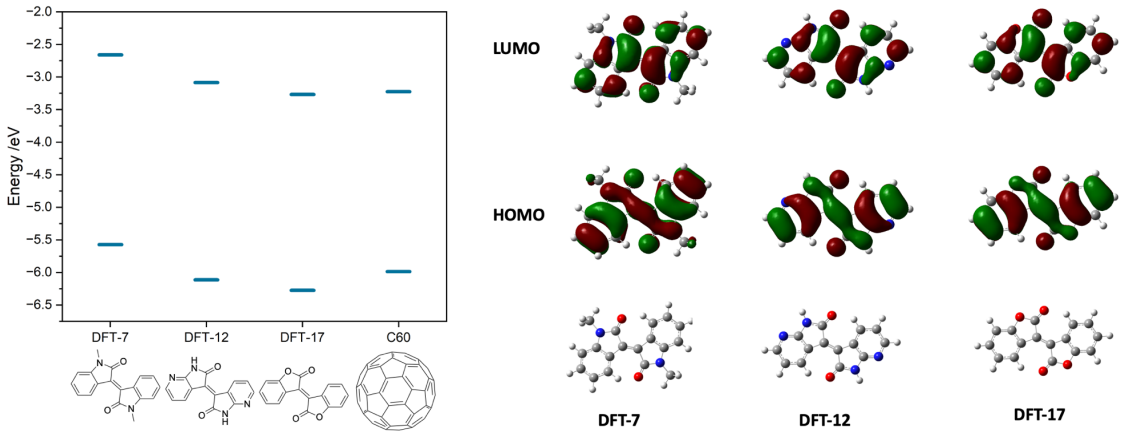

Figure 141. Left: DFT FMO estimations for narrowed down selection of isoindigo derivatives. Right: FMO distributions.

Molecule	DFT HOMO /eV	DFT LUMO /eV	Band gap /eV
DFT- 7	-5.57	-2.66	2.91
DFT-12	-6.11	-3.09	3.02
DFT-17	-6.27	-3.27	3.00
C_{60}	-5.99	-3.22	2.77

4.3. Synthesis

4.3.1. Isatin Dimerisation Attempt

In a first attempt to synthesise 1,1′-dimethylisoindigo (**DFT-7**), commercially available 1-methylisatin was reacted with phosphorous hexaethyltriamide shown in Figure 142. This was in accordance with reports of isoindigo being able to be synthesised by dimerisation of isatin using this reagent in a single step.[423–426]

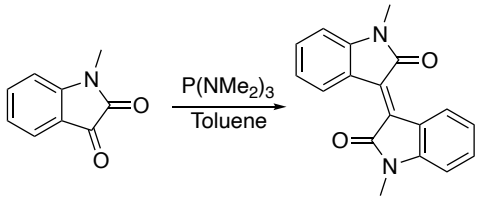

Figure 142. Attempted dimerisation of isatin

However, this reaction produced a messy distribution of products which was difficult to separate. The mechanism for this reaction is thought to proceed via deoxygenation forming a carbene intermediate at the 3-position, driven by the formation of the P=O bond in hexamethylphosphoramide. However it is reported that the side products include an epoxide bridged dimer, arising from intermediate carbene reaction with isatin,[427] which could explain the low yield and side products.

4.3.2. Aldol Condensation Strategy

Instead, a more conventional method of synthesising isoindigo via acid-catalysed aldol condensation of isatin and oxindole derivatives was adopted for all of the ETLs in the series, as shown in Figure 143.[428–430] This strategy was superior to dimerization approaches using the attempted phosphine[423–426] or Lawesson's reagent[419,431] conditions, because although oxindole derivates must be first synthesised with which to couple the isoindigo derivatives, once made they could be combined in different ways to form asymmetric isoindigo derivatives, opening up a wider range of possible molecules with finer control of energy levels.

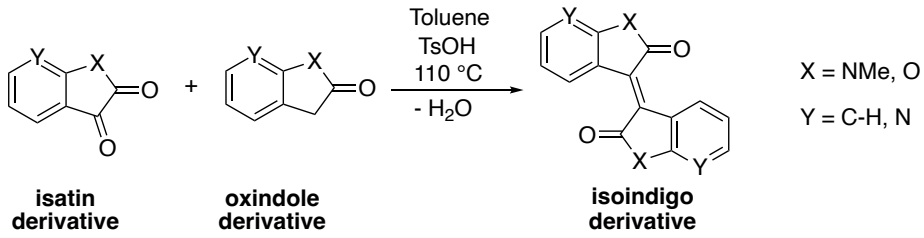

Figure 143. Aldol Condensation scheme

4.3.3. Aldol Condensation Precursor Targets

In order to synthesise the target molecules, the aldol condensation precursors in Figure 144 on the right had to be synthesised, while those on the left were commercially available.

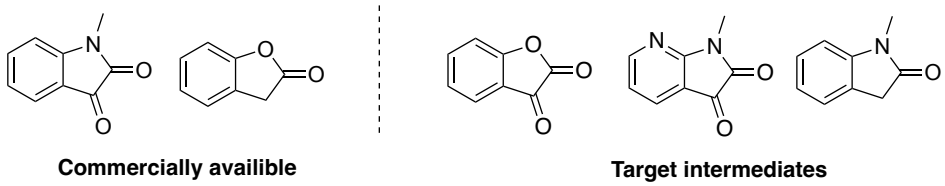

Figure 144. Commercially available (left) and target precursors (right)

4.3.4. Oxindole Methylation to Synthesise 19

19 was synthesised by deprotonation of the oxindole, and quenching with methyl iodide, shown in figure 145.

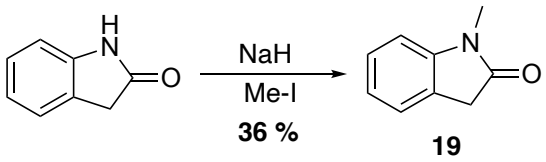

*Figure 145. Synthesis of intermediate **19***

4.3.5. Isatin Conversion to 2,3-Benzofurandione to Synthesise 20

Owing to the availability of isatin at low cost, the procedure shown in Figure 146 was followed to synthesise **20** from literature procedures.[432,433]

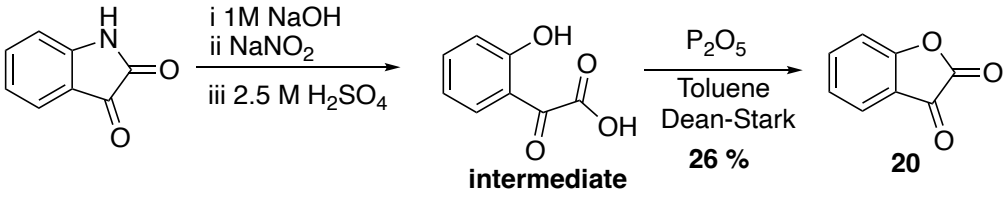

Figure 146. Synthesis of intermediate 20

A mechanism for the above transformation is given in Figure 147. First, addition of aqueous hydroxide hydrolyses isatin to form ring opened isatinic acid salt.[434,435] Addition of $NaNO_2$ with H_2SO_4 forms HNO_2 which decomposes to produce a reactive NO^+, which is attacked by the aryl amine to form an unstable diazonium salt which subsequently decomposes (in a controlled manner) driven by the evolution of N_2 gas, leaving an aryl cation which is attacked by water to form phenylglyoxylic acid.[56] This intermediate undergoes aqueous workup and extensive drying and is the directly subjected to ring closing dehydration by phosphorous pentoxide to form **2**.

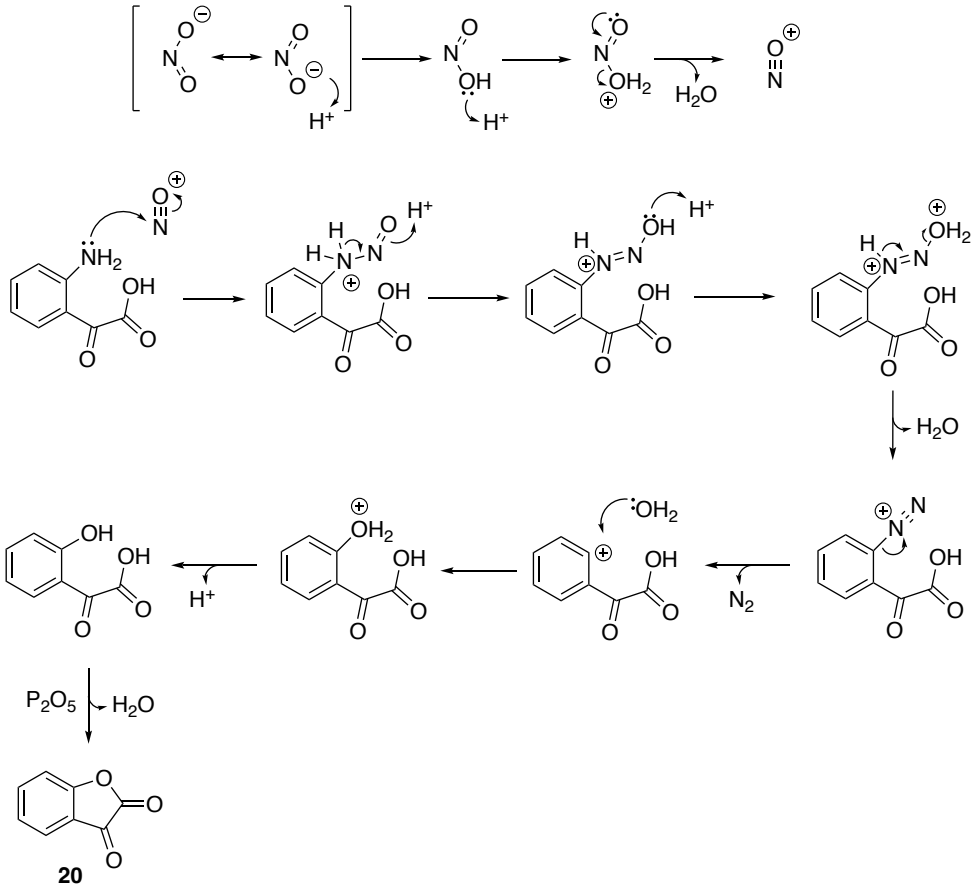

*Figure 147. Mechanism for synthesis of **20***

4.3.6. 1-Methyl Oxindole Oxidation to Produce 22

The last isatin derivative to complete the series was **22**, shown in Figure 148. This was synthesised by methylation of indole in the same manner as in section 4.3.1. to produce **21**. Next **21** was oxidised using pyridinium chlorochromate (PCC) in the presence of $AlCl_3$ Lewis acid catalyst, using a procedure which has been recently reported[436] and since reproduced for azaisatin synthesis.[424]

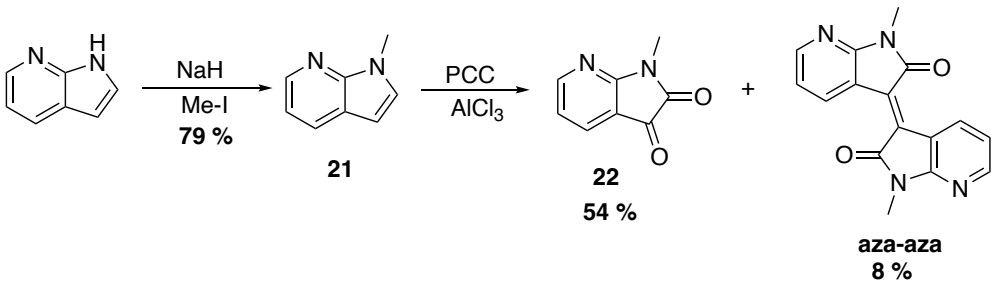

*Figure 148. Synthesis of intermediate **22**, and accidental synthesis of ETL **aza-aza***

During silica column chromatography purification, it was noticed that there were two distinct bands, with an orange one eluting first, followed by a red one. NMR and GC-MS analysis happily showed that the second fraction was actually the dimerised final target **DFT-12**, renamed here as **aza-aza**, while the first fraction was the intended target **22**. Such dimerisation has previously been reported as a side product to the reaction, though its mechanism is not yet understood.[424]

4.3.7. Aldol Condensations

Having synthesised the necessary isatin derivative and oxindole derivative precursors, they were combined. A representative mechanism for acid catalysed aldol condensation isoindigo formation is shown in Figure 159. It involves tautomerisation of the oxindole, followed by nucleophilic attack of the more electrophilic isatin carbonyl at the 3-position. This is followed by elimination of water forming the trans double bond.

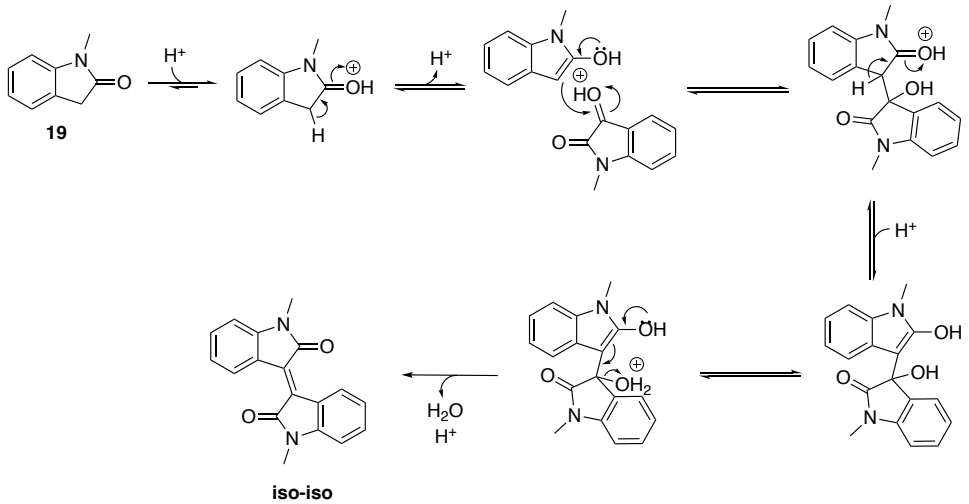

Figure 149. Mechanism for aldol condensation

The isatin and oxindole derivates were reacted in different combinations to give five isoindigo derivatives, with the sixth being the side-product from the synthesis of **22**. The final ETL are named in accordance with the composition of each half, with isoindigo as iso, azaisoindigo as aza and isoxindigo as isox. The final materials with labels are shown in Figure 150.

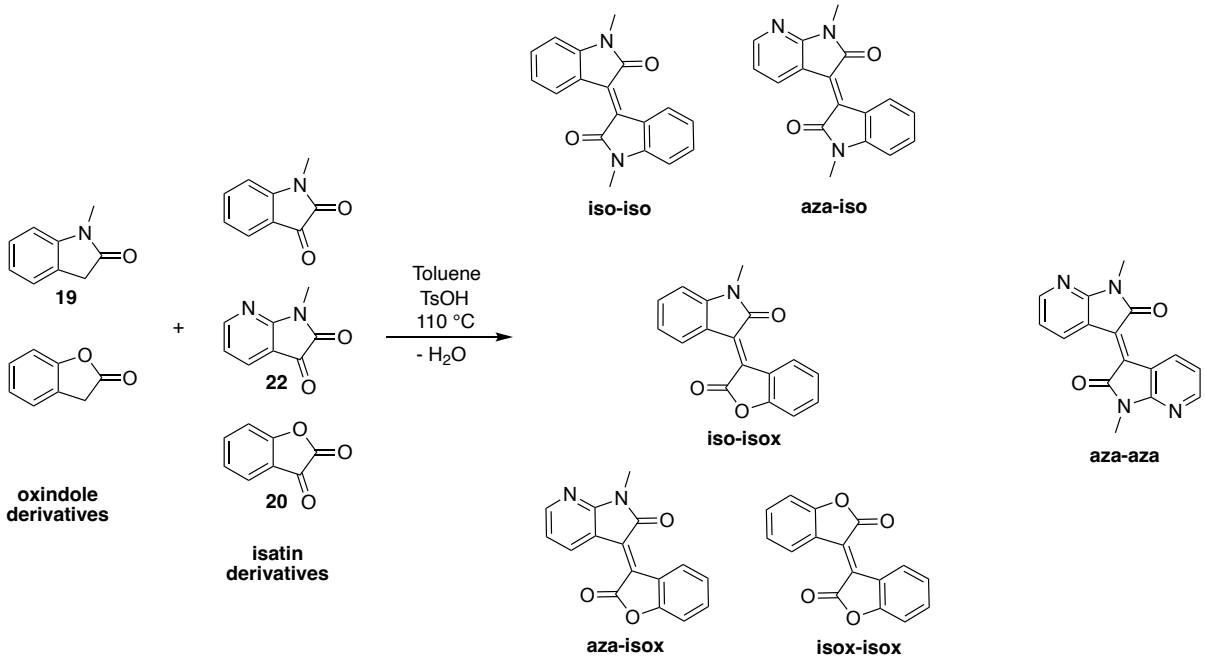

Figure 150. Final ETL materials

4.4. Characterisation

4.4.1. DFT Comparison Including Asymmetric ETLs

All of the now synthesised ETL materials are displayed in Figure 152.

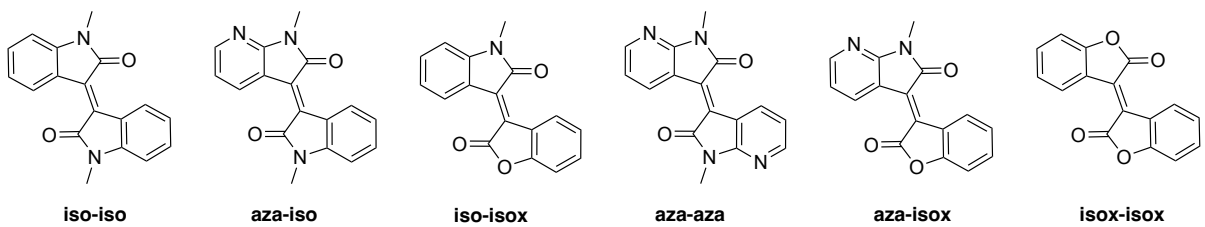

Figure 151. ETL materials in order of decreasing LUMO energy

After synthesising the asymmetric molecules, another DFT optimisation was conducted. It was found the calculated FMO energies lay between the symmetric parent molecules which they are a hybrid of, as would be expected. The FMO energies of the series are shown in Figure 152, in order of descending energy, and with **C_{60}** for comparison.

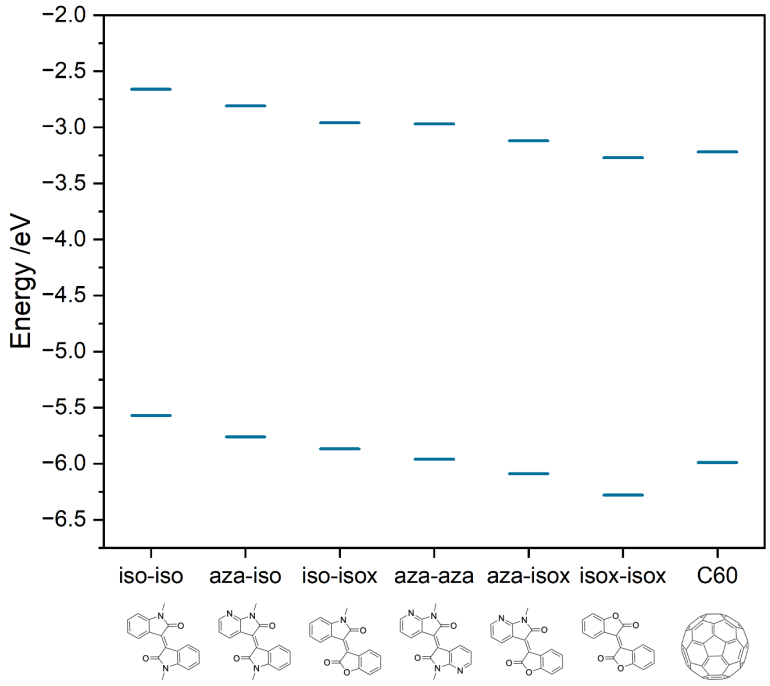

Figure 152. DFT calculated FMO energies.

The DFT calculated energy level properties are displayed below.

Molecule	DFT HOMO /eV	DFT LUMO /eV	Band gap /eV
Iso-iso	-5.57	-2.66	2.91
Aza-iso	-5.76	-2.81	2.95
Iso-isox	-5.87	-2.96	2.91
Aza-aza	-6.11	-3.09	3.00
Aza-isox	-6.09	-3.12	2.96
Isox-isox	-6.28	-3.27	3.00
C_{60}	-5.99	-3.22	2.77

4.4.2. Thermogravimetric Analysis (TGA)

In order to quantify the sublimation temperatures to see if the ETLs fulfilled the design criteria, TGA was conducted. This was done by adding between 1 and 2 mg of material into the TGA apparatus. The temperature was increased from 30 °C to 600 °C at a ramp rate of 10 °C min^{-1} under N_2 atmosphere at ambient pressure. The mass of the sample was measured as a function of temperature. The onset of mass loss was measured and shown below in Figure 154.

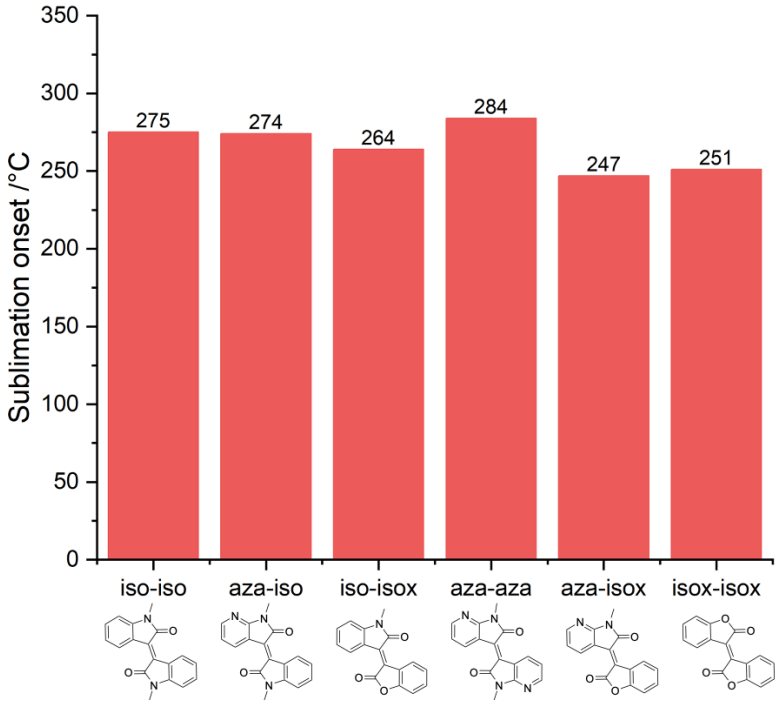

Figure 153. onset of mass loss under TGA for ETLs

They all displayed mass loss onset at ambient pressure between 240 °C and 290 °C. At the end, there was nothing left in the sample holder.

4.4.3. Sublimation Test

To test that the TGA mass loss was caused by sublimation rather than degradation, a laboratory sublimation kit was purchased. This allowed sample to be added to the sublimation chamber, put under high vacuum and while heated, enabling sublimation on a glass slide stuck to the chilled roof of the chamber, depicted in Figure 154 below.

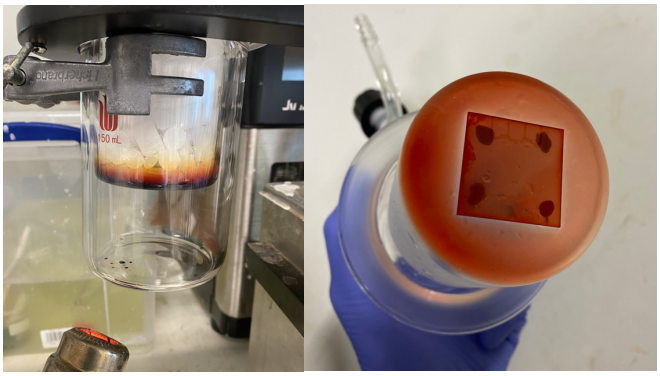

*Figure 154. Example sublimation of **iso-iso***

The sublimed compound was collected and tested for degradation by ^{1}H NMR. It showed an identical spectrum, indicating heating during the sublimation process did not cause any structural damage. This was the case for all of the materials.

4.4.4. UV-Vis Characterisation of Optical Bandgap

The same approach was then used to sublime thin films of material onto glass slides to conduct UV-vis spectroscopy. Given the intention was to use them sublimed in devices, it was thought that this method of processing films would better represent their intended application. The sublimed films are shown in Figure 155.

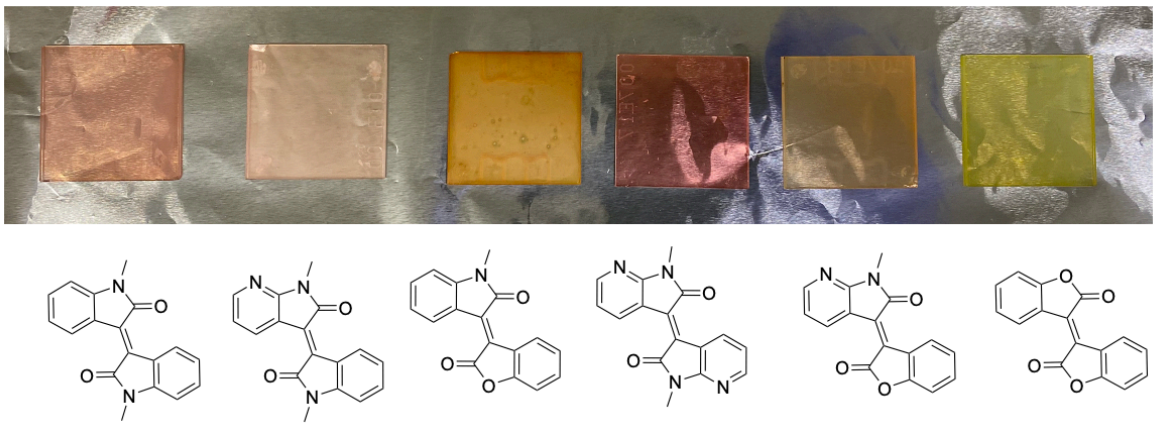

Figure 155. Sublimed ETLs on glass slides

UV-vis spectroscopy was also conducted for chloroform solutions of the materials for comparison. Both spectra are shown in Figure 156.

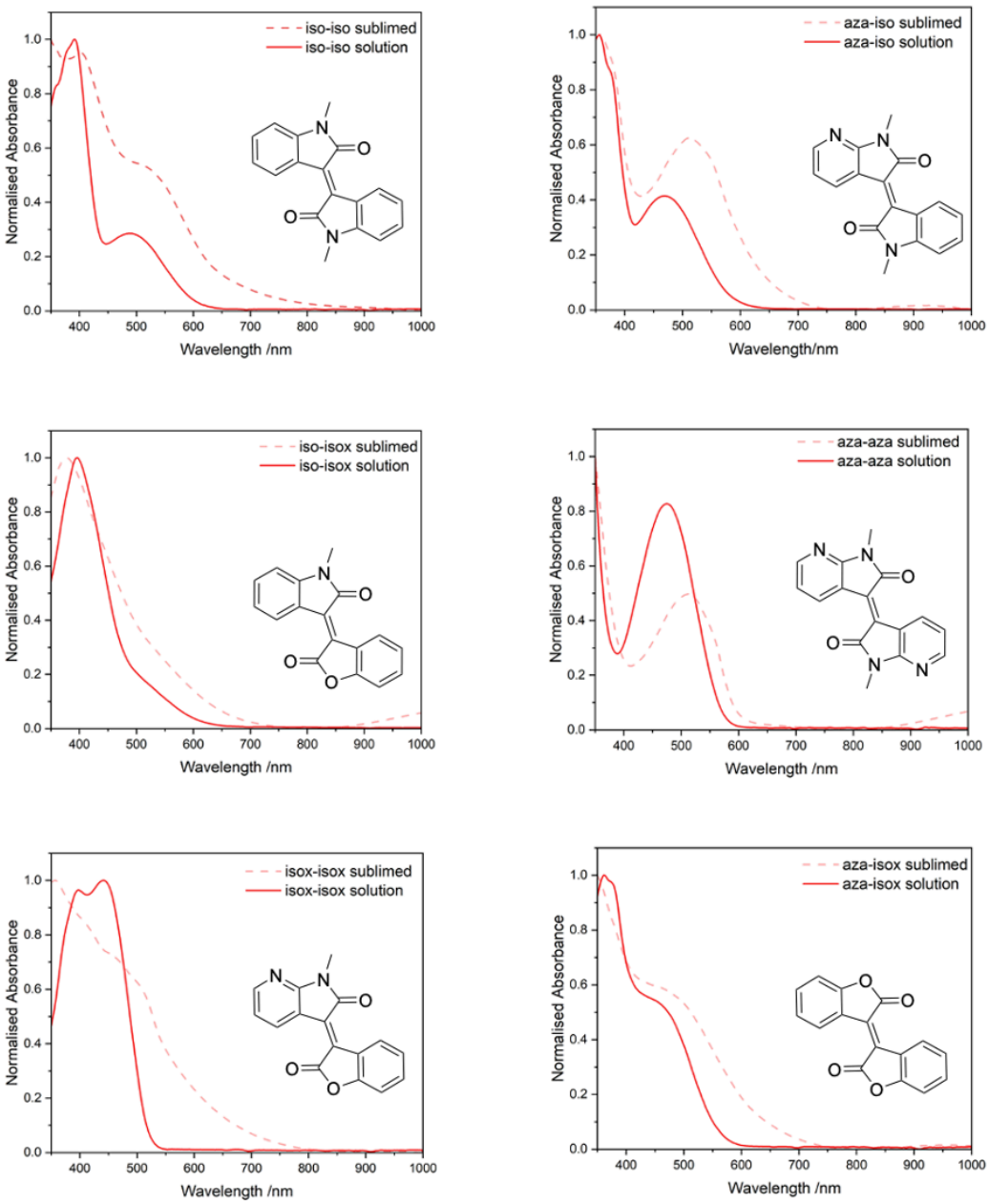

Figure 156 *UV-vis spectra for chloroform solution (solid line) and sublimed (dotted line)*

As can be seen from Figure 157, some of the sublimed films appeared slightly 'frosted' due to film roughness. This may be caused by crystallisation following sublimation, which seemed to cause scattering in the UV-vis spectra, making solid state optical bandgap estimation for some of the materials unreliable. Nonetheless, the optical bandgaps in solution are shown in the table below. They are all broadly similar, with isox-isox being the largest, accounting for its yellow colour.

Material	Solution Absorption onset /nm	Solution Optical Bandgap /eV
iso-iso	600	2.07
aza-iso	581	2.13
iso-isox	612	2.03
aza-aza	568	2.18
aza-isox	559	2.22
isox-isox	518	2.39

4.4.5. PESA Characterisation of HOMO Energies

PESA measurements were undertaken of the films to obtain estimates for their HOMO energies, however, going down the series, the data quality seemed to deteriorate, as shown in Figure 157. The magnitude of the photoemission signal was very small, making the signal to noise ratio high, such that reliable tangents could not be drawn to estimate the onset energy of photoemission. Several attempts on different films could not remedy this problem.

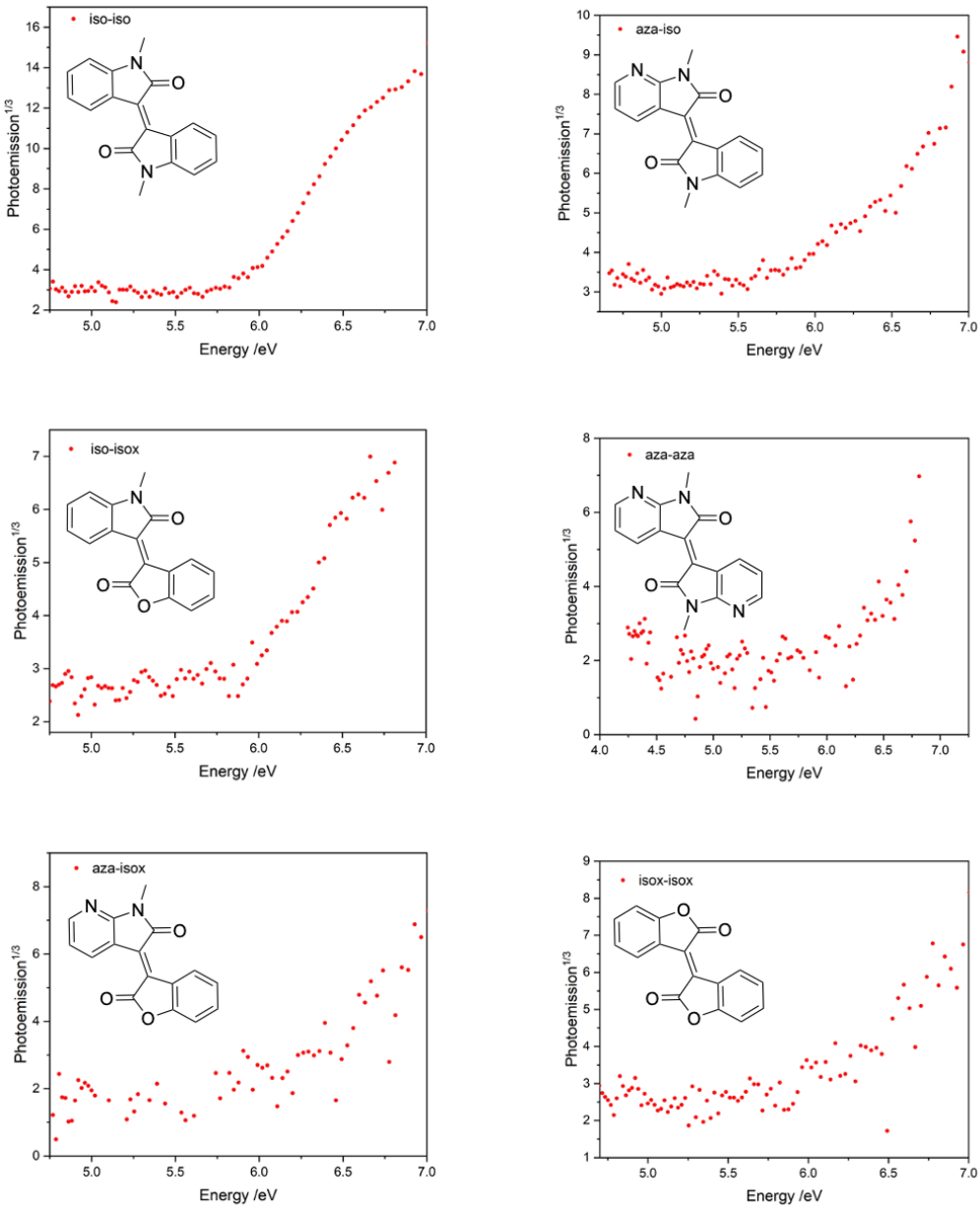

Figure 157. PESA spectra for sublimed ETI films

It was thought that the reason the signal was so low was because the maximum irradiation energy was 7.0 eV. Because of the presumably very deep HOMO energies, higher irradiation energies would be needed to get a big enough signal to draw a tangent.

Iso-iso was the only material to give an acceptable signal, and the onset of photoemission is at -5.9 eV. The sublimed absorption onset at 651 nm from UV-vis

spectroscopy gives an optical bandgap estimate of 1.90 eV. This puts the LUMO energy at -4.0 eV using PESA and optical bandgap. Though as previously discussed, the optical bandgap sits within the fundamental bandgap,[78–80,100] so this is likely to give an estimate of the LUMO which is too low in energy, while the true LUMO should be closer to vacuum energy.

This demonstrated that PESA is an unsuitable method to determine the energy of very deep HOMO materials. Nonetheless, for the material in the series whose HOMO was estimated by DFT calculation to be the highest in energy, using PESA and the optical bandgap from UV-vis placed its LUMO at -4.0 eV, with the caveat that this estimate will be too low, making it was at least close to the desired region.

4.4.6. Cyclic Voltammetry (CV) Characterisation

CV was an attractive method to determine the LUMO energy, given it does so more directly than PESA, which can only estimate HOMO energies and requires optical bandgap to estimate the LUMO energy. Owing to the solubility of the ETLs in acetonitrile, thin film CV using this electrolyte was not possible, while aqueous CV gave no signal. Therefore, solution CV in acetonitrile was conducted to estimate the LUMO energies.

This was done by degassing 0.1 M tetrabutylammonium hexafluorophosphate in anhydrous acetonitrile using N_2 for 30 minutes. This was added to a standard three-electrode potentiostat configuration, using a Pt mesh as counter electrode, glassy carbon rod as the working electrode and an $Ag/AgNO_3$ wire electrode as the reference. To this solution was added less than 1 mg of material which was gently stirred to dissolve. Cyclic voltammetry was conducted between +0.8 V to -1.5 V at a scan rate of 0.1 $V\,s^{-1}$ for 3 scans, with the second and third shown in Figure 159 for all of the materials.

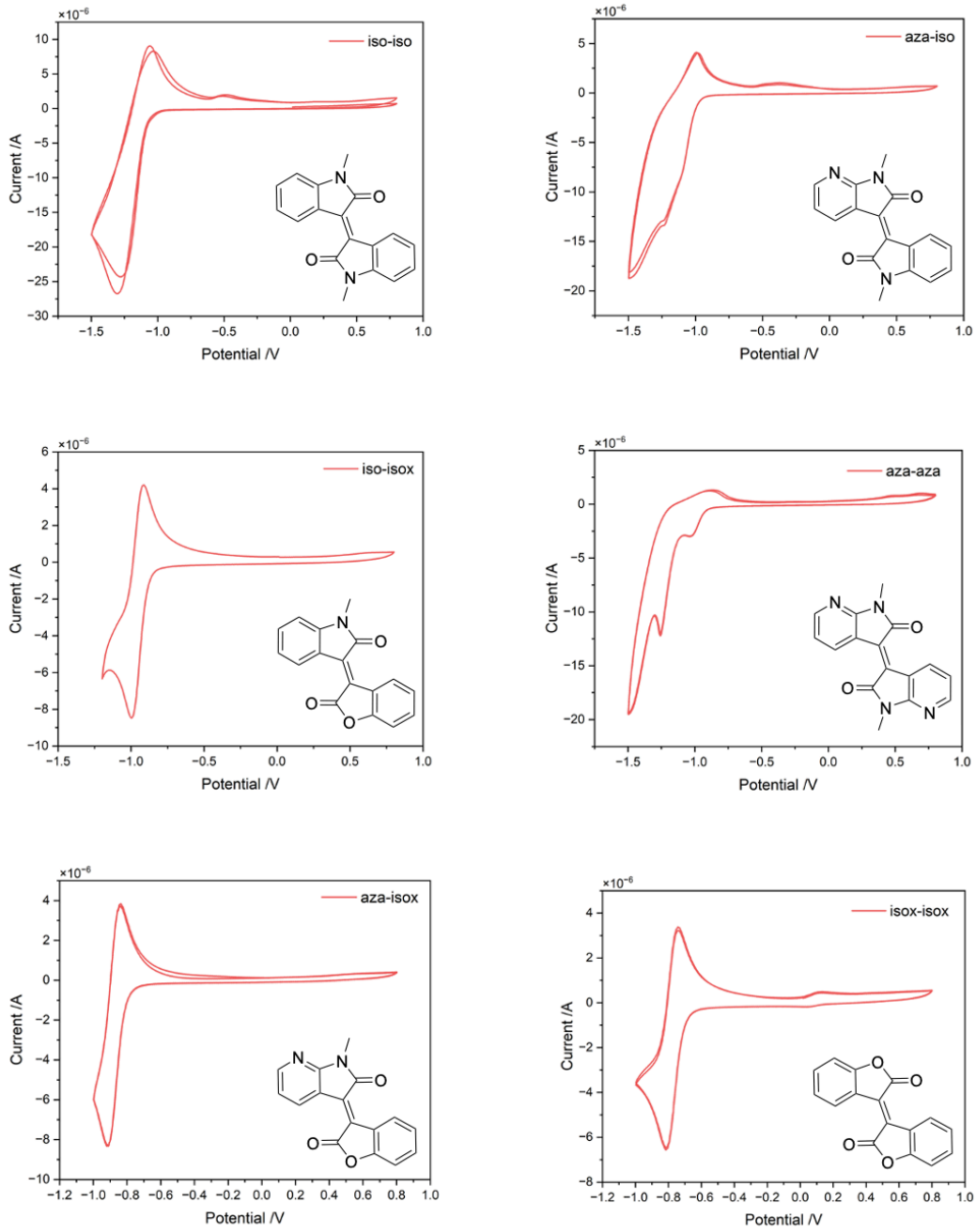

Figure 158. Solution CV spectra of ETLs in acetonitrile vs Ag/AgNO₃

All of the materials displayed reversible reduction events in the potential range, and drawing tangents for the cathodic peaks gave the reduction onsets. In order to convert these values to absolute estimates for LUMO energy, the ferrocene half wave potential was measured to be +0.064 V vs Ag/AgNO$_3$, and used in the equation below to calculate the LUMO energy on an absolute energy scale relative to vacuum, which is commonly used in literature.[316–319]

$$E_{eV} = 4.8 - \left(E_{Fc}\right) + E_{onset}$$

This gave estimations for the LUMO energies shown in the table below.

Material	Reduction onset /V	LUMO estimate /eV
iso-iso	-1.08	-3.66
aza-iso	-1.00	-3.74
iso-isox	-0.88	-3.86
aza-aza	-0.91	-3.83
aza-isox	-0.81	-3.93
isox-isox	-0.70	-4.04

Use of solution CV derived electron affinity estimates to determine the LUMO energy for small molecules in the solid state is far from ideal. This is because aggregation affects the local electronic environment of small molecules and facilitates varying degrees of electronic coupling which affects their bandgap, which is further complicated by the possible presence of crystalline and amorphous regions in the solid state.[100,437] Furthermore, the energy of a reduced molecule in solution is likely to be slightly different compared to thin film, owing to solvation effects.[80]

Nonetheless, this CV data shows a clear trend in estimated LUMO energy going down the series from iso-iso being the highest energy, to isox-isox with the lowest. The CV analysis furthermore placed the materials in a suitable region of energetic alignment with the perovskite, with a spread of estimated LUMOs was about 0.4 eV. Even though these values would be expected to diverge in the solid state, it was assumed that they would diverge by similar amounts, given the very similar geometries of the isoindigo derivative ETLs.

4.4.7. Comparison of Experimental Energies to DFT Calculations

Figure 159 displays the LUMO energies for the series calculated from DFT calculated and measured and estimated by solution CV. It shows that while their absolute energies are offset, the trend predicted by DFT is in good agreement with CV measurement.

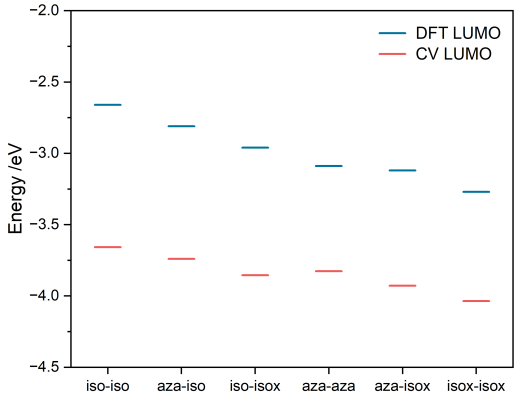

Figure 159. DFT and solution CV LUMO estimates comparison

Figure 161 (left) shows this good correlation between DFT LUMO and solution CV LUMO, while Figure 161 (right) compares the DFT bandgap estimations with those from solution UV-vis. This too shows reasonable agreement, though **aza-aza** appears to be slightly anomalous. Its CV appears different to the other materials, given its first reduction onset is a very small peak, followed by a larger one. However, when the onset of the larger peak is used, it makes the CV LUMO estimation more positive, which makes the data point even more of an outlier. Given that **aza-aza** also appears to be anomalous by UV-vis optical bandgap estimation, which is an independent measurement, it follows that the anomalous result likely comes from the DFT calculation of **aza-aza**.

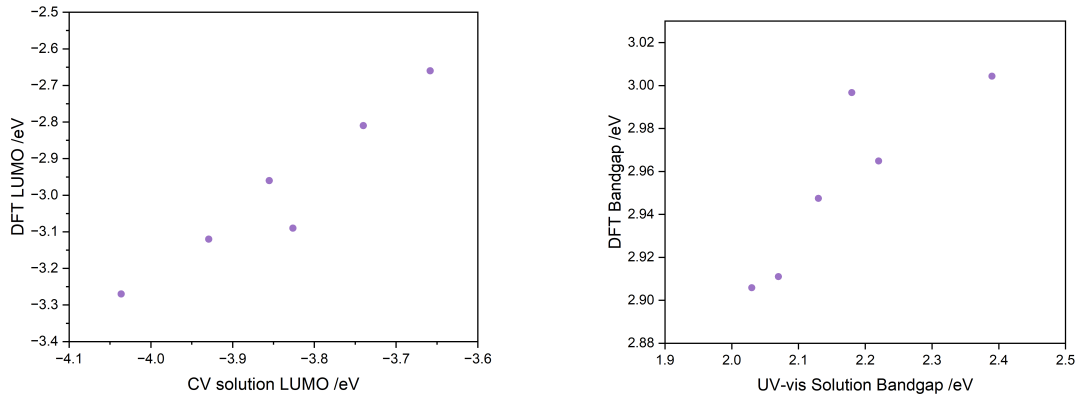

Figure 160. Correlations between DFT and CV LUMO estimations and UV-vis optical bandgaps

4.5. ETL Testing in Perovskite Solar Cells

The original intention was for these materials to be tested in perovskite solar cells using an advanced sublimation setup for rapid device fabrication and testing. However, when used in this setup, it was found that the ETLs sublimed at too low a temperature, given the extremely high vacuum. This made it not possible to test them in this setup. In lieu of this, while an alternative sublimation testing setup was found, the molecules in the series (except **isox-isox** which was poorly soluble) were fabricated into p-i-n perovskite solar cells by solution-processing in chloroform. The orientation p-i-n denotes the order in which the layered cell is fabricated: depositing the HTL onto the bottom anodic contact, followed by the perovskite active layer, followed by the ETL on top of this and finally the cathodic contact to carry electrons to the circuit.

The distribution of V_{OC}, $J_{SC,}$ and maximum power point values from the devices are summarised alongside the **C_{60}** control in Figure 162. These parameters are derived by measuring the current-voltage characterisations of the cells under simulated sunlight in order to evaluate solar cell performance. V_{OC} is the open circuit voltage. It represents the maximum photovoltage the device can generate under conditions of no current flow between anodic and cathodic contacts in the circuit. J_{SC} is the short circuit current density, which represents the maximum photocurrent the cell can

deliver. It can be thought of as the cell without a load resistance, where the anodic and cathodic contacts are 'short-circuited' so charge can flow between them without resistance. The maximum power point is the product of -V_{OC} and J_{SC} (given the convention to display photovoltage as negative).[438]

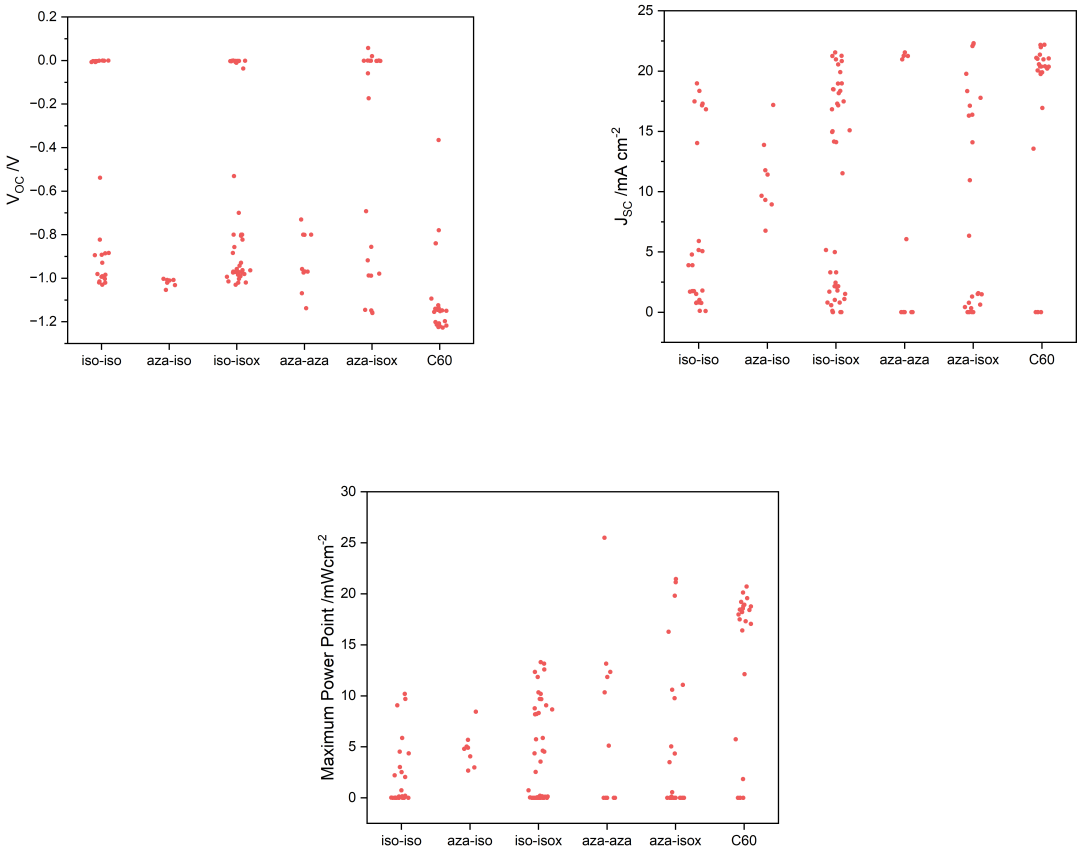

*Figure 161. V_{OC}, J_{SC} and maximum power points for ETLs in comparison to **C60**.*

It can be seen in Figure 162, that the best maximum power output values increase as LUMO energy decreases from **iso-iso** to **aza-isox**. This suggests that **iso-iso** has too high a LUMO energy, causing losses due to poor alignment. As the LUMO is decreased, the best devices show improvements in power output.

Nonetheless, these solution-processed materials do not consistently outperform **C_{60}**, and give much broader distributions in performance. In particular the V_{OC} values of **C_{60}** devices are greater than the devices using the novel ETLs. This is indicative of greater interfacial recombination caused the synthesised ETLs in devices.

Nonetheless, given these trends, it was thought that **isox-isox**, with the lowest energy LUMO could give better performance. Owing to the lower temperature sublimations of these ETLs, an alternative sublimation fabrication setup was found. However, when **aza-isox** and **isox-isox** were tested in this setup, all the devices failed to generate a significant photovoltage. This was thought to be due to poor coverage by the ETLs of the perovskite active layers, enabling contact of the perovskite with the cathodic contact leading to interfacial losses. However it was noted that this lower temperature sublimation setup was not optimised for perovskite fabrication, so this could have been a contributing factor.

Nonetheless, in terms of the structure of the ETL materials themselves, they crystallised very readily during purification owing to their planar π-conjugated structures. It is understood from the development of HTL materials that crystallisation can impair contact, impairing performance.[399]

4.6. Conclusions and Future Work

In this chapter, the project aims were to design and synthesise a series of novel ETL materials for perovskite solar cells, whose LUMO energies were spread across the region of -4.0 eV, with as deep HOMOs as possible, and to be sublimation processable. These design requirements were mostly satisfied.

DFT was used to estimate the relative effects of various molecular design strategies applied to the isoindigo motif, using **C_{60}** as a reference point. Six ETL materials were successfully synthesised. Although accurate determination of the LUMO energies in the solid state was not possible using the attempted methods owing to the ETLs' deep HOMO energies, solution CV characterisation of their electron affinities showed their LUMO energies were in the desired energy window. It was also shown that the experimentally estimated CV LUMOs and UV-vis optical bandgaps showed excellent agreement with the trends from DFT, save for **aza-aza** which was anomalous. Though given the red or yellow colour of all of the ETLs, the optical bandgap was clearly still too narrow. A potential solution to this could be to substitute isoindigo derivatives at

the 4,4' positions to provoke a steric clash and cause the dihedral angles to be more twisted to impair conjugation and increase the optical bandgap.

Furthermore, sublimation was demonstrated for all of the ETLs. In fact, the sublimation was too easily achieved, which proved a problem for testing the ETLs in their intended perovskite solar cell fabrication and characterisation setup. Solution processed ETLs showed a general improvement in efficiency as LUMO energy was decreased from **iso-iso** to **aza-isox**, while **isox-isox** was not able to be tested in solution owing to its lower solubility. Tests of **aza-isox** and **isox-isox** to make devices in a non-optimised sublimation setup however yielded failed devices, likely due to very poor coverage of the perovskite.

In order to improve these materials, it is likely that their crystallisation properties should be hindered in order to generate more uniform amorphous films.[357] Taking inspiration form HTLs, and satisfyingly returning to Chapter 1, use of the spiro motif is common in charge transport materials such as spiro-MeOTAD. This HTL uses the orthogonal spiro-fluorene motif functionalised with triarylamines. It has a relatively high glass transition temperatures owing to this spiro motif, which hinders its ability to form crystal domains, due to increased molecular motion near the glass transition temperature.[350,357] If ETL crystallisation properties are hindered sufficiently, and it is not at the expense of sublimation processability, then this could provide a pathway to overcome this issue.

Finally, more methods to characterise the optoelectronic properties in the solid state are required, such as ultraviolet photoelectron spectroscopy (UPS) in conjunction with low energy inverse photoelectron spectroscopy (IPES).

5. Thesis Conclusions

Chapter 1 outlined the numerous interrelated parameters which control the photocatalytic process. Chapter 2 aimed to more closely investigate the parameters of porosity and hydrophilicity. In order to do this, novel tert-butyl spirofluorene flanked polymers were synthesised, using protecting groups to control hydrophilicity and porosity to allowing thorough characterisation. By holding other factors such as polymer backbone constant, and quantifying particle size differences, it was found that porosity is beneficial for conjugated polymer photocatalysts, so long as it does not adversely affect other parameters. It was also shown that hydrophilicity was beneficial for performance. However, it was shown the presence of hydrophilic functional groups in conjunction with porosity gave the greatest increases in activity. It was shown by TAS that porous polymers are capable of intrinsic exciton separation, a rare property for organic semiconductors. This work lays the groundwork for further photophysical investigation into this behaviour for this class of materials.

In Chapter 3, these findings were reinforced, though by exploring more diverse polymer backbones it was found porosity and hydrophilicity were not always the best predictor of activity, when other factors such as energetic driving forces are inadequate. Understanding of the properties of this class of intrinsically microporous polymers was also enhanced. It was found the density of tert-butyl spirofluorene units along the backbone correlated with the porosity, but usually at the expense of solubility. Nonetheless it was shown that balancing these factors can lead to the generation of solution processable microporous polymers, demonstrating significant porosity in non-network materials. This solution processability is particularly advantageous, and in combination with suitable electronic properties, could have the potential to better enable heterojunction formation in organic semiconductors.

In Chapter 4, a series of novel sublimation processable ETL materials for perovskite solar cells were designed using DFT modelling and synthesised successfully. The DFT trends showed excellent correlation with the measured experimental FMOs, and a performance trend for the materials in perovskite solar cells was found, showing

decreasing LUMO energy correlated with higher performance. This was attributed to better energetic alignment with the perovskite CBM. Although the materials tested did not give greater performance than **C_{60}** on average, further work decreasing LUMO, energy, widening the bandgap and suppressing crystallisation are identified as a promising step.

In Chapter 1, the promise of solar driven H_2 derived from water was outlined and the potential for direct photocatalytic water splitting to deliver this was discussed. In order for this to be feasible, solar to hydrogen conversion efficiencies of 5 to 10 % are required for commercial viability. This target has already been met by inorganic semiconductors on the laboratory scale, with 5.2 % already reported for some of the highest performing inorganic systems,[177] which was raised to 9.2 % at elevated temperatures.[178] Nonetheless, this involves epitaxial growth and precise graduated impregnation with Mg. This technology is not scalable, limiting the utilisation of such systems outside of the laboratory.

Part of the promise of organic semiconductors is their low fabrication and processing costs, particularly when their soluble properties are fully exploited. Nonetheless, organic semiconductors are still lag behind their inorganic counterparts. In general, while they benefit from superior light harvesting and processing properties, they struggle with exciton separation and transport. Because of this, the field still exhibits extensive reliance on sacrificial electron donors. This is particularly problematic in systems such as those involving dibenzo[b,d]thiophene sulfone (which has somewhat dominated the field) which rely on the rapid interaction with sacrificial reagents for exciton separation. By contrast, while still employing sacrificial reagents to remove the long term build-up of holes, type-II heterojunction mixed semiconductor systems can display intrinsic charge generation and offer far greater potential to be integrated into overall water splitting single particle systems or Z-schemes, owing to their long-lived spatially separated electron and hole polarons. Furthermore, recent work on glycolated single component systems and the present work outlined in this thesis with porous organic semiconductors highlights a fascinating insight: water splitting takes place in water and its presence seems to produce a greater dielectric environment

making exciton separation more favourable and polaron recombination less favourable. This strongly suggests that getting ‘wetter’ via incorporation of hydrophilic moieties, or wettable porosity is a promising direction for the future design or photocatalytic organic semiconductors in order to capitalise on the beneficial photophysical consequences of the presence of water and ameliorate some of the disadvantages organic semiconductors have relative to their inorganic counterparts with respect to exciton separation.

Although a relatively new field, progress in performance and fundamental understanding has increased immensely. Furthermore, organic semiconductors are a broad family of materials with a diverse spectrum of applications; insight from photovoltaics has significantly enriched photocatalysis, and in turn the interplay of insight from light emitting diodes and transistors has also been added in, in a multi-directional symbiotic flow of understanding. This is likely only to increase as more is understood about the science of highly conjugated organic compounds.

6. References

[1] S. Pirani, *Burning Up: A Global History of Fossil Fuel Consumption*, Pluto Press, **2018**.
[2] M. K. Hubbert, *Science* **1949**, *109*, 103.
[3] International Energy Agency, *CO2 Emissions in 2022*, **2023**.
[4] L. Kemp, C. Xu, J. Depledge, K. L. Ebi, G. Gibbins, T. A. Kohler, J. Rockstrom, M. Scheffer, H. J. Schellnhuber, W. Steffen, T. M. Lenton, *Proc. Natl. Acad. Sci. U. S. A.* **2022**, *119*, e2108146119.
[5] United Nations, *Paris Agreement English*, Paris, **2015**.
[6] HM Government, *Net Zero Strategy: Build Back Greener*, **2021**.
[7] P. M. Forster, C. J. Smith, T. Walsh, W. F. Lamb, R. Lamboll, M. Hauser, A. Ribes, D. Rosen, N. Gillett, M. D. Palmer, J. Rogelj, K. Von Schuckmann, S. I. Seneviratne, B. Trewin, X. Zhang, M. Allen, R. Andrew, A. Birt, A. Borger, T. Boyer, J. A. Broersma, L. Cheng, F. Dentener, P. Friedlingstein, J. M. Gutiérrez, J. Gütschow, B. Hall, M. Ishii, S. Jenkins, X. Lan, J. Y. Lee, C. Morice, C. Kadow, J. Kennedy, R. Killick, J. C. Minx, V. Naik, G. P. Peters, A. Pirani, J. Pongratz, C. F. Schleussner, S. Szopa, P. Thorne, R. Rohde, M. Rojas Corradi, D. Schumacher, R. Vose, K. Zickfeld, V. Masson-Delmotte, P. Zhai, *Earth Syst. Sci. Data* **2023**, *15*, 2295.
[8] International Energy Agency, *World Energy Outlook 2023*, **2023**.
[9] The Royal Society, *Large-Scale Electricity Storage*, **2023**.
[10] M. A. Delucchi, M. Z. Jacobson, *Bull. At. Sci.* **2013**, *69*, 30.
[11] S. Rehman, L. M. Al-Hadhrami, M. M. Alam, *Renew. Sustain. Energy Rev.* **2015**, *44*, 586.
[12] D. Rastler, *Electricity Energy Storage Technology Options*, Palo Alto, **2010**.
[13] International Energy Agency, *Global Hydrogen Review 2022*, **2022**.
[14] F. Ustolin, A. Campari, R. Taccani, *J. Mar. Sci. Eng.* **2022**, *10*, 1222.
[15] X. Yang, C. P. Nielsen, S. Song, M. B. McElroy, *Nat. Energy* **2022**, *7*, 955.
[16] N. Rambhujun, M. S. Salman, T. Wang, C. Pratthana, P. Sapkota, M. Costalin, Q. Lai, K. F. Aguey-Zinsou, *MRS Energy Sustain.* **2020**, *7*, 1.
[17] M. Capdevila-Cortada, *Nat. Catal.* **2019**, *2*, 1055.
[18] International Energy Agency, *Ammonia Technology Roadmap Towards More Sustainable Nitrogen Fertiliser Production*, **2021**.
[19] G. Lopez, L. Santamaria, A. Lemonidou, S. Zhang, C. Wu, A. T. Sipra, N. Gao, *Nat. Rev. Methods Prim.* **2022**, *2*, 20.
[20] H. Balat, E. Kirtay, *Int. J. Hydrogen Energy* **2010**, *35*, 7416.
[21] M. G. Walter, E. L. Warren, J. R. McKone, S. W. Boettcher, Q. Mi, E. A. Santori, N. S. Lewis, *Chem. Rev.* **2010**, *110*, 6446.
[22] P. Nikolaidis, A. Poullikkas, *Renew. Sustain. Energy Rev.* **2017**, *67*, 597.
[23] K. Chelvam, M. M. Hanafiah, K. S. Woon, K. Al Ali, *Energy Reports* **2024**, *11*, 369.
[24] J. E. Funk, *Int. J. Hydrogen Energy* **2001**, *26*, 185.
[25] H. Ozcan, R. S. El-Emam, B. Amini Horri, *J. Clean. Prod.* **2023**, *382*, 135295.
[26] T. Markvart, *Solar Electricity*, John Wiley & Sons, Chichester, **2000**.
[27] M. Perez, R. Perez, *Sol. Energy Adv.* **2022**, *2*, 100014.
[28] J. Jia, L. C. Seitz, J. D. Benck, Y. Huo, Y. Chen, J. W. D. Ng, T. Bilir, J. S. Harris, T. F. Jaramillo, *Nat. Commun.* **2016**, *7*, 13237.
[29] Z. Li, T. R. Klein, D. H. Kim, M. Yang, J. J. Berry, M. F. A. M. Van Hest, K. Zhu, *Nat. Rev. Mater.* **2018**, *3*, 18017.
[30] N. A. Burton, R. V. Padilla, A. Rose, H. Habibullah, *Renew. Sustain. Energy Rev.* **2021**, *135*, 110255.
[31] A. Allouhi, S. Rehman, M. S. Buker, Z. Said, *J. Clean. Prod.* **2022**, *362*, 132339.
[32] B. Ehrler, E. Alarcón-Lladó, S. W. Tabernig, T. Veeken, E. C. Garnett, A. Polman, *ACS Energy Lett.* **2020**, *5*, 3029.
[33] G. Glenk, S. Reichelstein, *Nat. Commun.* **2022**, *13*, 1.
[34] G. A. Adedayo, A. B. Samson, *Int. J. Renew. Energy Technol. Res.* **2017**, *6*.
[35] A. Fujishima, K. Honda, *Nature* **1972**, *238*, 37.
[36] K. Maeda, *J. Photochem. Photobiol. C Photochem. Rev.* **2011**, *12*, 237.
[37] J. H. Kim, D. Hansora, P. Sharma, J. W. Jang, J. S. Lee, *Chem. Soc. Rev.* **2019**, *48*, 1908.
[38] S. C. Warren, K. Voïtchovsky, H. Dotan, C. M. Leroy, M. Cornuz, F. Stellacci, C. Hébert, A. Rothschild, M. Grätzel, *Nat. Mater.* **2013**, *12*, 842.
[39] D. K. Lee, D. Lee, M. A. Lumley, K. S. Choi, *Chem. Soc. Rev.* **2019**, *48*, 2126.
[40] V. Schröder, B. Emonts, H. Janßen, H. P. Schulze, *Chem. Eng. Technol.* **2004**, *27*, 847.
[41] A. M. K. Fehr, A. Agrawal, F. Mandani, C. L. Conrad, Q. Jiang, S. Y. Park, O. Alley, B. Li, S. Sidhik, I. Metcalf, C. Botello, J. L. Young, J. Even, J. C. Blancon, T. G. Deutsch, K. Zhu, S. Albrecht, F. M. Toma, M. Wong, A. D. Mohite, *Nat. Commun.* **2023**, *14*, 3797.
[42] B. A. Pinaud, J. D. Benck, L. C. Seitz, A. J. Forman, Z. Chen, T. G. Deutsch, B. D. James, K. N. Baum, G. N. Baum, S. Ardo, H. Wang, E. Miller, T. F. Jaramillo, *Energy Environ. Sci.* **2013**, *6*, 1983.
[43] B. James, G. Baum, J. Perez, K. Baum, *Technoeconomic Analysis of Photoelectrochemical (PEC) Hydrogen Production*, Arlington, **2009**.
[44] T. Hisatomi, K. Domen, *Nat. Catal.* **2019**, *2*, 387.
[45] Y. Goto, T. Hisatomi, Q. Wang, T. Higashi, K. Ishikiriyama, T. Maeda, Y. Sakata, S. Okunaka, H. Tokudome, M. Katayama, S. Akiyama, H. Nishiyama, Y. Inoue, T. Takewaki, T. Setoyama, T. Minegishi, T. Takata, T. Yamada, K. Domen, *Joule* **2018**, *2*, 509.
[46] M. Schrçder, K. Kailasam, J. Borgmeyer, M. Neumann, A. Thomas, R. Schomäcker, nd Michael Schwarze, M. Schrçder, K. ailasam, J. Borgmeyer, M. eumann, A. Thomas, R. Schomäcker, M. Schwarze, *Energy Technol.* **2015**, *3*, 1014.
[47] A. Xiong, G. Ma, K. Maeda, T. Takata, T. Hisatomi, T. Setoyama, J. Kubota, K. Domen, *Catal. Sci. Technol.* **2014**, *4*, 325.
[48] Q. Wang, Y. Li, T. Hisatomi, M. Nakabayashi, N. Shibata, J. Kubota, K. Domen, *J. Catal.* **2015**, *328*, 308.
[49] Q. Zhou, Y. Guo, Y. Zhu, *Nat. Catal.* **2023**, *6*, 574.

[50] H. Nishiyama, T. Yamada, M. Nakabayashi, Y. Maehara, M. Yamaguchi, Y. Kuromiya, Y. Nagatsuma, H. Tokudome, S. Akiyama, T. Watanabe, R. Narushima, S. Okunaka, N. Shibata, T. Takata, T. Hisatomi, K. Domen, *Nature* **2021**, *598*, 304.
[51] S. Nishioka, F. E. Osterloh, X. Wang, T. E. Mallouk, K. Maeda, *Nat. Rev. Methods Prim.* **2023**, *3*, 42.
[52] A. P. Sutton, *Electronic Structure of Materials*, Clarendon Press, Oxford, **1993**.
[53] J. M. Fiore, *Semiconductor Devices: Theory and Application*, **2018**.
[54] B. G. Streetman, S. Banerjee, *Solid State Electronic Devices*, Pearson, **2015**.
[55] B. V. Suresh, *Solid State Devices and Technology*, Pearson Education India, **2010**.
[56] J. Clayden, *Organic Chemistry*, Oxford, **2012**.
[57] P. Kordt, *Charge Dynamics in Organic Semiconductors*, De Gruyter, **2016**.
[58] L. Alcácer, *Electronic Structure of Organic Semiconductors*, Morgan And Claypool Publishers, **2018**.
[59] J. P. Gaspard, *Comptes Rendus Phys.* **2016**, *17*, 389.
[60] A. Kahn, *Mater. Horizons* **2016**, *3*, 7.
[61] D. Cahen, A. Kahn, *Adv. Mater.* **2003**, *15*, 271.
[62] J. L. Bredas, *Mater. Horizons* **2013**, *1*, 17.
[63] H. Bronstein, C. B. Nielsen, B. C. Schroeder, I. McCulloch, *Nat. Rev. Chem.* **2020**, *4*, 66.
[64] S. Trasatti, *Pure Appl. Chem.* **1986**, *58*, 955.
[65] A. J. Bard, L. R. Faulkner, H. S. White, *Electrochemical Methods: Fundamentals and Applications*, John Wiley & Sons, Ltd, **2022**.
[66] D. G. Patel, F. Feng, Y. Y. Ohnishi, K. A. Abboud, S. Hirata, K. S. Schanze, J. R. Reynolds, *J. Am. Chem. Soc.* **2012**, *134*, 2599.
[67] I. McCulloch, R. S. Ashraf, L. Biniek, H. Bronstein, C. Combe, J. E. Donaghey, D. I. James, C. B. Nielsen, B. C. Schroeder, W. Zhang, *Acc. Chem. Res.* **2012**, *45*, 714.
[68] C. M. Aitchison, R. S. Sprick, *Nanoscale* **2021**, *13*, 634.
[69] S. Chen, T. Takata, K. Domen, *Nat. Rev. Mater.* **2017**, *2*, 17050.
[70] N. J. Turro, *Modern Molecular Photochemistry of Organic Molecules*, University Science Books, **2010**.
[71] B. Valeur, M. Berberan-Santos, *Molecular Fluorescence Principles and Applications*, Wiley-VCH, Weinheim, **2013**.
[72] M. S. Vezie, S. Few, I. Meager, G. Pieridou, B. Dörling, R. S. Ashraf, A. R. Goñi, H. Bronstein, I. McCulloch, S. C. Hayes, M. Campoy-Quiles, J. Nelson, *Nat. Mater.* **2016**, *15*, 746.
[73] K. G. Jespersen, W. J. D. Beenken, Y. Zaushitsyn, A. Yartsev, M. Andersson, T. Pullerits, V. Sundström, *J. Chem. Phys.* **2004**, *121*, 12613.
[74] X. Liu, Z. Xu, J. M. Cole, *J. Phys. Chem. C* **2013**, *117*, 16584.
[75] O. P. Dimitriev, *Chem. Rev.* **2022**, *122*, 8487.
[76] J. Yan, X. Rodríguez-Martínez, D. Pearce, H. Douglas, D. Bili, M. Azzouzi, F. Eisner, A. Virbule, E. Rezasoltani, V. Belova, B. Dörling, S. Few, A. A. Szumska, X. Hou, G. Zhang, H. L. Yip, M. Campoy-Quiles, J. Nelson, *Energy Environ. Sci.* **2022**, *15*, 2958.
[77] T. M. Clarke, J. R. Durrant, *Chem. Rev.* **2010**, *110*, 6736.
[78] L. Zhu, Y. Yi, Z. Wei, *J. Phys. Chem. C* **2018**, *122*, 22309.
[79] L. Zhu, Z. Wei, Y. Yi, *J. Phys. Chem. C* **2022**, *126*, 14.
[80] J. Sworakowski, *Synth. Met.* **2018**, *235*, 125.
[81] P. Guiglion, C. Butchosa, M. A. Zwijnenburg, *Macromol. Chem. Phys.* **2016**, *217*, 344.
[82] N. Cho, C. W. Schlenker, K. M. Knesting, P. Koelsch, H.-L. Yip, D. S. Ginger, A. K-Y Jen, N. Cho, H. Yip, A. K-Y Jen, C. W. Schlenker, K. M. Knesting, D. S. Ginger, P. Koelsch, *Adv. Energy Mater.* **2014**, *4*, 1301857.
[83] R. Godin, J. R. Durrant, *Chem. Soc. Rev.* **2021**, *50*, 13372.
[84] A. Wadsworth, Z. Hamid, J. Kosco, N. Gasparini, I. Mcculloch, A. Wadsworth, Z. Hamid, N. Gasparini, J. Kosco, I. Mcculloch, *Adv. Mater.* **2020**, *32*, 2001763.
[85] K. Takanabe, *ACS Catal.* **2017**, *7*, 8006.
[86] O. V. Mikhnenko, P. W. M. Blom, T. Q. Nguyen, *Energy Environ. Sci.* **2015**, *8*, 1867.
[87] U. Scherf, E. Harth, A. Gügel, K. Müllen, U. Lemmer, J. Feldmann, *Phys. Rev. B* **1999**, *59*, 15346.
[88] B. E. Paul Shaw, A. Ruseckas, I. D. W Samuel, I. D. W Samuel, A. Ruseckas, P. E. Shaw, *Adv. Mater.* **2008**, *20*, 3516.
[89] A. Khasbaatar, Z. Xu, J. H. Lee, G. Campillo-Alvarado, C. Hwang, B. N. Onusaitis, Y. Diao, *Chem. Rev.* **2023**, *123*, 8395.
[90] Y. Firdaus, V. M. Le Corre, S. Karuthedath, W. Liu, A. Markina, W. Huang, S. Chattopadhyay, M. M. Nahid, M. I. Nugraha, Y. Lin, A. Seitkhan, A. Basu, W. Zhang, I. McCulloch, H. Ade, J. Labram, F. Laquai, D. Andrienko, L. J. A. Koster, T. D. Anthopoulos, *Nat. Commun.* **2020**, *11*, 5220.
[91] T. H. Thomas, D. J. Harkin, A. J. Gillett, V. Lemaur, M. Nikolka, A. Sadhanala, J. M. Richter, J. Armitage, H. Chen, I. McCulloch, S. M. Menke, Y. Olivier, D. Beljonne, H. Sirringhaus, *Nat. Commun.* **2019**, *10*, 2614.
[92] M. Sachs, R. S. Sprick, D. Pearce, S. A. J. Hillman, A. Monti, A. A. Y. Guilbert, N. J. Brownbill, S. Dimitrov, X. Shi, F. Blanc, M. A. Zwijnenburg, J. Nelson, J. R. Durrant, A. I. Cooper, *Nat. Commun.* **2018**, *9*, 4968.
[93] S. A. J. Hillman, R. S. Sprick, D. Pearce, D. J. Woods, W. Y. Sit, X. Shi, A. I. Cooper, J. R. Durrant, J. Nelson, *J. Am. Chem. Soc.* **2022**, *144*, 19382.
[94] V. L. Piercy, K. H. Saeed, A. W. Prentice, G. Neri, C. Li, A. M. Gardner, Y. Bai, R. S. Sprick, I. V. Sazanovich, A. I. Cooper, M. J. Rosseinsky, M. A. Zwijnenburg, A. J. Cowan, *J. Phys. Chem. Lett.* **2021**, *12*, 10899.
[95] M. Sachs, H. Cha, J. Kosco, C. M. Aitchison, L. Francàs, S. Corby, C.-L. Chiang, A. A. Wilson, R. Godin, A. Fahey-Williams, A. I. Cooper, R. S. Sprick, I. McCulloch, J. R. Durrant, *J. Am. Chem. Soc.* **2020**, *142*, 14574.
[96] M. C. Scharber, D. Mühlbacher, M. Koppe, P. Denk, C. Waldauf, A. J. Heeger, C. J. Brabec, *Adv. Mater.* **2006**, *18*, 789.
[97] J. Liu, S. Chen, D. Qian, B. Gautam, G. Yang, J. Zhao, J. Bergqvist, F. Zhang, W. Ma, H. Ade, O. Inganäs, K. Gundogdu, F. Gao, H. Yan, *Nat. Energy* **2016**, *1*, 16089.
[98] D. Baran, T. Kirchartz, S. Wheeler, S. Dimitrov, M. Abdelsamie, J. Gorman, R. S. Ashraf, S. Holliday, A. Wadsworth, N. Gasparini, P. Kaienburg, H. Yan, A. Amassian, C. J. Brabec, J. R. Durrant, I. McCulloch, *Energy Environ. Sci.*

2016, *9*, 3783.
[99] L. Perdigón-Toro, H. Zhang, A. Markina, J. Yuan, S. Mehrdad Hosseini, C. M. Wolff, G. Zuo, M. Stolterfoht, Y. Zou, F. Gao, D. Andrienko, S. Shoaee, D. Neher, L. Perdigón-Toro, C. M. Wolff, G. Zuo, M. Stolterfoht, D. Neher, S. M. Hosseini, S. Shoaee, H. Zhang, F. Gao, A. Markina, D. Andrienko, J. Yuan, Y. Zou, *Adv. Mater.* **2020**, *32*, 1906763.
[100] J. Bertrandie, J. Han, C. S. P. De Castro, E. Yengel, J. Gorenflot, T. Anthopoulos, F. Laquai, A. Sharma, D. Baran, *Adv. Mater.* **2022**, *34*, 2202575.
[101] T. Banerjee, F. Podjaski, J. Kröger, B. P. Biswal, B. V. Lotsch, *Nat. Rev. Mater.* **2020**, *6*, 168.
[102] V. Coropceanu, J. Cornil, D. A. da Silva Filho, Y. Olivier, R. Silbey, J. L. Brédas, *Chem. Rev.* **2007**, *107*, 926.
[103] L. Berencei, A. Grout-Smith, J. E. Poole, W. Barford, *J. Chem. Phys.* **2019**, *151*, 064120.
[104] F. C. Grozema, P. T. Van Duijnen, Y. A. Berlin, M. A. Ratner, L. D. A. Siebbeles, *J. Phys. Chem. B* **2002**, *106*, 7791.
[105] S. P. O. Danielsen, C. R. Bridges, R. A. Segalman, *Macromolecules* **2022**, *55*, 437.
[106] V. Lemaur, J. Cornil, R. Lazzaroni, H. Sirringhaus, D. Beljonne, Y. Olivier, *Chem. Mater.* **2019**, *31*, 6889.
[107] A. Wadsworth, H. Chen, K. J. Thorley, C. Cendra, M. Nikolka, H. Bristow, M. Moser, A. Salleo, T. D. Anthopoulos, H. Sirringhaus, I. McCulloch, *J. Am. Chem. Soc.* **2020**, *142*, 652.
[108] J. Yang, D. Wang, H. Han, C. Li, *Acc. Chem. Res.* **2013**, *46*, 1900.
[109] K. Wenderich, G. Mul, *Chem. Rev.* **2016**, *116*, 14587.
[110] H. G. Michaelson, *IBM J. Res. Dev.* **1978**, *22*, 72.
[111] M. Grätzel, *Heterogenous Photochemical Electron Transfer*, CRC Press, **2018**.
[112] M. Sadeghi, W. Liu, T. G. Zhang, P. Stavropoulos, B. Levy, *J. Phys. Chem.* **1996**, *100*, 19466.
[113] N. Lakshminarasimhan, A. D. Bokare, W. Choi, *J. Phys. Chem. C* **2012**, *116*, 17531.
[114] J. Kosco, S. Gonzalez-Carrero, C. T. Howells, T. Fei, Y. Dong, R. Sougrat, G. T. Harrison, Y. Firdaus, R. Sheelamanthula, B. Purushothaman, F. Moruzzi, W. Xu, L. Zhao, A. Basu, S. De Wolf, T. D. Anthopoulos, J. R. Durrant, I. McCulloch, *Nat. Energy* **2022**, *7*, 340.
[115] J. N. Hansen, H. Prats, K. K. Toudahl, N. Mørch Secher, K. Chan, J. Kibsgaard, I. Chorkendorff, *ACS Energy Lett.* **2021**, *6*, 1175.
[116] P. Quaino, F. Juarez, E. Santos, W. Schmickler, *Beilstein J. Nanotechnol. 596* **2014**, *5*, 846.
[117] S. Trasatti, *J. Electroanal. Chem. Interfacial Electrochem.* **1972**, *39*, 163.
[118] J. K. Nørskov, T. Bligaard, A. Logadottir, J. R. Kitchin, J. G. Chen, S. Pandelov, U. Stimming, *J. Electrochem. Soc.* **2005**, *152*, J23.
[119] S. Yanagida, A. Kabumoto, K. Mizumoto, C. Pac, K. Yoshino, *J. Chem. Soc. Chem. Commun.* **1985**, *8*.
[120] R. S. Sprick, J. X. Jiang, B. Bonillo, S. Ren, T. Ratvijitvech, P. Guiglion, M. A. Zwijnenburg, D. J. Adams, A. I. Cooper, *J. Am. Chem. Soc.* **2015**, *137*, 3265.
[121] L. Li, Z. Cai, Q. Wu, W. Y. Lo, N. Zhang, L. X. Chen, L. Yu, *J. Am. Chem. Soc.* **2016**, *138*, 7681.
[122] P. B. Pati, G. Damas, L. Tian, D. L. A. Fernandes, L. Zhang, I. B. Pehlivan, T. Edvinsson, C. M. Araujo, H. Tian, *Energy Environ. Sci.* **2017**, *10*, 1372.
[123] A. W. Prentice, M. A. Zwijnenburg, *Sustain. Energy Fuels* **2021**, *5*, 2622.
[124] A. W. Prentice, M. A. Zwijnenburg, *Sustain. Energy Fuels* **2022**, *6*, 3756.
[125] Y. Bai, D. J. Woods, L. Wilbraham, C. M. Aitchison, M. A. Zwijnenburg, R. S. Sprick, A. I. Cooper, *J. Mater. Chem. A* **2020**, *8*, 8700.
[126] J. Kosco, M. Sachs, R. Godin, M. Kirkus, L. Francas, M. Bidwell, M. Qureshi, D. Anjum, J. R. Durrant, I. McCulloch, *Adv. Energy Mater.* **2018**, 1802181.
[127] X. Wang, K. Maeda, A. Thomas, K. Takanabe, G. Xin, J. M. Carlsson, K. Domen, M. Antonietti, *Nat. Mater.* **2008**, *8*, 76.
[128] T. R. Simmons, G. Berggren, M. Bacchi, M. Fontecave, V. Artero, *Coord. Chem. Rev.* **2014**, *270–271*, 127.
[129] M. A. Gross, A. Reynal, J. R. Durrant, E. Reisner, *J. Am. Chem. Soc.* **2014**, *136*, 356.
[130] C. A. Caputo, M. A. Gross, V. W. Lau, C. Cavazza, B. V Lotsch, E. Reisner, C. A. Caputo, M. A. Gross, E. Reisner, V. W. Lau, B. V Lotsch, C. Cavazza, *Angew. Chemie Int. Ed.* **2014**, *53*, 11538.
[131] B. C. M. Martindale, G. A. M. Hutton, C. A. Caputo, E. Reisner, *J. Am. Chem. Soc.* **2015**, *137*, 6018.
[132] J. Ran, J. Zhang, J. Yu, M. Jaroniec, S. Z. Qiao, *Chem. Soc. Rev.* **2014**, *43*, 7787.
[133] F. E. Osterloh, *ACS Energy Lett.* **2017**, *2*, 445.
[134] J. Schneider, D. W. Bahnemann, *J. Phys. Chem. Lett.* **2013**, *4*, 3479.
[135] H. Kasap, C. A. Caputo, B. C. M. Martindale, R. Godin, V. W. H. Lau, B. V. Lotsch, J. R. Durrant, E. Reisner, *J. Am. Chem. Soc.* **2016**, *138*, 9183.
[136] Q. Wang, K. Domen, *Chem. Rev.* **2020**, *120*, 919.
[137] Y. Pellegrin, F. Odobel, *Comptes Rendus Chim.* **2017**, *20*, 283.
[138] D. Njus, P. M. Kelley, Y. J. Tu, H. B. Schlegel, *Free Radic. Biol. Med.* **2020**, *159*, 37.
[139] D. Bartlett, D. F. Church, P. L. Bounds, W. H. Koppenol, *Free Radic. Biol. Med.* **1995**, *18*, 85.
[140] D. R. S. Lima, M. Cossenza, C. G. Garcia, C. C. Portugal, F. F. D. C. Marques, R. Paes-De-Carvalho, A. D. Pereira Netto, *Anal. Methods* **2016**, *8*, 5441.
[141] J. Du, J. J. Cullen, G. R. Buettner, *Biochim. Biophys. Acta - Rev. Cancer* **2012**, *1826*, 443.
[142] X. Wang, L. Chen, S. Y. Chong, M. A. Little, Y. Wu, W. H. Zhu, R. Clowes, Y. Yan, M. A. Zwijnenburg, R. S. Sprick, A. I. Cooper, *Nat. Chem.* **2018**, *10*, 1180.
[143] J. Kosco, M. Bidwell, H. Cha, T. Martin, C. T. Howells, M. Sachs, D. H. Anjum, S. Gonzalez Lopez, L. Zou, A. Wadsworth, W. Zhang, L. Zhang, J. Tellam, R. Sougrat, F. Laquai, D. M. DeLongchamp, J. R. Durrant, I. McCulloch, *Nat. Mater.* **2020**, *19*, 559.
[144] H. Kasap, D. S. Achilleos, A. Huang, E. Reisner, *J. Am. Chem. Soc.* **2018**, *140*, 11604.
[145] T. Kawai, T. Sakata, *Nature* **1980**, *286*, 474.
[146] T. Uekert, C. M. Pichler, T. Schubert, E. Reisner, *Nat. Sustain.* **2020**, *4*, 383.
[147] E. McQueen, Y. Bai, R. S. Sprick, *Nanomaterials* **2022**, *12*, 4299.
[148] T. Le Bahers, M. Rérat, P. Sautet, *J. Phys. Chem. C* **2014**, *118*, 5997.
[149] Y. Wang, H. Suzuki, J. Xie, O. Tomita, D. J. Martin, M. Higashi, D. Kong, R. Abe, J. Tang, *Chem. Rev.* **2018**, *118*, 5201.

[150] M. F. Hohmann-Marriott, R. E. Blankenship, *Annu. Rev. Plant Biol.* **2011**, *62*, 515.
[151] A. Thilagam, *J. Math. Chem.* **2015**, *53*, 466.
[152] G. Ma, S. Chen, Y. Kuang, S. Akiyama, T. Hisatomi, M. Nakabayashi, N. Shibata, M. Katayama, T. Minegishi, K. Domen, *J. Phys. Chem. Lett.* **2016**, *7*, 3892.
[153] K. Maeda, M. Higashi, D. Lu, R. Abe, K. Domen, *J. Am. Chem. Soc.* **2010**, *132*, 5858.
[154] K. Sayama, K. Mukasa, R. Abe, Y. Abe, H. Arakawa, *Chem. Commun.* **2001**, *1*, 2416.
[155] R. Abe, *Bull. Chem. Soc. Jpn.* **2011**, *84*, 1000.
[156] Y. Qi, Y. Zhao, Y. Gao, D. Li, Z. Li, F. Zhang, C. Li, *Joule* **2018**, *2*, 2393.
[157] K. Tsuji, O. Tomita, M. Higashi, R. Abe, *ChemSusChem* **2016**, *9*, 2201.
[158] Y. Sasaki, H. Kato, A. Kudo, *J. Am. Chem. Soc.* **2013**, *135*, 5441.
[159] T. Ohno, D. Haga, K. Fujihara, K. Kaizaki, M. Matsumura, *J. Phys. Chem. B* **1997**, *101*, 6415.
[160] T. Ohno, F. Tanigawa, K. Fujihara, S. Izumi, M. Matsumura, *J. Photochem. Photobiol. A Chem.* **1998**, *118*, 41.
[161] Q. Wang, T. Hisatomi, Y. Suzuki, Z. Pan, J. Seo, M. Katayama, T. Minegishi, H. Nishiyama, T. Takata, K. Seki, A. Kudo, T. Yamada, K. Domen, *J. Am. Chem. Soc.* **2017**, *139*, 1675.
[162] A. Iwase, Y. H. Ng, Y. Ishiguro, A. Kudo, R. Amal, *J. Am. Chem. Soc.* **2011**, *133*, 11054.
[163] Q. Wang, T. Hisatomi, Q. Jia, H. Tokudome, M. Zhong, C. Wang, Z. Pan, T. Takata, M. Nakabayashi, N. Shibata, Y. Li, I. D. Sharp, A. Kudo, T. Yamada, K. Domen, *Nat. Mater.* **2016**, *15*, 611.
[164] Z. Zhang, J. T. Yates, *Chem. Rev.* **2012**, *112*, 5520.
[165] F. Williams, A. J. Nozik, *Nature* **1984**, *312*, 21.
[166] Z. Pan, J. A. Röhr, Z. Ye, Z. S. Fishman, Q. Zhu, X. Shen, S. Hu, *Sustain. Energy Fuels* **2019**, *3*, 850.
[167] T. Takata, J. Jiang, Y. Sakata, M. Nakabayashi, N. Shibata, V. Nandal, K. Seki, T. Hisatomi, K. Domen, *Nature* **2020**, *581*, 411.
[168] P. D. Evans, *Encyclopedia of Materials: Science and Technology*, **2001**.
[169] K. Maeda, K. Domen, *J. Phys. Chem. Lett.* **2010**, *1*, 2655.
[170] D. H. Shin, S. H. Choi, *Coatings 2018, Vol. 8, Page 329* **2018**, *8*, 329.
[171] K. Kalyanasundaram, E. Borgarello, D. Duonghong, M. Grätzel, *Angew. Chemie Int. Ed. English* **1981**, *20*, 987.
[172] X. Ning, G. Lu, *Nanoscale* **2020**, *12*, 1213.
[173] R. Abe, *J. Photochem. Photobiol. C Photochem. Rev.* **2010**, *11*, 179.
[174] K. Maeda, T. Takata, M. Hara, N. Saito, Y. Inoue, H. Kobayashi, K. Domen, *J. Am. Chem. Soc.* **2005**, *127*, 8286.
[175] M. G. Kibria, F. A. Chowdhury, S. Zhao, B. AlOtaibi, M. L. Trudeau, H. Guo, Z. Mi, *Nat. Commun.* **2015**, *6*, 6797.
[176] F. A. Chowdhury, M. L. Trudeau, H. Guo, Z. Mi, *Nat. Commun.* **2018**, *9*, 1707.
[177] Y. Wang, Y. Wu, K. Sun, Z. Mi, *Mater. Horizons* **2019**, *6*, 1454.
[178] P. Zhou, I. A. Navid, Y. Ma, Y. Xiao, P. Wang, Z. Ye, B. Zhou, K. Sun, Z. Mi, *Nature* **2023**, *613*, 66.
[179] B. Lee, D. Fan, S. R. Forrest, *Sustain. Energy Fuels* **2020**, *4*, 2035.
[180] O. Savateev, M. Antonietti, X. Wang, *Carbon Nitrides: Structure, Properties and Applications in Science and Technology*, Walter De Gruyter GmbH & Co KG, **2023**.
[181] Y. Wang, A. Vogel, M. Sachs, R. S. Sprick, L. Wilbraham, S. J. A. Moniz, R. Godin, M. A. Zwijnenburg, J. R. Durrant, A. I. Cooper, J. Tang, *Nat. Energy* **2019**, *4*, 746.
[182] B. V. Lotsch, M. Döblinger, J. Sehnert, L. Seyfarth, J. Senker, O. Oeckler, W. Schnick, *Chem. – A Eur. J.* **2007**, *13*, 4969.
[183] N. Chaoui, M. Trunk, R. Dawson, J. Schmidt, A. Thomas, *Chem. Soc. Rev.* **2017**, *46*, 3302.
[184] M. J. Bojdys, J. O. Müller, M. Antonietti, A. Thomas, *Chem. – A Eur. J.* **2008**, *14*, 8177.
[185] E. Wirnhier, M. Döblinger, D. Gunzelmann, J. Senker, B. V. Lotsch, W. Schnick, *Chem. – A Eur. J.* **2011**, *17*, 3213.
[186] K. Maeda, X. Wang, Y. Nishihara, D. Lu, M. Antonietti, K. Domen, *J. Phys. Chem. C* **2009**, *113*, 4940.
[187] G. Zhang, G. Li, Z.-A. Lan, L. Lin, A. Savateev, T. obias Heil, S. Zafeiratos, X. Wang, M. Antonietti, G. Li, Z. Lan, L. Lin, X. Wang, D. Zafeiratos, *Angew. Chemie* **2017**, *129*, 13630.
[188] V. S. Vyas, V. W. H. Lau, B. V. Lotsch, *Chem. Mater.* **2016**, *28*, 5191.
[189] R. Godin, Y. Wang, M. A. Zwijnenburg, J. Tang, J. R. Durrant, *J. Am. Chem. Soc.* **2017**, *139*, 5216.
[190] M. Z. Rahman, C. B. Mullins, *Acc. Chem. Res.* **2019**, *52*, 248.
[191] H. Wang, X. Sun, D. Li, X. Zhang, S. Chen, W. Shao, Y. Tian, Y. Xie, *J. Am. Chem. Soc.* **2017**, *139*, 2468.
[192] G. Zhao, S. Hao, J. Guo, Y. Xing, L. Zhang, X. Xu, *Chinese J. Catal.* **2021**, *42*, 501.
[193] S. Mazzanti, A. Savateev, *Chempluschem* **2020**, *85*, 2499.
[194] A. B. Jorge, D. J. Martin, M. T. S. Dhanoa, A. S. Rahman, N. Makwana, J. Tang, A. Sella, F. Corà, S. Firth, J. A. Darr, P. F. McMillan, *J. Phys. Chem. C* **2013**, *117*, 7178.
[195] J. Li, B. Shen, Z. Hong, B. Lin, B. Gao, Y. Chen, *Chem. Commun.* **2012**, *48*, 12017.
[196] D. J. Martin, K. Qiu, S. A. Shevlin, A. D. Handoko, X. Chen, Z. Guo, J. Tang, *Angew. Chemie Int. Ed.* **2014**, *53*, 9240.
[197] Y. Wang, J. Zhang, X. Wang, M. Antonietti, H. Li, *Angew. Chemie Int. Ed.* **2010**, *49*, 3356.
[198] G. Zhang, M. Zhang, X. Ye, X. Qiu, S. Lin, X. Wang, G. Zhang, M. Zhang, X. Ye, X. Qiu, S. Lin, X. Wang, *Adv. Mater.* **2014**, *26*, 805.
[199] Y. Wang, H. Li, J. Yao, X. Wang, M. Antonietti, *Chem. Sci.* **2011**, *2*, 446.
[200] L. Jiang, X. Yuan, Y. Pan, J. Liang, G. Zeng, Z. Wu, H. Wang, *Appl. Catal. B Environ.* **2017**, *217*, 388.
[201] G. Zhang, L. Lin, G. Li, Y. Zhang, A. Savateev, S. Zafeiratos, X. Wang, M. Antonietti, *Angew. Chemie* **2018**, *130*, 9516.
[202] G. Zhang, Z. A. Lan, L. Lin, S. Lin, X. Wang, *Chem. Sci.* **2016**, *7*, 3062.
[203] L. Lin, C. Wang, W. Ren, H. Ou, Y. Zhang, X. Wang, *Chem. Sci.* **2017**, *8*, 5506.
[204] D. Zhao, Y. Wang, C. L. Dong, Y. C. Huang, J. Chen, F. Xue, S. Shen, L. Guo, *Nat. Energy* **2021**, *6*, 388.
[205] D. J. Martin, P. J. T. Reardon, S. J. A. Moniz, J. Tang, *J. Am. Chem. Soc.* **2014**, *136*, 12568.
[206] Z. Pan, G. Zhang, X. Wang, *Angew. Chemie* **2019**, *131*, 7176.
[207] J. Yan, H. Wu, H. Chen, Y. Zhang, F. Zhang, S. F. Liu, *Appl. Catal. B Environ.* **2016**, *191*, 130.
[208] X. She, J. Wu, H. Xu, J. Zhong, Y. Wang, Y. Song, K. Nie, Y. Liu, Y. Yang, M.-T. F. Rodrigues, R. Vajtai, J. Lou, D. Du, H. Li, P. M. Ajayan, X. She, H. Xu, D. Du, H. Li, J. Wu, Y. Wang, Y. Song, Y. Liu, Y. Yang, M. F. Rodrigues, R. Vajtai, J. Lou, P. M. Ajayan, J. Zhong, K. Nie, *Adv. Energy Mater.* **2017**, *7*, 1700025.

[209] G. J. Hedley, A. Ruseckas, I. D. W. Samuel, *Chem. Rev.* **2017**, *117*, 796.
[210] I. D. W. Samuel, G. A. Turnbull, *Chem. Rev.* **2007**, *107*, 1272.
[211] H. Gu, S. Ming, K. Lin, S. Chen, X. Liu, B. Lu, J. Xu, *Electrochim. Acta* **2018**, *260*, 772.
[212] L. Ding, Z. Di Yu, X. Y. Wang, Z. F. Yao, Y. Lu, C. Y. Yang, J. Y. Wang, J. Pei, *Chem. Rev.* **2023**, *123*, 7421.
[213] X. Guo, A. Facchetti, *Nat. Mater.* **2020**, *19*, 922.
[214] Z. Qian, Z. J. Wang, K. A. I. Zhang, *Chem. Mater.* **2021**, *33*, 1909.
[215] L. Guo, Y. Niu, H. Xu, Q. Li, S. Razzaque, Q. Huang, S. Jin, B. Tan, *J. Mater. Chem. A* **2018**, *6*, 19775.
[216] A. I. Cooper, *Adv. Mater.* **2009**, *21*, 1291.
[217] R. S. Sprick, Y. Bai, A. A. Y. Guilbert, M. Zbiri, C. M. Aitchison, L. Wilbraham, Y. Yan, D. J. Woods, M. A. Zwijnenburg, A. I. Cooper, *Chem. Mater.* **2019**, *31*, 305.
[218] Y. Bai, L. Wilbraham, H. Gao, R. Clowes, H. Yang, M. A. Zwijnenburg, A. I. Cooper, R. S. Sprick, *J. Mater. Chem. A* **2021**, *9*, 19958.
[219] K. Lin, Z. Wang, Z. Hu, P. Luo, X. Yang, X. Zhang, M. Rafiq, F. Huang, Y. Cao, *J. Mater. Chem. A* **2019**, *7*, 19087.
[220] Z. A. Lan, W. Ren, X. Chen, Y. Zhang, X. Wang, *Appl. Catal. B Environ.* **2019**, *245*, 596.
[221] P. Corradini, F. Auriemma, C. De Rosa, *Acc. Chem. Res.* **2006**, *39*, 314.
[222] S. J. Rowan, S. J. Cantrill, G. R. L. Cousins, J. K. M. Sanders, J. F. Stoddart, *Angew. Chemie Int. Ed.* **2002**, *41*, 898.
[223] C. S. Diercks, O. M. Yaghi, *Science* **2017**, *355*.
[224] M. Liu, L. Guo, S. Jin, B. Tan, *J. Mater. Chem. A* **2019**, *7*, 5153.
[225] P. Kuhn, M. Antonietti, A. Thomas, *Angew. Chemie Int. Ed.* **2008**, *47*, 3450.
[226] P. Katekomol, J. Roeser, M. Bojdys, J. Weber, A. Thomas, *Chem. Mater.* **2013**, *25*, 1542.
[227] M. J. Bojdys, J. Jeromenok, A. Thomas, M. Antonietti, *Adv. Mater.* **2010**, *22*, 2202.
[228] S. Kuecken, A. Acharjya, L. Zhi, M. Schwarze, R. Schomäcker, A. Thomas, *Chem. Commun.* **2017**, *53*, 5854.
[229] K. Schwinghammer, S. Hug, M. B. Mesch, J. Senker, B. V. Lotsch, *Energy Environ. Sci.* **2015**, *8*, 3345.
[230] P. Kuhn, A. Forget, D. Su, A. Thomas, M. Antonietti, *J. Am. Chem. Soc.* **2008**, *130*, 13333.
[231] S. Kuecken, J. Schmidt, L. Zhi, A. Thomas, *J. Mater. Chem. A* **2015**, *3*, 24422.
[232] J. Xie, S. A. Shevlin, Q. Ruan, S. J. A. Moniz, Y. Liu, X. Liu, Y. Li, C. C. Lau, Z. X. Guo, J. Tang, *Energy Environ. Sci.* **2018**, *11*, 1617.
[233] M. Liu, Q. Huang, S. Wang, Z. Li, B. Li, S. Jin, B. Tan, *Angew. Chemie Int. Ed.* **2018**, *57*, 11968.
[234] S. Zhang, G. Cheng, L. Guo, N. Wang, B. Tan, S. Jin, *Angew. Chemie Int. Ed.* **2020**, *59*, 6007.
[235] J.-X. Jiang, F. Su, A. Trewin, C. D. Wood, H. Niu, J. T. A. Jones, Y. Z. Khimyak, A. I. Cooper, *J. Am. Chem. Soc.* **2008**, *130*, 7710.
[236] Y. Xu, D. Jiang, *Chem. Commun.* **2014**, *50*, 2781.
[237] J. Jiang, F. Su, A. Trewin, C. D. Wood, N. L. Campbell, H. Niu, C. Dickinson, A. Y. Ganin, M. J. Rosseinsky, Y. Z. Khimyak, A. I. Cooper, *Angew. Chemie Int. Ed.* **2007**, *46*, 8574.
[238] S. Dalapati, S. Jin, J. Gao, Y. Xu, A. Nagai, D. Jiang, *J. Am. Chem. Soc.* **2013**, *135*, 17310.
[239] V. S. Vyas, F. Haase, L. Stegbauer, G. Savasci, F. Podjaski, C. Ochsenfeld, B. V. Lotsch, *Nat. Commun.* **2015**, *6*, 8508.
[240] F. J. Uribe-Romo, C. J. Doonan, H. Furukawa, K. Oisaki, O. M. Yaghi, *J. Am. Chem. Soc.* **2011**, *133*, 11478.
[241] S. Kandambeth, A. Mallick, B. Lukose, M. V. Mane, T. Heine, R. Banerjee, *J. Am. Chem. Soc.* **2012**, *134*, 19524.
[242] B. P. Biswal, S. Chandra, S. Kandambeth, B. Lukose, T. Heine, R. Banerjee, *J. Am. Chem. Soc.* **2013**, *135*, 5328.
[243] T. Banerjee, F. Haase, G. Savasci, K. Gottschling, C. Ochsenfeld, B. V. Lotsch, *J. Am. Chem. Soc.* **2017**, *139*, 16228.
[244] S. Wan, F. Gándara, A. Asano, H. Furukawa, A. Saeki, S. K. Dey, L. Liao, M. W. Ambrogio, Y. Y. Botros, X. Duan, S. Seki, J. F. Stoddart, O. M. Yaghi, *Chem. Mater.* **2011**, *23*, 4094.
[245] V. Coropceanu, J. Cornil, D. A. da Silva Filho, Y. Olivier, R. Silbey, J. L. Brédas, *Chem. Rev.* **2007**, *107*, 926.
[246] T. Banerjee, K. Gottschling, G. Savasci, C. Ochsenfeld, B. V. Lotsch, *ACS Energy Lett.* **2018**, *3*, 400.
[247] T. Banerjee, B. V. Lotsch, *Nat. Chem.* **2018**, *10*, 1175.
[248] R. Dawson, A. Laybourn, R. Clowes, Y. Z. Khimyak, D. J. Adams, A. I. Cooper, *Macromolecules* **2009**, *42*, 8809.
[249] C. B. Meier, R. Clowes, E. Berardo, K. E. Jelfs, M. A. Zwijnenburg, R. S. Sprick, A. I. Cooper, *Chem. Mater.* **2019**, *31*, 44.
[250] R. S. Sprick, B. Bonillo, R. Clowes, P. Guiglion, N. J. Brownbill, B. J. Slater, F. Blanc, M. A. Zwijnenburg, D. J. Adams, A. I. Cooper, *Angew. Chemie Int. Ed.* **2016**, *55*, 1792.
[251] D. J. Woods, S. A. J. Hillman, D. Pearce, L. Wilbraham, L. Q. Flagg, W. Duffy, I. McCulloch, J. R. Durrant, A. A. Y. Guilbert, M. A. Zwijnenburg, R. S. Sprick, J. Nelson, A. I. Cooper, *Energy Environ. Sci.* **2020**, *13*, 1843.
[252] R. S. Sprick, B. Bonillo, M. Sachs, R. Clowes, J. R. Durrant, D. J. Adams, A. I. Cooper, *Chem. Commun.* **2016**, *52*, 10008.
[253] R. S. Sprick, Z. Chen, A. J. Cowan, Y. Bai, C. M. Aitchison, Y. Fang, M. A. Zwijnenburg, A. I. Cooper, X. Wang, *Angew. Chemie Int. Ed.* **2020**, *59*, 18695.
[254] Y. Bai, C. Li, L. Liu, Y. Yamaguchi, M. Bahri, H. Yang, A. Gardner, M. A. Zwijnenburg, N. D. Browning, A. J. Cowan, A. Kudo, A. I. Cooper, R. S. Sprick, *Angew. Chemie* **2022**, *134*, e202201299.
[255] C. M. Aitchison, S. Gonzalez-Carrero, S. Yao, M. Benkert, Z. Ding, N. P. Young, B. Willner, F. Moruzzi, Y. Lin, J. Tian, P. D. Nellist, J. R. Durrant, I. Mcculloch, *Adv. Mater.* **2023**, 2300037.
[256] K. Geng, T. He, R. Liu, S. Dalapati, K. T. Tan, Z. Li, S. Tao, Y. Gong, Q. Jiang, D. Jiang, *Chem. Rev.* **2020**, *120*, 8814.
[257] M. Barawi, L. Collado, M. Gomez-Mendoza, F. E. Oropeza, M. Liras, V. A. De La Peña O'shea, M. Barawi, L. Collado, M. Gomez-Mendoza, F. E. Oropeza, M. Liras, V. A. De La Peña O'shea, U. Rey, J. Carlos, C. / Tulipán, *Adv. Energy Mater.* **2021**, *11*, 2101530.
[258] J. Kosco, F. Moruzzi, B. Willner, I. Mcculloch, J. Kosco, I. Mcculloch, F. Moruzzi, B. Willner, *Adv. Energy Mater.* **2020**, *10*, 2001935.
[259] C. Yang, B. C. Ma, L. Zhang, S. Lin, S. Ghasimi, K. Landfester, K. A. I. Zhang, X. Wang, *Angew. Chemie Int. Ed.* **2016**, *55*, 9202.
[260] Y. Xiang, X. Wang, L. Rao, P. Wang, D. Huang, X. Ding, X. Zhang, S. Wang, H. Chen, Y. Zhu, *ACS Energy Lett.* **2018**, *3*, 2544.
[261] L. Li, W. Y. Lo, Z. Cai, N. Zhang, L. Yu, *Macromolecules* **2016**, *49*, 6903.

[262] J. Ritchie, J. A. Crayston, J. P. J. Markham, I. D. W. Samuel, *J. Mater. Chem.* **2006**, *16*, 1651.
[263] Y. Noda, C. Merschjann, J. Arμbek, N. Koch, M. J. Bojdys, Y. Noda, M. J. Bojdys, C. Merschjann, J. T. Arμbek, P. Amsalem, N. K. Och, *Angew. Chemie Int. Ed.* **2019**, *58*, 9394.
[264] J. Z. Cheng, L. L. Liu, G. Liao, Z. Q. Shen, Z. R. Tan, Y. Q. Xing, X. X. Li, K. Yang, L. Chen, S. Y. Liu, *J. Mater. Chem. A* **2020**, *8*, 5890.
[265] K. Schwinghammer, M. B. Mesch, V. Duppel, C. Ziegler, J. Senker, B. V. Lotsch, *J. Am. Chem. Soc.* **2014**, *136*, 1730.
[266] S. Wang, Y. Li, X. Wang, G. Zi, C. Zhou, B. Liu, G. Liu, L. Wang, W. Huang, *J. Mater. Sci. Technol.* **2022**, *104*, 155.
[267] K. Dill, S. Bromberg, *Molecular Driving Forces : Statistical Thermodynamics in Biology, Chemistry, Physics, and Nanoscience*, Garland Science, Boca Raton, FL, **2010**.
[268] B. C. Schroeder, C. B. Nielsen, P. Westacott, J. Smith, S. Rossbauer, T. D. Anthopoulos, N. Stingelin, I. McCulloch, *MRS Commun.* **2015**, *5*, 435.
[269] N. E. Jackson, K. L. Kohlstedt, B. M. Savoie, M. Olvera De La Cruz, G. C. Schatz, L. X. Chen, M. A. Ratner, *J. Am. Chem. Soc.* **2015**, *137*, 6254.
[270] C. Zhong, C. Duan, F. Huang, H. Wu, Y. Cao, *Chem. Mater.* **2011**, *23*, 326.
[271] A. Marks, S. Griggs, N. Gasparini, M. Moser, *Adv. Mater. Interfaces* **2022**, *9*, 2102039.
[272] Y. Hu, Y. Liu, J. Wu, Y. Li, J. Jiang, F. Wang, *ACS Appl. Mater. Interfaces* **2021**, *13*, 42753.
[273] F. Y. Cao, C. L. Huang, T. Y. Cheng, H. J. Cheng, T. K. Wu, Y. J. Cheng, *ACS Macro Lett.* **2023**, *12*, 468.
[274] A. Bruno, L. X. Reynolds, C. Dyer-Smith, J. Nelson, S. A. Haque, *J. Phys. Chem. C* **2013**, *117*, 19832.
[275] C. Szymanski, C. Wu, J. Hooper, M. A. Salazar, A. Perdomo, A. Dukes, J. McNeill, *J. Phys. Chem. B* **2005**, *109*, 8543.
[276] M. V. Pavliuk, S. Wrede, A. Liu, A. Brnovic, S. Wang, M. Axelsson, H. Tian, *Chem. Soc. Rev.* **2022**, *51*, 6909.
[277] N. Elgiddawy, N. Elnagar, H. Korri-Youssoufi, A. Yassar, *Microorg. 2023, Vol. 11, Page 2006* **2023**, *11*, 2006.
[278] C. Wu, C. Szymanski, Z. Cain, J. McNeill, *J. Am. Chem. Soc.* **2007**, *129*, 12904.
[279] J. Pecher, S. Mecking, *Chem. Rev.* **2010**, *110*, 6260.
[280] A. Holmes, H. Laval, M. Schmutz, S. Blanc, J. Allouche, B. Watts, G. Wantz, N. P. Holmes, K. Hirakawa, E. Deniau, S. Chambon, C. Lartigau-Dagron, A. Bousquet, *Mater. Today Chem.* **2022**, *26*, 101229.
[281] L. Wang, R. Fernández-Terán, L. Zhang, D. L. A. Fernandes, L. Tian, H. Chen, H. Tian, *Angew. Chemie Int. Ed.* **2016**, *55*, 12306.
[282] M. Yu, W. Zhang, Z. Guo, Y. Wu, W. Zhu, *Angew. Chemie Int. Ed.* **2021**, *60*, 15590.
[283] M. H. Elsayed, M. Abdellah, Y. H. Hung, J. Jayakumar, L. Y. Ting, A. M. Elewa, C. L. Chang, W. C. Lin, K. L. Wang, M. Abdel-Hafiez, H. W. Hung, M. Horie, H. H. Chou, *ACS Appl. Mater. Interfaces* **2021**, *13*, 56554.
[284] J. Ho Moon, R. Deans, E. Krueger, L. F. Hancock, *Chem. Commun.* **2003**, *1*, 104.
[285] D. Tuncel, H. V. Demir, *Nanoscale* **2010**, *2*, 484.
[286] K. Landfester, N. Bechthold, F. Tiarks, M. Antonietti, *Macromolecules* **1999**, *32*, 5222.
[287] K. Landfester, *Adv. Mater.* **2001**, *13*, DOI 10.1002/1521-4095.
[288] H. Yang, X. Li, R. S. Sprick, A. I. Cooper, *Chem. Commun.* **2020**, *56*, 6790.
[289] A. Dolan, J. M. De La Perrelle, T. D. Small, E. R. Milsom, G. F. Metha, X. Pan, M. R. Andersson, D. M. Huang, T. W. Kee, *ACS Appl. Nano Mater.* **2022**, *5*, 12154.
[290] S. Gärtner, M. Christmann, S. Sankaran, H. Röhm, E.-M. Prinz, F. Penth, A. Pütz, A. Emre Türeli, B. Penth, B. Baumstümmler, A. Colsmann, S. Gärtner, S. Sankaran, H. Röhm, A. Pütz, A. Colsmann, M. Christmann, E. Prinz, A. E. Türeli, B. Baumstümmler, *Adv. Mater.* **2014**, *26*, 6653.
[291] J. Cho, K. Hee Cheon, H. Ahn, K. Hun Park, S.-K. Kwon, Y.-H. Kim, D. Sung Chung, J. Cho, K. H. Cheon, D. S. Chung, H. Ahn, K. H. Park, S. Kwon, Y. Kim, *Adv. Mater.* **2015**, *27*, 5587.
[292] J. Cho, S. Yoon, K. Min Sim, Y. Jin Jeong, C. Eon Park, S. K. Kwon, Y. H. Kim, D. S. Chung, *Energy Environ. Sci.* **2017**, *10*, 2324.
[293] J. Luke, E. M. Speller, A. Wadsworth, M. F. Wyatt, S. Dimitrov, H. K. H. Lee, Z. Li, W. C. Tsoi, I. McCulloch, D. Bagnis, J. R. Durrant, J. S. Kim, *Adv. Energy Mater.* **2019**, *9*, 1803755.
[294] H. Rosenberg, *The Solid State*, Oxford University Press, Oxford, **1978**.
[295] P. J. Harrop, *Dielectrics*, Butterworths, London, **1972**.
[296] L. J. A. Koster, S. E. Shaheen, J. C. Hummelen, *Adv. Energy Mater.* **2012**, *2*, 1246.
[297] S. Torabi, F. Jahani, I. Van Severen, C. Kanimozhi, S. Patil, R. W. A. Havenith, R. C. Chiechi, L. Lutsen, D. J. M. Vanderzande, T. J. Cleij, J. C. Hummelen, L. J. A. Koster, *Adv. Funct. Mater.* **2015**, *25*, 150.
[298] Z. Chen, L. Yan, J. J. Rech, J. Hu, Q. Zhang, W. You, *ACS Appl. Polym. Mater.* **2019**, *1*, 804.
[299] S. Sami, R. Alessandri, R. Broer, R. W. A. Havenith, *ACS Appl. Mater. Interfaces* **2020**, *12*, 17783.
[300] A. A. Mohapatra, Y. Dong, P. Boregowda, A. Mohanty, A. Sadhanala, X. Jiao, A. Narayan, C. R. McNeill, J. R. Durrant, S. Patil, *J. Phys. Chem. C* **2021**, *125*, 6886.
[301] R. J. Sengwa, K. Kaur, R. Chaudhary, *Polym. Int.* **2000**, *49*, 599.
[302] J. Kosco, S. Gonzalez-Carrero, C. T. Howells, W. Zhang, M. Moser, R. Sheelamanthula, L. Zhao, B. Willner, T. C. Hidalgo, H. Faber, B. Purushothaman, M. Sachs, H. Cha, R. Sougrat, T. D. Anthopoulos, S. Inal, J. R. Durrant, I. McCulloch, *Adv. Mater.* **2021**, *34*, 2105007.
[303] A. Andryieuski, S. M. Kuznetsova, S. V. Zhukovsky, Y. S. Kivshar, A. V. Lavrinenko, *Sci. Rep.* **2015**, *5*, 13535.
[304] R. Diao, H. Ye, Z. Yang, S. Zhang, K. Kong, J. Hua, *Polym. Chem.* **2019**, *10*, 6473.
[305] Z. Hu, Z. Wang, X. Zhang, H. Tang, X. Liu, F. Huang, Y. Cao, *iScience* **2019**, *13*, 33.
[306] M. Qureshi, K. Takanabe, *Chem. Mater.* **2017**, *29*, 158.
[307] X. Yang, Z. Hu, Q. Yin, C. Shu, X.-F. Jiang, J. Zhang, X. Wang, J.-X. Jiang, F. Huang, Y. Cao, X. Yang, Z. Hu, Q. Yin, X. Jiang, J. Zhang, X. Wang, F. Huang, Y. Cao, C. Shu, J. Jiang, *Adv. Funct. Mater.* **2019**, *29*, 1808156.
[308] M. Schwarze, D. Stellmach, M. Schröder, K. Kailasam, R. Reske, A. Thomas, R. Schomäcker, *Phys. Chem. Chem. Phys.* **2013**, *15*, 3466.
[309] D. Yamashita, Y. Nakajima, M. Uda, *J. Surf. Anal.* **2008**, *14*, 433.
[310] H. Kirihata, M. Uda, *Rev. Sci. Instrum.* **1981**, *52*, 68.
[311] P. K. Santra, A. F. Palmstrom, J. T. Tanskanen, N. Yang, S. F. Bent, *J. Phys. Chem. C* **2015**, *119*, 2996.
[312] R. E. Aderne, B. G. A. L. Borges, H. C. Ávila, F. Von Kieseritzky, J. Hellberg, M. Koehler, M. Cremona, L. S. Roman, C. M. Araujo, M. L. M. Rocco, C. F. N. Marchiori, *Mater. Adv.* **2022**, *3*, 1791.

[313] J. C. S. Costa, R. J. S. Taveira, C. F. R. A. C. Lima, A. Mendes, L. M. N. B. F. Santos, *Opt. Mater. (Amst).* **2016**, *58*, 51.
[314] N. Elgrishi, K. J. Rountree, B. D. McCarthy, E. S. Rountree, T. T. Eisenhart, J. L. Dempsey, *J. Chem. Educ.* **2018**, *95*, 197.
[315] C. M. Cardona, W. Li, A. E. Kaifer, D. Stockdale, G. C. Bazan, C. M. Cardona, W. Li, A. E. Kaifer, D. Stockdale, G. C. Bazan, *Adv. Mater.* **2011**, *23*, 2367.
[316] A. A. Szumska, I. P. Maria, L. Q. Flagg, A. Savva, J. Surgailis, B. D. Paulsen, D. Moia, X. Chen, S. Griggs, J. T. Mefford, R. B. Rashid, A. Marks, S. Inal, D. S. Ginger, A. Giovannitti, J. Nelson, *J. Am. Chem. Soc.* **2021**, *143*, 14795.
[317] J. Hou, B. Zhang, D. Li, Y. Fu, G. Liu, Y. Chen, *J. Mater. Chem. C* **2019**, *7*, 14664.
[318] W. Hong, B. Sun, H. Aziz, W. T. Park, Y. Y. Noh, Y. Li, *Chem. Commun.* **2012**, *48*, 8413.
[319] J. Pommerehne, H. Vestweber, W. Guss, R. F. Mahrt, H. Bässler, M. Porsch, J. Daub, *Adv. Mater.* **1995**, *7*, 551.
[320] M. Naderi, *Prog. Filtr. Sep.* **2015**, 585.
[321] J. Rouquerol, F. Rouquerol, K. Sing, *Adsorption by Powders and Porous Solids: Principles, Methodology and Applications*, Elsevier Science & Technology, **1998**.
[322] Z. A. Alothman, *Materials (Basel).* **2012**, *5*, 2874.
[323] M. Thommes, K. Kaneko, A. V. Neimark, J. P. Olivier, F. Rodriguez-Reinoso, J. Rouquerol, K. S. W. Sing, *Pure Appl. Chem.* **2015**, *87*, 1051.
[324] Malvern, *A Basic Guide to Particle Characterization*, **2015**.
[325] C. M. Keck, R. H. Müller, *Int. J. Pharm.* **2008**, *355*, 150.
[326] Malvern, *Mastersizer 2000 User Manual*, **2007**.
[327] P. B. Kowalczuk, J. Drzymala, *Part. Sci. Technol.* **2016**, *34*, 645.
[328] R. Berera, R. van Grondelle, J. T. M. Kennis, *Photosynth. Res.* **2009**, *101*, 105.
[329] C. M. Aitchison, R. S. Sprick, A. I. Cooper, *J. Mater. Chem. A* **2019**, *7*, 2490.
[330] C. Cheng, X. Wang, Y. Lin, L. He, J. X. Jiang, Y. Xu, F. Wang, *Polym. Chem.* **2018**, *9*, 4468.
[331] J. Yin, M. P. Rainka, X. X. Zhang, S. L. Buchwald, *J. Am. Chem. Soc.* **2002**, *124*, 1162.
[332] J. W. M. Osterrieth, J. Rampersad, D. Madden, N. Rampal, L. Skoric, B. Connolly, M. D. Allendorf, V. Stavila, J. L. Snider, R. Ameloot, J. Marreiros, C. Ania, D. Azevedo, E. Vilarrasa-Garcia, B. F. Santos, X. H. Bu, Z. Chang, H. Bunzen, N. R. Champness, S. L. Griffin, B. Chen, R. B. Lin, B. Coasne, S. Cohen, J. C. Moreton, Y. J. Colón, L. Chen, R. Clowes, F. X. Coudert, Y. Cui, B. Hou, D. M. D'Alessandro, P. W. Doheny, M. Dincă, C. Sun, C. Doonan, M. T. Huxley, J. D. Evans, P. Falcaro, R. Ricco, O. Farha, K. B. Idrees, T. Islamoglu, P. Feng, H. Yang, R. S. Forgan, D. Bara, S. Furukawa, E. Sanchez, J. Gascon, S. Telalović, S. K. Ghosh, S. Mukherjee, M. R. Hill, M. M. Sadiq, P. Horcajada, P. Salcedo-Abraira, K. Kaneko, R. Kukobat, J. Kenvin, S. Keskin, S. Kitagawa, K. ichi Otake, R. P. Lively, S. J. A. DeWitt, P. Llewellyn, B. V. Lotsch, S. T. Emmerling, A. M. Pütz, C. Martí-Gastaldo, N. M. Padial, J. García-Martínez, N. Linares, D. Maspoch, J. A. Suárez del Pino, P. Moghadam, R. Oktavian, R. E. Morris, P. S. Wheatley, J. Navarro, C. Petit, D. Danaci, M. J. Rosseinsky, A. P. Katsoulidis, M. Schröder, X. Han, S. Yang, C. Serre, G. Mouchaham, D. S. Sholl, R. Thyagarajan, D. Siderius, R. Q. Snurr, R. B. Goncalves, S. Telfer, S. J. Lee, V. P. Ting, J. L. Rowlandson, T. Uemura, T. Iiyuka, M. A. van der Veen, D. Rega, V. Van Speybroeck, S. M. J. Rogge, A. Lamaire, K. S. Walton, L. W. Bingel, S. Wuttke, J. Andreo, O. Yaghi, B. Zhang, C. T. Yavuz, T. S. Nguyen, F. Zamora, C. Montoro, H. Zhou, A. Kirchon, D. Fairen-Jimenez, *Adv. Mater.* **2022**, *34*, 2201502.
[333] N. B. McKeown, P. M. Budd, *Macromolecules* **2010**, *43*, 5163.
[334] N. B. Mckeown, P. M. Budd, *Porous Polymers*, John Wiley And Sons, Hoboken, **2011**.
[335] N. B. McKeown, *ISRN Mater. Sci.* **2012**, *2012*, 1.
[336] M. A. Little, A. I. Cooper, M. A. Little, A. I. Cooper, *Adv. Funct. Mater.* **2020**, *30*, 1909842.
[337] P. M. Budd, E. S. Elabas, B. S. Ghanem, S. Makhseed, N. B. McKeown, K. J. Msayib, C. E. Tattershall, D. Wang, *Adv. Mater.* **2004**, *16*, 456.
[338] P. M. Budd, B. S. Ghanem, S. Makhseed, N. B. McKeown, K. J. Msayib, C. E. Tattershall, *Chem. Commun.* **2004**, *4*, 230.
[339] T. Emmler, K. Heinrich, D. Fritsch, P. M. Budd, N. Chaukura, D. Ehlers, K. Rätzke, F. Faupel, *Macromolecules* **2010**, *43*, 6075.
[340] T. P. I. Saragi, T. Spehr, A. Siebert, T. Fuhrmann-Lieker, J. Salbeck, *Chem. Rev.* **2007**, *107*, 1011.
[341] N. B. McKeown, P. M. Budd, K. J. Msayib, B. S. Ghanem, H. J. Kingston, C. E. Tattershall, S. Makhseed, K. J. Reynolds, D. Fritsch, *Chem. – A Eur. J.* **2005**, *11*, 2610.
[342] T. M. Figueira-Duarte, S. C. Simon, M. Wagner, S. I. Druzhinin, K. A. Zachariasse, K. Müllen, *Angew. Chemie Int. Ed.* **2008**, *47*, 10175.
[343] G. Cheng, B. Bonillo, R. S. Sprick, D. J. Adams, T. Hasell, A. I. Cooper, *Adv. Funct. Mater.* **2014**, *24*, 5219.
[344] T. M. Figueira-Duarte, P. G. Del Rosso, R. Trattnig, S. Sax, E. J. W. List, K. Mullen, *Adv. Mater.* **2010**, *22*, 990.
[345] F. Moruzzi, W. Zhang, B. Purushothaman, S. Gonzalez-Carrero, C. M. Aitchison, B. Willner, F. Ceugniet, Y. Lin, J. Kosco, H. Chen, J. Tian, M. Alsufyani, J. S. Gibson, E. Rattner, Y. Baghdadi, S. Eslava, M. Neophytou, J. R. Durrant, L. Steier, I. McCulloch, *Nat. Commun.* **2023**, *14*, 3443.
[346] D. Xia, C. Duan, S. Liu, D. Ding, M. Baumgarten, M. Wagner, D. Schollmeyer, H. Xu, K. Müllen, *New J. Chem.* **2019**, *43*, 3788.
[347] P. Klein, H. J. Jötten, C. M. Aitchison, R. Clowes, E. Preis, A. I. Cooper, R. S. Sprick, U. Scherf, *Polym. Chem.* **2019**, *10*, 5200.
[348] G. Cheng, T. Hasell, A. Trewin, D. J. Adams, A. I. Cooper, *Angew. Chemie Int. Ed.* **2012**, *51*, 12727.
[349] R. G. Clarkson, M. Gomberg, *J. Am. Chem. Soc.* **1930**, *52*, 2881.
[350] J. Salbeck, F. Weissörtel, J. Bauer, *Macromol. Symp.* **1998**, *125*, 121.
[351] D. Thirion, J. Rault-Berthelot, L. Vignau, C. Poriel, *Org. Lett.* **2011**, *13*, 4418.
[352] C. Poriel, J. J. Liang, J. Rault-Berthelot, F. Barrière, N. Cocherel, A. M. Z. Slawin, D. Horhant, M. Virboul, G. Alcaraz, N. Audebrand, L. Vignau, N. Huby, G. Wantz, L. Hirsch, *Chem. – A Eur. J.* **2007**, *13*, 10055.
[353] N. Cocherel, C. Poriel, L. Vignau, J. F. Bergamini, J. Rault-Berthelot, *Org. Lett.* **2010**, *12*, 452.
[354] Z. Jiang, H. Yao, Z. Liu, C. Yang, C. Zhong, J. Qin, G. Yu, Y. Liu, *Org. Lett.* **2009**, *11*, 4132.
[355] L. H. Xie, R. Zhu, Y. Qian, R. R. Liu, S. F. Chen, J. Lin, W. Huang, *J. Phys. Chem. Lett.* **2010**, *1*, 272.

[356] U. Bach, D. Lupo, P. Comte, J. E. Moser, F. Weissörtel, J. Salbeck, H. Spreitzer, M. Grätzel, *Nature* **1998**, *395*, 583.
[357] Z. Hawash, L. K. Ono, Y. Qi, *Adv. Mater. Interfaces* **2018**, *5*, 1700623.
[358] J. Yi, Y. Wang, Q. Luo, Y. Lin, H. Tan, H. Wang, C. Q. Ma, *Chem. Commun.* **2016**, *52*, 1649.
[359] X. F. Wu, W. F. Fu, Z. Xu, M. Shi, F. Liu, H. Z. Chen, J. H. Wan, T. P. Russell, *Adv. Funct. Mater.* **2015**, *25*, 5954.
[360] N. Kleinhenz, L. Yang, H. Zhou, S. C. Price, W. You, *Macromolecules* **2011**, *44*, 872.
[361] Y. Hernandez, V. Nicolosi, M. Lotya, F. M. Blighe, Z. Sun, S. De, I. T. McGovern, B. Holland, M. Byrne, Y. K. Gun'ko, J. J. Boland, P. Niraj, G. Duesberg, S. Krishnamurthy, R. Goodhue, J. Hutchison, V. Scardaci, A. C. Ferrari, J. N. Coleman, *Nat. Nanotechnol.* **2008**, *3*, 563.
[362] C. A. Furtado, U. J. Kim, H. R. Gutierrez, L. Pan, E. C. Dickey, P. C. Eklund, *J. Am. Chem. Soc.* **2004**, *126*, 6095.
[363] W. Y. Huang, Z. Q. Shen, J. Z. Cheng, L. L. Liu, K. Yang, X. Chen, H. R. Wen, S. Y. Liu, *J. Mater. Chem. A* **2019**, *7*, 24222.
[364] Z. R. Tan, Y. Q. Xing, J. Z. Cheng, G. Zhang, Z. Q. Shen, Y. J. Zhang, G. Liao, L. Chen, S. Y. Liu, *Chem. Sci.* **2022**, *13*, 1725.
[365] W. Zhang, J. Smith, S. E. Watkins, R. Gysel, M. McGehee, A. Salleo, J. Kirkpatrick, S. Ashraf, T. Anthopoulos, M. Heeney, I. McCulloch, *J. Am. Chem. Soc.* **2010**, *132*, 11437.
[366] J. K. Stille, *Angew. Chemie* **1986**, *98*, 504.
[367] P. Espinet, A. M. Echavarren, P. Espinet, A. M. Echavarren, *Angew. Chemie Int. Ed.* **2004**, *43*, 4704.
[368] A. Meijere, F. Diederich, *Metal-Catalyzed Cross-Coupling Reactions*, WILEY-VCH Verlag Gmbh, **2004**.
[369] C. Cordovilla, C. Bartolomé, J. M. Martínez-Ilarduya, P. Espinet, *ACS Catal.* **2015**, *5*, 3040.
[370] H. G. Klivilx, J. F. Reuwer, J. A. Mangravite, *Can. J. Chem.* **1963**, *41*, 3081.
[371] H. L. D. Hayes, R. Wei, M. Assante, K. J. Geogheghan, N. Jin, S. Tomasi, G. Noonan, A. G. Leach, G. C. Lloyd-Jones, *J. Am. Chem. Soc.* **2021**, *143*, 14814.
[372] P. A. Cox, A. G. Leach, A. D. Campbell, G. C. Lloyd-Jones, *J. Am. Chem. Soc.* **2016**, *138*, 9145.
[373] J. J. Li, *Name Reactions: A Collection of Detailed Mechanisms and Synthetic Applications*, Springer International Publishing AG, **2021**.
[374] L. Mohammadkhani, M. M. Heravi, *ChemistrySelect* **2019**, *4*, 6309.
[375] C. T. Chen, W. S. Chao, H. W. Liu, Y. Wei, J. H. Jou, S. Kumar, *RSC Adv.* **2013**, *3*, 9381.
[376] J. D. Peltier, B. Heinrich, B. Donnio, O. Jeannin, J. Rault-Berthelot, C. Poriel, *Chem. – A Eur. J.* **2017**, *23*, 17290.
[377] H. Usta, C. Risko, Z. Wang, H. Huang, M. K. Deliomeroglu, A. Zhukhovitskiy, A. Facchetti, T. J. Marks, *J. Am. Chem. Soc.* **2009**, *131*, 5586.
[378] J. Y. Lee, K. H. Lee, S. O. Kim, J. N. You, S. Kang, J. Y. Lee, K. S. Yook, S. O. Jeon, S. S. Yoon, *J. Mater. Chem.* **2012**, *22*, 5145.
[379] D. Venkateshvaran, M. Nikolka, A. Sadhanala, V. Lemaur, M. Zelazny, M. Kepa, M. Hurhangee, A. J. Kronemeijer, V. Pecunia, I. Nasrallah, I. Romanov, K. Broch, I. McCulloch, D. Emin, Y. Olivier, J. Cornil, D. Beljonne, H. Sirringhaus, *Nature* **2014**, *515*, 384.
[380] F. L. Tobiason, L. Huestis, C. Chandler, S. E. Pedersen, P. Peters, *J. Heterocycl. Chem.* **1973**, *10*, 773.
[381] D. C. Blakemore, *Synthetic Methods in Drug Discovery: Volume 1*, **2016**.
[382] B. S. Ghanem, M. Hashem, K. D. M. Harris, K. J. Msayib, M. Xu, P. M. Budd, N. Chaukura, D. Book, S. Tedds, A. Walton, N. B. McKeown, *Macromolecules* **2010**, *43*, 5287.
[383] R. W. Tilford, S. J. Mugavero, P. J. Pellechia, J. J. Lavigne, *Adv. Mater.* **2008**, *20*, 2741.
[384] E. J. Corey, A. Venkateswarlu, *J. Am. Chem. Soc* **1972**, 6190.
[385] T. W. Greene, P. G. M. Wuts, *Protective Groups In Organic Synthesis*, John Wiley & Sons, Ltd, New York, **1991**.
[386] E. Zhu, G. Ge, J. Shu, M. Yi, L. Bian, J. Hai, J. Yu, Y. Liu, J. Zhou, W. Tang, *J. Mater. Chem. A* **2014**, *2*, 13580.
[387] P. Patschinski, C. Zhang, H. Zipse, *J. Org. Chem.* **2014**, *79*, 8348.
[388] Y. J. Tu, D. Njus, H. B. Schlegel, *Org. Biomol. Chem.* **2017**, *15*, 4417.
[389] A. Giovannitti, K. J. Thorley, C. B. Nielsen, J. Li, M. J. Donahue, G. G. Malliaras, J. Rivnay, I. Mcculloch, A. Giovannitti, K. J. Thorley, J. Li, I. Mcculloch, C. B. Nielsen, M. J. Donahue, G. G. Malliaras, J. Rivnay, *Adv. Funct. Mater.* **2018**, *28*, 1706325.
[390] G. Ö. Atlı, E. A. Yılmaz, S. T. Aslan, Y. A. Udum, L. Toppare, A. Çırpan, *J. Electroanal. Chem.* **2020**, *862*, 114014.
[391] F. Tomás, J. L. M. Abboud, J. Laynez, R. Notario, L. Santos, S. O. Nilsson, J. Catalán, R. M. Claramunt, J. Elguero, *J. Am. Chem. Soc.* **1989**, *111*, 7348.
[392] Z. Hu, Z. Hu, Q. Huang, C. Liu, A. Song, L. Shao, Y. Bai, Z. Hu, K. Zhang, F. Huang, Y. Cao, *Org. Mater.* **2022**, *4*, 18.
[393] D. Kroh, F. Eller, K. Schötz, S. Wedler, L. Perdigón-Toro, G. Freychet, Q. Wei, M. Dörr, D. Jones, Y. Zou, E. M. Herzig, D. Neher, A. Köhler, *Adv. Funct. Mater.* **2022**, *32*, 2205711.
[394] X. Zhao, P. Pachfule, S. Li, T. Langenhahn, M. Ye, C. Schlesiger, S. Praetz, J. Schmidt, A. Thomas, *J. Am. Chem. Soc.* **2019**, *141*, 6623.
[395] Z. J. Wang, S. Ghasimi, K. Landfester, K. A. I. Zhang, *Chem. Commun.* **2014**, *50*, 8177.
[396] I. P. Maria, S. Griggs, R. B. Rashid, B. D. Paulsen, J. Surgailis, K. Thorley, V. N. Le, G. T. Harrison, C. Combe, R. Hallani, A. Giovannitti, A. F. Paterson, S. Inal, J. Rivnay, I. McCulloch, *Chem. Mater.* **2022**, *34*, 8593.
[397] J. Xu, B. Chen, J. Lv, D. Chang, D. Niu, S. Hu, X. Zhang, Z. Xin, L. Wang, *Dye. Pigment.* **2019**, *170*, 107559.
[398] M. Grzybowski, D. T. Gryko, *Adv. Opt. Mater.* **2015**, *3*, 280.
[399] J. P. Correa-Baena, A. Abate, M. Saliba, W. Tress, T. Jesper Jacobsson, M. Grätzel, A. Hagfeldt, *Energy Environ. Sci.* **2017**, *10*, 710.
[400] P. K. Nayak, S. Mahesh, H. J. Snaith, D. Cahen, *Nat. Rev. Mater.* **2019**, *4*, 269.
[401] J. Feng, X. Wang, J. Li, H. Liang, W. Wen, E. Alvianto, C. W. Qiu, R. Su, Y. Hou, *Nat. Commun.* **2023**, *14*, 5392.
[402] J. Y. Kim, J. W. Lee, H. S. Jung, H. Shin, N. G. Park, *Chem. Rev.* **2020**, *120*, 7867.
[403] J. M. Luther, L. T. Schelhas, *Science* **2022**, *376*, 28.
[404] O. Malinkiewicz, A. Yella, Y. H. Lee, G. M. Espallargas, M. Graetzel, M. K. Nazeeruddin, H. J. Bolink, *Nat. Photonics* **2013**, *8*, 128.
[405] T. Leijtens, K. A. Bush, R. Prasanna, M. D. McGehee, *Nat. Energy* **2018**, *3*, 828.
[406] S. Foo, M. Thambidurai, P. Senthil Kumar, R. Yuvakkumar, Y. Huang, C. Dang, *Int. J. Energy Res.* **2022**, *46*, 21441.
[407] B. Roose, K. C. Gödel, S. Pathak, A. Sadhanala, J. Pablo Correa Baena, B. D. Wilts, H. J. Snaith, U. Wiesner, M.

Grätzel, U. Steiner, A. Abate, B. Roose, B. D. Wilts, U. Steiner, A. Abate, K. C. Gödel, A. Sadhanala, S. Pathak, H. J. Snaith, J. P. Correa Baena, M. Grätzel, U. Wiesner, *Adv. Energy Mater.* **2016**, *6*, 1501868.
[408] B. Roose, J. P. C. Baena, K. C. Gödel, M. Graetzel, A. Hagfeldt, U. Steiner, A. Abate, *Nano Energy* **2016**, *30*, 517.
[409] A. J. Ramadan, R. D. J. Oliver, M. B. Johnston, H. J. Snaith, *Nat. Rev. Mater.* **2023**, *8*, 822.
[410] K. Wojciechowski, T. Leijtens, S. Siprova, C. Schlueter, M. T. Hörantner, J. T. W. Wang, C. Z. Li, A. K. Y. Jen, T. L. Lee, H. J. Snaith, *J. Phys. Chem. Lett.* **2015**, *6*, 2399.
[411] A. Wadsworth, M. Moser, A. Marks, M. S. Little, N. Gasparini, C. J. Brabec, D. Baran, I. McCulloch, *Chem. Soc. Rev.* **2019**, *48*, 1596.
[412] A. Kojima, K. Teshima, Y. Shirai, T. Miyasaka, *J. Am. Chem. Soc.* **2009**, *131*, 6050.
[413] F. Zu, D. Shin, N. Koch, *Mater. Horizons* **2022**, *9*, 17.
[414] P. Kaienburg, A. Jungbluth, I. Habib, S. V. Kesava, M. Nyman, M. K. Riede, *Adv. Mater.* **2022**, *34*, 2107584.
[415] Gaussian Inc., **2016**.
[416] R. Stalder, J. Mei, K. R. Graham, L. A. Estrada, J. R. Reynolds, *Chem. Mater.* **2014**, *26*, 664.
[417] X. Wei, W. Zhang, G. Yu, *Adv. Funct. Mater.* **2021**, *31*, 2010979.
[418] M. Irimia-Vladu, E. D. Gåowacki, P. A. Troshin, G. Schwabegger, L. Leonat, D. K. Susarova, O. Krystal, M. Ullah, Y. Kanbur, M. A. Bodea, V. F. Razumov, H. Sitter, S. Bauer, N. S. Sariciftci, *Adv. Mater.* **2012**, *24*, 375.
[419] R. S. Ashraf, A. J. Kronemeijer, D. I. James, H. Sirringhaus, I. McCulloch, *Chem. Commun.* **2012**, *48*, 3939.
[420] W. Yue, M. Nikolka, M. Xiao, A. Sadhanala, C. B. Nielsen, A. J. P. White, H. Y. Chen, A. Onwubiko, H. Sirringhaus, I. McCulloch, *J. Mater. Chem. C* **2016**, *4*, 9704.
[421] P. Nesvadba, *Synth. 2000* **1999**, 355.
[422] F. Bigi, G. Casiraghi, G. Sartori, *Tetrahedron* **1983**, *39*, 2147.
[423] V. Bogdanov, V. F. Mironov, L. I. Musin, B. I. Buzykin, A. I. Konovalov, *Russ. J. Gen. Chem.* **2008**, *78*, 1741.
[424] J. Huang, Z. Mao, Z. Chen, D. Gao, C. Wei, W. Zhang, G. Yu, *Chem. Mater.* **2016**, *28*, 2209.
[425] A. V. Bogdanov, V. F. Mironov, L. I. Musin, R. Z. Musin, D. B. Krivolapov, I. A. Litvinov, *Synth. Commun.* **2012**, *42*, 2388.
[426] D. Kleeblatt, B. Siyo, M. Hein, V. O. Iaroshenko, J. Iqbal, A. Villinger, P. Langer, *Org. Biomol. Chem.* **2013**, *11*, 886.
[427] L. I. Musin, A. V. Bogdanov, D. B. Krivolapov, A. B. Dobrynin, I. A. Litvinov, V. F. Mironov, *Russ. J. Org. Chem.* **2014**, *50*, 822.
[428] C. Papageorgiou, X. Borer, *Helv. Chim. Acta* **1988**, *71*, 1079.
[429] J. Mei, K. R. Graham, R. Stalder, J. R. Reynolds, *Org. Lett.* **2010**, *12*, 660.
[430] A. Onwubiko, W. Yue, C. Jellett, M. Xiao, H. Y. Chen, M. K. Ravva, D. A. Hanifi, A. C. Knall, B. Purushothaman, M. Nikolka, J. C. Flores, A. Salleo, J. L. Bredas, H. Sirringhaus, P. Hayoz, I. McCulloch, *Nat. Commun.* **2018**, *9*, 416.
[431] G. Kollenz, G. Penn, R. Theuer, W. M. F. Fabian, H. A. Abd El-Nabi, X. Zhang, K. Peters, E. M. Peters, H. G. Von Schnering, *Tetrahedron* **1996**, *52*, 5427.
[432] T. Itoh, J. Tatsugi, H. Tomioka, *Bull. Chem. Soc. Jpn.* **2009**, *82*, 475.
[433] K. Albertshofer, B. Tan, C. F. Barbas, *Org. Lett.* **2013**, *15*, 2958.
[434] L. A. Casey, R. Galt, M. I. Page, *J. Chem. Soc. Perkin Trans. 2* **1993**, 23.
[435] W. Pfitzinger, *J. Prakt. Chem* **1886**, *33*, 100.
[436] R. Sriram, C. N. Sesha Sai Pavan Kumar, N. Raghunandan, V. Ramesh, M. Sarangapani, V. J. Rao, *Synth. Commun.* **2012**, *42*, 3419.
[437] M. Pasini, B. Vercelli, G. Zotti, A. Berlin, *Electrochim. Acta* **2016**, *193*, 261.
[438] J. Nelson, *The Physics Of Solar Cells*, World Scientific Publishing Company, **2003**.

7. Supplementary Information

Intermediate 1

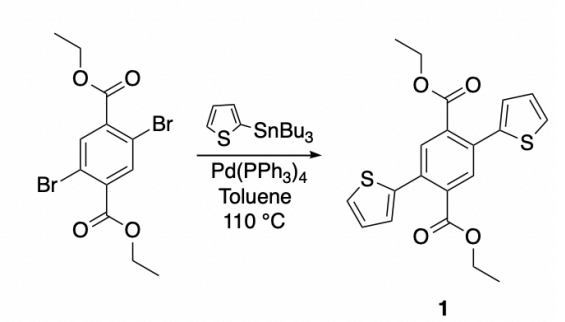

1

1,4-Diethyl 2,5-dibromo-1,4-benzenedicarboxylate (11.49 g, 30.2 mmol, 1 eq) and tetrakis(triphenylphosphine) (0.92 g, 0.8 mmol, 0.03 eq) were added to a 2-neck round bottom flask and purged with nitrogen. 2-(tributylstannyl)thiophene (24 mL, 75.6 mmol, 2.5 eq) was added, followed by anhydrous toluene (60 mL). The solution was refluxed at 110 °C overnight. The next day after the reaction was complete, the solvent was removed under reduced pressure and the crude mixture was passed through a silica plug wetted with petroleum ether: ethyl acetate (80:20), using more eluent to wash it all through. The filtrate was kept, and the solvent was removed under reduced pressure to give a yellow solid. This was recrystallised in hexane: dichloromethane overnight to give large colourless crystals **1** (9.73 g, 83%).

^{1}H NMR (400 MHz, $CDCl_3$) δ 7.81 (s, 2H), 7.39 (dd, J = 4.9, 1.4 Hz, 4H), 7.10-7.06 (m, 4 H), 4.22 (q, J = 7.1 Hz, 4H), 1.15 (t, J=7.1 Hz, 6H)

^{13}C NMR (400 MHz, $CDCl_3$) δ 167.83, 140.65, 134.23, 133.60, 132.02, 127.48, 127.12, 126.60, 61.79, 13.95.

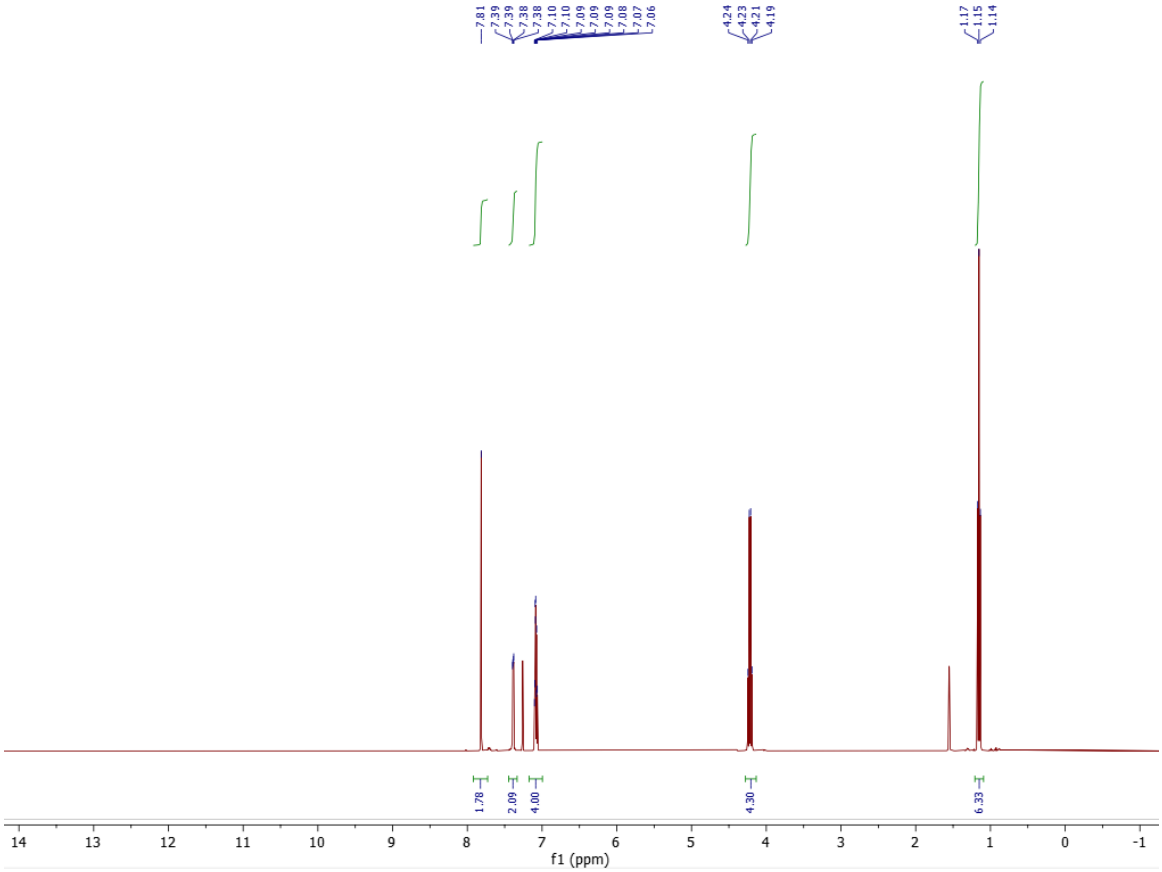
7.81
7.39
7.39
7.38
7.38
7.10
7.09
7.09
7.09
7.08
7.07
7.06
4.24
4.23
4.21
4.19
1.17
1.15
1.14
1.78
2.09
4.00
4.30
6.33
f1 (ppm)

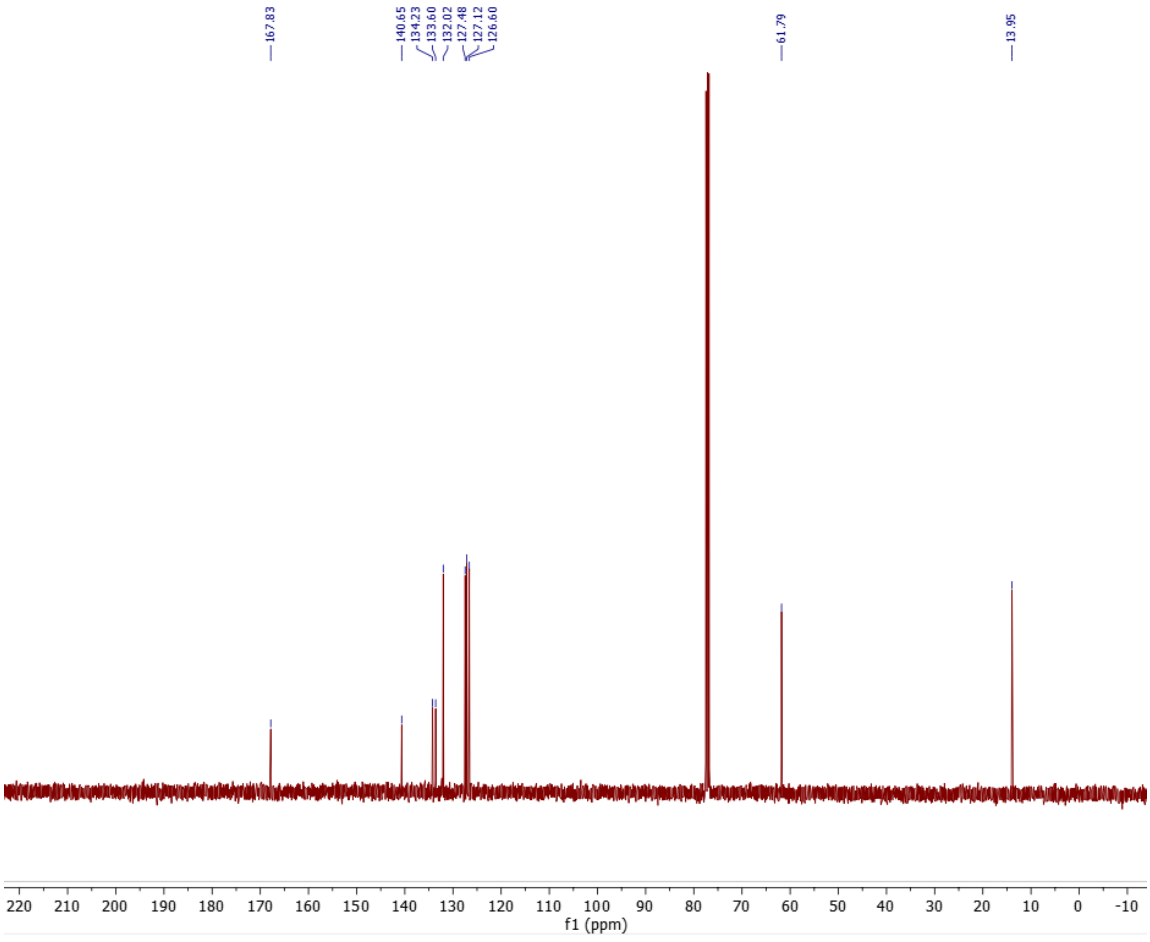
167.83
140.65
134.23
133.60
132.02
127.48
127.12
126.60
61.79
13.95
f1 (ppm)

Intermediate 2

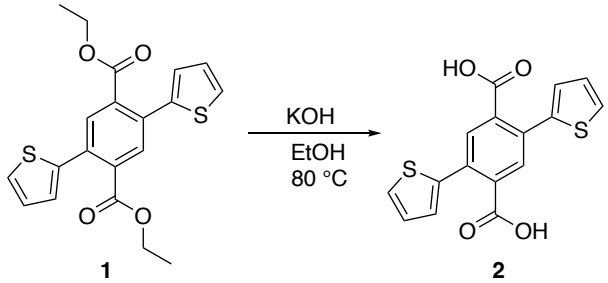

1 **2**

1 (9.66 g, 25.0 mmol, 1 eq) was stirred in ethanol (300 mL) and potassium hydroxide (14.00 g, 249.9 mmol, 10 eq) was added. The solution was refluxed at 80 °C overnight. The next day the product had precipitated somewhat, and the solution was cooled. It was subsequently poured onto ice and neutralised with hydrochloric acid solution. The precipitate was collected by vacuum filtration, washing thoroughly with deionised water followed by methanol. The solid was collected and dried in a vacuum oven overnight to give a white powder **2** (6.81 g, 80%).

^{1}H NMR (400 MHz, d_6-DMSO) δ 13.43 (s, 2H), 7.70 (s, 2H), 7.67 (dd, J = 5.0, 1.2 Hz, 2H), 7.25 (dd J = 3.6, 1.2 Hz, 2H), 7.15 (dd, J = 5.0, 3.6 Hz, 2H)

^{13}C NMR (400 MHz, d_6-DMSO) δ 168.73, 139.68, 134.52, 131.44, 130.17, 127.88, 127.50, 127.12.

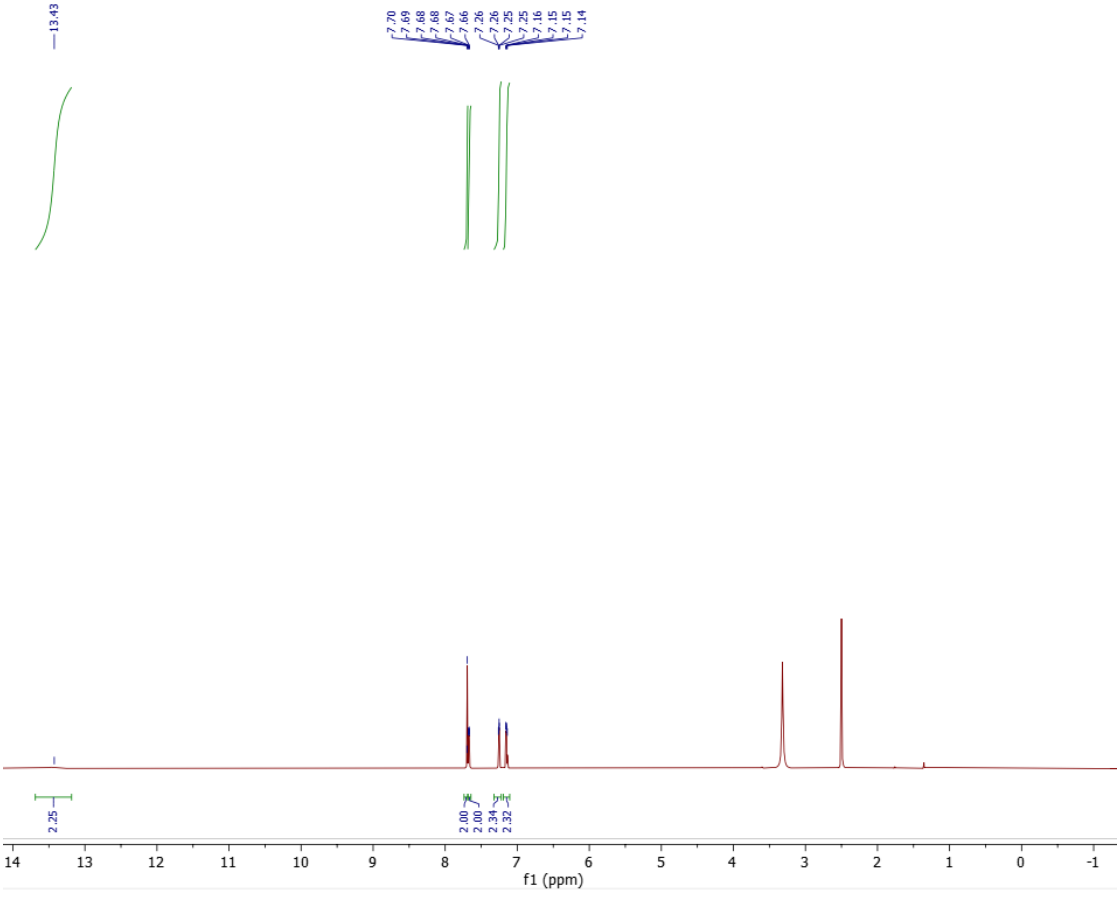

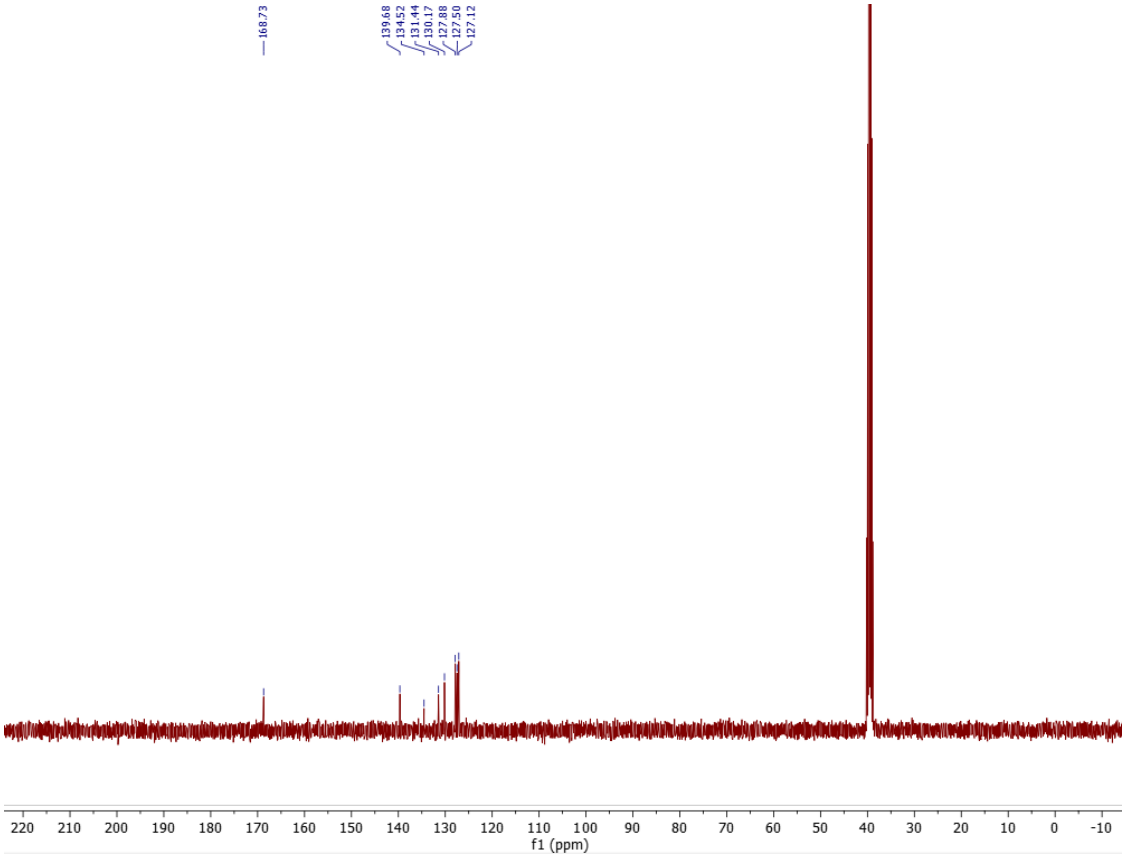
168.73
139.68
134.52
131.44
130.17
127.88
127.50
127.12
220 210 200 190 180 170 160 150 140 130 120 110 100 90 80 70 60 50 40 30 20 10 0 -10
f1 (ppm)

Intermediate 4

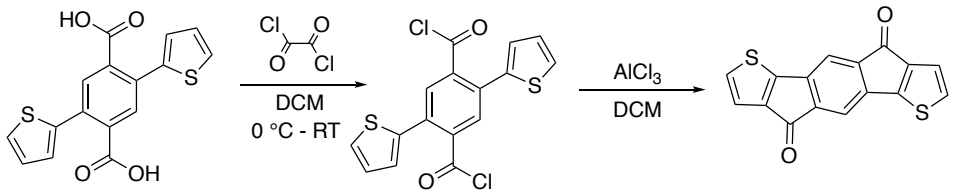

2 **3** **4**

2 (6.11g, 18.5 mmol, 1 eq), was added to a 2-neck round bottom flask and put under high vacuum attached to a Schlenk line while being heated with a heat gun for several minutes, then purged with nitrogen. Anhydrous dichloromethane (300 mL) was added, and the suspension was stirred at room temperature under nitrogen. Oxalyl chloride (6.4 mL, 74.0 mmol, 4 eq) was added, followed by anhydrous dimethylformamide (2 mL) dropwise, to keep the rate of gas evolution manageable. The suspension, which became a solution and turned slightly yellowish, was stirred at room temperature for 3 h under nitrogen, after which time the solvent and excess oxalyl chloride was removed under reduced pressure. The resultant yellowish solid intermediate **3** was purged with nitrogen and dissolved in anhydrous dichloromethane (200 mL). Aluminium trichloride (9.87 g, 74.0 mmol, 4 eq) was added through the side neck of the round bottom flask under a positive nitrogen pressure and it was stirred at room temperature overnight under nitrogen. The next day it was poured into 2 M hydrochloride acid in ice, then the solid precipitate underwent vacuum filtration, washing sequentially with deionised water, methanol, acetone, dichloromethane and diethyl ether. The solid was dried in a vacuum oven overnight to give a blue powder **4** (5.06 g, 93%). This was too insoluble for ^{13}C NMR.

^{1}H NMR (400 MHz, d_6-DMSO) δ 7.59 (d, J = 4.9 Hz, 2H), 7.52 (s, 2H), 7.19 (d, J = 4.9 Hz, 2 H)

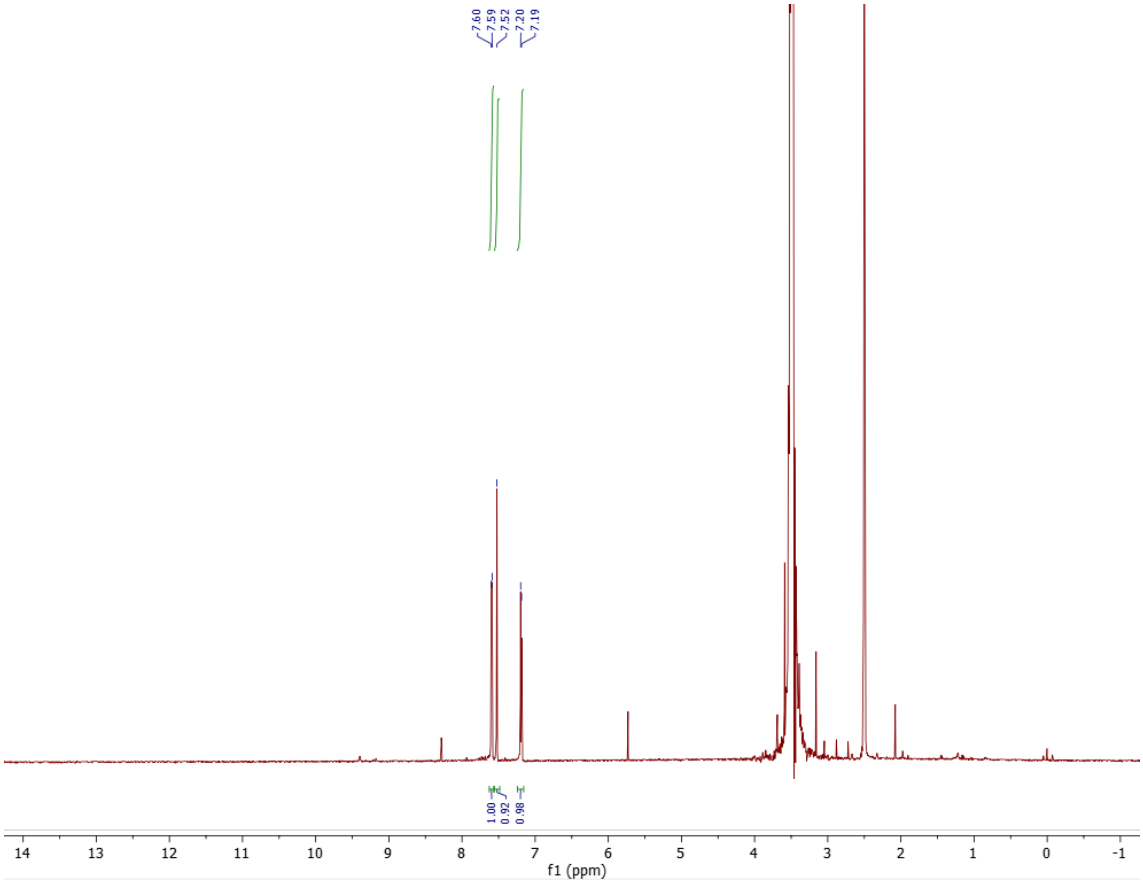
7.60
7.59
7.52
7.20
7.19
1.00
0.92
0.98
14
13
12
11
10
9
8
7
6
5
4
3
2
1
0
-1
f1 (ppm)

Intermediate 5

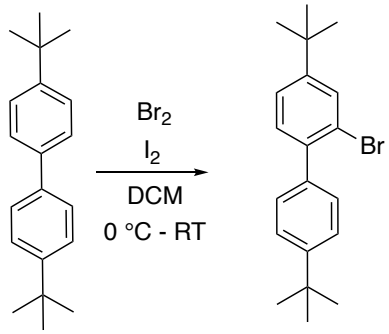

5

4,4′-Bis(1,1-dimethylethyl)-1,1′-biphenyl (31.63 g, 139.7 mmol, 1 eq) and iodine (1.21 g, 4.7 mmol 0.03 eq) were dissolved in dichloromethane and cooled to 0 °C in a 2-neck round bottom flask fitted with a bubbler containing bromine quencher (1M sodium sulfate and 1 M sodium hydroxide solution). Bromine (9.52 mL, 150.9 mmol, 1.08 eq) was added and it was stirred at room temperature for 2 days, monitoring the reaction by crude NMR. After complete reaction, water and bromine quencher were added and it was transferred to a separating funnel. The organic phase was collected and washed with water, brine and sodium sulfate was added. The dried organic phase was filtered, then the solvent was removed under reduced pressure to give a colourless solid. This was recrystallised in hexane and the colourless crystals were collected by vacuum filtration. The recrystallisation filtrate was kept and the solvent removed under reduced pressure. A second recrystallisation was conducted with this, and the two batches were combined to give colourless crystals **5** (41.5 g, 86%)

^{1}H NMR (400 MHz, $CDCl_3$) δ 7.66 (d, J = 2.0 Hz, 1H), 7.45-7.42 (m, 2H), 7.37-7.34 (m, 3H) 7.26 (d, J = 8.0 Hz, 1 H), 1.37 (s, 9H), 1.35 (s, 9H)

^{13}C NMR (400 MHz, $CDCl_3$) δ 151.98, 150.24, 139.45, 138.02, 131.01, 130.16, 129.09, 124.84, 124.53, 122.47, 34.62, 31.41, 31.25.

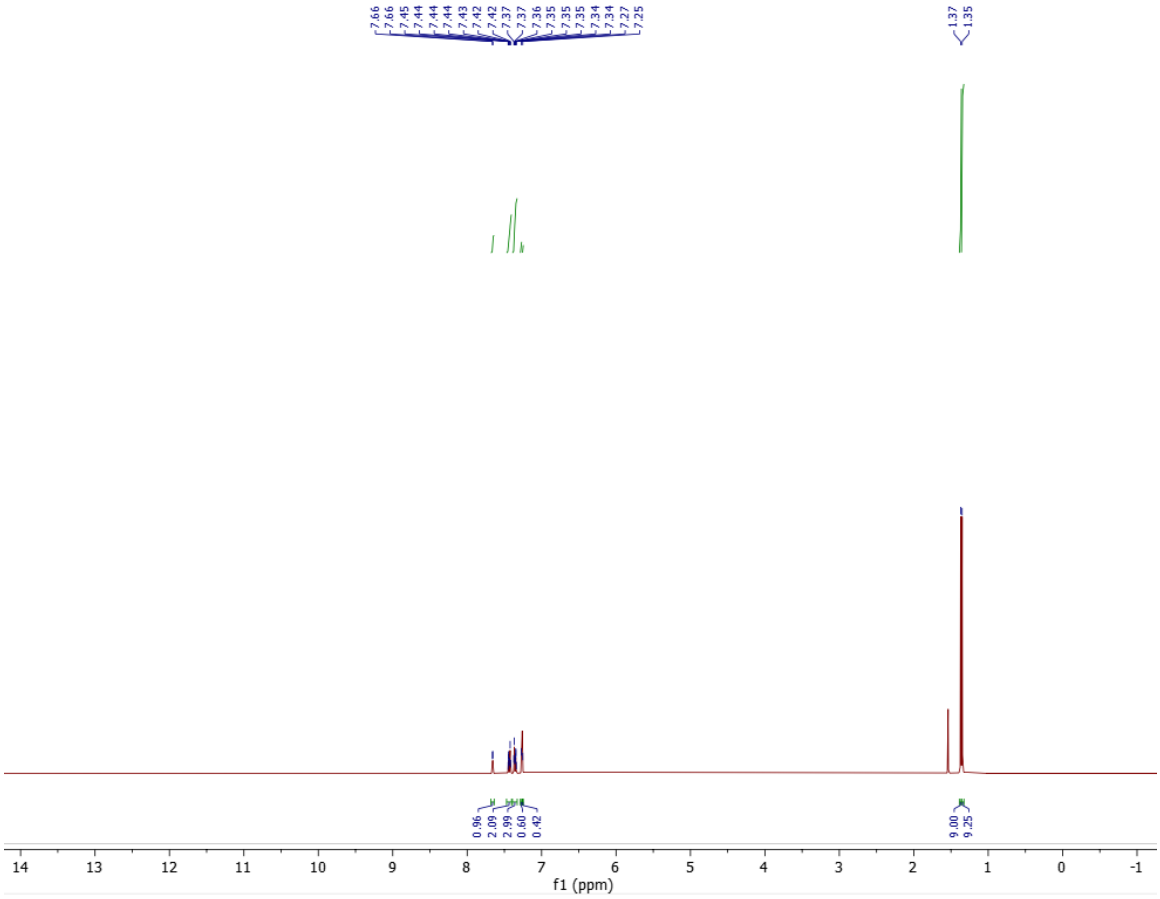
7.66
7.66
7.45
7.44
7.44
7.44
7.43
7.42
7.42
7.37
7.37
7.36
7.35
7.35
7.35
7.34
7.34
7.27
7.25
1.37
1.35
0.96
2.09
2.99
0.60
0.42
9.00
9.25
14
13
12
11
10
9
8
7
6
5
4
3
2
1
0
-1
f1 (ppm)

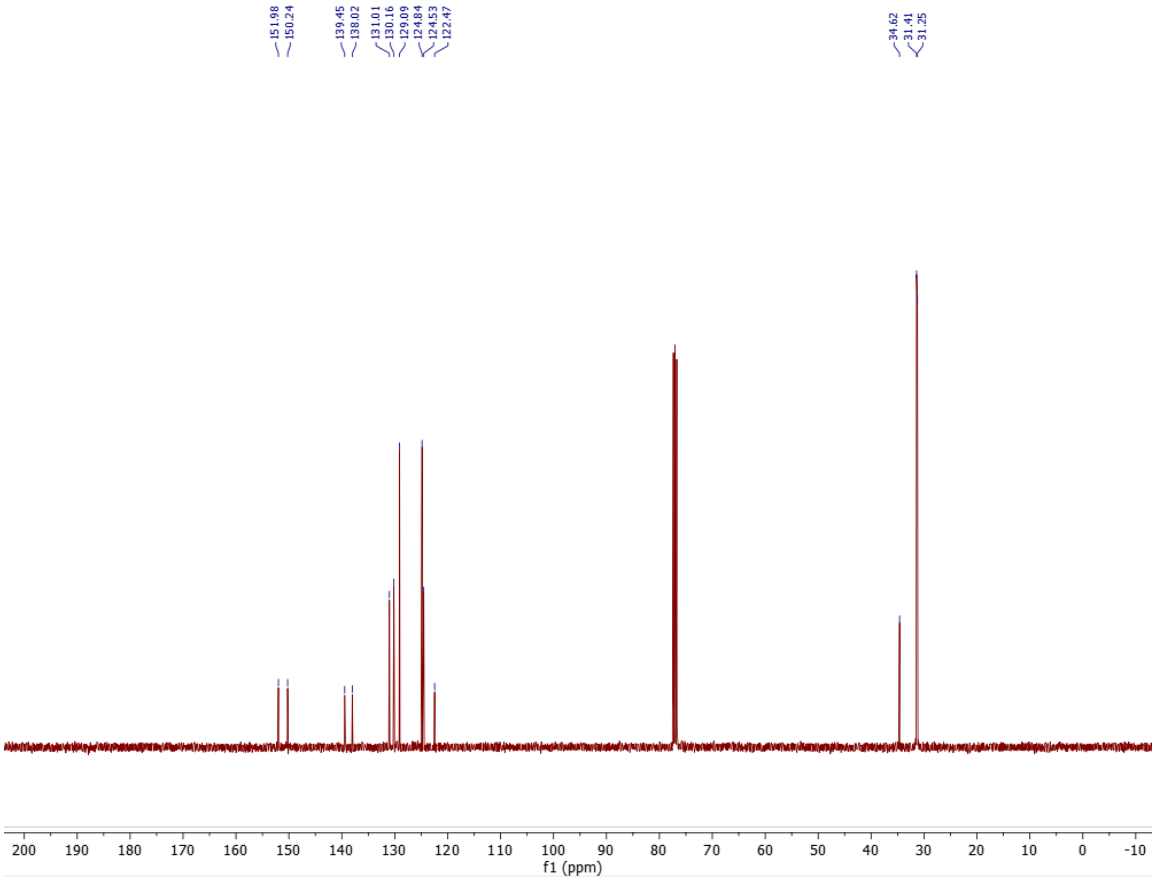
151.98
150.24
139.45
138.02
131.01
130.16
129.09
124.84
124.53
122.47
34.62
31.41
31.25
200 190 180 170 160 150 140 130 120 110 100 90 80 70 60 50 40 30 20 10 0 -10
f1 (ppm)

Unfunctionalized Sp-IDT

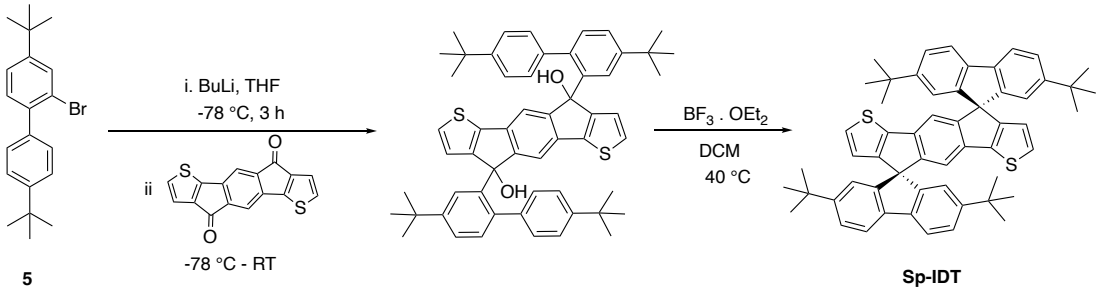

5 (17.60 g, 51.0 mmol, 5 eq) was added to a 2-neck round bottom flask and put under high vacuum attached to a Schlenk line for 30 minutes, then purged with nitrogen. It was dissolved in anhydrous tetrahydrofuran (300 mL) and cooled to -78 °C. n-butyllithium (31.9 mL, 1.6 M, 5 eq) was added slowly whereupon the solution turned yellow and solid began to precipitate. This was left stirring at -78 °C for 3 h under nitrogen. Finely divided and vacuum oven dried **4** (3.00 g, 10.2 mmol, 1 eq) was quickly added through the side neck under a positive pressure of nitrogen. This was left stirring overnight under nitrogen and allowed to reach room temperature. The tetrahydrofuran was removed under reduced pressure, then the alcohol intermediate was extracted with dichloromethane in a separating funnel, washing with water, brine and sodium sulfate was added to dry. This underwent gravity filtration and was transferred to a round bottom flask, with more dichloromethane added such that the total volume was about 200 mL. This was stirred vigorously and boron trifluoride etherate (1 mL) was added dropwise. The solution was refluxed for 2 h. After complete reaction, everything was poured through a short silica plug eluting with dichloromethane. The filtrate was collected, and the solvent was removed under reduced pressure, then purified by dry loading on a silica column, eluting with a graduated eluent, from pure petroleum ether to petroleum ether: dichloromethane (90:10). The columned material was subsequently collected, dispersed in hot chloroform (20 mL) and pipetted into stirring methanol to precipitate. This was then collected by vacuum filtration and washed with methanol. A white solid was recovered **unfunctionalized Sp-IDT**(1.89 g, 23%)

^{1}H NMR (400 MHz, $CDCl_3$) δ 7.75 (dd, J = 8.1, 0.6 Hz, 4H), 7.42 (dd, J = 8.1, 1.8 Hz, 4 H), 7.08 (d, J = 4.9 Hz, 2H), 6.79 (s, 2H), 6.76 (dd, J = 1.6, 0.6 Hz, 4 H), 6.41 (d, J = 4.9 Hz, 2H), 1.19 (s, 36 H)

^{13}C NMR (400 MHz, $CDCl_3$) δ 152.65, 152.56, 150.88, 147.21, 143.50, 139.35, 136.55, 127.30, 125.05, 121.69, 120.66, 119.32, 114.73, 63.89, 34.99, 31.62.

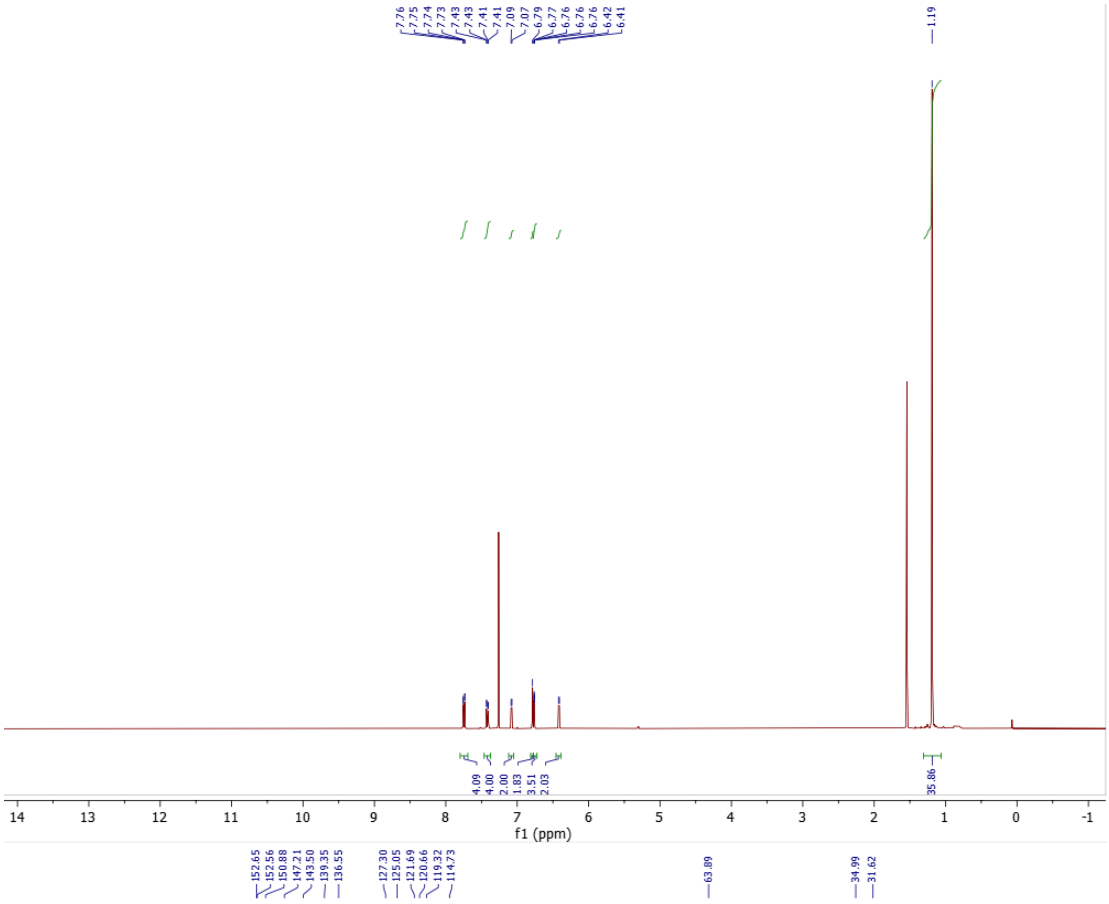
7.76
7.75
7.74
7.73
7.43
7.41
7.09
7.07
6.79
6.77
6.76
6.76
6.76
6.42
6.41
1.19
4.09
4.00
2.00
1.83
3.51
2.03
35.86
f1 (ppm)
152.65
152.56
150.88
147.21
143.50
139.35
136.55
127.30
125.05
121.69
120.66
119.32
114.73
63.89
34.99
31.62
f1 (ppm)

Distannylated Sp-IDT Monomer

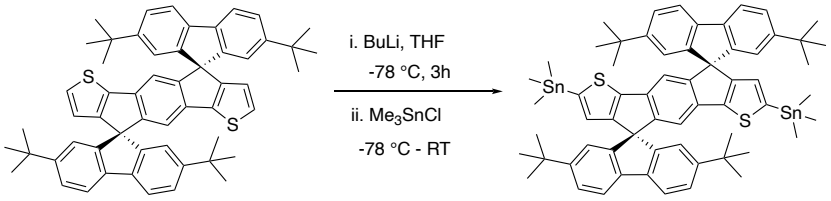

Sp-IDT **Distannylated Sp-IDT**

Unfunctionalised Sp-IDT (947 mg, 1.20 mmol, 1 eq) was purged with nitrogen and dissolved in anhydrous tetrahydrofuran (100 mL). This was cooled to -78 °C and n-butyllithium (1.9 mL, 1.6 M, 2.5 eq) was added dropwise and it was stirred under nitrogen for 3 h. Trimethyltin chloride (3.6, 1M, 3 eq) was added and it was allowed to stir under nitrogen reaching room temperature overnight. The next day the product was extracted with dichloromethane in a separating funnel, washing twice with water, brine and sodium sulfate was added. Gravity filtration was undertaken, and the solvent was removed under reduced pressure. The off-white solid was recrystallised in chloroform: isopropanol overnight to recover a white crystalline solid **distannylated Sp-IDT** (670 mg, 60%)

^{1}H NMR (400 MHz, $CDCl_3$) δ 7.75 (d, J = 8.0 Hz, 4H), 7.42 (dd, J = 8.0, 1.8 Hz, 4H), 6.77 (d, J = 1.8 Hz, 4H), 6.74 (s, 2H), 6.46 (s, 2H), 1.19 (s, 36H), 0.22 (s, 18 H)

^{13}C NMR (400 MHz, $CDCl_3$) δ 154.42, 152.84, 150.79, 149.45, 147.66, 140.80, 139.33, 136.29, 129.36, 124.89, 120.83, 119.21, 114.85, 63.39, 35.00, 31.63, -8.05.

MS (MALDI-TOF): MS calculated for $[C_{62}H_{70}S_2Sn_2]^+$: m/z = 1116.30; measured m/z = 1116.46

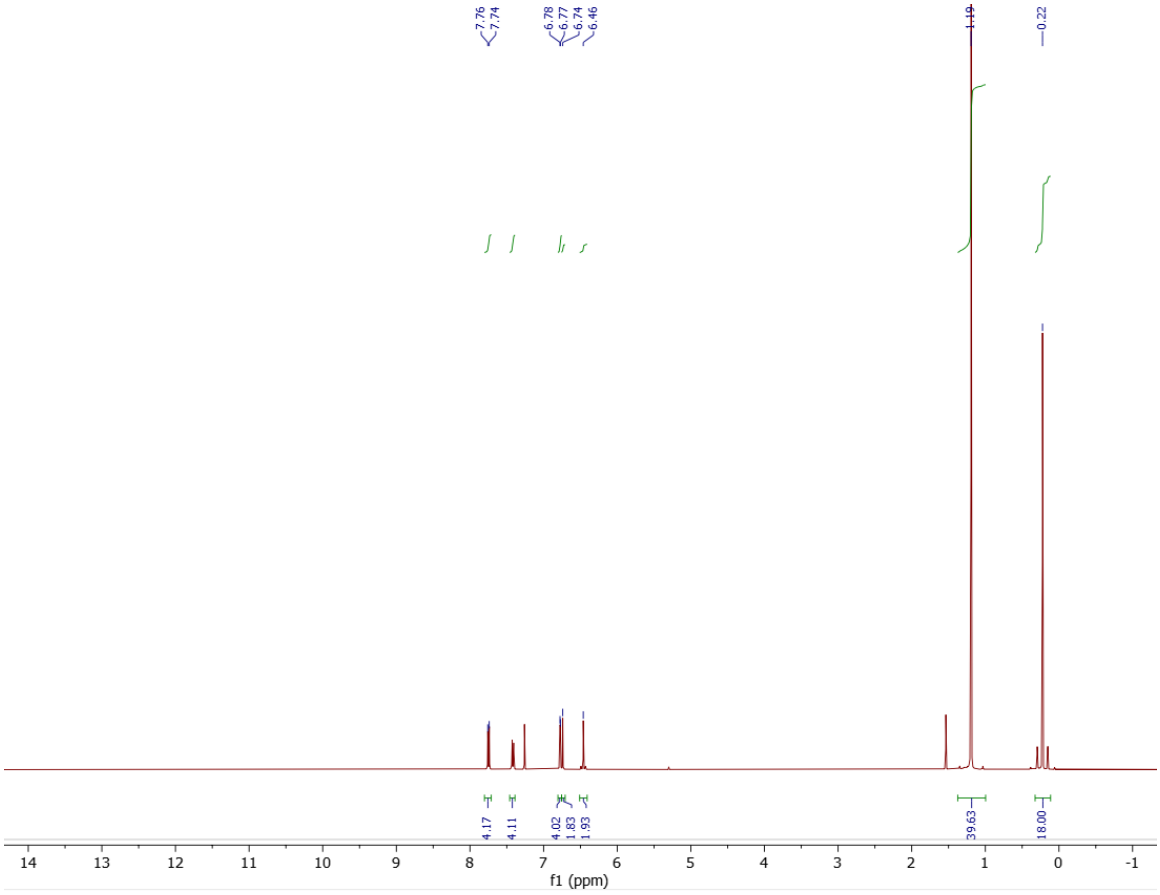
7.76
7.74
6.78
6.77
6.74
6.46
1.10
0.22
4.17
4.11
4.02
1.83
1.93
39.63
18.00
f1 (ppm)

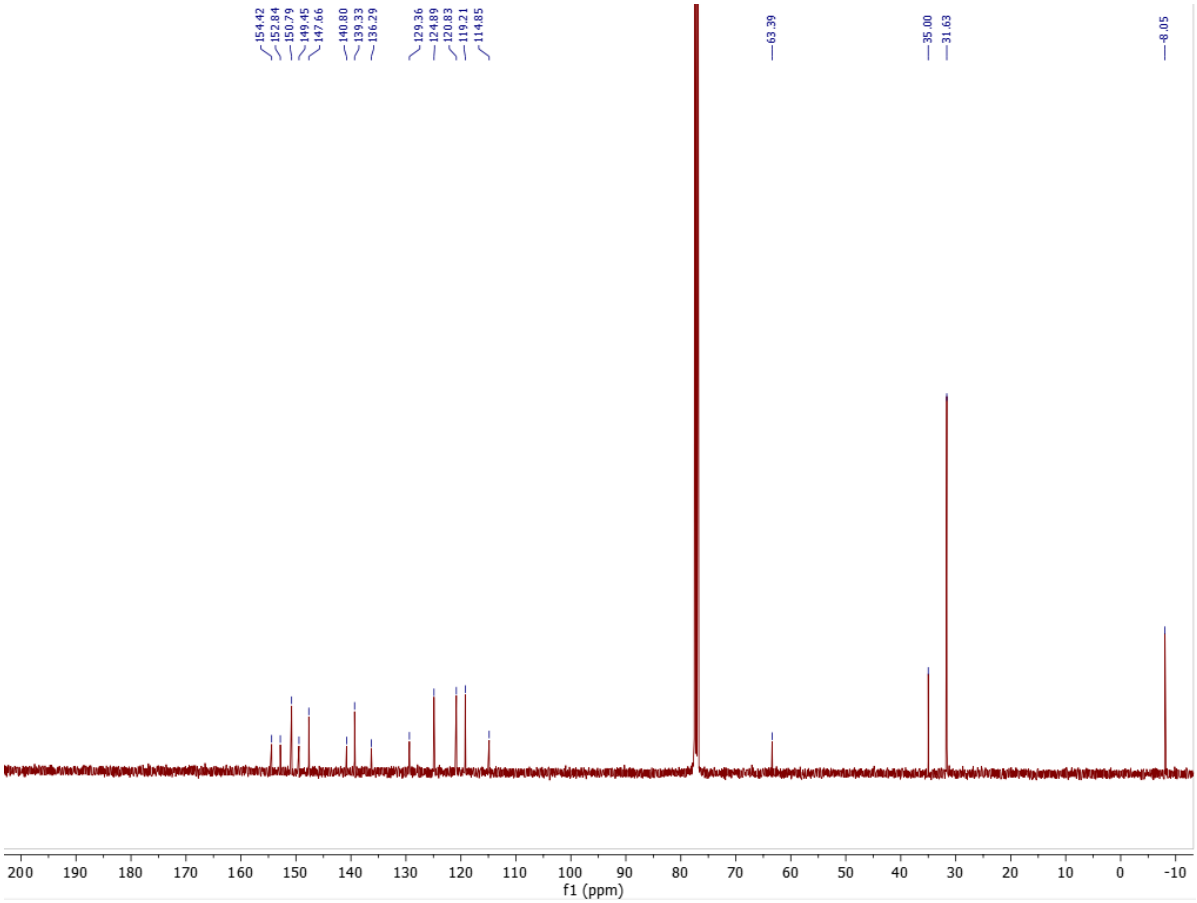
154.42
152.84
150.79
149.45
147.66
140.80
139.33
136.29
129.36
124.89
120.83
119.21
114.85
63.39
35.00
31.63
8.05
f1 (ppm)

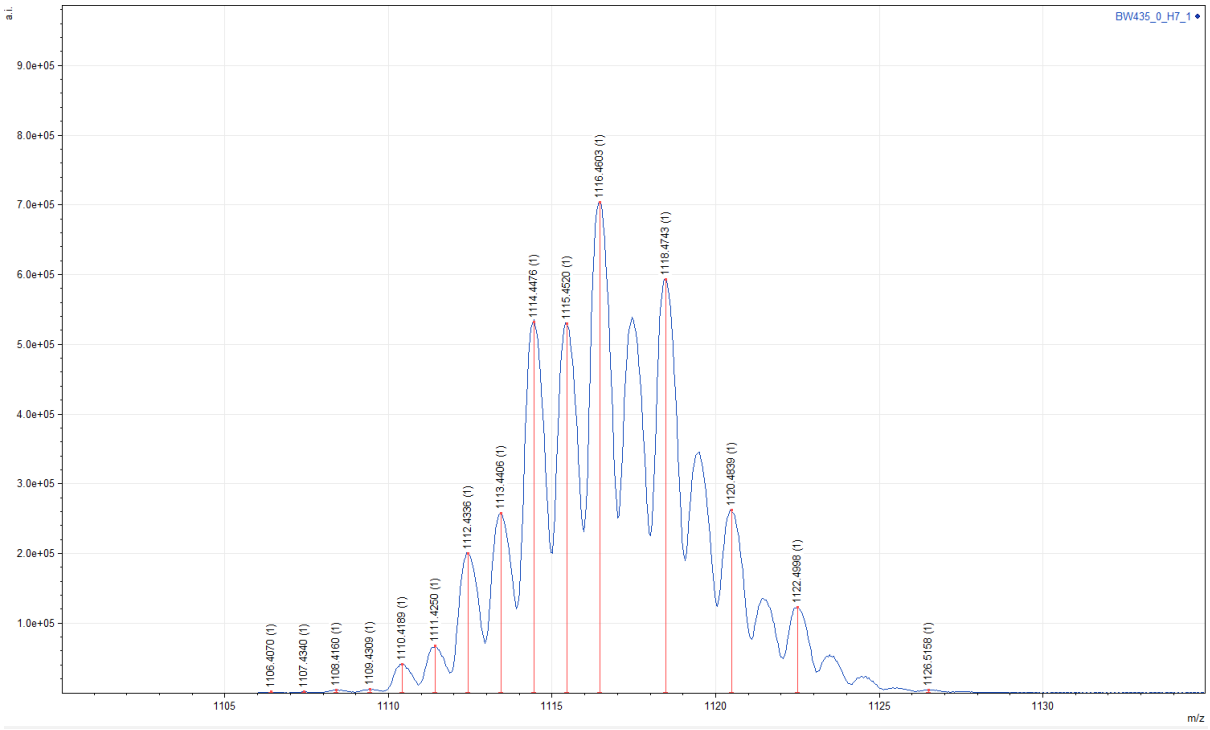
BW435_0_H7_1
a.i.
9.0e+05
8.0e+05
7.0e+05
6.0e+05
5.0e+05
4.0e+05
3.0e+05
2.0e+05
1.0e+05
1106.4070 (1)
1107.4340 (1)
1108.4160 (1)
1109.4309 (1)
1110.4169 (1)
1111.4250 (1)
1112.4336 (1)
1113.4406 (1)
1114.4476 (1)
1115.4520 (1)
1116.4603 (1)
1118.4743 (1)
1120.4839 (1)
1122.4998 (1)
1126.5158 (1)
1105
1110
1115
1120
1125
1130
m/z

Dibrominated Sp-IDT Monomer

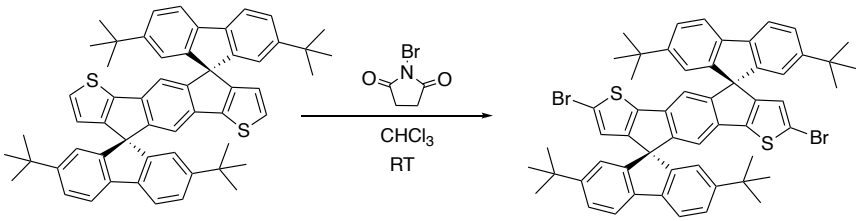

Sp-IDT **dibrominated Sp-IDT**

5 (275 mg, 0.347 mmol, 1 eq) was dissolved in chloroform (50 mL) and N-bromo-succinimide (136 mg, 0.765 mg 2.2 eq) was added. This was stirred at room temperature overnight. After complete reaction, it was poured into a separating funnel and washed with water, brine and sodium sulfate was added. This underwent gravity filtration and the solvent was removed under reduced pressure. This was dispersed using 20 mL chloroform and pipetted into stirring methanol. The precipitate was collected by vacuum filtration, washed with methanol and dried to give am off-white powder **dibrominated Sp-IDT** (303 mg, 92%)

^{1}H NMR (400 MHz, $CDCl_3$) δ 7.74 (d, J = 8.0 Hz, 4H), 7.43 (dd, J = 8.0, 1.8 Hz, 4H), 6.75 (d, 1.8 Hz, 4H), 6.71 (s, 2H), 6.43 (s, 2H) 1.21 (s, 36H)

MS (MALDI-TOF): MS calculated for $[C_{56}H_{52}Br_2S_2]^+$: m/z = 948.19; measured m/z = 948.30

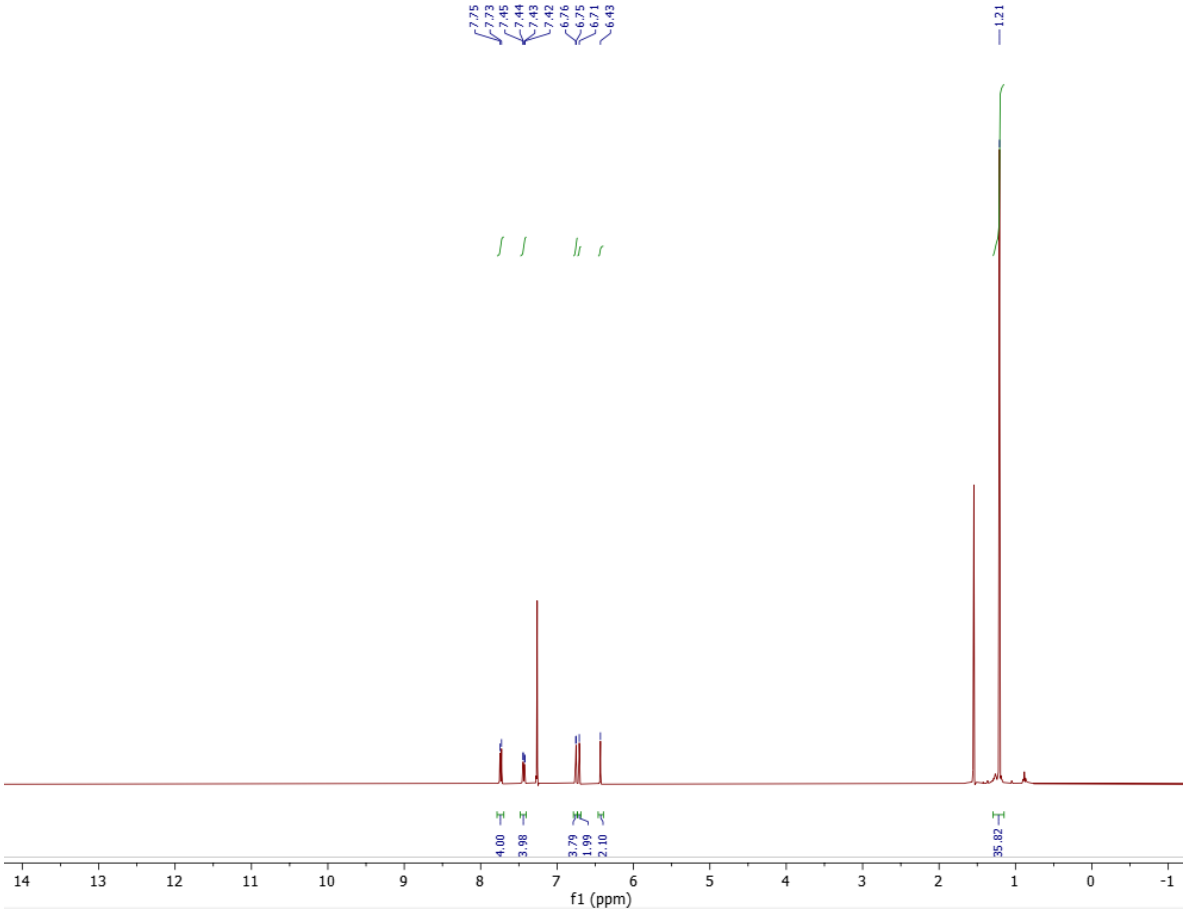
7.75
7.73
7.45
7.44
7.43
7.42
6.76
6.75
6.71
6.43
1.21
4.00
3.98
3.79
1.99
2.10
35.82
14
13
12
11
10
9
8
7
6
5
4
3
2
1
0
-1
f1 (ppm)

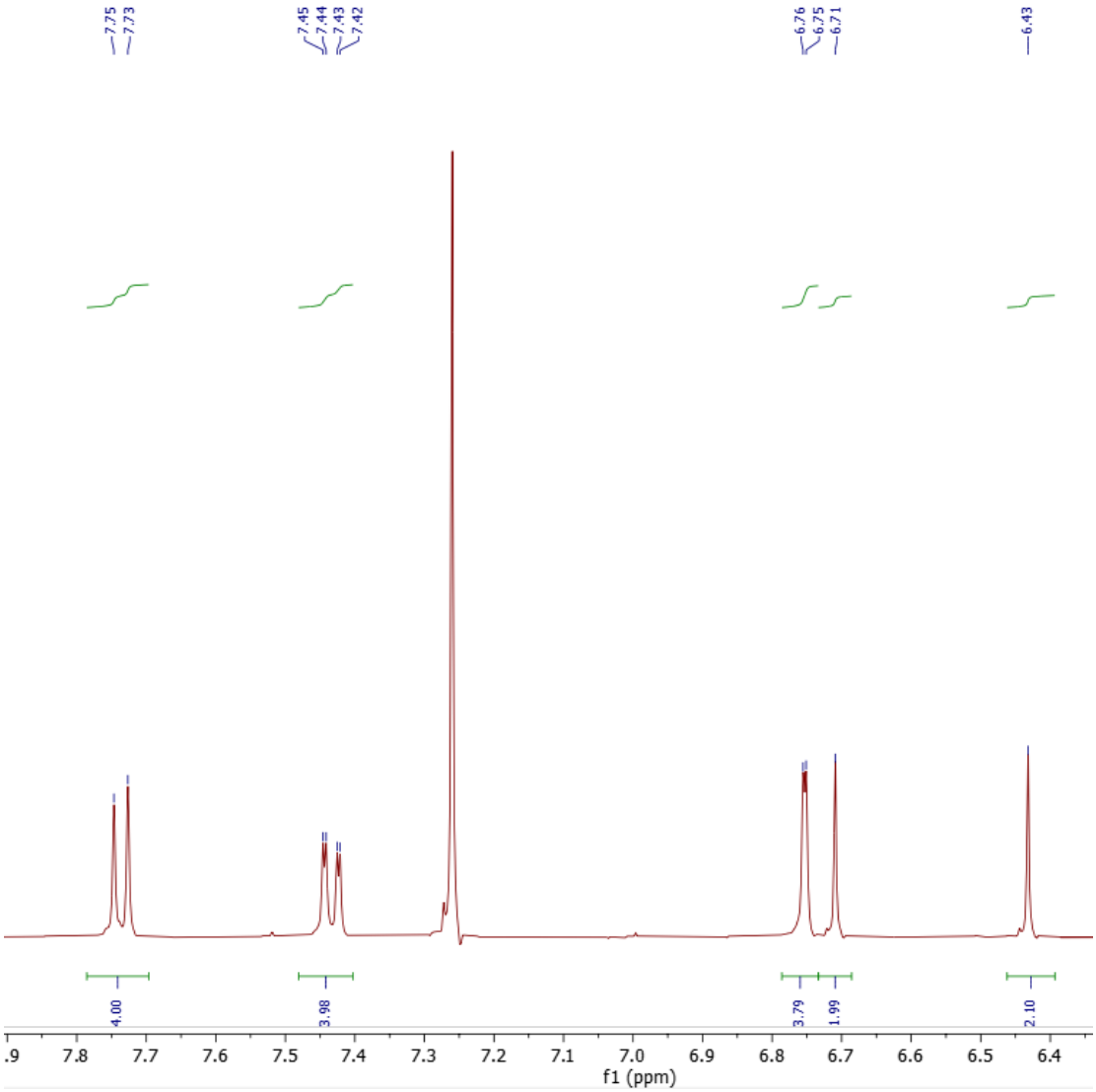
7.75
7.73
7.45
7.44
7.43
7.42
6.76
6.75
6.71
6.43
4.00
3.98
3.79
1.99
2.10
f1 (ppm)

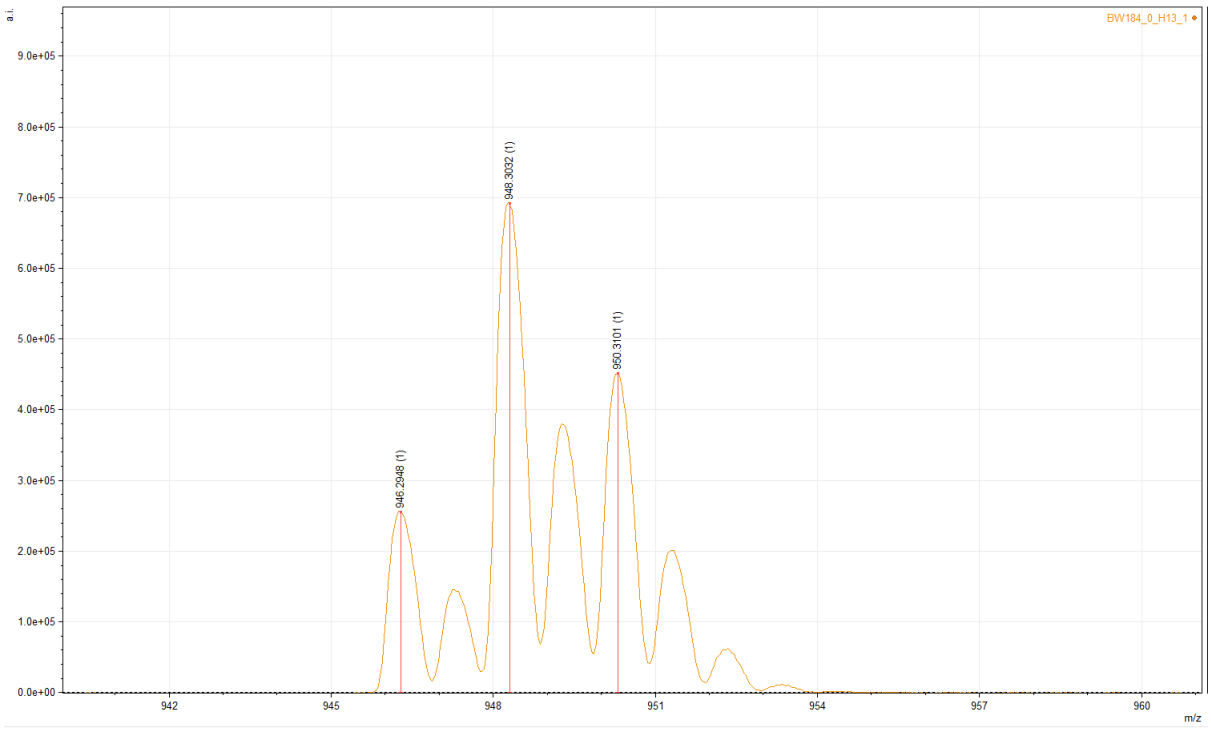
BW184_0_H13_1
948.3032 (1)
950.3101 (1)
946.2948 (1)
m/z

Intermediate 6

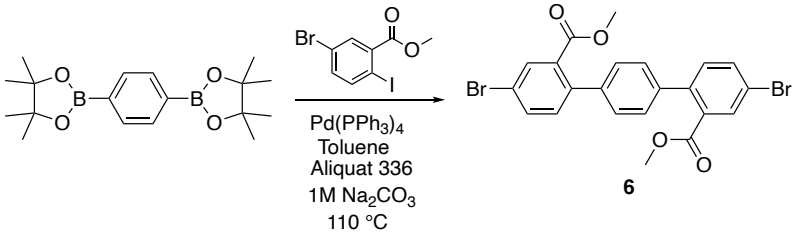

1 M aqueous sodium carbonate solution (122 mL) was degassed with nitrogen for 1 h. At the same time, 1,4-bis(4,4,5,5-tetramethyl-1,3,2-dioxaborolan-2-yl)benzene (10.05 g, 30.4 mmol, 1 eq), methyl 5-bromo-2-iodobenzoate (18.49 g, 67.0 mmol, 2.2 eq) and Aliquat 336 (2 drops) were added to a 2-neck round bottom flask and purged with nitrogen. Degassed toluene (200 mL) was added and the solution was degassed for 30 minutes. All of the degassed sodium carbonate solution was added, followed by palladium tetrakis(triphenylphosphine) (0.70 g, 0.61 mmol, 0.02 eq). It was refluxed overnight and monitored by crude NMR. Once the reaction was complete it was poured into a separating funnel, using ethyl acetate to extract from the aqueous layer. The organic fraction was washed with water, brine and sodium sulfate was added. This underwent gravity filtration, and the solvent was removed under reduced pressure. The brown solid was purified on a silica column eluting with petroleum ether: dichloromethane (60:40) and subsequently recrystallised in dichloromethane: methanol to recover a white crystalline solid **6** (4.93 g, 27%)

^{1}H NMR (400 MHz, d_8-THF) δ 7.93 (d, J = 2.2 Hz, 2H), 7.73 (dd, J = 8.2, 2.2 Hz, 2H), 7.38 (d, J = 8.2 Hz, 2H) 7.31 (s, 4H), 3.62 (s, 6H)

^{13}C NMR (400 MHz, d_8-THF) δ 167.81, 141.82, 140.42, 134.89, 134.14, 133.26, 133.16, 128.90, 121.76, 52.24.

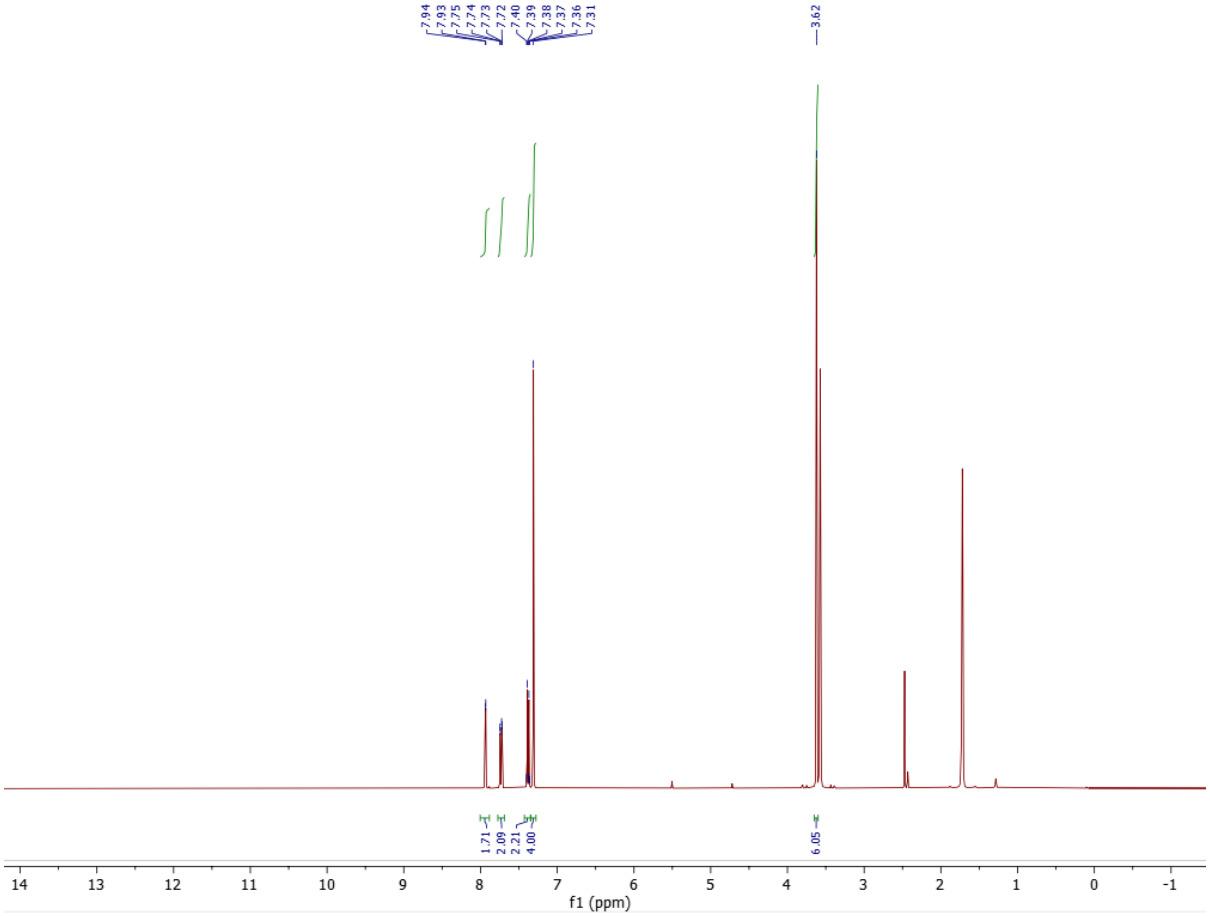
7.94
7.93
7.75
7.74
7.73
7.72
7.40
7.39
7.38
7.37
7.36
7.31
3.62
1.71
2.09
2.21
4.00
6.05
f1 (ppm)

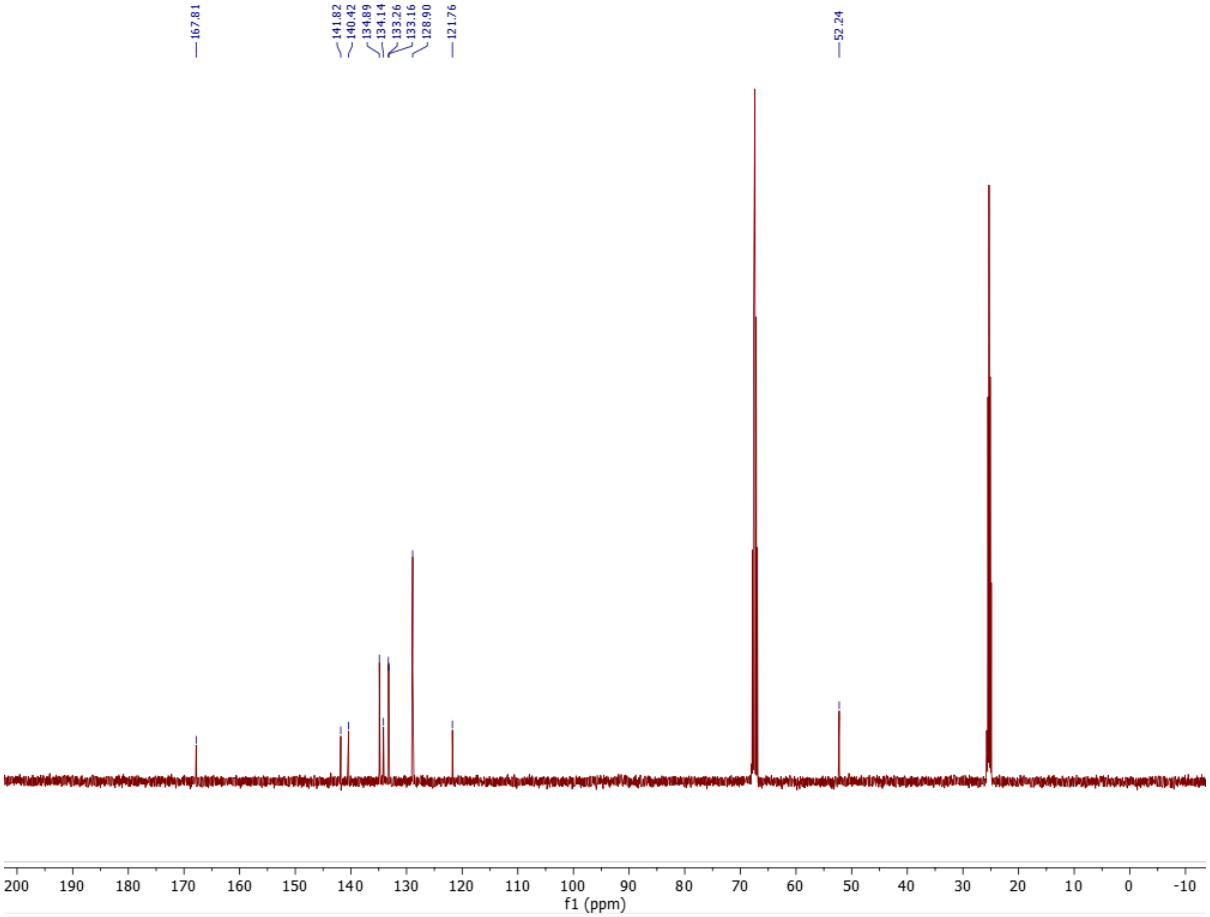
167.81
141.82
140.42
134.89
134.14
133.26
133.16
128.90
121.76
52.24
f1 (ppm)

Intermediate 7

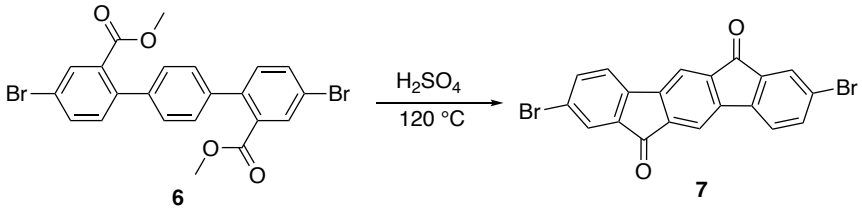

6 (4.14 g, 8.2 mmol, 1 eq) was added to concentrated sulfuric acid (300mL) and stirred at 120 °C overnight. The next day it was cooled then poured into ice water and collected by vacuum filtration, washing sequentially with deionised water, methanol, acetone, dichloromethane, diethyl ether and dried in a vacuum oven to recover a bright pink powder **7** (3.03 g, 84%) This was too insoluble for NMR.

Sp-IF Monomer

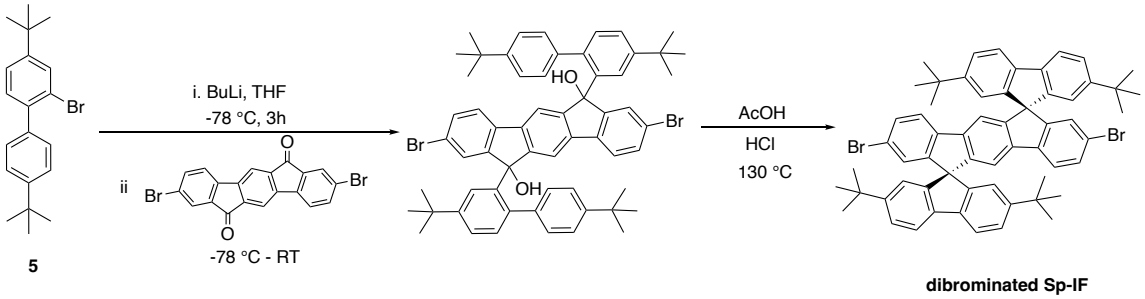

5 (4.86 g, 14.1 mmol, 4 eq) was added to a 2-neck round bottom flask and put under high vacuum attached to a Schlenk line for 30 minutes, then purged with nitrogen. It was dissolved in anhydrous tetrahydrofuran (100 mL) and cooled to -78 °C. n-butyllithium (31.9 mL, 1.6 M, 5 eq) was added slowly whereupon the solution turned yellow and solid began to precipitate. This was left stirring at -78 °C for 3 h under nitrogen. Finely divided and vacuum oven dried **7** (1.55 g, 3.5 mmol, 1 eq) was quickly added through the side neck under a positive pressure of nitrogen. This was left stirring overnight under nitrogen and allowed to reach room temperature. The tetrahydrofuran was removed under reduced pressure, then the alcohol intermediate was extracted with dichloromethane in a separating funnel, washing with water, brine and sodium sulfate was added to dry. This underwent gravity filtration, and the solvent was removed under reduced pressure. Acetic acid (100 mL) and 37% aqueous hydrochloric acid solution (10 mL) were added, and it was refluxed overnight. This was then cooled and poured into icy water, then neutralised with sodium hydroxide solution. The precipitate was collected by vacuum filtration, washing thoroughly with deionised water and methanol. After drying, the powder was collected and dissolved in a minimum volume of chloroform. Methanol (300 mL) was added under stirring to cause the product to precipitate. This was collected by vacuum filtration, washed again with methanol, acetonitrile and acetone, then dried in a vacuum oven, to give a white powder (2.51 g, 76%). This was too insoluble for ^{13}C NMR

^{1}H NMR (400 MHz, $CDCl_3$) δ 7.78 (d, J = 8.1 Hz 4H), 7.46-7.43 (m, 6H), 7.35 (dd, J = 8.2, 1.8 Hz, 2H), 7.12 (s, 2H), 6.80 (d, 1.8 Hz, 2H), 6.69 (d, J = 1.7 Hz, 4H), 1.18 (s, 36H)

MS (MALDI-TOF): MS calculated for $[C_{60}H_{56}Br_2]^+$: m/z =936.27; measured m/z = 936.44

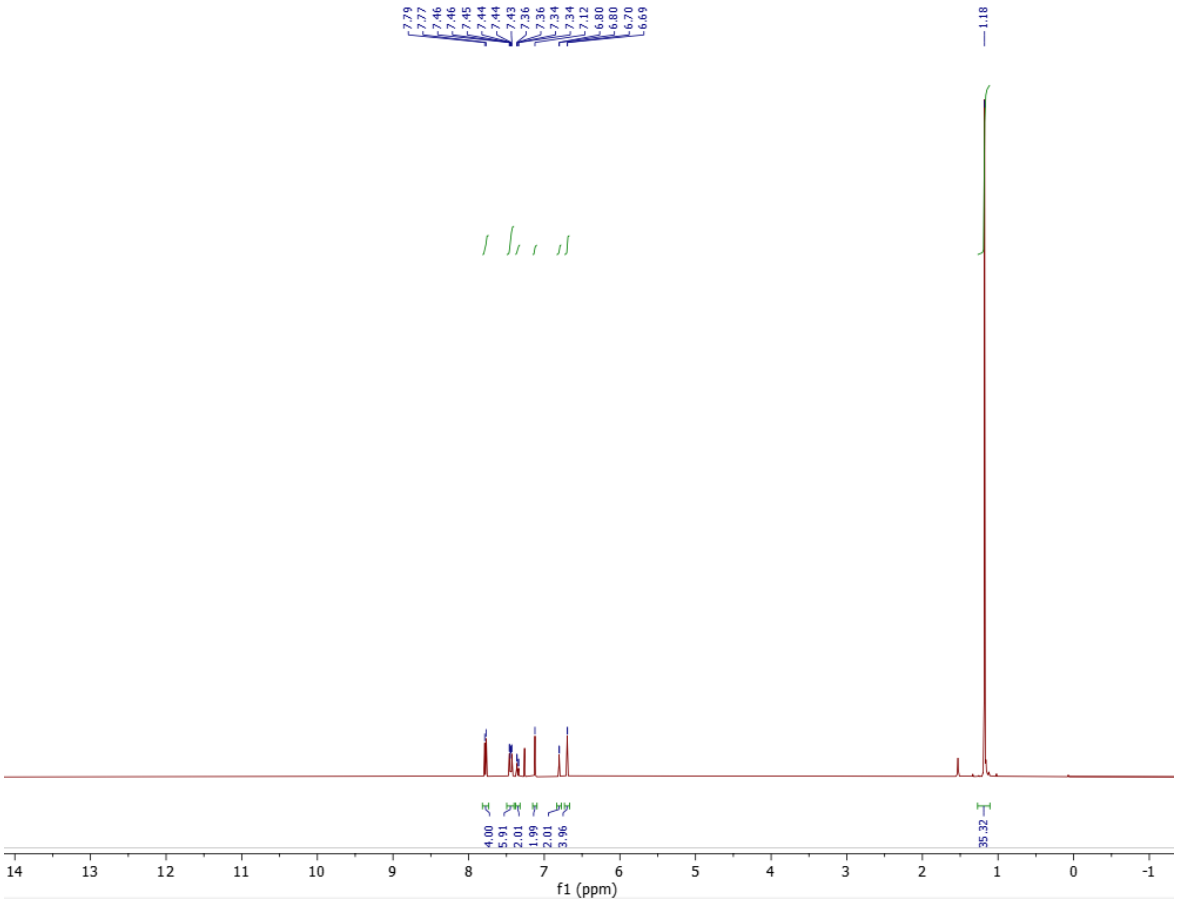

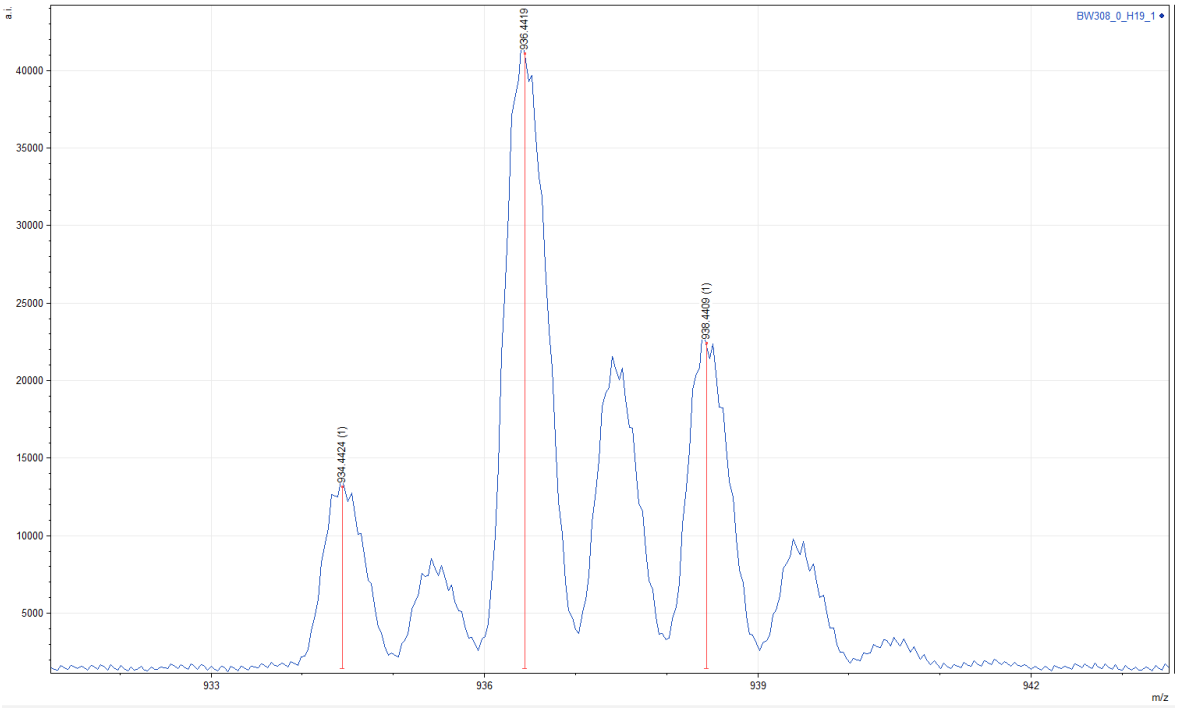
a.i.
BW308_0_H19_1
40000
35000
30000
25000
20000
15000
10000
5000
934.4424 (1)
936.4419
938.4409 (1)
933
936
939
942
m/z

Sp-IDT-BT Polymer

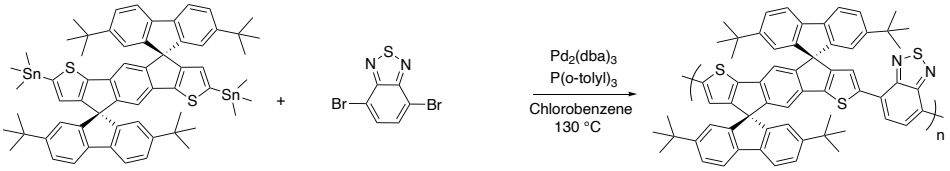

Sp-IDT-BT

Distannylated IDT-Sp (79.59 mg, 71 µmol, 1 eq), 4,7-dibromo-2,1,3-benzothiadiazole (20.95 mg, 71 µmol, 1 eq), tri(o-tolyl)phosphine (1.7 mg, 6 µmol, 0.08 eq) and tris(dibenzylideneacetone)dipalladium(0) (1.3 mg, 1 µmol, 0.02 eq) were added to a microwave vial, it was capped then degassed with nitrogen for 30 minutes. Anhydrous chlorobenzene (1.5 mL) was added and it was heated to 130 °C overnight. This was cooled, precipitated into methanol and poured into a cellulose Soxhlet thimble. This underwent a Soxhlet extraction washing with acetone followed by hexane, ethyl acetate then extracted with chloroform followed by another extraction with chlorobenzene. The insoluble polymer remained in the Soxhlet thimble. This was collected to give a dark blue powder polymer **Sp-IDT-BT** (60 mg, 92 %). This was not soluble enough for NMR.

Intermediate 8

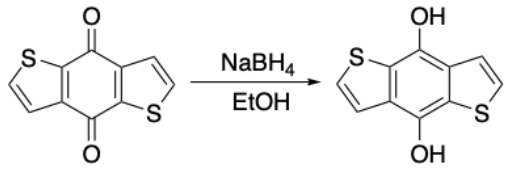

8

Benzo[1,2-b:4,5-b′]dithiophene-4,8-dione (5.00 g, 22.7 mmol, 1 eq) was stirred under nitrogen in degassed ethanol (400 mL). Sodium borohydride (3.40 g, 90.1 eq, 4 eq) was added in several portions to prevent an uncontrolled increase in temperate and gas evolution. This formed a blood red solution which was stirred vigerously at room temperature overnight under nitrogen. This was poured into a mixture of ice and 1M hydrochloric acid to form a green precipitate which was filtered, washing with water and methanol then dried in a vacuum oven to give a dark green solid **8**, which was stored under nitrogen at low temperature to avoid oxidation in air (4.69 g, 93 %). It was too insoluble for ^{13}C NMR.

^{1}H NMR (400 MHz, d-DMSO) δ 9.79 (s, 2H), 7.61 (d, J = 5.5 Hz, 2H), 7.54 (d, J = 5.5 Hz, 2H)

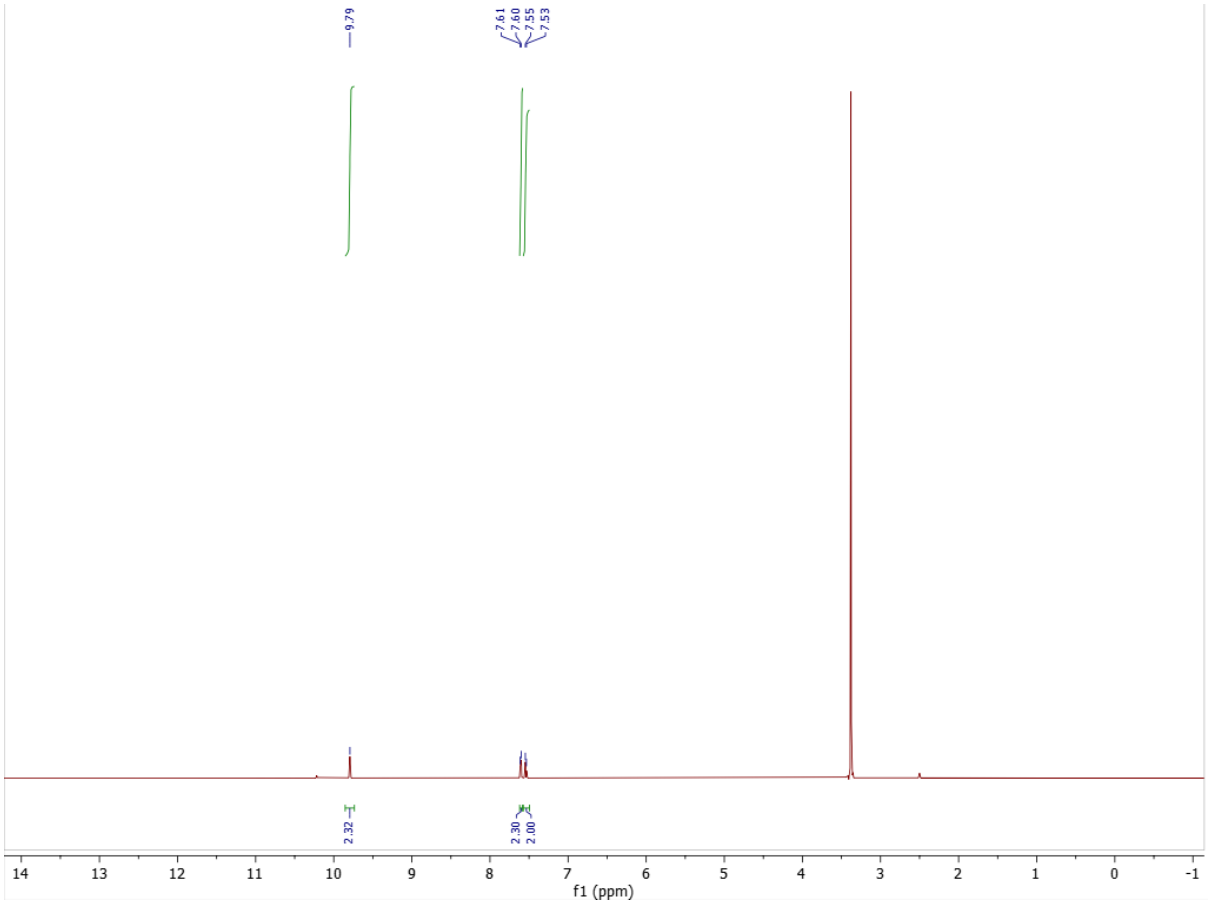
9.79
7.61
7.60
7.55
7.53
2.32
2.30
2.00
14
13
12
11
10
9
8
7
6
5
4
3
2
1
0
-1
f1 (ppm)

Intermediate 9

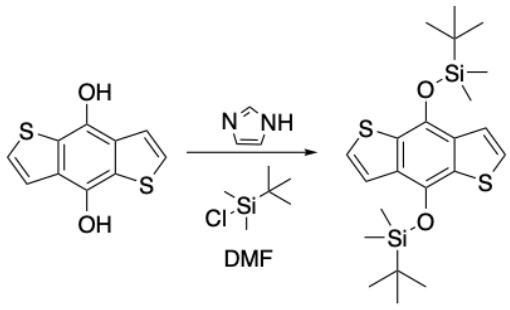

8 **9**

8 (3.50 g, 15.7 mmol, 1 eq), tert-butyldimethylsilyl chloride (11.87 g, 78.7, 5 eq) and imidazole (10.72 g, 157.5 mmol, 10 eq) were added to a 2-neck round bottom flask and purged with nitrogen. Anhydrous dimethylformamide (200 mL) was added and it was stirred at 50 °C overnight under nitrogen. Most of the solvent was removed under reduced pressure, then it was poured into a separating funnel with water. The product was extracted with dichloromethane and washed twice with water, once with brine and sodium sulfate was added. This underwent gravity filtration, and the solvent was removed under reduced pressure. The resultant yellow-green solid was purified on a silica column, eluting with petroleum ether: dichloromethane (20:80) giving a colourless solid **9** (4.59 g, 64%)

^{1}H NMR (400 MHz, $CDCl_3$) δ 7.38 (d, *J* = 5.6 Hz, 2H), 7.28 (d, *J* = 5.6 Hz, 2H), 1.14 (s, 18H), 0.25 (s, 12H).

^{13}C NMR (400 MHz, $CDCl_3$) δ 139.40, 130.63, 129.39, 124.86, 120.79, 25.98, 18.57, -3.41.

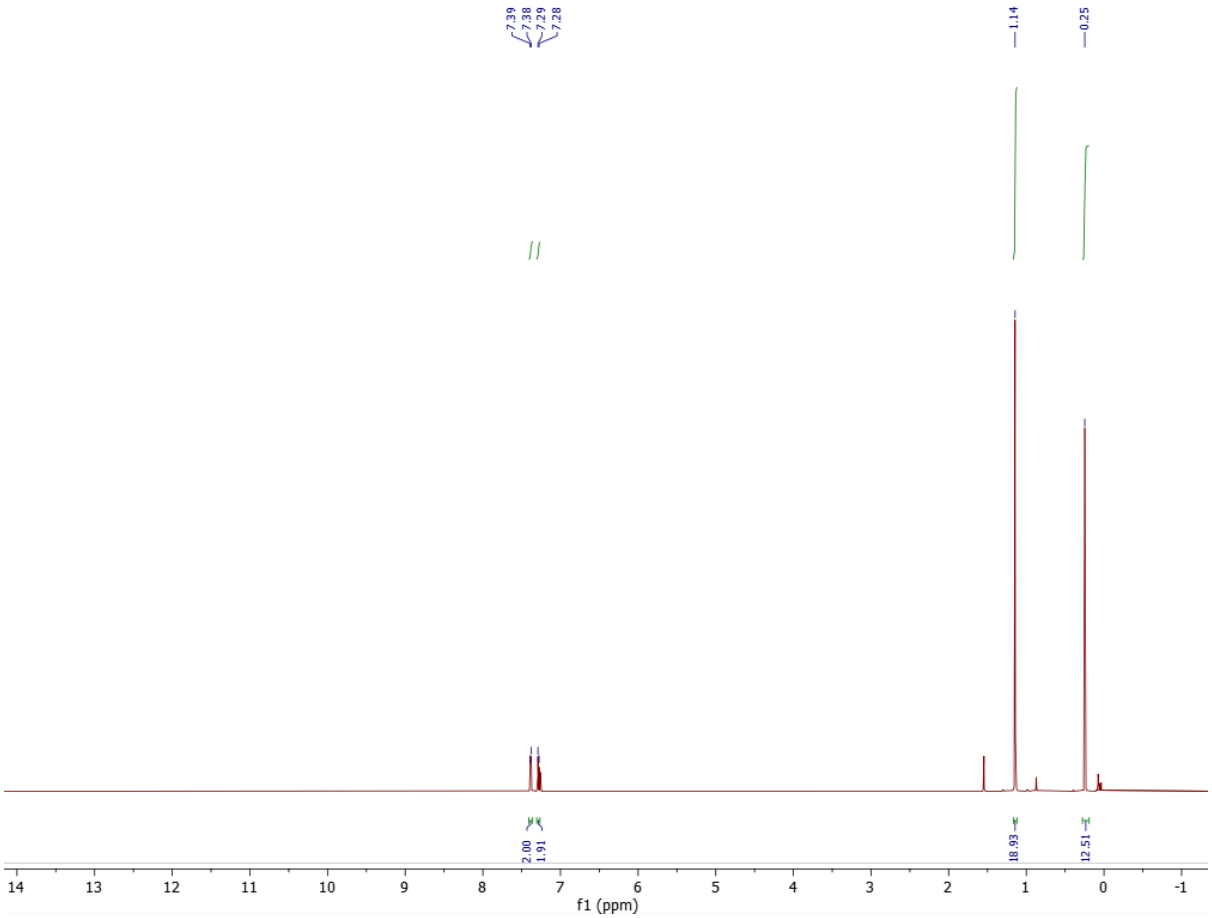
7.39
7.38
7.29
7.28
1.14
0.25
2.00
1.91
18.93
12.51
14
13
12
11
10
9
8
7
6
5
4
3
2
1
0
-1
f1 (ppm)

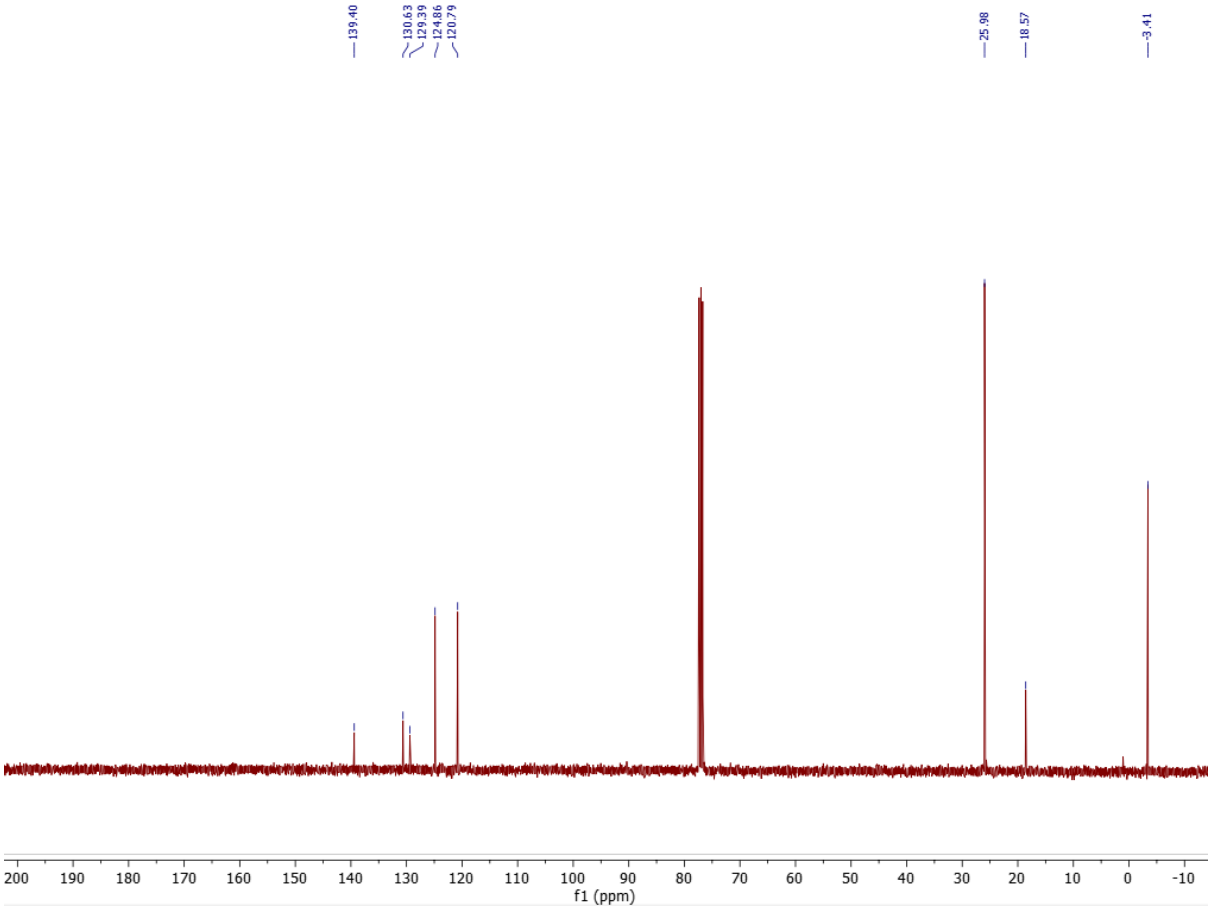
139.40
130.63
129.39
124.86
120.79
25.98
18.57
-3.41
200 190 180 170 160 150 140 130 120 110 100 90 80 70 60 50 40 30 20 10 0 -10
f1 (ppm)

DBDT-Si Monomer

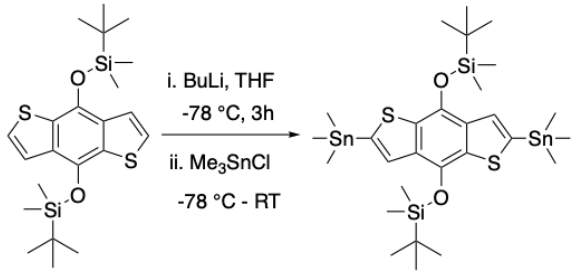

9 distannylated BDT-Si

9 (400 mg, 0.89 mmol, 1 eq) was purged with nitrogen and dissolved in anhydrous tetrahydrofuran (50 mL). This was cooled to -78 °C and n-butyllithium (1.4 mL, 1.6 M, 2.5 eq) was added dropwise and it was stirred under nitrogen for 3 h. Trimethyltin chloride (2.7 mL, 1M, 3 eq) was added and it was allowed to stir under nitrogen reaching room temperature overnight. The next day the product was extracted with dichloromethane in a separating funnel, washing twice with water, brine and sodium sulfate was added. Gravity filtration was undertaken, and the solvent was removed under reduced pressure. The off-white solid was recrystallised in dichloromethane: methanol to recover a colourless crystalline solid (590 mg, 86%)

^{1}H NMR (400 MHz, $CDCl_3$) δ 7.44 (s, 2H), 1.16 (s, 18H), 0.42 (s, 18H), 0.25 (s, 12H)

^{13}C NMR (400 MHz, $CDCl_3$) δ 139.12, 138.18, 133.72, 132.01, 129.00, 26.21, 18.77, -3.24, -8.23.

MS (MALDI-TOF): MS calculated for $[C_{28}H_{50}O_2S_2Si_2Sn_2]^+$: m/z = 776.08; measured m/z = 776.21

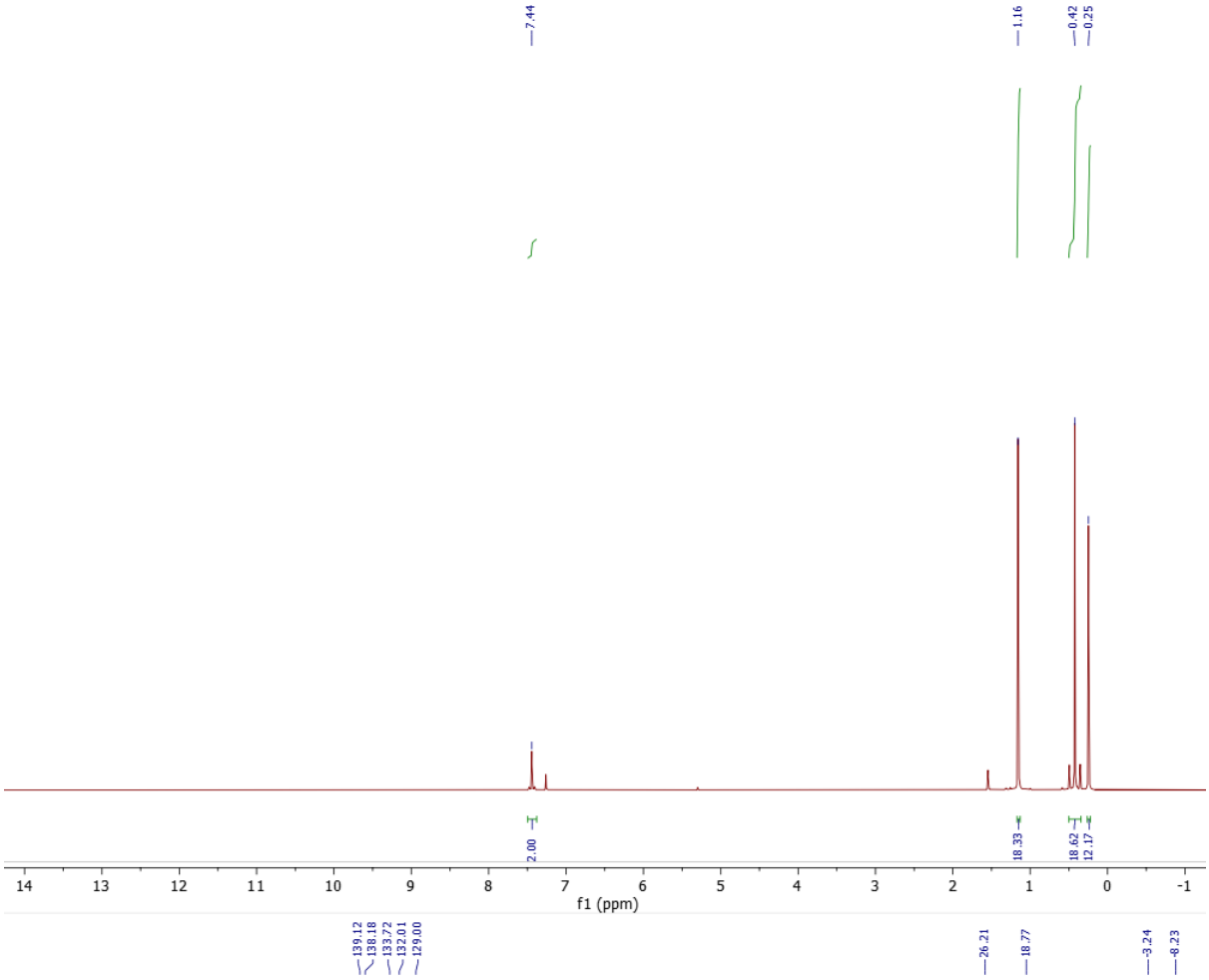
7.44
1.16
0.42
0.25
2.00
18.33
18.62
12.17
f1 (ppm)
139.12
138.18
133.72
132.01
129.00
26.21
18.77
-3.24
-8.23
f1 (ppm)

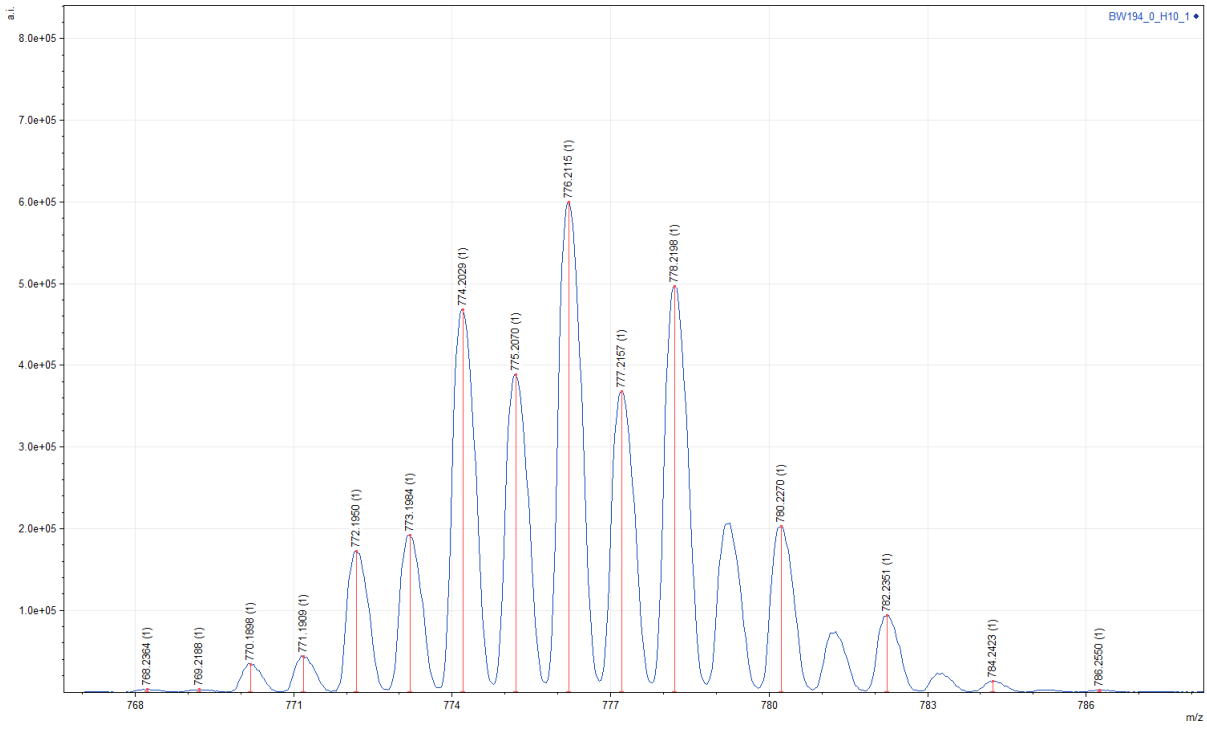
BW194_0_H10_1
a.i.
8.0e+05
7.0e+05
6.0e+05
5.0e+05
4.0e+05
3.0e+05
2.0e+05
1.0e+05
768.2364 (1)
769.2188 (1)
770.1898 (1)
771.1909 (1)
772.1950 (1)
773.1984 (1)
774.2029 (1)
775.2070 (1)
776.2115 (1)
777.2157 (1)
778.2198 (1)
780.2270 (1)
782.2351 (1)
784.2423 (1)
786.2550 (1)
768
771
774
777
780
783
786
m/z

Sp-IDT-BDT-Si Polymer

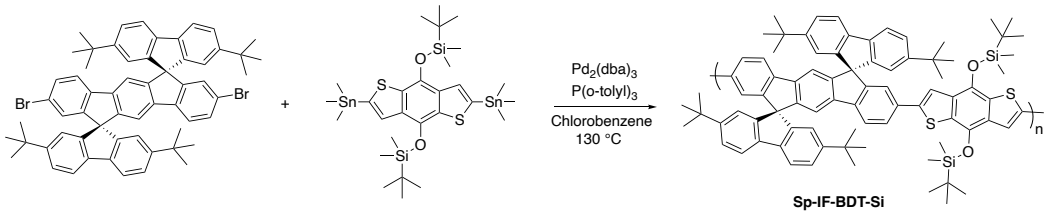

Sp-IF-BDT-Si

BDT-Si (98.67 mg, 127 µmol, 1 eq), Sp-IF (119.07 mg, 127 µmol, 1 eq), tri(o-tolyl)phosphine (3.1 mg, 12 µmol, 0.08 eq) and tris(dibenzylideneacetone) dipalladium(0) (2.3 mg, 3 µmol, 0.02 eq) were added to a microwave vial, it was capped then degassed with nitrogen for 30 minutes. Anhydrous chlorobenzene (2.5 mL) was added, and it was heated to 130 °C overnight. This was cooled, precipitated into methanol and poured into a cellulose Soxhlet thimble. This underwent a Soxhlet extraction washing with acetone followed by hexane, ethyl acetate then extracted with chloroform followed by another extraction with chlorobenzene. The chloroform fraction and chlorobenzene fractions were combined, concentrated under reduced pressure, then precipitated into methanol and collected by vacuum filtration to give a yellow-orange solid polymer **Sp-IF-BDT-Si** (55 mg, 35%). It was too poorly soluble for chloroform NMR.

GPC chlorobenzene M_N 5894 gmol^{-1}, M_W 6970 gmol^{-1}, PD 1.183

Intermediate 10

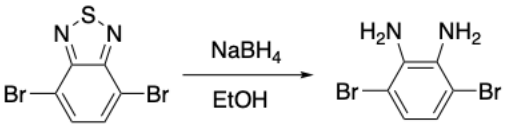

10

4,7-Dibromo-2,1,3-benzothiadiazole (20.0 g, 68.0 mmol, 1 eq) and ethanol (500 mL) were cooled to 0 °C. Sodium borohydride (25.7 g, 680.4 mmol, 10 eq) was added in portions with under stirring and it was allowed to reach room temperature overnight. The ethanol was removed under reduced pressure, ethyl acetate was added and everything was transferred to a separating funnel along with water. The organic fraction was extracted and washed with water, brine and sodium sulfate was added. This underwent gravity filtration, and the solvent was removed. This was purified on a silica column, eluting with petroleum ether: (40:60). After removing the solvent from the fractions containing product, a white solid **10** was recovered (15.4 g, 84%)

^{1}H NMR (400 MHz, d$_6$-DMSO) δ 6.64 (s, 2H), 5.01 (s, 4H)

^{13}C NMR (400 MHz, d$_6$-DMSO) δ 133.17, 120.68, 106.63.

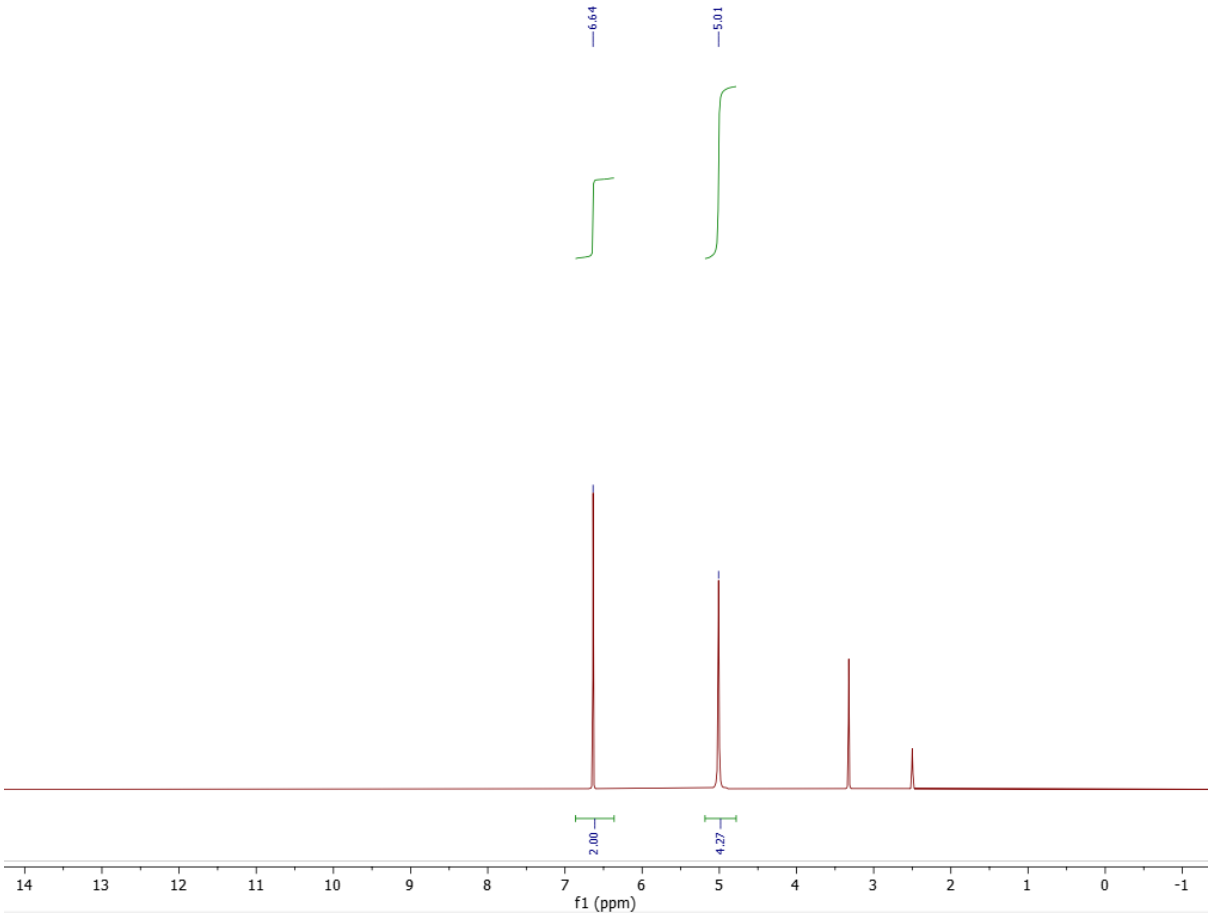
6.64
5.01
2.00
4.27
14 13 12 11 10 9 8 7 6 5 4 3 2 1 0 -1
f1 (ppm)

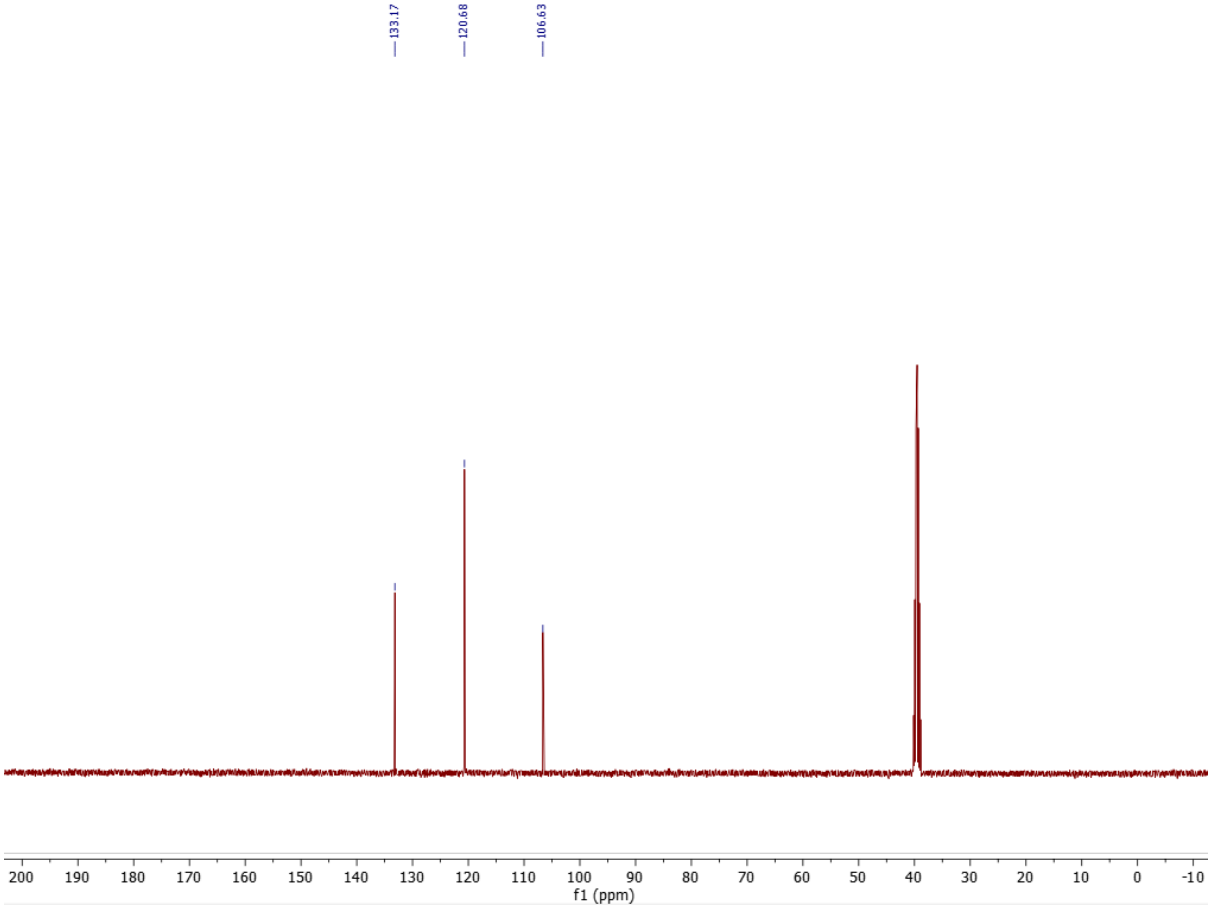
133.17
120.68
106.63
200 190 180 170 160 150 140 130 120 110 100 90 80 70 60 50 40 30 20 10 0 -10
f1 (ppm)

Intermediate 11

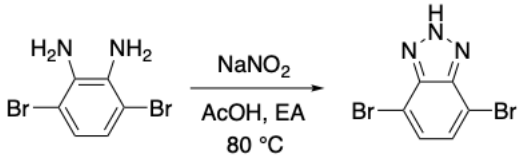

10 **11**

10 (3.69 g, 18.9 mmol, 1 eq) was dissolved in acetic acid (50 mL) and ethyl acetate (20 mL). Sodium nitrite (1.15 g, 16.7 mmol, 1.2 eq) was added in portions under stirring and it was refluxed for 4 h, by which time product had precipitated out somewhat. This was poured into ice water, neutralised with sodium hydroxide solution then transferred to a separating funnel. Ethyl acetate was added to extract the product, which was subsequently washed with water, brine and sodium sulfate was added. This underwent gravity filtration, and the solvent was removed to give a pale slightly pink solid **11** (3.41, 89%). This was too insoluble for ^{13}C NMR.

^{1}H NMR (400 MHz, $CDCl_3$) δ 12.14 (s, br, 1H) 7.51 (s, 2H)

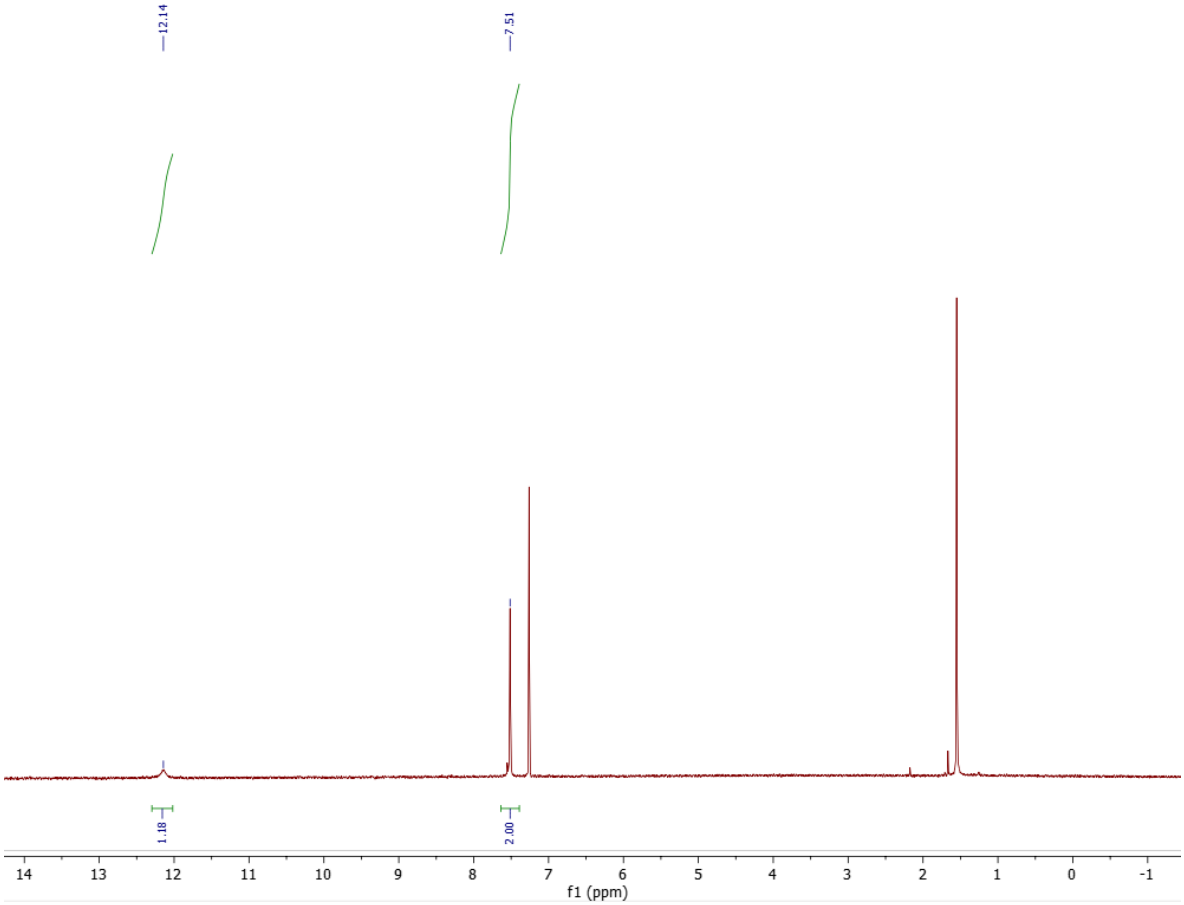

Intermediate 12

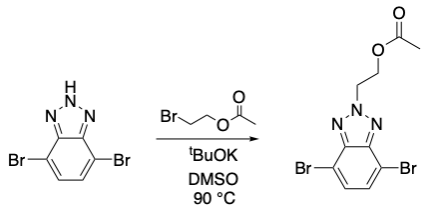

11 (1.5 g, 5.4 mmol, 1 eq), and potassium tert-butoxide (0.73, 6.5 mmol, 1.2 eq) were added to a 2-neck round bottom flask and purged with nitrogen. Anhydrous dimethyl sulfoxide (50 mL) was added and it was stirred at 90 °C for 10 minutes, whereupon the solution turned blue following deprotonation. 2-bromoethyl acetate (0.9 mL, 1.27 g, 7.6 mmol, 1.4 eq) was added dropwise and it was left stirring at 90 °C for 4 h. After complete reaction it was poured into a separating funnel along with water. The product was extracted with ethyl acetate and washed twice with water, once with brine and sodium sulfate was added. This underwent gravity filtration, and the solvent was removed under reduced pressure. This was purified on a silica column, eluting with a graduated eluent, from pure dichloromethane to dichloromethane: ethyl acetate (95:5). The first fraction was collected and removal of solvent from the gave a colourless solid **12** (0.98 g, 50%).

^{1}H NMR (400 MHz, $CDCl_3$) δ 7.45 (s, 2H), 5.02 (t, J = 5.2 Hz, 2H), 4.74 (t, J = 5.2 Hz, 2H), 2.03 (s, 2H)

^{13}C NMR (400 MHz, $CDCl_3$) δ 170.62, 144.13, 130.05, 110.22, 61.92, 56.00, 20.83.

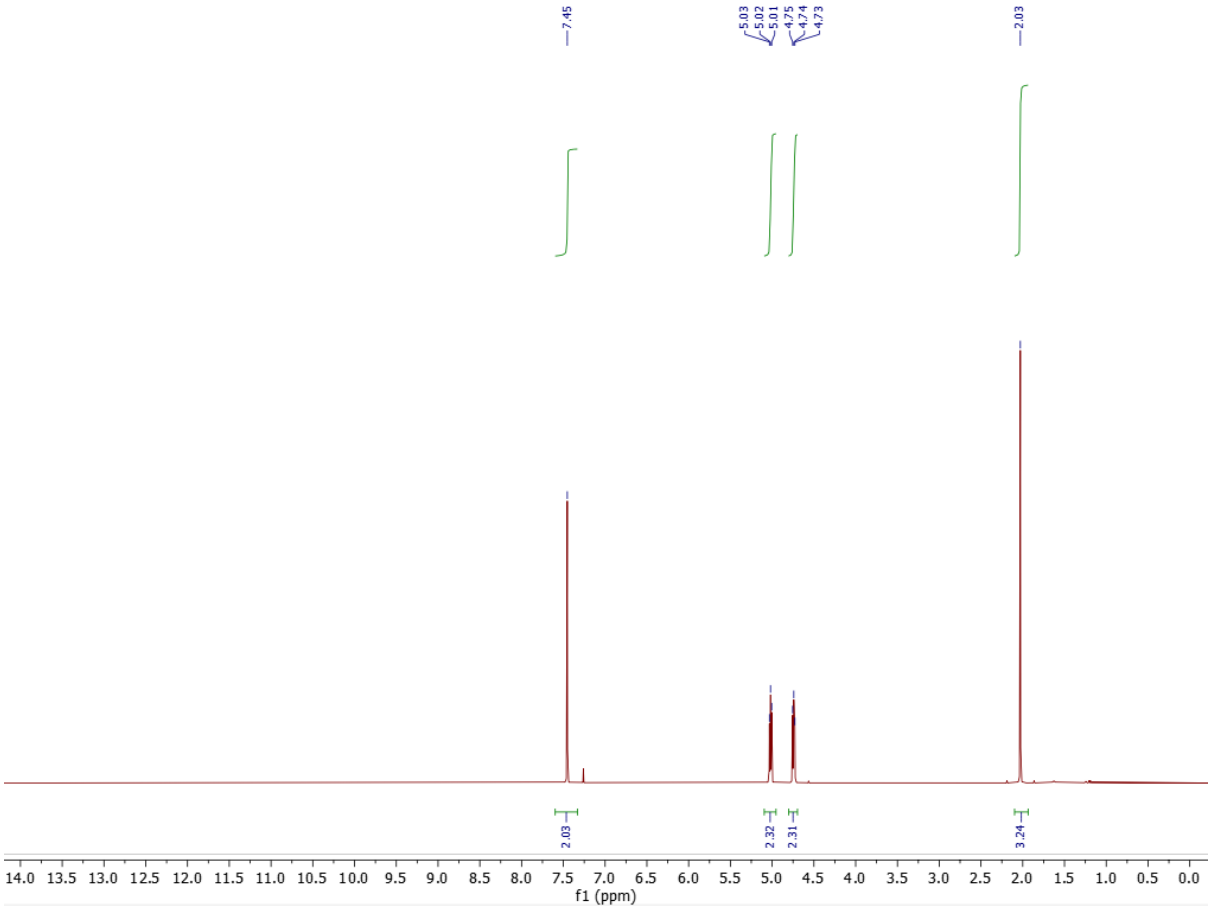
7.45
5.03
5.02
5.01
4.75
4.74
4.73
2.03
2.03
2.32
2.31
3.24
14.0 13.5 13.0 12.5 12.0 11.5 11.0 10.5 10.0 9.5 9.0 8.5 8.0 7.5 7.0 6.5 6.0 5.5 5.0 4.5 4.0 3.5 3.0 2.5 2.0 1.5 1.0 0.5 0.0
f1 (ppm)

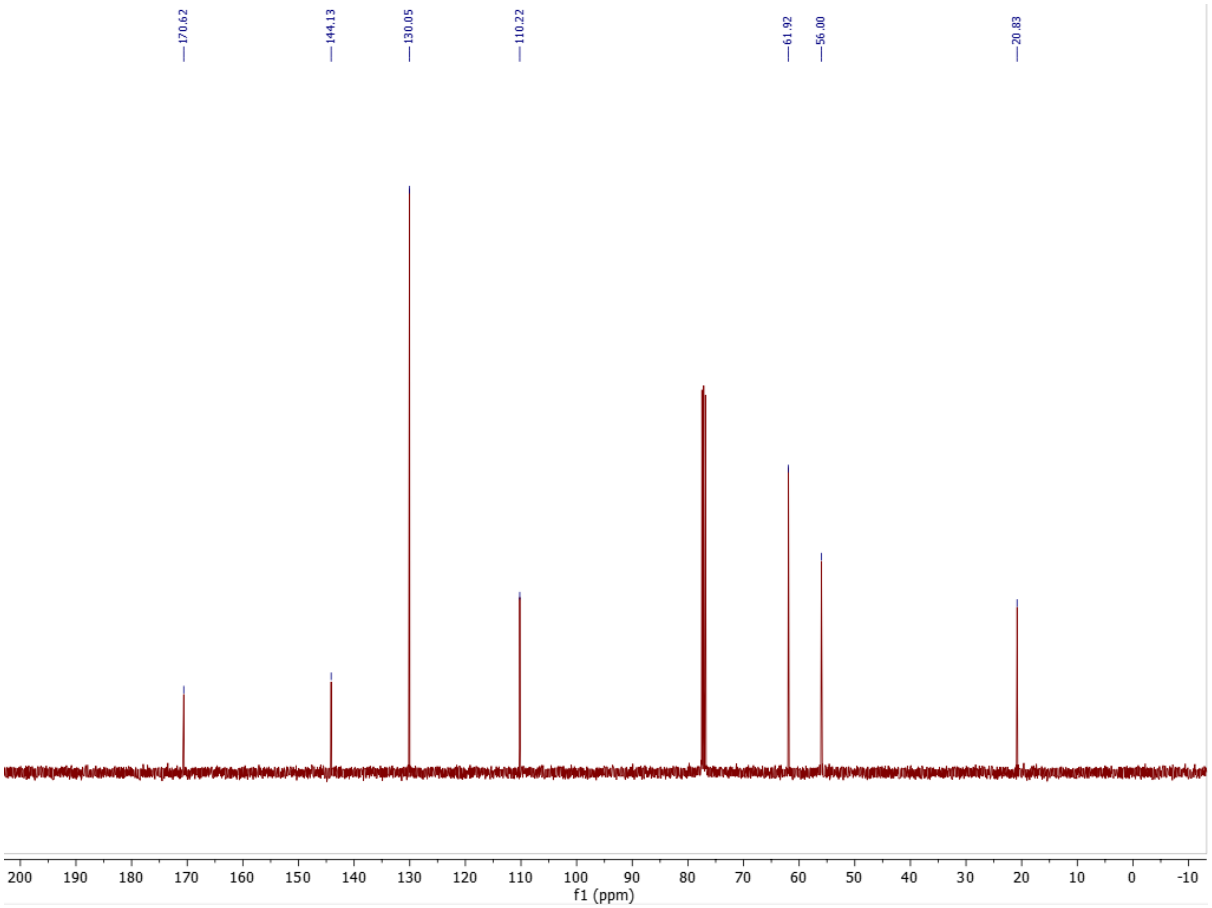
170.62
144.13
130.05
110.22
61.92
56.00
20.83
200 190 180 170 160 150 140 130 120 110 100 90 80 70 60 50 40 30 20 10 0 -10
f1 (ppm)

Intermediate 13

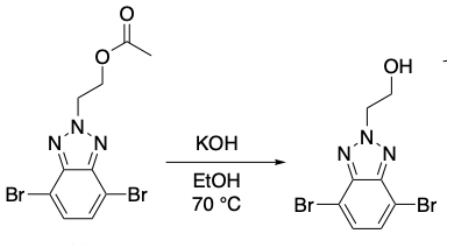

12 13

12 (0.97 g, 2.7 mmol, 1 eq), potassium hydroxide (0.6 g, 10.7 mmol, 4 eq) and ethanol (300 mL) were refluxed overnight. Most of the ethanol was removed under reduced pressure, then the solution was poured into a separating funnel with ethyl acetate and water. The product was extracted with ethyl acetate and washed twice with water, once with brine and sodium sulfate was added. This underwent gravity filtration, and the solvent was removed under reduced pressure. This was recrystallised in ethanol to give colourless crystals (0.57 g, 66%)

^{1}H NMR (400 MHz, $CDCl_3$) δ 7.46 (s, 2H), 4.95 (t, J = 5.0 Hz, 2H), 4.31 (t, J = 5.0 Hz, 2H), 2.80 (s, 2H)

^{13}C NMR (400 MHz, $CDCl_3$) δ 143.92, 130.12, 110.14, 61.05, 59.35

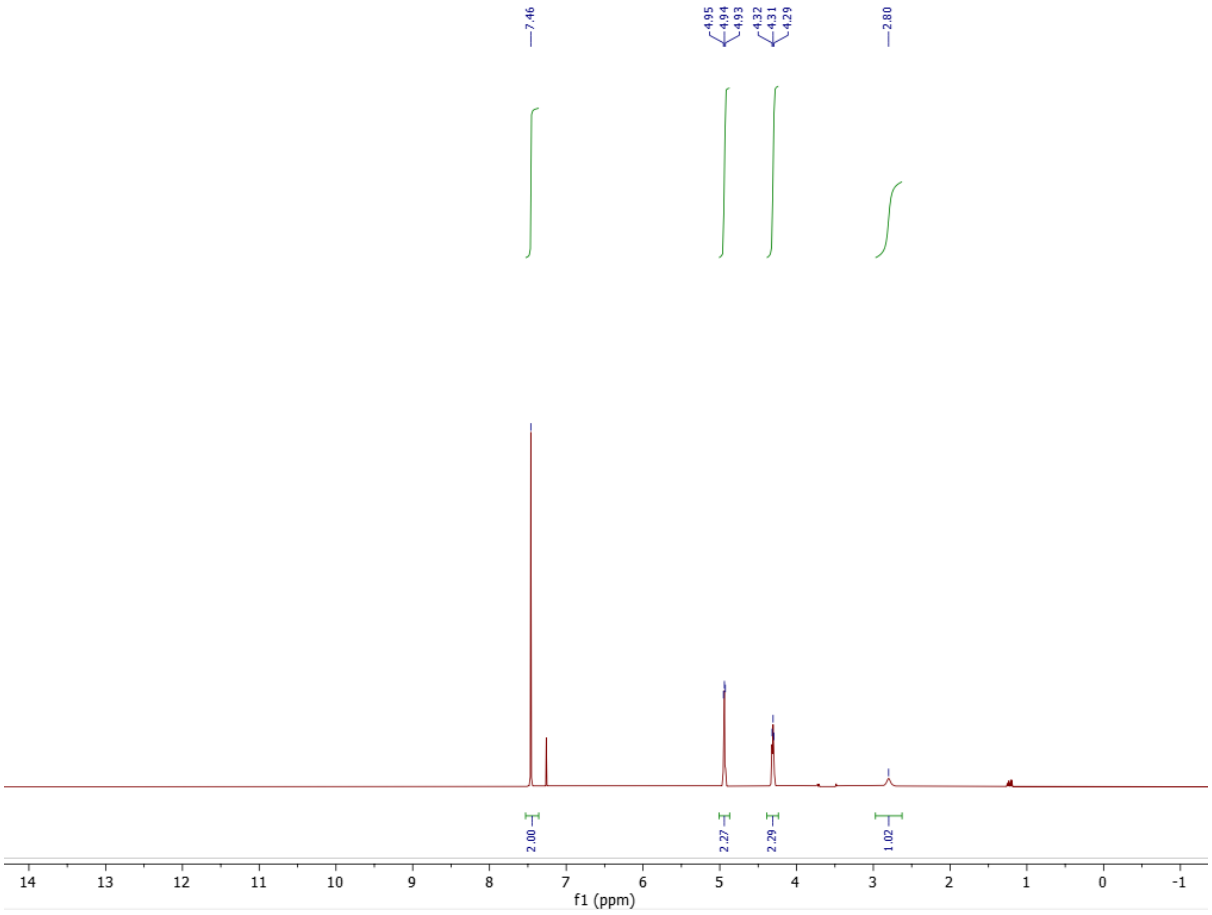
7.46
4.95
4.94
4.93
4.32
4.31
4.29
2.80
2.00
2.27
2.29
1.02
14 13 12 11 10 9 8 7 6 5 4 3 2 1 0 -1
f1 (ppm)

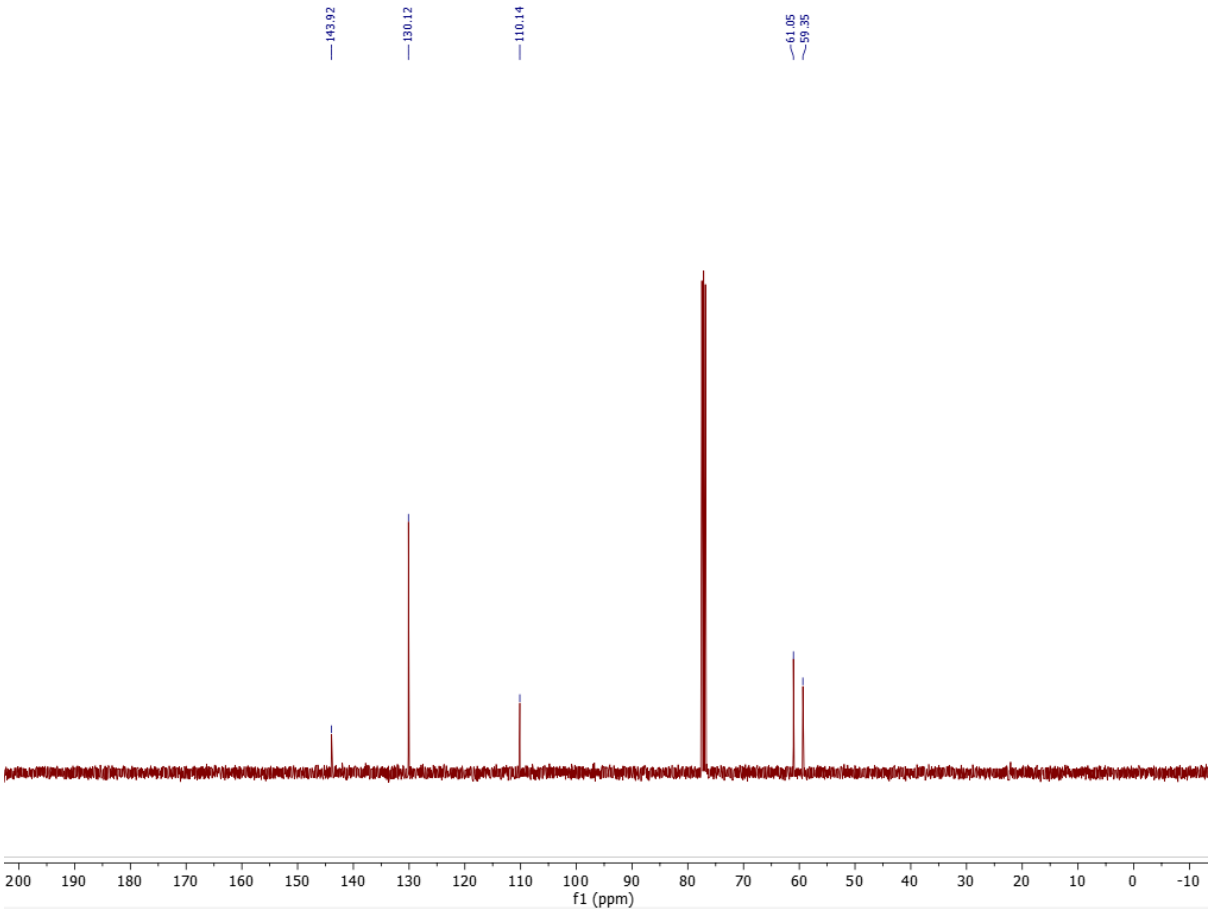
143.92
130.12
110.14
61.05
59.35
200 190 180 170 160 150 140 130 120 110 100 90 80 70 60 50 40 30 20 10 0 -10
f1 (ppm)

Intermediate 14

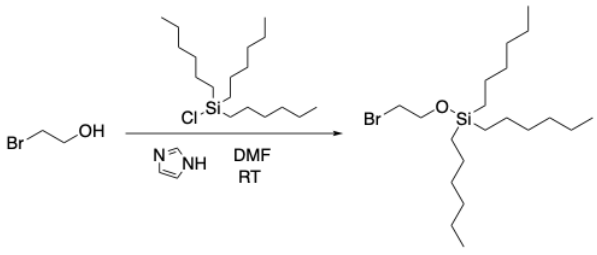

14

2-bromoethanol (1.77 g, 14.2 mmol, 0.9 eq) trihexylsilyl chloride (5.03 g, 15.8 mmol, 1 eq) and imidazole (2.15g, 31.5 mmol, 2 eq) were purged with nitrogen and dissolved in anhydrous dimethylformamide (100 mL). This was stirred for 4 h then poured into a separating funnel. The product was extracted with dichloromethane and washed twice with water, once with brine and sodium sulfate was added. This underwent gravity filtration, and the solvent was removed under reduced pressure to recover a colourless oil **14** which was used without further purification (4.98 g, 86%).

^{1}H NMR (400 MHz, $CDCl_3$) δ 3.86 (t, J = 6.7 Hz, 2H), 3.38 (t, J = 6.7 Hz, 2H), 1.32-1.26 (m, 24H), 0.90-0.87 (m, 9H), 0.62-0.58 (m, 6H)

^{13}C NMR (400 MHz, $CDCl_3$) δ 63.37, 33.43, 33.16, 31.67, 23.19, 22.75, 14.26, 13.72.

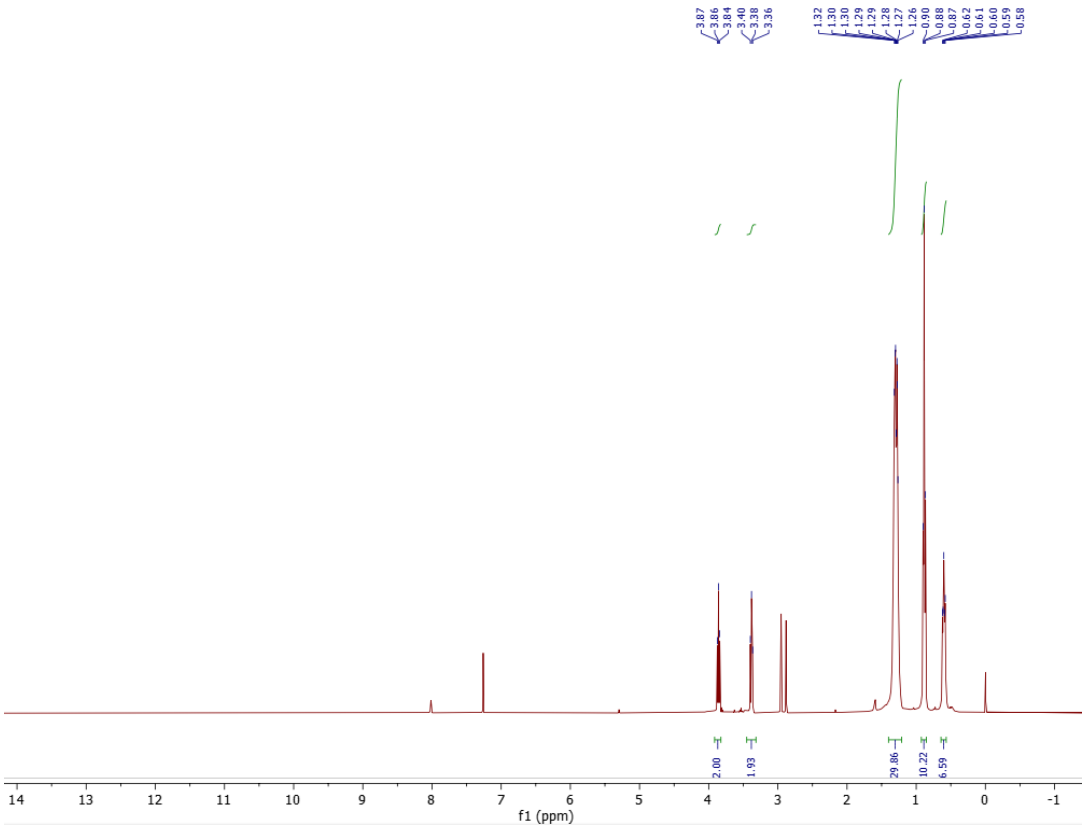

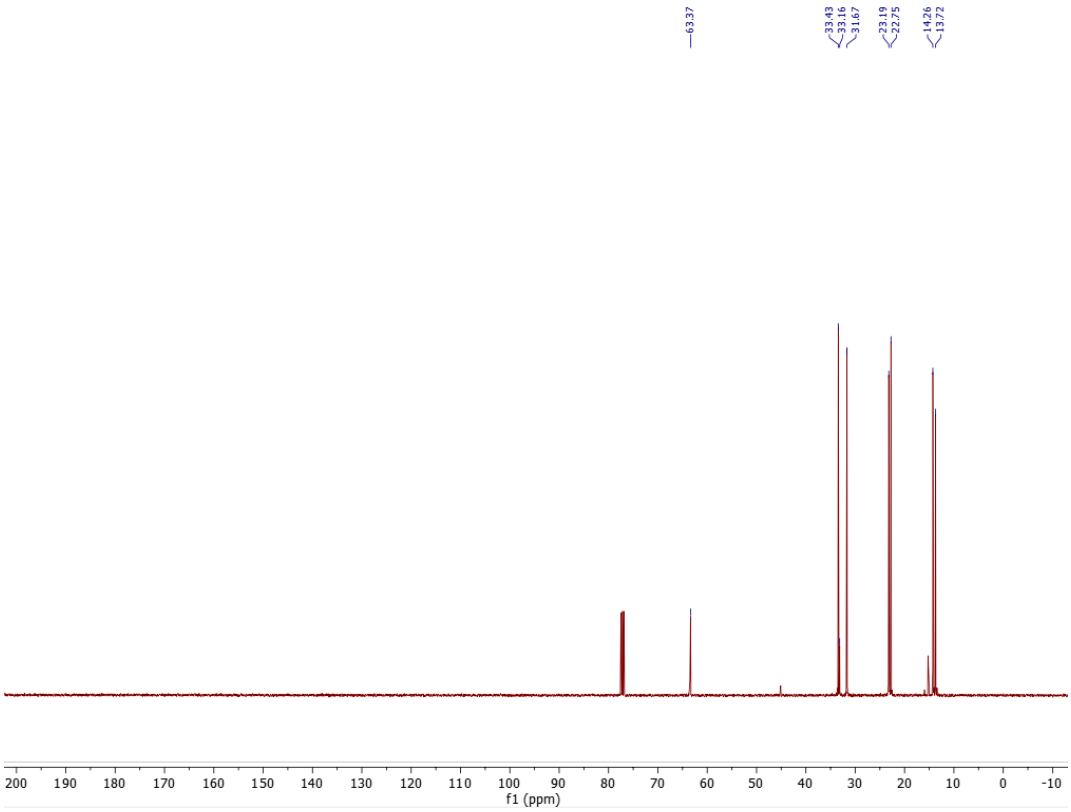
63.37
33.43
33.16
31.67
23.19
22.75
14.26
13.72
200 190 180 170 160 150 140 130 120 110 100 90 80 70 60 50 40 30 20 10 0 -10
f1 (ppm)

BTz-Si Monomer Pathway 1

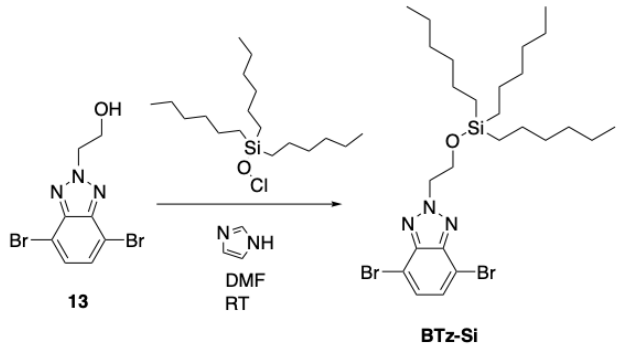

13 (0.5 mg, 1.6 mmol, 1 eq) and imidazole (1.1 g, 15.6 mmol, 10 eq) were added to a 250 mL round-bottom flask, put under high vacuum for 30 minutes then with nitrogen. Chlorotrihexylsilane (2.4 mL, 2.0 g, 6.2 mmol, 4 eq) and anhydrous dimethylformamide (100 mL) were added and I was stirred at 50 °C overnight. After complete reaction it was poured into a separating funnel along with water. The product was extracted with dichloromethane and washed twice with water, once with brine and sodium sulfate was added. This underwent gravity filtration, and the solvent was removed under reduced pressure. Most of the excess chlorotrihexylsilane was removed by distillation, applying high vacuum and heating with a heat gun until the evaporation stopped. The remaining oil was thenpurified on a silica column, eluting with a graduated eluent, from pure petroleum ether to petroleum ether: dichloromethane (80:20). Removal of solvent gave a colourless viscous oil **BTz-Si** (0.66 g, 71%). See pathway 2 for characterisation.

BTz-Si Monomer Pathway 2

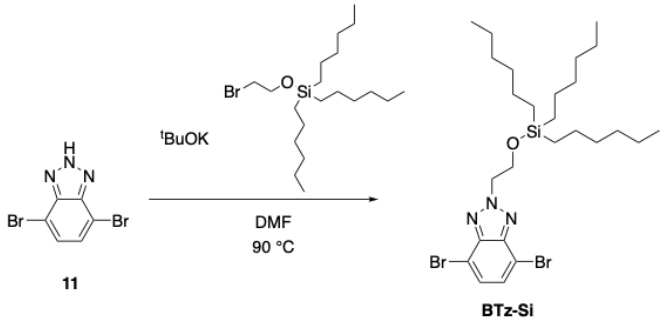

11 (1.89 g, 6.8 mmol, 1 eq), and potassium tert-butoxide (0.92, 8.2 mmol, 1.2 eq) were added to a 2-neck round bottom flask and purged with nitrogen. Anhydrous dimethylformamide (50 mL) followed by **14** (3.34g, 8.2 mmol, 1.2 eq) and it was stirred at 90 °C for 4 h. After complete reaction it was poured into a separating funnel along with water. The product was extracted with dichloromethane and washed twice with water, once with brine and sodium sulfate was added. This underwent gravity filtration, and the solvent was removed under reduced pressure. The resultant oil was purified on a silica column, eluting with a graduated eluent, from pure petroleum ether to

petroleum ether: dichloromethane (70:30). Removal of solvent from the product fractions gave a colourless viscous oil **BTz-Si** (1.6 g, 39%).

^{1}H NMR (400 MHz, $CDCl_3$) δ 7.44 (s, 2H), 4.88 (t, *J* = 5.6 Hz, 2H), 4.28 (t, *J* = 5.6 Hz, 2H), 1.30 – 1.06 (m, 24H), 0.86 (t, *J* = 7.0 Hz, 9H), 0.54 – 0.36 (m, 6H).

^{13}C NMR (400 MHz, $CDCl_3$) δ 143.97, 129.70, 110.19, 61.58, 59.61, 33.37, 31.59, 23.02, 22.74, 14.28, 13.49.

HSMS (ESI): HR-MS calculated for $[C_{26}H_{45}Br_2N_3OSi+H]^+$: m/z = 602.1771; measured m/z = 602.1784

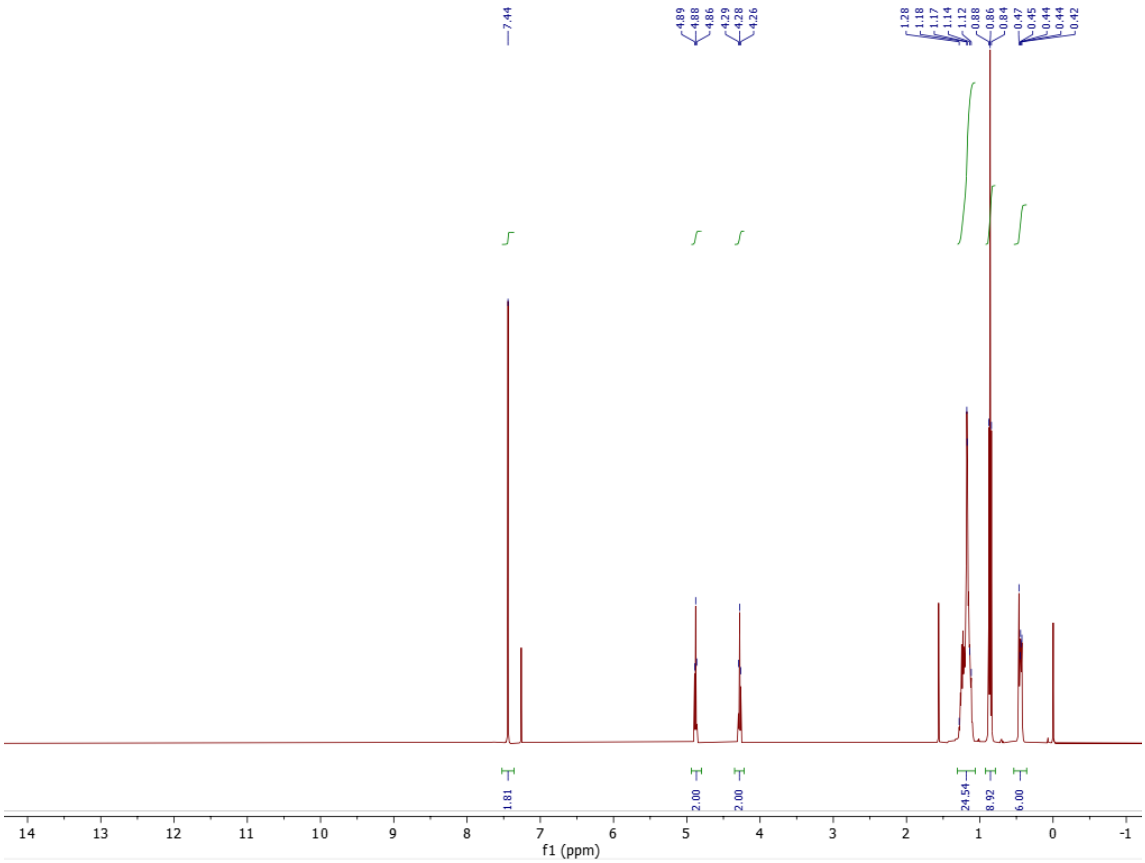

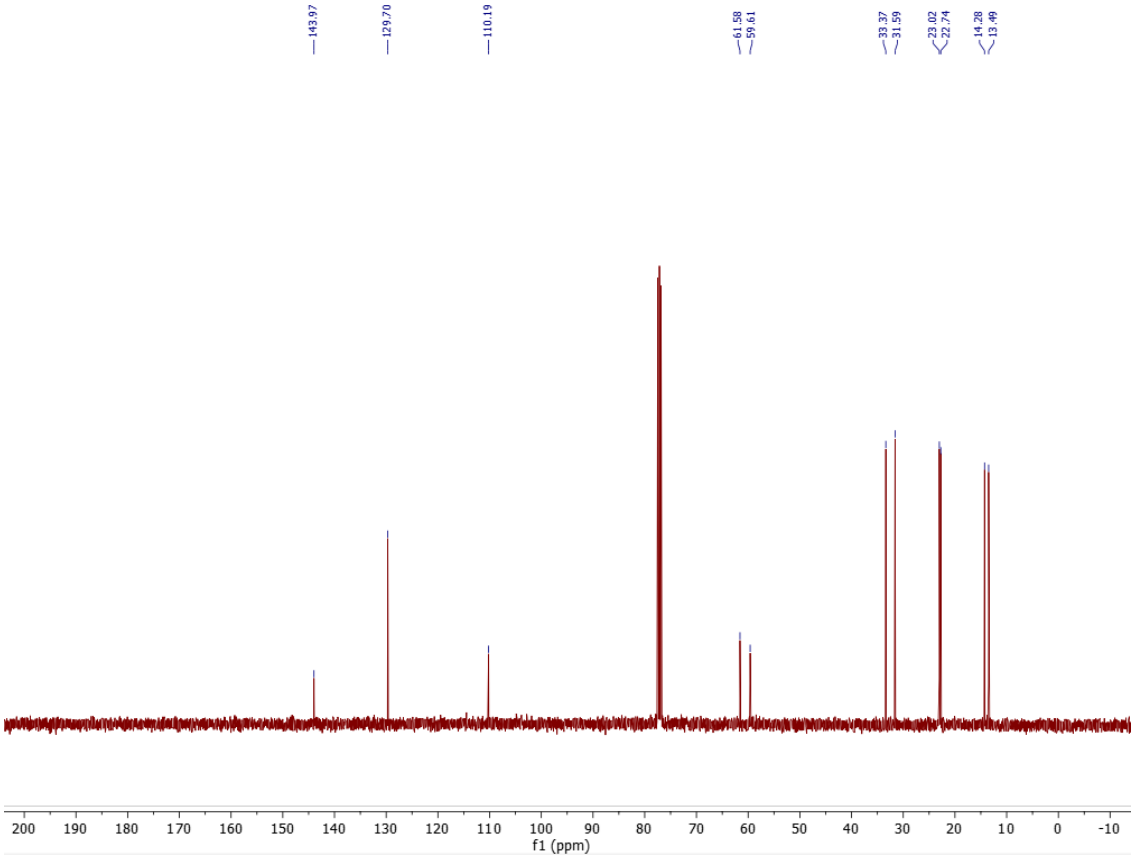
143.97
129.70
110.19
61.58
59.61
33.37
31.59
23.02
22.74
14.28
13.49
200 190 180 170 160 150 140 130 120 110 100 90 80 70 60 50 40 30 20 10 0 -10
f1 (ppm)

Expanded Spectrum RT 0.10, NL 864813, Peak [1], Target Mass 602.1771

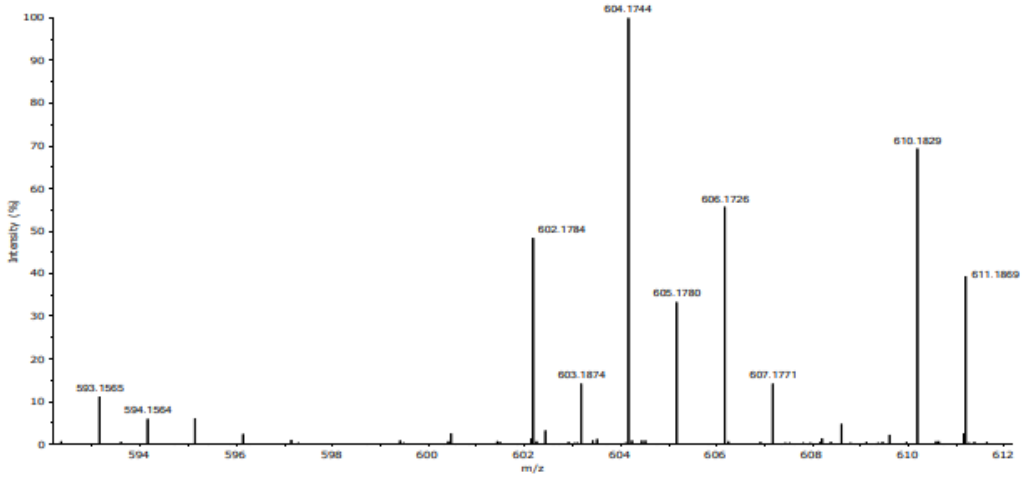

Theoretical Spectrum for C26H46Br2N3OSi, Minimum Abundance 0.01%

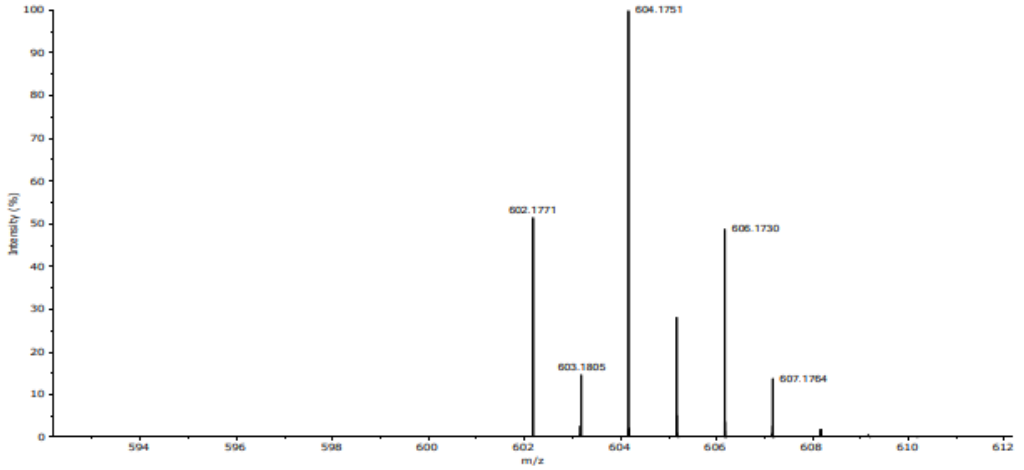

Sp-IDT-BTz-Si Polymer

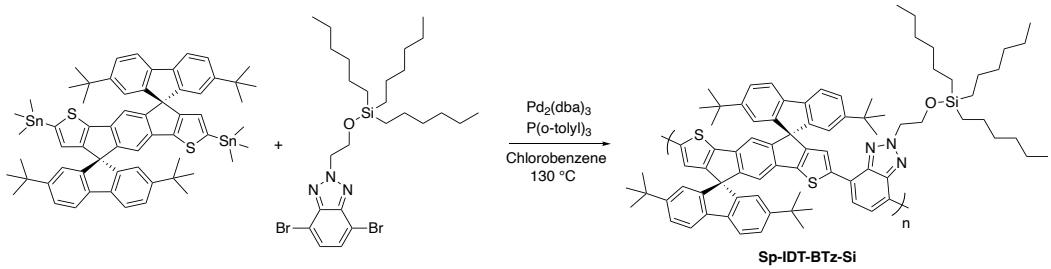

Distannylated Sp-IDT (241.34 mg, 216 µmol, 1 eq), **BTz-Si** (130.43 mg, 216µmol, 1 eq), tri(o-tolyl)phosphine (5.3 mg, 17 µmol, 0.08 eq) and tris(dibenzylideneacetone) dipalladium(0) (4.0 mg, 4 µmol, 0.02 eq) were added to a microwave vial, it was capped then degassed with nitrogen for 30 minutes. Anhydrous chlorobenzene (4.3 mL) was added and it was heated to 130 °C overnight. This was cooled, precipitated into methanol and poured into a cellulose Soxhlet thimble. This underwent a Soxhlet extraction washing with acetone followed by hexane, ethyl acetate then extracted with chlorobenzene. This was concentrated under reduced pressure, then precipitated into methanol and collected by vacuum filtration to give a yellow solid polymer **Sp-IDT-BTz-Si** (225 mg, 84%).

^{1}H NMR (500 MHz, $CDCl_3$) δ 7.75 (br,, d, J = 8.0 Hz, 4H), 7.45-7.31 (br, m, 6H), 7.17 (br, 2H), 6.84-6.70 (br, m,6H), 4.72 (br, 2H), 4.13 (br, 2H), 1.19-0.98, (br, m, 60H), 0.73 (t, J = 7.2 Hz, 9H), 0.31 (br, 6H)

GPC chlorobenzene M_N 24107 gmol^{-1}, M_W 61073 gmol^{-1}, PD 2.53

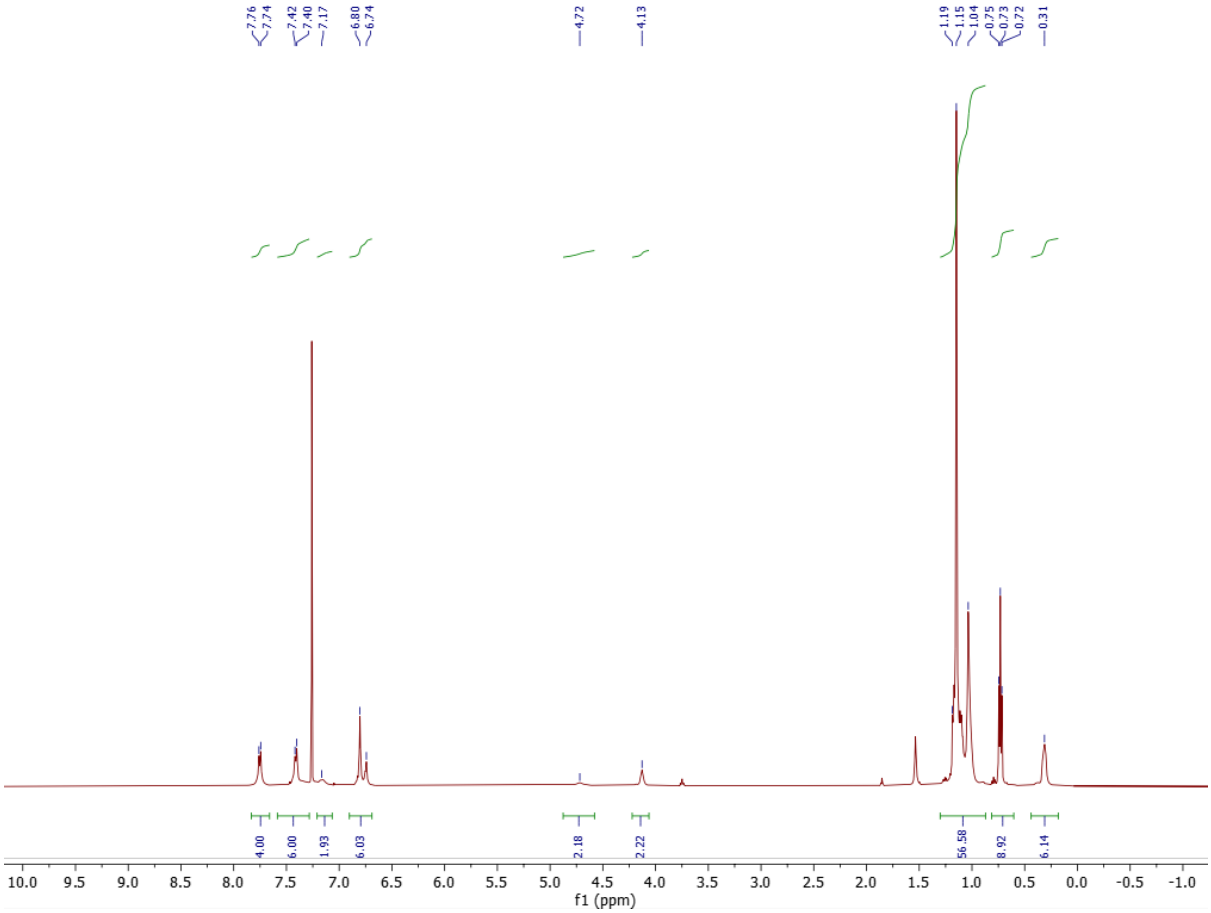
7.76
7.74
7.42
7.40
7.17
6.80
6.74
4.72
4.13
1.19
1.15
1.04
0.75
0.73
0.72
0.31
4.00
6.00
1.93
6.03
2.18
2.22
56.58
8.92
6.14
10.0 9.5 9.0 8.5 8.0 7.5 7.0 6.5 6.0 5.5 5.0 4.5 4.0 3.5 3.0 2.5 2.0 1.5 1.0 0.5 0.0 -0.5 -1.0
f1 (ppm)

BTz-Et Monomer

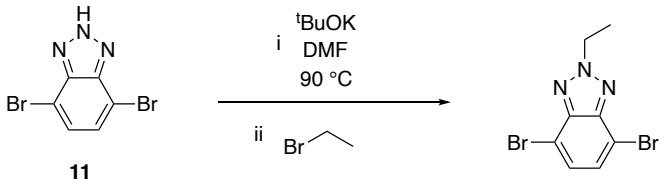

11 (270 mg, 0.957 mmol, 1 eq) and potassium tert-butoxide (131 mg, 1.170 mmol, 1.2 eq) were added to a microwave vial and purged with nitrogen. Anhydrous dimethylformamide (2 mL) followed by bromoethane (0.1 mL, 1.365 mmol, 1.4 eq) and it was stirred at 90 °C for 4 h. After complete reaction it was poured into a separating funnel along with water. The product was extracted with dichloromethane and washed twice with water, once with brine and sodium sulfate was added. This underwent gravity filtration, and the solvent was removed under reduced pressure. The resultant solid was purified on a silica column, eluting with a graduated eluent, from petroleum ether: dichloromethane (90: 10) to petroleum ether: dichloromethane (80:20). Removal of solvent from the product fractions gave a colourless solid, which was subsequently recrystallised in ethanol to give large colourless crystals **BTz-Et** (111 mg g, 37%).

^{1}H NMR (400 MHz, $CDCl_3$) δ 7.45 (s, 2H), 4.85 (q, *J* = 7.3 Hz, 2H), 1.75 (t, *J* = 7.3 Hz, 3H).

^{13}C NMR (400 MHz, $CDCl_3$) δ 143.90, 129.68, 110.12, 52.69, 15.44.

HSMS (ESI): HR-MS calculated for $[C8H7Br2N3+H]^+$: m/z = 303.9079; measured m/z = 303.9075

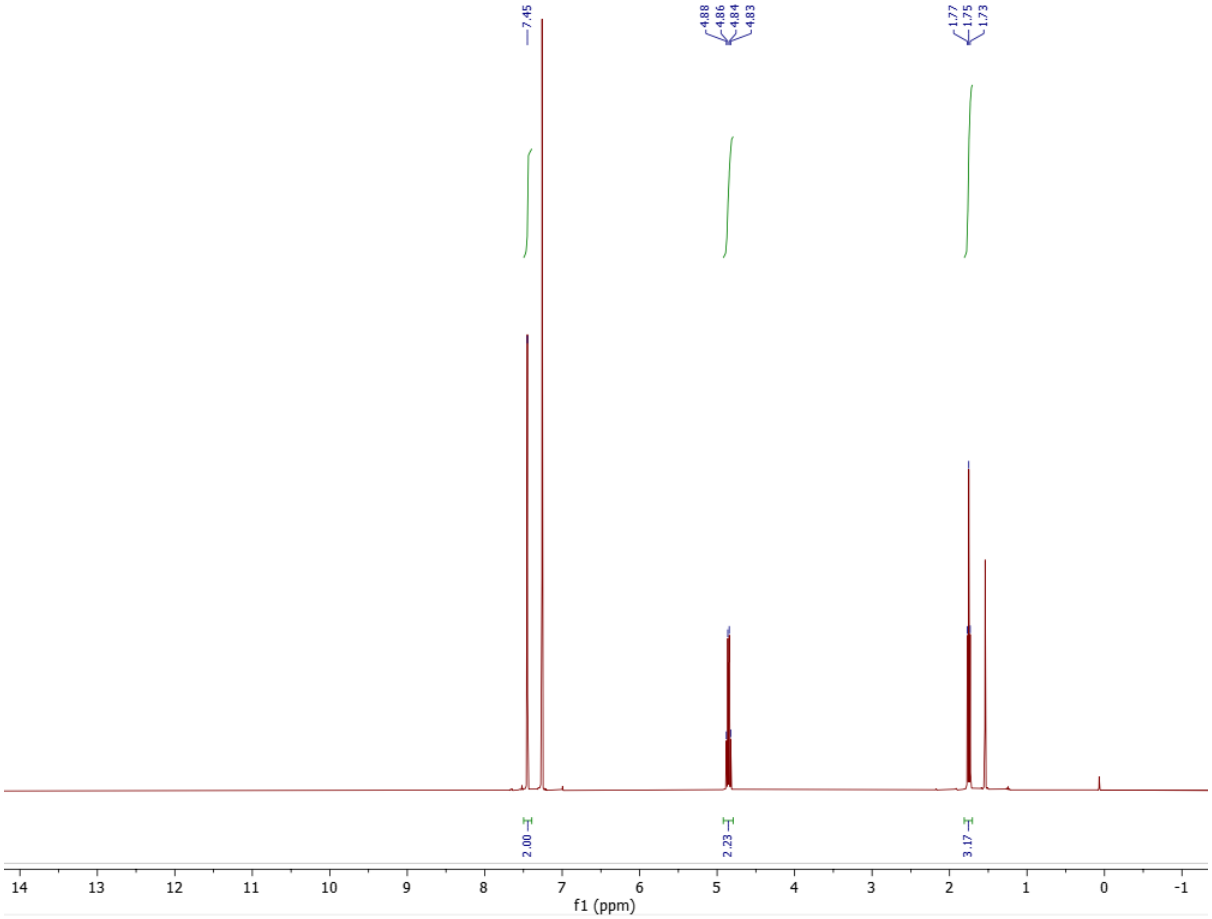
7.45
4.88
4.86
4.84
4.83
1.77
1.75
1.73
2.00
2.23
3.17
14 13 12 11 10 9 8 7 6 5 4 3 2 1 0 -1
f1 (ppm)

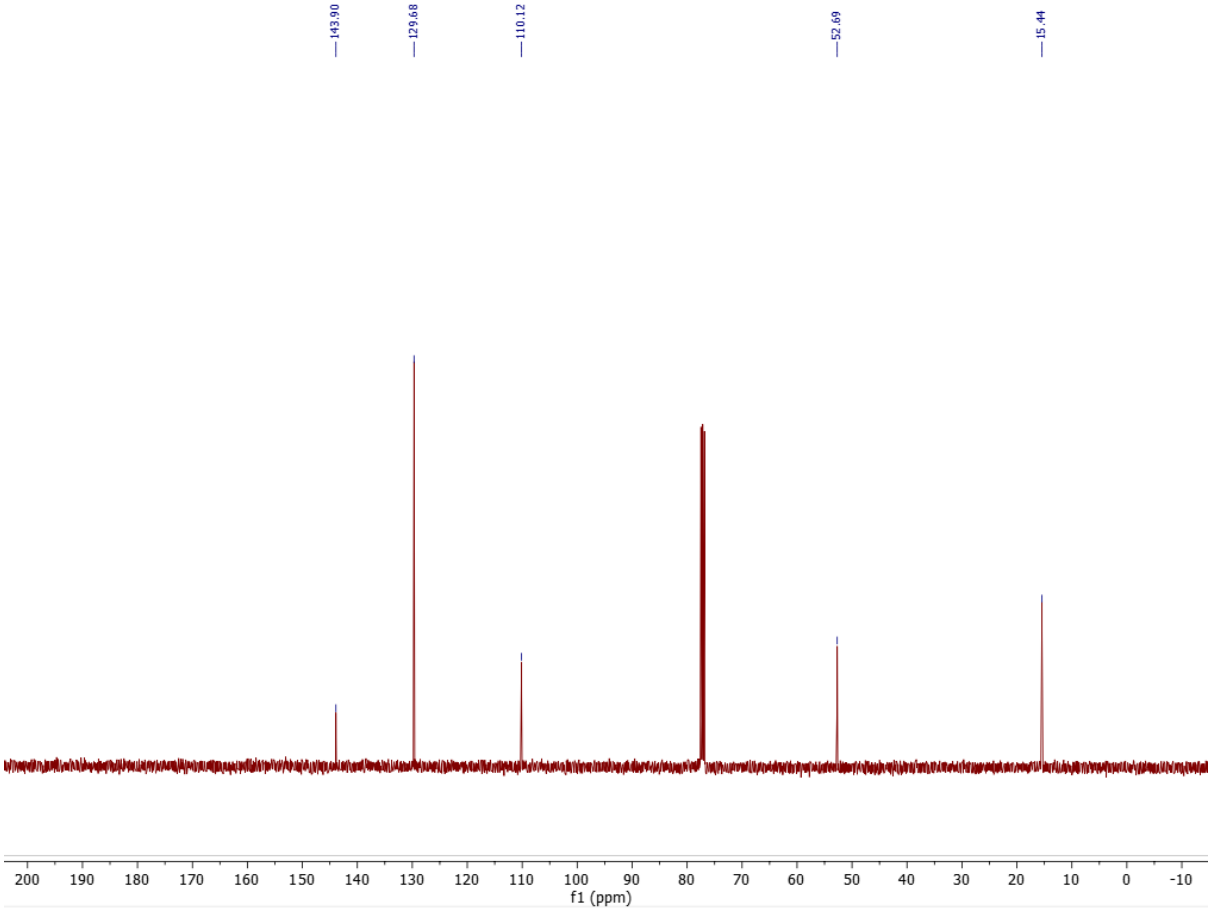
143.90
129.68
110.12
52.69
15.44
200 190 180 170 160 150 140 130 120 110 100 90 80 70 60 50 40 30 20 10 0 -10
f1 (ppm)

Expanded Spectrum RT 0.12, NL 781414, Peak [1], Target Mass 303.9079

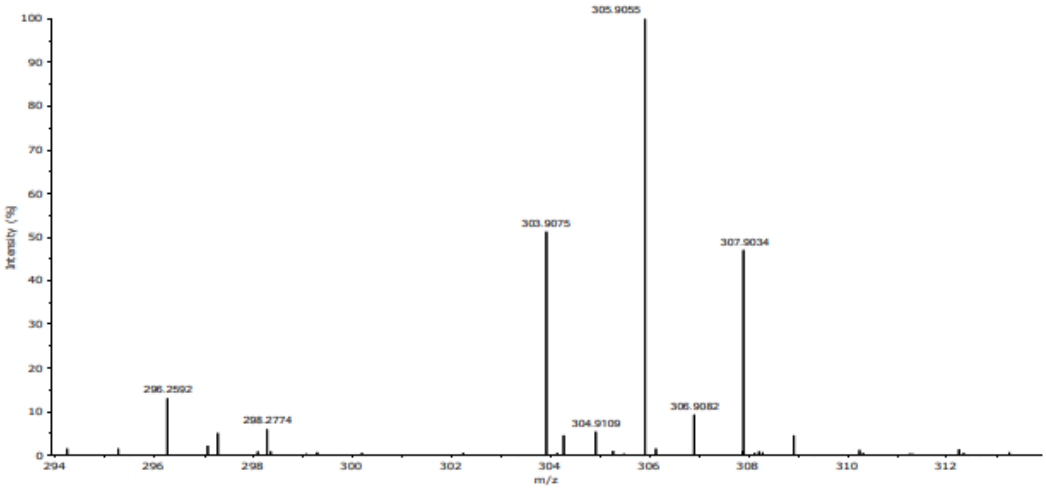

Theoretical Spectrum for C8H8Br2N3, Minimum Abundance 0.01%

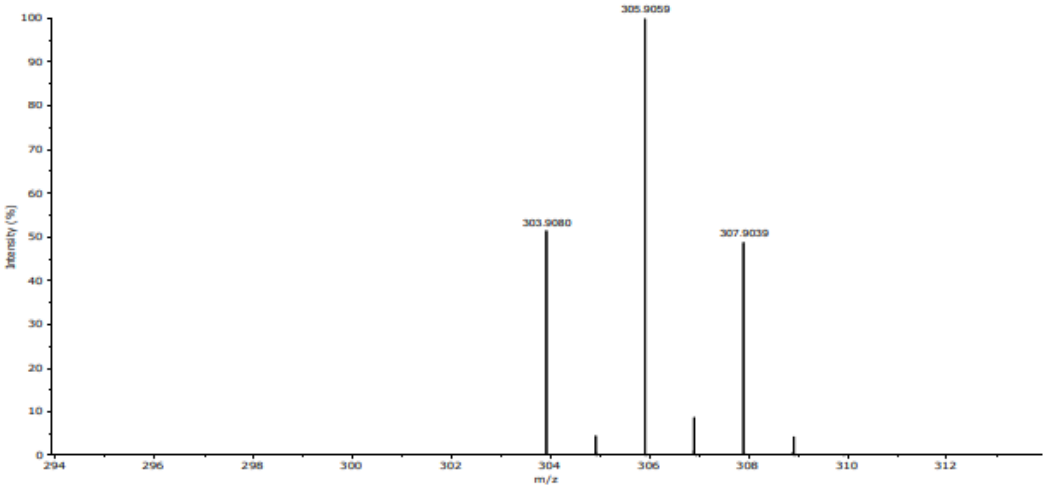

BTz-Hex Monomer

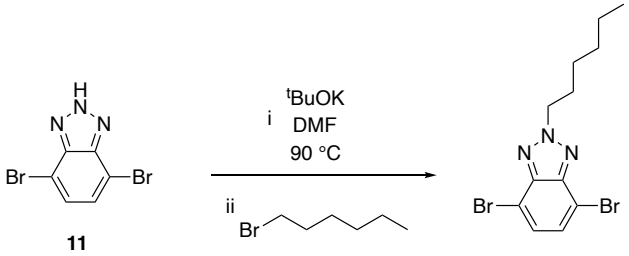

11 (500 mg, 1.81 mmol, 1 eq), and potassium tert-butoxide (243 mg, 2.17 mmol, 1.2 eq) were added to a microwave vial and purged with nitrogen. Anhydrous dimethylformamide (10 mL) followed by 1-bromohexane (0.3 mL, 2.17 mmol, 1.2 eq) and it was stirred at 90 °C for 4 h. After complete reaction it was poured into a separating funnel along with water. The product was extracted with dichloromethane and washed twice with water, once with brine and sodium sulfate was added. This underwent gravity filtration, and the solvent was removed under reduced pressure. The resultant oil was purified on a silica column, eluting with a graduated eluent, from petroleum ether: dichloromethane (90: 10) to petroleum ether: dichloromethane (80:20). Removal of solvent from the product fractions gave a colourless oil **BTz-Hex** (328 mg g, 50%).

^{1}H NMR (400 MHz, $CDCl_3$) δ 7.44 (s, 2H), 4.77 (t, J = 7.5 Hz, 2H), 2.18 – 2.10 (m, 2H), 1.40 – 1.28 (m, 6H), 0.88 (t, J = 6.9 Hz, 3H).

^{13}C NMR (400 MHz, $CDCl_3$) δ 143.82, 129.62, 110.09, 57.58, 31.25, 30.29, 26.29, 22.50, 14.05.

HSMS (ESI): HR-MS calculated for $[C_{12}H_{15}Br_2N_3+H]^+$: m/z = 359.9705; measured m/z = 359.9716

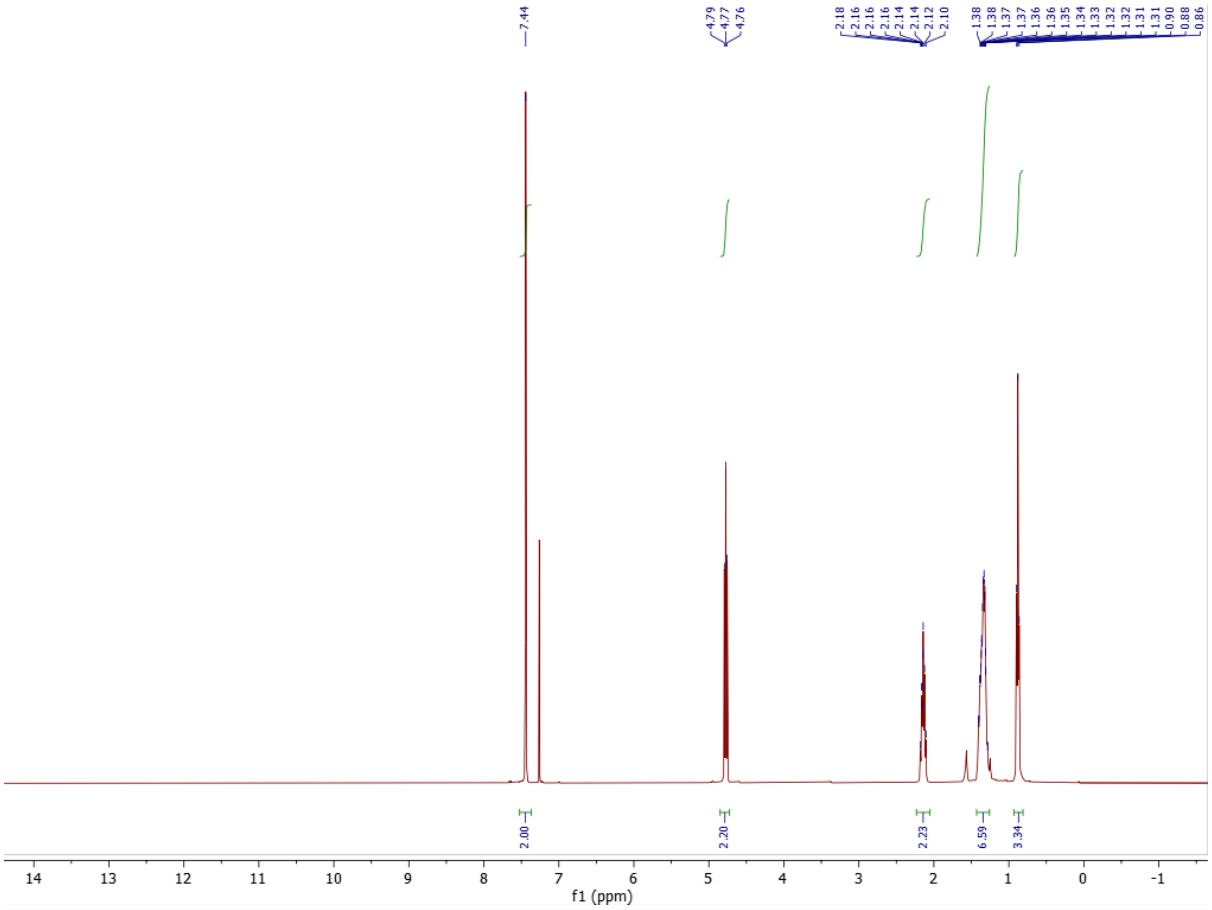
7.44
4.79
4.77
4.76
2.18
2.16
2.16
2.16
2.14
2.14
2.12
2.10
1.38
1.38
1.37
1.37
1.36
1.36
1.35
1.34
1.33
1.32
1.32
1.31
1.31
0.90
0.88
0.86
2.00
2.20
2.23
6.59
3.34
f1 (ppm)

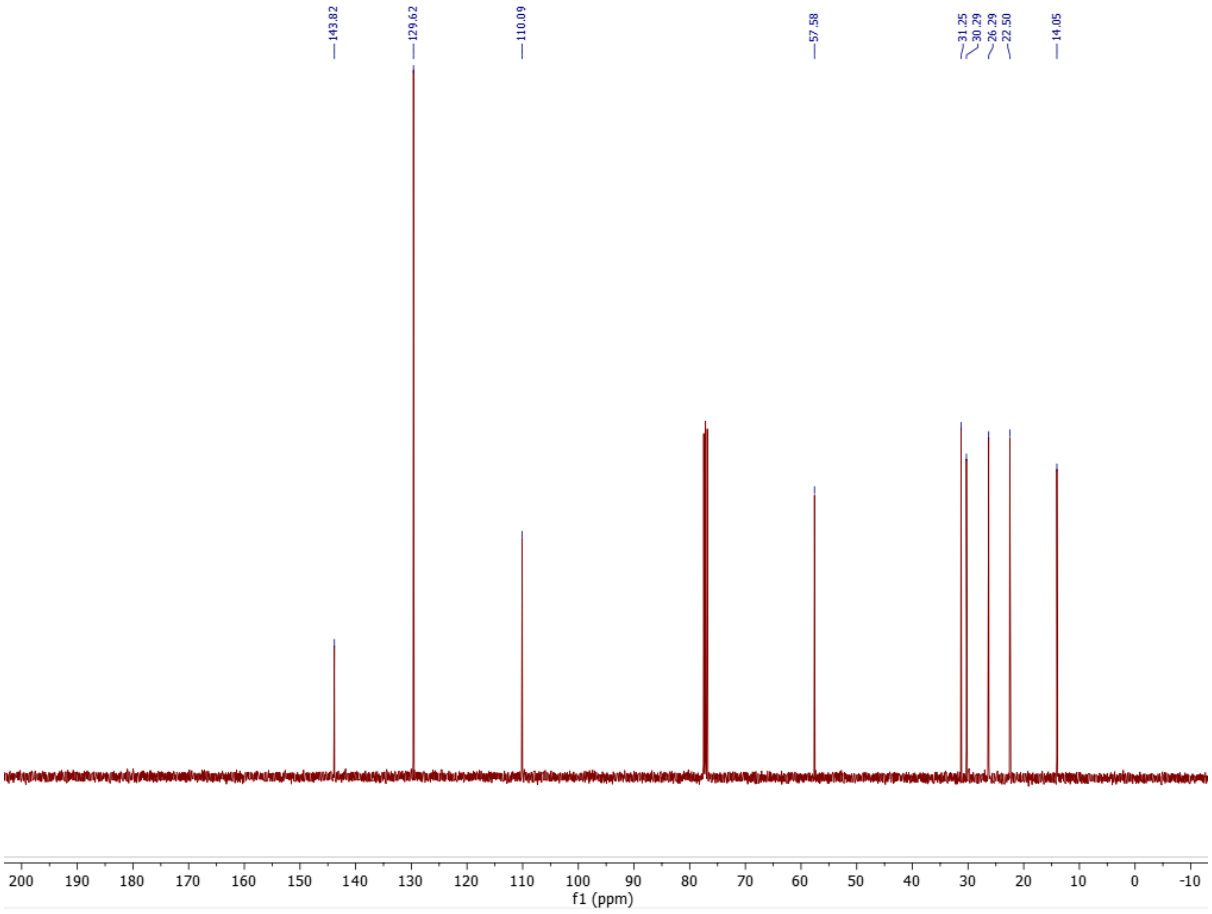
143.82
129.62
110.09
57.58
31.25
30.29
26.29
22.50
14.05
f1 (ppm)

Expanded Spectrum RT 0.18, NL 1268956, Peak [1], Target Mass 359.9705

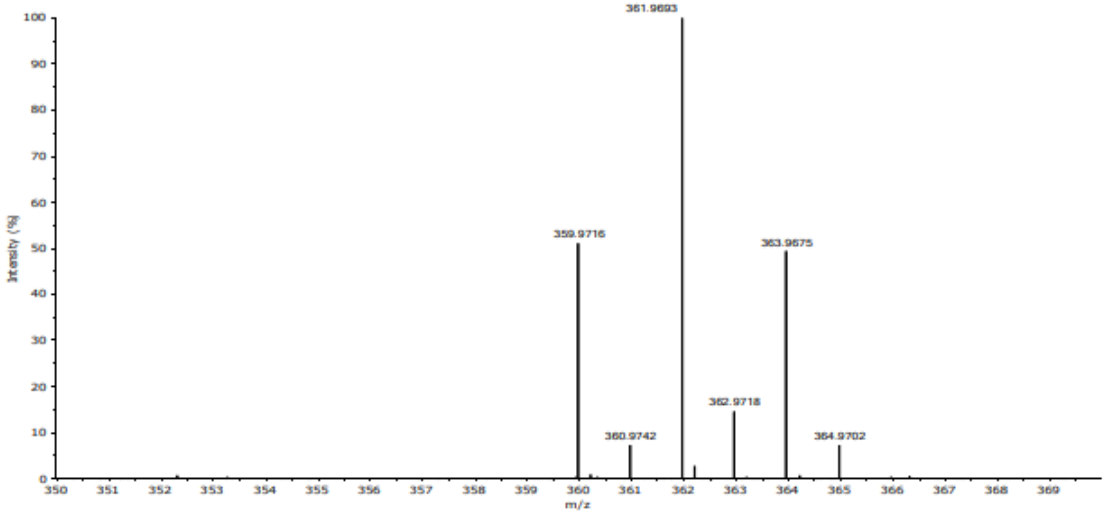

Theoretical Spectrum for C12H16Br2N3, Minimum Abundance 0.01%

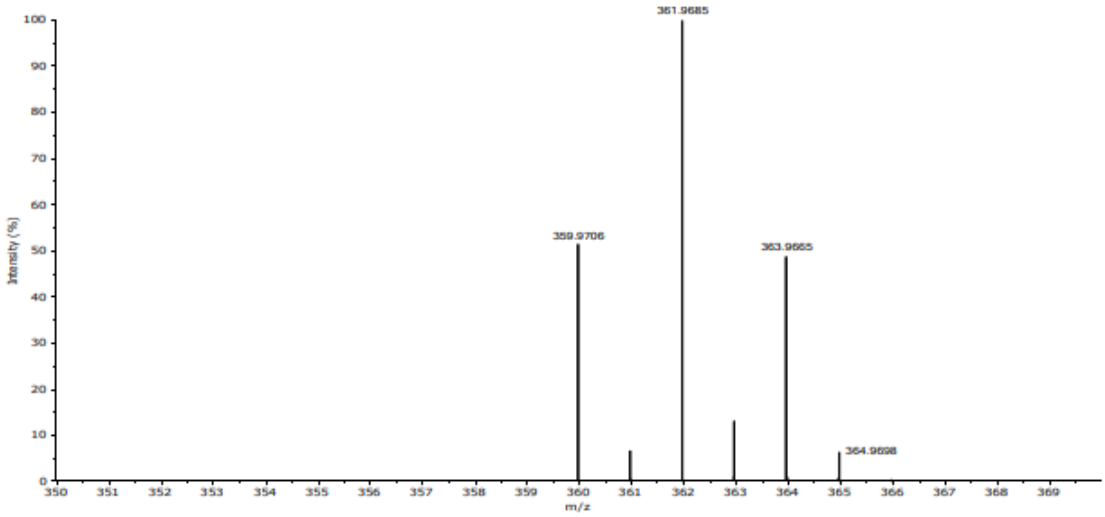

BTz-Dec Monomer

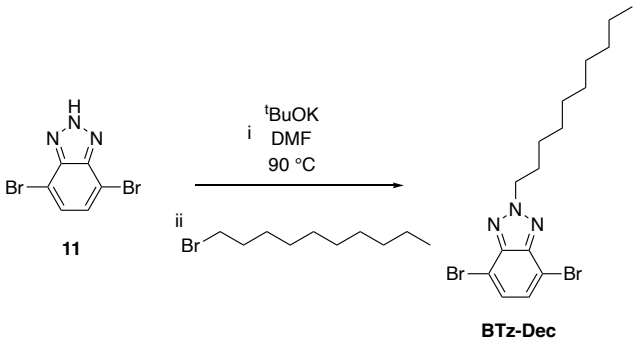

11 (500 mg, 1.81 mmol, 1 eq) and potassium tert-butoxide (243 mg, 2.17 mmol, 1.2 eq) were added to a microwave vial and purged with nitrogen. Anhydrous dimethylformamide (10 mL) followed by 1-bromodecane (0.3 mL, 1.81 mmol, 1.2 eq) and it was stirred at 90 °C for 4 h. After complete reaction it was poured into a separating funnel along with water. The product was extracted with dichloromethane and washed twice with water, once with brine and sodium sulfate was added. This underwent gravity filtration, and the solvent was removed under reduced pressure. The resultant oil was purified on a silica column, eluting with petroleum ether: dichloromethane (90: 10). Removal of solvent from the product fractions gave a colourless oil **BTz-Dec** (304 mg g, 40%).

^{1}H NMR (400 MHz, $CDCl_3$) δ 7.44 (s, 2H), 4.77 (t, J = 7.4 Hz, 2H), 2.18-2.10 (m, 2H), 1.37-1.25 (m, 14H), 0.87 (t, J = 6.7 Hz, 3H)

^{13}C NMR (400 MHz, $CDCl_3$) δ 143.72, 129.51, 109.98, 57.49, 31.85, 30.22, 29.44, 29.34, 29.24, 28.97, 26.50, 22.66, 14.11.

HSMS (ESI): HR-MS calculated for $[C16H23Br2N3 +H]^+$: m/z = 416.0331; measured m/z = 416.0325

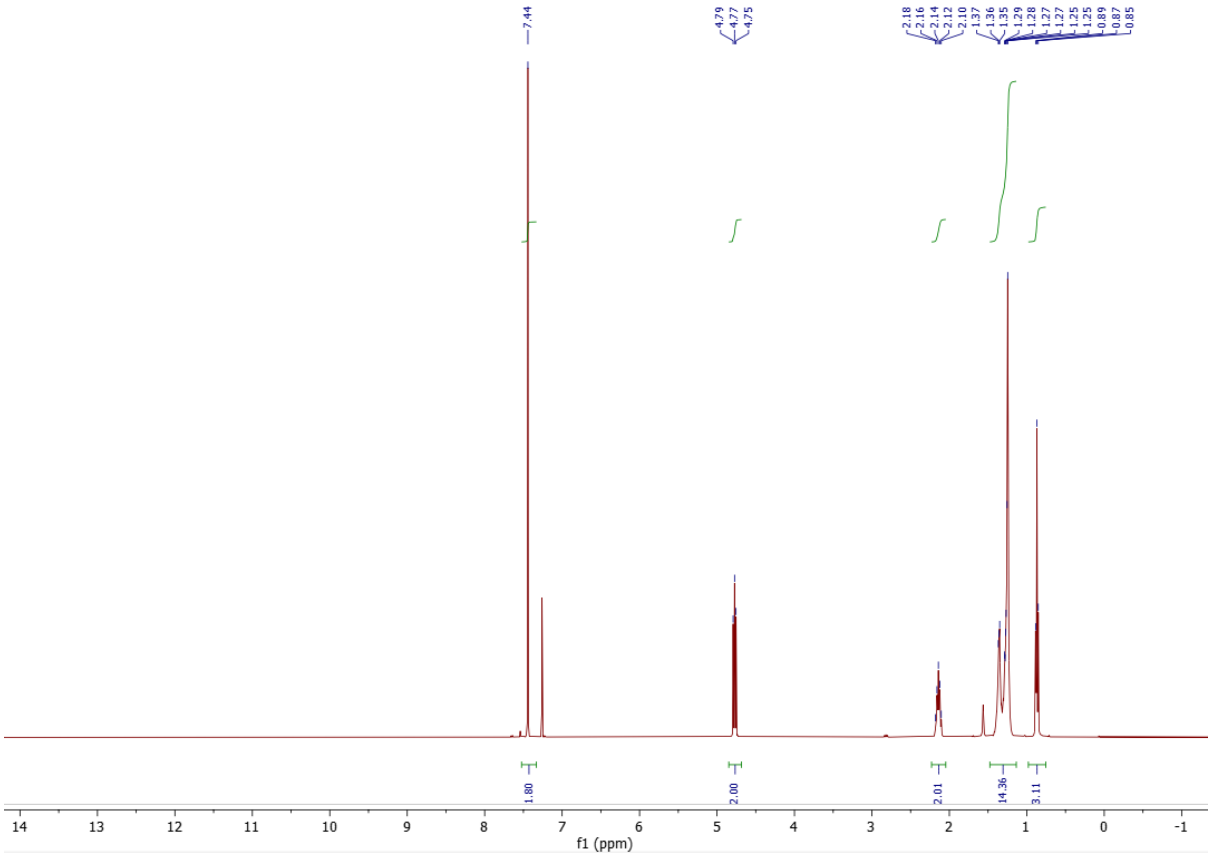
7.44
4.79
4.77
4.75
2.18
2.16
2.14
2.12
2.10
1.37
1.36
1.35
1.29
1.28
1.27
1.27
1.25
1.25
0.89
0.87
0.85
1.80
2.00
2.01
14.36
3.11
f1 (ppm)

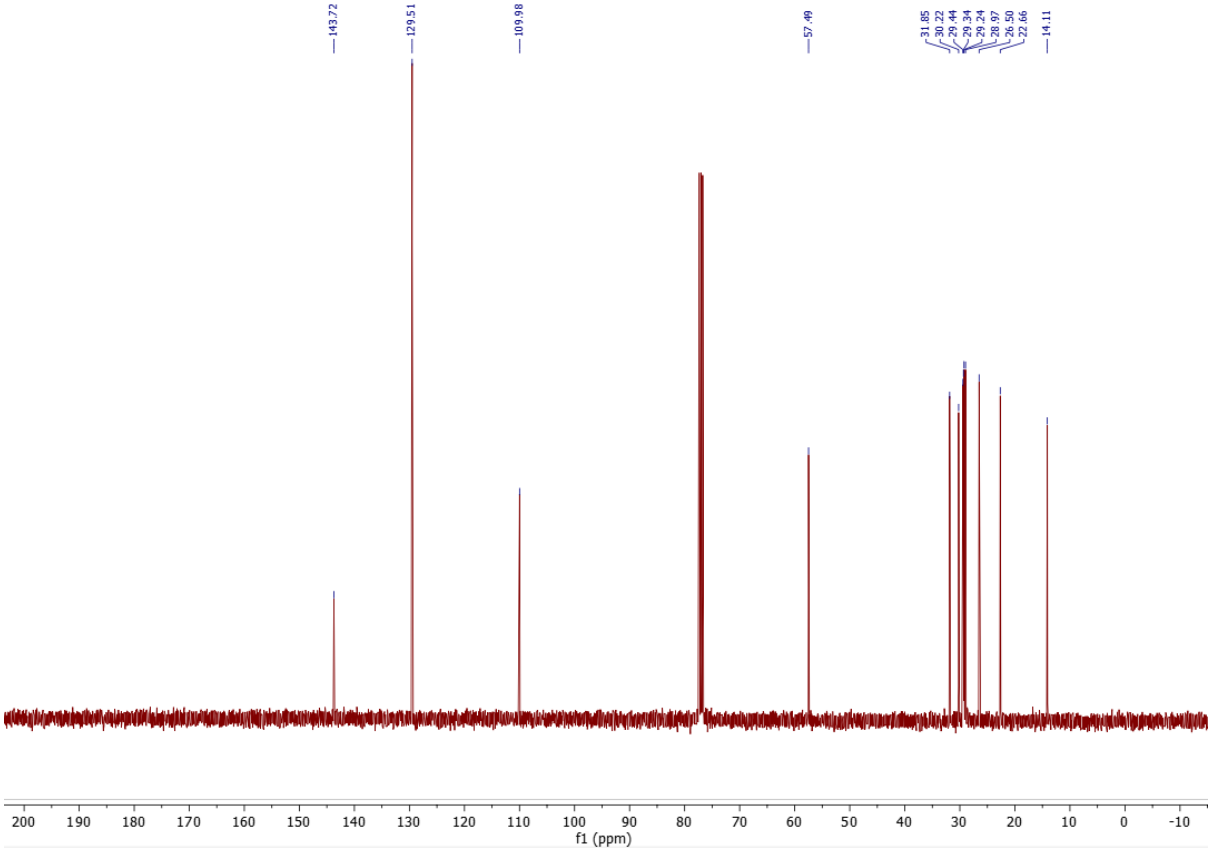
143.72
129.51
109.98
57.49
31.85
30.22
29.44
29.34
29.24
28.97
26.50
22.66
14.11
f1 (ppm)

Expanded Spectrum RT 0.11, NL 1104935, Peak [1], Target Mass 416.0331

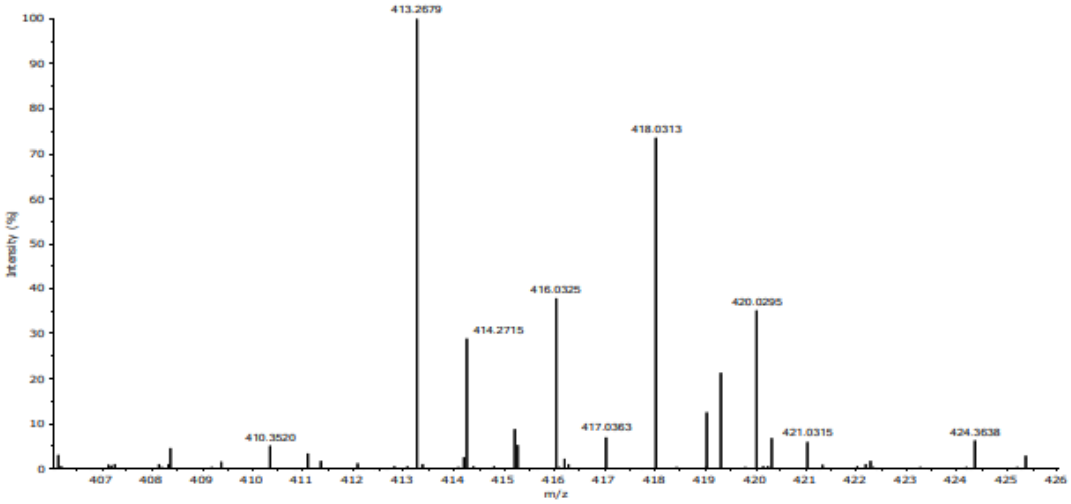

Theoretical Spectrum for C16H24Br2N3, Minimum Abundance 0.01%

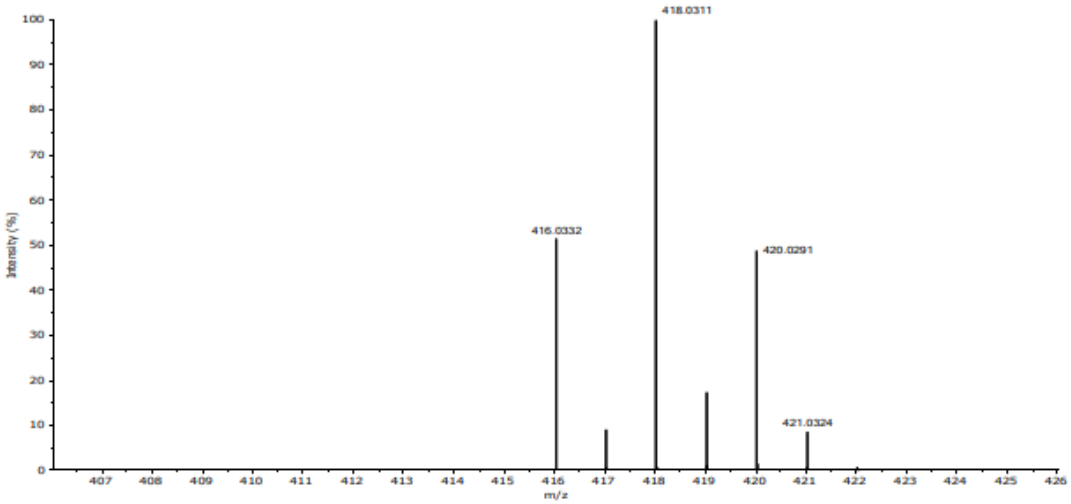

Sp-IDT-BTz-Et Polymer

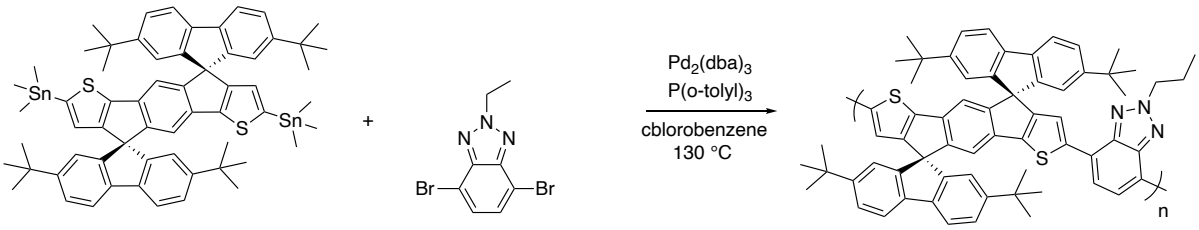

Distannylated Sp-IDT (91.20 mg, 82 µmol, 1 eq), **BTz-Et** (24.90 mg, 82 µmol, 1 eq), tri(o-tolyl)phosphine (2.0 mg, 7 µmol, 0.08 eq) and tris(dibenzylideneacetone) dipalladium(0) (1.5 mg, 2 µmol, 0.02 eq) were added to a microwave vial, it was capped then degassed with nitrogen for 30 minutes. Anhydrous chlorobenzene (1.7 mL) was added and it was heated to 130 °C overnight. This was cooled, precipitated into methanol and collected by vacuum filtration. In the filter it was washed with hot acetone, hot hexane, hot ethyl acetate followed by more methanol, then collected to give a dark purple solid (65 mg, 85%). Due to poor solubility NMR and GPC was not performed.

Sp-IDT-BTz-Hex Polymer

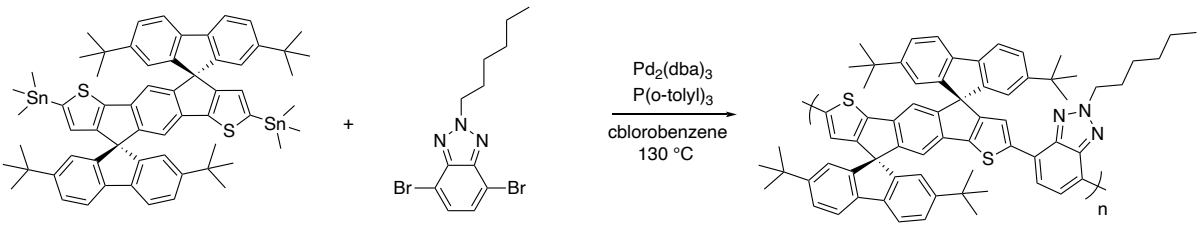

Distannylated Sp-IDT (129.87 mg, 116 µmol, 1 eq), **BTz-Hex** (41.99 mg, 116 µmol, 1 eq), tri(o-tolyl)phosphine (2.8 mg, 9 µmol, 0.08 eq) and tris(dibenzylideneacetone) dipalladium(0) (2.1 mg, 2 µmol, 0.02 eq) were added to a microwave vial, it was capped then degassed with nitrogen for 30 minutes. Anhydrous chlorobenzene (2.7 mL) was added and it was heated to 130 °C overnight. This was cooled, precipitated into methanol and collected by vacuum filtration. In the filter it was washed with hot acetone, hot hexane, hot ethyl acetate followed by more methanol, then collected to give a dark purple solid (107 mg, 93%). Due to poor solubility NMR and GPC was not performed.

Sp-IDT-BTz-Dec Polymer

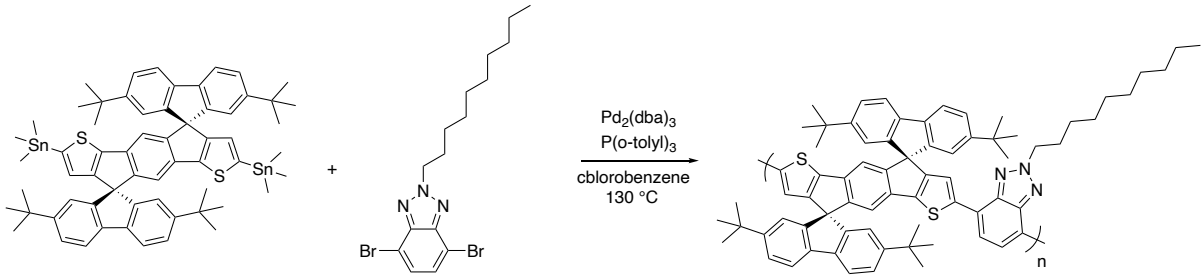

BW457

Distannylated Sp-IDT (151.11 mg, 135 µmol, 1 eq), **BTz-Hex** (56.45 mg, 135 µmol, 1 eq), tri(o-tolyl)phosphine (3.3 mg, 11 µmol, 0.08 eq) and tris(dibenzylideneacetone) dipalladium(0) (2.5 mg, 3 µmol, 0.02 eq) were added to a microwave vial, it was capped then degassed with nitrogen for 30 minutes. Anhydrous chlorobenzene (2.7 mL) was added and it was heated to 130 °C overnight. This was cooled, precipitated into methanol and collected by vacuum filtration. In the filter it was washed with hot acetone, hot hexane, hot ethyl acetate followed by more methanol, then collected to give a dark purple solid (138 mg, 96 %). NMR and GPC was not performed.

Intermediate 15

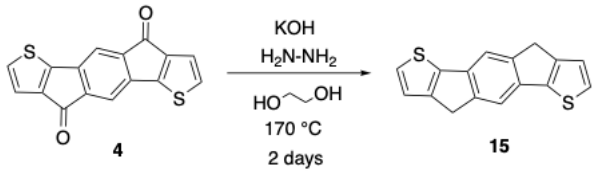

4 (4.70 g, 16.0 mmol, 1eq), potassium hydroxide (17.9 g, 319.4 mmol, 20 eq) and diethylene glycol (400 mL) were purged with nitrogen for 20 minutes, then hydrazine monohydrate (8.0 mL, 20 eq) was added and it was heated to 150 °C with a condenser fitted for 2 days. This was cooled then added to ice and 2 M HCl then underwent vacuum filtration to recover a dark brown solid. This was washed with water and acetone then collected by dissolving in chloroform. The solid was purified on a silica plug, eluting with dichloromethane: petroleum ether (70:30) to revover a light brown solid **15** (451 mg, 11 %)

^{1}H NMR (400 MHz, $CDCl_3$) δ 7.62 (s, 1H), 7.29 (d, *J* = 4.8 Hz, 1H), 7.12 (d, *J* = 4.8 Hz, 1H), 3.75 (s, 2H).

^{13}C NMR (400 MHz, $CDCl_3$) δ 147.10, 145.57, 143.60, 136.26, 126.48, 122.98, 115.99, 34.06

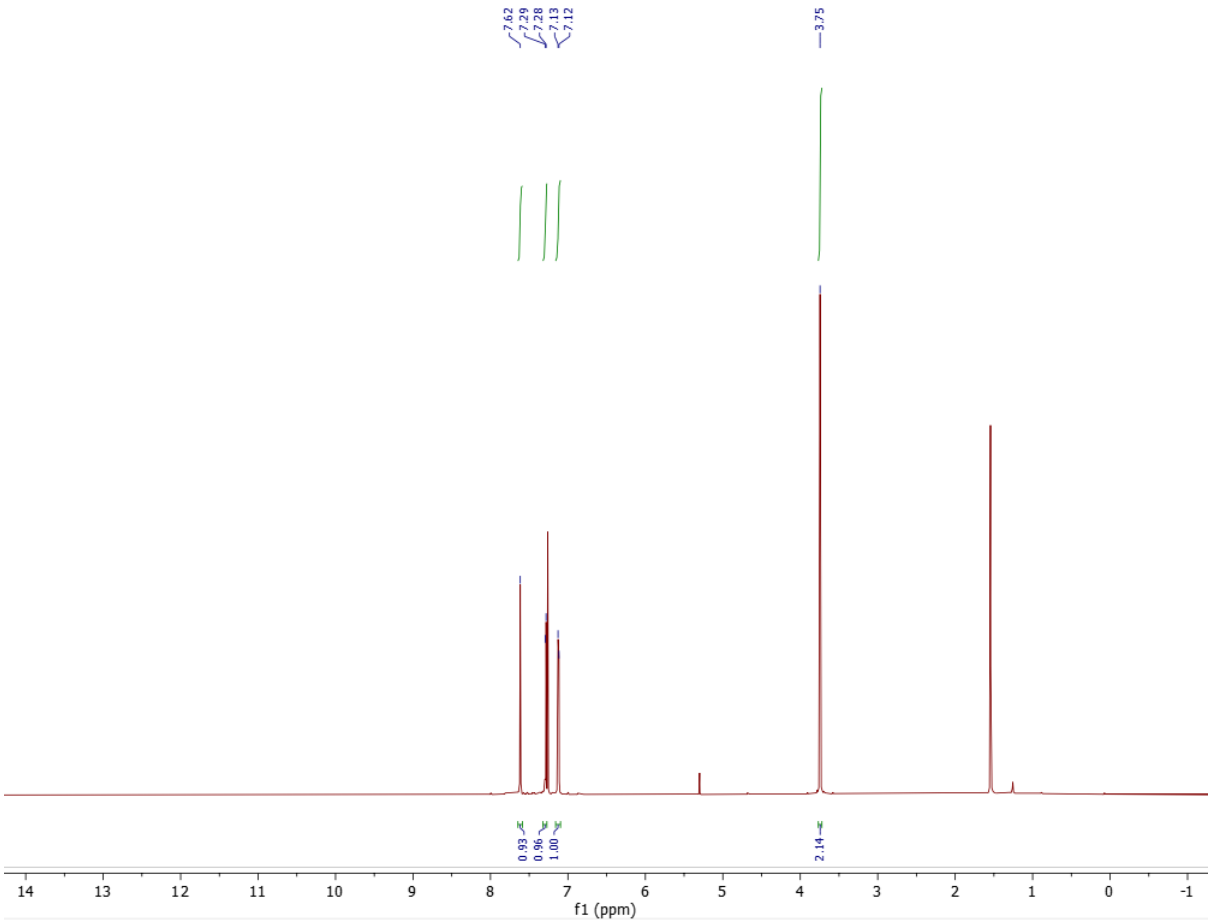
7.62
7.29
7.28
7.13
7.12
3.75
0.93
0.96
1.00
2.14
14
13
12
11
10
9
8
7
6
5
4
3
2
1
0
-1
f1 (ppm)

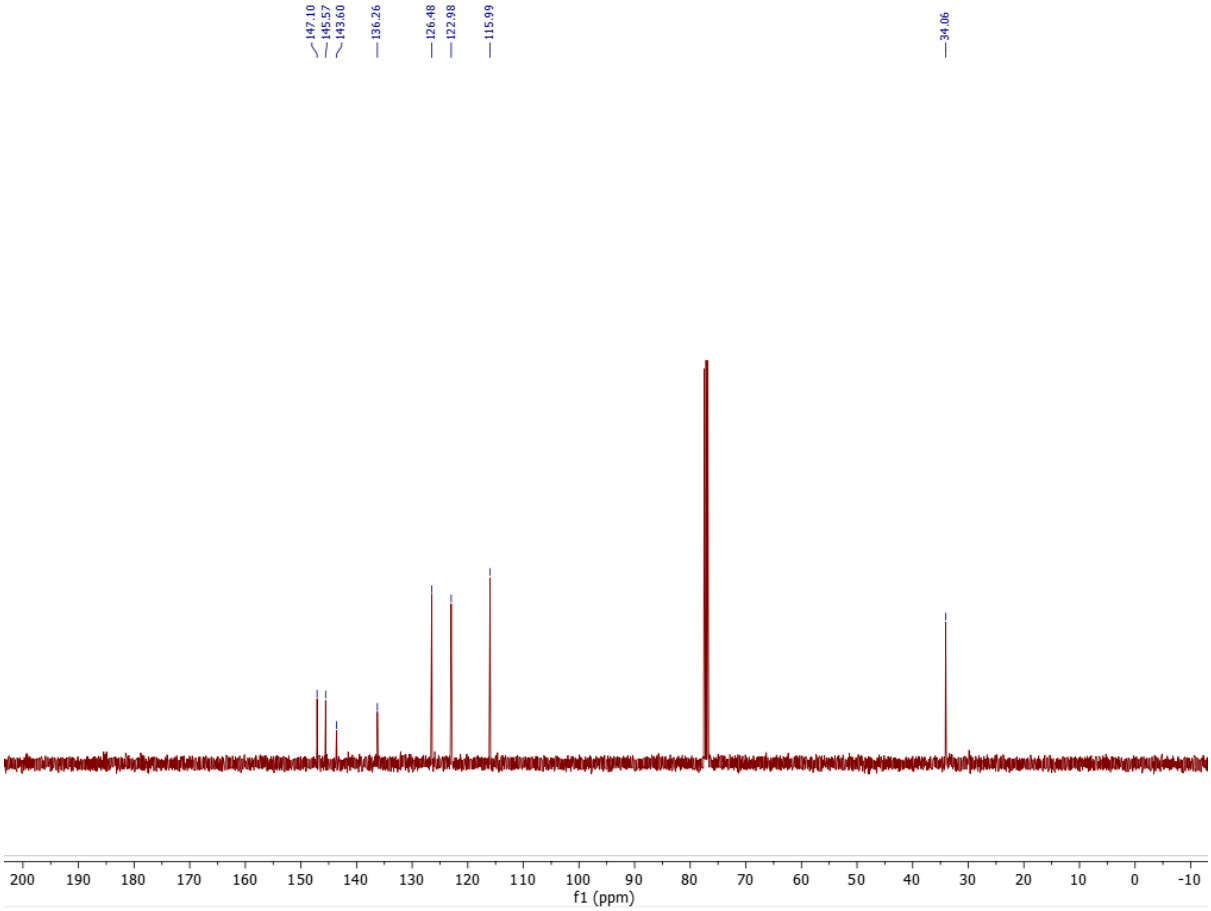
147.10
145.57
143.60
136.26
126.48
122.98
115.99
34.06
200
190
180
170
160
150
140
130
120
110
100
90
80
70
60
50
40
30
20
10
0
-10
f1 (ppm)

Intermediate Unfunctionalized Bu-IDT

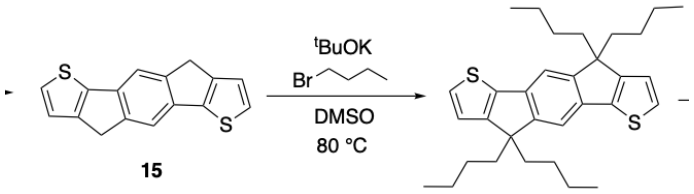

15 Bu-IDT

15 (0.24 g, 0.9 mmol, 1 eq) was added to a 2-neck round bottom flask and dried under high vacuum, then purged with nitrogen. Anhydrous dimethyl sulfoxide (10 mL) followed by potassium tert-butoxide (0.61, 5.4 mmol, 6 eq) portion wise while under stirring under nitrogen, whereupon the suspension turned red-brown. This was heated to 80 °C and stirred for 1 h, after which 1-bromobutane (0.6 mL, 5.4 mmol, 6 eq) was added dropwise and continued to stir at 80 °C under nitrogen overnight. After complete reaction, it was cooled then poured into a separating funnel with water and extracted with dichloromethane, washing with water and brine, then sodium sulfate was added. This underwent gravity filtration, and the solvent was removed under reduced pressure to give a brown residue. This was purified on a silica column, eluting with petroleum ether to recover a pale brown crystalline solid/ This was finally recrystallised in dichloromethane: methanol to give slightly orange-brown crystals **unfunctionalized Bu-IDT** (0.19 g, 41%)

^{1}H NMR (400 MHz, CD_2Cl_2) δ 7.33 (s, 2H), 7.29 (d, J = 4.8 Hz, 2H), 7.00 (d, J = 4.8 Hz, 2H), 2.04-1.97 (m, 4H), 1.92 (m, 4H), 1.18-1.09 (m, 8H), 0.82-0.75 (m, 8H), 0.72 (t, J = 7.4 Hz, 12H)

^{13}C NMR (400 MHz, $CDCl_3$) δ 155.27, 153.38, 141.78, 135.71, 126.27, 121.90, 113.31, 53.72, 39.14, 26.57, 23.26, 14.08.

GC-MS calculated for $[C_{32}H_{42}S_2]$+: *m*/*z* = 490.27; found: *m*/*z* = 490.3

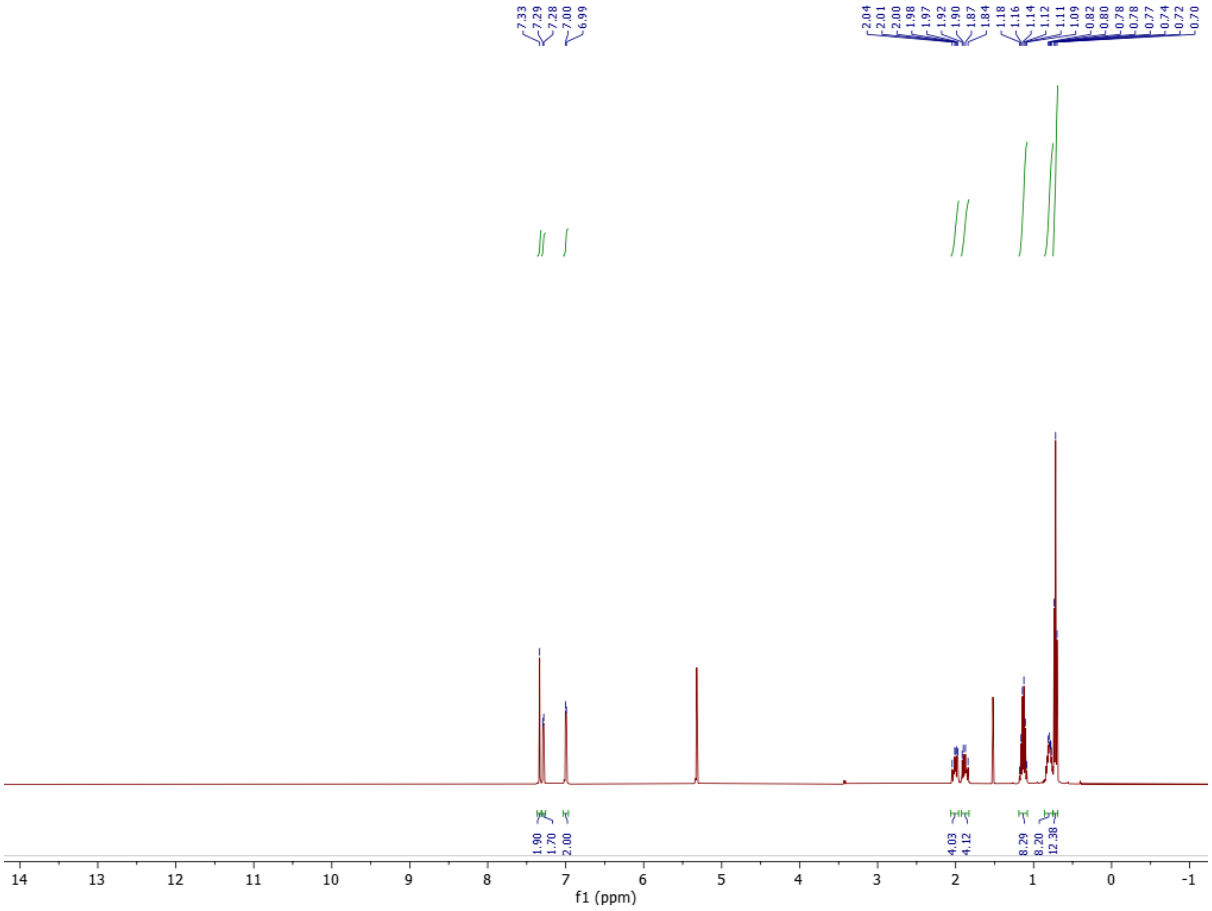
7.33
7.29
7.28
7.00
6.99
2.04
2.01
2.00
1.98
1.97
1.92
1.90
1.87
1.84
1.18
1.16
1.14
1.12
1.11
1.09
0.82
0.80
0.78
0.78
0.77
0.74
0.72
0.70
1.90
1.70
2.00
4.03
4.12
8.29
8.20
12.38
14 13 12 11 10 9 8 7 6 5 4 3 2 1 0 -1
f1 (ppm)

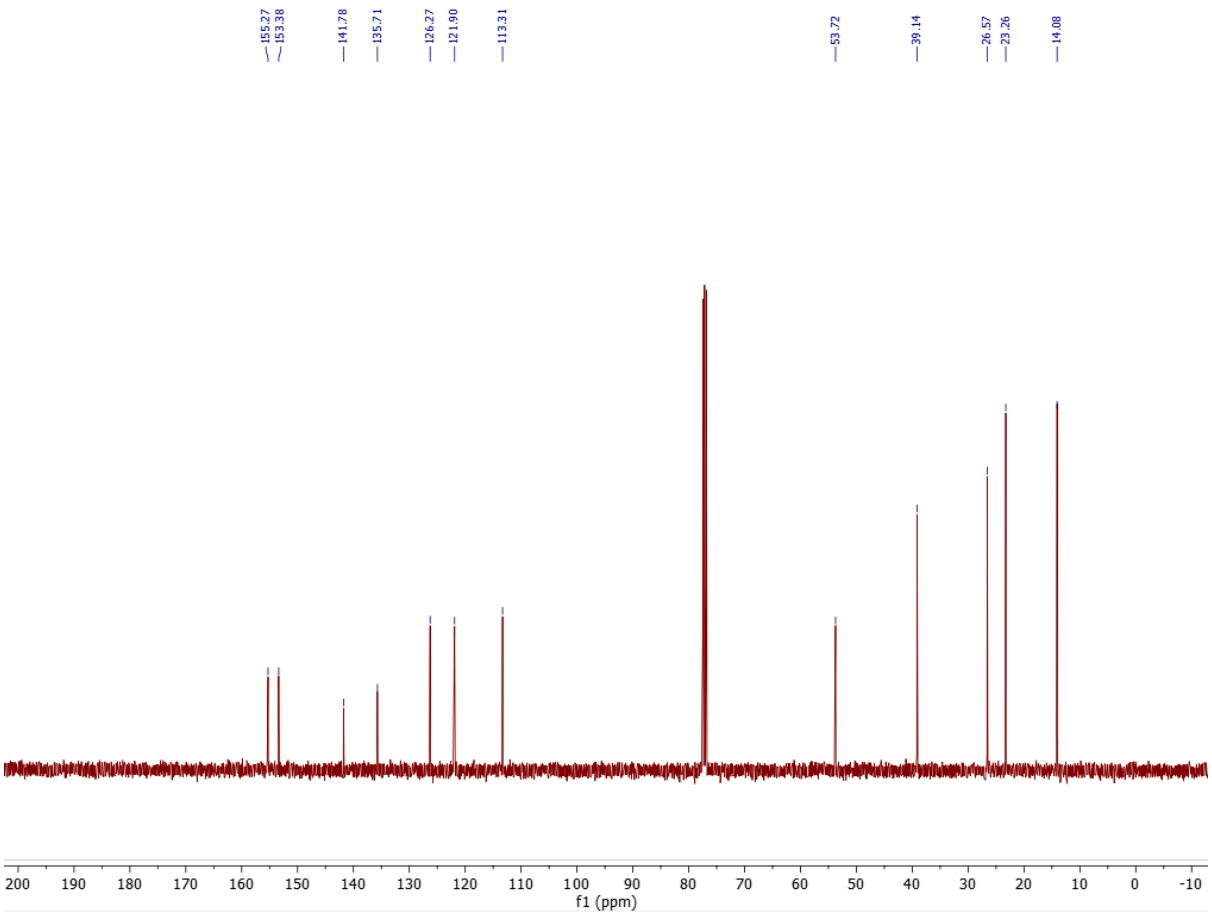
155.27
153.38
141.78
135.71
126.27
121.90
113.31
53.72
39.14
26.57
23.26
14.08
200 190 180 170 160 150 140 130 120 110 100 90 80 70 60 50 40 30 20 10 0 -10
f1 (ppm)

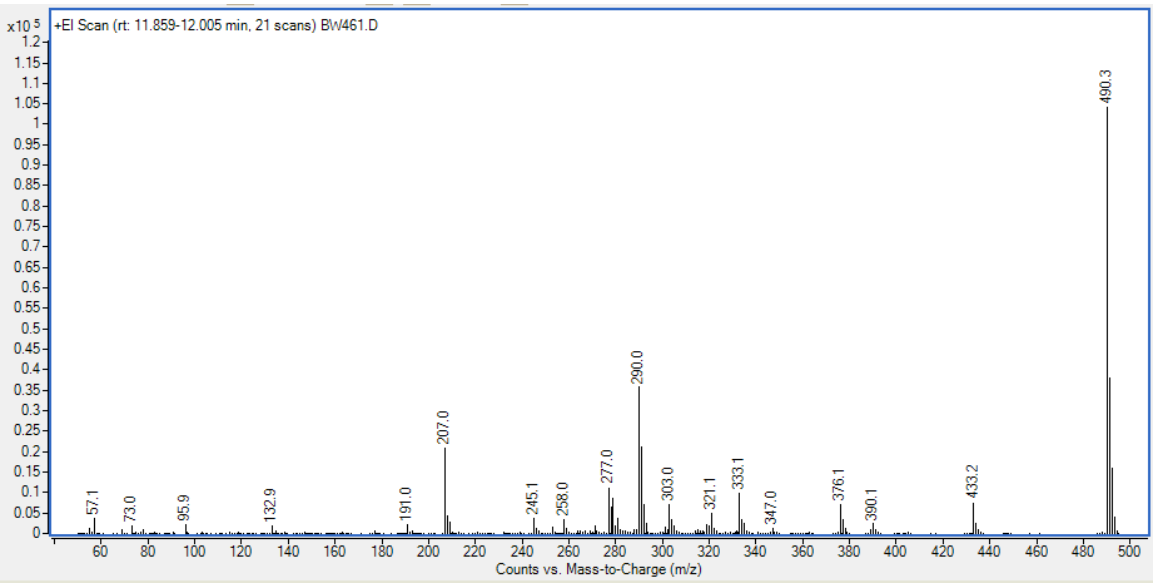
+EI Scan (rt: 11.859-12.005 min, 21 scans) BW461.D
x10 5
1.2
1.15
1.1
1.05
1
0.95
0.9
0.85
0.8
0.75
0.7
0.65
0.6
0.55
0.5
0.45
0.4
0.35
0.3
0.25
0.2
0.15
0.1
0.05
0
57.1
73.0
95.9
132.9
191.0
207.0
245.1
258.0
277.0
290.0
303.0
321.1
333.1
347.0
376.1
390.1
433.2
490.3
60
80
100
120
140
160
180
200
220
240
260
280
300
320
340
360
380
400
420
440
460
480
500
Counts vs. Mass-to-Charge (m/z)

Distannylated Bu-IDT Monomer

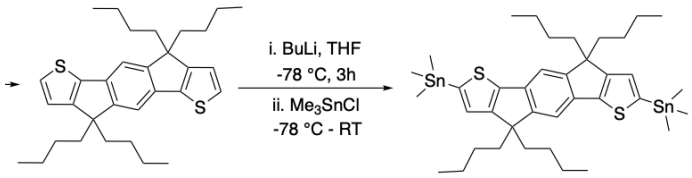

Bu-IDT distannylated Bu-IDT

Bu-IDT (170 mg, 0.35 mmol, 1 eq) was added to a 2-neck round bottom flask and dried under high vacuum, then purged with nitrogen. Anhydrous tetrahydrofuran (10 mL) was added to fully dissolve the compound and it was colled to -78 °C. n-butyl lithium (0.6 mL, 1.6 M, 2.5 eq) was added dropwise whereupon the solution turned slightly red and precipitate formed. This was continued to stir for 2 h and trimethyltin chloride (1.0 mL, 1.0 M, 3 eq) was added dropwise to quench the intermediate, whereupon the precipitate redissolved. This was stirred and allowed to reach room temperature overnight. This was poured into a separating funnel with water and extracted with dichloromethane, washing with water and brine, then sodium sulfate was added. This underwent gravity filtration, and the solvent was removed under reduced pressure to give a light brown solid. This was recrystallised in dichloromethane: methanol to give colourless crystals (199 mg, 70 %)

^{1}H NMR (400 MHz, CD_2Cl_2) δ 7.31 (s, 2H), 7.03 (s, 2H), 1.94 – 2.03(m, 4H), 1.81 – 1.90 (m, 4H), 1.13 (m, 8H), 0.77 – 0.89 (m, 8H), 0.72 (t, J = 7.3 Hz, 12H), 0.40 (s, 18H).

^{13}C NMR (400 MHz, $CDCl_3$) δ 157.33, 153.60, 147.80, 139.46, 135.42, 129.55, 113.59, 53.12, 39.17, 26.58, 23.29, 14.08, -7.89.

HSMS (ESI): HR-MS calculated for $[C_{38}H_{58}S_2Sn_2+H]^+$: m/z = 819.2097; measured m/z = 819.2126

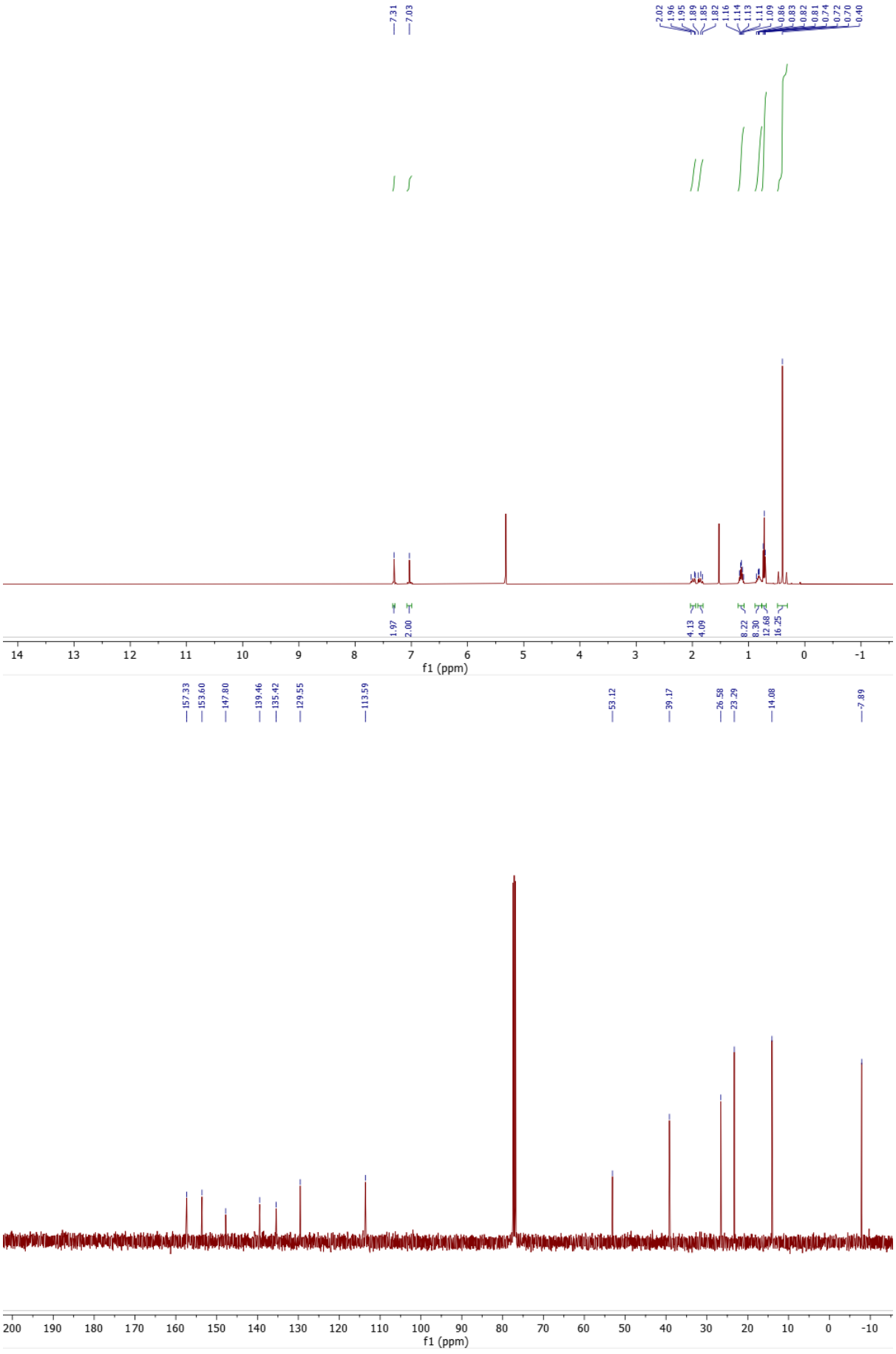
7.31
7.03
2.02
1.96
1.95
1.89
1.85
1.82
1.16
1.14
1.13
1.11
1.09
0.86
0.83
0.82
0.81
0.74
0.72
0.70
0.40
1.97
2.00
4.13
4.09
8.22
8.30
12.68
16.25
f1 (ppm)
157.33
153.60
147.80
139.46
135.42
129.55
113.59
53.12
39.17
26.58
23.29
14.08
-7.89
f1 (ppm)

Expanded Spectrum RT 0.10, NL 387721, Peak [1], Target Mass 819.2097

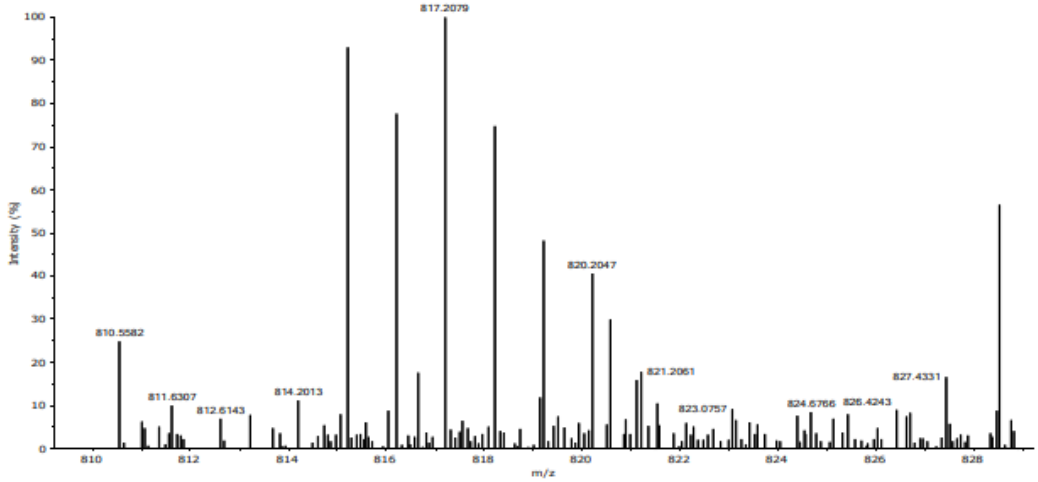

Theoretical Spectrum for C38H59S2Sn2, Minimum Abundance 0.01%

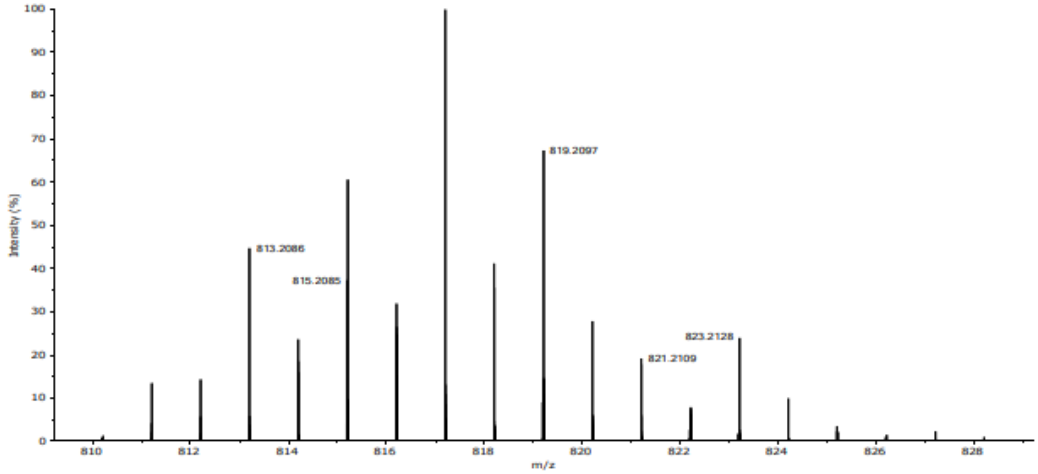

Bu-IDT-BTz-Si Polymer

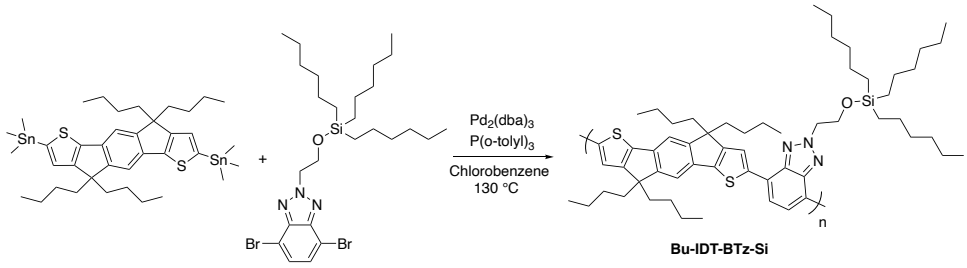

Distannylated Bu-IDT (165.43 mg, 203 µmol, 1 eq), **BTz-Si (**122.30 mg, 203 µmol, 1 eq), tri(o-tolyl)phosphine (4.9 mg, 16 µmol, 0.08 eq) and tris(dibenzylideneacetone) dipalladium(0) (3.7 mg, 4 µmol, 0.02 eq) were added to a microwave vial, it was capped then degassed with nitrogen for 30 minutes. Anhydrous chlorobenzene (4.0 mL) was added and it was heated to 130 °C overnight. This was cooled, precipitated into methanol and poured into a cellulose Soxhlet thimble. This underwent a Soxhlet extraction washing with methanol followed by hexane then extracted with chloroform. The chloroform fraction was concentrated under reduced pressure then precipitated into methanol and collected by vacuum filtration to give a dark purple solid polymer **Bu-IDT-BTz-Si** (121 mg, 64%)

GPC (chlorobenzene) M_N 27027 $gmol^{-1}$, MW 45072 $gmol^{-1}$, PD 1.66

^1H NMR (500 MHz, $CDCl_3$) δ 7.99 (br, 2H), 7.72 (br, 2H), 7.38 (br, 2H), 5.03 (br, 2H), 4.46 (br, 2H), 2.17-1.92 (b, m, 8H), 1.33-0.71 (br, m, 69H), 0.54 (br, 6H)

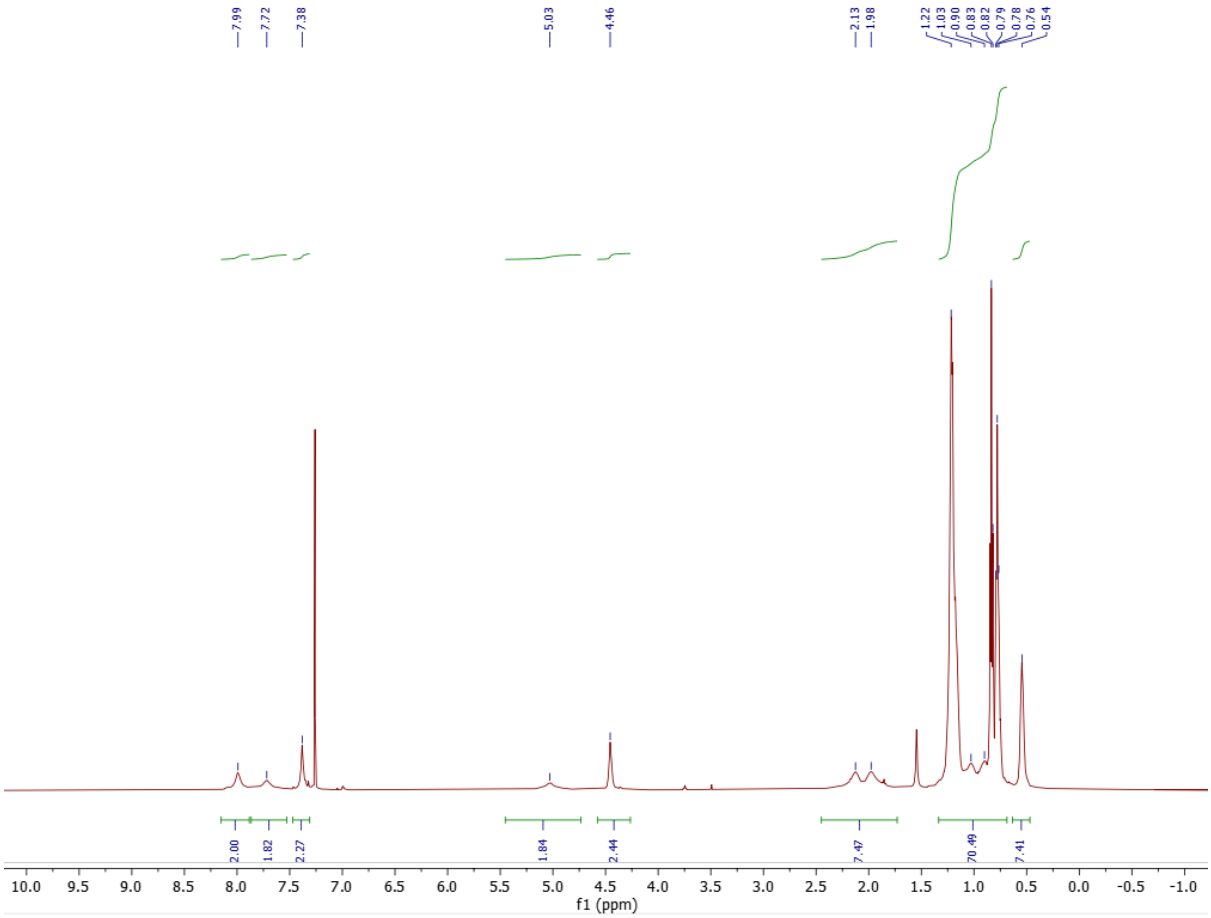

Sp-IDT-IF-Sp Polymer

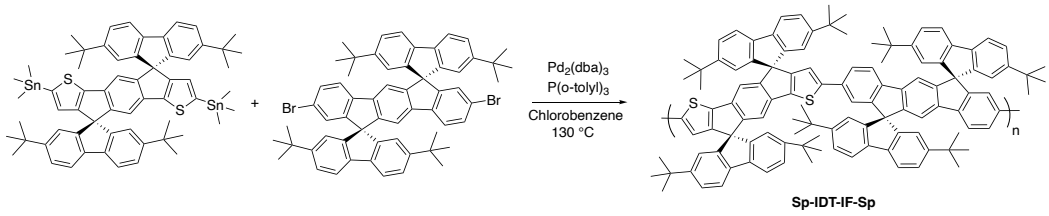

Distannylated Sp-IDT (102.66 mg, 92 µmol, 1 eq), **Sp-IF** (86.13 mg, 92 µmol, 1 eq), tri(o-tolyl)phosphine (2.2 mg, 7 µmol, 0.08 eq) and tris(dibenzylideneacetone) dipalladium(0) (1.7 mg, 2 µmol, 0.02 eq) were added to a microwave vial, it was capped then degassed with nitrogen for 30 minutes. Anhydrous chlorobenzene (1.8 mL) was added and it was heated to 130 °C overnight. This was cooled, precipitated into methanol and collected by vacuum filtration. In the filter it was washed with hot acetone, hot hexane, hot ethyl acetate followed by more methanol, then collected to give a dark purple solid (125 mg, 90%). Due to poor solubility NMR and GPC was not performed.

Dibrominated Sp-F Intermediate

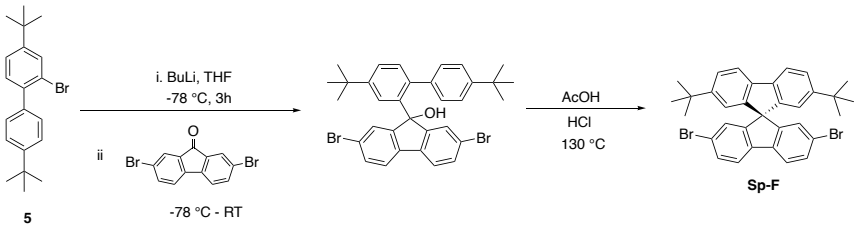

5 (10.00 g, 29.0 mmol, 3 eq) was added to a 2-neck round bottom flask and put under high vacuum attached to a Schlenk line for 30 minutes, then purged with nitrogen. It was dissolved in anhydrous tetrahydrofuran (200 mL) and cooled to -78 °C. n-butyllithium (18.0 mL, 1.6 M, 3 eq) was added slowly whereupon the solution turned yellow and solid began to precipitate. This was left stirring at -78 °C for 3 h under nitrogen. Finely divided and vacuum oven dried 2,7-dibromo-9-fluorenone (3.26 g, 9.7 mmol, 1 eq) was quickly added through the side neck under a positive pressure of nitrogen. This was left stirring overnight under nitrogen and allowed to reach room temperature. The tetrahydrofuran was removed under reduced pressure, then the alcohol intermediate was extracted with ethyl acetate in a separating funnel, washing with water, brine and sodium sulfate was added to dry. This underwent gravity filtration, and the solvent was removed under reduced pressure. Acetic acid (200 mL) and 37% aqueous hydrochloric acid solution (20 mL) were added, and it was refluxed overnight. This was then cooled and poured into icy water, then neutralised with sodium hydroxide solution. The precipitate was collected by vacuum filtration, washing thoroughly with deionised water and methanol. After drying, the powder recrystallised in ethanol: dichloromethane to give a white crystalline powder **dibrominated Sp-F** (2.97 g, 53%)

^{13}H NMR (400 MHz, $CDCl_3$) δ 7.71 (d, J = 8.1 Hz, 2H), 7.68 (d J = 8.1 Hz, 2H), 7.49 (dd, J = 8.1, 1.8 Hz, 2H), 7.42 (dd, J = 8.1, 1.8 Hz, 2H), 6.83 (d, J = 1.8 Hz, 2H), 6.62 (d, J = 1.8 Hz, 2H), 1.18 (s, 18H)

^{13}C NMR (400 MHz, $CDCl_3$) δ 151.49, 151.26, 147.32, 139.75, 139.29, 131.05, 127.54, 125.63, 121.93, 121.46, 120.59, 119.51, 35.03, 31.57.

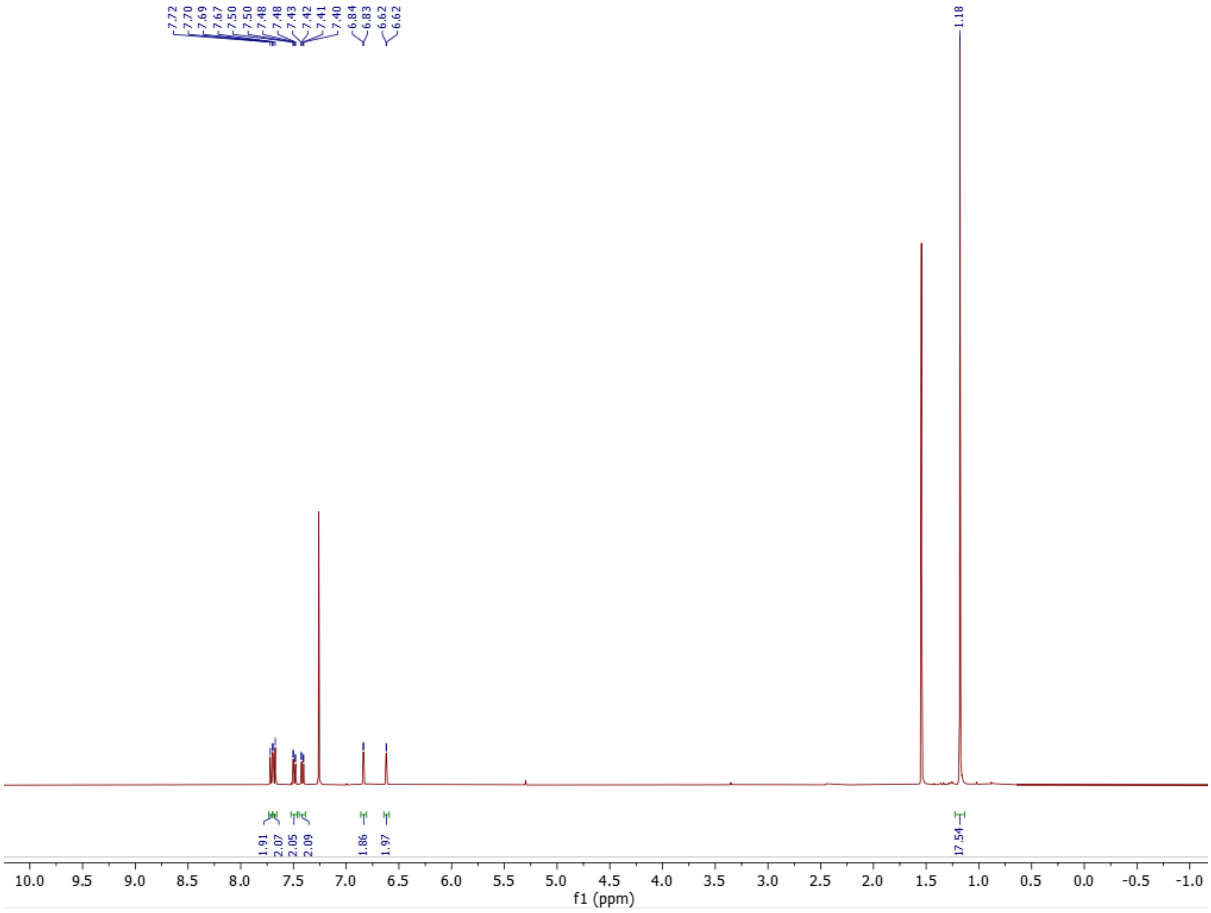
7.72
7.70
7.69
7.67
7.50
7.50
7.48
7.48
7.43
7.42
7.41
7.40
6.84
6.83
6.62
6.62
1.18
1.91
2.07
2.05
2.09
1.86
1.97
17.54
10.0 9.5 9.0 8.5 8.0 7.5 7.0 6.5 6.0 5.5 5.0 4.5 4.0 3.5 3.0 2.5 2.0 1.5 1.0 0.5 0.0 -0.5 -1.0
f1 (ppm)

Diborylated Sp-F Monomer

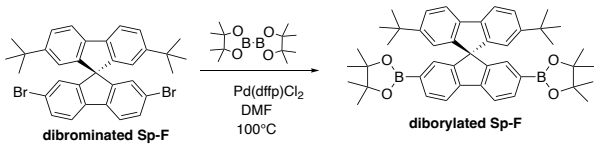

Dibrominated Sp-F (1.71 g, 2.9 mmol, 1 eq), bis(pinacolato)diborane (1.64 g, 6.5 mmol, 2.2 eq) and potassium acetate (0.64 g, 6.5 mmol, 2.2 eq) were added to a 2-neck round bottom flask and heated to 100 °C under high vacuum for 30 minutes. This was purged with nitrogen and [1,1′-Bis(diphenylphosphino) ferrocene]dichloropalladium(II) (0.04 g, 58 μmol, 0.02 eq) was added along with anhydrous dimethylformamide (40 mL) and it was refluxed overnight. After complete reaction it was cooled then poured into a separating funnel with water and extracted with dichloromethane, washing with water and brine, then sodium sulfate was added. This underwent gravity filtration, and the solvent was removed under reduced pressure to give a dark sludge. This was dissolved in a minimum amount of chloroform and pipetted into stirring hexane to cause impurities to precipitate. This was poured through and celite plug, washing with hexane. The filtrate was recovered and the solvent was removed under reduced pressure and it was recrystallised in ethanol: dichloromethane to give a white crystalline powder diborylated Sp-F (0.98 g, 49%)

^{1}H NMR (400 MHz, $CDCl_3$) δ 7.89 – 7.84 (m, 4H), 7.69 (d, J = 8.0 Hz, 2H), 7.36 (dd, J = 8.0, 1.8 Hz, 2H), 7.13 – 7.12 (m, 2H), 6.59 (d, J = 1.8 Hz, 2H), 1.26 (s, 24H), 1.13 (s, 18H).

^{13}C NMR (101 MHz, $CDCl_3$) δ 150.68, 149.65, 148.65, 144.62, 139.71, 134.54, 130.47, 124.89, 121.01, 119.67, 119.18, 83.83, 34.94, 31.59, 24.93.

MS (MALDI-TOF): MS calculated for $[C_{45}H_{54}B_2O_4]^+$: m/z =680.42; measured m/z = 680.70

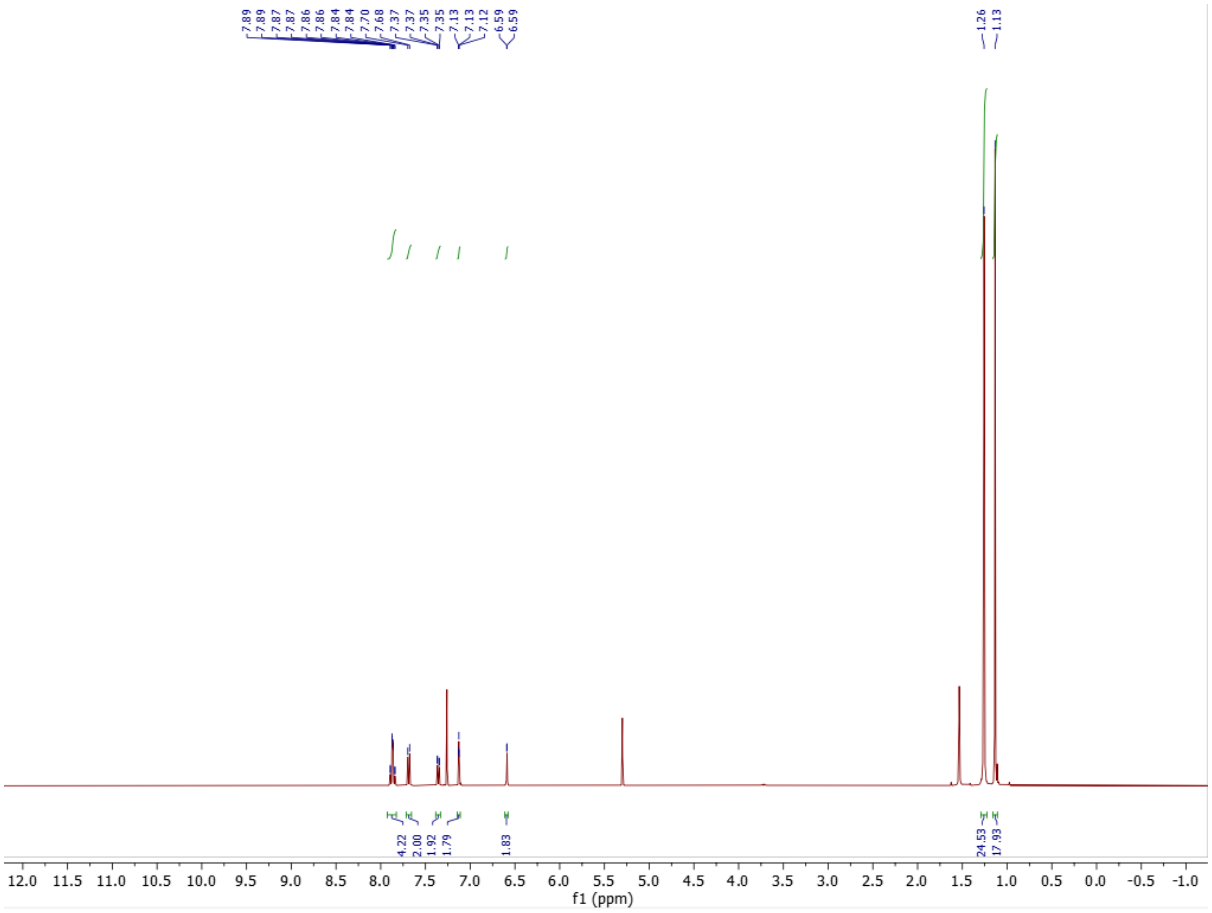
7.89
7.89
7.87
7.87
7.86
7.86
7.84
7.84
7.70
7.68
7.37
7.37
7.35
7.35
7.13
7.13
7.12
6.59
6.59
1.26
1.13
4.22
2.00
1.92
1.79
1.83
24.53
17.93
12.0 11.5 11.0 10.5 10.0 9.5 9.0 8.5 8.0 7.5 7.0 6.5 6.0 5.5 5.0 4.5 4.0 3.5 3.0 2.5 2.0 1.5 1.0 0.5 0.0 -0.5 -1.0
f1 (ppm)

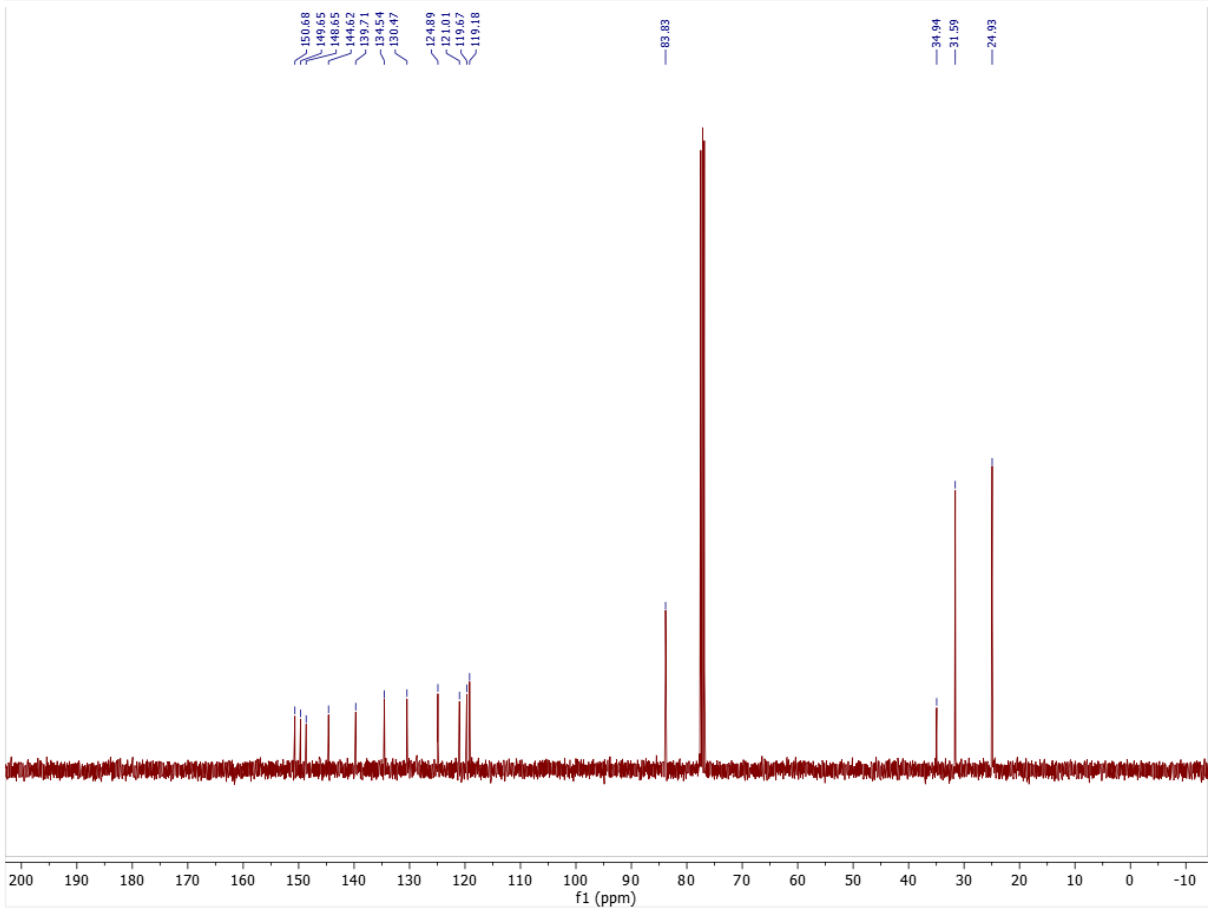
150.68
149.65
148.65
144.62
139.71
134.54
130.47
124.89
121.01
119.67
119.18
83.83
34.94
31.59
24.93
200 190 180 170 160 150 140 130 120 110 100 90 80 70 60 50 40 30 20 10 0 -10
f1 (ppm)

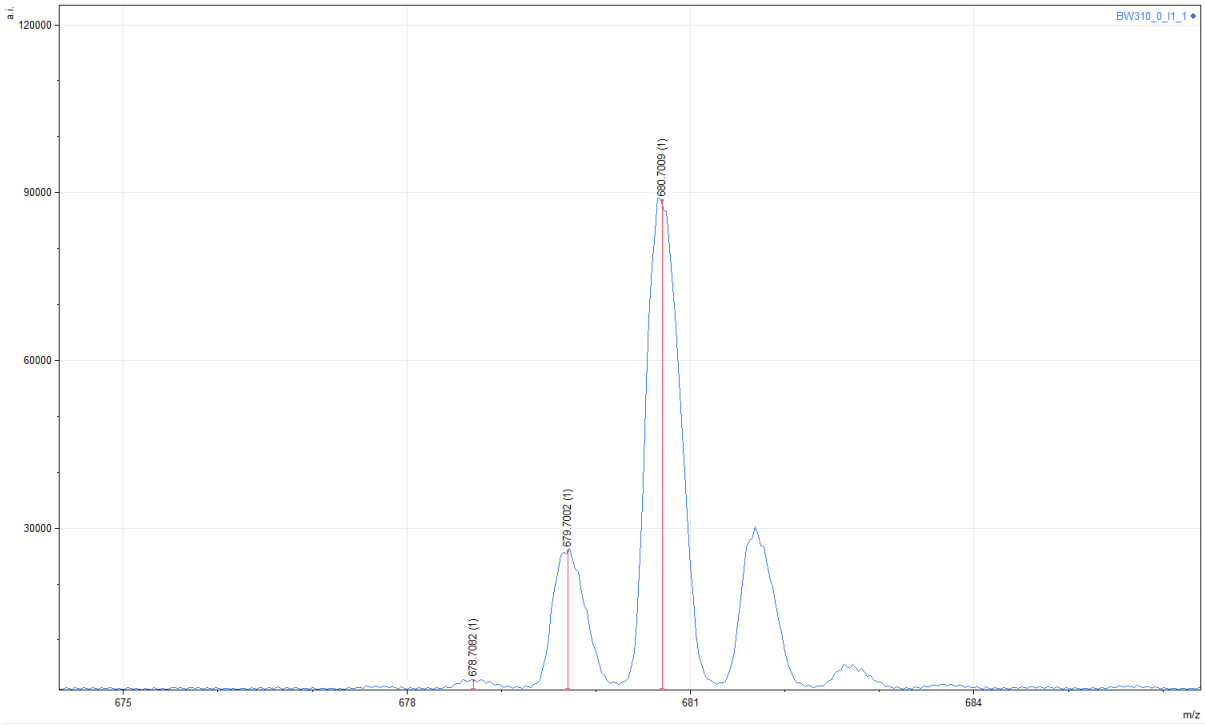
a.i.
120000
90000
60000
30000
BW310_0_I1_1
680.7009 (1)
679.7002 (1)
678.7082 (1)
675
678
681
684
m/z

Sp-F-BTz-Si Polymer

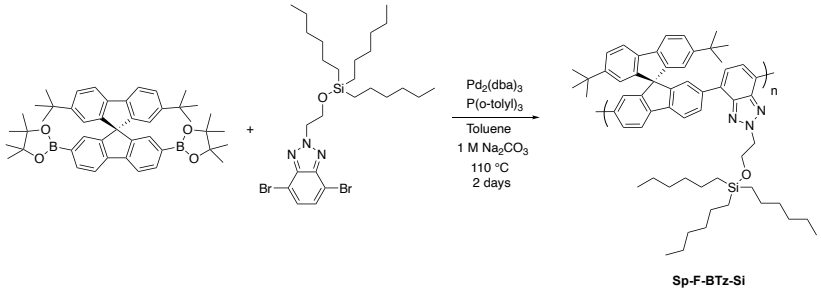

Sp-F-BTz-Si

Diborylated Sp-F (471.74 mg, 693 µmol, 1 eq), **BTz-Si** (418.38 mg, 693µmol, 1 eq), tri(o-tolyl)phosphine (16.9mg, 55 µmol, 0.08 eq), tris(dibenzylideneacetone) dipalladium(0) (12.7 mg, 14 µmol, 0.02 eq) and Aliquat 336 (1 drop) were added to a microwave vial. It was capped then degassed with nitrogen for 30 minutes. Anhydrous toluene (15.0 mL) and degassed sodium carbonate (1M, 5.0 mL) were added and it was heated to 130 °C overnight. This was cooled, precipitated into methanol and poured into a cellulose Soxhlet thimble. This underwent Soxhlet extraction washing with acetone followed by hexane, ethyl acetate then extracted with chloroform. The chloroform fraction was concentrated under reduced pressure then precipitated into methanol and collected by vacuum filtration to give a dark purple solid (146 mg, 24%)

GPC (chlorobenzene) M_N 22460 $gmol^{-1}$, M_W 30,383 $gmol^{-1}$ PD 1.35

^{1}H NMR (500 MHz, $CDCl_3$) δ 8.31 (br, m, 2H), 8.00 (d, J = 8.2 Hz, 2H), 7.70 (d, J = 8.0 Hz, 2H), 7.36 (d, J = 6.8 Hz, 2H), 7.23 (br, 2H), 7.15 (br, 2H), 6.75 (s, 2H), 4.80 (br, 2H), 4.21 (m, 2H), 1.28-1.09 (br, m, 42H), 0.83 (t, J = 7.0 Hz, 8H), 0.48 (m, 6H)

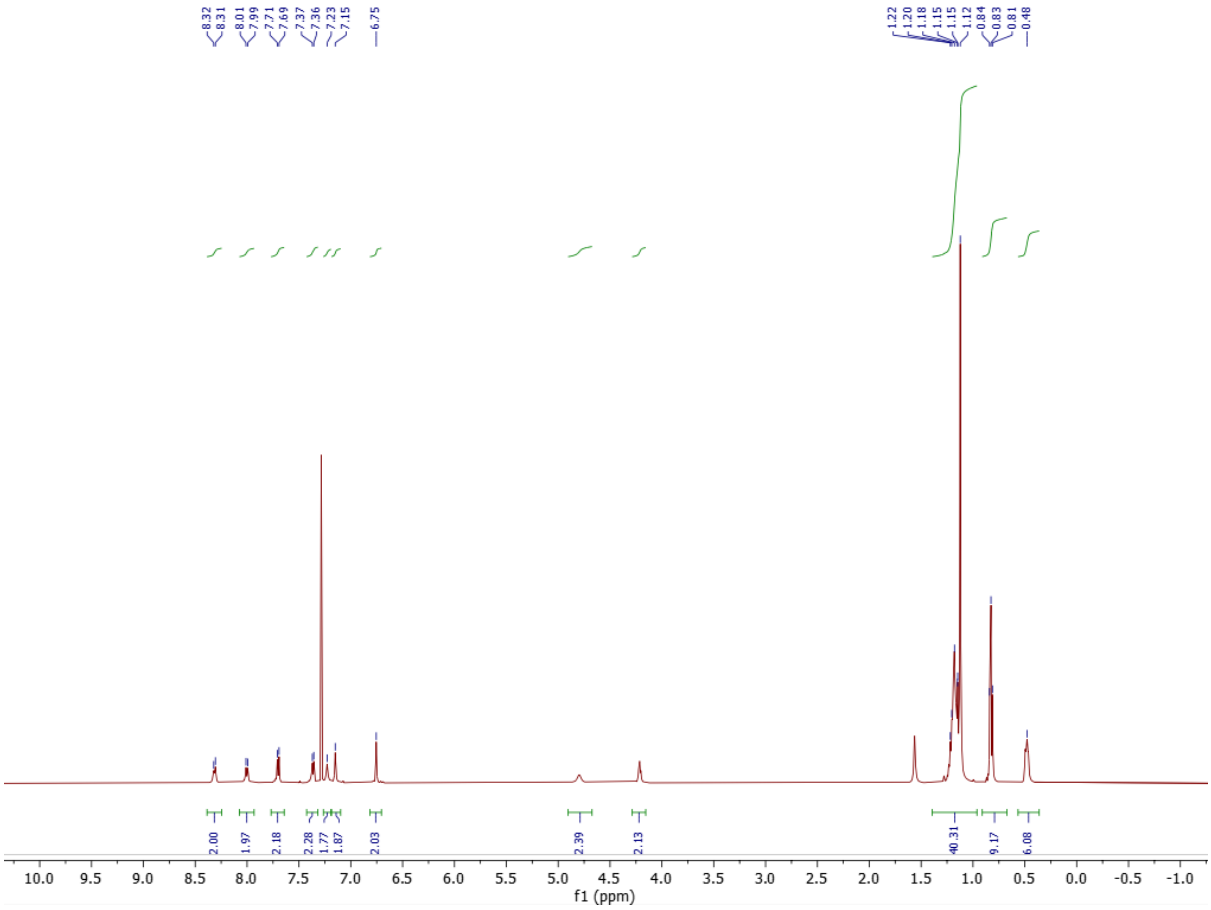
8.32
8.31
8.01
7.99
7.71
7.69
7.37
7.36
7.23
7.15
6.75
1.22
1.20
1.18
1.15
1.15
1.12
0.84
0.83
0.81
0.48
2.00
1.97
2.18
2.28
1.77
1.87
2.03
2.39
2.13
40.31
9.17
6.08
10.0 9.5 9.0 8.5 8.0 7.5 7.0 6.5 6.0 5.5 5.0 4.5 4.0 3.5 3.0 2.5 2.0 1.5 1.0 0.5 0.0 -0.5 -1.0
f1 (ppm)

Intermediate 16

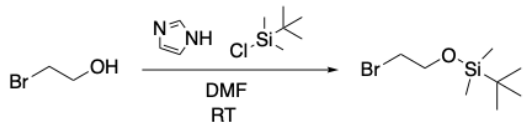

16

2-bromoethanol (2.93 g, 23.4 mmol, 0.9 eq) tert-butyldimethylsilyl chloride (3.92 g, 26.0 mmol, 1 eq) and imidazole (3.54g, 52.0 mmol, 2 eq) were purged with nitrogen and dissolved in anhydrous dimethylformamide (100 mL). This was stirred for 4 h then poured into a separating funnel. The product was extracted with dichloromethane and washed twice with water, once with brine and sodium sulfate was added. This underwent gravity filtration, and the solvent was removed under reduced pressure to recover a colourless oil **16** and was used without further (5.07 g, 90%).

^{1}H NMR (400 MHz, $CDCl_3$) δ 3.89 (t, J = 6.5 Hz, 2H), 3.39 (t, J = 6.5 Hz, 2H), 0.90 (s, 9H), 0.09 (s, 6H)

^{13}C NMR (400 MHz, $CDCl_3$) δ 63.63, 33.36, 25.94, 18.43, -5.16.

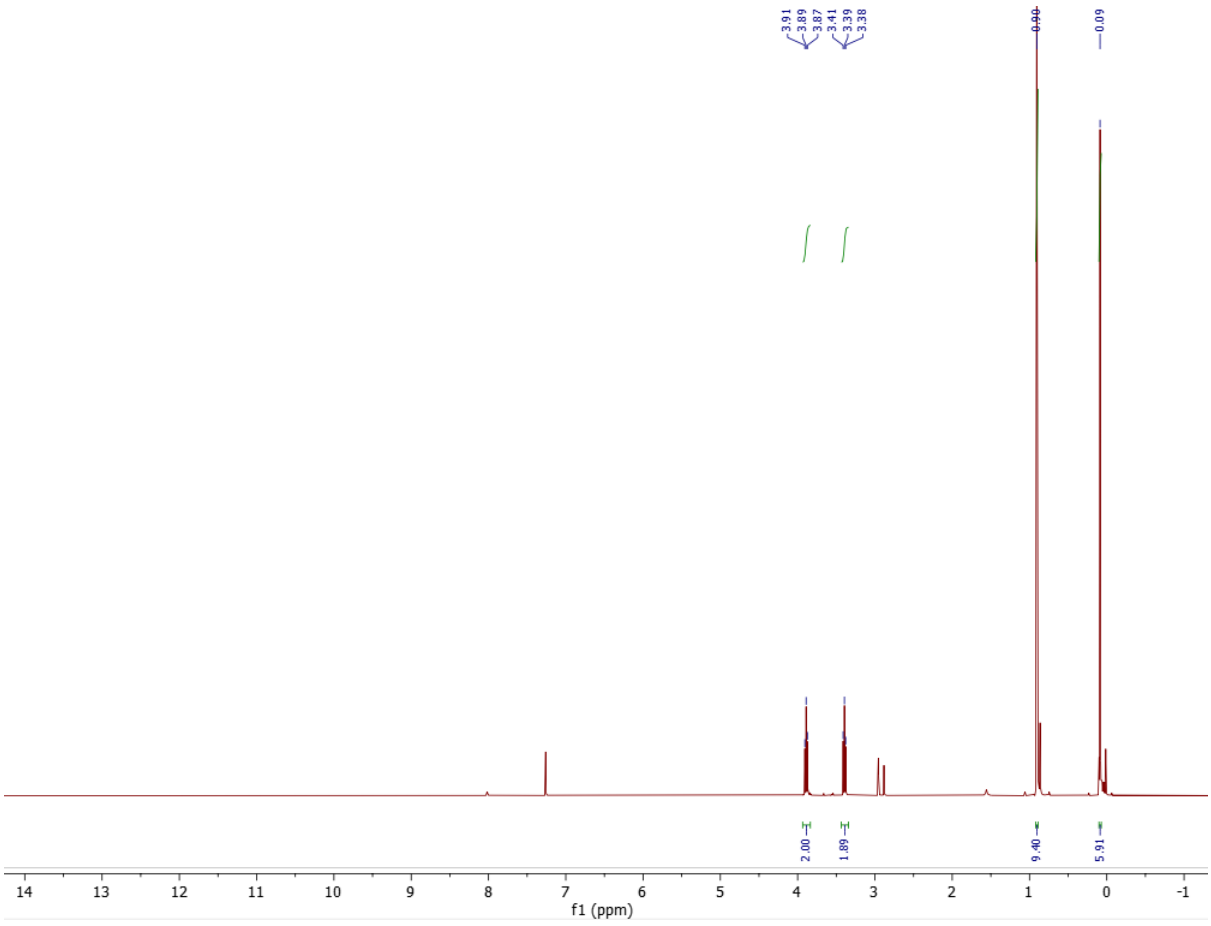

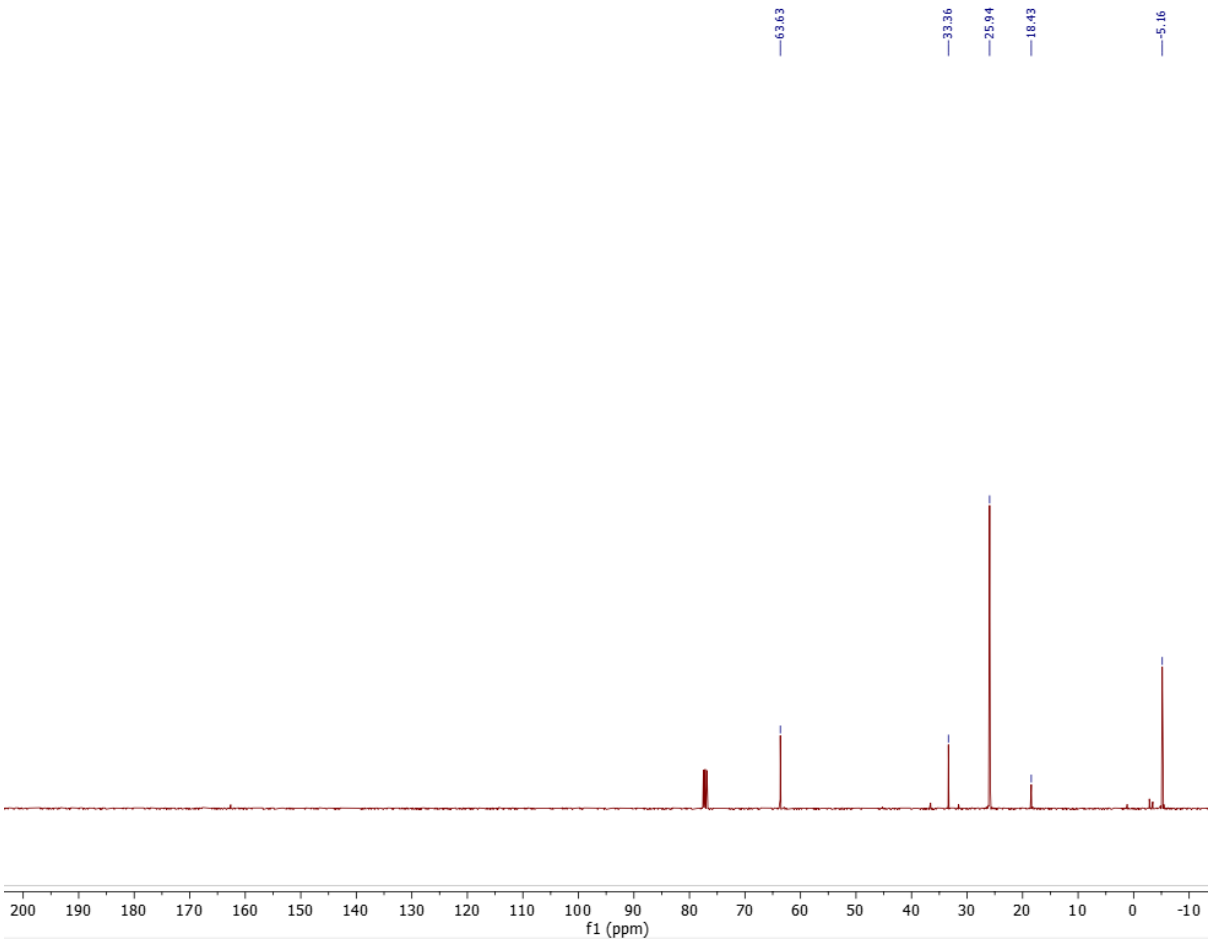
63.63
33.36
25.94
18.43
-5.16
200 190 180 170 160 150 140 130 120 110 100 90 80 70 60 50 40 30 20 10 0 -10
f1 (ppm)

F-Si Monomer

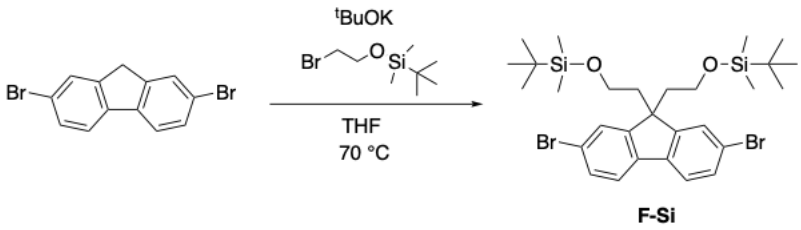

F-Si

2,7-dibromofluorene (1.50 g, 4.6 mmol, 1 eq) and potassium tert-butoxide (1.56 g,13.9 mmol, 3 eq) were purged with nitrogen in a 2 neck round bottom flask and anhydrous tetrahydrofuran (50 mL) was added, whereupon it generated a red solution. It was stirred at room temperature under nitrogen for 10 minutes, then **16** (3.32 g, 13.9 mmol, 3 eq) was added and it was refluxed overnight. After complete reaction, the solution was poured into a separating funnel. The product was extracted with dichloromethane and washed with water, brine and sodium sulfate was added. This underwent gravity filtration, and the solvent was removed under reduced pressure to get a brown residue. This was purified on a silica column, eluting with a graduated eluent, from pure petroleum ether to petroleum ether: diethyl ether (98:2). The columned material was subsequently collected and recrystallised in dichloromethane: ethanol to give a colourless crystalline solid **F-Si** (1.60 g, 54%)

^{1}H NMR (400 MHz, $CDCl_3$) δ 7.52-7.50 (m, 4H), 7.45 (dd, J = 8.1, 1.7 Hz, 2H), 2.98 (t, J = 7.0 Hz, 4H), 2.26 (t, J = 7.0 Hz, 4H), 0.73 (s, 18H), -0.2 (s, 12H)

^{13}C NMR (400 MHz, $CDCl_3$) δ 151.39, 138.60, 130.62, 126.83, 121.71, 121.40, 59.03, 52.35, 42.91, 25.95, 18.25, -5.45

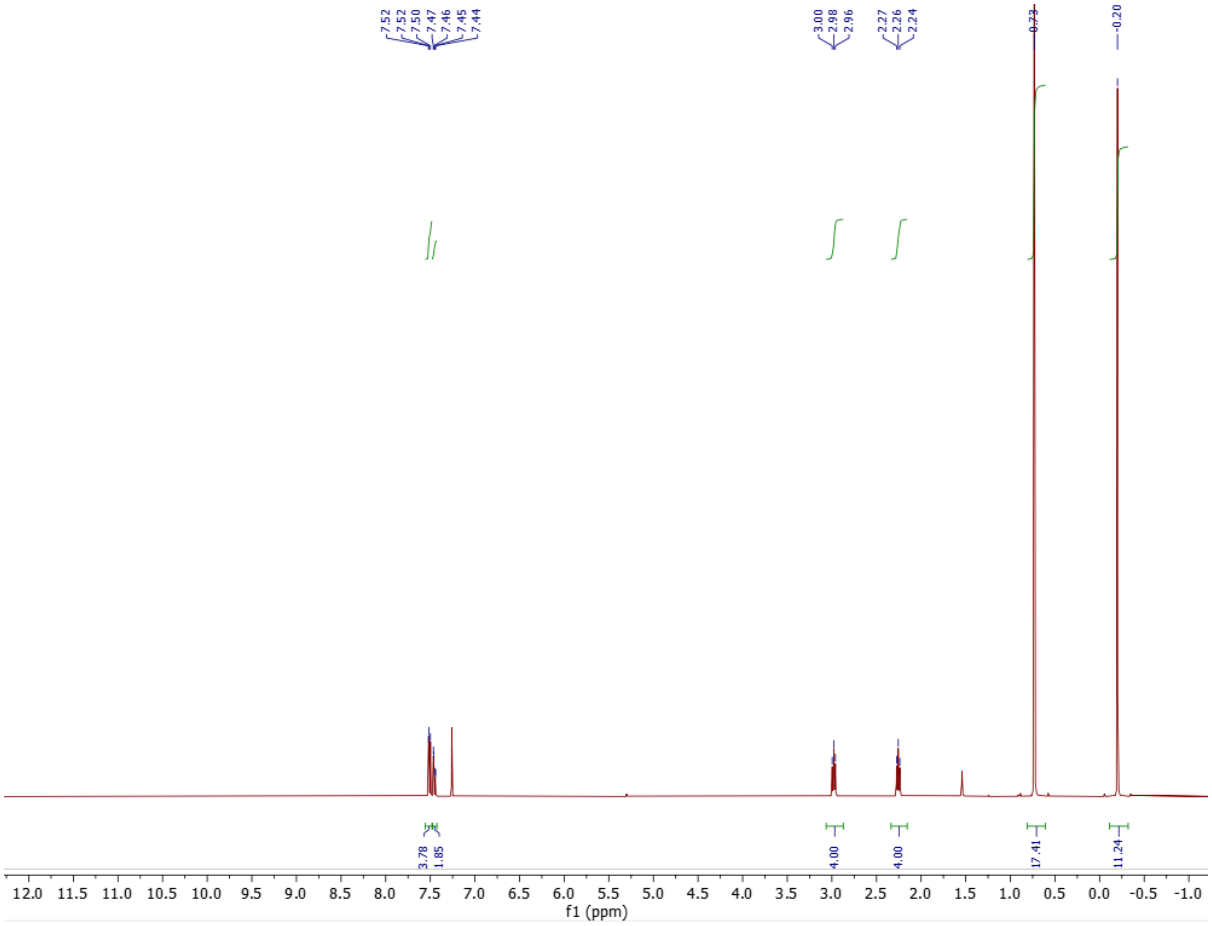
7.52
7.52
7.50
7.47
7.46
7.45
7.44
3.00
2.98
2.96
2.27
2.26
2.24
0.73
-0.20
3.78
1.85
4.00
4.00
17.41
11.24
12.0 11.5 11.0 10.5 10.0 9.5 9.0 8.5 8.0 7.5 7.0 6.5 6.0 5.5 5.0 4.5 4.0 3.5 3.0 2.5 2.0 1.5 1.0 0.5 0.0 -0.5 -1.0
f1 (ppm)

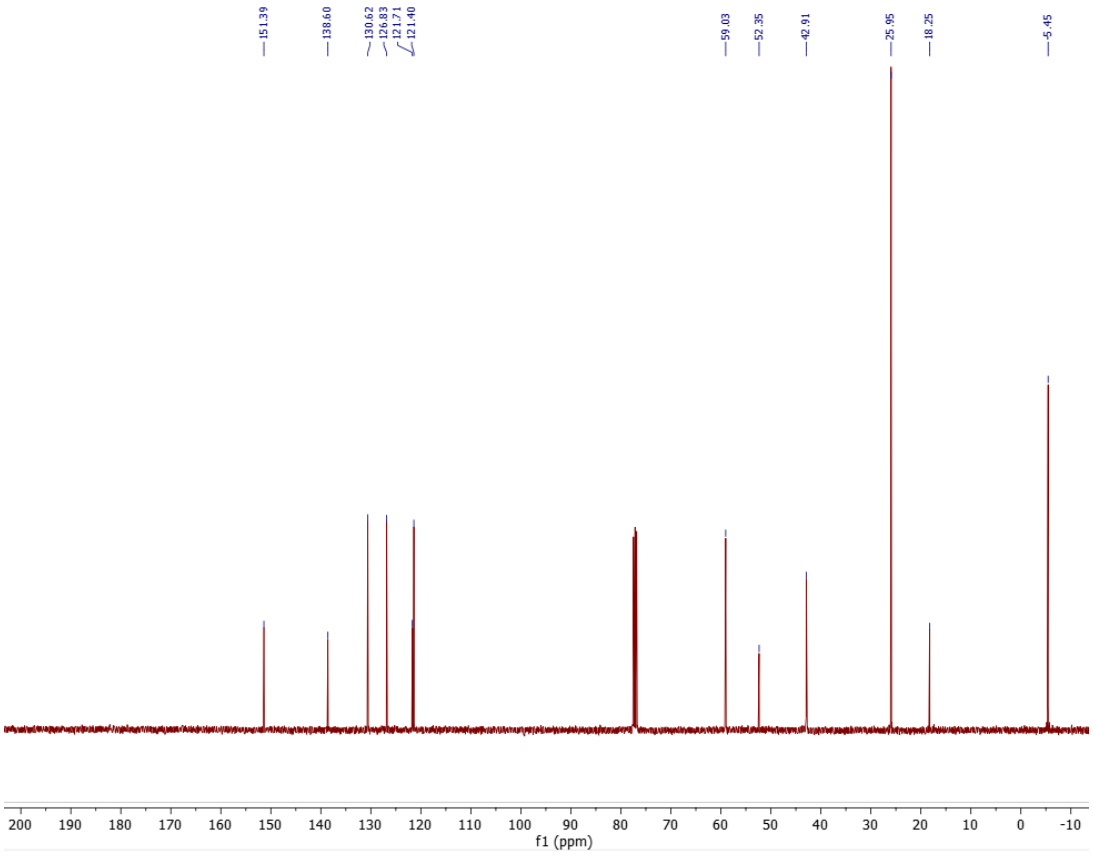
151.39
138.60
130.62
126.83
121.71
121.40
59.03
52.35
42.91
25.95
18.25
5.45
200 190 180 170 160 150 140 130 120 110 100 90 80 70 60 50 40 30 20 10 0 -10
f1 (ppm)

Sp-IDT-Si Polymer

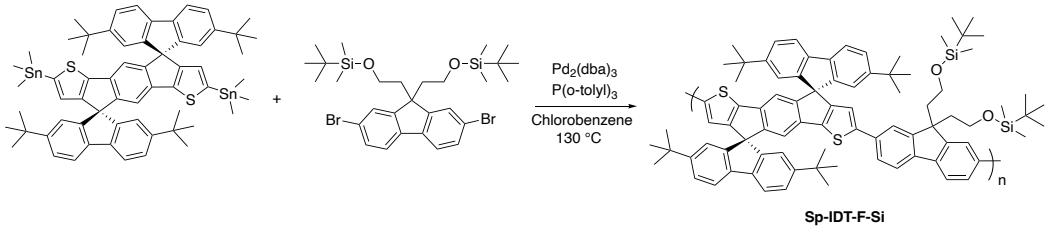

Sp-IDT-F-Si

Distannylated Sp-IDT (381.10 mg, 341 µmol, 1 eq), **F-Si** (218.62 mg, 341 µmol, 1 eq), tri(o-tolyl)phosphine (8.3 mg, 27 µmol, 0.08 eq) and tris(dibenzylideneacetone) dipalladium(0) (6.3 mg, 7 µmol, 0.02 eq) were added to a microwave vial, it was capped then degassed with nitrogen for 30 minutes. Anhydrous chlorobenzene (6.8 mL) was added and it was heated to 130 °C overnight. This was cooled, precipitated into methanol and poured into a cellulose Soxhlet thimble. This underwent a Soxhlet extraction washing with acetone followed by hexane, ethyl acetate then extracted with chlorobenzene. This was concentrated under reduced pressure, then precipitated into methanol and collected by vacuum filtration to give a yellow solid (317 mg, 73 %).

^{1}H NMR (500 MHz, $CDCl_3$) δ 7.78 (d, J= 7.9 Hz, 4 H), 7.48-7.35 (br, m, 10 H), 6.87-6.79 (br, m, 6H), 6.68 (br, s, 2H), 2.83 (br, 4H), 2.15 (br, 4H), 1.20 (s, 36 H), 0.56 (s, 18H), -0.39 (s, 12H)

GPC chlorobenzene M_N 12593 gmol^{-1} M_W 23139 gmol^{-1} PD: 1.84

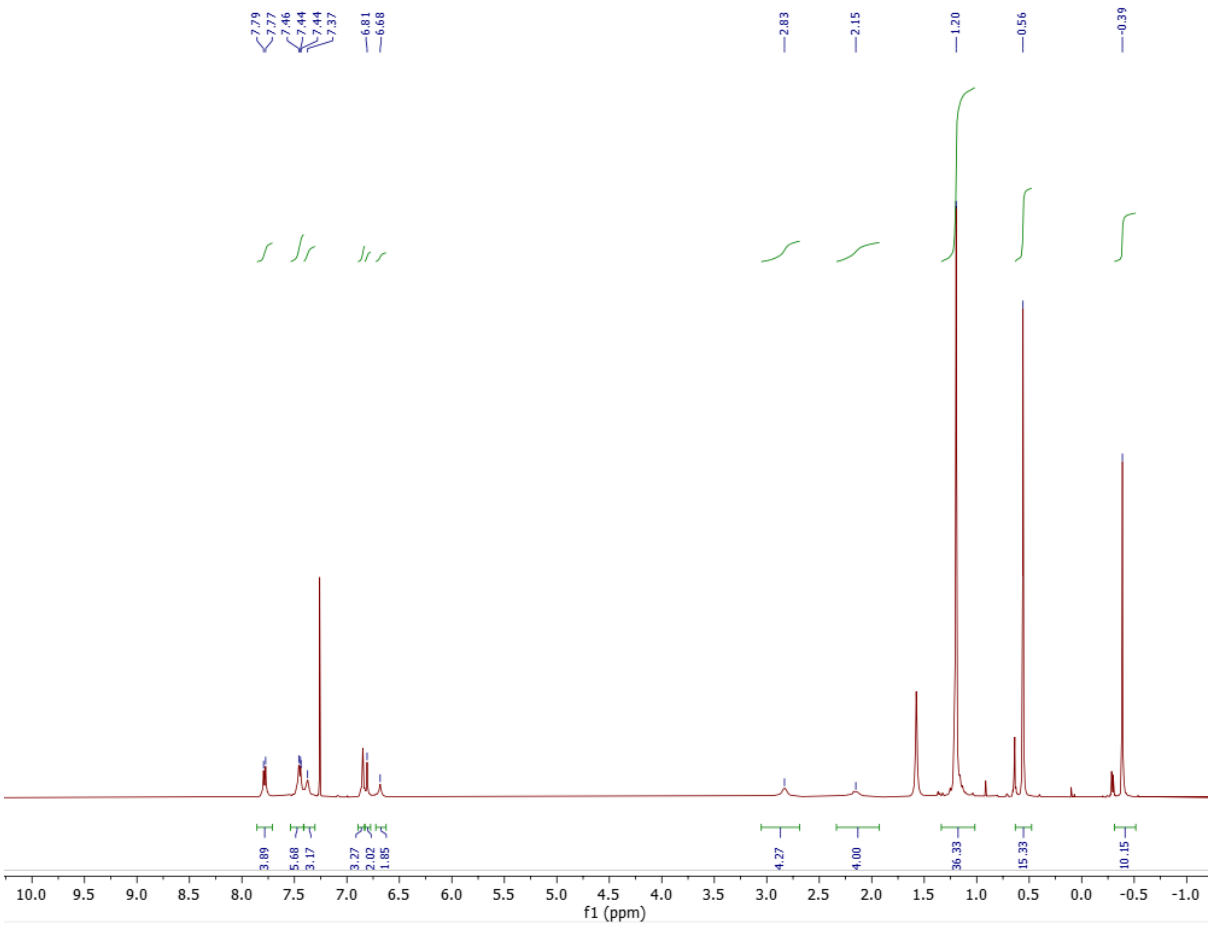

Intermediate 16

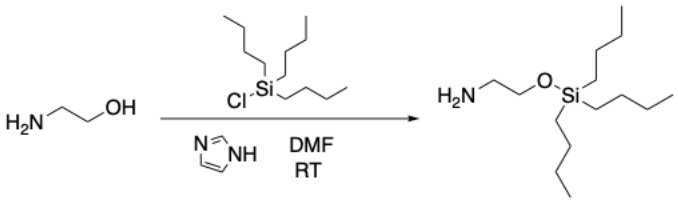

16

Ethanolamine (0.89 g, 14.5 mmol, 1.1 eq), tributylsilyl chloride (3.10 g, 13.2 mmol, 1 eq) and imidazole (1.17g, 17.2 mmol, 1.3 eq) were purged with nitrogen and dissolved in anhydrous dimethylformamide (30 mL). This was stirred for 4 h then poured into a separating funnel. The product was extracted with dichloromethane and washed twice with water, once with brine and sodium sulfate was added. This underwent gravity filtration, and the solvent was removed under reduced pressure. The resultant oil was purified on a silica column, eluting with a graduated eluent, from petroleum ether: ethyl acetate (50:50) to (80:20). Removal of solvent from the product fractions gave a colourless oil **16** (2.13 g, 62%).

^{1}H NMR (400 MHz, $CDCl_3$) δ 3.87 (t, J = 7.0, 2H), 3.39 (t, J = 7.0 Hz, 2H), 1.36-1.29 (m, 12H), 0.89 (t, 7.0 Hz, 9H), 0.63-0.59 (m, 6H)

^{13}C NMR (400 MHz, $CDCl_3$) δ 63.37, 33.18, 26.71, 25.45, 13.90, 13.41.

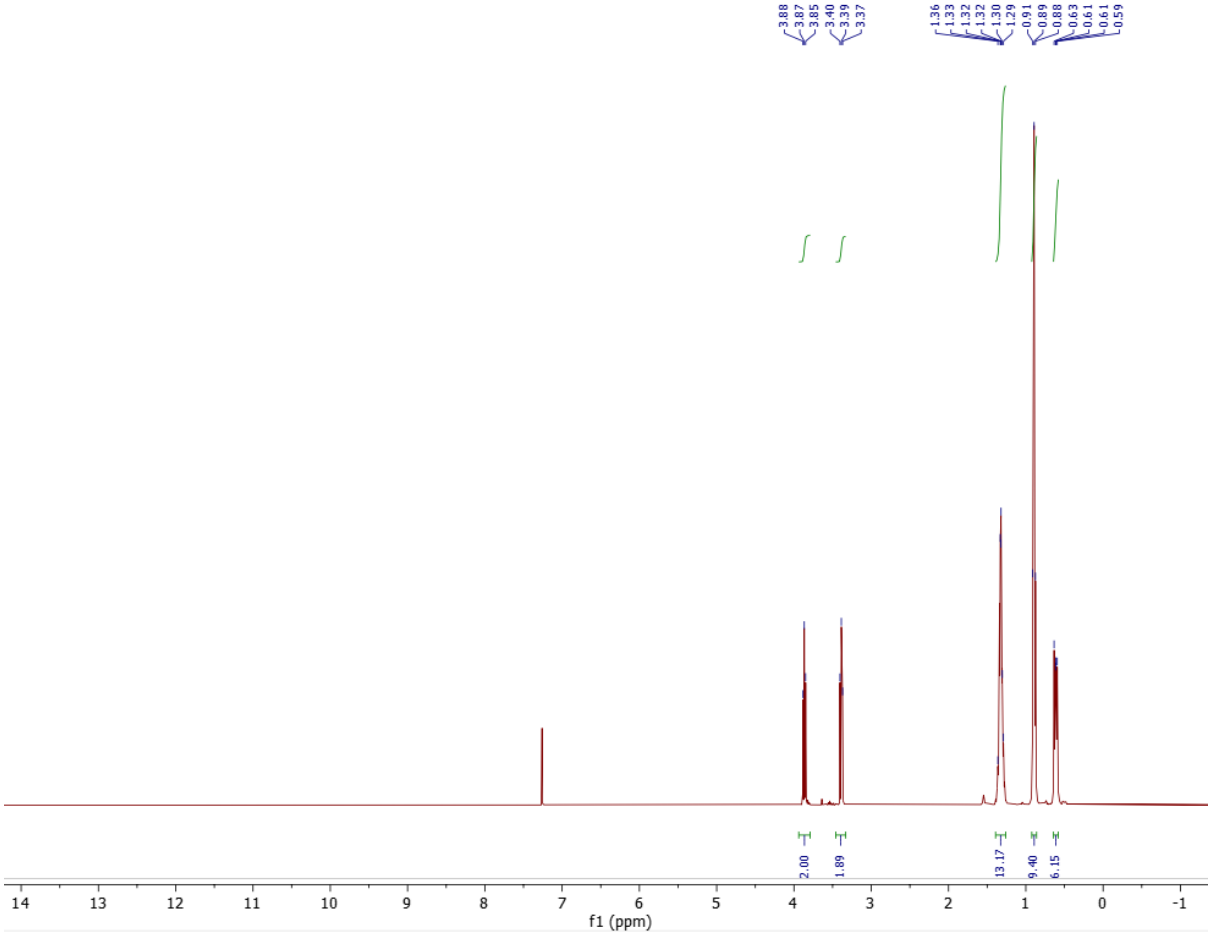

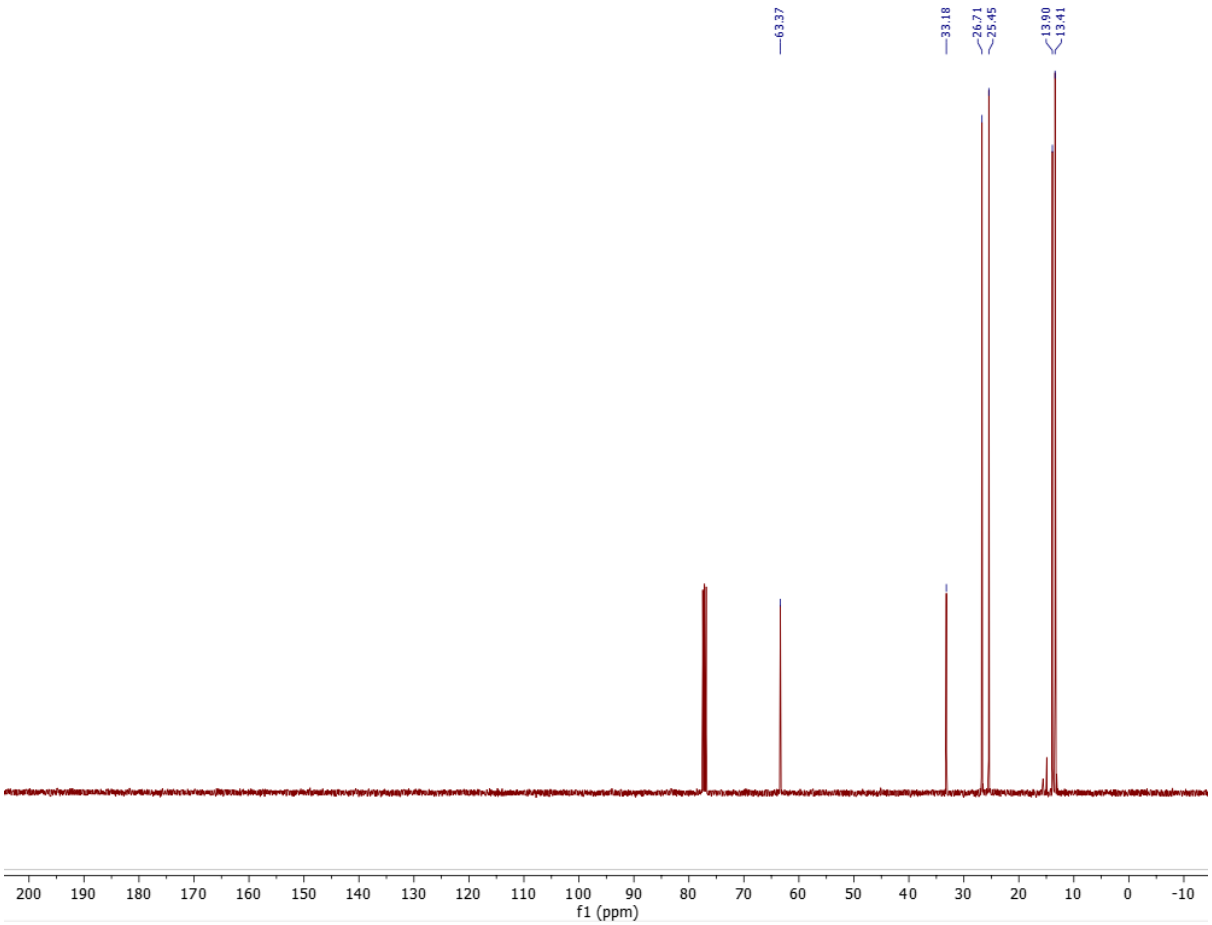

NDI-Si Monomer

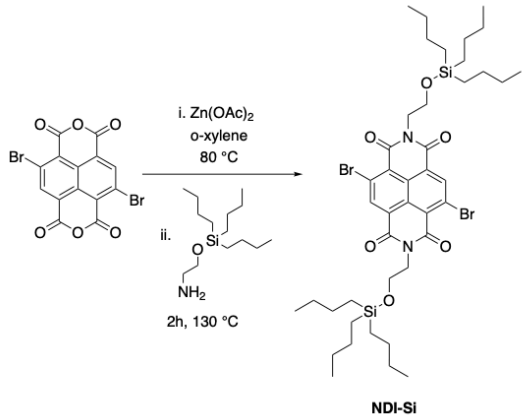

2,6-Dibromonaphthalene-1,4,5,8-tetracarboxylic dianhydride (0.50g, 1.2 mmol, 1 eq) and anhydrous zinc acetate (0.43g, 2.35 mmol, 2 eq) were added to a 2-neck round bottom flask and put under high vacuum attached to a Schlenk line for 30 minutes, then purged with nitrogen. Anhydrous o-xylene was added and the pale-yellow suspension was stirred at 80 °C under nitrogen. **16** (0.67 g, 2.6 mmol, 2.2 eq) was added dropwise and the temperature was increase to 130 °C. This was allowed to

react for 2h, after which time the suspension had become a clear solution and had begun to turn slightly red. It was cooled and poured into a separating funnel with water and extracted with dichloromethane, washing with water, brine, and sodium sulfate was added. This underwent gravity filtration, and the solvent was removed under reduced pressure to give a slightly red oil. This was purified on a silica column, eluting with a graduated eluent, from pure petroleum ether to petroleum ether: ethyl acetate (90:10). The fractions with product were collected, the solvent was removed under reduced pressure, recrystallised in dichloromethane: methanol and underwent vacuum filtration to recover fluffy pale-yellow crystals **NDI-Si** (0.19 g, 18%)

^{1}H NMR (400 MHz, $CDCl_3$) δ 9.00 (s, 2H), 4.41 (t, J = 6.0 Hz, 4H), 3.93 (t, J = 6.0 Hz, 4H), 1.25-1.18 (m, 24 H), 0.79 (t, J = 6.8 Hz, 18H), 0.54-0.50 (m, 12H)

^{13}C NMR (400 MHz, $CDCl_3$) δ 161.00, 160.87, 139.22, 128.52, 127.86, 125.49, 124.23, 59.40, 42.99, 26.67, 25.40, 13.87, 13.34.

MS (MALDI-TOF): MS calculated for $[C_{42}H_{64}Br_2N_2O_6Si_2]^+$: m/z = 908.27; measured m/z = 907.90

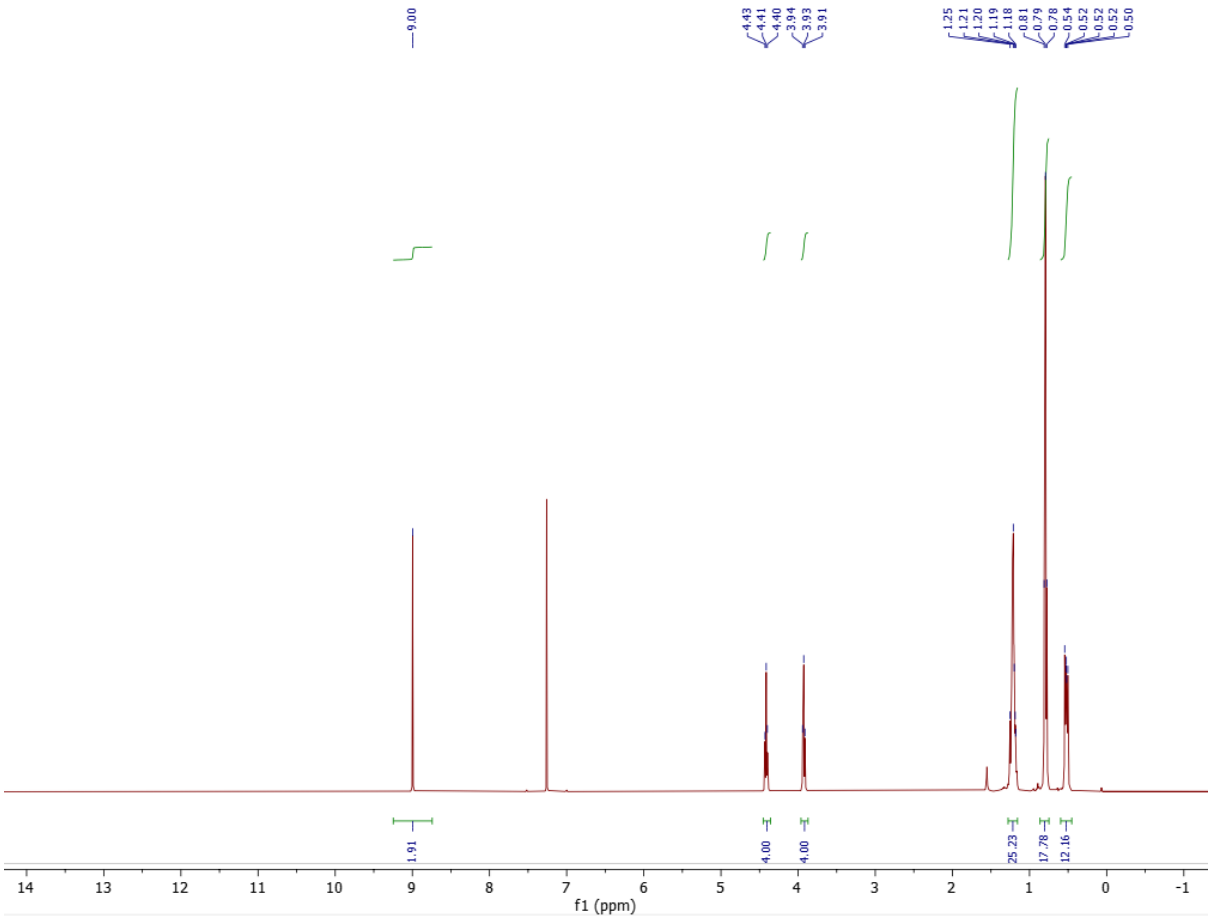

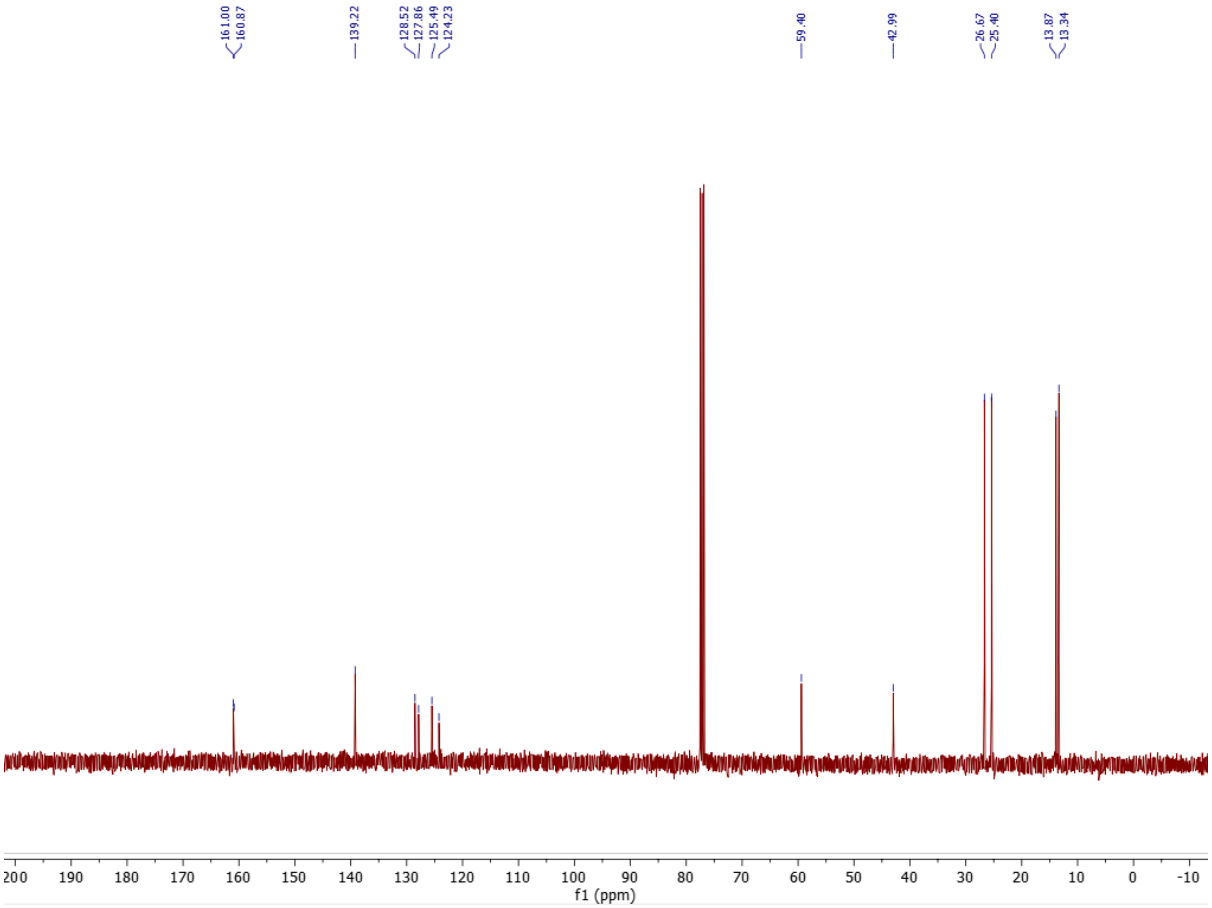

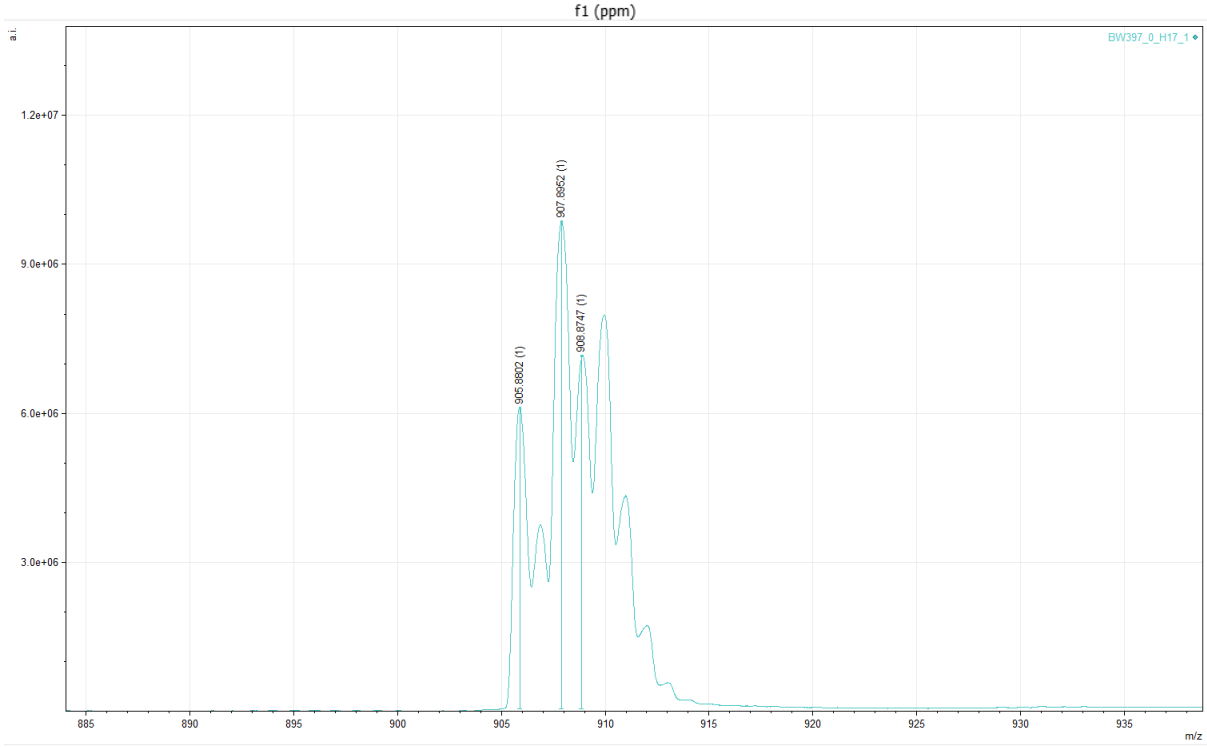

Sp-IDT-NDI-Si Polymer

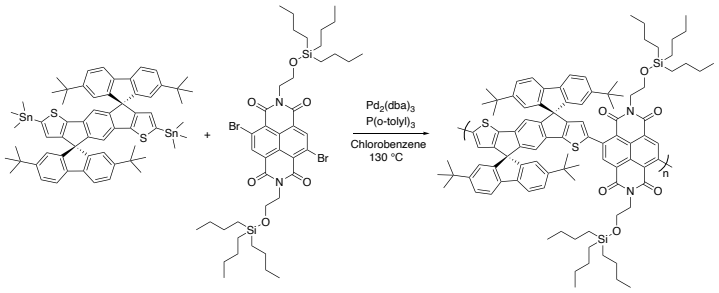

Distannylated Sp-IDT (263.25 mg, 236 µmol, 1 eq), **NDI-Si** (214.26 mg, 236 µmol, 1 eq), tri(o-tolyl)phosphine (5.7 mg, 19 µmol, 0.08 eq) and tris(dibenzylideneacetone)dipalladium(0) (4.3 mg, 5 µmol, 0.02 eq) were added to a microwave vial, it was capped then degassed with nitrogen for 30 minutes. Anhydrous chlorobenzene (4.7 mL) was added and it was heated to 130 °C overnight. This was cooled, precipitated into methanol and poured into a cellulose Soxhlet thimble. This underwent a Soxhlet extraction washing with acetone followed by hexane, ethyl acetate then extracted with chloroform. The chloroform fraction was then precipitated into methanol and collected by vacuum filtration to give a deep purple solid (141 mg, 35 %).

GPC (chlorobenzene) M_N 27,864 gmol^{-1}, M_W 41290 gmol^{-1}, PD 1.48 gmol^{-1}

^{1}H NMR (400 MHz, $CDCl_3$) δ 8.54 (s, 2H), 7.72 (d, J = 7.9 Hz, 4H), 7.42 (d, J = 7.4 Hz, 4H), 6.92 (br, 4H), 6.84 (s, 2H), 6.66 (s, 2H), 4.16 (br, 4H), 3.69 (br, 4H), 1.25-1.03 (br, m, 60H), 0.64 (br, 18H), 0.39 (br, 12H)

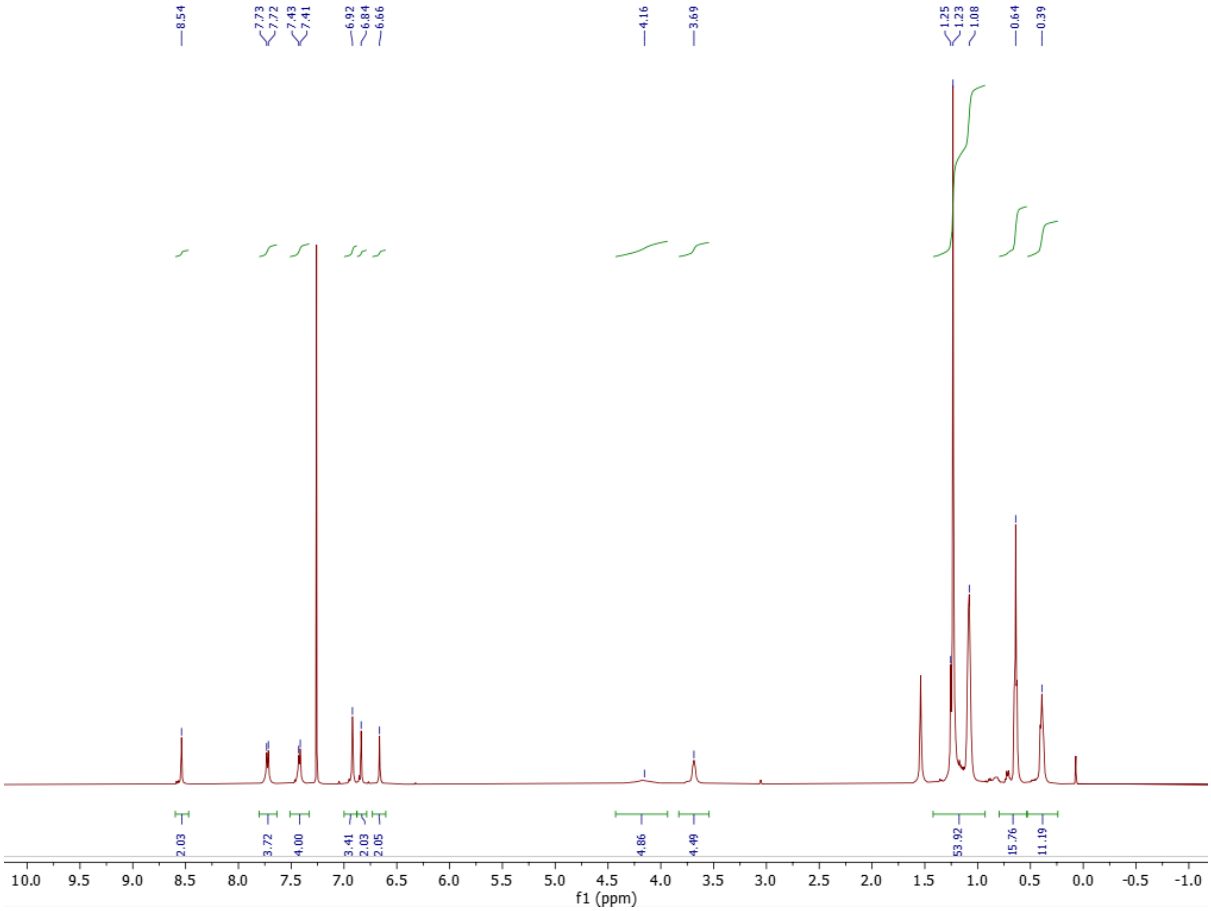

Intermediate 17

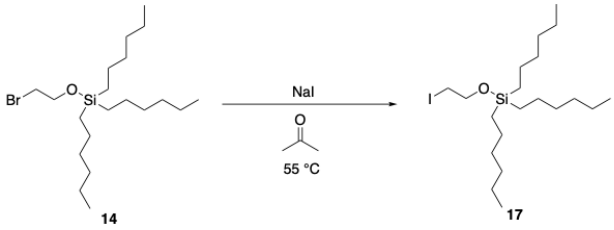

14 (5.91 g, 14.5 mmol, 1 eq), sodium iodide (8.70 g, 58.0 mmol, 4 eq) and acetone (50 mL) were added to a round bottom flask and refluxed overnight. It was cooled and poured into a separating funnel with water and extracted with dichloromethane, washing with water, brine, and sodium sulfate was added. This underwent gravity filtration, and the solvent was removed under reduced pressure to give a colourless oil and used without further purification (6.33 g, 96%)

^{1}H NMR (400 MHz, $CDCl_3$) δ 3.82-3.79 (m, 2H), 3.20-3.16 (m, 2H), 1.32-1.28 (m, 24H), 0.9-0.97 (m, 9H), 0.62-0.58 (m, 6H)

^{13}C NMR (400 MHz, $CDCl_3$) δ 64.20, 33.42, 31.67, 23.21, 22.75, 14.28, 13.77, 6.88.

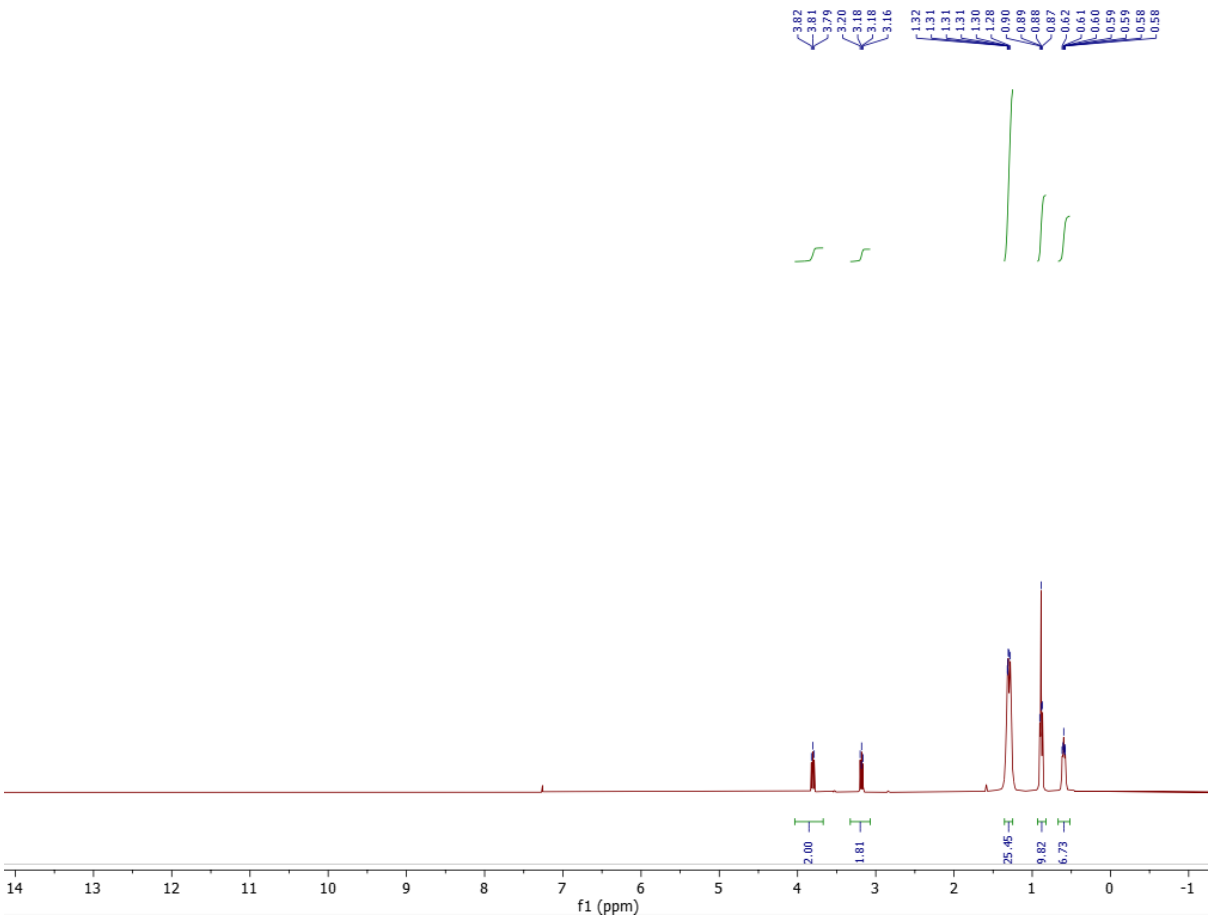
3.82
3.81
3.79
3.20
3.18
3.18
3.16
1.32
1.31
1.31
1.31
1.30
1.28
0.90
0.89
0.88
0.87
0.62
0.61
0.60
0.59
0.59
0.58
0.58
2.00
1.81
25.45
9.82
6.73
14
13
12
11
10
9
8
7
6
5
4
3
2
1
0
-1
f1 (ppm)

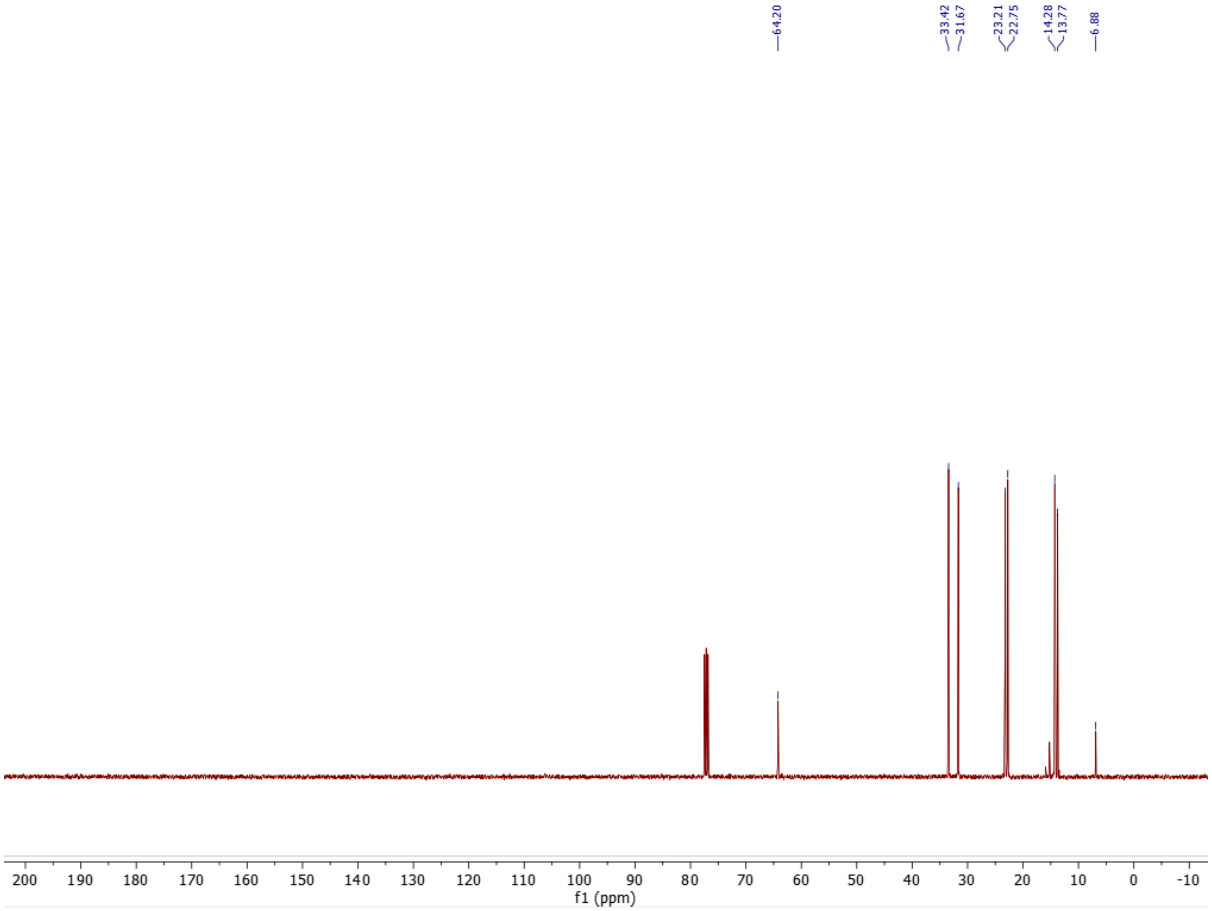
64.20
33.42
31.67
23.21
22.75
14.28
13.77
6.88
f1 (ppm)

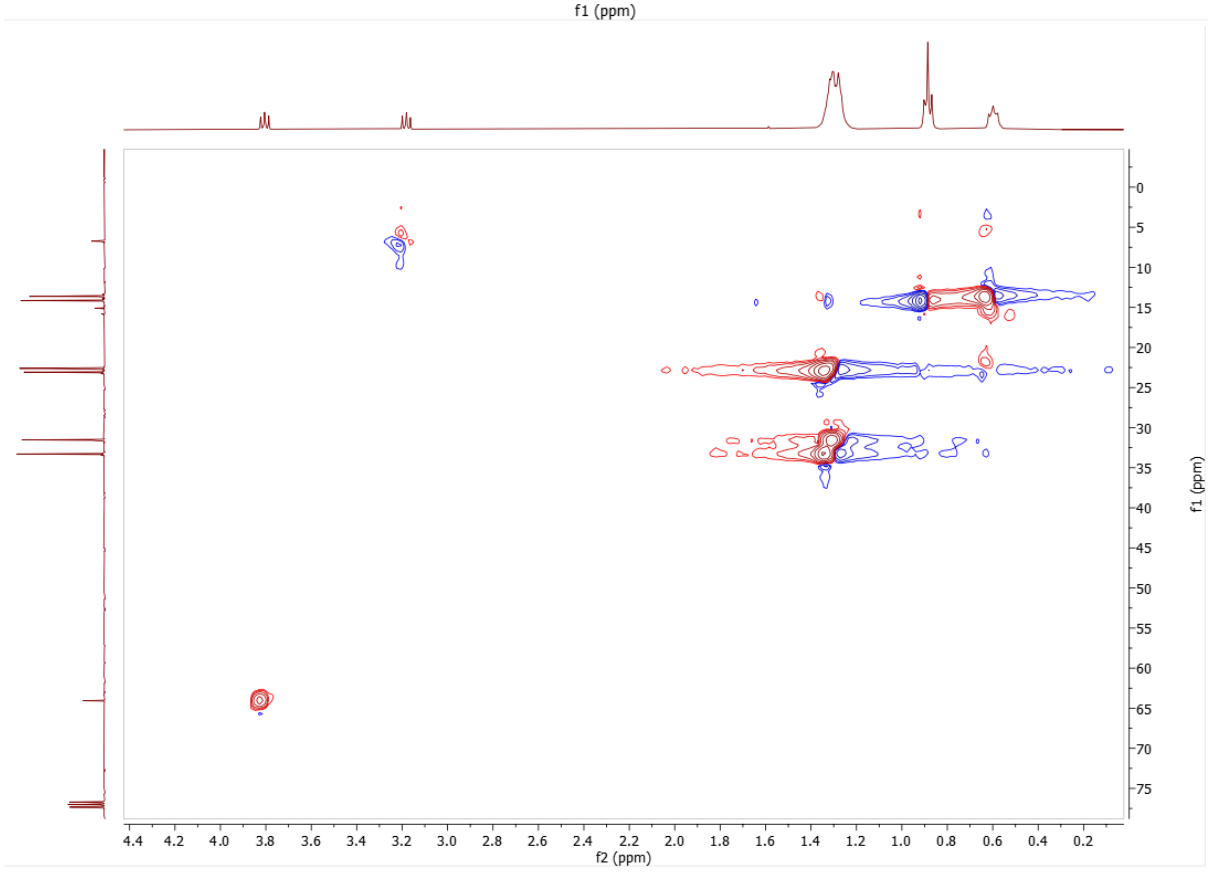
f2 (ppm)
f1 (ppm)

Intermediate 18

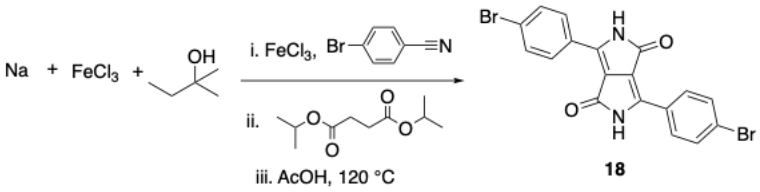

Sodium (1.00 g, 43.5 mmol, 6 eq) and iron (III) chloride (0.04 g, 0.2 mmol, 0.03 eq) were added to a round bottom flask and purged with nitrogen. 2-methyl-2-butanol (15 mL) was added and it was stirred at 50 °C for 20 minutes to react. 4-bromobenzonitrile (3.96 g, 21.7 mmol, 3 eq) was added and heated to 100 °C. Diisopropylsuccinimate (1.5 mL, 7.3 mmol, 1 eq) was added and the solution quickly turned dark purple. This was refluxed overnight. The next day acetic acid (10 mL) was added and it was heated to 120 °C under reflux for 1 hour, whereupon red solid precipitated. This was cooled then filtered, washed thoroughly with methanol and dried in a vacuum oven to give a deep red solid (2.62 g, 81%). This was too insoluble for NMR.

NDI-Si Monomer

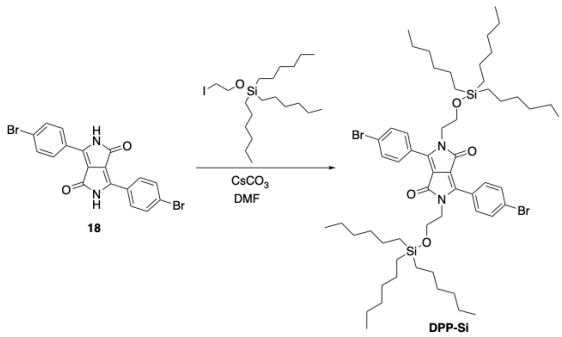

18 (1.50 g, 3.6 mmol, 1 eq) and caesium carbonate (2.40 g, 7.9 mmol, 2.2 eq) were thoroughly dried in a vacuum oven then added to a 2-neck round bottom flask and purged with nitrogen. Anhydrous dimethylformamide (100 mL) was added and it was stirred at 80 °C for 15 minutes under nitrogen, followed by addition of **17** (6.10 g, 13.4 mmol, 4 eq), then the reaction was continued overnight. It was cooled and poured into a separating funnel with water and extracted with dichloromethane, washing with water, brine, and sodium sulfate was added. This underwent gravity filtration, and the solvent was removed under reduced pressure. This was purified on a silica column, eluting with a graduated eluent from pure petroleum ether to petroleum ether: diethyl ether (95:5). Since unreacted **17** had a similar R_f to the product in silica, this was subsequently purified by size exclusion chromatography

(bio-beads X-3) eluting with chloroform. Finally, this was recrystallised in isopropanol to give an orange crystalline solid (0.92 g, 25 %)

^{1}H NMR (400 MHz, $CDCl_3$) δ 7.92 (d, J = 8.6, 4H), 7.56 (d, J = 8.6, 4H), 3.82 (d, J = 4.4 Hz, 4H), 3.79 (d, J = 4.4 Hz, 4H), 1.19-1.13 (m, 48H), 0.78 (t, J = 6.9 Hz, 28H), 0.46-0.42 (m, 12H)

^{13}C NMR (400 MHz, $CDCl_3$) δ 162.91, 148.37, 132.15, 131.16, 109.68, 60.95, 44.79, 33.47, 31.64, 29.84, 23.16, 22.75, 14.27, 13.51.

HSMS (ESI): HR-MS calculated for $[C_{58}H_{94}Br_2N_2O_4Si_2+H]^+$: m/z = 1097.5192; measured m/z = 1097.5213

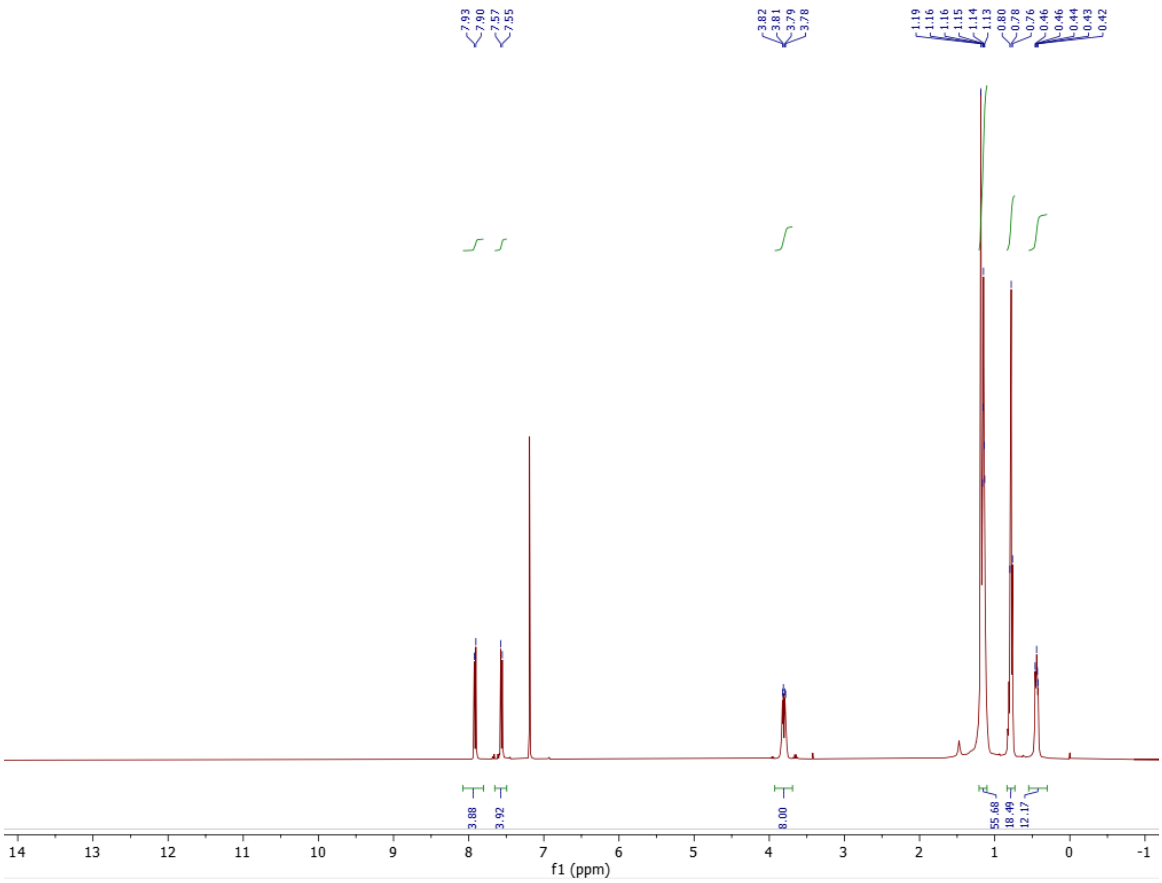

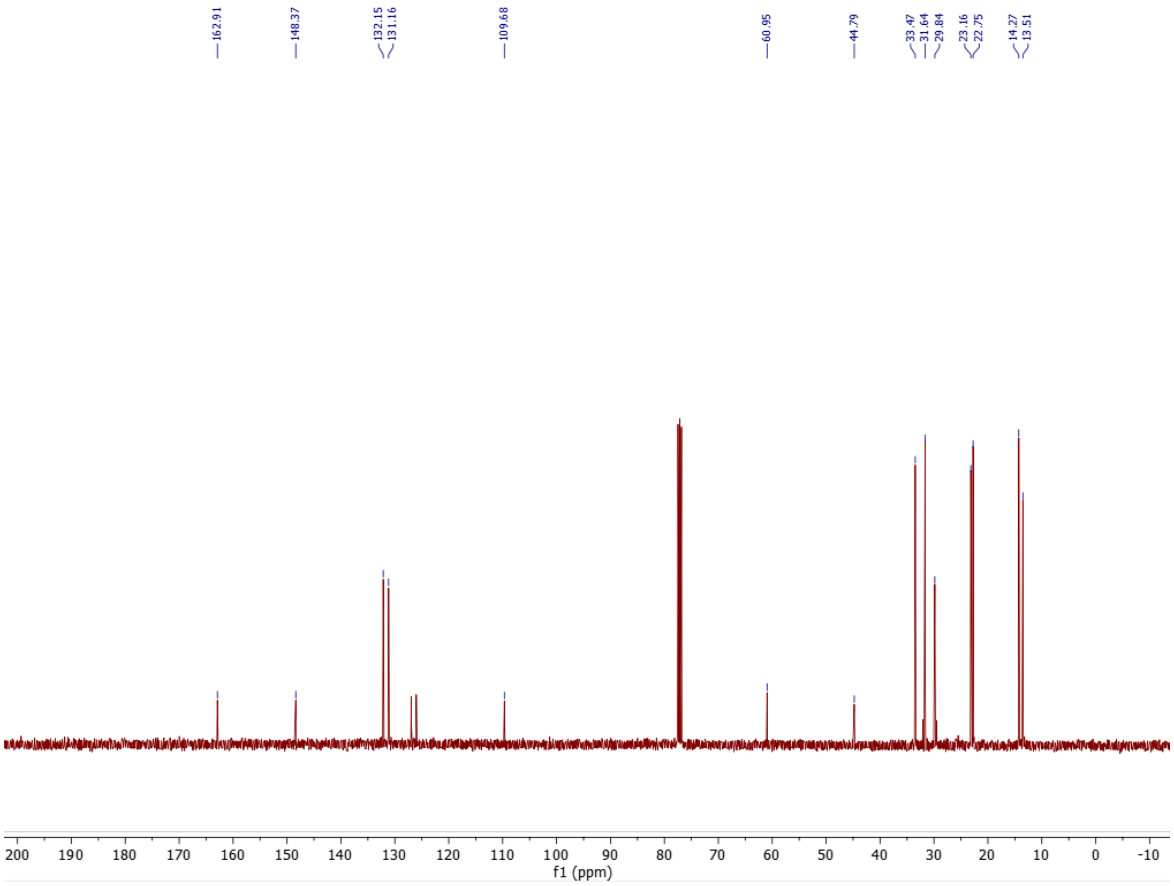
162.91
148.37
132.15
131.16
109.68
60.95
44.79
33.47
31.64
29.84
23.16
22.75
14.27
13.51
200 190 180 170 160 150 140 130 120 110 100 90 80 70 60 50 40 30 20 10 0 -10
f1 (ppm)

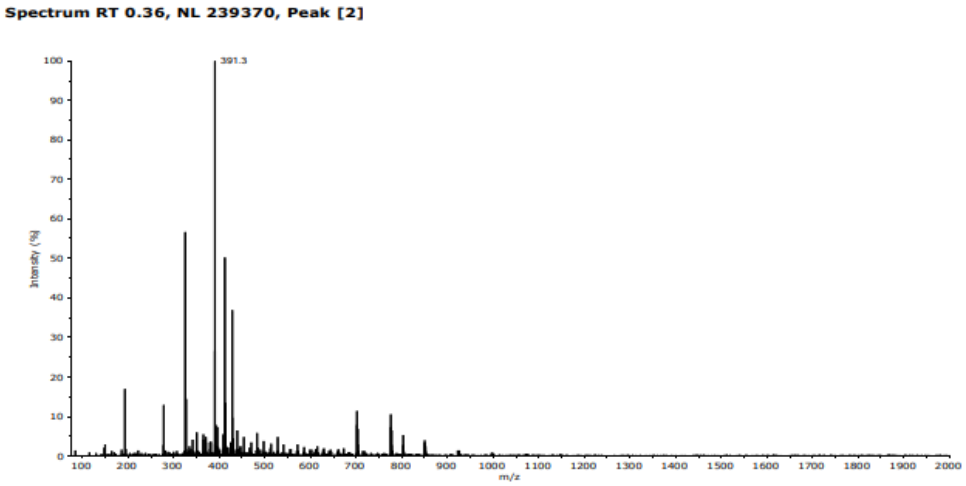

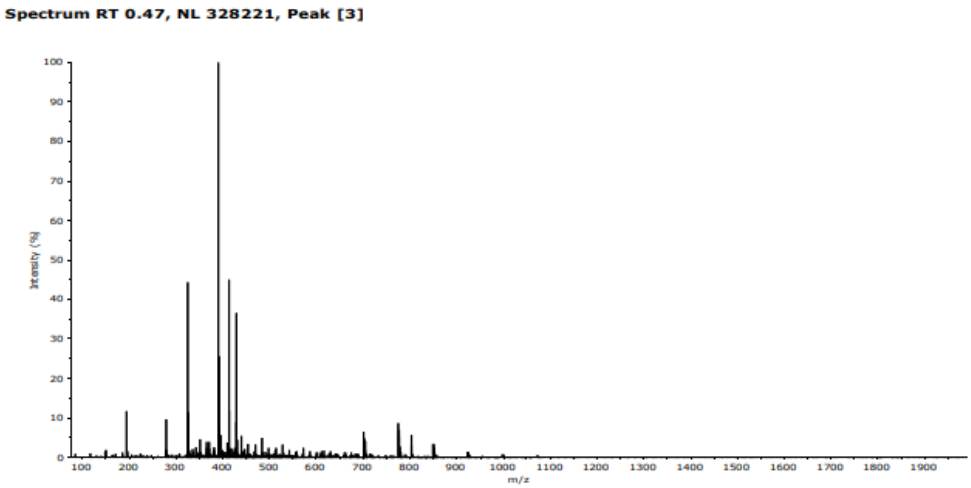

Sp-IDT-DPP-Si Polymer

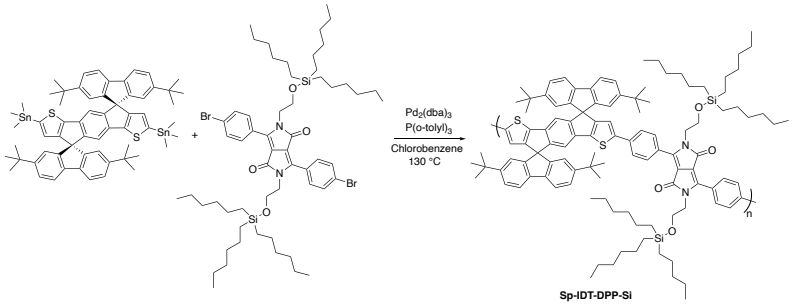

Distannylated Sp-IDT (276.20 mg, 247 µmol, 1 eq), **DPP-Si** (271.90 mg, 247 µmol, 1 eq), tri(o-tolyl)phosphine (6.0 mg, 20 µmol, 0.08 eq) and tris(dibenzylideneacetone) dipalladium(0) (4.5 mg, 5 µmol, 0.02 eq) were added to a microwave vial, it was capped then degassed with nitrogen for 30 minutes. Anhydrous chlorobenzene (4.9 mL) was added and it was heated to 130 °C overnight. This was cooled, precipitated into methanol and poured into a cellulose Soxhlet thimble. This underwent a Soxhlet extraction washing with acetone followed by hexane, ethyl acetate then extracted

with chloroform. The chloroform fraction was then precipitated into methanol and collected by vacuum filtration to give a deep purple solid (336 mg, 79%).

GPC (chlorobenzene) M_N 45168 gmol^{-1}, M_W 91113 gmol^{-1}, PD 2.02

^{1}H NMR (500 MHz, $CDCl_3$) δ 7.98 (br, 4H), 7.78 (br, 4H), 7.56-7.41 (br, m, 8H), 6.83-6.77 (br, m, 8H), 3.83 (br, 8H), 1.28-1.02 (br, m, 84H), 0.72 (t, J = 6.7 Hz, 18H), 0.44 (br, 12H)

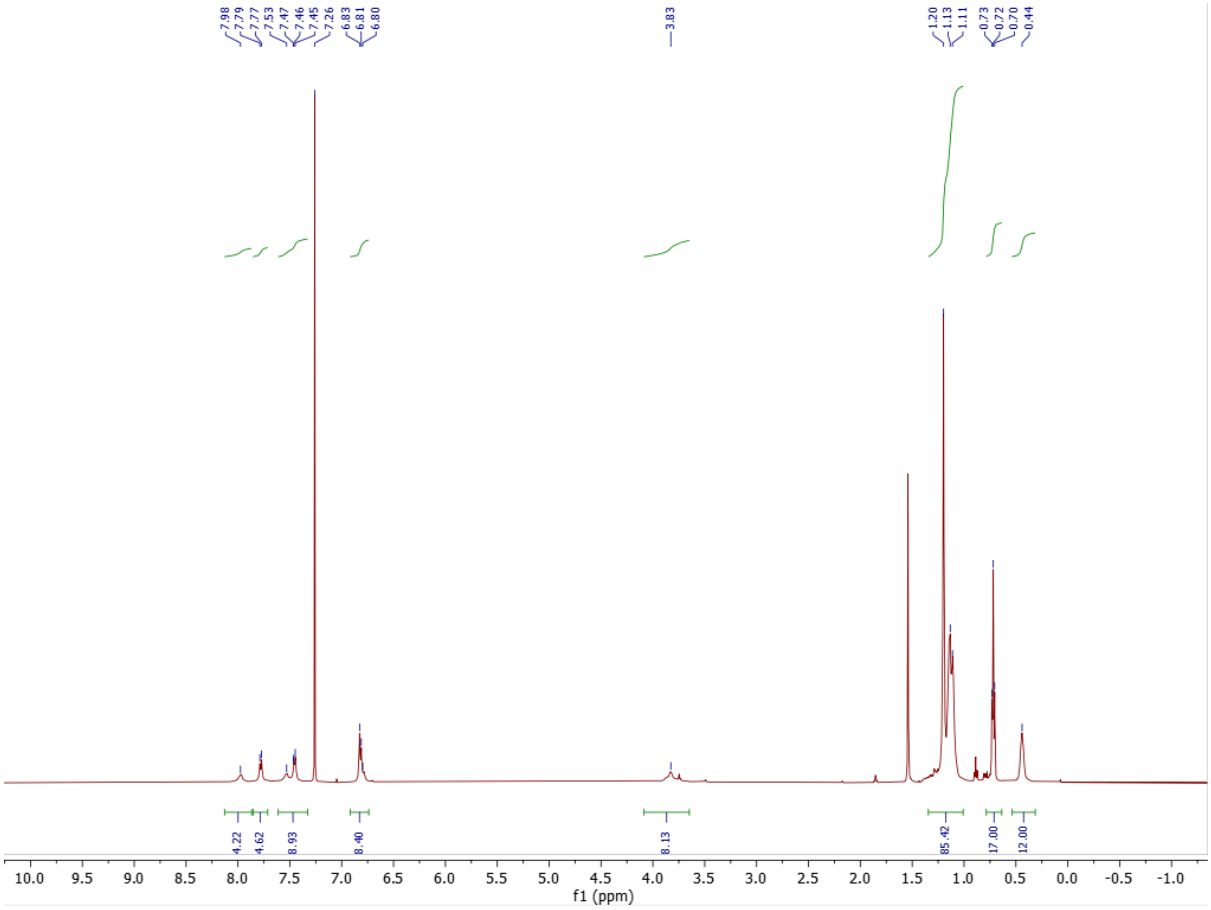

Intermediate 19

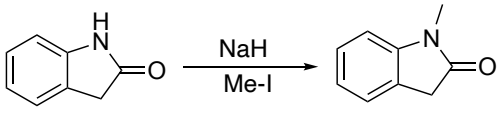

19

Oxindole (10.6 g, 79.6 mmol, 1 eq), and 60 wt% sodium hydride in mineral oil (3.36 g, 84.0 mmol, 1.05 eq) were added to a 2-neck round bottom flask and purged with nitrogen. Anhydrous toluene (300 mL) was added and the suspension was stirred at 60 °C under nitrogen. Dimethylsulfate (6.6 mL, 95.5 mmol, 1.2 eq) was added and

the reaction was left stirring overnight under nitrogen at 60 °C. It was cooled and poured into a separating funnel with water and extracted with ethyl acetate, washing with water, brine, and sodium sulfate was added. This underwent gravity filtration, and the solvent was removed under reduced pressure to give a red-brown solid. This was purified on a silica column eluting with dichloromethane, then recrystallised in dichloromethane: hexane to give colourless crystals **19** (4.26 g, 36 %).

^{1}H NMR (400 MHz, d_8-THF) δ 7.22-7.18 (m, 2H), 6.95-6.91 (m, 1H), 6.83-6.81 (m, 1H), 3.40 (s, 2H), 3.12 (s, 3H)

^{13}C NMR (400 MHz, $CDCl_3$) δ 175.16, 145.30, 127.97, 124.59, 124.38, 122.42, 108.15, 35.83, 26.23.

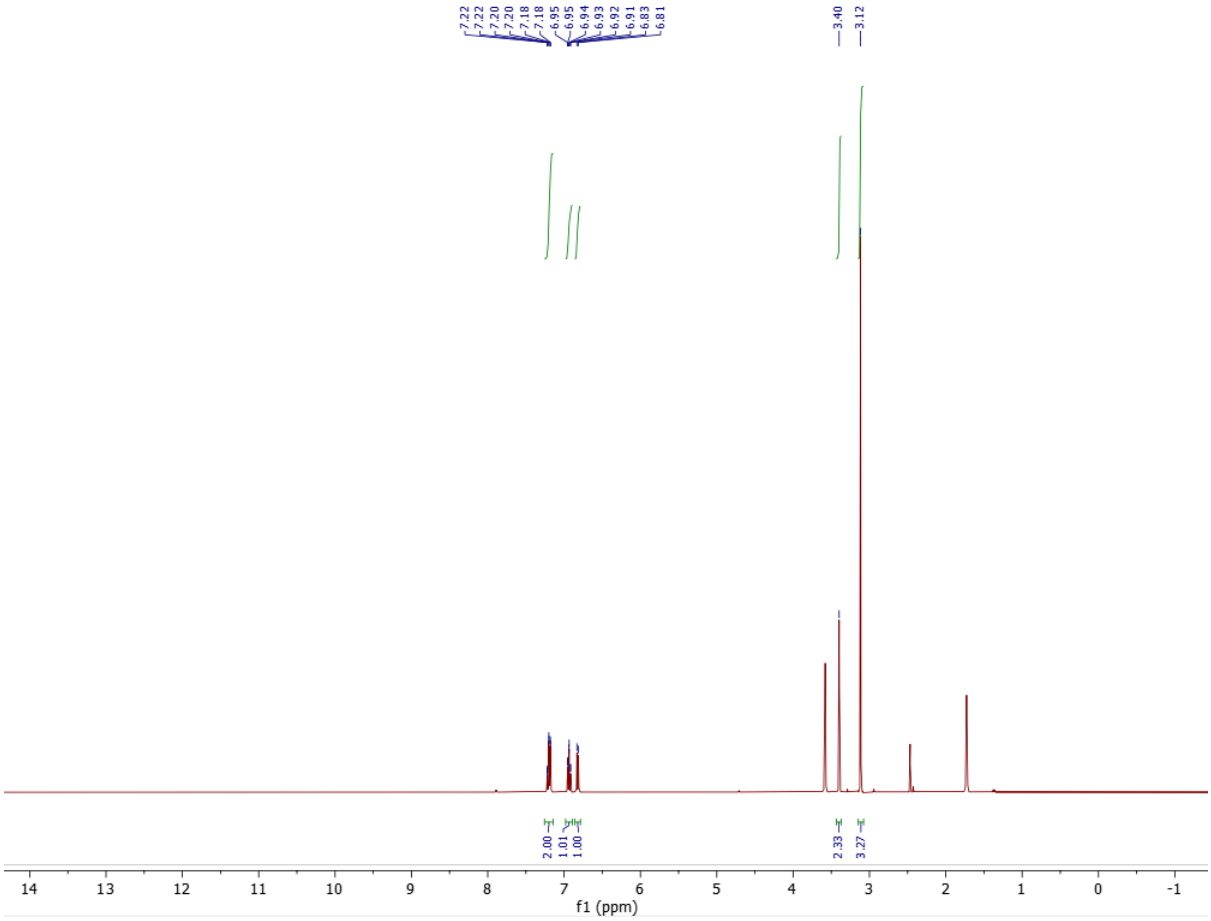

Intermediate 20

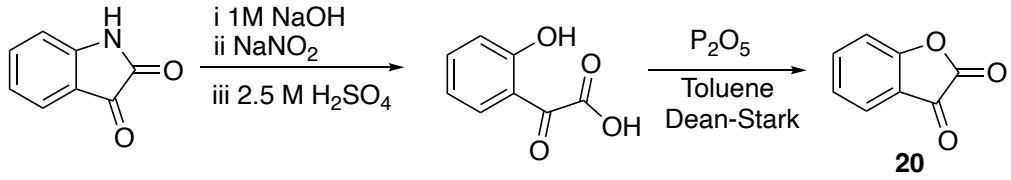

20

Isatin (10.0 g, 68.0 mmol, 1 eq) was dissolved in sodium hydroxide solution (1.0 M, 100 mL, 102.0 mmol, 1.5 eq) in a 1 L round bottom flask and chilled to 0 °C on an ice bath. After turning darkening in colour following deprotonation, sodium nitrite was added (5.2 g, 74.8 mmol, 1.1 eq) followed by slow addition sulfuric acid solution (2.5 M, 109 mL, 271.9 mmol, 4 eq), whereupon it foamed considerably. Stirring was ceased and it was heated to 60 °C and left to stand for 3 h. It was then very gently stirred until gas bubbles stopped being produced for 1 h more. Care must be taken to allow nitrogen evolution to occur slowly to avoid potentially dangerous decomposition of the diazonium salt intermediate, by stopping stirring and gently warming to temperature. After the bubbling had finished, it was cooled and poured into a separating funnel. Water was added and the organic phase was extracted, washed again with brine then dried with magnesium sulfate and underwent gravity filtration. The residue was dried under high vacuum for 4 hours, anhydrous toluene (300 mL) and phosphorous pentoxide (39 g, 137.3 mmol, 2 eq) were added then it fitted to Dean-Stark apparatus and refluxed overnight. It then underwent gravity filtration to recover a yellowish solution and the solvent was removed under reduced pressure to get a slightly yellow solid (2.60 g, 26 %). GCMS showed a single peak with an m/z of 147.98, matching the predicted m/z of 148.02

^{1}H NMR (400 MHz, $CDCl_3$) δ 7.82-7.74 (m, 2H), 7.36-7.32 (m, 1H), 7.22-7.24 (m, 1 H)

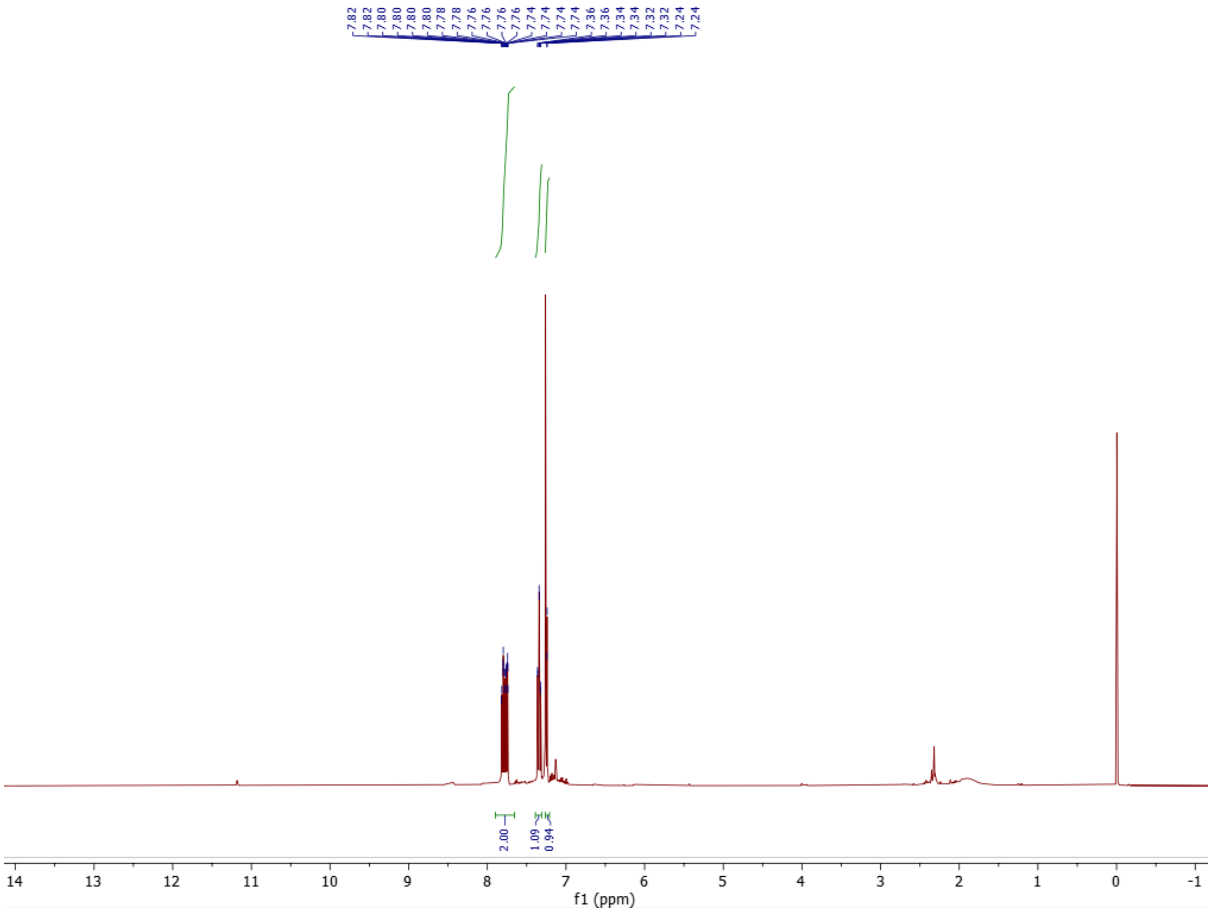
7.82
7.82
7.80
7.80
7.80
7.80
7.78
7.78
7.76
7.76
7.76
7.76
7.74
7.74
7.74
7.74
7.36
7.36
7.34
7.34
7.32
7.32
7.24
7.24
2.00
1.09
0.94
14
13
12
11
10
9
8
7
6
5
4
3
2
1
0
-1
f1 (ppm)

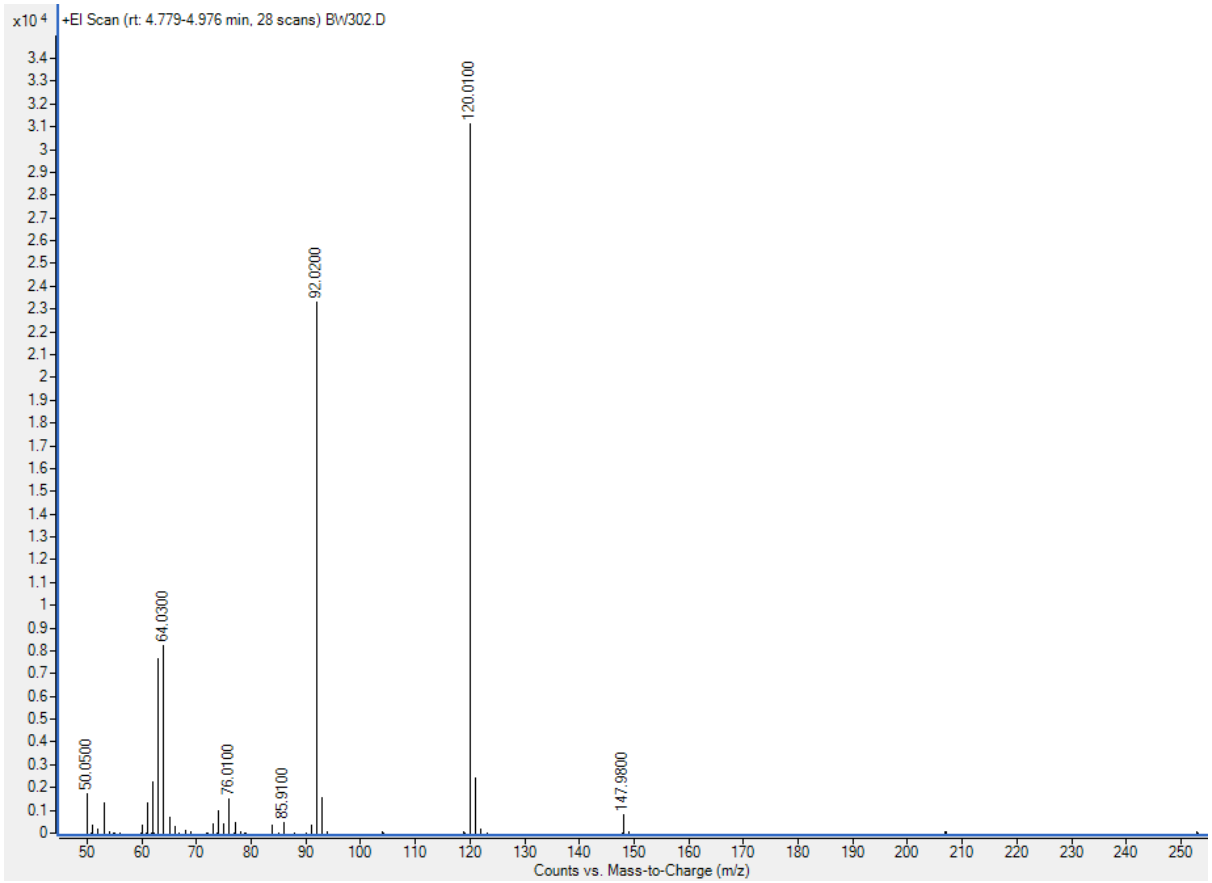
x10 4
+EI Scan (rt: 4.779-4.976 min, 28 scans) BW302.D
120.0100
92.0200
64.0300
50.0500
76.0100
85.9100
147.9800
Counts vs. Mass-to-Charge (m/z)

Intermediate 21

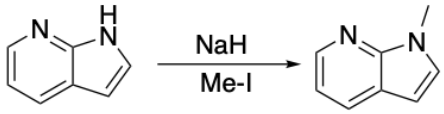

21

Indole (10.0 g, 84.7 mmol, 1 eq), and 60 wt% sodium hydride in mineral oil (3.72 g, 93.1 mmol, 1.1 eq) were added to a 2-neck round bottom flask and purged with nitrogen. Anhydrous dimethylformamide (100 mL) was added and it was stirred at 0 °C under nitrogen. Methyl iodide (7.9 mL, 127.0 mmol, 1.5 eq) was added and the reaction was left stirring overnight under nitrogen and allowed to reach room temperature. The solvent and excess methyl iodide was subsequently removed under reduced pressure, then it was purified on a silica plug eluting with hexane to give a slightly yellow oil **21** (8.82 g, 79 %).

^{1}H NMR (400 MHz, $CDCl_3$) δ 8.34 (dd, J = 4.8, 1.6 Hz, 1H) 7.90 (dd, J = 7.8, 1.6Hz), 7.18 (d, J = 3.4 Hz, 1H), 7.06 (dd, J = 7.8, 4.8 Hz, 1H) 6.45 (d, J = 3.4 Hz, 1H), 3.90 (s, 3H)

^{13}C NMR (400 MHz, $CDCl_3$) δ 147.91, 142.91, 129.10, 128.82, 120.64, 115.58, 99.38, 31.34.

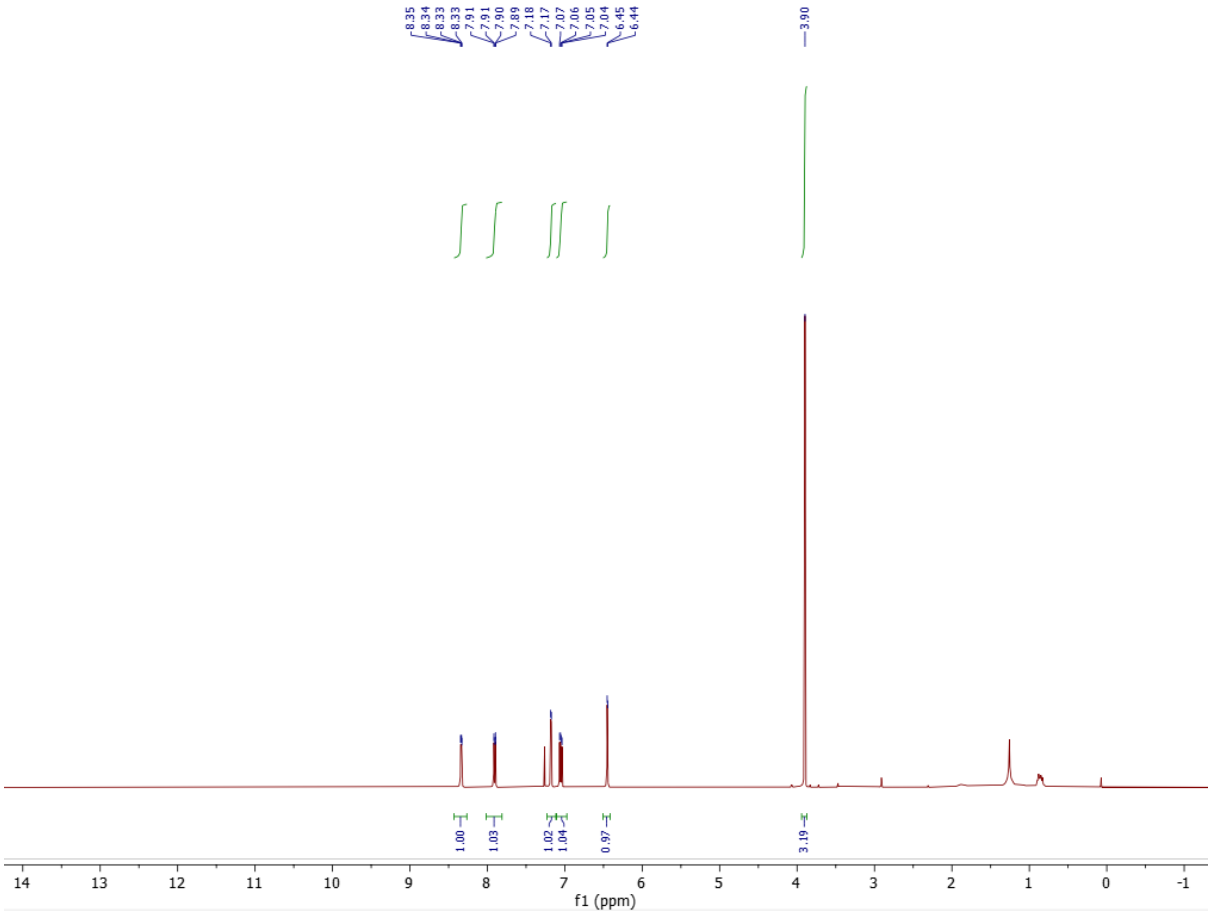
8.35
8.34
8.33
8.33
7.91
7.91
7.90
7.89
7.18
7.17
7.07
7.06
7.05
7.04
6.45
6.44
3.90
1.00
1.03
1.02
1.04
0.97
3.19
14
13
12
11
10
9
8
7
6
5
4
3
2
1
0
-1
f1 (ppm)

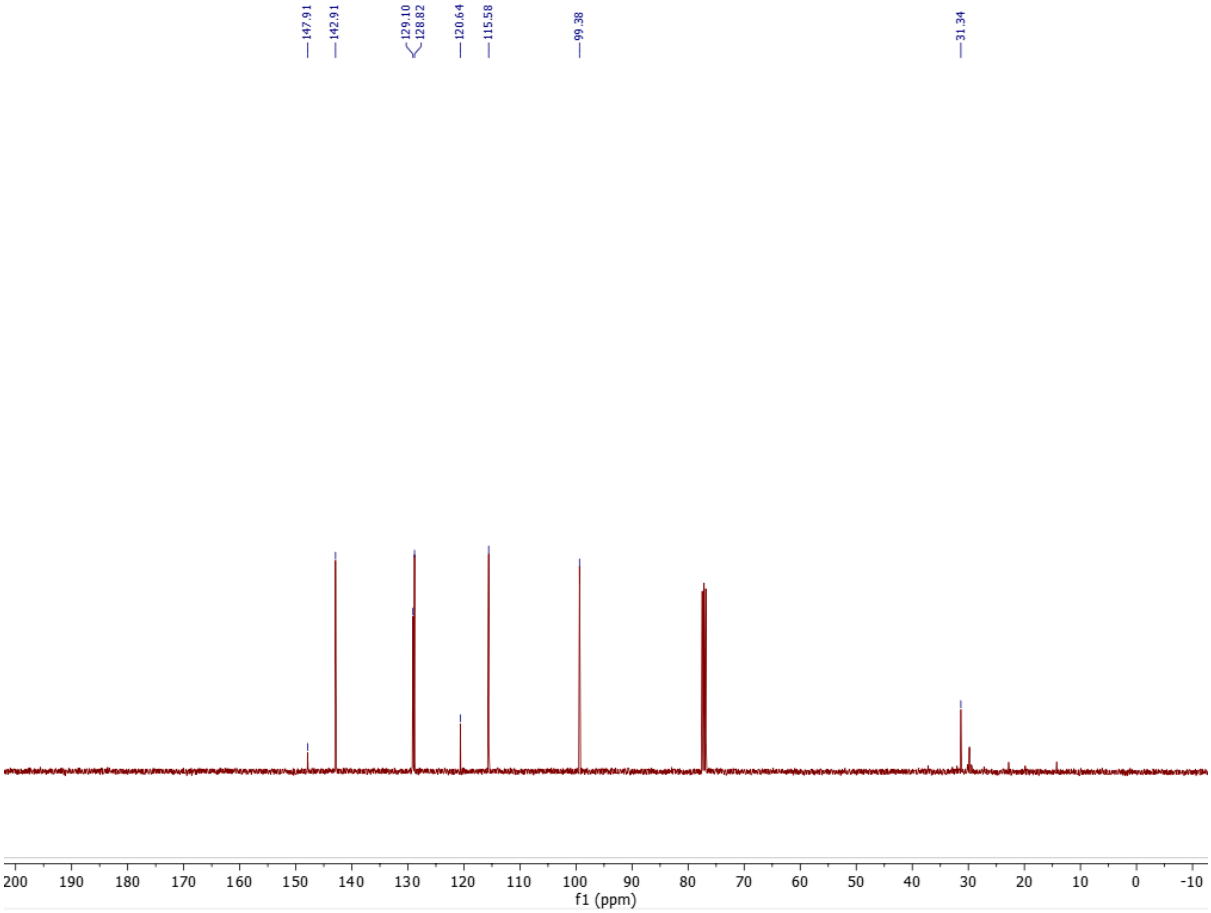

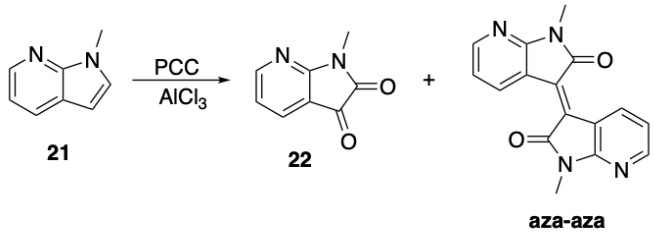

21 (3.60 g, 27.2 mmol, 1 eq) was added to a microwave vial and degassed with nitrogen. Pyridinium chlorochromate (14.68 g, 68.1 mmol, 2.5 eq), silica (14.6 g) and aluminium trichloride (0.07 g, 0.5 mmol, 0.02 eq) were added to a 2-neck round bottom flask and heated to 50 °C under high vacuum for 30 minutes using a Schlenk line. This was subsequently purged with nitrogen and anhydrous dichloroethane (30 mL) and anhydrous acetonitrile (30 mL) were added and stirred under nitrogen. The degassed oil **21** was added dropwise to the other reagents, using more anhydrous dichloroethane (10 mL) to wash everything in. This was then refluxed under nitrogen overnight. The mixture underwent gravity filtration to remove the chromium and silica solid, washing with dichloromethane. The filtrate was collected, and the solvent

removed under reduced pressure. The crude red solid was purified on a silica column eluting with dichloromethane. This separated orange **22** and red **aza-aza**. Orange **22** eluted first to give an orange solid (2.40 g, 54%).

22

^{1}H NMR (400 MHz, $CDCl_3$) δ 8.46 (dd, *J* = 5.3, 1.7 Hz, 1H), 7.82 (dd, *J* = 7.3, 1.7 Hz, 1H), 7.09 (dd, *J* = 7.3, 5.3 Hz, 1H), 3.36 (s, 3H).

^{13}C NMR (400 MHz, $CDCl_3$) δ 181.97, 163.97, 158.44, 155.95, 132.84, 119.67, 112.13, 25.13.

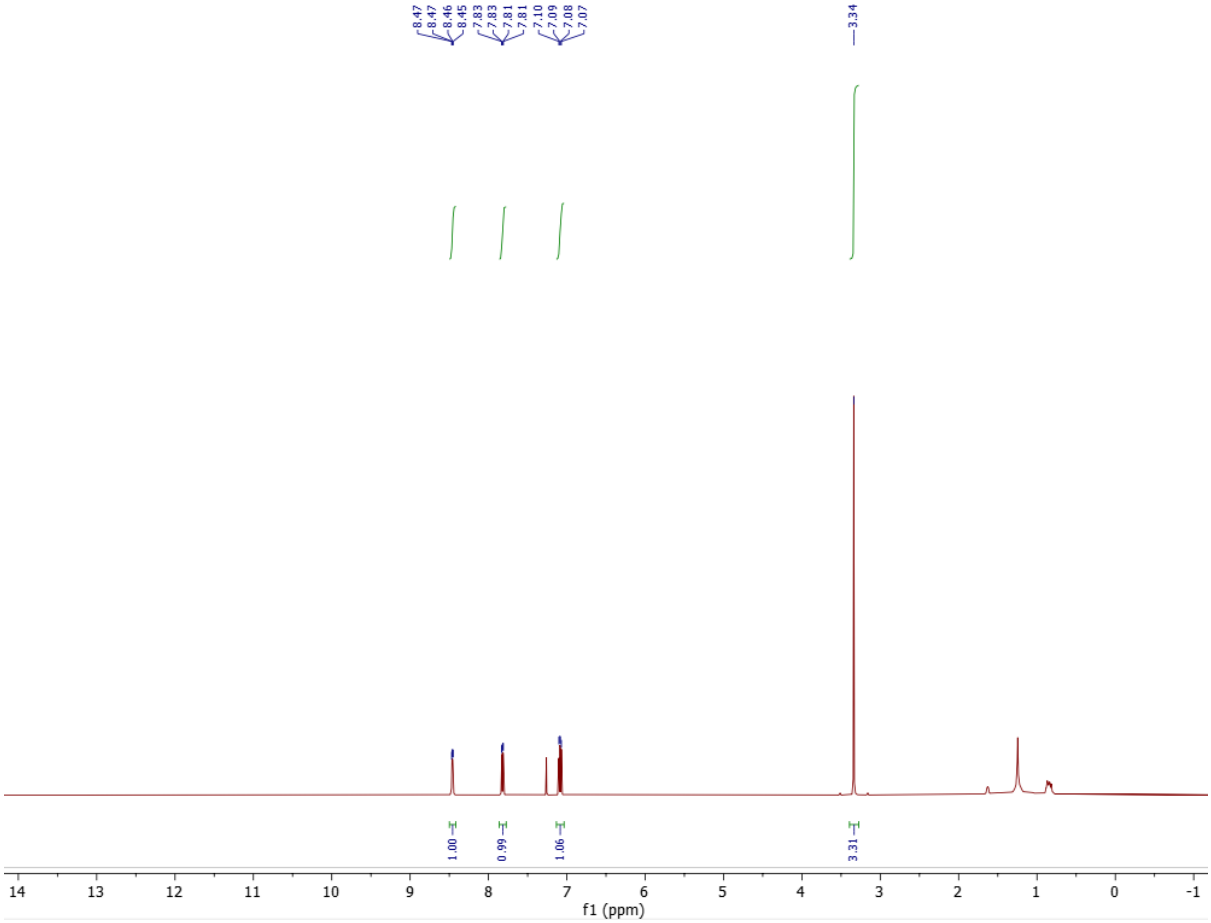

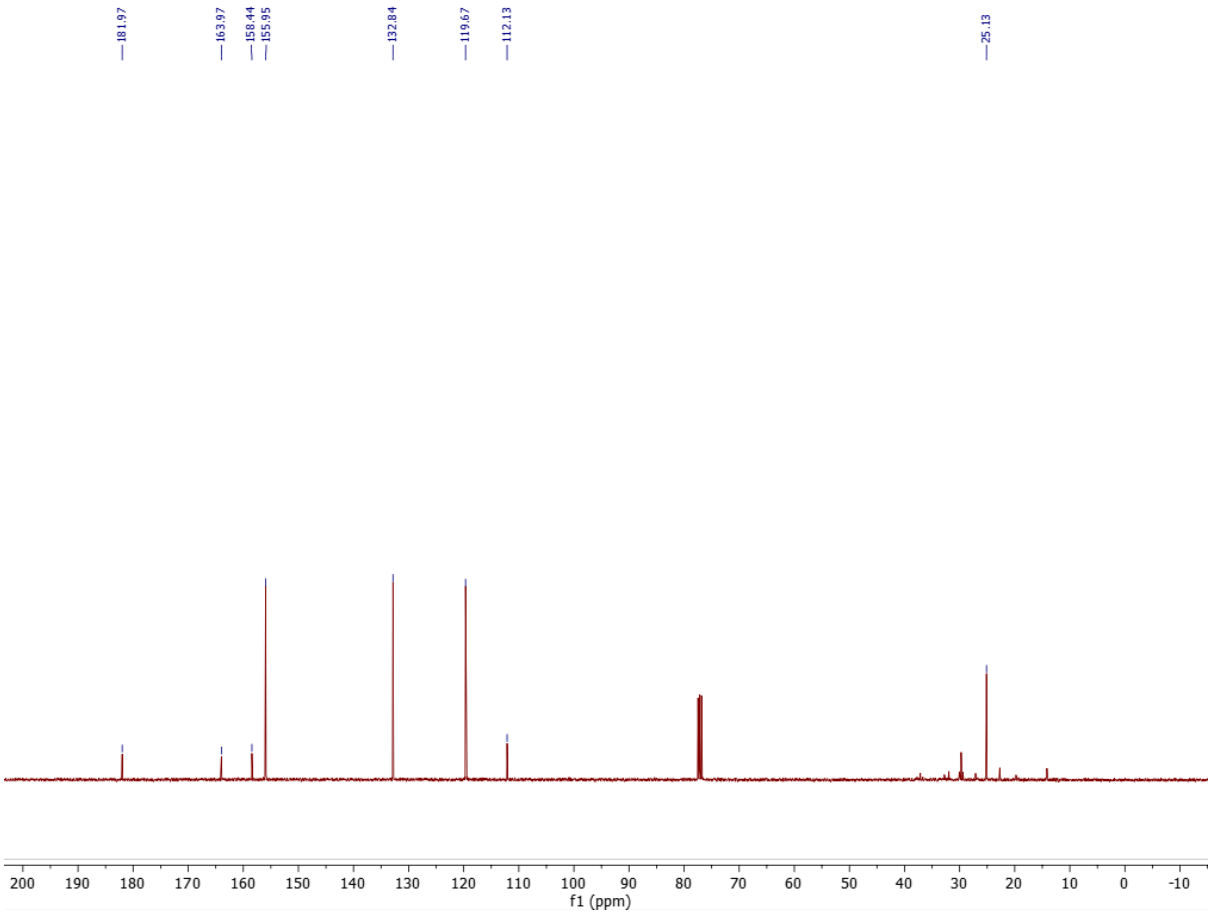

ETL aza-aza

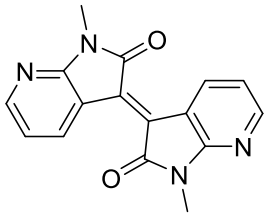

The red second fraction of the above reaction was clllected, partially dissolved in chloroform (10 mL), precipitated into stirring hexane (100 mL), then collected by vacuum filtration. This was recrystallised in toluene to give a red crystalline solid (0.34 g, 8.0%)

^{1}H NMR (400 MHz, $CDCl_3$) δ 9.48 (dd, *J* = 7.9, 1.6 Hz, 2H), 8.25 (dd, *J* = 5.1, 1.6 Hz, 2H), 7.04 (dd, *J* = 7.9, 5.1 Hz, 2H), 3.40 (s, 6H)

^{13}C NMR (400 MHz, $CDCl_3$) δ 167.80, 157.85, 150.20, 137.80, 132.33, 118.78, 116.37, 25.61

HSMS (ESI): HR-MS calculated for $[C_{16}H_{12}N_4O_2]^+$: m/z = 292.0955; measured m/z = 292.4429

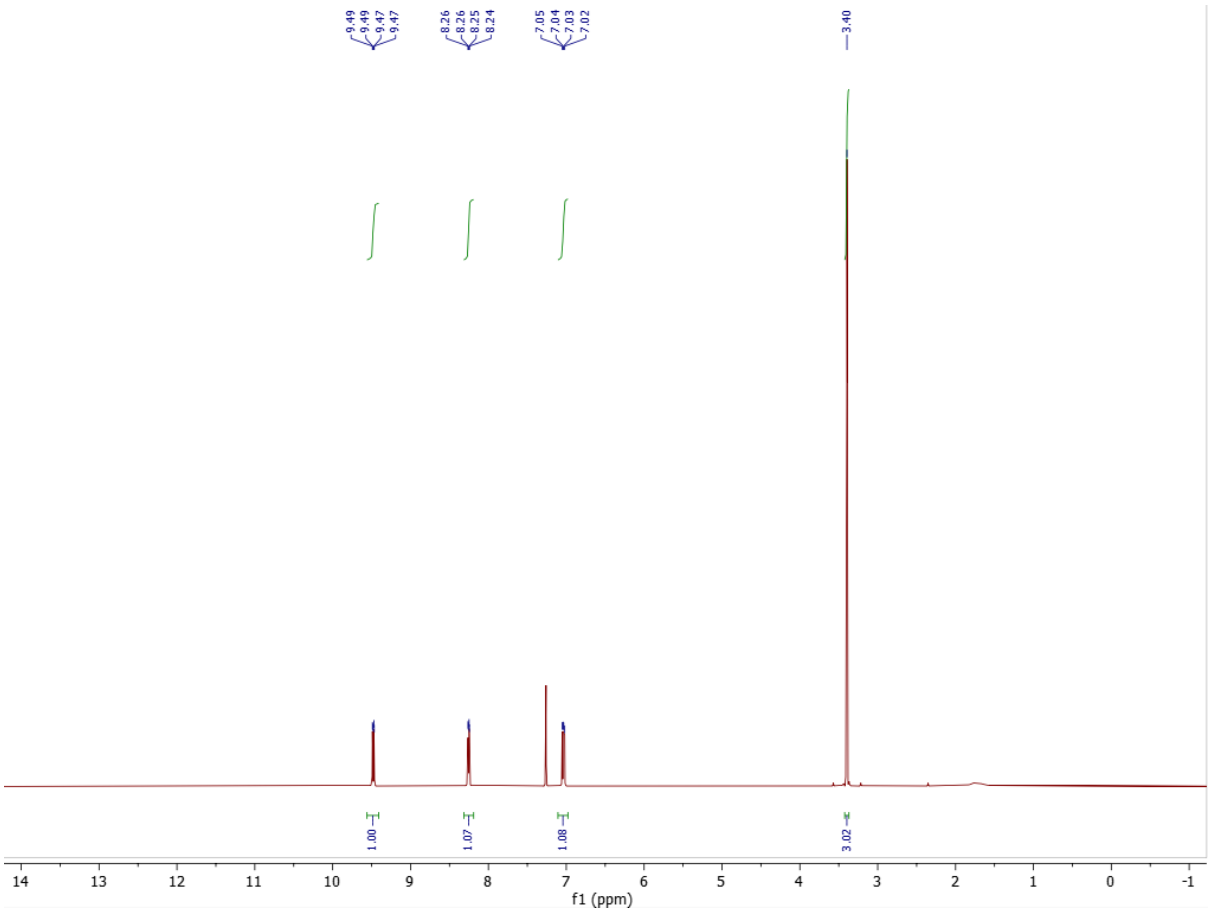

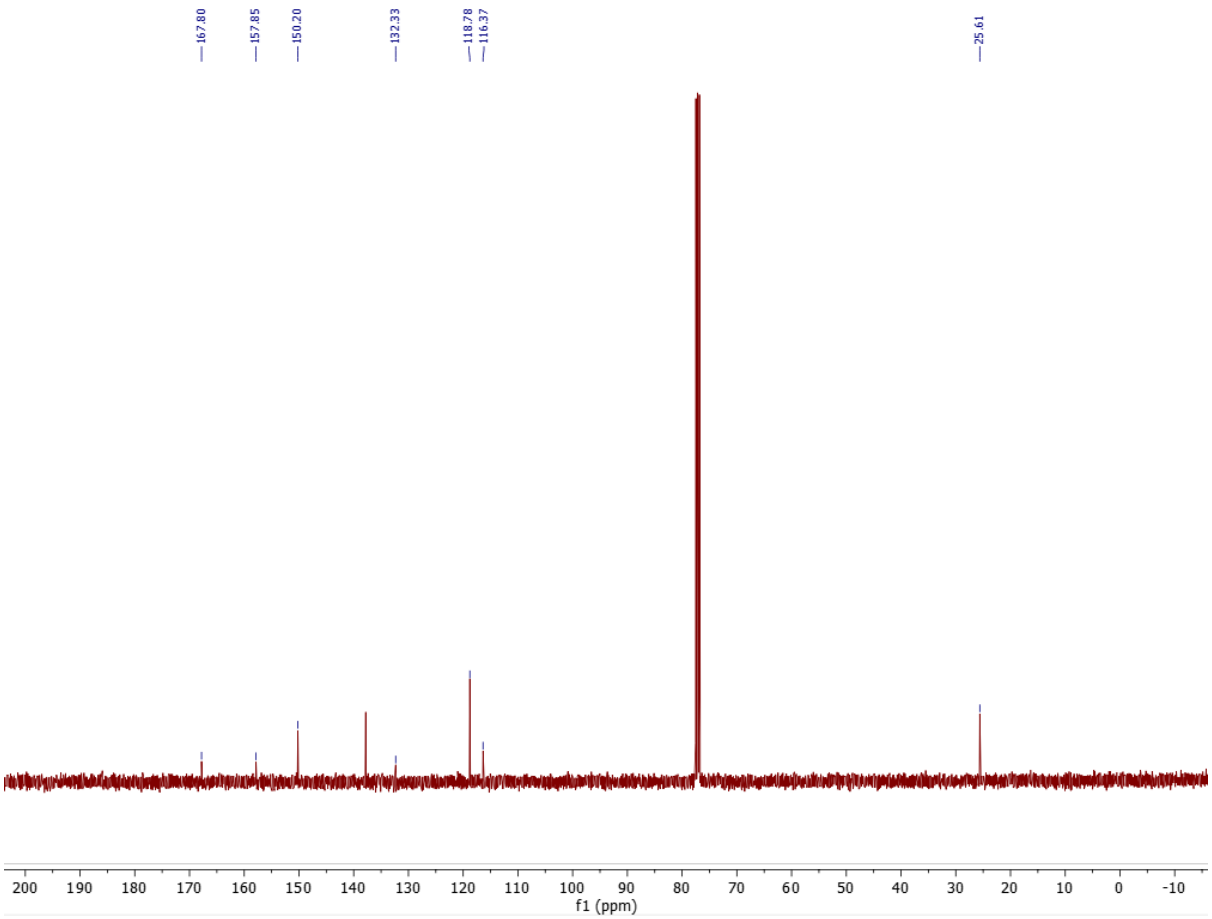
167.80
157.85
150.20
132.33
118.78
116.37
25.61
200 190 180 170 160 150 140 130 120 110 100 90 80 70 60 50 40 30 20 10 0 -10
f1 (ppm)

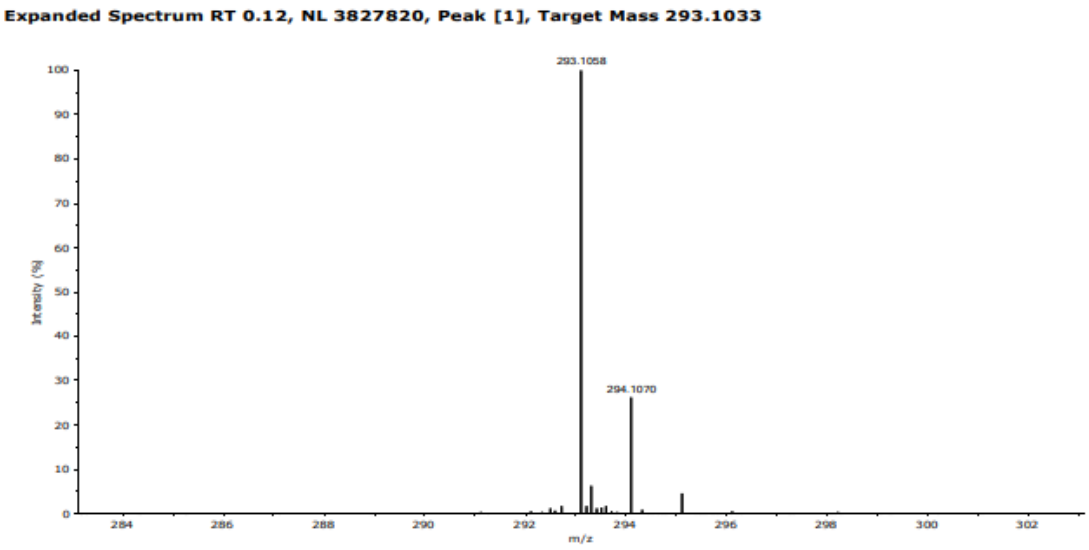

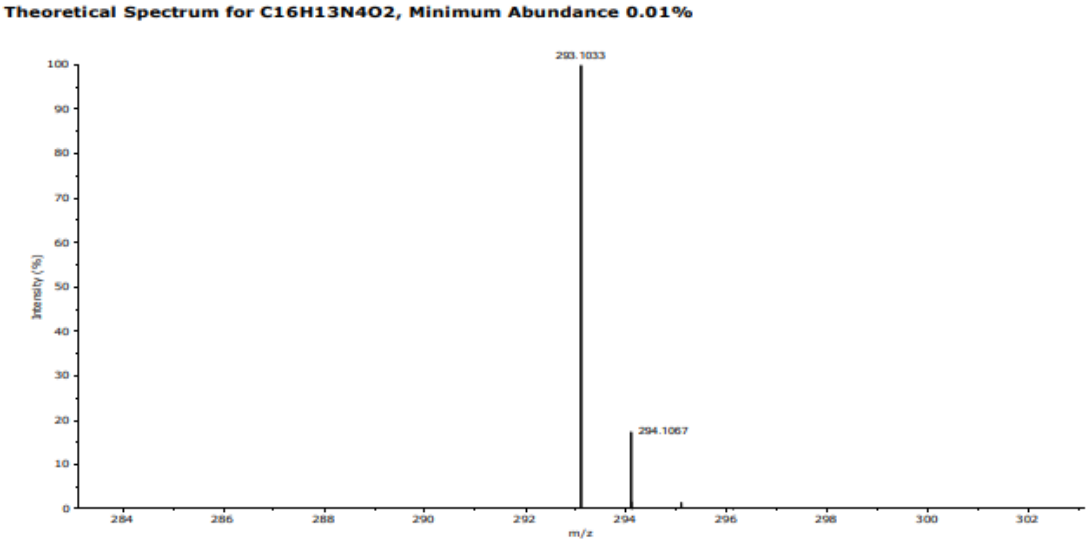

ETL iso-iso

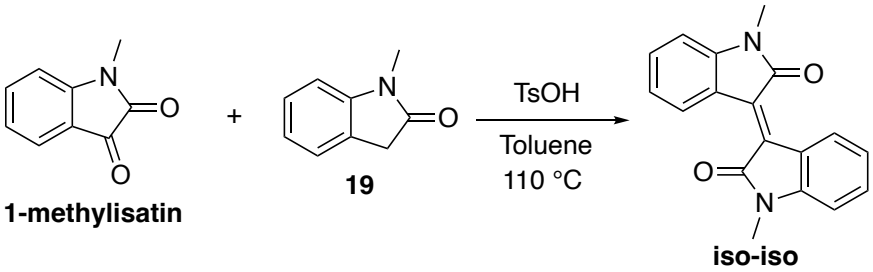

1-methylisatin **iso-iso**

19 (1.00 g, 6.79 mmol, 1eq), 1-methylisatin (1.15 g, 7.13 mmol, 1.05 eq) and p-toluene sulfonic acid monohydrate (0.06 g, 0.34 mmol, 0.05 eq) were stirred under nitrogen in anhydrous toluene (100 mL) with some molecular sieves at 110 °C overnight. This was poured into a separating funnel with water and extracted with dichloromethane,

then washed with brine then sodium sulfate was added and underwent gravity filtration. This was purified on a silica column eluting with dichloromethane: petroleum ether (80:2-) then recrystallised in toluene to give a needle like red crystals **iso-iso** (0.54 g, 27%)

^{1}H NMR (400 MHz, $CDCl_3$) δ 9.20 (d, J = 9.2 Hz, 1H), 7.38-7.35 (m, 1H), 7.08-7.04 (m, 1H), 6.77 (d, 7.7 Hz, 1H), 3.27 (s, 3H)

^{13}C NMR (400 MHz, $CDCl_3$) δ 168.11, 145.33, 133.55, 132.49, 129.97, 122.53, 121.70, 107.77, 26.25.

HSMS (ESI): HR-MS calculated for $[C18H15N2O2+H]^+$: m/z = 291.1128; measured m/z = 291.1140

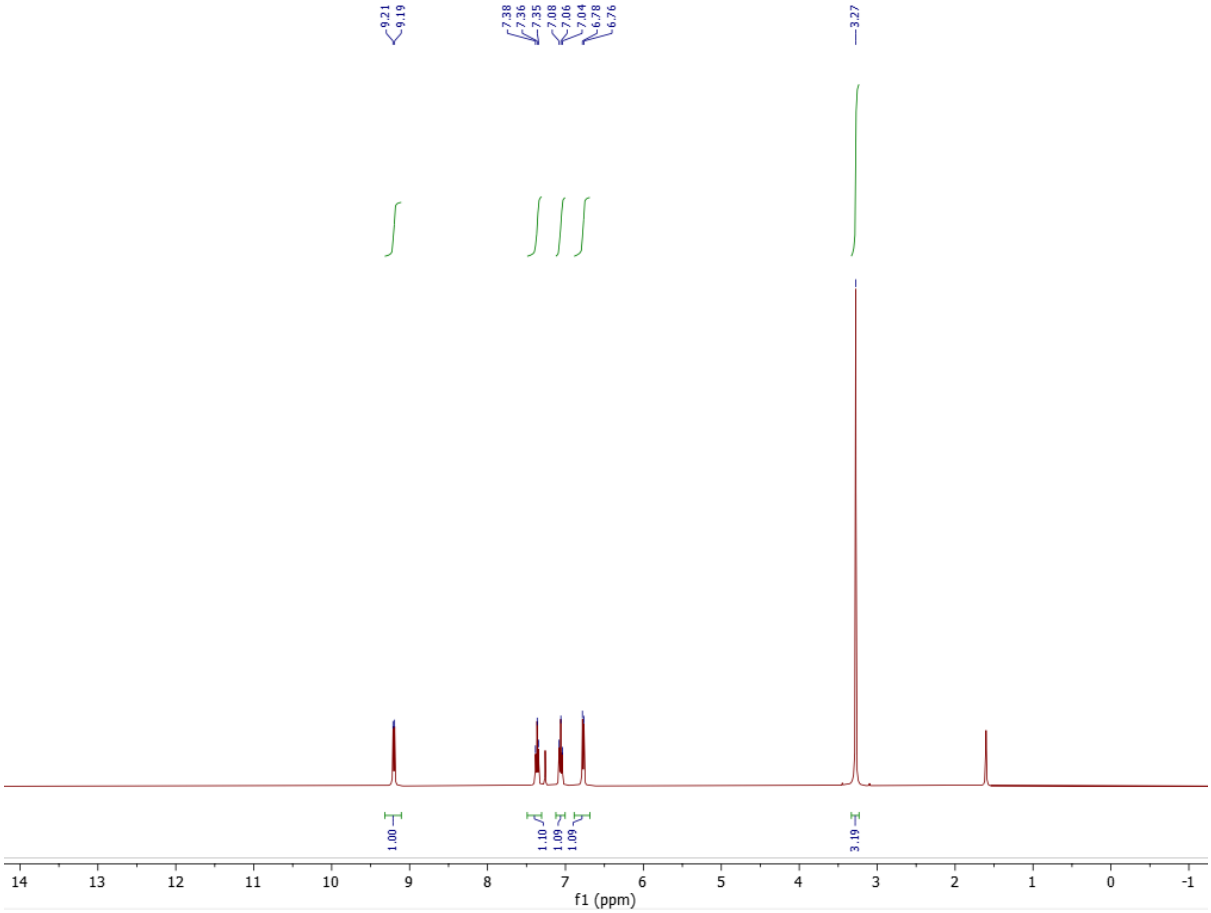

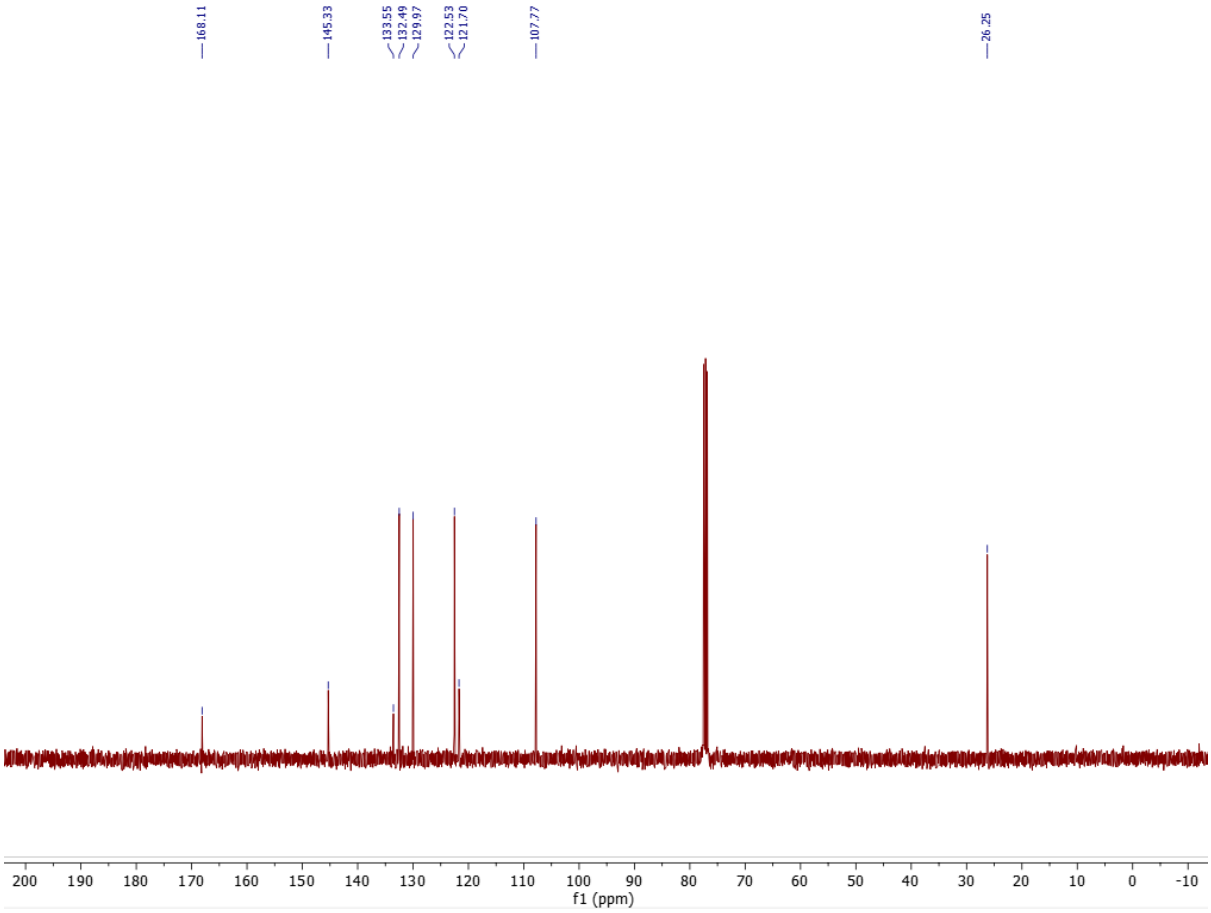
168.11
145.33
133.55
132.49
129.97
122.53
121.70
107.77
26.25
200 190 180 170 160 150 140 130 120 110 100 90 80 70 60 50 40 30 20 10 0 -10
f1 (ppm)

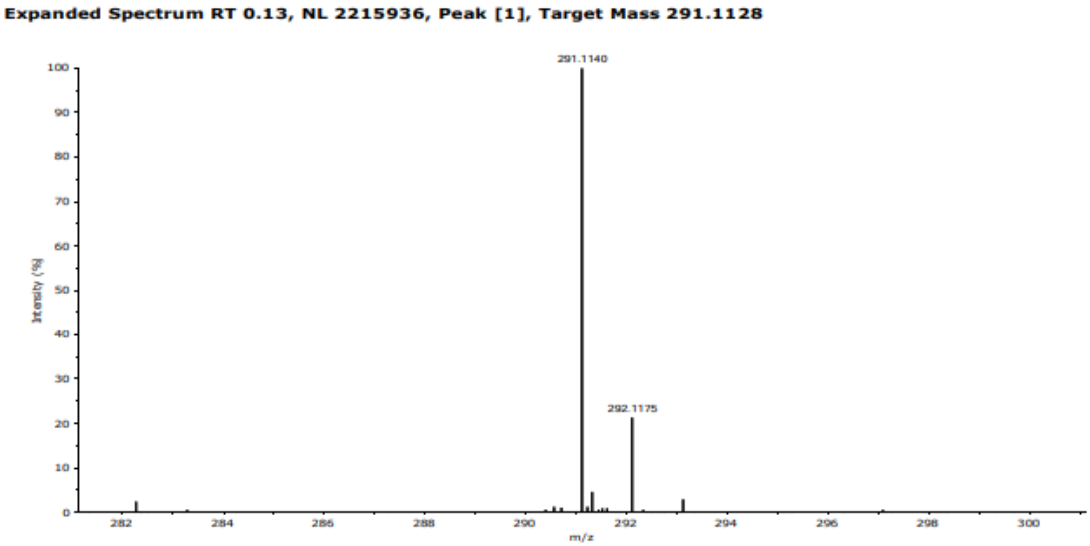

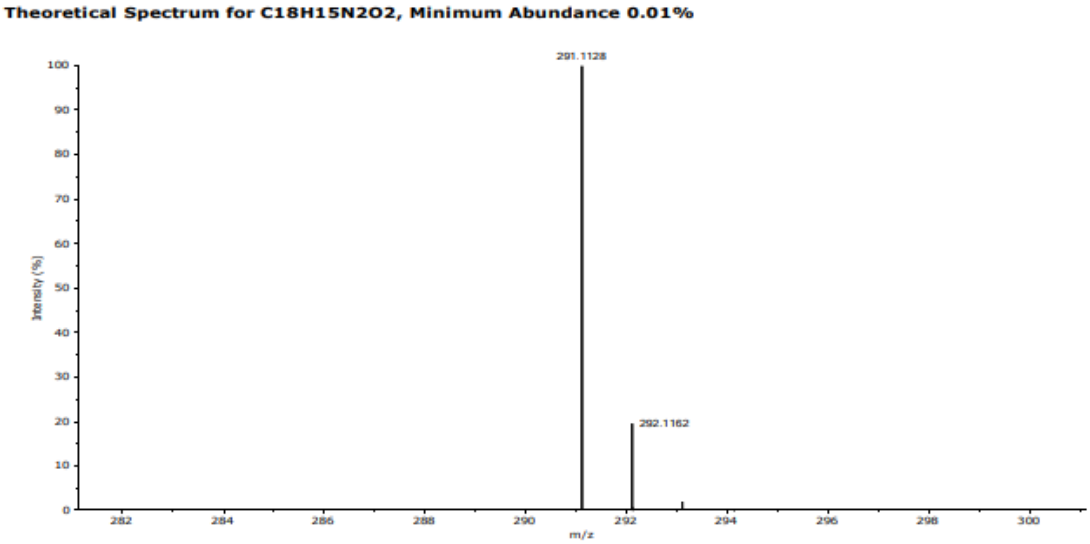

ETL aza-iso

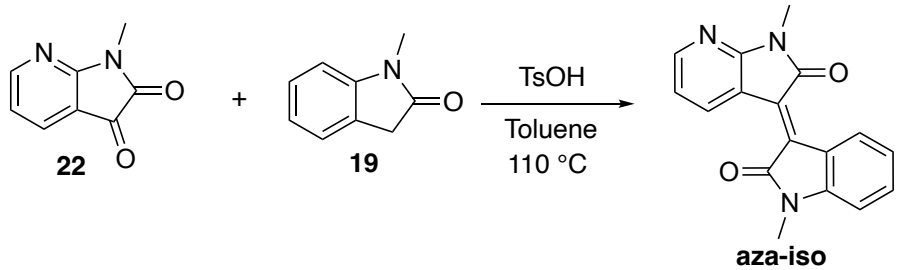

19 (551 mg, 3.40 mmol, 1eq), **22** (500 mg, 3.40 mmol, 1 eq) and p-toluene sulfonic acid monohydrate (64 mg, 0.34 mmol, 0.1 eq) were stirred under nitogen in anhydrous toluene (10 mL) with some molecular sieves at 110 °C overnight. This was poured into

a separating funnel with water and extracted with dichloromethane, then washed with brine then sodium sulfate was added and underwent gravity filtration. This was purified on a silica plug eluting with dichloromethane then recrystallised in toluene to give fluffy red crystals **aza-iso** (223 mg, 23%)

^{1}H NMR (400 MHz, CD_2Cl_2) δ 9.44 (dd, *J* = 7.9, 1.6 Hz, 1H), 9. 27–9.25 (m, 1H), 8.22-8.20 (m, 1H), 7.45-7.41 (m, 1H), 7.11-7.06 (m, 1H), 7.00 (dd, *J* = 7.9, 5.1 Hz, 1H), 6.85-6.82 (m, 1H), 3.35 (s, 3H), 3.27 (s, 3H).

^{13}C NMR (400 MHz, $CDCl_3$) δ 168.07, 167.85, 157.55, 149.73, 145.71, 137.24, 134.85, 133.18, 130.88, 130.41, 122.83, 121.36, 118.45, 116.67, 107.92, 26.26, 25.44.

HSMS (ESI): HR-MS calculated for $[C17H13N3O2+H]^+$: m/z = 292.1081; measured m/z = 292.1115

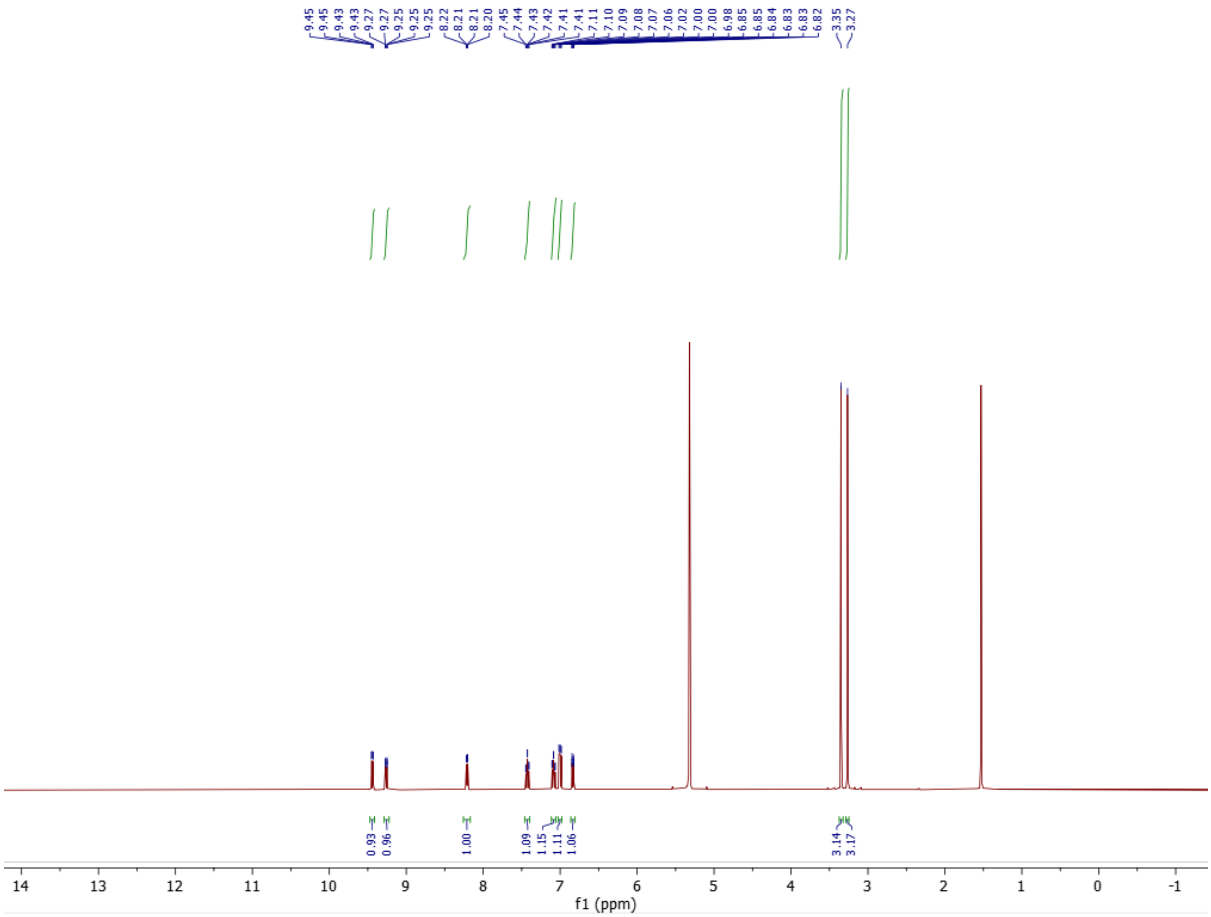

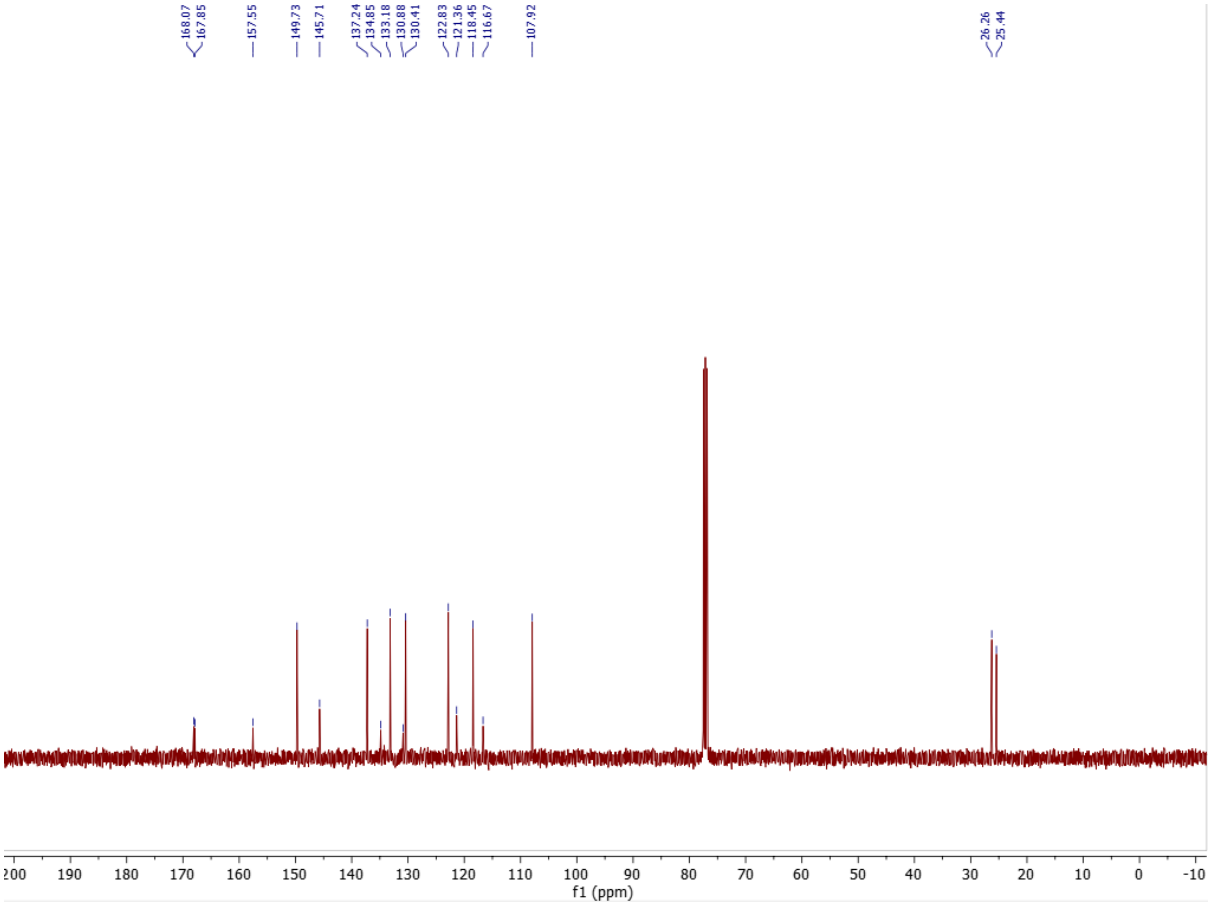
168.07
167.85
157.55
149.73
145.71
137.24
134.85
133.18
130.88
130.41
122.83
121.36
118.45
116.67
107.92
26.26
25.44
200
190
180
170
160
150
140
130
120
110
100
90
80
70
60
50
40
30
20
10
0
-10
f1 (ppm)

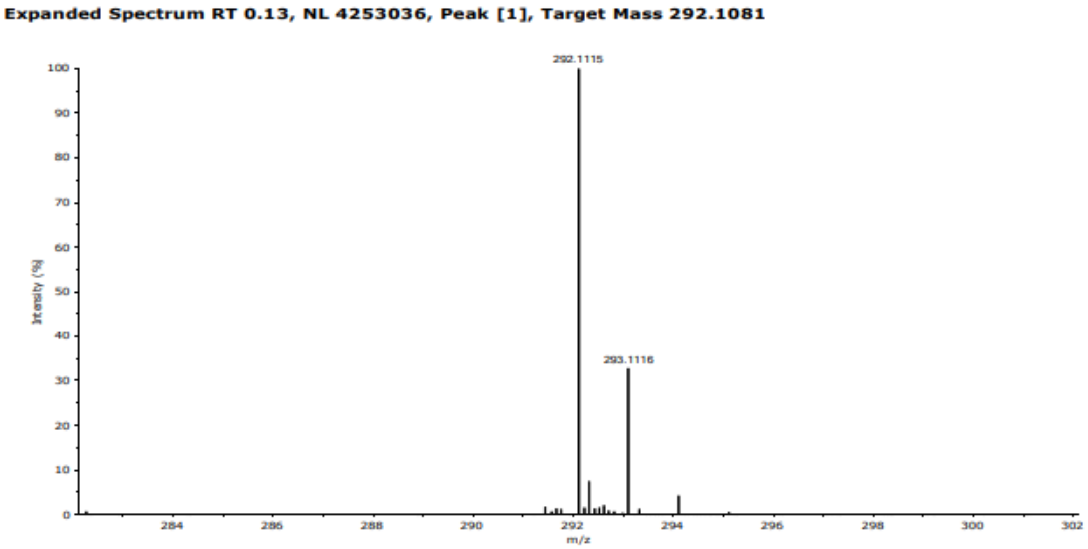

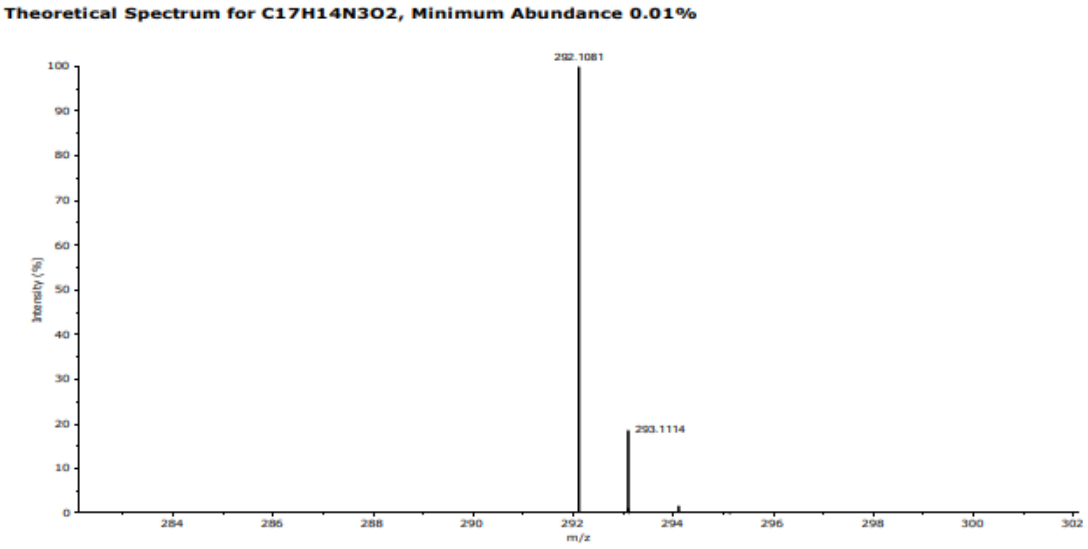

ETL iso-isox

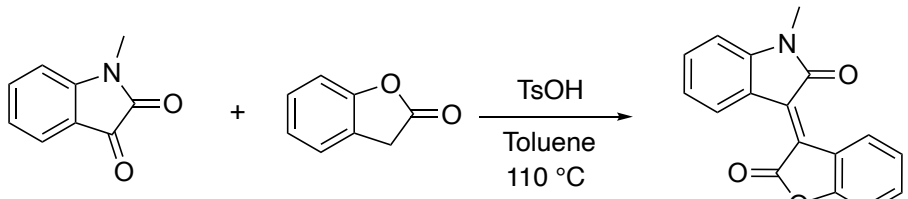

1-methylisatin **2-coumaranone** **iso-isox**

1-methylisatin (601 mg, 3.72 mmol, 1eq), 2-coumaranone (500 mg, 3.72 mmol, 1 eq) and hydrochloric acid (1 drop, 4M in anhydrous dioxane) were stirred in acetic acid (15 mL) with some molecular sieves at 110 °C overnight. This was poured into a separating funnel with water and extracted with dichloromethane, then washed with brine then sodium sulfate was added and underwent gravity filtration. This was purified

on a silica plug eluting with petroleum ether: dichloromethane (20:80) then recrystallised in toluene to give a dark brown-red fluffy crystals **iso-isox** (284 mg, 27%)

^{1}H NMR (400 MHz, $CDCl_3$) δ 9.32-9.30 (m, 1H) 9.07-9.04 (m, 1H), 7.52-7.42 (m, 2H), 7.27-7.22 (m, 1H), 7.16-7.10 (m, 2H), 6.85-6.83 (m, 1H), 3.32 (s, 3H)

^{13}C NMR (101 MHz, $CDCl_3$) δ 167.56, 167.49, 155.53, 145.88, 135.41, 133.62, 133.41, 130.07, 129.98, 127.16, 124.24, 123.13, 122.89, 121.09, 110.50, 108.11, 26.26.

HSMS (ESI): HR-MS calculated for $[C_{17}H_{11}NO_3+H]^+$: m/z = 278.0812; measured m/z = 278.0817

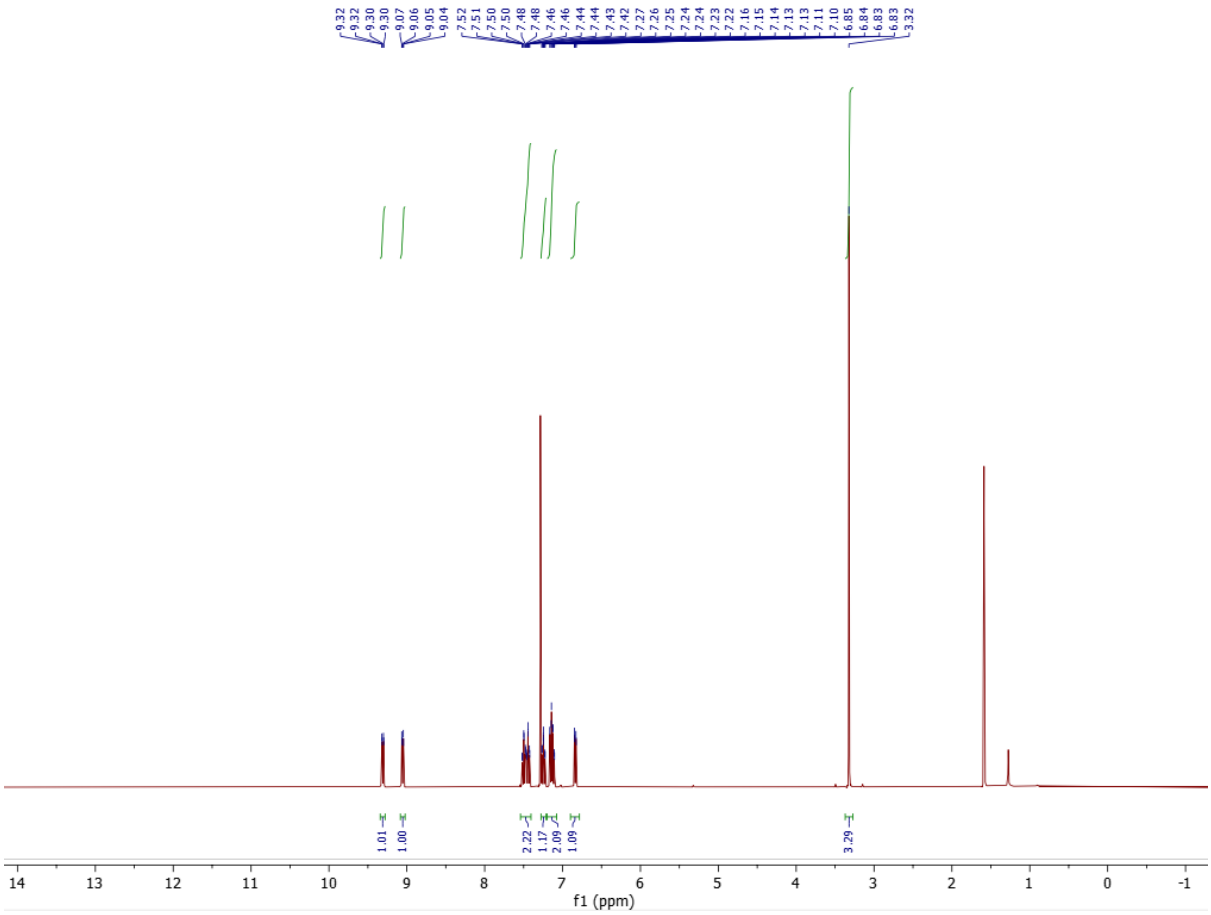

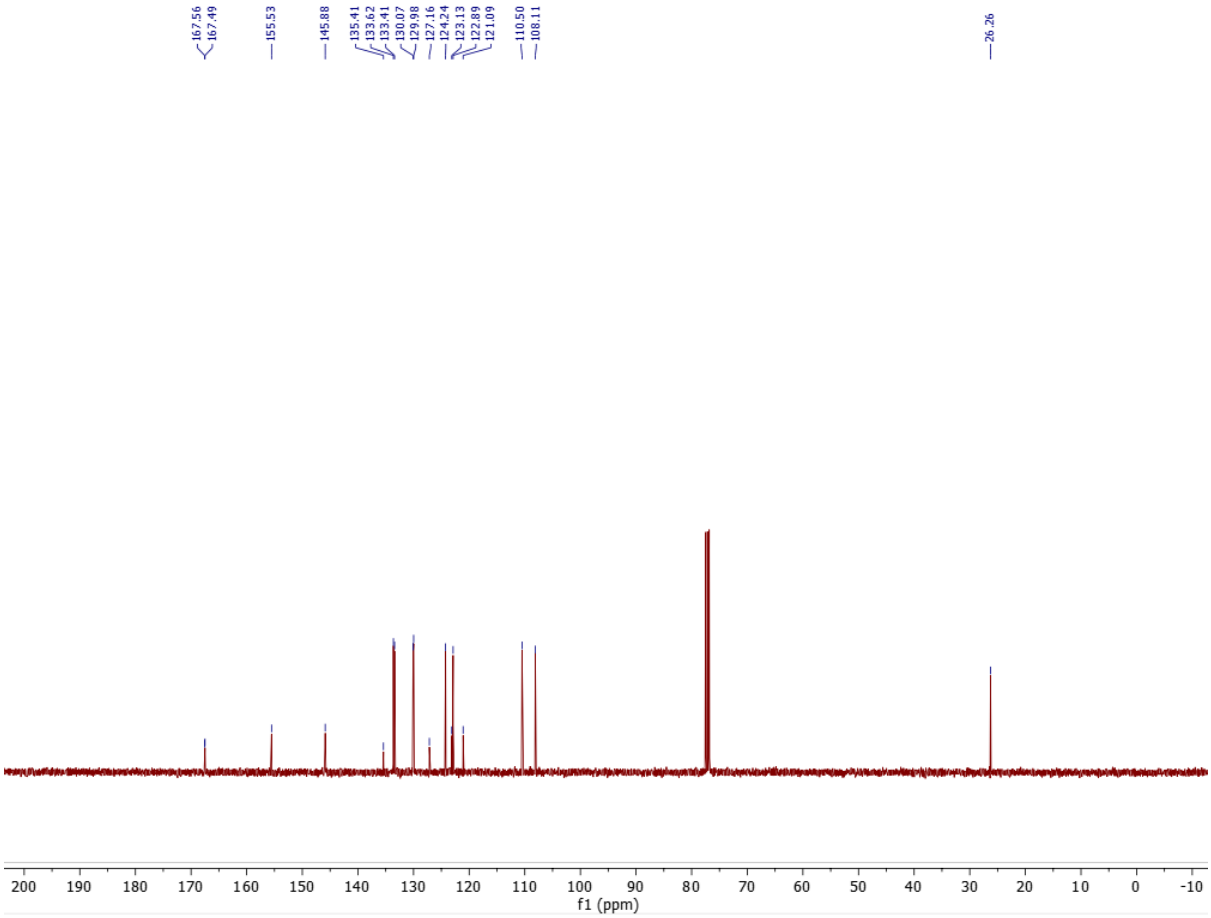
167.56
167.49
155.53
145.88
135.41
133.62
133.41
130.07
129.98
127.16
124.24
123.13
122.89
121.09
110.50
108.11
26.26
200 190 180 170 160 150 140 130 120 110 100 90 80 70 60 50 40 30 20 10 0 -10
f1 (ppm)

Expanded Spectrum RT 0.15, NL 885019, Peak [1], Target Mass 278.0812

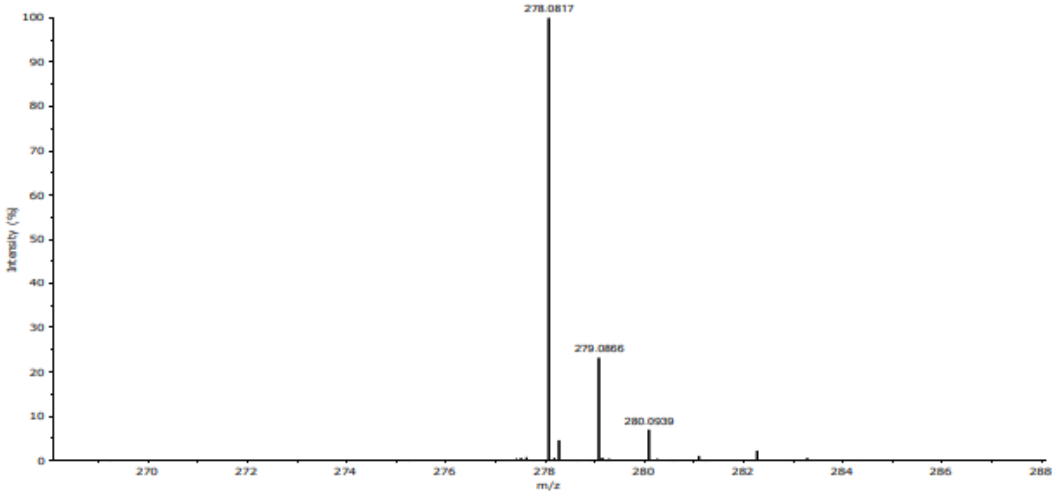

Theoretical Spectrum for C17H12NO3, Minimum Abundance 0.01%

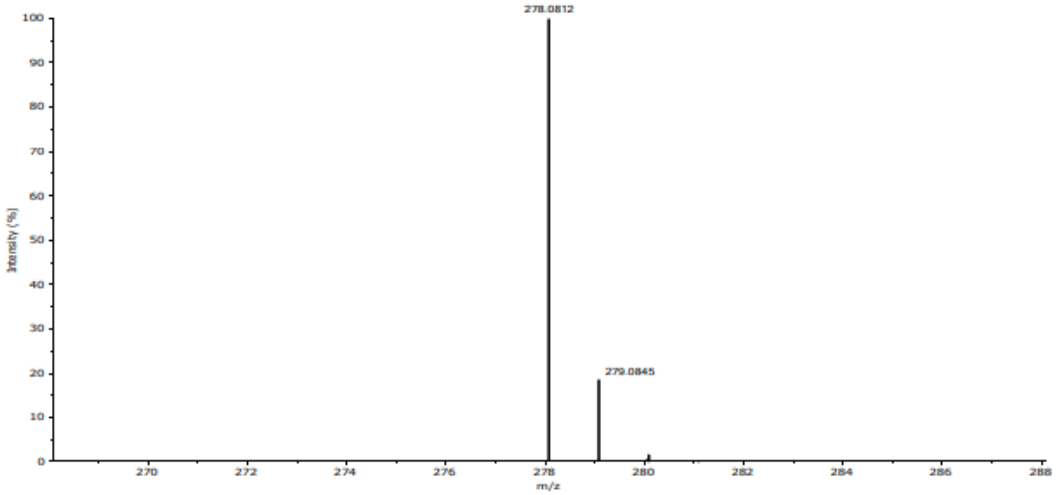

ETL aza-isox

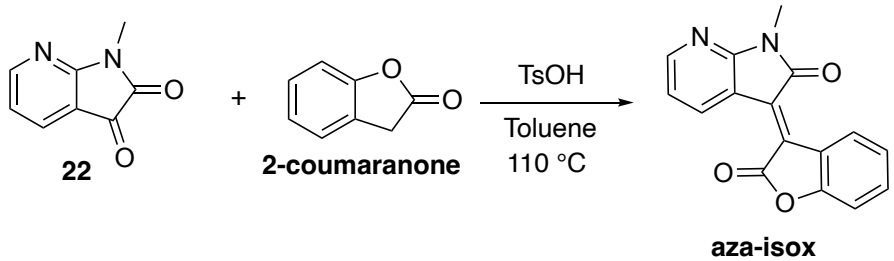

22 + **2-coumaranone** → **aza-isox**

22 (604 mg, 3.73 mmol, 1eq), 2-coumaranone (500 mg, 3.73 mmol, 1 eq) and p-toluene sulfonic acid monohydrate (70 mg, 0.37 mmol, 0.1 eq) were stirred under nitrogen in anhydrous toluene (10 mL) with some molecular sieves at 110 °C overnight. This was poured into a separating funnel with water and extracted with dichloromethane, then washed with brine then sodium sulfate was added and underwent gravity filtration. This was purified on a silica plug eluting with dichloromethane then recrystallised in toluene to give fluffy red crystals **aza-isox** (218 mg, 21%)

^{1}H NMR (400 MHz, CD_2Cl_2) δ 9.33-9.30 (m, 1H), 9.20 (dd, *J* = 7.9, 1.6 Hz, 1H), 8.26 (dd, *J* = 5.1, 1.6 Hz, 1H), 7.56-5.51 (m, 1H), 7.29-7.24 (m, 1H), 7.18-7.15 (m, 1H), 7.04 (dd, *J* = 7.9, 5.1 Hz, 1H), 3.36 (s, 4H).

^{13}C NMR (101 MHz, $CDCl_3$) δ 167.53, 167.21, 158.00, 155.92, 150.60, 137.07, 134.42, 132.76, 130.37, 128.66, 124.57, 122.73, 118.73, 116.01, 110.68, 25.49.

HSMS (ESI): HR-MS calculated for $[C16H10N2O3+H]^+$: m/z = 279.0764; measured m/z = 279.0775

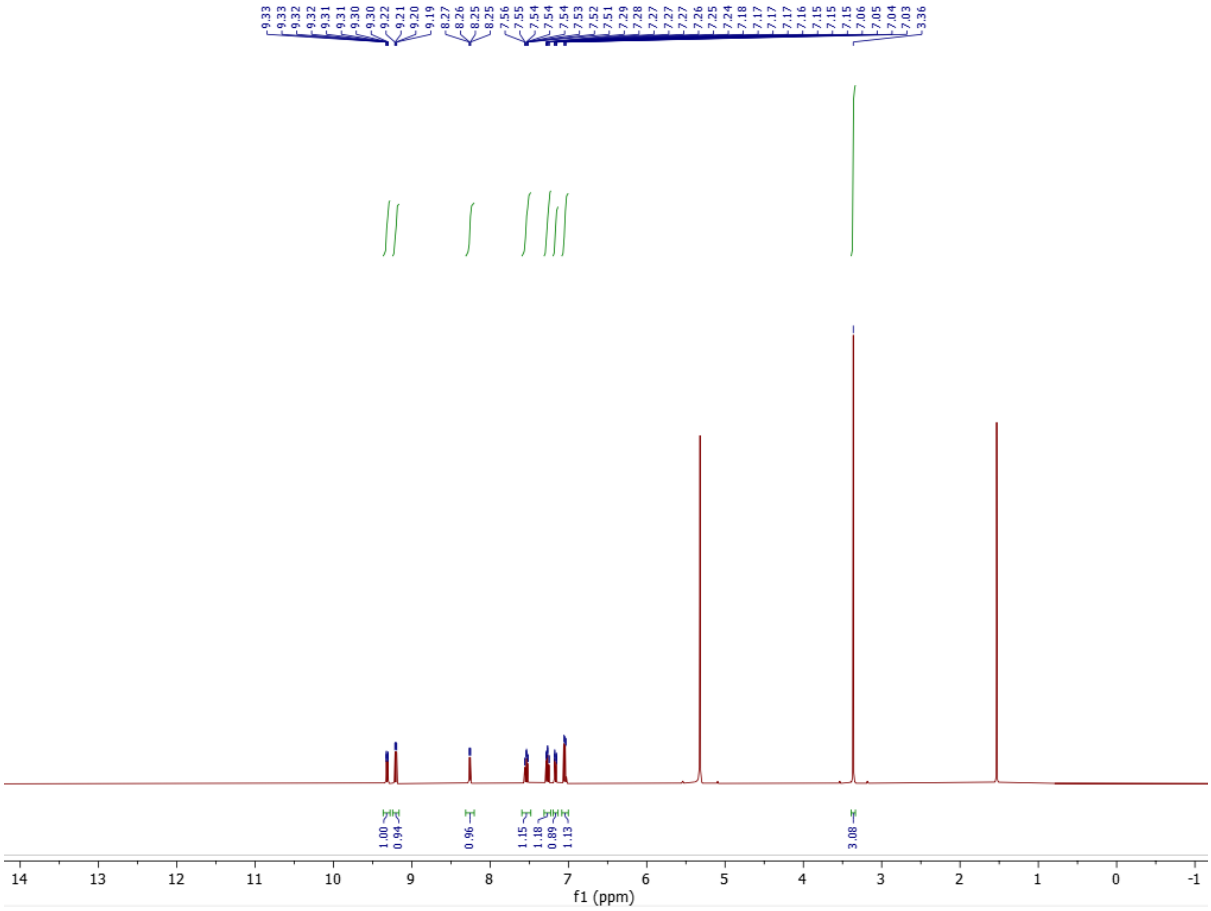
9.33
9.33
9.32
9.32
9.31
9.31
9.30
9.30
9.22
9.21
9.20
9.19
8.27
8.26
8.25
8.25
7.56
7.55
7.54
7.54
7.54
7.53
7.52
7.51
7.29
7.28
7.27
7.27
7.27
7.26
7.25
7.24
7.18
7.17
7.17
7.17
7.16
7.15
7.15
7.15
7.06
7.05
7.04
7.03
3.36
1.00
0.94
0.96
1.15
1.18
0.89
1.13
3.08
14
13
12
11
10
9
8
7
6
5
4
3
2
1
0
-1
f1 (ppm)

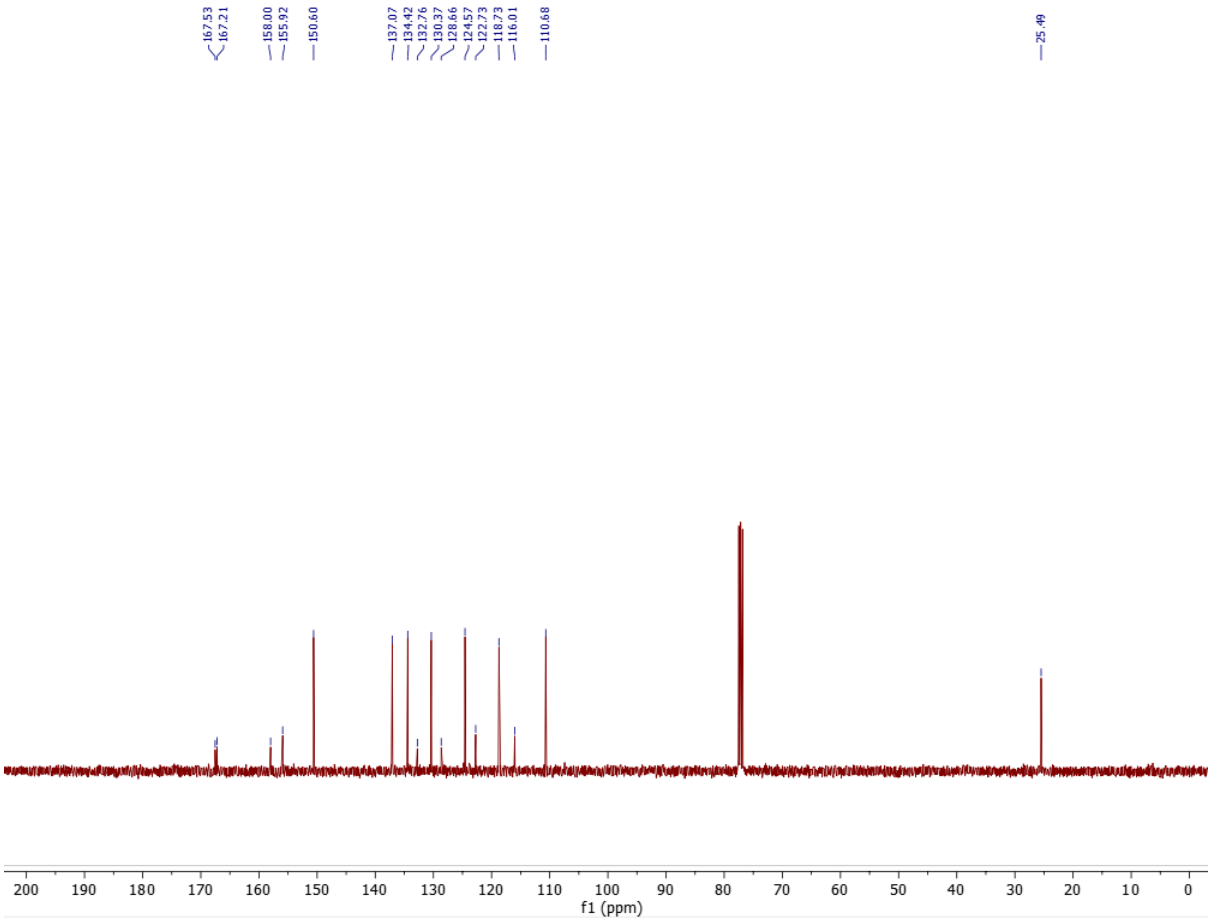

ETL isox-isox

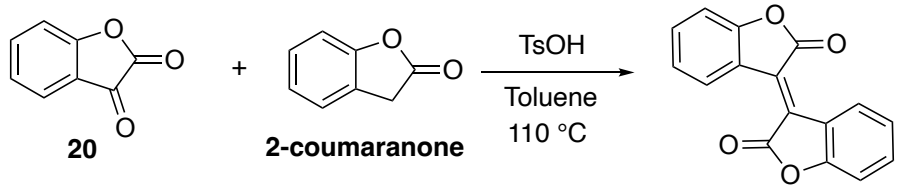

20 **2-coumaranone** **isox-isox**

x (500 mg, 3.38 mmol, 1eq), 2-coumaranone (453 mg, 3.38 mmol, 1 eq) and p-toluene sulfonic acid monohydrate (32 mg, 0.17 mmol, 0.05 eq) were stirred under nitrogen in anhydrous toluene (20 mL) with some molecular sieves at 110 °C overnight. This was poured into a separating funnel with water and extracted with dichloromethane, then washed with brine then sodium sulfate was added and underwent gravity filtration. This was purified on a silica column eluting with dichloromethane: petroleum ether (30:70) then recrystallised in toluene to give a an orange crystalline solid **isox-isox** (357mg, 40%)

^{1}H NMR (400 MHz, CD_2Cl_2) δ 9.07 (dd, J = 8.4, 1.3 Hz, 1H), 7.58-7.54 (m, 1H), 7.31-7.27 (m, 1H), 7.19 (dd, *J* = 8.1, 1.1 Hz, 1H)

HSMS (ESI): HR-MS calculated for $[C_{16}H_8O_4+H]^+$: m/z = 265.0495; measured m/z = 265.0516

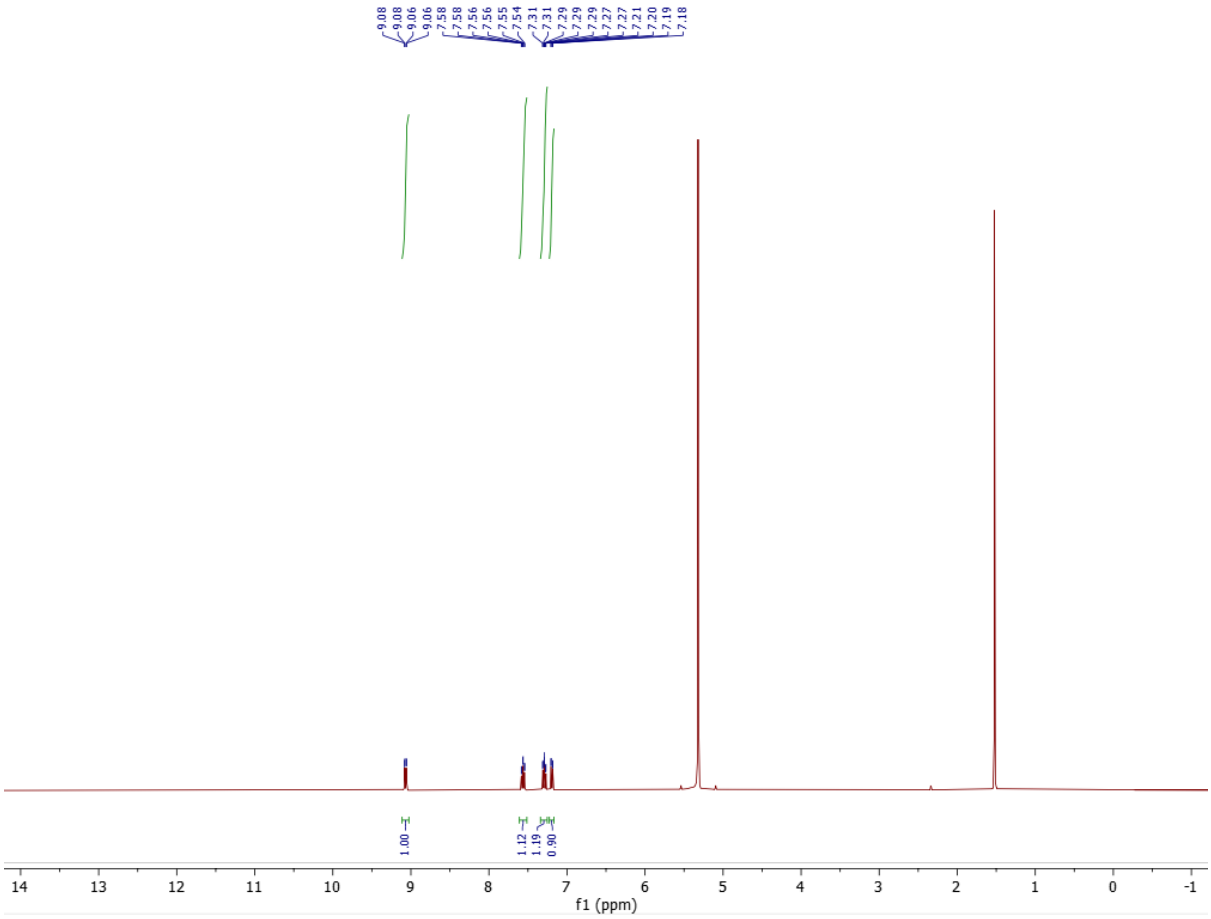

Expanded Spectrum RT 0.13, NL 1226378, Peak [1], Target Mass 265.0495

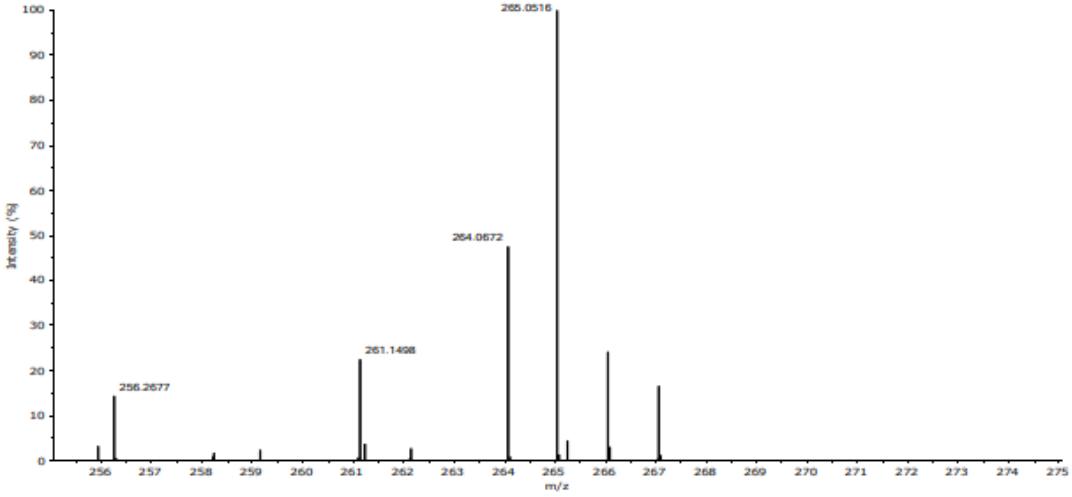

Theoretical Spectrum for C16H9O4, Minimum Abundance 0.01%

